

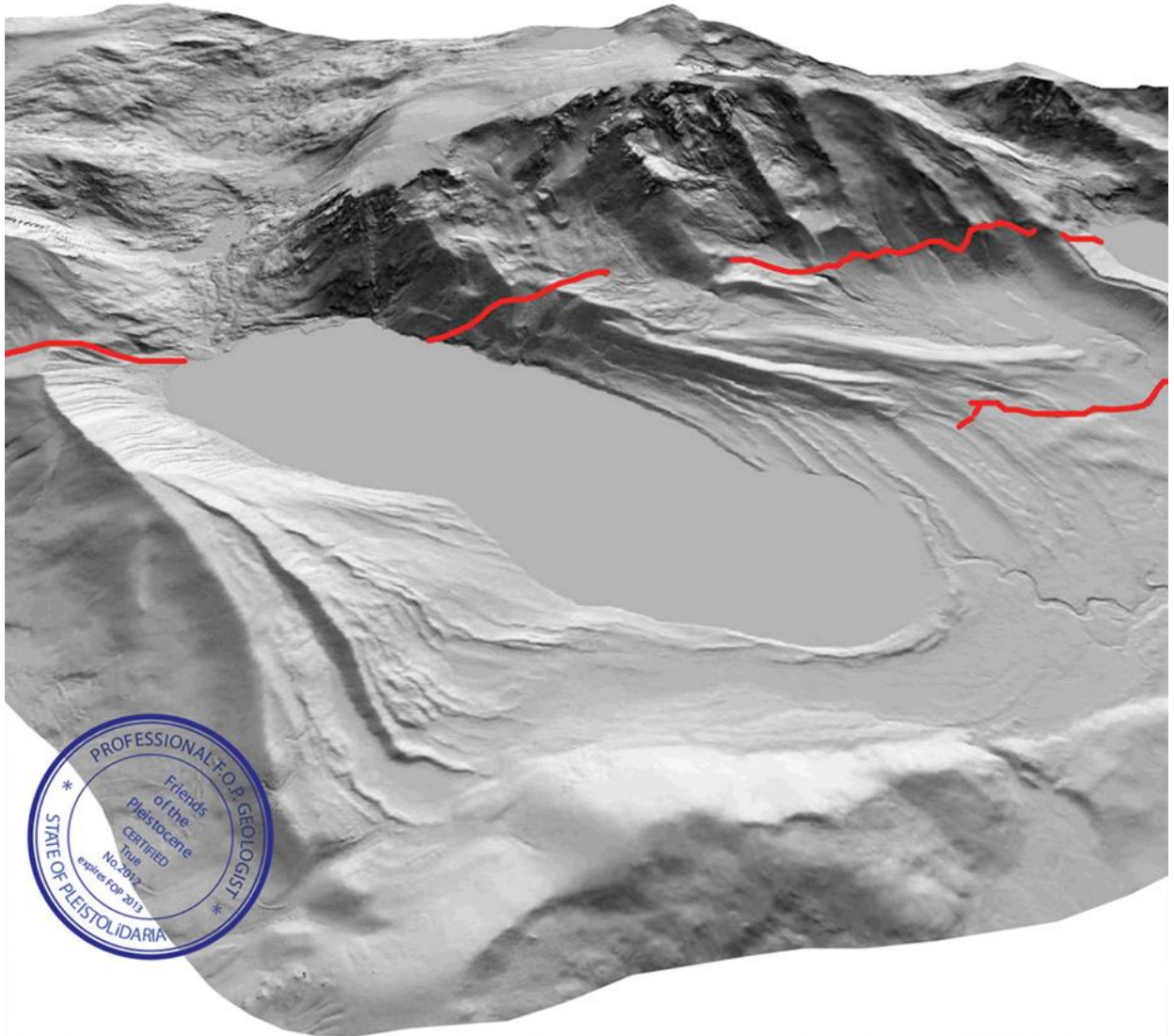
Guidebook

Neotectonics of the Lake Tahoe and Carson and Sierra Valleys

Compiled by: Gordon Seitz

F.O.P. 2012 · Sept. 13-16

Friends of the Pleistocene Pacific Cell Meeting



Compiled by Gordon Seitz, California Geological Survey, Menlo Park

Layout: Gordon Seitz and Tahia Moseley

Website: Beth Haddon, SFSU, CGS

Leaders:

Dylan H. Rood, Scottish Universities Environmental Research Centre,
Dylan.Rood@glasgow.ac.uk

Alan R. Ramelli, Nevada Bureau of Mines and Geology, ramelli@unr.edu

Gordon Seitz, California Geological Survey,
Gordon.Seitz@conservation.ca.gov

Graham M. Kent, Nevada Seismological Laboratory, University of Nevada,
Reno and South Tahoe High School, gkent@seismo.unr.edu

Shane Smith, University of Nevada, shanebsmith@gmail.com

Bill Hammond, Nevada Bureau of Mines and Geology and Nevada
Geodetic Laboratory, whammond@unr.edu

Jayne Bormann, University of Nevada, Nevada Bureau of Mines and
Geology and Nevada Geodetic Laboratory, bormannj@unr.edu

Ryan Gold, Geologic Hazards Science Center
U.S. Geological Survey, rgold@usgs.gov

Rich Briggs, Geologic Hazards Science Center, U.S. Geological Survey,
rbriggs@usgs.gov

Table of Contents

- Introduction
- Rules 1
- Directions to campsites and beer and fire
- Itinerary - Directions/Summary of Program Stops
- Day 1, Stop 1 – Genoa Fault
- Day 1, Stop 2 – Tahoe/Tioga Moraines
- Day 1, Stop 3 – West Tahoe Fault
- Day 1, Stop 4 – West Tahoe Fault
- Day 1, Stop 5 – Taylor Creek Amphitheater
- Day 1, Stop 6 – Submerged Tree Stumps
- Day 2, Stop 1 – Eagle Rock
- Day 2, Stop 2 – Incline Village Fault Trench Site
- Day 2, Stop 3 – Grizzly Valley Fault
- Day 3, Stop 1 – Fort Sage Fault Trench
- Day 3, Stop 2 – Honey Lake Fault
- Legal

Introduction

The neotectonic understanding of the Lake Tahoe basin has gone through three major accelerations in recent times, first the multibeam bathymetry survey in 1998, followed by intensive and ongoing Chirp seismic surveys starting in 1999, and most recently a basin wide LiDAR survey.

We will present research that involves these methods. The LiDAR survey was conducted by Watershed Sciences, Inc. (WSI) from August 11th to August 24th, 2010. The requested area of interest (AOI), excluding the actual lake, was 232,536 acres of delivered LiDAR data. The Leica systems were set to acquire $\geq 83,000 - 105,900$ laser pulses per second and flown at 900 - 1300 meters above ground level, capturing a scan angle of $\pm 14^\circ$. These settings were developed to yield points with an average native pulse density of >8 pulses per square meter over terrestrial surfaces. The resulting average first-return density of delivered dataset is 11.82 points per square meter with an average ground point density of 2.26 points per square meter. The vertical accuracy was estimated at 3.5 cm. All TRPA LiDAR data is in the public domain.

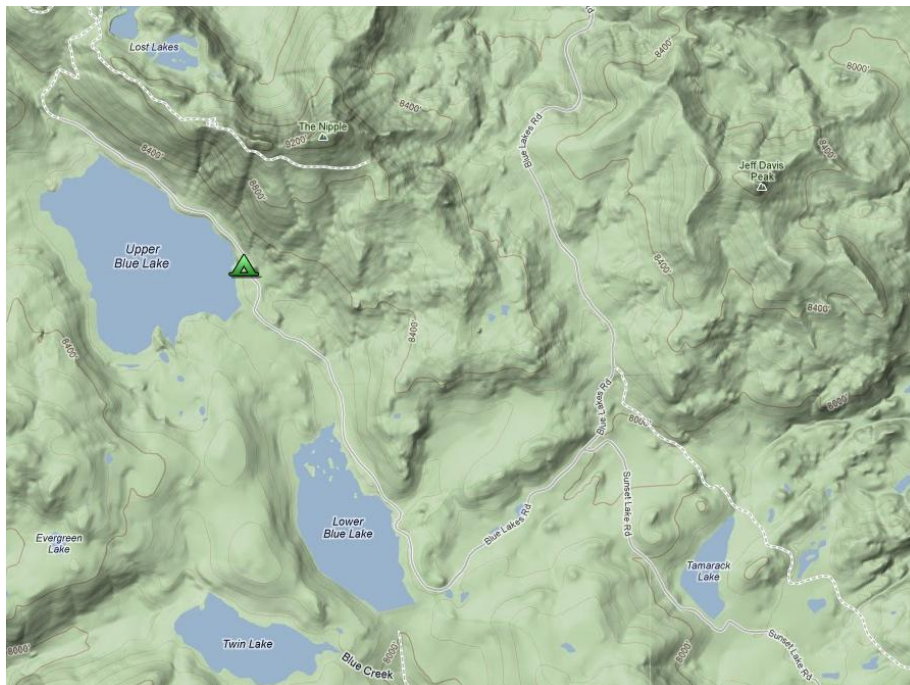
This FOP field trip will first visit two similar active normal faults, the Genoa and West Tahoe Faults, located in two adjacent basins of similar size. The glacial geomorphology is spectacularly captured by the bare-earth LiDAR. We hope to give Friends of the Pleistocene, a truly Pleistocene experience. We will try to focus on observing field relationships with accompanying presentations, and we are providing a selection of what we feel are representative research results in various forms of maturity. At the northern end of the Walker Lane the Tahoe basin forms the last extensional basin before strike-slip motions become more dominant in the Truckee, Sierra Valleys, and the Honey Lake fault systems.

Thanks for participating,

Gordon

Directions to Campsites and Beer and Fire

THURSDAY AND FRIDAY NIGHT: Upper Blue Lake Damsite Campground



LOCATION:

We will camp at the Upper Blue Lake Damsite Campground (of the Blue Lake Campgrounds) on Thursday and Friday night. We have arranged for the Upper Blue Lake

Damsite Campground to be exclusive for the FOP party. If there is a gate, please open it to get thru. Close afterwards.

The Blue Lakes (elevation 8100 ft.) are located 12 miles south of **HIGHWAY 88** in Hope Valley. The lakes serve as water storage for downstream hydroelectric plants operated by Pacific Gas and Electric Company.

The campground manager will re-open the campground on the 13th to host our group. For the most privacy, we will settle at the Upper Blue Lake Damsite Campground.

To manage the cost, we need to park **three vehicles per site**. They are large sites, so no worries. Costs are higher on this trip mainly due to camp fees. Dogs are a buck extra per night, seriously. Tahoe isn't the middle of nowhere like we usually get to enjoy—that said, we'll be based in the higher Sierras with lots of blue water, so it's still a deal. You will be able to leave your camping set-up out for Friday night.

TIME:

Arrive from 2pm or later (we recommend to get there before dark) for Opening FOP ceremonies. Sunset at approximately 7:30pm. Happy hour from 6pm - midnite.

BE PREPARED:

We expect temperatures at night in the 30's. Daytime should be perfect. Please bring layers and be prepared like a field geologist.

NEARBY ATTRACTION:

The Nipple at approximately 9,200 ft.

THURSDAY AND FRIDAY NIGHT: Upper Blue Lake Damsite Campground (Cont'd)

WE WILL SUPPLY:

Beer. Fire. Toilets. No showers. But there is a lake.

MORE INFORMATION:

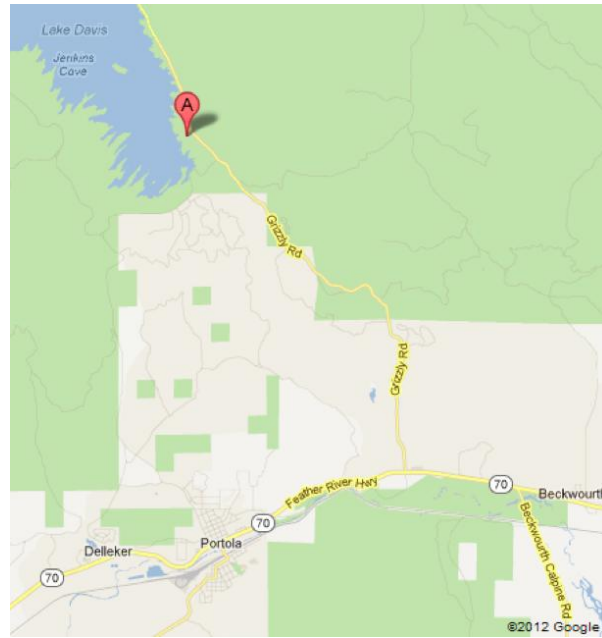
http://www.carsonpass.com/lodging/blue_lakes_camping.html

SATURDAY NIGHT: Lake Davis - Grasshopper Flat Campground at Plumas National Forest

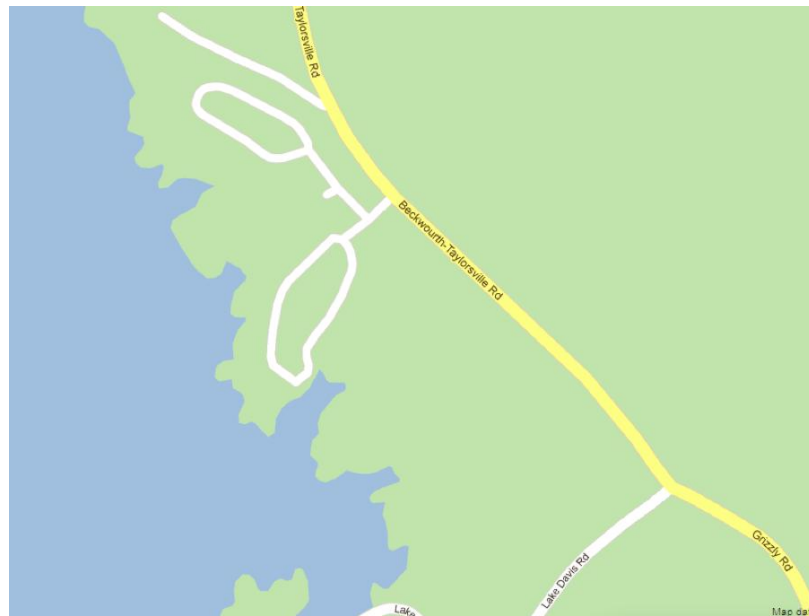
LOCATION:

We will be staying at Grasshopper Flat on the final night and closing ceremony. Grasshopper flat is at an elevation of 5,900 feet. Access is gained from **HIGHWAY 70**, to the south. On Map 1 (upper left), point A is the campground. On Map 2 (upper right, detail), the site is located on loop 1 (upper loop). On Map 3, (lower left, even more

detail), the site is located on the upper loop. Again, we will occupy the sites with multiple vehicles.



Map 1



MAP 2

LIST of STOPS

FRIDAY

Stop 1 - Mott Canyon at base of Kingsbury Grade [38.928364° -119.839596°] (D. Rood and A. Ramelli)

Stop 2 - Fallen Leaf Lateral Moraines [38.887141° -120.050923°](G. Seitz)

Stop 3 - Angora Lakes [38.871860° -120.064267°]

West Tahoe Fault (**WTF**) well-defined multiple-event scarp (G. Seitz)

Fallen Leaf Lake Paleoseismology of **WTF** (G. Kent)

Stop 4 - West Tahoe Fault (WTF) North Fallen Leaf Lake Lateral Tioga-age Moraines [38.926747° -120.069884°] (G. Seitz)

Stop 5 - Taylor Creek Visitor Center [38.937850° -120.055221°] (Hammond, Smith)

Stop 6- Beach-Submerged Trees Swim and Dive (Seitz, Kent)

Saturday

Stop 1 - Eagle Rock - [39.107091° -120.161469°]

McKinney Bay slide and offshore fault architecture (G. Kent)

Stop 2 - Incline Village Fault, Southwood School trench site [39.248936° -119.963720°] (Seitz, Kent)

Stop 3 - Grizzly Valley fault system, Sierra Valley CA [39.792875°-120.316098°] (R. Gold)

Sunday

Stop 1 - Fort Sage fault, Doyle CA [40.057852°-120.088482°](Briggs)

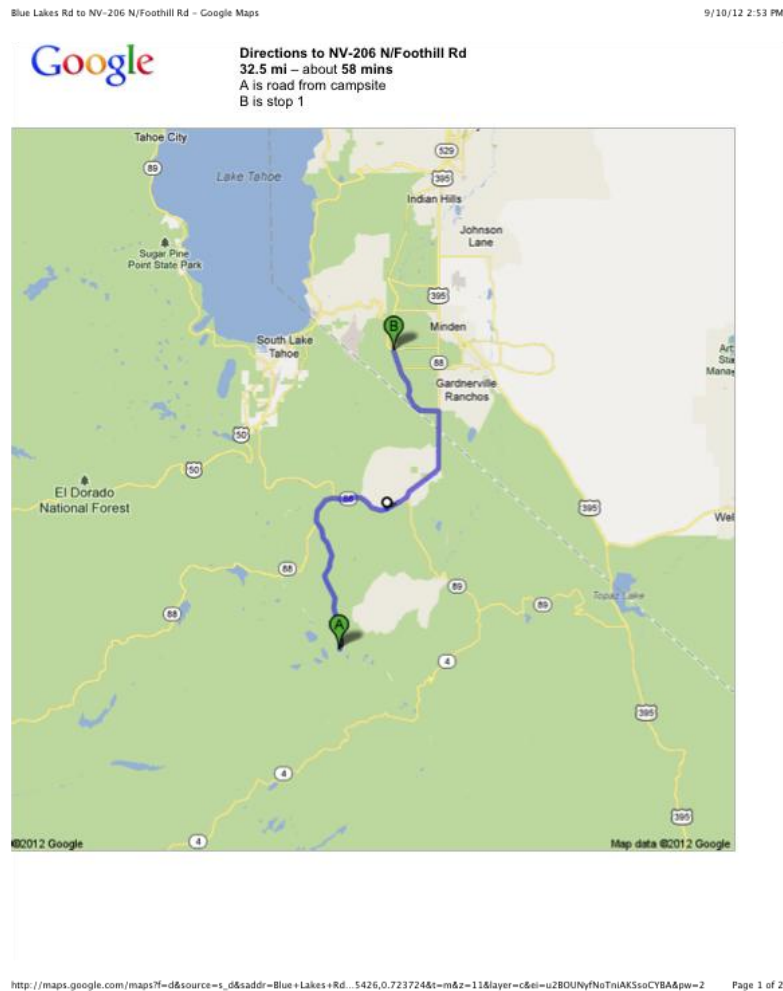
Stop 2 - Honey Lake fault, Doyle CA [40.054694°-
120.122511°](Briggs et al.)

DAY 1: FRIDAY

- **Day 1, Stop 1 – Genoa Fault – Meet at 9:30 AM**

Location: [38.928364° -119.839596°]. Mott Canyon at base of Kingsbury Grade. Park at Park-and-Ride lot.

Summary: Genoa fault at Mott Canyon: Slip rate determined from cosmogenically dated surface boulders and depth profiles of the faulted alluvial fan (Dylan Rood and Allan



Ramelli).

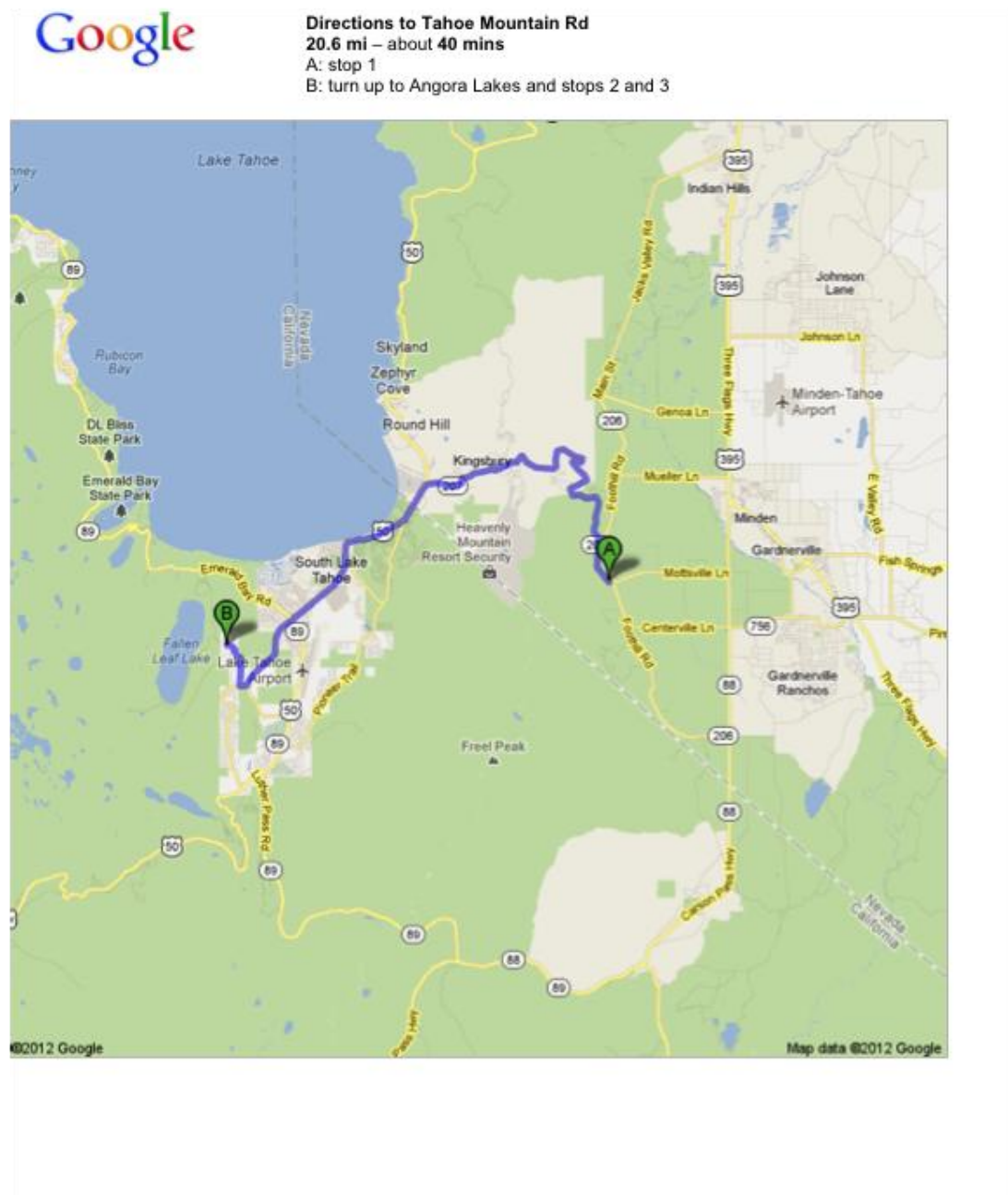
- **Day 1, Stop 2 – Tahoe/Tioga Moraines ~11:30 AM**

Location: [38.887141° -120.050923°]. Overview of Fallen Leaf Lateral Moraines and Fallen Leaf Lake

Summary: Tahoe- (60 ka) and Tioga-aged (19 ka) lateral moraine crests.
Geomorphology, differences in crest profile roundness and boulder surface weathering.
(Gordon Seitz and Graham Kent)

NV-207 W/Kingsbury Grade Rd to Tahoe Mountain Rd - Google Maps

9/10/12 2:56 PM



http://maps.google.com/maps?f=d&source=s_d&saddr=NV-207+W%2FK...391,0.361862&t=m&z=12&layer=c&ei=yWFOUJKoDaSSiQL_zlCQCQ&pw=2

Page 1 of 2

- Day 1, Stop 3 – West Tahoe Fault ~12:15 PM

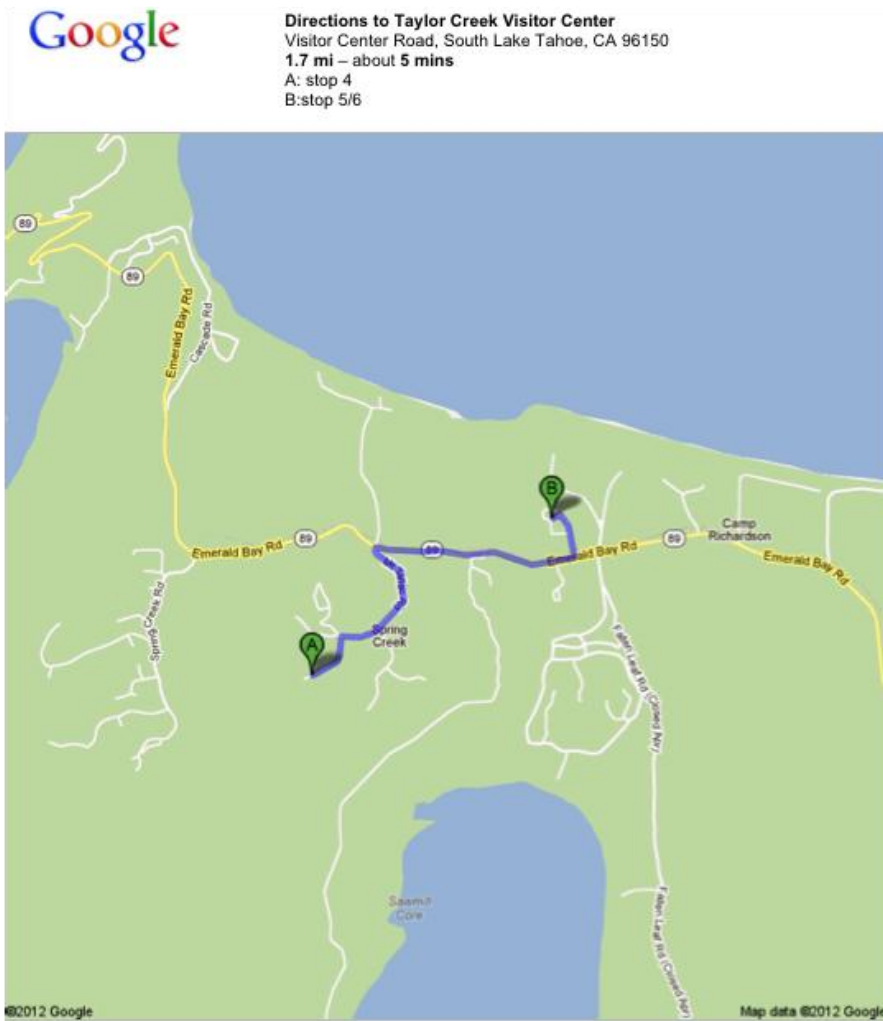
- **Day 1, Stop 5 – Taylor Creek Amphitheater ~3:30 PM**

Location: [38.937850° -120.055221°]. Taylor Creek Visitor Center. The Taylor Creek Visitor Center is located on the south shore of beautiful Lake Tahoe.

Summary: Holocene Subaqueous Paleoseismology of Lake Tahoe (Smith). Geodetic Constraints (W. Hammond). Offshore Faulting (G. Kent). Onshore Extend of West Tahoe Fault based on LiDAR (G. Seitz).

Mt Tallac Rd C to Taylor Creek Visitor Center – Google Maps

9/11/12 1:09 AM



http://maps.google.com/maps?d&source=s_d&saddr=Mt+Tallac+Rd...z=15&ie=UTF8&t=m&z=15&layer=c&ei=M_FOUmq3No2GIQKVzoDICQ&pw=2

Page 1 of 2

Itinerary - Directions/Summary of Program Stops

DAY 1: FRIDAY PM

More Info: The visitor center is the hub of 4 self-guided trails start and the home of the **Stream Profile Chamber**, a primary attraction. For everyone that doesn't plan on getting wet at the next Stop 6, another possibility is to get a live underwater perspective. The Stream Profile Chamber, located 1/4 mile down the Rainbow Trail, provides a view of the stream environment via a 180-degree curved diorama.

- **Day 1, Stop 6 – Submerged Tree Stumps ~5:00 PM**

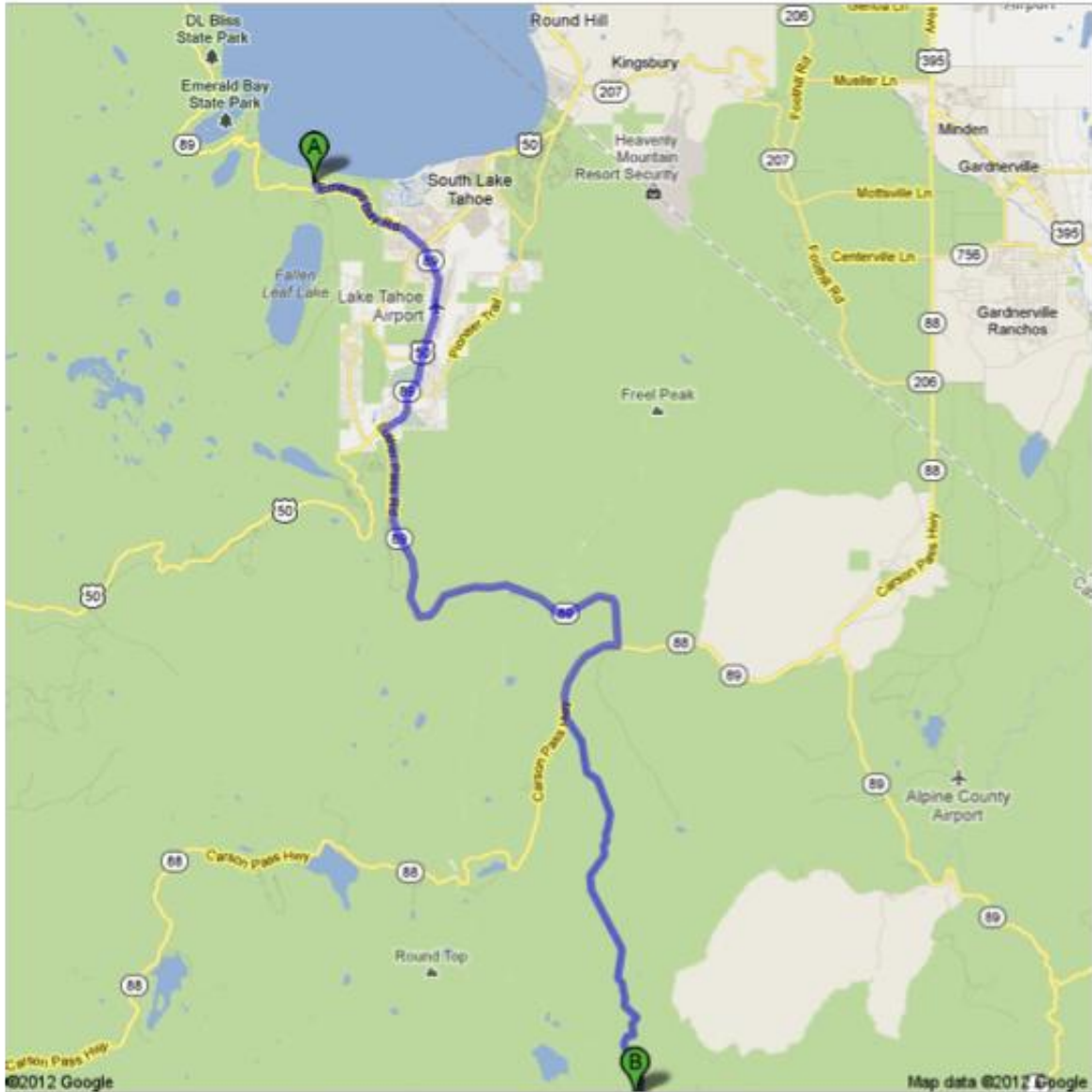
Location: Baldwin Beach, walk to beach.

Summary: By design Stop 6 will provide cooling off, as needed. You'll have the opportunity to get wet and examine submerged tree stumps, which we have sampled and radiocarbon dated.

Return to Blue Lakes Camp via Hwy 50, 89, 88 ~ 60 minutes



Directions to Blue Lakes Rd
32.4 mi – about 1 hour 0 mins
A: stops 5/6
B: Blue Lakes camp



Itinerary - Directions/Summary of Program Stops

DAY 2: SATURDAY

Leave camp at **9:00 AM**

Drive north on Hwy 88 & 89 around the west shore of Lake Tahoe.

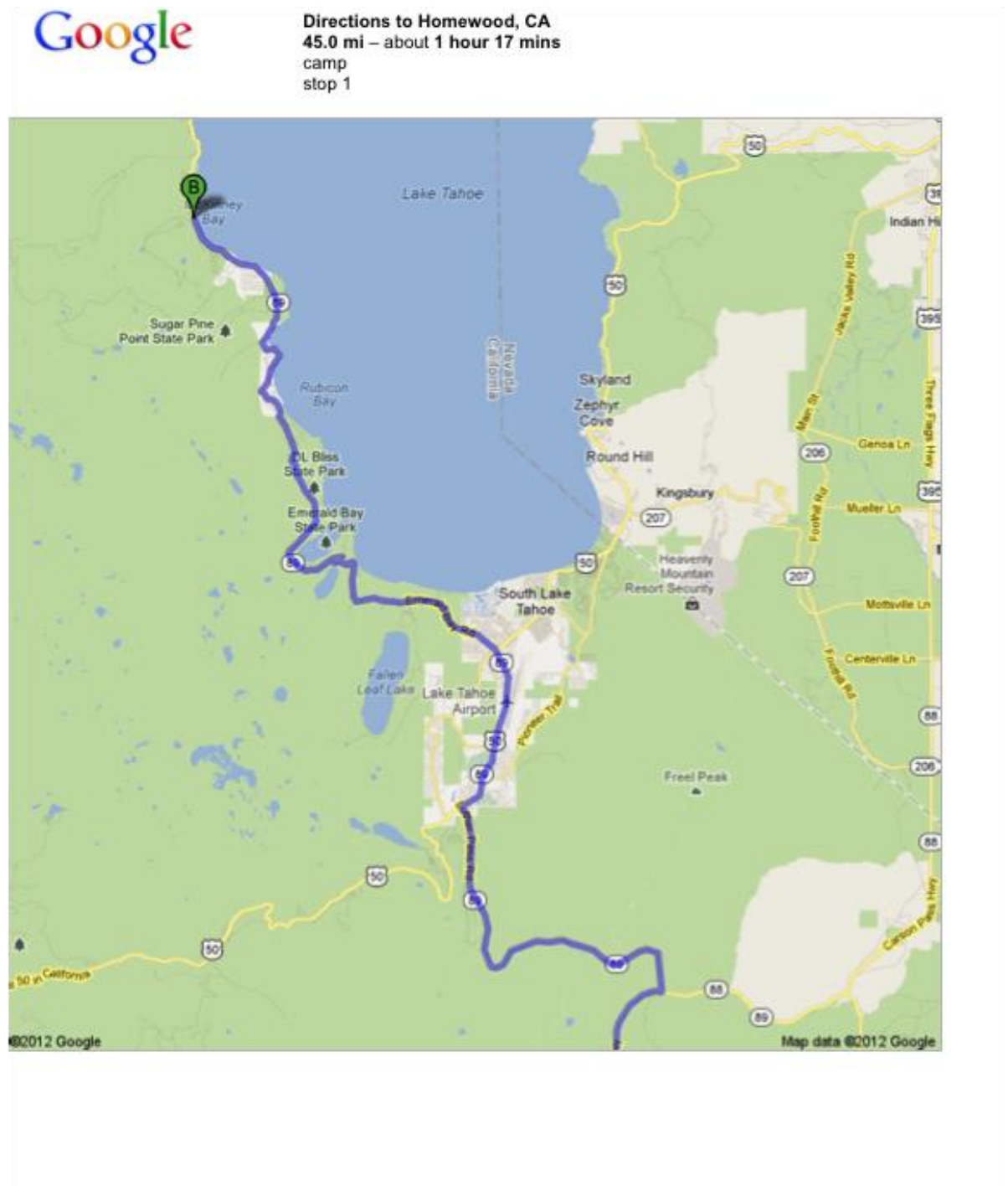
- **Day 2, Stop 1 – Eagle Rock**

Location: [39.107091° -120.161469°]. Eagle Rock.

Summary: McKinney Bay slide and offshore fault architecture (G. Kent)

Blue Lakes Rd, Markleeville, CA 96120 to Homewood, CA - Google Maps

9/11/12 1:40 AM



http://maps.google.com/maps?f=d&source=s_d&saddr=Blue+Lakes+Ro...0876,0.271912&t=m&z=12&layer=c&ei=x_dOUNGYIeGIIAKcwoGIDA&pw=2

Page 1 of 2



Park at B on right side of road. Walk south to trailhead. Caution crossing the road. It's a 20 minute hike to the top of Eagle Rock.

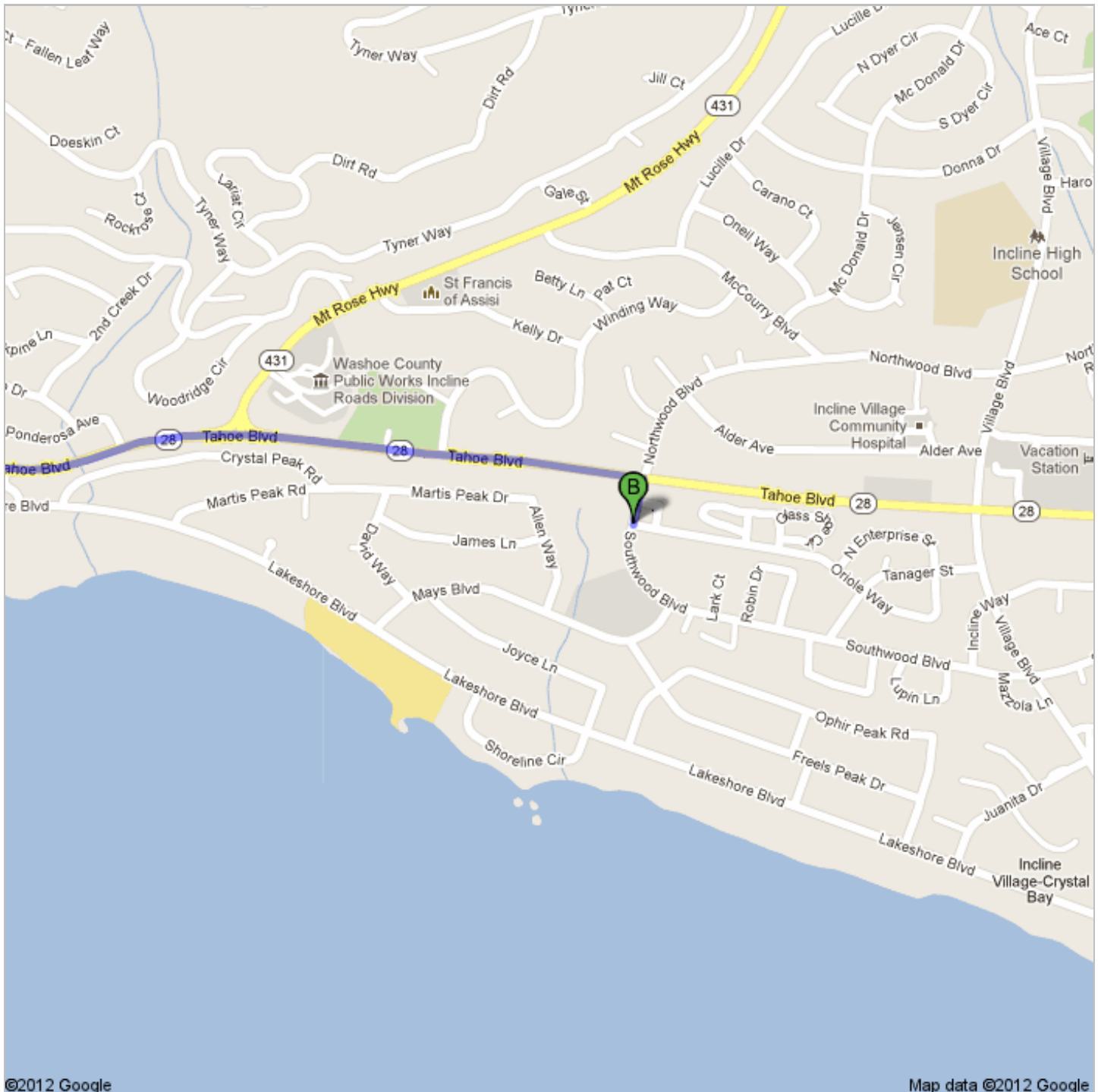
- **Day 2, Stop 2 – Incline Village Fault Trench Site**

Location: [39.248936° -119.963720°]. Incline Village Fault.

Summary: Southwood School trench site (Seitz, Kent).



Directions to Southwood Blvd
19.1 mi – about 29 mins
Southwood school



©2012 Google

Map data ©2012 Google

 CA-89 N/W Lake Blvd

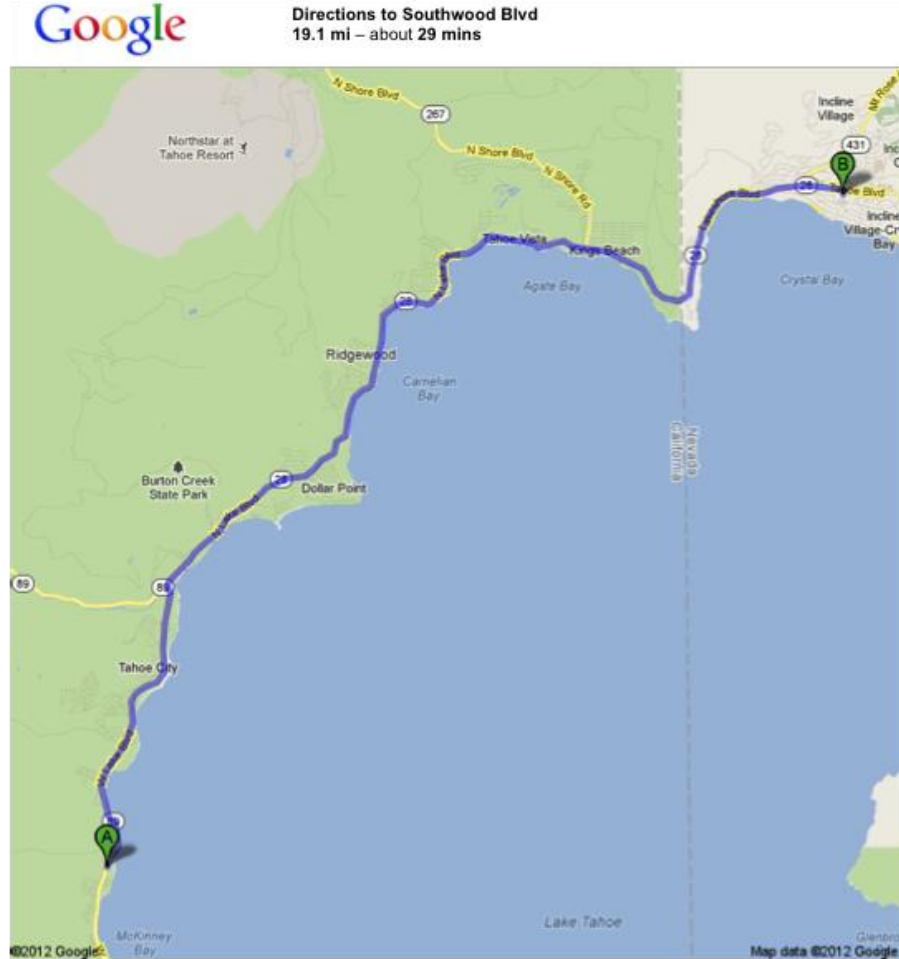
- 89
 1. Head **north** on **CA-89 N/W Lake Blvd** toward **Idylwild Way** go 4.6 mi
total 4.6 mi
 About 6 mins
- 28
 2. Turn right onto **CA-28 E/N Lake Blvd** go 11.0 mi
total 15.5 mi
 Continue to follow CA-28 E
 About 17 mins
- 28
 3. Continue onto **NV-28 E** go 3.5 mi
total 19.0 mi
 Entering Nevada
 About 5 mins
- 4. Turn right onto **Southwood Blvd** go 374 ft
total 19.1 mi

 Southwood Blvd

These directions are for planning purposes only. You may find that construction projects, traffic, weather, or other events may cause conditions to differ from the map results, and you should plan your route accordingly. You must obey all signs or notices regarding your route.

Map data ©2012 Google

Directions weren't right? Please find your route on maps.google.com and click "Report a problem" at the bottom left.



http://maps.google.com/maps?f=d&source=s_d&saddr=CA-89+N%2FW+...5179,0.135956&t=m&z=13&layer=c&ei=qv10UPisluXjALvoYCWAw&pw=2 Page 1 of 2

Large magnitude Holocene earthquakes recorded on and offshore on the Incline Village fault, Lake Tahoe: Although onshore faulting is obscured by a Pleistocene-age glacial overprint with many fault-like scarps, basin-wide bare-earth LiDAR has improved our ability to accurately map tectonic scarps. High-resolution Chirp seismic profiles confirms the onshore fault location of the Incline Village fault prior to LiDAR survey. A cross-fault excavation exposed stacked, scarp-derived colluvial wedge deposits that provide evidence for 3 events. Reconstructions of the onshore exposures indicate vertical displacements ranging from 3.5 to 4.2 meters per event. The most recent event shows a vertical throw of 3.5 m and 3.3 m on and offshore, respectively.



Directions to Unknown road
58.8 mi – about 1 hour 26 mins

A Southwood Blvd



1. Head north on Southwood Blvd toward Tahoe Blvd

go 374 ft
total 374 ft



2. Take the 1st left onto Tahoe Blvd
About 3 mins

go 1.1 mi
total 1.2 mi



3. Continue straight onto NV-28 W/Lakeshore Blvd
Continue to follow NV-28 W
Entering California
About 3 mins

go 2.3 mi
total 3.5 mi



28

4. Continue onto **CA-28 W**
About 3 mins

go 1.7 mi
total 5.2 mi



267

5. Turn right onto **CA-267 W**
About 17 mins

go 11.8 mi
total 17.0 mi



89

6. Continue onto **CA-89 N**
About 1 min

go 0.2 mi
total 17.2 mi



89

7. At the traffic circle, continue straight onto **CA-89**
About 26 mins

go 22.9 mi
total 40.1 mi



49

8. Turn right onto **CA-49 N/Golden Chain Highway N/E Main St** (signs for **Loyalton**)

go 9.7 mi
total 49.7 mi

Continue to follow CA-49 N/Golden Chain Highway N

About 11 mins



9. Turn left onto **Heriot Ln**

About 6 mins

go 2.0 mi
total 51.7 mi



10. Continue onto **Harriet Ln**

About 7 mins

go 3.0 mi
total 54.7 mi



11. Turn left onto **Co Route A24/Dyson Ln**

Continue to follow Dyson Ln

About 4 mins

go 1.7 mi
total 56.4 mi



12. Continue onto **Co Route A24**

About 3 mins

go 1.7 mi
total 58.1 mi



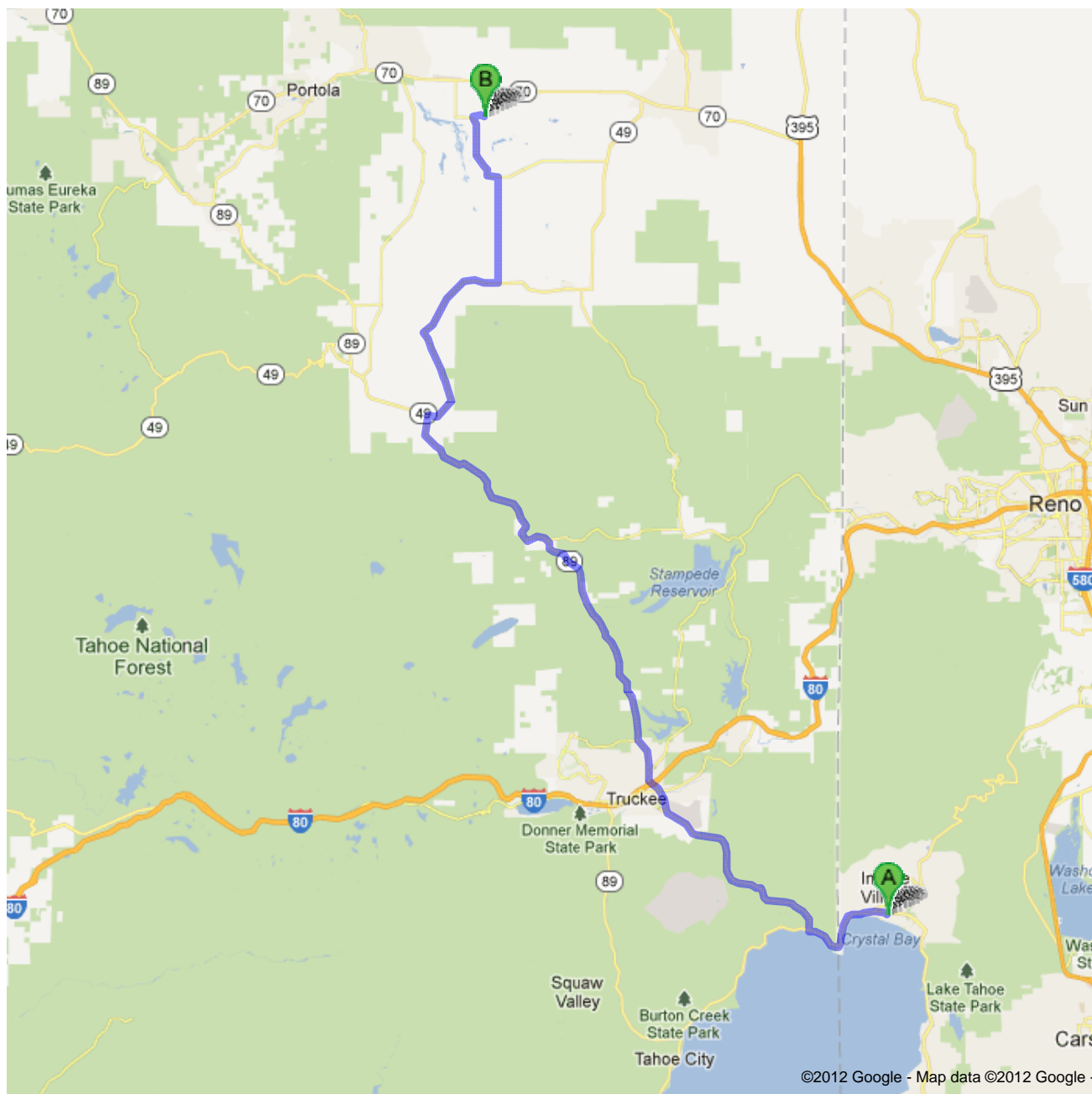
 13. Turn right
Unknown road
About 2 mins

go 0.8 mi
total 58.8 mi





Directions to Unknown road
58.8 mi – about 1 hour 26 mins



 Southwood Blvd

- | | | |
|---|---|-----------------------------|
| | 1. Head north on Southwood Blvd toward Tahoe Blvd | go 374 ft
total 374 ft |
|  | 2. Take the 1st left onto Tahoe Blvd
About 3 mins | go 1.1 mi
total 1.2 mi |
|  | 3. Continue straight onto NV-28 W/Lakeshore Blvd
Continue to follow NV-28 W
Entering California
About 3 mins | go 2.3 mi
total 3.5 mi |
|  | 4. Continue onto CA-28 W
About 3 mins | go 1.7 mi
total 5.2 mi |
|  | 5. Turn right onto CA-267 W
About 17 mins | go 11.8 mi
total 17.0 mi |
|  | 6. Continue onto CA-89 N
About 1 min | go 0.2 mi
total 17.2 mi |
|  | 7. At the traffic circle, continue straight onto CA-89
About 26 mins | go 22.9 mi
total 40.1 mi |
|  | 8. Turn right onto CA-49 N/Golden Chain Highway N/E Main St (signs for Loyalton)
Continue to follow CA-49 N/Golden Chain Highway N
About 11 mins | go 9.7 mi
total 49.7 mi |
|  | 9. Turn left onto Heriot Ln
About 6 mins | go 2.0 mi
total 51.7 mi |
| | 10. Continue onto Harriet Ln
About 7 mins | go 3.0 mi
total 54.7 mi |
|  | 11. Turn left onto Co Route A24/Dyson Ln
Continue to follow Dyson Ln
About 4 mins | go 1.7 mi
total 56.4 mi |
| | 12. Continue onto Co Route A24
About 3 mins | go 1.7 mi
total 58.1 mi |
|  | 13. Turn right
About 2 mins | go 0.8 mi
total 58.8 mi |

 Unknown road

These directions are for planning purposes only. You may find that construction projects, traffic, weather, or other events may cause conditions to differ from the map results, and you should plan your route accordingly. You must obey all signs or notices regarding your route.

Map data ©2012 Google

Directions weren't right? Please find your route on maps.google.com and click "Report a problem" at the bottom left.

- **Day 2, Stop 3 – Grizzly Valley Fault**

Location: [39.792875°-120.316098°]

Summary: Grizzly Valley fault system, Sierra Valley CA (R. Gold), Transition to the Translational Regime (J. Bormann)

More Info: Airborne LiDAR data show evidence of surface deformation on the floor of Sierra Valley. In October 2011, we acquired high-resolution shallow-seismic reflection data to evaluate deformation in the shallow subsurface. The reflection data reveal sub-vertical faulting in the Plio-Pleistocene lacustrine deposits in Sierra Valley, coincident with the subtle surface morphology that indicates faulting. The best-preserved evidence for recent faulting exists in Sierra Valley, it'll be combined with an examination of the shallow-seismic reflection data.

- **Drive to Saturday night camp.**

-

DAY 3: SUNDAY

- **Day 3, Stop 1 – Fort Sage Fault Trench**

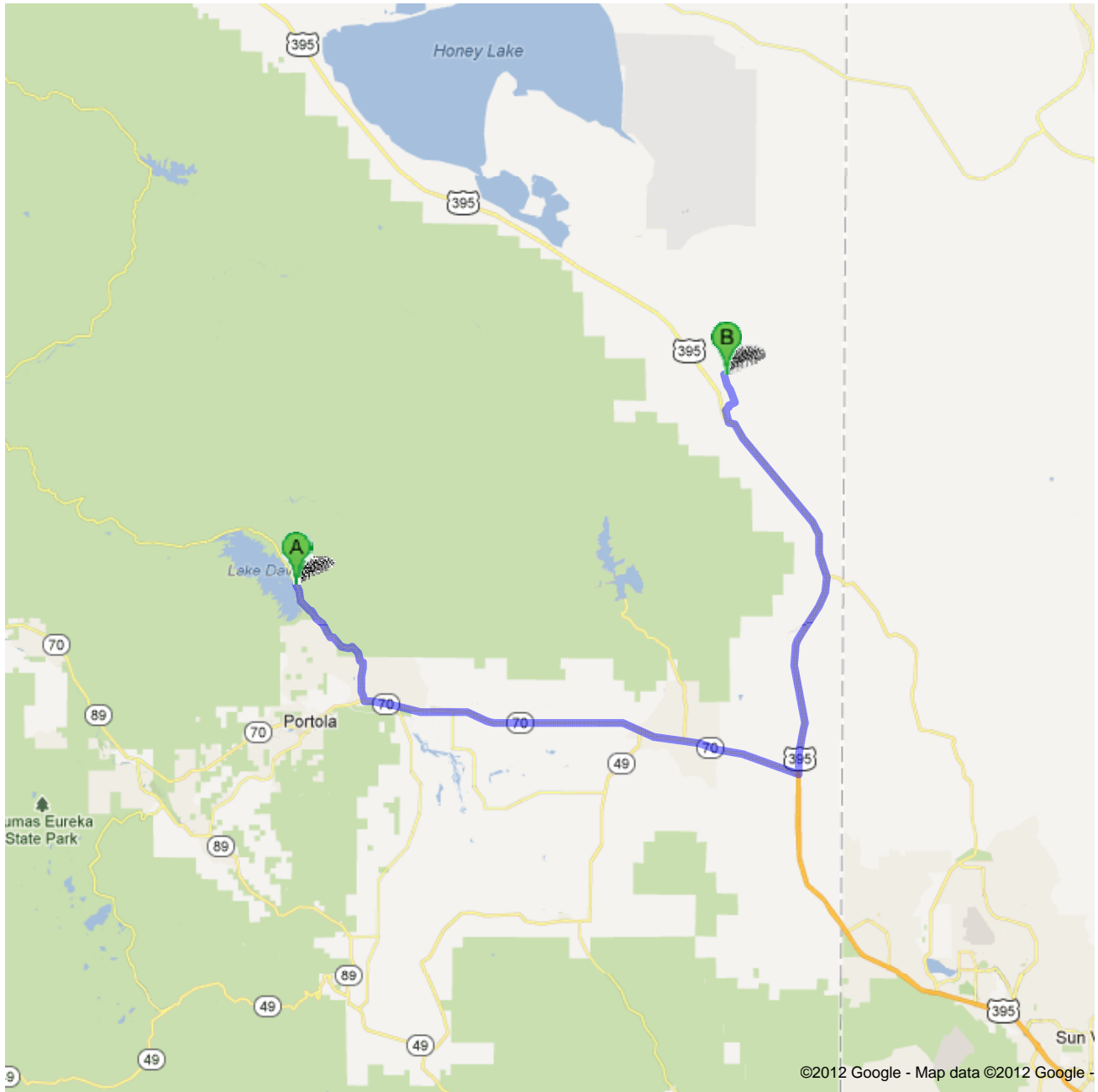
Location: [40.057852°-120.088482°]

Summary: Fort Sage fault, Doyle CA (Briggs).

More Info: This fault experienced a surface-rupturing earthquake in 1950. Trenches reveal evidence for two, pre-1950 earthquakes. These events are considered in relationship to previously identified precariously balanced rocks (PBR) in the footwall of the Fort Sage Mountains.



Directions to Co Rd 322/Hackstaff Rd
49.2 mi – about 1 hour 3 mins



Beckwourth-Taylorsville Rd

1. Head **southeast** on **Beckwourth-Taylorsville Rd** go 1.4 mi
total 1.4 mi
About 2 mins

2. Continue onto **Grizzly Rd** go 5.7 mi
total 7.1 mi
About 10 mins

 3. Turn left onto **CA-70 E/Feather River Hwy** go 21.0 mi
total 28.0 mi
Continue to follow CA-70 E
About 24 mins

 4. Turn left to merge onto **US-395 N** go 18.5 mi
total 46.6 mi
About 20 mins

 5. Turn right onto **Doyle Loop** go 0.6 mi
total 47.2 mi
About 2 mins

 6. Slight right onto **Hackstaff Rd** go 2.1 mi
total 49.2 mi
About 5 mins

Co Rd 322/Hackstaff Rd

These directions are for planning purposes only. You may find that construction projects, traffic, weather, or other events may cause conditions to differ from the map results, and you should plan your route accordingly. You must obey all signs or notices regarding your route.

Map data ©2012 Google

Directions weren't right? Please find your route on maps.google.com and click "Report a problem" at the bottom left.

- **Day 3, Stop 2 – Honey Lake Fault**

Location: [40.054694°-120.122511°]

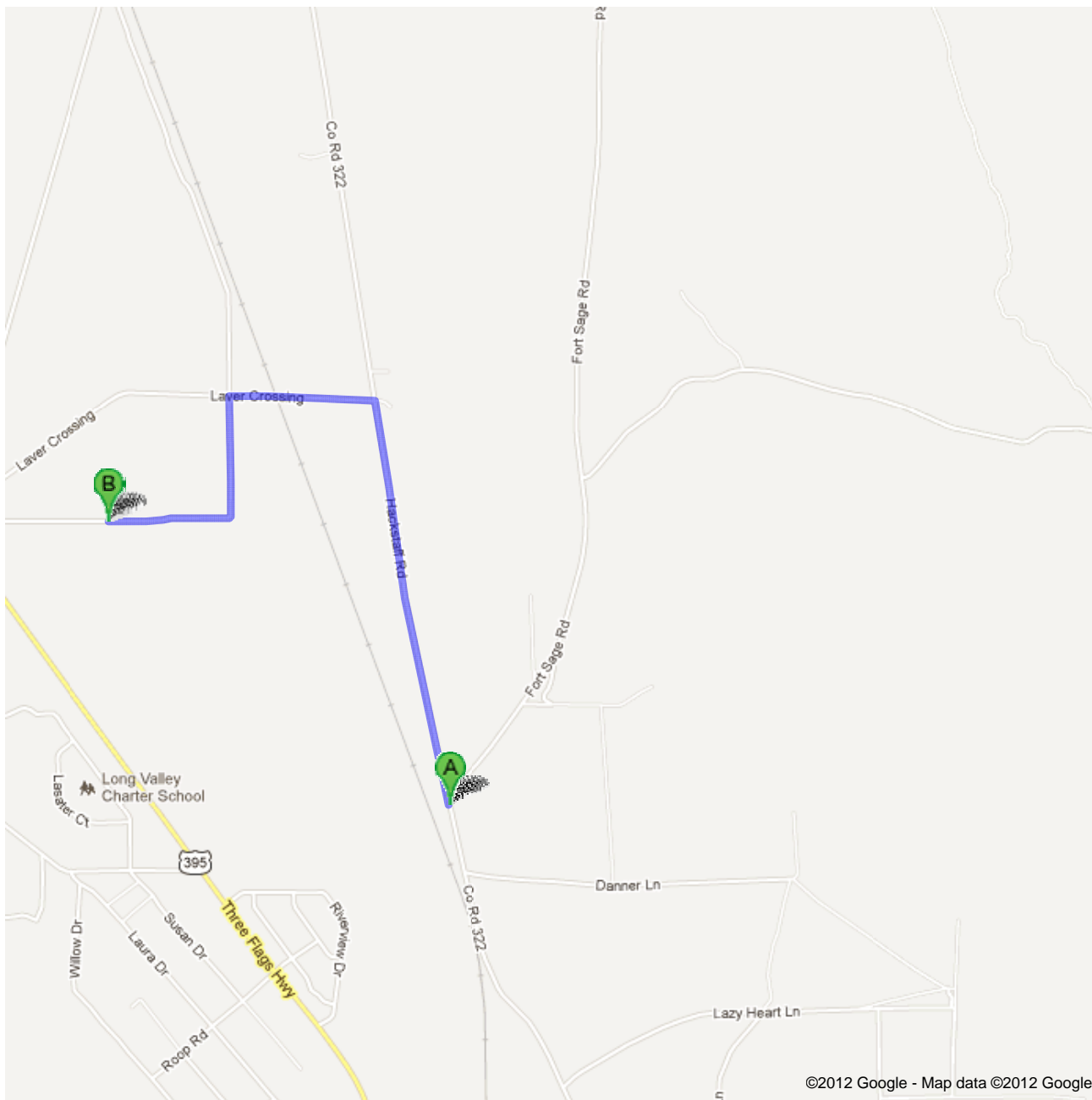
Summary: Honey Lake fault, Doyle CA (Briggs et al.)

More Info: The Honey Lake fault is among the best-studied structures in the northern Walker Lane, including both paleoseismic investigations and mid-Holocene slip-rate studies on the basis of a lateral faulted terrace riser along Long Valley Creek. New airborne LiDAR data reveal details regarding the slip rate along this structure. In particular, two terrace riser offsets along the Honey Lake fault place new constraints on this fault's Holocene slip rate.

- **Thanks for another great FOP. Have a safe drive home.**



Directions to Unknown road
2.3 mi – about 7 mins



A Co Rd 322/Hackstaff Rd

- 1. Head **north** on **Co Rd 322/Hackstaff Rd** toward **Fort Sage Rd**
About 3 mins

go 1.2 mi
total 1.2 mi

- 2. Take the 1st left onto **Laver Crossing**
About 1 min

go 0.4 mi
total 1.6 mi



© 2012 Google

- 3. Turn **left**
About 3 mins

go 0.7 mi
total 2.3 mi



© 2012 Google

B Unknown road

These directions are for planning purposes only. You may find that construction projects, traffic, weather, or other events may cause conditions to differ from the map results, and you should plan your route accordingly. You must obey all signs or notices regarding your route.

Map data ©2012 Google

Directions weren't right? Please find your route on maps.google.com and click "Report a problem" at the bottom left.

Day 1, Stop 1 – Genoa Fault

Stop 1: Genoa fault at Mott Canyon (38.928364° -119.839596°, park cars on the shoulder or in Park and Ride lot at intersection of Hwy 207-Kingsbury Grade and Foothill Rd., walk 0.5 miles up Kingsbury Grade to Forest Service road [on left], which leads to scarp (stop 1 is about 0.5 miles south of Hwy 207).

At this stop, we will look at the Genoa fault scarp, alluvial-fan geomorphology and fault offset, and an outcrop of the fault in a stream cut. We will discuss ^{10}Be dating results of the fan, offset calculation from ground-based LiDAR, modeling of slip rate and uncertainty, along-strike patterns in slip rate on the Genoa fault, and earthquake chronology from previous and new paleoseismic trenching of the Genoa fault.



Fig. 1. Low sun angle aerial photo of Mott Canyon site showing the Genoa fault scarp and offset alluvial fans. View to northwest.

Temporal fault slip rate and rupture patterns on the Genoa fault, central eastern Sierra Nevada, integrating ground-based LiDAR, ^{10}Be surface exposure dating, and paleoseismology

Dylan Rood^{1,2}, Alan Ramelli³, Jonathan Harvey⁴, Douglas Burbank⁴, Bodo Bookhagen⁴

¹ AMS Laboratory, Scottish Universities Environmental Research Centre (SUERC), East Kilbride, Scotland, UK.

² Earth Research Institute, University of California, Santa Barbara, CA, USA.

³ Nevada Bureau of Mines and Geology, University of Nevada, Reno, NV, USA.

⁴ Department of Earth Science, University of California, Santa Barbara, CA, USA.

Introduction and Methods

Using an integrated geomorphic-paleoseismic approach, we evaluate temporal patterns of fault-related, late Quaternary deformation along the Genoa fault at the eastern boundary of the Carson Range (central Sierra Nevada-Basin and Range transition zone), California-Nevada. The Genoa fault is experiencing some of the highest strain rates and fastest Holocene slip rates in the western Great Basin (c.f., Wesnousky et al., 2012), and poses a significant hazard to the Carson City-Reno urban corridor and Lake Tahoe. This fault was the site of at least two late Holocene M~7 earthquakes, including a pre-historic, but less

than ~600 yr BP event with co-seismic displacement of 4-6 m and a penultimate event at less than ~2000-2500 yr BP (Ramelli et al., 1999). The fault's long-term slip rate history is only well studied at one site on the southern segment: $0.4 \pm 0.3/-0.1$ mm/yr over both ~20 ky and ~150 ky time scales along the West Fork of the Carson River at Woodfords, CA (Rood et al, 2011a).

Over 10- to 200-ky time scales, our geomorphic approach is to quantify fault displacements of multiple geomorphic features, including two glacial outwash terraces and two alluvial fans. We use ground-based LiDAR topographic data to model fault slip at the Woodfords, Mott Canyon, and Corsser Creek sites. We determine the age of offset features using ^{10}Be surface exposure dating techniques, including ~50 new ^{10}Be analyses from surface boulders and depth profiles. By comparing offsets of different ages along individual fault segments and modeling their slip rates and uncertainties, we define how the locus, magnitude, and rate of fault slip changes through time.

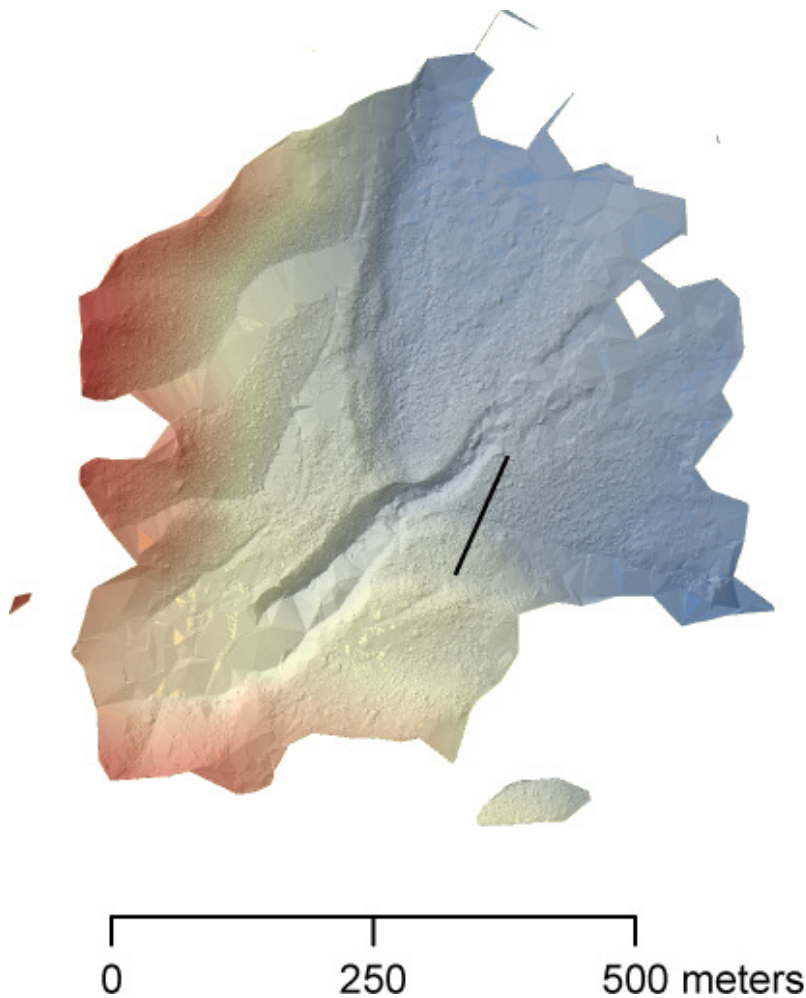


Fig. 2 (left). Ground-based LiDAR 25-cm DEM of scarp and youngest fan at Mott Canyon. Black line shows location of cross-profile. North is up.

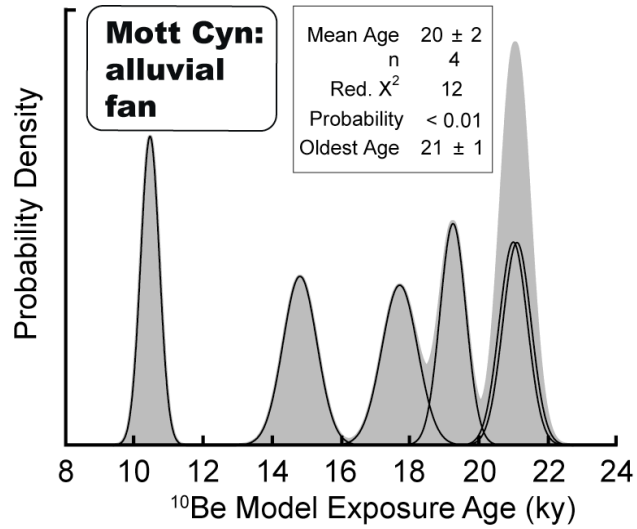
New paleoseismic data from two trenches at the Fay Canyon site permits comparison of rupture patterns on the neighboring central and southern fault segments, where differences in the timing of earthquake events, displacement magnitude/event, and geometry of underlying faults are compared to the slip rates calculated from offset geomorphic

features. By integrating geologic and paleoseismic datasets, we investigate what frequency and magnitudes of earthquake rupture were required to build observed geomorphic offsets, and, specifically, whether the last and penultimate events ruptured across an ostensibly important fault-segment boundary.

Slip rate on the central section of the Genoa fault at Mott Canyon

At Mott Canyon, multiple alluvial fan surfaces are offset by the central section of the Genoa fault (Fig. 1). Ground-based LiDAR survey data was collected at Mott Canyon to image the ~10 m scarp and offset in the youngest fan surface. Topographic cross-profiles were extracted from a 25-cm digital elevation model (DEM; Fig. 2). Samples for ¹⁰Be surface exposure dating were collected from the tops of abundant large (>1 m tall) boulders on the fan surface located above and below the scarp. We used the LiDAR and cosmogenic nuclide data with Monte Carlo simulation methods (c.f., Rood et al., 2011a) to model the slip and slip rate across the fault scarp.

Fig. 3 (right). Probability density function for ¹⁰Be boulder ages from the Mott Canyon fan with summary statistics. Black curves are individual sample PDFs defined by the age and 1σ analytical error. A cumulative probability density function (grey curve) is calculated by summing individual PDFs for all boulders from each deposit.



Modeling of the LiDAR data gives a slip estimate of 11.7 +5.5/-1.4 m (mode and 95% confidence limits).

¹⁰Be data give an exposure age of 19.7 +/- 1.6 ka (average and standard deviation; Fig. 3), which is similar in age to deposits of the Tioga glaciation associated with the Last Glacial

Maximum (LGM) (Rood et al., 2011b). Taken together, Monte Carlo simulation results give a slip rate of 0.6 +0.3/-0.1 mm/yr (Fig. 4) for the central section of the Genoa fault at this site, which is located near the southern end of the central section.

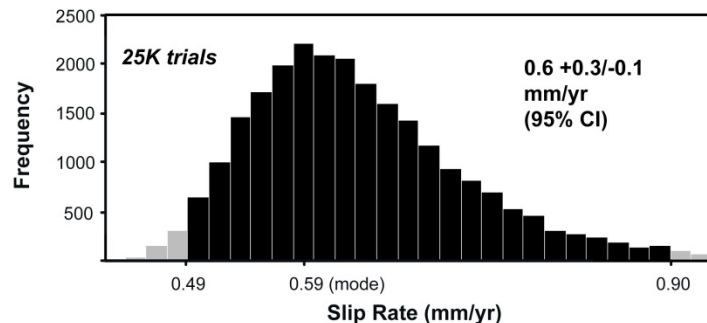
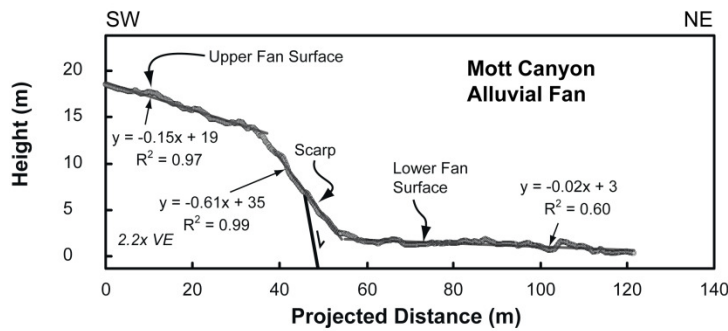


Fig. 4 (left). Calculations associated with the alluvial fan surface at Mott Canyon using parameters measured from the survey profile (upper) and Monte Carlo simulation output (lower) that gives the slip rate and 95% confidence intervals.

Paleoseismology of the southern section of the Genoa fault at Fay Canyon

Data from two paleoseismic trenches at Fay Canyon (Luther Creek) provide information on the southern section of Genoa fault. 19 new radiocarbon ages on charcoal samples bound the ages of the last and penultimate events at the site. In the southern trench, a sample that pre-dated the most recent event (MRE) gives an age of 405 +/- 30 cal years BP (1σ) while a sample that post-dated the MRE gives an age of 380 +/- 30 cal years BP. In the northern trench, the age of the penultimate event is bracketed by samples that pre- and post-date the earthquake, which give ages of 2050 +/- 30 and 1885 +/- 30 cal years BP, respectively. The ages for the last two events at the Fay Canyon site fall within the uncertainty of the ages for earthquakes dated on the central section of the Genoa fault (Ramelli et al., 1999; Fig. 5).

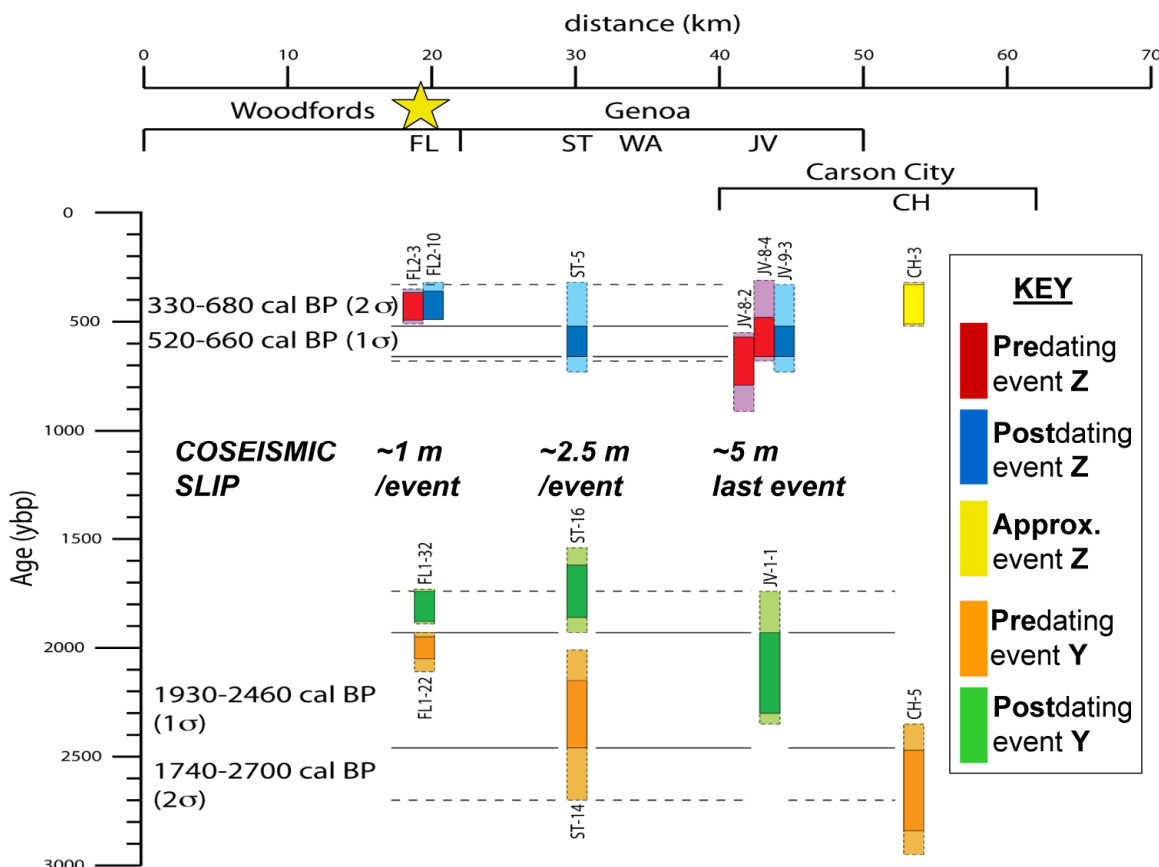


Fig. 5. Summary of paleoseismic data for the Genoa fault. FL=Fay Canyon site (star) on the southern section of the Genoa fault (this study). Central section sites include: ST=Corsser Creek/Sturgis Ranch, WA=Walley's Hot Springs, and JV=Jacks Valley (after Ramelli et al, 1999).

Conclusions

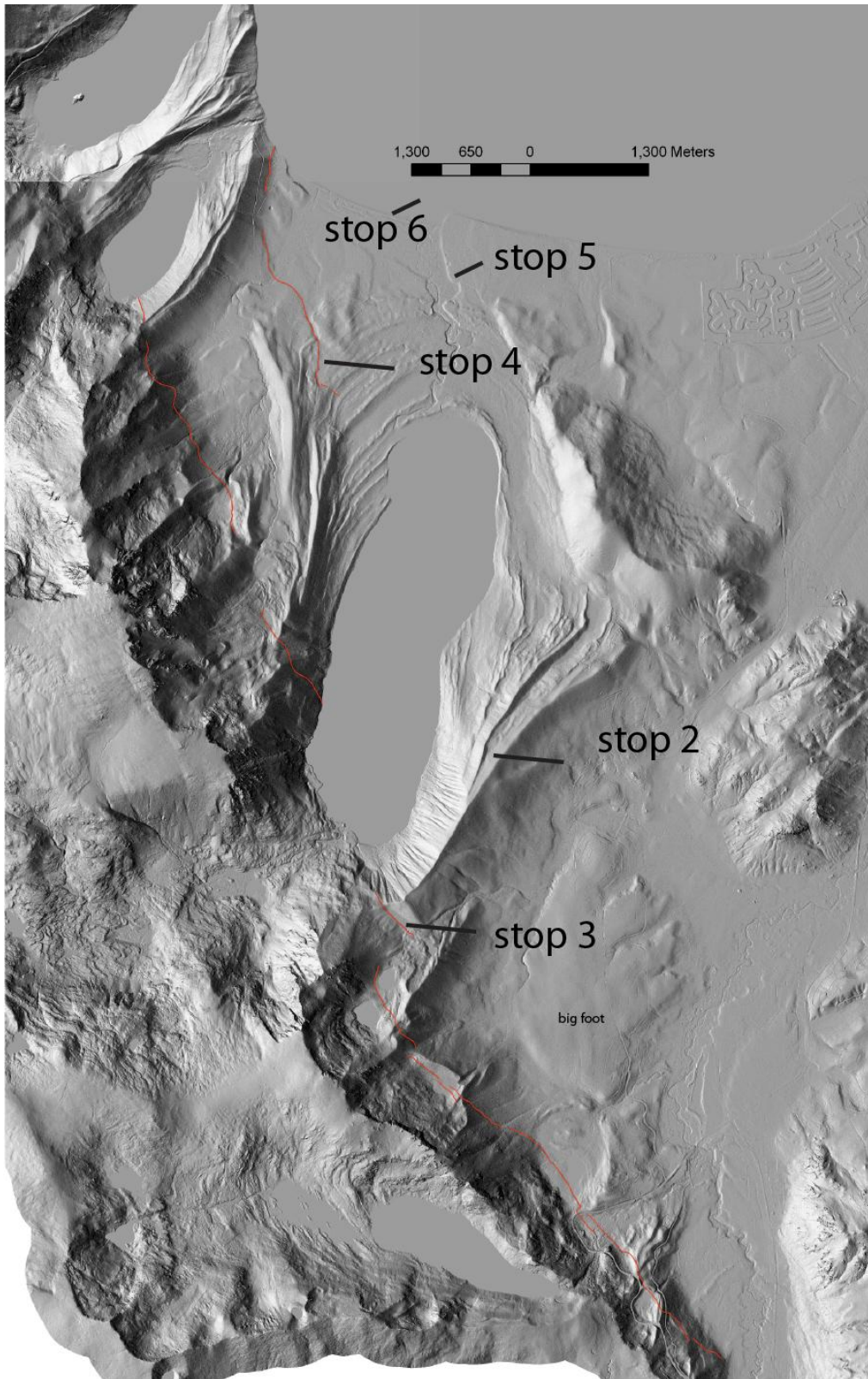
- Data permit that slip rates were relatively constant over ~20 and ~150 ky timescales on the southern section of the Genoa fault at Woodfords

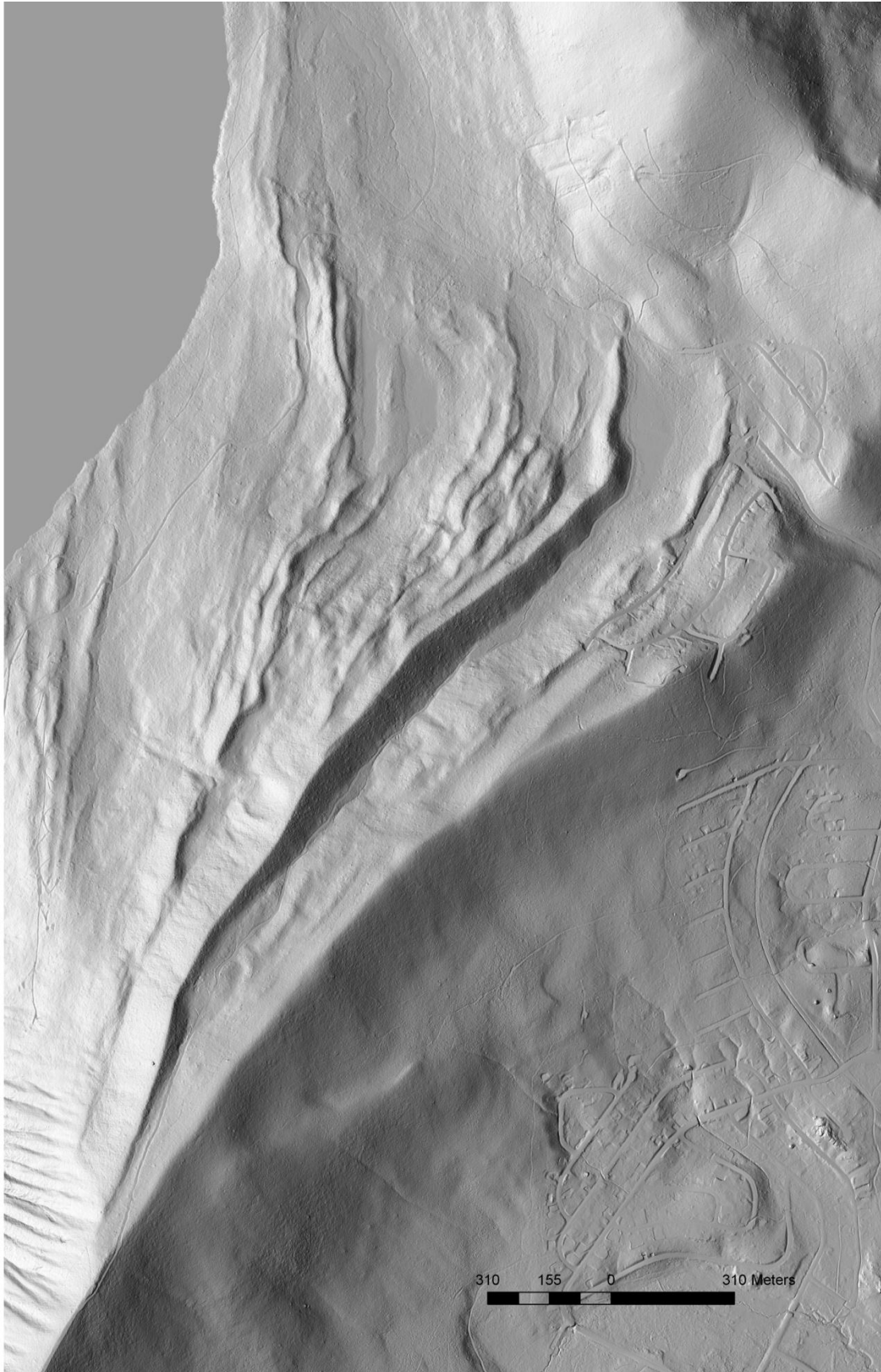
- Slip rates are variable in space over the ~20 ky timescale, with a possible ~1.5-2-fold change over 20 km
- Paleoseismic data permit that the last 2 earthquakes ruptured across the possible segment boundary at Jobs Canyon (Fig. 5)
- Smaller slip per event (e.g., 1 m versus 2.5 m; Fig. 5) permits consistent through-going ruptures on the southern and central sections

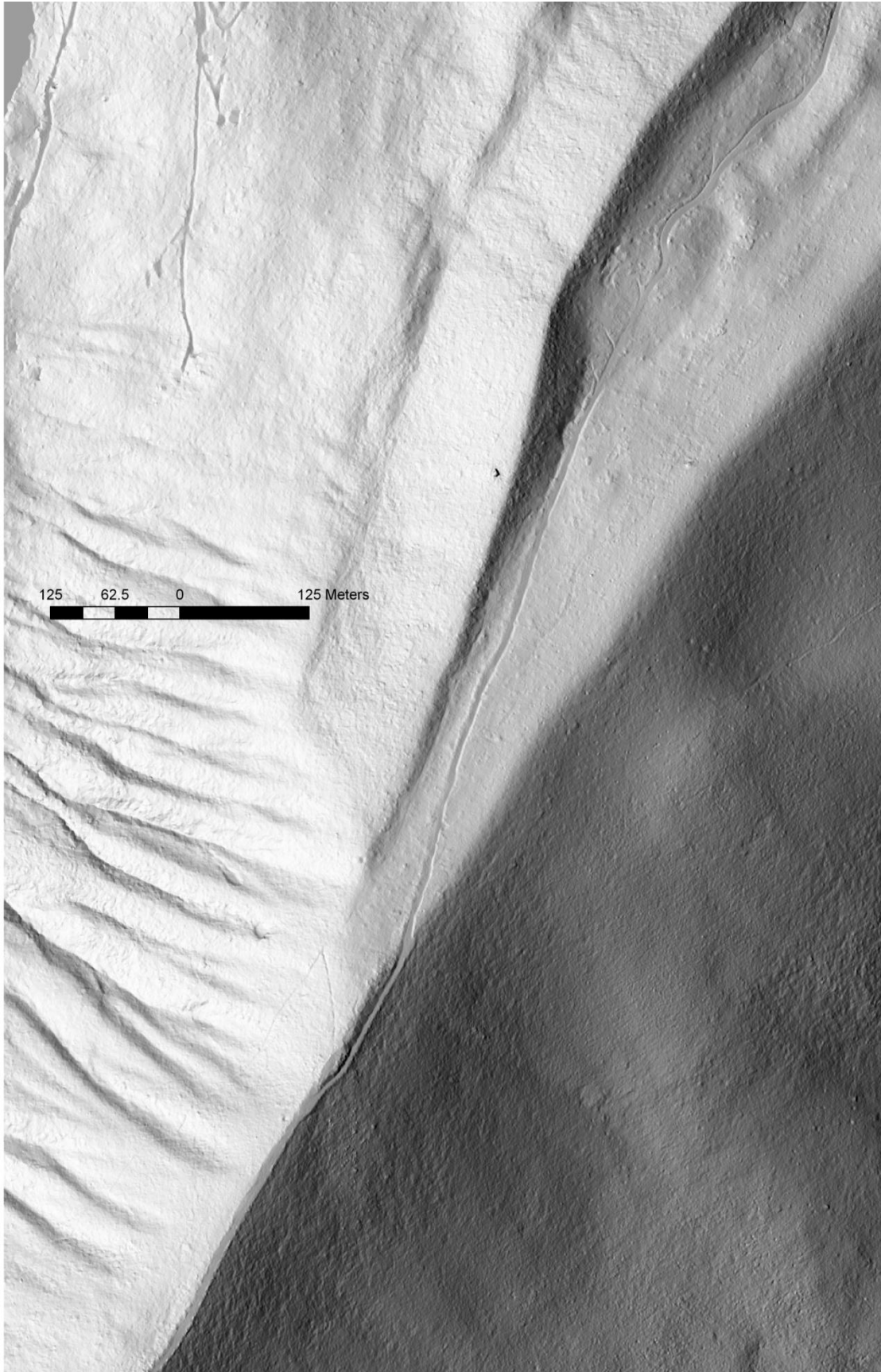
References

- Ramelli, A.R., Bell, J.W., dePolo, C.M., Yount, J.C., 1999, Large-Magnitude, Late Holocene Earthquakes on the Genoa Fault, West-Central Nevada and Eastern California, *Bulletin of the Seismological Society of America*, 89, 6, 1458-1472.
- Rood, D.H., Burbank, D.W., Finkel, R.C., 2011a, Spatiotemporal patterns of fault slip rates across the central Sierra Nevada Frontal Fault Zone, *Earth and Planetary Science Letters*, 301, 457-468, doi:10.1016/j.epsl.2010.11.006.
- Rood, D.H., Burbank, D.W., Finkel, R.C., 2011b, Chronology of glaciations in the Sierra Nevada, California from ¹⁰Be surface exposure dating, *Quaternary Science Reviews*, 30, 646-661, doi:10.1016/j.quascirev.2010.12.001.
- Wesnousky, S.G., Bormann, J.M., Kreemer, C., Hammond, W.D., Brune, J.N., 2012, Neotectonics, geodesy, and seismic hazard in the Northern Walker Lane of Western North America: Thirty kilometers of crustal shear and no strike-slip?, *Earth and Planetary Science Letters*, 329-330, 133-140.

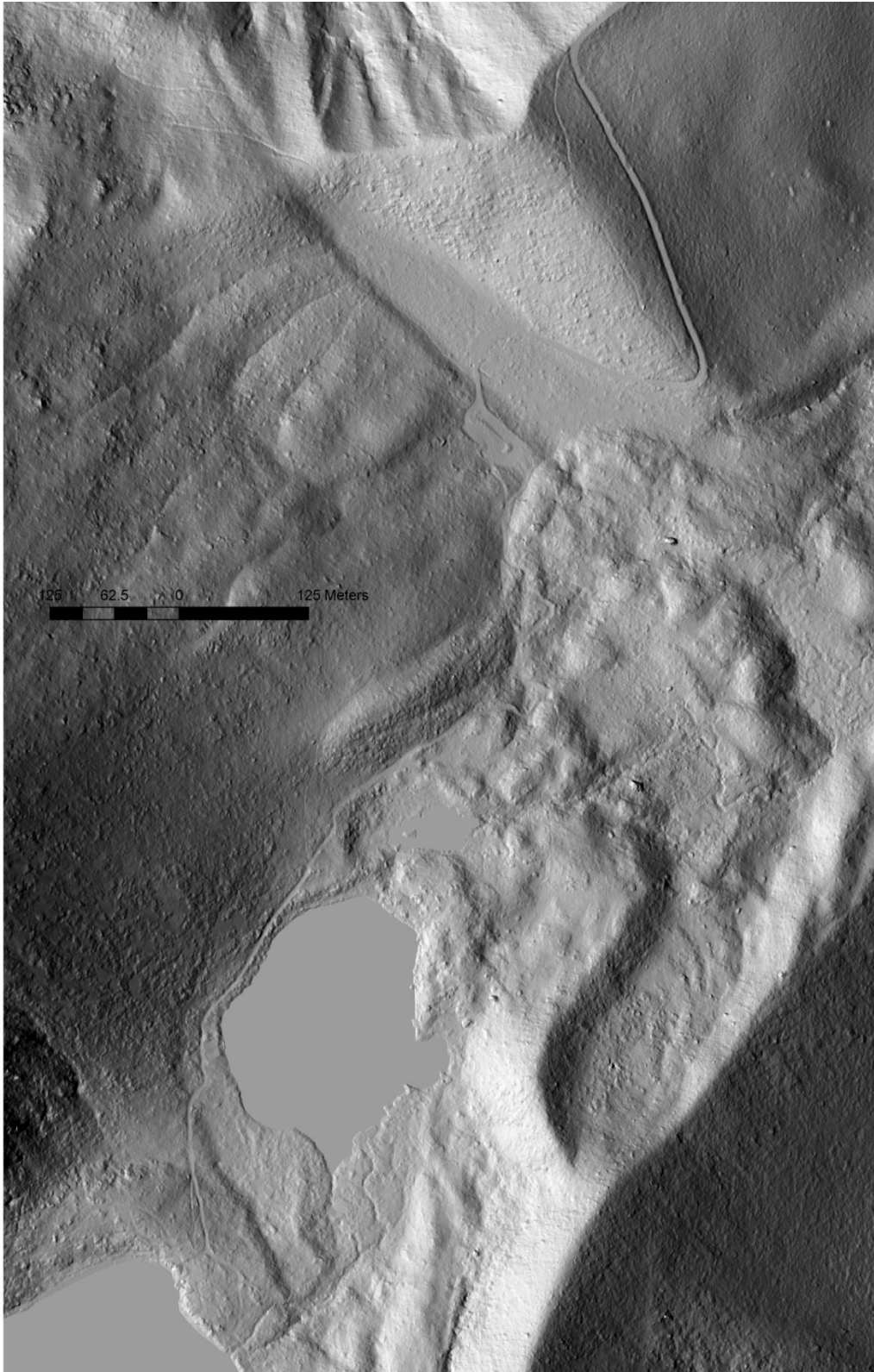
Day 1, Stop 2 – Tahoe/ Tioga Moraines







Day 1, Stop 3 – West Tahoe Fault



Paleoseismic History Of The Fallen Leaf Segment Of The West-Tahoe Fault Discerned From Lacustrine Slide Deposits In The Lake Tahoe Basin, California-Nevada

Jillian M. Maloney, Paula J. Noble, Neal W. Driscoll, Graham M. Kent, Shane B. Smith, Gretchen C. Schmauder, Jeffrey M. Babcock, Robert L. Baskin, Robert Karlin, Annie M. Kell, Gordon G. Seitz and John A. Kleppe

Abstract

Previous research in the Lake Tahoe Basin (LTB) has identified major faults and associated deformation across the region. The West Tahoe–Dollar Point Fault (WTDPF) extends along the western margin of the LTB and is characterized as its most hazardous fault. Fallen Leaf Lake (FLL), Cascade Lake (CL), and Emerald Bay are three sub-basins of the LTB, located south of Lake Tahoe, that provide an opportunity to image primary earthquake deformation along the WTDPF and associated landslide deposits. Here we present results from high-resolution seismic CHIRP surveys in FLL and CL, as well as multibeam bathymetry coverage of FLL, and onshore LiDAR data of the southern LTB. CHIRP profiles beneath FLL image slide deposits that appear synchronous with slides in Emerald Bay and Lake Tahoe. The temporal correlation of slides between multiple basins suggests triggering by events on the WTDPF system. If this correlation is correct, we postulate a recurrence interval for the FLL section of the WTDPF of ~3–4 k.y., indicating that the WTDPF is near or beyond its characteristic seismic recurrence cycle. In addition, CHIRP data beneath CL image strands of the WTDPF offsetting the lake floor as much as ~7 m. The CL data combined with onshore LiDAR allow us to map the WTDPF continuously between FLL and CL. This improved mapping of the WTDPF elucidates fault geometry south of Lake Tahoe and improves geohazard assessment of the region. The new data presented here build on previous research to provide a robust understanding of the tectonics of the entire Lake

Tahoe Basin.

I. Introduction

Onshore and offshore research in the Lake Tahoe Basin (LTB) has defined the geometry and slip-rates of the major faults accommodating extension across the basin (Brothers et al., 2009; Dingler et al., 2009; Gardner et al., 2000; Karlin et al., 2005; Kent et al., 2005; Schweickert et al., 2004; Seitz et al., 2006; Seitz et al., 2005). These faults, the Stateline–North Tahoe Fault (SLNTF), Incline Village Fault (IVF), and the West Tahoe–Dollar Point Fault (WTDPF), exhibit down to the east normal displacement (Dingler et al., 2009) (Fig. 1). Recent work in Fallen Leaf Lake (FLL) has helped identify the WTDPF as potentially the most hazardous fault in the LTB, with the potential to produce $M > 7.0$ earthquakes (Brothers et al., 2009). The WTDPF is a major N-S striking normal fault, extending >50 km along the western margin of the LTB, and is divided by geomorphic discontinuities into three segments: the southern Fallen Leaf segment (FLS), central Rubicon segment (RS), and northern Dollar Point segment (DPS) (Fig. 1a) (Brothers et al., 2009). The most recent event (MRE) on the FLS was initially dated at 4.1-4.5 k.y. BP (Brothers et al., 2009), and is refined herein as 4.57-4.85 k.y. BP based on data presented subsequently. The MRE on the RS was broadly dated to lie between 3-10 k.y. BP (Brothers et al., 2009) and later constrained to ~ 5.3 -5.6 k.y. BP (Smith et al., in press). Kent et al. (2005) estimated a recurrence interval for the WTDPF of ~ 4.8 k.y. based on slip-rate models, but the paleoseismic record has not been extended past the most recent events on the FLS and RS. Furthermore, rupture-timing patterns between the three WTDPF sections, IVF, and SLNTF remain poorly understood.

Historic earthquakes have been shown to trigger mass movements in lacustrine and marine environments (Hampton et al., 1996; Lee et al., 2009). Based on this observation, recent studies have used slump or slide deposits observed in sediment cores and seismic reflection data to estimate earthquake recurrence intervals (Schnellmann et al., 2002; Strasser et al., 2006; Upton and Osterberg, 2007). Several lines of evidence argue for seismic triggering of slide deposits, but most convincing is a record of synchronous deposits across broad areas and multiple basins. CHIRP data beneath Lake Tahoe sub-basins FLL, Cascade Lake (CL), and Emerald Bay (EB) image several large slide deposits. The slides are correlated temporally between the three sub-basins, as well as with previously dated slides in Lake Tahoe (Smith et al., in press). Based on extent and timing, we suggest the slides were triggered by strong shaking on the WTDPF. These co-seismic slides extend the paleoseismic record for the WTDPF and provide new insights into the rupture patterns along strike, and possibly between faults. Based on the extended paleoseismic record, we estimate a recurrence interval of $\sim 3\text{-}4$ k.y. on the FLL section of the WTDPF, which is vital in assessing geohazards posed by the WTDPF to the populated LTB.

II. Background

The LTB lies within the actively deforming Walker Lane belt. The Walker Lane belt is located between the Sierra Nevada block and the central Great Basin, and is characterized by transtensional deformation caused by the oblique divergence of the Sierra Nevada-Central Valley microplate and stable North America (Fig. 1b) (Argus and Gordon, 2001; Oldow, 2003; Unruh et al., 2003). Geodetic studies indicate 9-13 mm/yr of dextral

shear in the Walker Lane belt, which amounts to ~20-25% of the total plate motion between the North American and Pacific plates (Bennett et al., 2003; Dixon et al., 2000; Hammond and Thatcher, 2004; Svarc et al., 2002). The LTB is located in the northern Walker Lane belt, and is the westernmost basin in a series of N-S trending basins and mountain ranges bounded by normal faults (Surpless et al., 2002; Faulds et al., 2005).

The LTB is an asymmetric half-graben located between the Sierra Nevada and Carson mountain ranges, and has been tectonically active for at least 3 Ma (Dingler et al., 2009; Faulds et al., 2005; Hyne et al., 1972; Kent et al., 2005; Schweickert et al., 2004; Surpless et al., 2002). Extension across the basin is accommodated by three primary normal fault systems: the WTDPF, SLNTF, and IVF (Kent et al., 2005), which have vertical slip rates of 0.4-0.8 mm/yr, 0.35-0.6 mm/yr, and 0.18-0.30 mm/yr, respectively (Brothers et al., 2009; Dingler et al., 2009). Based on CHIRP data and dating of sediment cores, the MRE on the FLL section of the WTDPF occurred 4.57 -4.85 k.y. BP. A coarse-grained deposit fills accommodation created by the MRE and infills bathymetric lows basin wide (Brothers et al., 2009). Based on onshore trenching, the MRE on the IVF occurred ~500 yrs BP with the penultimate event occurring between 20-30 k.y. BP (Seitz et al., 2005). The MRE on the SLNTF has not been determined, but seismic data across the fault show a ~10 m scarp on the floor of Lake Tahoe and ~21-25 m offset of the McKinney Bay debris complex (~60 ka) (Dingler et al., 2009; Kent et al., 2005).

The other major regional fault that may produce strong shaking in the LTB is the Genoa Fault. The Genoa Fault lies just east of LTB and trends >50 km along the eastern edge of the Carson Range. The Holocene slip rate on the Genoa Fault is ~2-3 mm/yr, with

the two most recent events occurring at 500-600 yrs BP and 2.0-2.2 k.y. yrs BP (Ramelli et al., 1999). Paleoseismic evidence suggests both events were $M > 7.0$ (Ramelli et al., 1999).

FLL, CL, and EB are small moraine-bounded depressions shaped by glacial processes with similar sedimentary histories. All three basins are bounded by lateral Tioga (24,500-13,600 ^{14}C yrs BP; Benson et al., 1998) and Tahoe glacial moraines on their eastern and western shores (Saucedo et al., 2005). FLL and CL are separated from Lake Tahoe by recessional end moraines, while EB connects with Lake Tahoe to the north at Emerald Point. Input of modern sediment to FLL is sourced mainly from Glen Alpine Creek, which drains an area of $\sim 42 \text{ km}^2$ from the Desolation Wilderness to the south. Additional input to the lake is sourced from Cathedral Creek and several unnamed creeks along the western shore that drain from the mountains to the southwest. Input to CL is mainly from Cascade Creek, which drains an area of $\sim 12 \text{ km}^2$. Input to EB is mainly from Eagle Creek, which drains an area of $\sim 25 \text{ km}^2$ from the mountains to the southwest. Granitic rocks of the Sierra Nevada batholith and metamorphosed roof pendants primarily characterize the geology of the drainage areas for all three sub-basins (Saucedo et al., 2005). Several Pleistocene-Holocene age landslide deposits have been mapped onshore near the sub-basins (Saucedo et al., 2005). Slides are mapped above the southernmost shores of both EB and CL and appear to spill into the basins (Fig. 2). Two slides are also mapped slightly northwest from Cathedral Creek, above FLL.

Previously collected CHIRP profiles in FLL and EB image glacial deposits mantled by younger lacustrine deposits, which thin to the north in both basins (Brothers et al., 2009; Dingler et al., 2009). In FLL, the youngest sediments also thicken towards the center of the lake and were proposed to represent drift deposits formed by bottom currents (Brothers et

al., 2009). Previously collected piston cores from FLL contain predominantly fine silt and diatomaceous clay, interrupted by episodic layers of coarser sediment (Brothers et al., 2009).

Debris flow and turbidite deposits have been identified in cores and seismic reflection data in LT sediments, and seismic triggering of the deposits has been suggested (Dingler et al., 2009; Karlin et al., 2005; Kent et al., 2005; Seitz et al., 2006; Smith et al., 2006). Smith et al. (in press) mapped and dated 18 debris flow and turbidite deposits in LT, four of which appear to be triggered by events on the LTB faults. They proposed that the youngest deposit, A (630-120 yrs BP), was triggered by an event on the IVF, a 4.51-4.07 k.y. BP deposit (F) by an event on southern segments of the WTDPF, a 5.60-5.33 k.y. BP deposit (G) by an event on the northern and central segments of the WTDPF, and a 7.89-7.19 k.y. BP deposit (J) by an event on the WTDPF. Several deposits younger than deposit J were also linked to events on faults outside the LTB. Older event deposits were identified and dated as deposits K (9.45-8.77 k.y. BP), L (9.73-9.32 k.y. BP), M (10.16-9.80 k.y. BP), N (11.26-10.48 k.y. BP), and O (12.49-11.20 k.y. BP), but the triggering mechanism for these deposits was not definitive, and in some cases may be related to motion on the Stateline–North Tahoe Fault.

III. Methods

Fallen Leaf Lake bathymetric data were collected in July 2010 using a pole-mounted Reson 7125 multibeam system operated at 200 kHz (Fig. 3). The system generates 256 steered and focused equi-angle beams across a 128° swath. Individual beamwidth is 1° x 2°. Pulse length was set to 33 μ s, giving a range resolution of ~2.5 cm. Vessel motion was

measured using a POS MV WaveMaster inertial measurement unit, providing roll, pitch, and true heading accuracy to 0.030° . Positions were calculated through the POS MV WaveMaster and dual-differential GPS system, providing position accuracy to better than 2 m. A fixed Reson SVP 71 measured sound velocity at the transducer head and vertical velocity profiles were collected with a Reson SVP 20. Both sound velocity profilers use direct soundings to determine velocity. Position, motion, and sound velocity data were applied to the multibeam soundings during acquisition through the Reson PDS2000 software.

Subsequent to the field effort, data were further processed using Caris HIPS and SIPS software, and interpreted with Caris HIPS and SIPS, IVS Fledermaus, and ArcGIS software packages. Depths were converted to elevations referenced to the USGS Fallen Leaf Lake water level datum of 1944 m (NAVD 88) in order to align it with onshore LiDAR data. Lake level varied by ~ 3 cm over the course of the survey, and daily lake level corrections were applied to the data.

In June 2011, ~ 45 line km of Compressed High Intensity Radar Pulse (CHIRP) seismic data were acquired from FLL and CL (Fig. 2). All surveys employed SIO's Edgetech SUBSCAN CHIRP profiler. The CHIRP profiler was operated with a 50 ms swept pulse of 1-15 kHz, and provided decimeter vertical resolution and sub-bottom penetration >50 m. All data were digitally recorded in JSF format (and later converted to SEG-Y format) with real-time GPS navigation, providing location accuracy to within 5 m. Data were processed using SIOSEIS (Henkart, 2003) and imported to Kingdom Suite and IVS Fledermaus software packages for interpretation. A nominal water and sediment velocity of 1450 m/s was assumed for all depth and sediment thickness conversions.

Previously acquired CHIRP data were also used to supplement the new seismic imagery during interpretation (Fig. 2; Dingler et al., 2009). The new data were collected with a higher frequency swept signal and provide improved resolution data, which allowed for more precise mapping of acoustic horizons and correlation to piston cores.

Five piston cores from four locations were acquired in FLL during November 2010 using a Kullenberg piston coring system from LaCore (University of Minnesota; Fig. 2). The two longest cores, BC1A and BC2D, recovered ~9.8 m and ~11.5 m, respectively. Three of the piston cores (BC1A, BC2D, and BC3A) were logged for lithology and magnetic susceptibility, and sampled for micropaleontology, geochemistry, and radiocarbon dating by a team at UNR (Karlin et al., 2011). Plant macrofossils were extracted from the cores for radiocarbon dating in order to avoid problems with reservoir ages. The macrofossil samples were dated at the Lawrence Livermore National Center for Applied Mass Spectrometry (CAMS) Laboratory. Calibrated radiocarbon ages were determined using OxCal v. 4.0.5 (Bronk Ramsey, 2001) and the IntCal 04 calibration curve (Reimer et al., 2004). The ages of the two youngest event deposits in FLL were modeled as a sequence in OxCal v. 4.0.5 (Bronk Ramsey, 2001), using bounding dates from multiple cores. Older event deposit ages were determined by assuming a constant sedimentation rate for sediment older than ~8 k.y. BP. The sedimentation rates were calculated based on the age model for cores BC1A and BC2D (Karlin et al., 2011).

A previously collected piston core (EB2) from EB (Dingler et al., 2009) was used to calculate ages for event deposits observed in EB CHIRP data. Three macrofossil samples were analyzed at the CAMS Laboratory and calibrated radiocarbon ages were determined

using OxCal v. 4.1.7 (Bronk Ramsey, 2009) and the IntCal 04 calibration curve (Reimer et al., 2004).

IV. Results

IV - A. Fallen Leaf Lake Bathymetry

The maximum depth of FLL as recorded in the multibeam data is ~114 m below the USGS datum at 1944 m elevation (Fig. 3). The minimum depth was limited by equipment set-up and shallow water hazards. Steep slopes bound the basin on the southern, eastern, and western shorelines (~15-40°), with a more gently dipping slope to the north (~10°). Several prominent features with high slope and rugosity are observed along the basin slopes. The steep basin slopes change abruptly to the basin floor, which is gently sloping with low rugosity. The deepest areas of the basin are represented by two moats that run along the base of the eastern and western slopes in the southern basin. The moats are separated by a sub-parallel mound with a crest ~4 m higher than the moats. There are other small mounds and depressions on the basin floor, but regionally it slopes gently up to the north.

The expression of the WTDPF is observed on the basin floor as a linear depression that trends ~N20°W. A second splay may also trend along the base of the steeply sloping southern wall, which slopes up to ~40°. These expressions of the fault on the lake floor align well with traces of the WTDPF splays mapped in CHIRP data.

Along the basin slopes, several ridges extend from the shore to the basin floor. Three prominent ridges are located near the center of the eastern slope and three additional ridges are located along the northwestern slope. The crests range in height between ~3-10 m. Several less prominent ridges are located along the western slope. A fan shaped ridge feature on the eastern slope lies offshore the mouth of Cathedral Creek.

Several erosional features are observed on the eastern slope, south of the moraine crests. Five sub-parallel, linear striations trend $\sim N10^\circ E$ for ~ 900 m along the slope. These striations do not follow lake contours, but rather cut across them. Immediately south of the striations are three prominent, parallel scarps near the base of the eastern slope. The scarps are evenly spaced at ~ 220 m apart, trend $\sim N20^\circ W$, and each exhibits ~ 10 m of down the southwest vertical offset. These features are between, and trend parallel to, the WTDPF and the Midlake Fault mapped by Brothers et al. (2009). We observe a topographic high in the acoustic basement adjacent to these features, but we do not observe evidence for associated faulting of basin sediments.

Along the southern slope, two small headland features slope up to $\sim 80^\circ$ to the contact with the basin floor. Above the southeastern headland is a circular, flat area at ~ 40 m water depth. Shoreward to the southeast, the plateau is bounded by steeply dipping slopes (up to $\sim 60^\circ$) leading up to the modern shoreline. Shoreward to the northeast a more gently sloping ($\sim 5-10^\circ$) ramp leads up to the shore. The ramp is bordered on the basinward edge by a ridge trending $S55^\circ E$. The ridge crest is highest (~ 5 m) nearshore, and decreases as it wraps around the basinward edge of the plateau (~ 1 m). The ridge ends where it meets the southeastern headland on the slope to the basin floor. In this area over the fan, a channel like feature is observed extending from the plateau out over the fan. This feature is linear, ~ 25 m across, and 1-2 m deeper than the plateau. The mouth of Glen Alpine Creek empties adjacent to the southeast of the plateau, headland, and channel. A small debris fan sits adjacent to the northwestern headland and spills slightly out onto the basin floor. Above this fan there are three scarps oriented $\sim N5^\circ W$. The scarps are $\sim 10-15$ m high.

IV - B. Seismic Stratigraphy

IV - B - 1. Fallen Leaf Lake

Here we present new CHIRP and core data that places important constraints on the long-term earthquake history in the LTB and how deformation is accommodated on the various segments of the WTDPF. In order to compare deposits between sub-basins, we will first describe the acoustic character of sediments in FLL. FLL lake sediments are divided into two major groups, Section I and Section II, based on their acoustic character. Section I is further subdivided into units A, B, and C (e.g., Brothers et al., 2009). Sub-horizontal, parallel reflectors characterize Section II; in contrast, Section I exhibit a distinct lenticular geometry. An additional sedimentary package is observed, Section III, which infills topographic lows in the northern basin.

We will describe the observed sequences from oldest to youngest. The acoustic basement (AB) is the basal layer imaged by the CHIRP data and the relief on this surface is shown in Figure 4. Little to no lacustrine sediment is observed on the steep basin walls. The depth to basement is greatest in the southern basin and shoals to the north. In the deepest areas, the AB is not visible in the CHIRP profiles, and thus the depth is a minimum estimate (Figure 4). The AB is hummocky throughout the basin, with several mounds and ridges forming complex topography. A large topographic high in the AB is located adjacent to prominent modern scarps observed on the southeast basin slope in bathymetry data (Figs. 3 & 4). The central basin winds north in a tortuous path and is interrupted by several features. A large mound at the center of the basin has a long axis that runs roughly N-S and the height tapers to the north (Figs. 4 & 5). Other topographic highs in the northern basin form ridges that extend across the basin trending roughly NW-SE. The ridges observed in

the AB relief map (Fig. 4) occur near the bathymetric ridges mapped along the eastern slope (Fig. 3). These features divide the basin into a southern and northern zone, and are hereafter referred to as the mid-lake moraines (Figs. 4 & 6). The southern zone is a deep basin with steeply sloping walls and isolated topographic highs. The northern zone is shallower, with more gently sloping walls and highly variable topography in the AB (Fig. 4). The shape of the AB in these two zones appears to control sediment dispersal and results in differential deposition between the northern and southern zones.

Section III is observed between the AB horizon and Section I north of the mid-lake moraines. This package is chaotic, with some wavy, high amplitude, discontinuous reflectors (Fig. 6). The package infills lows and thins onto highs in the AB topography of the northern basin, particularly around the mid-lake moraine complex. The upper contact of Section III is wavy and in some locations hummocky. Generally the unit is more chaotic near the base and systematically exhibits more acoustic reflectors towards the upper contact. There is a marked contrast between Section III and the more transparent units of Section I above. Section III was beyond the penetration depth for all sediment cores.

Section II is only observed in the southern zone of the basin and has a maximum thickness of >40 m. The section consists of parallel, continuous reflectors separating semi-transparent layers of varying thickness (Fig. 5, 6). Both high and low amplitude reflectors are observed within Section II with large thickness variability between reflectors. The high amplitude reflectors are vertically farther apart near the base of Section II and become more numerous and closely spaced near the upper contact (ranging from ~1 to several meter spacing). Where visible, the low amplitude reflectors are very closely spaced (decimeter scale). They appear to form clusters of closely spaced reflectors separated by

transparent units. In the deepest part of the basin, the reflectors remain mostly horizontal, except where offset by the WTDPF. The contact of the reflectors and the steep basin walls is generally a straight, lateral onlap. To the north, reflectors of Section II shoal, converge, and eventually onlap the AB as it slopes upward toward the mid-lake moraines (Fig. 6). The reflectors appear to maintain a constant amplitude signal throughout the southern basin.

The base of Section II was identified as the AB where visible, but it was beyond the penetration depth of the CHIRP in the deepest portions of the southern basin. The high amplitude upper contact of Section II cannot be confidently traced to the north because it onlaps a high in the mid-lake moraines. However, we do not observe a package of sediment with similar acoustic character anywhere north of the mid-lake moraines. Nevertheless, we cannot rule out that there may be a highly condensed unit of Section II that we grouped either with Section III or Section I. The upper contact of Section II marks a change in stratal geometry from flat lying beds below to lenticular shaped beds in Section I above (Fig. 5). This contact was recovered in core BC1A at 850 cm down-core where it is marked by a thin turbidite that we interpret to be laterally traceable to a slide deposit observed in CHIRP data (Fig. 7). The proximal expression of this slide is observed to the west in the CHIRP data at the upper contact of Section II (Fig. 5). The upper contact of Section II is placed directly below the turbidite. Lithologically, there is a change in sediment character below the turbidite into a 0.6 m interval of laminated silty clay. Below the laminated interval is a thin layer of bluish clay, below which is 0.6 m of glacial silt. The upper contact of Section II also marks a change in magnetic susceptibility, which is almost zero at the base of Section I, and increases downward in the laminated interval to $\sim 1 \times 10^{-4}$ SI in the glacial silt unit below the bluish clay layer (Fig. 7). We calculate the age of the upper contact of Section II to

be ~11.24-11.64 k.y. BP (95% confidence level) based on our age model with a median age of 11.44 k.y. BP (Table 2, Fig. 7).

Section I is divided into three units, separated by slide deposits; units A and B are separated by the MRE slide and units B and C are separated by the TA slide (Fig. 5). The slide deposits are easily identified in CHIRP data because they infill topographic lows associated with the lenticular deposits that characterize Section I. These topographic lows are observed on the lake floor adjacent to the steep walls and form moats (Fig. 3). The slides preferentially infill the moats, obscuring in part the relief, and are used as marker beds for correlation to sediment cores (Fig. 7). The units of Section I exhibit lateral variation in thickness across the basin. The maximum thickness of units A, B, and C is ~5.2 m, ~4.1 m, and ~7.3 m, respectively. All three units were recovered in piston cores (Fig. 7). Unit C is characterized by olive and yellow clay with banding partially disturbed by bioturbation. Unit B is characterized by yellowish olive clay with subtle banding and mottling. The lower section of unit A is similar in lithology to unit B, with an upper section characterized by homogenous olive mud (Fig. 7). The magnetic susceptibility of all three units tends to be near zero with intermittent spikes that often correlate to dark bands observed in the core sediments. In many cases, these spikes correspond to high-amplitude reflectors observed in CHIRP data; however, some spikes do not appear to correspond to obvious reflectors. Units A, B, and C exhibit similar acoustic character to one another. Each unit consists of variable thickness transparent layers separated by thin, continuous reflectors of low to high amplitude. Unit C contains more high amplitude reflectors than units A and B. To the north, the transparent packages for all units thin and the reflectors converge and decrease in amplitude (Fig. 6). Layers within units A, B, and C bend upwards

at basin slopes to onlap the AB horizon well above the lake floor (Fig. 5). This onlap morphology is most prominent on the eastern and western slopes, and appears more pronounced in units A and B than in unit C. In the southern basin, each unit exhibits a lenticular geometry that is thickest near the basin center and thins toward the eastern and western basin slopes (Brothers et al., 2009) (Fig. 5). The reflectors within each unit converge toward the eastern and western slopes where moats are observed in the bathymetry (Fig. 2). In some profiles, the reflectors appear truncated by slide deposits. The lenticular pattern does not extend to the northern basin. Instead, the units in the northern basin thin towards highs in topography and are fairly uniform in thickness moving east-west across the basin.

IV - B - 2. Cascade Lake

The acoustic character of the stratigraphic packages of CL is similar to that observed in FLL and allowed us to make a jump correlation between the two basins. The AB horizon is hummocky, with steep slopes on the southern, eastern, and western sides and a gentler slope up to the north. (Figs. 8 & 9). The deepest part of the basin is in the south. Based on the acoustic character, the stratigraphy can be divided into three sections that have similar character to Sections I, II, and III in FLL (Fig. 8). The oldest sedimentary unit, Section III, is chaotic and homogenous with some discontinuous and wavy low to high amplitude reflectors that infill lows and thin onto basement highs. In the deepest area of the basin, the uppermost part of Section III is represented by thinly spaced (decimeter scale), high amplitude, wavy, and mostly continuous reflectors that separate semi-transparent layers. The upper contact of Section III is a high-amplitude reflector that separates the thinly

spaced reflectors below from Section II above. Continuous, sub-parallel, high-amplitude reflectors that separate semi-transparent layers of variable thickness (~decimeter to meter scale) are characteristic of Section II. These beds thin onto highs in topography, but do not extend north beyond the southern depocenter. The high amplitude reflectors maintain a strong signal throughout the basin. Some thinly spaced (decimeter scale), low-amplitude reflectors are apparent within the semi-transparent layers (Fig. 8). The uppermost package, Section I, is divided into two units separated by the dashed line in Figure 8. The lower unit is characterized by semi-transparent layers that are separated by high amplitude reflectors. The reflectors become more closely spaced moving up-section. This unit was grouped with Section I rather than Section II because it drapes over highs in topography away from the southern depocenter, while Section II onlaps topographic relief and is restricted to the southern depocenter. Within Section I, the lower unit is separated from the upper unit by a high amplitude reflector that maintains acoustic strength throughout the basin. The upper unit of Section I is mostly transparent with numerous thinly spaced (decimeter scale), low amplitude reflectors (Fig. 8). These reflectors decrease in amplitude moving from south to north. A single high amplitude reflector is observed in the lower third of Section I that appears to correlate with the base of a slide deposit. This reflector decreases in amplitude away from the slide deposit.

Along the base of the southern slope we observe two major strands of the WTDPF that trend ~N30°W (Figs. 8 & 9). The trend of the southern strand appears to extend onshore to the east and correlates with the trace of the WTDPF scarp identified in LiDAR data (Fig. 2). Both strands produce offset of the lake floor, which increases down section to the basement. It is difficult to identify discrete offset of individual reflectors because of the

antecedent topography on the AB horizon. However, the maximum observed offset on the northern strand is ~6.7 m at the seafloor and ~21.2 m at the AB horizon. The maximum offset on the southern strand is ~7.5 m at the seafloor and ~17 m at the AB horizon. Offset of the southern strand could not be measured in every CHIRP profile due to the intersection with the steeply sloping southern basin wall. Horizons are generally horizontal, but may exhibit some deformation as they approach the fault. The two strands become less well pronounced to the northwest. In the northwestern most NE-SW trending CHIRP profile we do not observe two distinct fault strands with obvious normal displacement, but rather several strands that deform basin sediments (Fig. 9). Some strands in this line are characterized by chevron folds, while some exhibit normal displacement. This CHIRP profile is located on the western slope of CL and the steep topography may obscure significant offset of the basement observed in eastern profiles. The shallowest horizon deformed by these faults is a low amplitude reflector within Section I, which appears to correlate with a slide deposit (CLS1). We did not identify strong evidence for a scarp extending onshore to the west from CL in the LiDAR data (Fig. 2); the distributed nature of offset in CL, along with no focused fault scarp seen west of the lake, may represent the horse tailing of the WTDPF as it dies out to the west, toward EB.

IV - B - 3. Emerald Bay

We use the same acoustic character observations in FL and CL to identify the stratigraphy of EB (Fig. 10). In general, Section III is the oldest sediment that is characterized in large part by a chaotic acoustic character with some high amplitude wavy and discontinuous reflectors. The acoustic character of Section II is variably spaced low to

high amplitude reflectors between semi-transparent packages. Section I is mostly transparent with many low amplitude reflectors and a few higher amplitude reflectors. In EB, the reflectors of Section I generally decrease in amplitude from south to north; however, some locations show more lateral variation in acoustic amplitude.

Sediment core EB2 recovered from EB penetrated to a depth of ~5.3 m below the lake floor and three radiocarbon dates were determined (Table 1). We calculated a constant sedimentation rate of ~1 mm/yr between the youngest and oldest dated samples. The dates also suggest an increase in sedimentation rate with depth. Between the youngest samples, we calculate a sedimentation rate of ~0.98 mm/yr, but the time spanning the oldest samples gave a sedimentation rate as high as ~1.25 mm/yr.

In EB, the WTDPF is not observed in the CHIRP data (Figs. 10 & 11). Nevertheless, we do observe gas wipeout to the northeast of the island located in the southern part of the bay (Fig. 11). In a single profile, we observe acoustic reflectors diverging to the south, into a gas wipeout (Fig. 11). The diverging beds are not observed in the CHIRP lines to the north or south. The youngest horizon that exhibits rotation and divergence into the gas wipeout is Horizon 1. While the sediment package between Horizon 1 and Horizon 2 thickens toward the gas wipeout, Horizon 2 does not dip towards the south where it intersects the gas wipeout. Reflectors above Horizon 2 are sub-horizontal and do not slope towards the south.

VI - C. Event Deposits

IV - C - 1. Fallen Leaf Lake

We observe four recurring slide deposits in CHIRP data and sediment cores from FLL: the MRE slide, the TA slide, the ~11.5 ka slide, and the ~13 ka slide (Fig. 12). The MRE and TA slides are morphologically similar. Both consist of a proximal and a distal component that have a measurable thickness in CHIRP data (Fig. 13). The ~11.5 ka and ~13 ka slides do not have a distal component with a thickness that is resolved in the CHIRP data. Nevertheless, the ~11.5 ka distal slide was recovered in one piston core and both slides may have distal components represented by high amplitude reflectors. The proximal slides are identified in CHIRP as chaotic, homogenous units that disrupt previously deposited horizontal reflectors (Figs. 5 & 13). For these slides, we are able to identify the youngest acoustic horizons disrupted by the proximal slides. These horizons also correspond to the base of the associated distal component for the MRE and TA slides. In all cases, these are strong reflectors that can be traced throughout the basin. The reflectors representing the top of the MRE and TA distal slides are not as high-amplitude. However, we are able to trace them over much of the basin, providing thickness estimates for each deposit. The tops of the proximal slides were identified by a hummocky surface and a change from chaotic, homogenous units below to transparent laminated units above (Fig. 13). The bases of the proximal slides were not always apparent due to acoustic attenuation and scattering.

MRE Slide

The MRE slide in FLL was first identified and described by Brothers et al. (2009). They described the distal portion of the slide as a diverging unit that onlaps bathymetric highs, thickens into lows, and infills accommodation created during the MRE. The proximal slide sampled by a piston core is coarse-grained and contains several large pieces of wood

and twigs. With the addition of the newly collected, high-resolution CHIRP data we are able to map the extent of the proximal, massive slide deposits in more detail and calculate the thickness of the distal slide (Fig. 12). We observe two apparently synchronous proximal slide deposits located in the southwestern and southeastern corners of the lake. The maximum observed thickness of the proximal MRE slides is ~ 4.1 m, and they cover a total area of ~ 0.40 km². The youngest acoustic horizon disrupted by the MRE slide deposits is the MRE horizon. The proximal slides appear to grade into the distal slide, which lies on top of the MRE horizon (Figs. 5 & 13). The distal slide is transparent in CHIRP profiles and infills accommodation created by the MRE as well as other topographic lows (Fig. 5). The maximum thickness of the distal slide is ~ 2.0 m over the mapped extent (~ 2.08 km²) (Fig. 12). The calculated areal extent is based on where the thickness of the deposit was discernable in CHIRP data and is therefore likely an underestimate. The slide does extend beyond the area mapped in Figure 12 at least as far north as piston core BC3A, where it was recovered as a ~ 5 cm thick deposit. The horizon correlated to the base of the distal slide remains highly reflective throughout the basin indicating that the slide may cover the entire area of the basin.

The MRE distal slide mapped in CHIRP data was correlated to piston cores and radiocarbon dates were acquired for organic material bracketing the MRE slide in four different cores (core IDs BC3A, BC2D, BC1A, and PC3; Fig. 2). The conservative age range of the slide determined from these dates is 2890-5690 cal yrs BP, using the oldest and youngest modeled dates. The preferred age model, which is a composite model for all cores, constrains the age of the MRE slide to 4570-4850 Cal yrs BP (Fig. 14).

TA Slide

The TA slide is so named because it lies directly above the Tsoyowata ash marker bed. The Tsoyowata ash was recovered in piston cores BC1A and BC2D and was correlated to CHIRP data and mapped throughout the basin. The ash is 7700-8000 Cal yrs BP and was sourced from a Mount Mazama eruption (Bacon, 1983; Sarna-Wojcicki et al., 1991). In the piston cores, the distal portion of the TA slide was recovered directly on top of the Tsoyowata Ash. In CHIRP data, we observe both a massive, proximal slide and the associated distal deposits that were recovered in the cores (Fig. 5 & 13). The proximal slide is located in the southwestern area of FLL covering an area of $\sim 0.39 \text{ km}^2$ (Fig. 12). The chaotic deposit disrupts horizontal reflectors that are folded adjacent to the margin of the deposit. The youngest disrupted horizon is correlated to the TA deposit. Although the base of the proximal slide is not always visible due to acoustic scattering and attenuation, the distal margin of the slide disrupts $\sim 7.9 \text{ m}$ of previously deposited sediment. In some areas, the slide unit contains fragments of folded and tilted horizons. None of the sediment cores penetrated into the proximal section of the TA slide. We also image two local slides near the central basin that are deposited directly above the TA horizon (Fig. 12).

The distal portion of the TA slide is acoustically transparent and infills topographic lows (Fig. 5). The maximum thickness of the distal slide is $\sim 1.1 \text{ m}$ over the mapped extent ($\sim 1.37 \text{ km}^2$). As with the MRE slide, the TA distal slide may extend across the entire basin, but it is not resolved in the CHIRP data. The TA distal deposit was recovered as a $< 5 \text{ cm}$ deposit in the northernmost core BC3A, and the horizon corresponding to the base of the TA distal slide deposit remains highly reflective throughout the basin.

Modeled radiocarbon ages for the TA slide yield a conservative age range of 7060-7930 cal yrs BP and a preferred age range of 7620-7900 cal yrs BP (Fig. 14). These results

are based on dates from three piston cores bracketing the slide. The preferred model is a composite of dates from all three cores.

~11.5 ka Slide

The proximal slide is imaged in the CHIRP data covering $\sim 0.12 \text{ km}^2$ with a maximum thickness of $\sim 1.3 \text{ m}$ (Fig. 5, Fig. 12). This slide appears to have a distal component that reaches at least 550 m across the lake where it was recovered in core BC1A. The distal component is observed as a strong reflector in the CHIRP data, but the thickness is not determined because the layer is at or below the resolution of the system. This slide correlates to the top of Section II in CHIRP data and the age was previously mentioned to be $\sim 11.24\text{-}11.64 \text{ k.y. BP}$.

~13 ka Slide

The $\sim 13 \text{ ka}$ slide is observed in CHIRP data only as a massive, proximal slide deposit in the southern lake basin covering an area of $\sim 0.7 \text{ km}^2$ (Fig. 6, Fig. 12). A small slide is also observed along the western slope in the central basin, which may not be directly linked to the southern slide, but does appear synchronous (Fig. 12). In some areas, the top of the slide is not well defined by an acoustic reflector, but the base of the slide is often marked by a high-amplitude sub-horizontal reflector. The character of the deposit is chaotic and the slide disturbs previously deposited horizontal reflectors. The maximum slide thickness is $\sim 2.9 \text{ m}$. The $\sim 13 \text{ ka}$ slide is chaotic, and returns from within the deposit are of lower amplitude than those observed in MRE and TA proximal slides. Also, the MRE and TA slides are located at the base of the steep southern basin slope, whereas the $\sim 13 \text{ ka}$ slide is located near the center of the southern basin and along the western basin slope (Fig. 12). The youngest reflector that is disrupted by the slide lies below the depth of the deepest

penetrating piston core. This reflector can be traced throughout the basin. To date this horizon we calculated a sedimentation rate of $\sim 0.56\text{-}0.64$ mm/yr for sediments below the Tsoyowata ash in core BC1A. Using this sedimentation rate, and a nominal 1450 m/s sediment velocity, we extrapolate the age of the disrupted reflector to be $\sim 13.7\text{-}14.9$ k.y. BP (Table 2). An ~ 2 m transparent unit lies above the disrupted reflector and the slide extends upward into this unit. Therefore, the slide may be slightly younger than calculated because the traced reflector is located near the base of the slide.

Additional Slides

We observe several small, isolated slide deposits in northern CHIRP profiles (Fig. 6). These slides do not appear to have a distal component that is pervasive throughout the lake. Stratigraphy is highly condensed in northern lake sediments making it difficult to trace horizons continuously to the north. The slides are stratigraphically below the MRE and TA horizons and may correlate with the older slides observed in the southern basin. The slide deposits occur near a distinct transition in the seismic stratigraphy of the northern basin between homogenous, chaotic units below (Section III) and thinly bedded, acoustically transparent layers above (Section I). As such the northern slides may be correlated to one another. The combined area covered by these deposits is ~ 0.15 km².

IV - C - 2. Cascade Lake

We observe two major slide deposits in CL (Fig. 8). The youngest slide, CLS1, is located at the base of the steep southern basin slope. The slide lies south of the southern WTDPF strand and laterally between the two WTDPF strands. Slide CLS1 has a hummocky upper surface that contacts the transparent sediments of Section I. The slide covers an area

of $\sim 0.1 \text{ km}^2$ and reaches a maximum thickness of $\sim 2.1 \text{ m}$. CLS1 marks the uppermost high amplitude reflector of Section I. Even though the WTDPF makes direct tracing of this horizon difficult, we assume based on acoustic character, that the horizon north of the WTDPF corresponding to the slide is also the uppermost high amplitude reflector. This allows us to compare the age of the slide with slide CLS2. Slide CLS2 is made up of two apparently synchronous slides (Fig. 8). Both have similar acoustic characteristics and so are described as one. CLS2 is stratigraphically lower than CLS1, and is located north of both strands of the WTDPF in the depocenter of the lake. The slide is acoustically chaotic with a hummocky surface. It disturbs several horizons within Section II sediments. The uppermost horizon disturbed by CLS2 was used to determine the relative age of the slide. CLS2 covers $\sim 0.09 \text{ km}^2$ and has a maximum thickness of $\sim 3.8 \text{ m}$.

IV - C - 3. Emerald Bay

We observe two major slide deposits in sediments beneath EB (Fig. 10). The youngest slide, EBS1, has a hummocky upper contact with transparent to laminated units above and a maximum thickness of $\sim 4.5 \text{ m}$. The slide is acoustically chaotic, disturbs previously deposited horizons, and covers an approximate area of 0.06 km^2 . The uppermost horizon disturbed by EBS1 is a reflector that maintains a high amplitude signal throughout the basin, and corresponds to Horizon 1 in Figure 11. The slide is located in the central basin near the base of the gently northeast sloping AB horizon. The older slide, EBS2, is similar in character to EBS1 and is located slightly to the southeast (Fig. 10). The maximum thickness of slide EBS2 is $\sim 2.9 \text{ m}$ and it covers an area of $\sim 0.26 \text{ km}^2$.

By extrapolating below the bottom of sediment core EB2 using a 1 mm/yr sedimentation rate and accounting for potential overpenetration of up to 0.5 m, we date slide EBS1 as ~9.3-10.2 k.y. BP, and slide EBS2 as ~12.6-13.6 k.y. BP. Sedimentation rates most likely vary through time and appear to increase with depth in the lake sediments. Using the radiocarbon ages from core EB2 we calculate a sedimentation rate of ~1mm/yr between the two youngest dates and an increase in sedimentation rate up to ~1.2 mm/yr between the two oldest dates. Additionally, during the Tioga glacial period, glaciers would have eroded previously deposited sediments and ice would have been in contact with the CHIRP AB horizon. Greater than 25 m of sediment are observed above the AB horizon at the location of EB2. If the AB horizon represents the retreat of the last Tioga glacial period (~14 k.y. BP), this would require a faster sedimentation rate to account for over 25 m of sediment at this location. Furthermore, we observe an increase in sedimentation rate with depth in FLL sediments, and we expect these two basins to have somewhat similar patterns in sedimentation (Table 2). If we use the increased sedimentation rate of ~1.2 mm/yr below the bottom of core EB2, we obtain age ranges for EBS1 of ~8.7-9.4 k.y. BP, and for EBS2 of ~11.5-12.1 k.y. BP. These estimates also include uncertainty due to the possibility of up to 0.5 m of overpenetration of core EB2.

V. Discussion

V - A. Stratigraphic Interpretation

The Tioga glaciation, which lasted from ~24.5 to ~13.6 ¹⁴C yr BP, consisted of several cycles of glacial advance and retreat (Benson et al., 1998; Phillips et al., 2009). A series of arched terminal and recessional Tioga moraines bound FLL, CL, and EB to the

north (Saucedo et al., 2005). These moraines delineate the farthest advance of Tioga glaciation. The mid-lake moraine complex, mapped in FLL CHIRP data, was likely deposited during a stillstand in glacial retreat or a subsequent, less extensive advance. The ridges observed in the CHIRP AB horizon align with ridges observed in lake bathymetry and with mapped Tioga aged moraines onshore. These moraines created topography on the basin floor that has impacted sedimentation patterns in FLL.

We assume the glaciers that formed FLL, EB, and CL were in contact with the AB horizon during the Tioga glaciation. Therefore, the sedimentary packages above the AB horizon were deposited after the retreat of the glaciers from these lakes at the end of the Tioga glaciation, ~15.8-16.6 k.y. BP (Calibrated with OxCal 4.1.7 and IntCal 04). In FLL, the basin also records stalls in the glacial retreat as evidenced by the mid-lake moraines. Section III infills lows created by the mid-lake moraine complex (Fig. 6). We interpret these deposits as sub-glacial or pro-glacial outwash deposits. The chaotic and strongly reflective acoustic nature of these deposits is consistent with such a depositional scenario and suggests that they are coarse-grained and lack internal structure. Some horizons can be distinguished and may represent coarser material deposited as an outburst flood event (Uchupi and Ross, 2000). Section III is only observed north of the mid-lake moraines, but similar deposits may be beyond the penetration depth of the CHIRP data in the deep southern basin. We interpret Section III as the oldest sedimentary section deposited when the glacier extended to the mid-lake moraines.

Subsequent to deposition of Section III, the glacier retreated up the valley, and sedimentation of Section II began in the deep accommodation created by the glacier and the WTDPF in the southern basin. We interpret Section II as sediment carried by glacial

meltwater and deposited in a pro-glacial lake (Figs. 5, 6, & 7). Sedimentation rates were high during deposition of Section II as the rapidly melting glacier carried sediment to the basin. The age of the upper contact of Section II is ~11.4-12.3 k.y. BP and the maximum thickness of Section II is >40 m indicating an average sedimentation rate of >9 mm/yr. Furthermore, the onlap of layers within Section II on to basin slopes is flat and sub-horizontal, and horizons maintain a strong amplitude laterally throughout the section. This may indicate rapid deposition from glacial outburst floods. Section II sediments are not observed north of the mid-lake moraine complex, however it is possible that we are not able to separate a highly condensed Section II from Section I or III. These topographic highs may have acted as depositional barriers for sediments that mainly entered the basin from glacial melt in the Desolation Wilderness and Glen Alpine Creek to the south.

The upper contact of Section II appears to mark the transition from glacial deposits below to lacustrine sediments in Section I above. This transition was captured in core BC1A where we observe glacial silt and high magnetic susceptibility below the upper contact of Section II, and lacustrine sediments and low magnetic susceptibility above the upper contact of Section II (Fig. 7). In CHIRP data, a change from uniform thickness and flat onlap at basement highs to lenticular deposits that onlap high onto basement walls also suggests a change from glacial to lacustrine deposition (Fig. 5). The diminished amplitude of reflectors to the north indicates that the source of sediment for Section I is primarily from the south.

In CL and EB, we do not observe the lenticular pattern of Section I, but are able to identify the correlated sections based on acoustic character. Section I in EB and CL is primarily identified by characteristic onlap high at basin walls. Section I in these basins has

high-amplitude reflections near the base, but is mostly transparent in the upper sediments. As with Section I in FLL, we interpret these deposits to be lacustrine deposits. Section II and Section III are considered glacial deposits, similar to FLL. Section III is the older of the units and the entire sequence from Section III through Section II is interpreted to be a transition from sub-glacial, to proximal pro-glacial, to distal pro-glacial deposits.

Slide Deposits: Character

The slide deposits observed in FLL sediments are characteristic of debris flow and turbidite deposits. The MRE and TA slides are indicative of large proximal debris flow deposits with associated distal turbidites. The turbidite deposits are easily identifiable in FLL because they infill lows in topography created by scour and differential deposition observed in Sequence I. We only observe a proximal debris flow deposit associated with the ~11.5 ka and ~13 ka slides in the FLL CHIRP data. Both of these slides, however, correspond to a high amplitude reflector that maintains strength throughout the basin and may represent a distal deposit.

The MRE proximal slides appear sourced from the southeastern and southwestern corners of FLL (Fig. 12). While we do not observe evidence for well-defined deltas, these are both areas of water and sediment input to the lake. The southeastern slide is located near the Glen Alpine Creek input and the southwestern slide is located near several small, un-named creeks that drain from the steep slopes of Cathedral Peak (Fig. 2). The southwestern slide may be sourced from the small apron extending slightly onto the basin floor from the slope. Above the slope is a set of ridges that may be scarps from the MRE slide (Fig. 3). The large TA proximal slide also appears sourced from the southeastern area

of the lake near the Glen Alpine Creek input (Fig. 12). The southern source area for the MRE and TA slides is also adjacent to the WTDPF and the steepest basin wall slopes, where slide deposits triggered by an event on the fault would be expected. The two smaller proximal slides associated with the TA deposits are located near the Cathedral Creek input to the lake on the western shore (Fig. 12). The ~11.5 ka slide is sourced from the western slope, just south of the input from Cathedral Creek (Fig. 12). The ~13 ka slide extends throughout much of the southern basin. In the south, the source of the slide appears to be the southern slope, whereas to the north the source appears to be the western slope, near Cathedral Creek (Fig. 12). This suggests the ~13 ka slide may be two distinct slides that coalesce near the center of the southern basin. Several slides are sourced on the western slope near Cathedral Creek. This is directly below two slide deposits mapped onshore that lie adjacent to the WTDPF fault trace (Saucedo et al., 2005). In LiDAR data, the toe of the eastern slide is located on the footwall side of the fault trace (Fig. 2). The westernmost slide is larger and is deposited across the trace. We do not observe a distinct fault trace across the western slide deposit, so it appears that the slide occurred post-MRE. It is also possible that the slide was synchronous with the MRE, but we lack sufficient data to determine an age. We also cannot determine if these slides were synchronous with older slide deposits in FLL.

In EB, the slide deposits appear sourced from the northwestward sloping basin wall. This is toward the mouth of the bay. A slide is mapped onshore spilling into the southern part of EB (Saucedo et al., 2005, Fig. 2), but we do not observe a slide sourced from this area in the available CHIRP data. In CL, CLS1 appears sourced from the southern slope on the footwall of the WTDPF. CLS2 is deposited in the basin depocenter and appears sourced from both the northern and southern basin slopes. An onshore slide is also mapped at the

southernmost shore of CL (Saucedo et al., 2005). In LiDAR data the onshore slide is directly adjacent to the WTDPF on the footwall side of the trace (Fig. 2). With currently available data, it is difficult to determine if the onshore slide is related to any of the slides observed in the CHIRP data.

Slide Deposits: Timing

Age ranges for the slide deposits observed in FLL, EB, CL (this study), and Lake Tahoe (Smith et al., in press) are plotted in Figure 15. The dated slide deposits in EB and CL are considered estimates and more detailed radiocarbon dating is needed to confirm temporal correlations with slides in FLL and Lake Tahoe. While the ages of the EB and CL slides are considered speculative, we have much more confidence in slide deposit dates for FLL (Table 2).

The age model determined from new piston cores in FLL constrains the age range of the MRE slide to 4.57-4.85 k.y. BP. We suggest that the MRE slide in FLL is synchronous with the MRE on the WTDPF-FLS, and an event deposit in Lake Tahoe. The age range for the most closely synchronous Deposit F in Lake Tahoe is 4.07-4.51 k.y. BP. Deposit F in Lake Tahoe is characterized by a debris flow and multiple turbidites that appear to originate from, and are constrained to, the northern Lake Tahoe basin (Smith et al., in press). Despite the slight incongruity in ages, we suggest that Deposit F and the MRE slide in FLL were both triggered by the same seismic event on the WTDPF-FLS. The overlap in preferred age models between Deposit F and the MRE slide in FLL indicates that the age of this event is ~4.5 k.y. BP. Errors in the modeled age range of the MRE slide in FLL or

Deposit F in Lake Tahoe could be due to sparseness of dates in pre 2010 cores, uncertainty in model calculations, or non-uniform deposition rates at the sites.

Based on our current age constraints and correlation of depositional packages through seismic stratigraphy, no evidence of a MRE-related slide is observed in either EB or CL. Based on radiocarbon ages from core EB2 in EB, we infer that the uppermost transparent stratigraphic unit of EB and CL was being deposited earlier than ~5.3 k.y. BP. A major MRE-related slide event within in CL and EB would necessarily have to be found within this uppermost transparent unit, but are not observed in CL or EB seismic lines.

The age model for the TA slide in FLL constrains the age of the slide to 7.62-7.9 k.y. BP. In sediment cores, the distal component of the TA slide is observed directly above the Tsoyowata Ash deposit. The ash bed provides a distinct marker bed to correlate with other sub-basins. In Lake Tahoe, the age range for the synchronous Deposit J is 7.19-7.89 k.y. BP (Smith et al., 2011). Deposit J also overlays the Tsoyowata Ash in cores from Lake Tahoe and is characterized by multiple debris flows originating along the southwestern basin and a single turbidite deposit that extends to the central and northern basin (Smith et al., in press). Both the TA slide and Deposit J are characterized by large proximal slides relative to basin size and turbidite deposits that extend laterally throughout most of each basin.

Based on a comparison of the stratigraphy between FLL, Lake Tahoe, EB, and CL, it is possible that slides observed in EB or CL were synchronous with the TA slide and Deposit J. The stratigraphic horizon representing slide EBS1 appears to mark a transition in acoustic character. Below the slide, we observe alternating semi-transparent layers and high amplitude reflectors. Above the slide we observe a more transparent unit with low amplitude reflectors and a few high amplitude reflectors (Fig. 10). In Lake Tahoe, CHIRP

data interpreted by Smith et al. (in press) illustrates that Deposit J (7.19-7.89 k.y. BP) marks this same acoustic transition. In FLL, the transition to acoustically transparent units is less clear because we do observe several high-amplitude reflectors even in the youngest units. In the northern part of the basin, where the sedimentary section is more condensed, the transition to transparent units is more apparent. In the northern basin, unit C of Section I has several closely spaced, medium to high amplitude reflectors, while units A & B above have fewer, and lower amplitude reflectors. This difference between unit C and units A & B is also observed where the basement slopes up to the north near the mid-lake moraine complex (Fig. 6). In this area, unit C more closely resembles Section II below than units A & B above. The upper contact of unit C is the TA slide deposit. Based on the similar transitions in acoustic character in EB, FLL, and Lake Tahoe, slide EBS1 appears correlated with the TA slide in FLL and Deposit J in Lake Tahoe. This is a reasonable assumption given the estimated age of ~8.7-9.5 k.y. BP calculated from core EB2. A slightly greater increase in sedimentation rate than predicted would push the age of the slide towards the younger age of the TA slide.

Following this stratigraphic interpretation in CL, we interpret the youngest, strong reflector that can be traced basin-wide as the ~8 ka or TA horizon (dashed horizon in Fig. 8). This reflector is actually resolved as two closely spaced high-amplitude reflectors in some parts of the basin. This is consistent with the TA horizon in FLL CHIRP data. In FLL, two closely spaced high-amplitude reflectors are observed, which may define the ash layer, with a lower amplitude reflector above marking the top of the TA turbidite. Several closely spaced, high amplitude reflectors characterize the unit below this TA horizon in CL, similar to the EB stratigraphy. Using this correlation, slide CLS1 is younger than the TA slide, and

CLS2 is older than the TA slide. Nevertheless, we cannot rule out the presence of a slide associated with the TA horizon. There is some evidence that the youngest slide may obscure an older slide below (Fig. 8). This interpretation of the TA horizon results in a sedimentation rate of ~ 0.39 mm/yr for sediments above the TA in the deep southern basin. This would generate an age estimate for the younger slide of ~ 5.1 - 5.3 k.y. BP. This age is close to the age range of Deposit G in Lake Tahoe (5330-5600), which was associated with the age of a drowned tree near Baldwin Beach in Lake Tahoe and the MRE on the Rubicon Section of the WTDPF (Smith et al., in press).

The ~ 11.5 ka and ~ 13 ka slide age ranges are ~ 11.4 - 12.3 k.y. BP and ~ 13.7 - 14.9 k.y. BP, respectively. The ~ 11.5 ka slide is synchronous with Deposit O in Lake Tahoe, which was dated 11.20-12.49 k.y. BP (Smith et al., in press). Additionally, the lithostratigraphic evidence suggests the ~ 11.5 ka slide and Deposit O are synchronous. Both event deposits mark the transition between bluish glacial silt and organic laminae below to olive lacustrine silt and clay above. The turbidite component of Deposit O was mapped throughout Lake Tahoe above a major liquefaction feature, and the associated debris flow was mapped in the south-central part of the basin (Smith et al., in press). The older ~ 13 ka slide is observed within FLL glacial sediments of Section II. Although deposits older than Deposit O were identified in Lake Tahoe, dates were not determined for these slides and we therefore cannot correlate the ~ 13 ka slide to a slide in Lake Tahoe.

We can also estimate the ages of the older slides in EB and CL based on calculated sedimentation rates and stratigraphic correlations. In EB, the previously estimated age of EBS2 is ~ 11.5 - 12.1 k.y. BP, which correlates with the ~ 11.5 ka slide in FLL and Deposit O in Lake Tahoe. The stratigraphy also suggests this horizon may mark a transition from glacial

sediments below to lacustrine sediments above, providing further evidence that the slide is synchronous with the ~11.5 ka slide and Deposit O. If the younger slide is ~8 ka and the older slide is ~12 ka in EB, this yields a sedimentation rate between the two slides of ~0.8 mm/yr. This rate is lower than rates determined for younger sediments in EB, and therefore does not appear reasonable because we would expect faster sedimentation rates for older sediments. This suggests that either our assumption of increasing sedimentation rates is incorrect, or our stratigraphic correlation is incorrect. An alternative interpretation would be that the transition to glacial sediments is deeper than EBS2, which would make EBS2 younger than the ~11.5 ka slide and Deposit O (solid circles and lines in Fig. 15). It is also plausible that EBS2 does represent the transition to glacial sediments, which would indicate that the age of EBS1 is slightly older than the TA slide and Deposit J (hollow circles and dashed lines in Fig. 15). Longer piston cores and more detailed radiocarbon dating are necessary to constrain further the ages of EB slide deposits.

In CL, CLS2 appears synchronous with a transition in seismic stratigraphy. Deposits above the slide horizon appear to drape high onto basin walls, whereas sediments below the horizon are observed only in topographic lows with slight onlap onto basin highs. We interpreted this change to represent the transition from glacially derived sediment input to more pelagic, lacustrine sedimentation. A similar shift is observed in FLL stratigraphy associated with the top of Section II and the ~11.5 ka slide. Assuming our pick for the TA horizon in CL is correct, and CLS2 is synchronous with the ~11.5 ka slide in FLL, we calculate a sedimentation rate between the TA horizon and CLS2 of 0.38-0.44 mm/yr. This range is reasonable given the sedimentation rate of ~0.39 mm/yr previously calculated for sediments younger than the TA horizon.

Slide Deposits: Triggering

Several potential triggering mechanisms for the Tahoe Basin slide deposits exist. These include lake level fluctuations, storms, and earthquakes. There is evidence that FLL has experienced significant droughts and undergone major changes in lake level during the mid- to late- Holocene. These droughts may have occurred every 650-1150 yrs (Kleppe et al., 2011). Submerged paleo-shorelines and upright and rooted trees observed below the lake surface suggest that lake level may have dropped 40-60 m below present elevation during the late Holocene (Kleppe et al., 2011). The region has also experienced longer-term climatic variability throughout the Holocene (Benson et al., 2002), which may have impacted FLL sedimentation patterns and induced lake level fluctuations. Significant drops in lake level may trigger landslides by exposing upper slope deposits to wave action and shifting the location of water and sediment input. Although lake level has fluctuated greatly in FLL, we do not think the MRE and TA slides were triggered by this mechanism. The submerged trees in FLL are dated ~1250 AD (Kleppe et al., 2011), but we do not observe major slide events in the uppermost sediments of FLL. Additionally, lake level fluctuations likely have occurred with a much shorter recurrence interval than the recurrence interval observed for slides in FLL. This evidence, together with coincident slides in Lake Tahoe, suggests a regional trigger for the slides observed in FLL.

Storms are another potential triggering mechanism for slides in FLL. Storms may be associated with flooding and increased sediment input to the lake as well as wave erosion and loading in shallow water. Flooding associated with storms may cause hyperpycnal flows, rapid accumulation, oversteepening, and pore pressure loading near stream mouths,

all of which may lead to failures. Furthermore, waves associated with storms may erode nearshore sediment and generate hyperpycnal flows, or may increase pore pressure and weaken slopes due to loading. As with lake level fluctuations, we anticipate the recurrence interval of major storms to be much shorter than the interval determined for FLL slide deposits.

Seismic triggering is also a potential cause of the slides observed beneath FLL. Earthquakes may trigger slides by strong shaking, increased pore pressure due to ground motion, gas escape, and down-drop of the hanging wall that influences slope stability and lake level. We do not observe direct evidence for gas in FLL in CHIRP or bathymetry data. We do, however, observe gas wipeout of CHIRP data in EB and Lake Tahoe. The WTDPF is directly identified beneath FLL and CL and presumably extends (and dies) into southern EB as evidenced by localized diverging beds. In FLL and CL, the WTDPF scarp creates a steep basin slope that would be susceptible to earthquake associated slope destabilization. The source area for the MRE, TA, and ~13 ka slides appears to be the steep WTDPF scarp that forms the southern basin wall. We confirm the observation by Brothers et al. (2009) that the MRE fills accommodation created by the MRE on the FLL section of the WTDPF. Additionally, the MRE horizon is the youngest horizon disrupted by the MRE proximal slide. These stratigraphic relationships suggest that the MRE slide was triggered by an earthquake. The correlation of direct evidence (offset of the MRE horizon) and indirect evidence (MRE slide) make a convincing case for earthquake-triggered slides in FLL. We extend this logic to the TA slide. The morphology, source area, and extent of the TA slide are very similar to the MRE slide. Furthermore, the TA slide is correlated to a significant slide in Lake Tahoe and possibly EB and CL. Although we lack primary evidence of offset on

the fault beneath FLL, the TA horizon appears to diverge slightly toward the southern splay of the WTDPF. Additionally, the potentially synchronous slide in EB does appear correlated with horizons diverging towards the WTDPF (Fig. 11).

In summary, we infer that the MRE and TA slides were triggered by an earthquake in the Lake Tahoe Basin for the following reasons: 1. The MRE and TA slides appear sourced from the steep slope above the trace of the WTDPF. 2. The observed slide recurrence interval of ~3-4 k.y. is much longer than expected for storm or lake level fluctuation triggers. 3. The coincident timing of deposits between basins suggests triggering by a regional, rather than local event. 4. We observe primary and secondary earthquake evidence for the MRE.

While the evidence is less robust for the ~11.5 ka slide, we speculate that this slide was also triggered by an earthquake. The ~11.5 ka slide appears synchronous with Deposit O in Lake Tahoe and possibly with slides in CL and EB. The ~11.5 ka slide is smaller than the MRE and TA slides, but this may reflect the short time period after the ~13 ka slide, which could have re-set slope stability around the lake. Additionally, the slide occurred near the transition from glacial sediments to lacustrine sediments, so we cannot rule out triggering by flooding. The ~13 ka slide was deposited within glacial sediments and does not appear correlated to slides in other sub-basins. Therefore, this slide was more likely triggered by local forces such as a glacial outburst flood (e.g., jokulhlaup).

We also observe a slide and deformation along the WTDPF estimated to be ~5.2 k.y. BP in CL. This age estimate is highly speculative and therefore we cannot confirm temporal correlation between this event and other basins. However, Smith et al. (in press) did date the MRE on the Rubicon section of the WTDPF and a slide deposit ~5.3-5.6 k.y. BP.

Paleoseismic Implications

The slide deposits observed in the sub-basins of the LTB provide secondary evidence for seismic events as old as ~11.5 k.y. BP and can be used to calculate a recurrence interval for basin-wide shaking events. The interval between the MRE and TA event is ~3.1 k.y. and the interval between the TA event and the ~11.5 ka event is ~3.7 k.y. Therefore, we calculate a closed recurrence interval for the two slide events in FLL of ~3.4 k.y.; if the most recent open interval is included, then a recurrence time of 3.8 k.y. is calculated along the WTDPF-FS. Given these three slides were likely triggered by earthquakes, one might be tempted to also include the ~5.3 k.y. Rubicon event, which reduces the recurrence interval to ~2.9 k.y. for events on the WTDPF, irrespective of whether the event was confined to one segment or ruptured across several. In either case, the MRE occurred ~4.5 k.y. BP indicating that the WTDPF is well beyond its characteristic earthquake cycle and can be considered “overdue” for a major seismic event. In addition to the direct hazard posed by an earthquake in the Lake Tahoe basin, seismically triggered slides also pose a threat due to the potential to generate seiche waves. We have shown a correlation between coseismic deformation and submarine slides in both EB and FLL providing strong evidence for earthquake-triggered slides in the Lake Tahoe Basin.

The slide deposits and observed primary deformation also may help constrain rupture patterns in the Lake Tahoe Basin. We observe primary and/or secondary evidence for four potential seismic events in sediments beneath FLL, CL, EB, and Lake Tahoe (Fig. 16). The MRE on the FLL section of the WTDPF is dated ~4.57-4.85 k.y. BP based on the age of co-seismic slide deposits. We suggest that Deposit F in northern LT, with a modeled age

of 4.07-4.51 k.y. BP (Smith et al., in press) was deposited during the same seismic event, and the overlap of these 2 ages constrains the event to be ~4.5 k.y. BP. In CL, we may observe both primary and secondary evidence of an ~5.2 k.y. event. This is roughly correlated to the MRE on the WTDPF-RS and a slide deposit in Lake Tahoe dated ~5.3-5.6 k.y. BP (Smith et al., in press). We observe multiple lines of evidence for an event on the WTDPF at ~8 k.y. in Lake Tahoe (Smith et al., in press), FLL (this study), and potentially EB and CL (this study). Finally, we observe only secondary evidence for an event ~11.5 k.y. BP. This event is represented by slides in Lake Tahoe (Smith et al., in press) and FLL (this study), and potentially CL (this study).

We have mapped the WTDPF-FLS in CHIRP and LiDAR extending from southern FLL to CL. Diverging beds in EB also suggest that this segment may continue and die into EB in a disorganized way. The WTDPF-RS is mapped along the steep western slope of LT all the way to the change in shoreline azimuth just north of EB (Fig. 2). This step between the FLS and RS is ~2 km as mapped in Figure 2. This is a reasonable distance for rupture propagation across the stepover. In strike-slip settings, ruptures have been shown to propagate across steps of up to 3-4 km (Wesnousky, 2006).

The geographic distribution of slides illustrated in Figure 16 may suggest that the entire basin experienced shaking ~11.5 k.y. BP and ~8 k.y. BP, which might be due to rupture of all three segments of the WTDPF. Although speculative, the younger events, however, may reflect segmented rupture. The ~5.3-5.6 k.y. event on the Rubicon section may have only ruptured the northern and central segments of the WTDPF, while a ~4.57-4.85 k.y. BP event may have ruptured only the FLL segment of the WTDPF. Nevertheless, the alternative also needs to be considered – that is, rupture of even one segment of the

WTDPF might generate sufficient ground motion to trigger failures basin-wide. For example, the MRE slide on the FLL section of the WTDPF might have triggered a slide as far away as the northern part of Lake Tahoe. Clearly additional work is warranted to understand how the segments of the WTDPF accommodate deformation whether they rupture in concert or alone.

Conclusions

Coincident slides in FLL, Lake Tahoe, and perhaps CL and EB suggest earthquake shaking as the most plausible triggering mechanism. The geographic distribution of the slide events and primary offset evidence further suggests that the WTDPF may sometimes rupture in segments, and other times along the entire length of the fault. The recurrence time for events, including the open interval on the WTDPF is ~2.9 k.y. As such, given the MRE is ~4.5 k.y.BP, the WTDPF is well beyond its characteristic earthquake cycle and appears “overdue” for a large magnitude event. The next event may rupture only the FLL or Rubicon/Dollar Point sections of the fault, or may rupture the entire length of the fault. Our research indicates that the WTDPF represents a significant geohazard for the Lake Tahoe Basin.

Acknowledgements

Research highlighted in this manuscript was supported by USGS NEHRP grants 10HQPA1000, 06HQGR0064 and 02HQGR0072. We wish to express our thanks to Brig Ebright for his permission to allow us to conduct research on Cascade Lake, and to Paul Baker for access to a critical boat ramp on his property. We are also indebted to Fire Chief Gary Gerren for access to the Fallen Leaf Lake boat ramp and invasive species boat wash.

The 2010 multibeam survey would have been impossible without the generous support of Bill Craven and access to his work boat. We also thank Shane Romsos and Tahoe Regional Planning Agency for access to the critical airborne LiDAR data collected in 2010. Lastly, we thanks Danny Brothers for conversations regarding previously collected CHIRP profiles and sedimentary cores.

References

- Argus, D. F., and Gordon, R. G., 2001, Present tectonic motion across the Coast Ranges and San Andreas fault system in central California: *Bulletin of the Geological Society of America*, v. 113, no. 12, p. 1580-1592.
- Bacon, C. R., 1983, Eruptive history of Mount Mazama and Crater Lake Caldera, Cascade Range, USA: *Journal of Volcanology and Geothermal Research*, vol. v. 18, p. 1-4.
- Bennett, R. A., Wernicke, B. P., Niemi, N. A., Friedrich, A. M., and Davis, J. L., 2003, Contemporary strain rates in the northern Basin and Range Province from GPS data: *Tectonics*, v. 22, p. no.2, 31.
- Benson, L., Kashgarian, M., Rye, R. O., Lund, S. P., Paillet, F. L., Smoot, J. P., Kester, C. L., Mensing, S., Meko, D., and Lindstrom, S., 2002, Holocene multidecadal and multicentennial droughts affecting Northern California and Nevada: *Quaternary Science Reviews*, v. 21, no. 4-6, p. 659-682.
- Benson, L. V., May, H. M., Antweiler, R. C., Brinton, T. I., Kashgarian, M., Smoot, J. P., and Lund, S. P., 1998, Continuous Lake-Sediment Records of Glaciation in the Sierra Nevada between 52,600 and 12,500 Radiocarbon yrs B.P.: *Quaternary Research*, v. 50, p. 113-127.
- Bronk Ramsey, C., 2001, Development of the Radiocarbon Calibration Program: *Radiocarbon*, v. 43, no. Nr 2A, p. 355-363.
- , 2009, Bayesian Analysis of Radiocarbon Dates: *Radiocarbon*, v. 51, no. 1, p. 337-360.
- Brothers, D. S., Kent, G. M., Driscoll, N. W., Smith, S. B., Karlin, R., Dingle, J. A., Harding, A. J., Seitz, G. G., and Babcock, J. M., 2009, New constraints on deformation, slip rate, and timing of the most recent earthquake on the West Tahoe-Dollar Point Fault, Lake Tahoe Basin, California: *Bulletin of the Seismological Society of America*, v. 99, no. 2A, p. 499-519.
- Dingle, J., Kent, G., Driscoll, N., Babcock, J., Harding, A., Seitz, G., Karlin, B., and Goldman, C., 2009, A high-resolution seismic CHIRP investigation of active normal faulting across Lake Tahoe basin, California-Nevada: *Geological Society of America Bulletin*, v. 121, no. 7-8, p. 1089-1107.
- Dixon, T. H., Miller, M., Farina, F., Wang, H., and Johnson, D., 2000, Present-day motion of the Sierra Nevada block and some tectonic implications for the Basin and Range Province, North American Cordillera: *Tectonics*, v. 19, no. 1, p. 1-24.
- Faulds, J. E., Henry, C. D., and Hinz, N. H., 2005, Kinematics of the northern Walker Lane: An incipient transform fault along the Pacific-North American plate boundary: *Geology*, v. 33, no. 6, p. 505-508.

- Gardner, J. V., Mayer, L. A., and Hughs Clarke, J. E., 2000, Morphology and processes in Lake Tahoe (California-Nevada): Bulletin of the Geological Society of America [Bull. Geol. Soc. Am.]. Vol. v. 112, no. 5, p. 736-746.
- Hammond, W. C., and Thatcher, W., 2004, Contemporary tectonic deformation of the Basin and Range Province, Western United States; 10 years of observation with the Global Positioning System: Journal of Geophysical Research, v. 109, p. no.B8, 21.
- Hampton, M. A., Lee, H. J., and Locat, J., 1996, Submarine landslides: Reviews of Geophysics, v. 34, no. 1, p. 33-59.
- Henkart, P., 2003, SIOSEIS software. Scripps Institution of Oceanography, La Jolla, California. <http://sioseis.ucsd.edu>.
- Hyne, N. J., Chelminski, P., Court, J. E., Gorsline, D. S., and Goldman, C. R., 1972, Quaternary History of Lake Tahoe, California-Nevada: Geological Society of America Bulletin, v. 83, no. 5, p. 1435-1448.
- Karlin, R., Noble, P. J., Zimmerman, S. H., Stratton, L., Smith, S. B., Kent, G., Maloney, J., and Driscoll, N. W., 2011, BOLLY Project - Preliminary Multi-Proxy Data from Holocene Cores, Fallen Leaf Lake, Tahoe Basin, California, USA, Abstract 189-33, presented at 2011 GSA Annual Meeting, Minneapolis, Minnesota, 9-12 October.
- Karlin, R. E., Smith, S., Seitz, G. G., Kent, G. M., Driscoll, N. W., Anderson, J. G., and von Seggern, D., 2005, Landslides, active faulting, and paleoseismicity in Lake Tahoe: Seismological Research Letters, v. 76, no. 2, p. 250.
- Kent, G. M., Babcock, J. M., Driscoll, N. W., Harding, A. J., Dingler, J. A., Seitz, G. G., Gardner, J. V., Mayer, L. A., Goldman, C. R., Heyvaert, A. C., Richards, R. C., Karlin, R., Morgan, C. W., Gayes, P. T., and Owen, L. A., 2005, 60 k.y. record of extension across the western boundary of the Basin and Range province: Estimate of slip rates from offset shoreline terraces and a catastrophic slide beneath Lake Tahoe: Geology, v. 33, no. 5, p. 365-368.
- Kleppe, J. A., Brothers, D. S., Kent, G. M., Biondi, F., Jensen, S., and Driscoll, N. W., 2011, Duration and severity of Medieval drought in the Lake Tahoe Basin: Quaternary Science Reviews, v. 30, p. 3269-3279.
- Lee, H. J., Greene, H. G., Edwards, B. D., Fisher, M. A., and Normark, W. R., 2009, Submarine landslides of the Southern California Borderland: Special Paper - Geological Society of America, v. 454, p. 251-269.
- Oldow, J. S., 2003, Active transtensional boundary zone between the western Great Basin and Sierra Nevada block, Western U.S. Cordillera: Geology, v. 31, no. 12, p. 1033-1036.
- Ramelli, A. R., Bell, J. W., dePolo, C. M., and Yount, J. C., 1999, Large-magnitude, late Holocene earthquakes on the Genoa Fault, west-central Nevada and eastern California: Bulletin of the Seismological Society of America, v. 89, no. 6, p. 1458-1472.
- Reimer, P. J., Baillie, M. G. L., Bard, E., Bayliss, A., Beck, J. W., Bertrand, C. J. H., Blackwell, P. G., Buck, C. E., Burr, G. S., Cutler, K. B., Damon, P. E., Edwards, R. L., Fairbanks, R. G., Friedrich, M., Guilderson, T. P., Hogg, A. G., Hughen, K. A., Kromer, B., McCormac, G., Manning, S., Ramsey, C. B., Reimer, R. W., Remmele, S., Southon, J. R., Stuiver, M., Talamo, S., Taylor, F. W., van der Plicht, J., and Weyhenmeyer, C. E., 2004, IntCal04 terrestrial radiocarbon age calibration, 0-26 cal kyr BP: Radiocarbon, v. 46, no. Nr 3, p. 1029-1058.

- Sarna-Wojcicki, A. M., Lajoie, K. R., Meyer, C. E., Adam, D. P., and Rieck, H. J., 1991, Tephrochronology correlation of upper Neogene sediments along the Pacific margin, conterminous United States, *in* Morrison, R. B., ed., Quaternary Non-Glacial Geology: Conterminous United States, *in* The Decade of North American Geology, Volume K-2, Geological Society of America, Boulder, Colorado, p. 117-140.
- Saucedo, G. J., Little, J. D., Watkins, S. E., Davis, J. R., Mascorro, M. T., Walker, V. D., and Ford, E. W., 2005, Geologic map of the Lake Tahoe Basin, California and Nevada.
- Schnellmann, M., Anselmetti, F. S., Giardini, D., McKenzie, J. A., and Ward, S. N., 2002, Prehistoric earthquake history revealed by lacustrine slump deposits: *Geology*, v. 30, no. 12, p. 1131-1134.
- Schweickert, R. A., Lahren, M. M., Smith, K. D., Howle, J. F., and Ichinose, G. A., 2004, Transtensional deformation in the Lake Tahoe region, California and Nevada, USA: *Tectonophysics*, v. 392, no. 1-4, p. 303-323.
- Seitz, G., Kent, G., Smith, S., Dingler, J., Driscoll, N., Karlin, R., Babcock, J., Harding, A., Prentice, C., Ellsworth, W., and Hellweg, P., 2006, Multi-method paleoseismology; combining on and offshore data to build a basin wide record of earthquakes at Lake Tahoe: *Seismological Research Letters*, v. 77, no. 2, p. 274.
- Seitz, G. G., Kent, G. M., Dingler, J. A., Karlin, B., Turner, R., Anderson, J. G., and von Seggern, D., 2005, First paleoseismic results from the Lake Tahoe basin; evidence for three M 7 range earthquakes on the Incline Village Fault: *Seismological Research Letters*, v. 76, no. 2, p. 239-240.
- Smith, S. B., Karlin, B., Seitz, G., Kent, G., and Anonymous, 2006, Seismically-induced landslides, debris flows, and turbidites in Lake Tahoe: Abstracts with Programs - Geological Society of America, v. 38, no. 7, p. 549.
- Smith, S. B., Karlin, R. E., Kent, G., Seitz, G., and Driscoll, N. W., 2011, Holocene Submarine Paleoseismology of Lake Tahoe: submitted.
- Strasser, M., Anselmetti, F. S., Faeh, D., Giardini, D., and Schnellmann, M., 2006, Magnitudes and source areas of large prehistoric northern Alpine earthquakes revealed by slope failures in lakes: *Geology*, v. 34, no. 12, p. 1005-1008.
- Surpless, B. E., Stockli, D. F., Dumitru, T. A., and Miller, E. L., 2002, Two-phase westward encroachment of Basin and Range extension into the northern Sierra Nevada: *Tectonics*, v. 21, p. no. 1, 13.
- Svarc, J. L., Savage, J. C., Prescott, W. H., and Ramelli, A. R., 2002, Strain accumulation and rotation in western Nevada, 1993-2000: *Journal of Geophysical Research*, v. 107, p. no.B5, 13.
- Uchupi, E., and Ross, D. A., 2000, Early Holocene marine flooding of the Black Sea: *Quaternary Research*, v. 54, no. 1, p. 68-71.
- Unruh, J., Humphrey, J., and Barron, A., 2003, Transtensional model for the Sierra Nevada frontal fault system, eastern California: *Geology*, v. 31, no. 4, p. 327-330.
- Upton, P., and Osterberg, E. C., 2007, Paleoseismicity and mass movements interpreted from seismic-reflection data, Lake Tekapo, South Canterbury, New Zealand: *New Zealand Journal of Geology and Geophysics*, v. 50, no. 4, p. 343-356.
- Wesnousky, S. G., 2006, Predicting the endpoints of earthquake ruptures: *Nature*, v. 444, p. 358-360.

Figure Captions

Figure 1: A. Map of the Lake Tahoe Basin and surrounding area showing generalized fault traces of the West Tahoe-Dollar Point Fault (WTDPF), Stateline-North Tahoe Fault (SNTF), and Incline Village Fault (IVF). Three segments of the WTDPF are also labeled: the northern Dollar Point Section (DPS), central Rubicon Section (RS), and southern Fallen Leaf Section (FLS). WTDPF segment divisions and fault traces modified from Brothers et al. (2009). B. Regional plate boundary map showing location of the San Andreas Fault (SAF), Walker Lane Belt (WLB), Sierra Nevada Range (SN), and the Great Basin (GB). The Lake Tahoe Basin is located within the northwestern WLB.

Figure 2: Map of the southern Lake Tahoe Basin including the sub-basins Emerald Bay, Cascade Lake, and Fallen Leaf Lake. Bathymetry of Lake Tahoe and Emerald Bay is from Gardner et al. (2000) retrieved from (U.S.G.S., 2011). The WTDPF is mapped as a red line that is dashed where inferred. Trace of the WTDPF beneath Lake Tahoe is from Brothers et al. (2009) and Dingler et al. (2009). Topography is from aerial LiDAR surveys (TRPAWS, 2011). Bathymetry and topography are 1 m grids shaded from an azimuth of 315° and elevation of 45°.

Abbreviations: Angora Lakes (AL), Cascade Creek (CsC), Cathedral Lake (CtL), Cathedral Creek (CtC), Eagle Lake (EL), Eagle Creek (EC), Gilmore Lake (GL), Glenn Alpine Creek (GAC), Mt. Tallac (MT), Snow Lake (SL), and Taylor Creek (TC).

Figure 3: A. Hillshaded bathymetry of Fallen Leaf Lake from the 2010 multibeam survey with 10 m contours from -10 m to -110 m. Depths are below the USGS 1944 m lake level.

Solid gray areas between the bathymetry and lakeshore are areas of no data. B. Hillshaded bathymetry without contours to highlight lakefloor features. Also shown are Cathedral Creek (CtC) and Glen Alpine Creek (GAC) inputs to the lake. Labeled features are described in detail in the text. For both figures, the topography is from aerial LiDAR surveys. Bathymetry and topography are 1 m grids shaded from an azimuth of 315° and elevation of 45°.

Figure 4: Topography of the Acoustic Basement (AB) traced in and gridded between CHIRP profiles. Labeled features are discussed in the text.

Figure 5: E-W CHIRP profile showing distal MRE slide (yellow), distal TA slide (blue), ~11.5 ka slide (green), and ~13 ka slide (pink). The MRE horizon is at the base of the MRE slide complex (~4.57-4.85 k.y. BP) and the base of the TA slide is the TA horizon (~7.6-7.9 k.y. BP). This profile also illustrates the sedimentary packages defined in the text. Section II, Section I, and Section I sub-units A, B, and C are labeled. The topographic high in the AB at the center of the profile is oriented N-S and tapers in height to the north. The blowup near Core 1A is shown in Figure 7.

Figure 6: N-S trending CHIRP profile showing variability in character of sediment packages between the northern and southern parts of the basin, separated by the mid-lake moraines. The base of Section I is marked in white, the TA horizon is marked in blue, and the MRE horizon is marked in yellow. The MRE distal slide is also colored in yellow where resolved. Section II is below Section I to the south of the mid-lake moraines, and Section III to the

north. Section I is divided into units A, B, and C. On the slope up towards the mid-lake moraines reflectors converge and layers thin. This is also the area where highly reflective layers below the TA horizon and more transparent units above are observed. The location and penetration depth of piston cores 2D, 4, and 3A are illustrated.

Figure 7: Blow-up section from Figure 5 CHIRP profile correlated to sediment core BC1A. The three slide deposits observed in the core are easily identified in the CHIRP data and were used to correlate the core to the CHIRP imagery. The three slides are the MRE slide (yellow), TA slide (blue), and ~11.5 ka slide (green). See inset legend for detailed core lithology. Magnetic susceptibility is displayed to the right of the core log.

Figure 8: NE-SW trending CHIRP profile from Cascade Lake illustrating two strands of the WTDPF (solid black lines), slide deposits, and acoustic character of the lake stratigraphy. Offset on the two WTDPF strands is measured at the seafloor and the basement at locations indicated (a-a', b-b', c-c', and d-d'). The dashed horizon is interpreted to be synchronous with the TA horizon in FLL and Lake Tahoe based on acoustic character. Section boundaries are marked in solid white.

Figure 9: Three-dimensional CHIRP fence diagram from Cascade Lake looking west. Strands of the WTDPF are dashed in red. The WTDPF appears as two distinct strands in the eastern and central basin with obvious vertical offset. In the westernmost profile, however, the faults become more distributed with evidence of transtensional deformation.

Figure 10: NE-SW CHIRP profile from Emerald Bay showing acoustic character of the sequences and slide deposits. The dashed line corresponds to Horizon 1 in Fig. 11. Location and approximate penetration depth of piston core EB2 is also shown. Solid white lines mark Section boundaries. In the southern basin, Section II and III are differentiated because a distinct boundary is not identified. The depth to acoustic basement (AB) is also not identified in the southern basin. The estimated age of EBS1 is ~8.7-9.4 k.y. BP, and the estimated age of EBS2 is ~11.5-12.1 k.y. BP.

Figure 11: SW-NE trending CHIRP profile beneath EB images diverging beds. Horizon 1 is correlated to the dashed horizon in Fig. 10. Above Horizon 2, divergence is not observed. The basement at the far left of the profile slopes up to the island in EB.

Figure 12: Mapped location of slide deposits: A. MRE Slide, B. TA Slide, C. ~11.5 ka Slide, D. ~13 ka Slide.

Figure 13: N-S trending CHIRP profile showing proximal MRE and TA slides. Also highlights sedimentation pattern over southern AB topographic high showing drape over the top of the high starting at the TA horizon.

Figure 14: The modeled event ages of the MRE Slide (a) and the TA Slide (b). The probability distribution for each radiocarbon date is shown in gray, the modeled dates for individual cores are white, and the combined preferred model is shown in red.

Figure 15: Plot showing timing of direct (fault offset) and indirect (slide deposits) evidence for earthquakes in LT, FLL, EB, and CL. Where evidence is correlated across basins, the symbols are color coded by event age (see legend). Gray symbols represent evidence not correlated across multiple basins. The age ranges for observed direct earthquake deformation on the FLS and RS of the WTDPF are highlighted in gray and marked with a triangle. Proposed events based on synchronous slides across basins are also shaded gray. All Lake Tahoe slides are modeled event dates with name convention from Smith et al. (in press). The two youngest FLL slides are modeled event dates. The age range of the two oldest slides was calculated by extrapolating a constant sedimentation rate below the Tsoyowata Ash. Two models of Emerald Bay event age ranges are shown. The solid symbols represent ages based on stratigraphic interpretation where EBS1 is synchronous with the FLL TA slide and assigned the same age range of 7.6-7.9 k.y. BP. The EBS2 age is calculated based on a sedimentation rate of 1-1.2 mm/yr below EBS1. The dashed symbols were determined based on calculated sedimentation rates from core EB2 of 1 mm/yr above ~5.3 k.y. at 4.26 m depth and 1.2 mm/yr below. Cascade Lake event ages were determined based on acoustic character correlation. Slide CLS2 appears synchronous with the transition from glacial to lacustrine sedimentation yielding an age of ~12 ka that falls within the age range of this transition for FLL and LT. We also interpret the dashed horizon in Figure 8 as the TA horizon based on acoustic character. We then assume a constant sedimentation rate between the TA horizon and lake floor and interpolate the age of CLS1 using this rate. We also place a hollow circle at Event 2 because there is some inconclusive evidence of a slide associated with the TA horizon in CL.

Figure 16: Map of the Lake Tahoe Basin showing direct and indirect evidence of seismic events in the four sub-basins (Lake Tahoe, FLL, EB, and CL). Circles represent slide deposits, colored by their age range. The WTDPF is colored by event age (see legend) and marked with a triangle where direct evidence of faulting is observed.

Table 1: Radiocarbon ages from core EB2 in Emerald Bay (location in Figure 2). Sample analysis performed at the Lawrence Livermore National Center for Applied Mass Spectrometry (CAMS) Laboratory. $\delta^{13}\text{C}$ values of -25 were not measured, but are the assumed values according to Stuiver and Polach (1977). Calibrated ages determined using OxCal Version 4.1.7 (Bronk Ramsey, 2009) and IntCal04 atmospheric curve (Reimer et al., 2004).

Table 2: Ages of horizons and associated slide deposits in FLL. The MRE and Post TA horizons represent the MRE and TA slides, respectively, and the ages are the modeled radiocarbon ages (Fig. 14). The TA horizon age is the age range for the Tsoyowata Ash deposit (Bacon, 1983; Sarna-Wojcicki et al., 1991). Sedimentation rates were calculated using each horizon depth in the core and the age range. These rates were then used to determine older slide dates (~11.5 ka and ~13 ka deposits) with the depth of the horizons in CHIRP data.

New Constraints on Deformation, Slip Rate, and Timing of the Most Recent Earthquake on the West Tahoe–Dollar Point Fault, Lake Tahoe Basin, California

by Daniel S. Brothers, Graham M. Kent, Neal W. Driscoll, Shane B. Smith, Robert Karlin, Jeffrey A. Dingler, Alistair J. Harding, Gordon G. Seitz, and Jeffrey M. Babcock

Abstract High-resolution seismic compressed high intensity Radar pulse (CHIRP) data and piston cores acquired in Fallen Leaf Lake (FLL) and Lake Tahoe provide new paleoseismic constraints on the West Tahoe–Dollar Point fault (WTDPF), the westernmost normal fault in the Lake Tahoe Basin, California. Paleearthquake records along three sections of the WTDPF are investigated to determine the magnitude and recency of coseismic slip. CHIRP profiles image vertically offset and folded strata along the southern and central sections that record deformation associated with the most recent event (MRE) on the WTDPF. Three faults are imaged beneath FLL, and the maximum vertical offset observed across the primary trace of the WTDPF is ~ 3.7 m. Core-registered piston cores in FLL recovered sediment and organic material above and below the MRE horizon. Radiocarbon dating of organic material constrained the age of the MRE to be between 3.6 and 4.9 k.y. B.P., with a preferred age of 4.1–4.5 k.y. B.P. In Lake Tahoe near Rubicon Point, approximately 2.0 m of vertical offset is observed across the WTDPF. Based on nearby core data, the timing of this offset occurred between ~ 3 –10 k.y. B.P., which is consistent with the MRE age in FLL. Offset of Tioga-aged glacial deposits provides a long-term record of vertical deformation on the WTDPF since ~ 13 –14 k.y. B.P., yielding a slip rate of 0.4–0.8 mm/yr. In summary, the slip rate and earthquake potential along the WTDPF is comparable to the nearby Genoa fault, making it the most active and potentially hazardous fault in the Lake Tahoe Basin.

Introduction

The Lake Tahoe Basin (LTB) is one of several fault-controlled basins within the northern Walker Lane deformation belt (Unruh *et al.*, 2003). Based on westward dipping lake deposits and the structural tilt of the Carson Range, the LTB appears to be an asymmetric half-graben (Hyne *et al.*, 1972; Schweickert *et al.*, 1999; Surpless *et al.*, 2002; Dingler, 2007) separating the Sierra Nevada Range to the west from the Carson Range to the east (Fig. 1). Extension occurs along three primary normal fault systems: the West Tahoe–Dollar Point fault (WTDPF), the Stateline–North Tahoe fault (SLNTF), and the Incline Village fault (IVF). Each fault exhibits down-to-the-east normal displacement during the last 10 k.y. (Dingler, 2007). Until recently, geologic slip rates, earthquake timing, and magnitude estimates across faults in the LTB were poorly constrained. Offshore swath bathymetry and compressed high intensity Radar pulse (CHIRP) sub-bottom surveys combined with cores and onshore paleoseismic excavations have defined the regional distribution of faults and the first precise estimates on slip rates (Gardner

et al., 2000; Kent *et al.*, 2005; Dingler, 2007). Despite such advances, one of the most active, but poorly understood, structures is the north–south striking WTDPF (Fig. 1). Along strike fault morphology (Fig. 1), large cumulative displacement beneath Lake Tahoe and vertically offset Pleistocene glacial moraines in the southern LTB indicate the WTDPF has a relatively high slip rate. Nevertheless, relaxed scarp profiles measured south of Lake Tahoe suggest the fault has not experienced a ground-rupturing event for several thousand years.

In 2006, we acquired CHIRP sub-bottom data and piston cores along the southern section of the WTDPF between Emerald Bay and Christmas Valley to define the age, coseismic offset, and rupture length of the most recent event (MRE; Fig. 2). High-resolution marine geophysics provides an opportunity not only to identify offset strata associated with individual earthquakes, but also to define the regional fault architecture in an area that is inaccessible by traditional onshore methods. Our results, combined with previous sub-

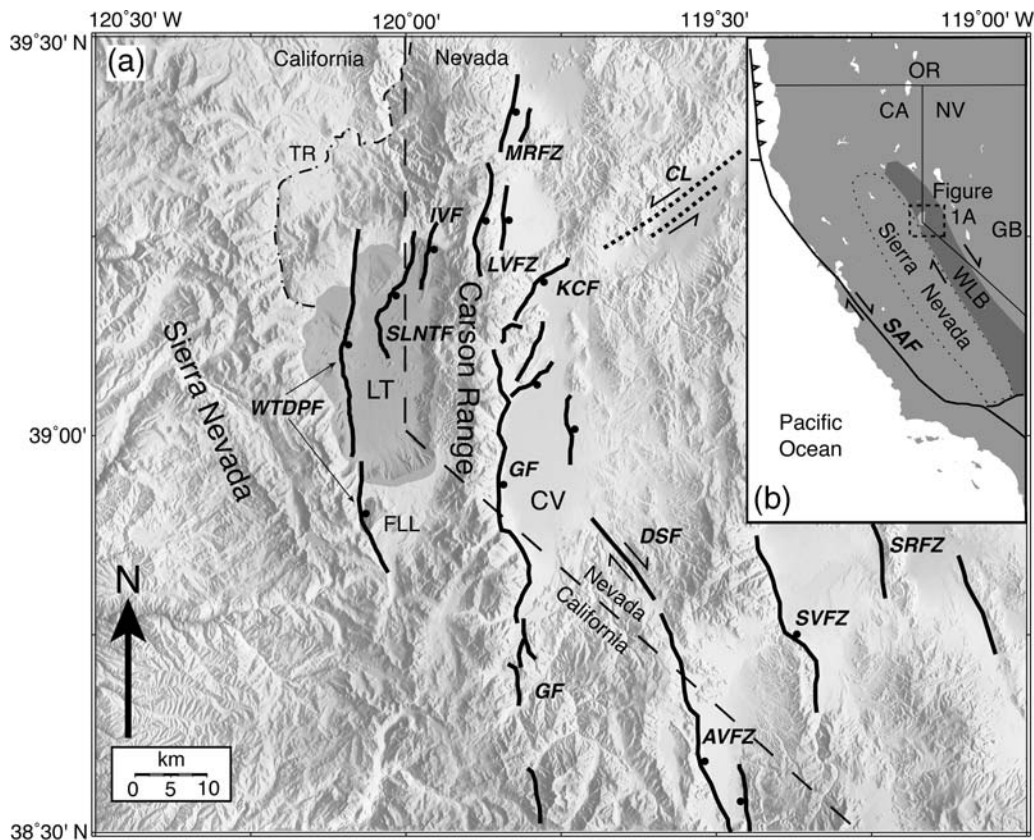


Figure 1. (a) Generalized fault and shaded relief map of eastern California and western Nevada. The LTB lies between the Sierra Nevada and Carson Ranges. Lake Tahoe (LT) and FLL are shaded gray. Solid black lines are active fault systems; dashed black lines are inferred faults. Abbreviations: West Tahoe–Dollar Point fault, WTDPF; Stateline–North Tahoe fault, SLNTF; Incline Village fault, IVF; Genoa fault, GF; Mount Rose fault zone, MRFZ; Little Valley fault zone, LVFZ; Carson Lineament, CL; Kings Canyon fault, KCF; Deep Springs fault, DSF; Antelope Valley fault zone, AVFZ; Smith Valley fault, SVF; Smith Range fault zone, SRFZ; Truckee River, TR; and Carson Valley CV. (b) Simplified plate boundary highlighting the San Andreas fault (SAF), Walker Lane belt (WLB; shaded gray area), Sierra Nevada block (thin dashed line), and the Great Basin (GB).

bottom and piston core data collected in Lake Tahoe (Dingler, 2007), indicate the WTDPF is the most active and hazardous fault in the LTB. The relatively high slip rate and rupture potential of the WTDPF provides essential information for geohazards assessments, including probability estimates for a future, large-magnitude event.

Quaternary Geology and Tectonics

Walker Lane

The Walker Lane belt (WLB) is an actively deforming tectonic province situated between the relatively stable Sierra Nevada microplate on the west and the central Great Basin to the east (Stewart, 1988; Argus and Gordon, 2001). The WLB is a complex zone of dextral transtension responding to the oblique-divergent motion of the Sierra Nevada microplate relative to the central Great Basin (Fig. 1b; Bennett *et al.*, 2003; Oldow, 2003; Unruh *et al.*, 2003). A suite of geodetic studies have detected 9–13 mm/yr of mostly dextral shear partitioned across numerous strike-slip, dip-slip, and

oblique-slip faults in the Walker Lane, accounting for ~25% of the total plate motion between the North American and Pacific plates (Hearn and Humphreys, 1998; Dixon *et al.*, 2000; Svarc *et al.*, 2002; Bennett *et al.*, 2003; Hammond and Thatcher, 2004, 2007).

Lake Tahoe is within the northern WLB, which consists of a series of north–south trending, normal fault bounded mountain ranges, northwest striking dextral faults, and northeast striking sinistral faults (Faulds *et al.*, 2005). At the latitude of Lake Tahoe and east of the Sierra Nevada Range the topography is dominated by several uplifted mountain ranges (Wassuk, Singatse, Pine Nut, and Carson) that are bounded by north–south striking normal faults. Although Surpluss *et al.* (2002) document larger cumulative offset along normal fault systems to the east than those to the west, geodetic studies indicate that the majority of extension (between 2–3 mm/yr) is focused around the Sierra Nevada frontal fault system. Near Lake Tahoe, the Sierra Nevada frontal fault system splays into two extensional domains separated by the Carson Range: the LTB and Carson Valley (Unruh *et al.*, 2003). Measured geodetic rates across the LTB

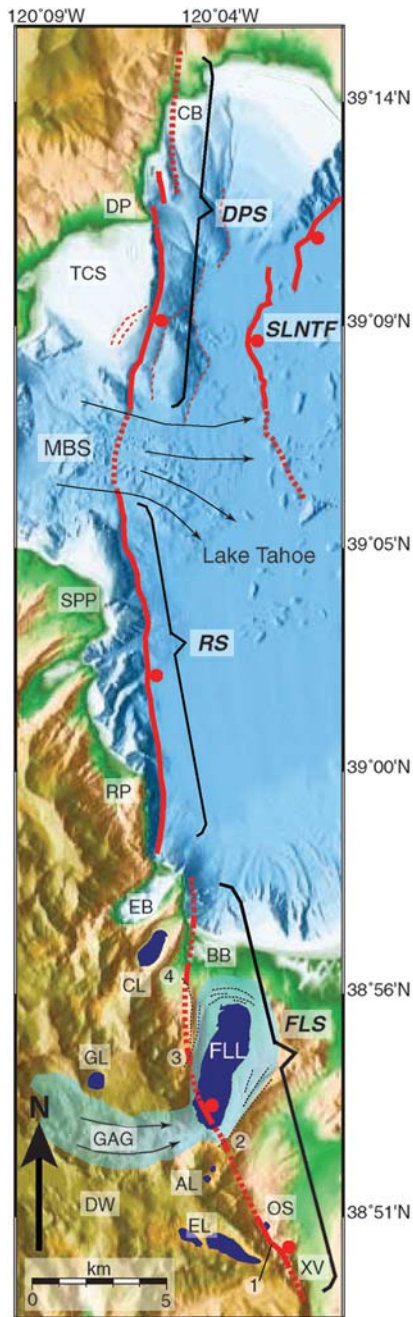


Figure 2. Map showing the three sections of the WTDPF (solid red lines—where known, and dashed red lines—where inferred): Dollar Point section (DPS), Rubicon section (RS), and Fallen Leaf section (FLS). Thin dashed red lines surrounding the DPS represent slump scarps. Abbreviations: Christmas Valley, XV; Osgood Swamp, OS; Echo Lakes, EL; Desolation Wilderness, DW; Angora Lakes, AL; Glenn Alpine glacier (also where the present Glen Alpine Creek is sourced), GAG; Gilmore Lake, GL; Cascade Lake, CL; Baldwin Beach, BB; Emerald Bay, EB; Rubicon Point, RP; Sugar Pine Point, SPP; McKinney Bay slide, MBS; Tahoe City shelf, TCS; Dollar Point, DP; and Carnelian Bay, CB. Black arrows represent flow directions for the MBS and GAG (also shaded blue). Dashed black lines surrounding FLL are approximate locations of moraine crests; arcuate crests north of FLL are recessional moraines. Numbered features: (1) photographed scarp in Figure 14, (2) and (3) 2–3 m scarps offsetting Tioga-aged moraine crests on either side of FLL, and (4) 2–3 m meadow scarp.

are poorly resolved due to sparse coverage on the western side of the Basin. Results of geologic and geodetic studies in the region, point to a westward encroachment of extension from the western Basin and Range province into the eastern Sierra Nevada block (Henry and Perkins, 2001; Surpless *et al.*, 2002). The present day Sierra Nevada–WLB boundary is located along the WTDPF. North of the LTB, Global Positioning System (GPS) studies measured ~ 7 mm/yr of dextral shear across the northern WLB, representing $\sim 15\%$ of the total plate motion (Bennett *et al.*, 2003; Hammond and Thatcher, 2004, 2007). Paleoseismic studies in the northern WLB have uncovered evidence for large-magnitude Holocene ruptures along normal, dextral, and sinistral fault systems, including the IVF (Dingler, 2007), Genoa fault (GF; Ramelli *et al.*, 1999), Pyramid Lake fault (Briggs and Wesnousky, 2004), and the Olinghouse fault (Briggs and Wesnousky, 2005).

Lake Tahoe Basin

The LTB has been tectonically active since at least 3 Ma (Henry and Perkins, 2001; Surpless *et al.*, 2002; Faulds *et al.*, 2005) with extension occurring along a series of east-dipping normal faults. The Quaternary landscape has been shaped by several Wisconsin glacial advances between 79 and 15 k.y. B.P. (Bischoff and Cummins, 2001), forming several moraine-bounded valleys along the range fronts within the LTB. The Sierra Nevada and Carson Ranges are predominantly composed of granodiorite and related metamorphic roof pendants of the Sierra Nevada batholith (Saucedo *et al.*, 2005), but also Miocene and younger volcanic rocks are found in the northern LTB (Birkeland, 1963; Saucedo *et al.*, 2005). Seismic reflection data collected in Lake Tahoe have imaged up to ~ 300 m of sediment below the lake floor without reaching the acoustic basement (AB, Hyne *et al.*, 1972).

The basin exhibits abundant low-magnitude seismicity (Ichinose *et al.*, 1999, 2003; Smith *et al.*, 2004). New paleoseismic evidence suggests there have been large-magnitude Holocene events (Kent *et al.*, 2005; Dingler, 2007). Late-Pleistocene to present geologic slip-rate estimates were calculated based on offset geomorphic markers observed in sub-bottom CHIRP profiles (Kent *et al.*, 2005; Dingler, 2007). An offset 19.2 ± 1.8 ka wave-cut paleoterrace, which correlates temporally with a 19 ± 1 ka glacial advance during the Tioga glaciation (Phillips *et al.*, 1996), was used to calculate a minimum basin extension rate of ~ 0.5 mm/yr (Kent *et al.*, 2005). In addition to offshore studies, an excavation across the IVF revealed the first direct evidence for multiple $M \approx 7$ Holocene events in the LTB (Dingler, 2007).

West Tahoe–Dollar Point Fault. The WTDPF is the north–south striking, range bounding normal fault along the western margin of the LTB (Figs. 1 and 2). Most of the fault’s length is located beneath Lake Tahoe where, presumably, the cumulative throw is greatest. Swath bathymetry and sub-bottom CHIRP surveys reveal well-defined scarps through

debris aprons, slides, and lake bottom sediments (Hyne *et al.*, 1972; Gardner *et al.*, 2000; Kent *et al.*, 2005; Dingler, 2007). We divide the WTDPF into three sections that are defined by apparent discontinuities or geomorphic boundaries (Fig. 2). The Fallen Leaf section extends from Christmas Valley at the south through Fallen Leaf Lake (FLL) and offshore into Lake Tahoe at the western edge of Baldwin Beach. Prior to this study, the Fallen Leaf section was poorly understood. Fault scarps within the transition between the Fallen Leaf and Rubicon sections are not well expressed by the local morphology and may include more than one splay. After an apparent ~1 km northwestward step from below Eagle Point to the base of the submerged slope off Emerald Point, the Rubicon section continues northward to McKinney Bay. Although the trends of the two northern sections are nearly equivalent and evidence for a tectonic boundary has not been observed, we treat the McKinney Bay slide (MBS) as a section boundary because faulting beneath the slide is poorly imaged and scarps have been overprinted or eroded by debris aprons and/or landslides. The southern extent of the Dollar Point section begins at the northern edge of the MBS and continues to the north along the eastern edge of the Tahoe City shelf (TCS) then eventually steps onshore in the vicinity of Carnelian Bay. A series of scarps and offset strata below the TCS appear to be caused by slumping (Dingler, 2007). The total length of the WTDPF is greater than 50 km.

Fallen Leaf Lake. FLL, located ~2 km south of Baldwin Beach, provides another lacustrine environment in which the WTDPF can be imaged using marine seismic methods. FLL is ~45 m higher than Lake Tahoe and fills a narrow moraine-bounded glacial valley (Fig. 2). The overall morphology has been shaped by Pleistocene glaciers sourced in the Desolation Wilderness (Fig. 2) where Tahoe-aged glaciers seem to have been more significant than the more recent Tioga-aged glaciers that merely reworked the inner slopes of Tahoe moraines (Saucedo *et al.*, 2005). The entire valley is bounded on either side by > 300 m high-lateral moraines (measured from the lake floor) that extend towards Lake Tahoe for > 5 km from the range front. Near its northern shoreline, FLL is bounded by a series of Tioga-aged recessional and terminal moraines that separate it from Lake Tahoe (Saucedo *et al.*, 2005). Based on the dimensions of lateral and end moraines, the Tahoe and Tioga glaciers in Fallen Leaf Valley appear to have been much larger than the adjacent valley glaciers that occupied Cascade Lake and Emerald Bay. Sediment discharge from Glen Alpine Creek, the most significant modern sediment input to FLL, would have been strongly modulated by glacial melt water. Like much of the LTB, glacial morphology, fluvial incision, and dense vegetation surrounding FLL make onshore identification of fault scarps difficult. Offshore geophysical surveys offer an alternative method to study the interactions between tectonic and glacial or fluvial processes.

Methods

Detailed geophysical surveys and field reconnaissance mapping were conducted between Christmas Valley and Emerald Bay in July 2006 (Figs. 2 and 3). Two sub-bottom surveys conducted in FLL and offshore Baldwin Beach in Lake Tahoe employed the Scripps Institution of Oceanography's Edgetech CHIRP profiler. In FLL, the CHIRP profiler was mounted on an aluminum frame held afloat by two inflatable pontoons and towed by a small (~20 × 10 ft) platform barge operated by the Fallen Leaf Marina. More than 40 line-km of data were collected at a constant tow depth of ~1 m. Offshore Baldwin Beach the CHIRP was towed off the stern of the R/V LeConte (operated by University of California, Davis) at 2–3 m below the surface; over 12 line-km of data were collected. All data were digitally recorded in SEG-Y format with real-time GPS navigation recorded with each shot, providing absolute location accuracy to within 5 m. SEG-Y files were processed using SIOSEIS then imported into the Kingdom Suite and Fledermaus software packages for interpretation. The 1–6 kHz swept frequency acoustic source provided sub-bottom penetration to > 50 m in lacustrine sediments, but in some places penetration was limited by the AB. All depth conversions assumed a 1500 m/sec sediment velocity unless otherwise stated. Onshore field reconnaissance between Baldwin Beach and Christmas Valley identified scarps along the Fallen Leaf lateral moraines as well as a several kilometer-long scarp south of FLL near Osgood Swamp (Fig. 2). The onshore and offshore results were integrated with datasets collected in 2000, 2002, and 2006 along the Rubicon and Dollar Point sections of the WTDPF (Kent *et al.*, 2005; Dingler, 2007).

During October 2006, five piston cores were collected in FLL (Figs. 3 and 4) from a platform barge using a modified Kullenberg piston corer. The coring device includes an ~250 kg weight stand, a 5 m long, 3 inch diameter core barrel and, depending on the sediment type, typically recovers between 3 and 5 m of sediment. The cores were acquired in the southern half of FLL in the vicinity of the WTDPF in an effort to construct a chronostratigraphic framework that can be used to estimate the timing of the MRE. Each of the piston cores recovered > 3.5 m of sediment. Lithologic and magnetic susceptibility logs were produced for all cores. The stratigraphy in all cores except one, PC5, was easily correlated based on color, texture, lithology, and magnetic susceptibility patterns (Fig. 4). Increases in magnetic susceptibility generally reflect increased concentrations of magnetite-rich siliciclastic sediments and may be correlated with periods of increased sediment contribution from the basin margins or in this case from Glen Alpine Creek. Conversely, low magnetic susceptibility appears to correlate with increased amounts of nonmagnetic clays and silts. PC5 was located at a shallower depth along the eastern basin slope. Six detrital wood samples and one organic fiber sample extracted from cores PC3, PC4, and PC5 were radiocarbon dated using an accelerator mass spectrometer. PC5 was the

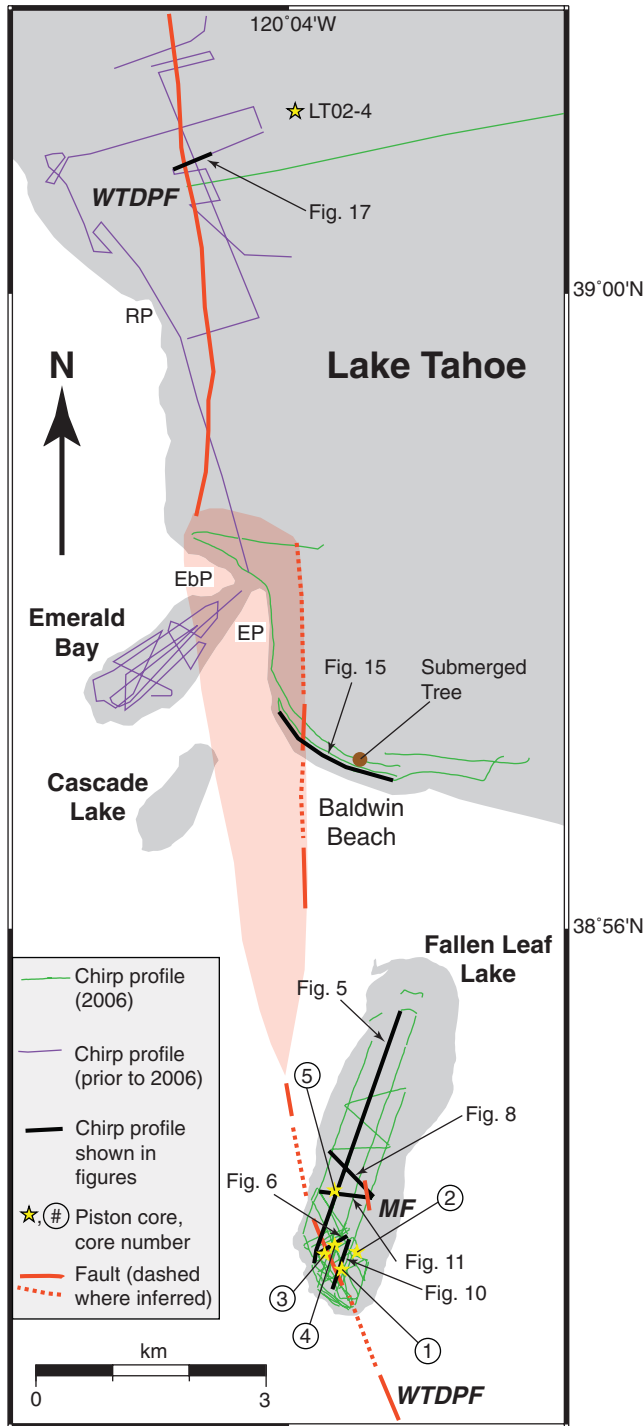


Figure 3. CHIRP profiles and sediment core locations in FLL and southwestern Lake Tahoe. Red lines mark the location of the WTDPF and MF (solid red line—where known, and dashed red line—where inferred). Abbreviations: RP, Rubicon Point; Eagle Point, EP; and Emerald Point, EmP. The submerged tree (brown circle) was sampled and radiocarbon dated to test for coincident timing of its submersion and the MRE on the WTDPF (Table 1). LT02-4 is the location of a piston core used to constrain sedimentation rates near the Rubicon section of the WTDPF shown in Figure 17 (Smith *et al.*, 2007). The precise location of faulting between FLL and EmP is not clear and may be distributed across a complex relay zone (red shaded area).

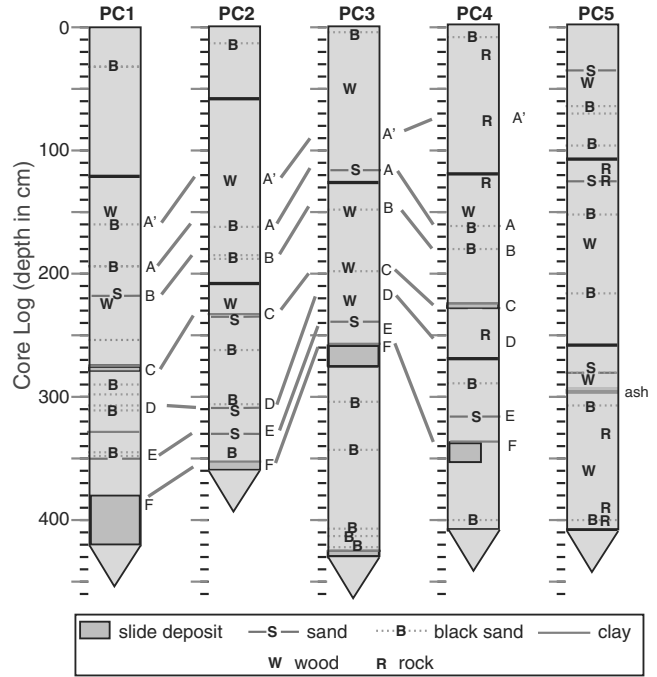


Figure 4. Piston core logs. Stratigraphic correlations are based on color, lithology, and magnetic susceptibility. Note the distinct slide deposit that is recognized in four of the cores. The ash labeled in PC5 is the 7.6–8.0 k.y. B.P. Tsoyowata Ash (Bacon, 1983).

only core that contained the 7.5–8.0 k.y. old Tsoyowata Ash as a chronological marker bed (Bacon, 1983; Sarna-Wojkicki *et al.*, 1991). Once the chronostratigraphy was established based on core data, we correlated distinct marker beds in the cores with corresponding layers in the seismic stratigraphy, allowing us to constrain the age of tectonically offset seismic horizons.

Faulting and Stratigraphic Framework

Fallen Leaf Lake

A high-density grid of sub-bottom CHIRP profiles was collected in the southern portion of the lake surrounding the WTDPF and a less dense grid collected in the northern lake (Fig. 3). The survey afforded three-dimensional, basin-wide correlation between seismic horizons and a nearly complete characterization of recent tectonic, glacial, and sedimentary processes beneath FLL. A low-resolution bathymetric elevation model was constructed by gridding lake-floor elevations measured in the CHIRP profiles. The basin depocenter is in the southern lake and is bounded to the south by a steep, ~100 m high escarpment that trends obliquely to the long axis of the valley and glacial flow direction. The base of the slope and its trend are coincident with the WTDPF, which is delineated by vertically offset and folded lacustrine horizons. In general, horizontally layered lacustrine deposits infill topographic relief in the underlying AB (Fig. 5). Three faults beneath FLL are observed in the CHIRP profiles. Two parallel faults separated by ~80 m trend ~N25°W along

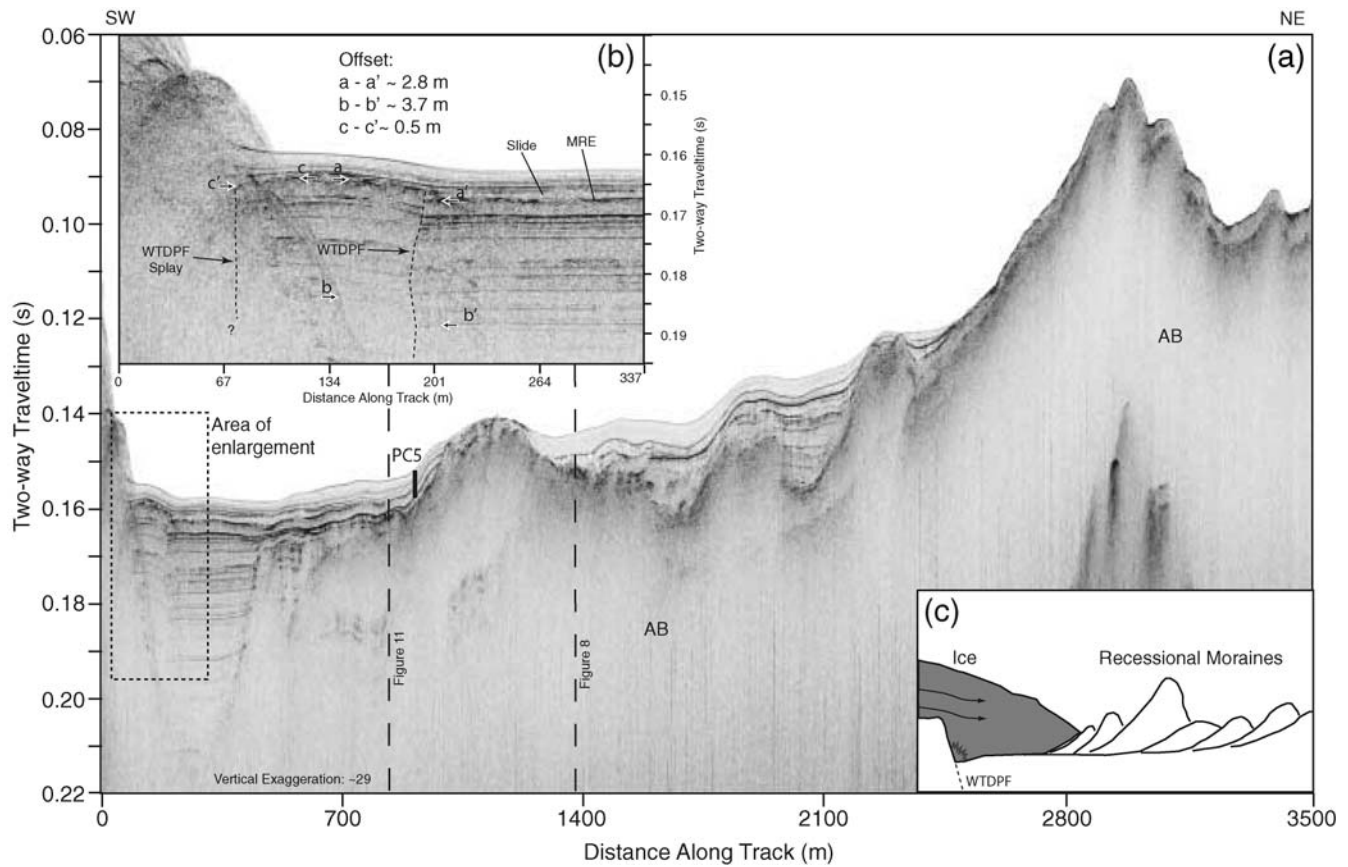


Figure 5. (a) Northeast–southwest trending CHIRP profile spanning over two-thirds of FLL. The WTDPF is seen toward the southern end, adjacent to a steep, fault-parallel escarpment. (b) Enlarged section of the two splays of the WTDPF (dashed box in 5a). Offset across both faults creates anticlinal folding in the sediments. A divergent bed labeled “slide” thickens into the fault and infills accommodation created during the MRE. The slide is an important marker bed that is seen in the seismic stratigraphy and in four of the piston cores (Fig. 4) throughout most of the southern lake. Piercing points (white arrows) on the footwall were selected near the apex of the anticline; beds are assumed to have been deposited approximately horizontal, then were subsequently folded and offset during the MRE. Offset increases with depth from ~ 2.8 m across the MRE horizon (aa') to ~ 3.7 m across horizon bb' due to increased compaction and dewatering with depth (all travel time to depth conversions assume 1500 m/sec velocity). Piston core PC5 is ~ 40 m to the west of this profile. (c) Hummocky topography in the acoustic basement (AB) is seen in several profiles. This type of morphology is typical for moraines formed by glacier fronts by temporary still stands or readvancements during an overall glacial retreat. Similar morphology is observed as a series of arcuate recessional moraines between FLL and Lake Tahoe (Saucedo, 2005). The relief toward the southern end of the profile, adjacent to the WTDPF, may be formed by a combination of glacial and tectonic processes, much like a roche moutonnée, but glacial plucking may have been facilitated by the location of the fault.

the base of the steep escarpment in the southern lake and project onto scarps mapped on the moraine crests above FLL (Fig. 2). Based on their proximity and synthetic nature, the two faults are collectively referred to as the WTDPF. The third fault, termed the Midlake fault (MF), is located ~ 1 km to the northeast of the WTDPF (Fig. 3) and is observed in only two profiles.

Coseismic deformations in the shallow sub-bottom are identified as vertically folded strata, but down-section layers show greater separation and exhibit distinct offset, suggesting that extensional fault-propagation-folding has occurred (Gawthorpe *et al.*, 1997; Hardy and McClay, 1999). East-side-down folding (~ 5 m below the lake floor) demarcates the MRE horizon on both the WTDPF and MF (Figs. 6–8). The MRE horizon on the hanging wall dips into the fault and is overlain by a thin divergent layer that thickens toward

the fault reflecting syntectonic deposition and infill of the accommodation created during the MRE. A striking observation is that the MRE horizon and the thin divergent bed overlying the MRE horizon can be traced across both the WTDPF and the MF (Fig. 9). Throughout the southern half of the lake the divergent layer onlaps bathymetric highs and diverges and thickens into lows, ranging in thickness from 0– ~ 1.5 m. Near the southeastern slope, strata beneath the layer abruptly changes in character, where it becomes chaotic and appears to have been disrupted (Fig. 10). Based on acoustic character and core logs (discussed later), we refer to this layer as a slide deposit. The stratal geometry and acoustic character seen in Figures 8 and 11 provide a stratigraphic framework that is used for basin-wide interpretations. The smooth lenticular shaped units labeled A, B, and C in package I thicken away from the bathymetric lows and down lap

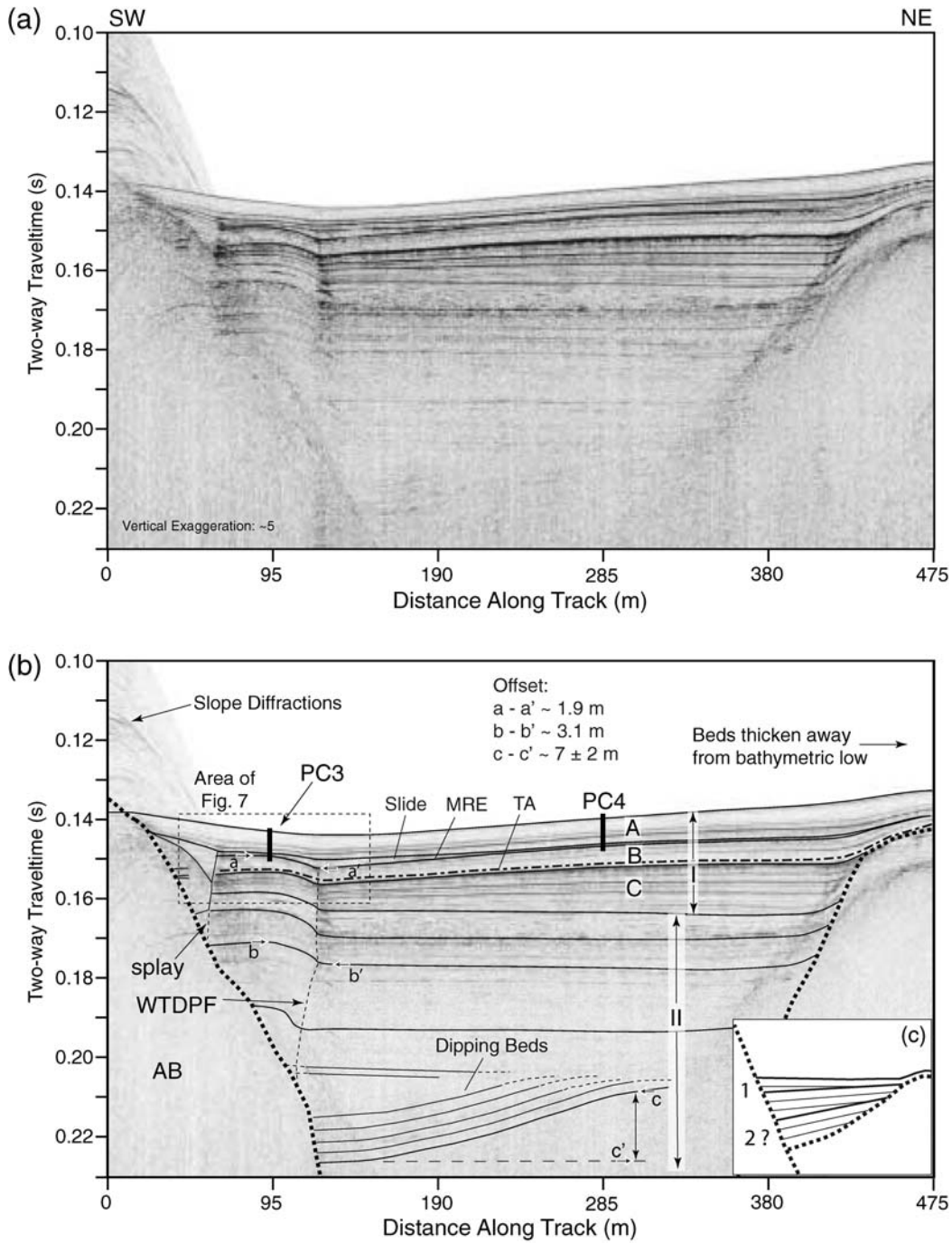


Figure 6. (a) Uninterpreted, and (b) interpreted fault-perpendicular profile. Locations of two nearby cores are projected onto the cross section. Piercing points (white arrows) measure slip that occurred during the MRE. Although offset of the MRE horizon is ~ 1.9 m then increases to ~ 3.1 m over deeper horizons, we do not observe stratigraphic evidence for multiple events (e.g., increase in dip or divergence down section) in the upper ~ 35 m. The deformation resembles a normal fault propagation fold, where offset at depth is attenuated in the shallow, unconsolidated sediments and is expressed as a fold. A slide deposit directly above the MRE horizon infills accommodation created during the MRE. Piston core PC3 sampled the slide near the WTDPF, which is used as a marker bed throughout the lake. Radiocarbon samples from PC3 constrain the timing of the MRE to 4.1–4.5 k.y. B.P. (Table 1). Units A, B and C in section I represent fine-grained layers (low amplitude reflections) that are separated by thin, coarse-grained layers (high-amplitude reflections). The fine-grained layers appear to thicken away from the basin depocenter suggesting current-controlled deposition (see text). The approximate position of the Tsoyowata Ash (dashed line labeled TA; ~ 7 m depth adjacent to the WTDPF) is correlated from seismic sections near piston core PC5 and provides an independent constraint on sedimentation rate. Section II exhibits more uniform deposition. Faintly imaged strata in the hanging wall dip at $\sim 4^\circ$. Assuming the beds were deposited horizontally then subsequently tilted during a penultimate event, the vertical offset is estimated at 7 ± 2 m. (c) Conceptual model for syntectonic deposition, where divergent beds record subsidence along the fault and multiple events can be recognized by increased dip down section.

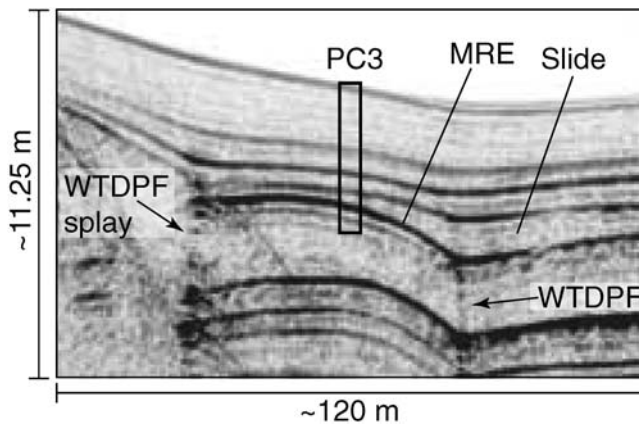


Figure 7. Enlarged section (dashed box) from Figure 6 highlighting the MRE horizon and overlying slide deposit. The two faults are separated by ~ 60 m. Piston core PC3 sampled material above and below the MRE horizon.

onto underlying beds. In contrast, the intervening layers diverge and thicken into low points along the basin margins. Package II does not exhibit the same geometric relationships and deposition appears more uniform.

Matching cores with the nearby seismic profiles allowed us to define relationships between seismic stratigraphy and the corresponding lithostratigraphy. Distinct marker beds sampled by the cores were traced onto adjacent CHIRP profiles (Fig. 9). Lithostratigraphy documented in all the piston cores except PC5 includes a distinct coarse-grained slide deposit (Fig. 4). At the base of PC1 is a coarse-grained, massive bed that contained several large pieces of wood and twigs, where PC2, PC3, and PC4 sampled the distal, fine-grained extent of the equivalent layer. The coarse-grained slide deposit observed in the cores correlates well with the divergent bed overlying the MRE horizon seen in the seismic profiles (Figs. 6 and 10). All cores except PC5 are within 30 m of a CHIRP profile; PC5 is within 45 m. The horizontal offset may result in a slight mismatch (< 0.5 m) between seismic stratigraphy and core logs. Another potential source for mismatch is overpenetration (< 0.5 m), which was noted during recovery by mud on the weights above the core barrel.

The age of the MRE was estimated by radiocarbon dating organic material from either side of the MRE horizon. The analysis was based solely on radiocarbon data from core PC3 (Fig. 12), which was located nearest the WTDPF. Sediment recovered by PC3 extended > 1.5 m below the MRE horizon and contained abundant organic matter for radiocarbon dating. Four samples (all > 5 mg) were analyzed with an accelerator mass spectrometer (Table 1). The radiocarbon dates were converted to calendar years B.P. using the OxCal 4.0 radiocarbon calibration software and calibration curve IntCal04.14c (Ramsey, 1995, 2001; Reimer *et al.*, 2004). All further discussions will be in terms of calendar years B.P. The sample at 3.40 m depth was anomalously old for its stratigraphic position suggesting it had a long-residence time in the watershed before deposition in FLL and was excluded

from the analysis. Of the remaining samples, the deepest and oldest (5.3–5.6 k.y. B.P.) was sampled by the core catcher at a depth of ~ 4.3 m, meaning the actual depth is between 4.3 and 4.8 m (accounting for possible overpenetration). Dividing the depth range by the age range resulted in an average sedimentation rate adjacent to the WTDPF between 0.8 and 0.9 mm/yr. An independent comparison can be made using the 7.5–8.0 k.y. B.P. Tsoyowata Ash that was sampled at a depth of 2.95 m in PC5 between two thin sand beds (Fig. 4). The relative stratigraphic position of the ash layer can be projected onto the nearest profile (Fig. 11; ~ 50 m away) and correlated basin wide. The ash is inferred at a depth of 7 ± 2 m adjacent to the WTDPF (labeled TA in Fig. 6), again resulting in an average sedimentation rate of ~ 1 mm/yr.

The age of the MRE horizon is confined by the age of samples 1 and 3 in PC3 (Fig. 13, Table 1). The absolute lower and upper bounds are 3.6 and 4.9 k.y. B.P. based on the radiocarbon ages, but a more precise estimate was calculated by linearly interpolating the age as a function of depth between samples 1 and 3 (Fig. 13). We assume the slide deposit was emplaced rapidly and removed its thickness from the interpolation. The total thickness between samples after removing the slide is 173 cm (the slide is only $\sim 10\%$ of the total thickness between samples) and the MRE horizon is 65 cm below sample 1. Interpolating the age as a function of depth for both the upper and lower age bounds on each sample confines the MRE to 4.1–4.5 k.y. B.P. Uncertainty in this estimate would be introduced by nonlinear sedimentation rates or nonlinear compaction within the interpolation interval during core collection. However, these effects are not quantifiable with the available data, and we do not observe evidence for either.

Piercing points in the seismic stratigraphy are selected to measure vertical offset (white arrows in Figs. 5, 6, and 8). The 1–6 kHz CHIRP source can resolve layers that are vertically separated by greater than ~ 0.4 m. Travel-time intervals between piercing points are measured directly then converted to depth intervals by assuming an interval velocity. We use a nominal velocity (1500 m/sec) for all depth conversions to avoid overestimating the offset measurements, and we incorporate a pick error of ± 0.2 m. At greater depths (> 10 m) where compaction and dewatering are likely, it is possible that seismic velocities reach ~ 1800 m/sec. On the main splay of the WTDPF, deformation within the shallow, poorly consolidated sediments appears to become distributed as folding and possibly minor faulting, which results in an attenuated offset up-section similar to analog models for extensional fault propagation folds (Hardy and McClay, 1999). Offset measurements show a gradual increase in offset with depth from ~ 2 m over the folded MRE horizon to > 3 m across horizons at depths greater than ~ 10 m (Table 2; Figs. 5–7). Because we do not observe any stratigraphic evidence (e.g., divergent beds, increasing dip with depth) for multiple events in the upper 0.05 sec (~ 38 m) of sediment, it is assumed that the deeper measurements provide our best

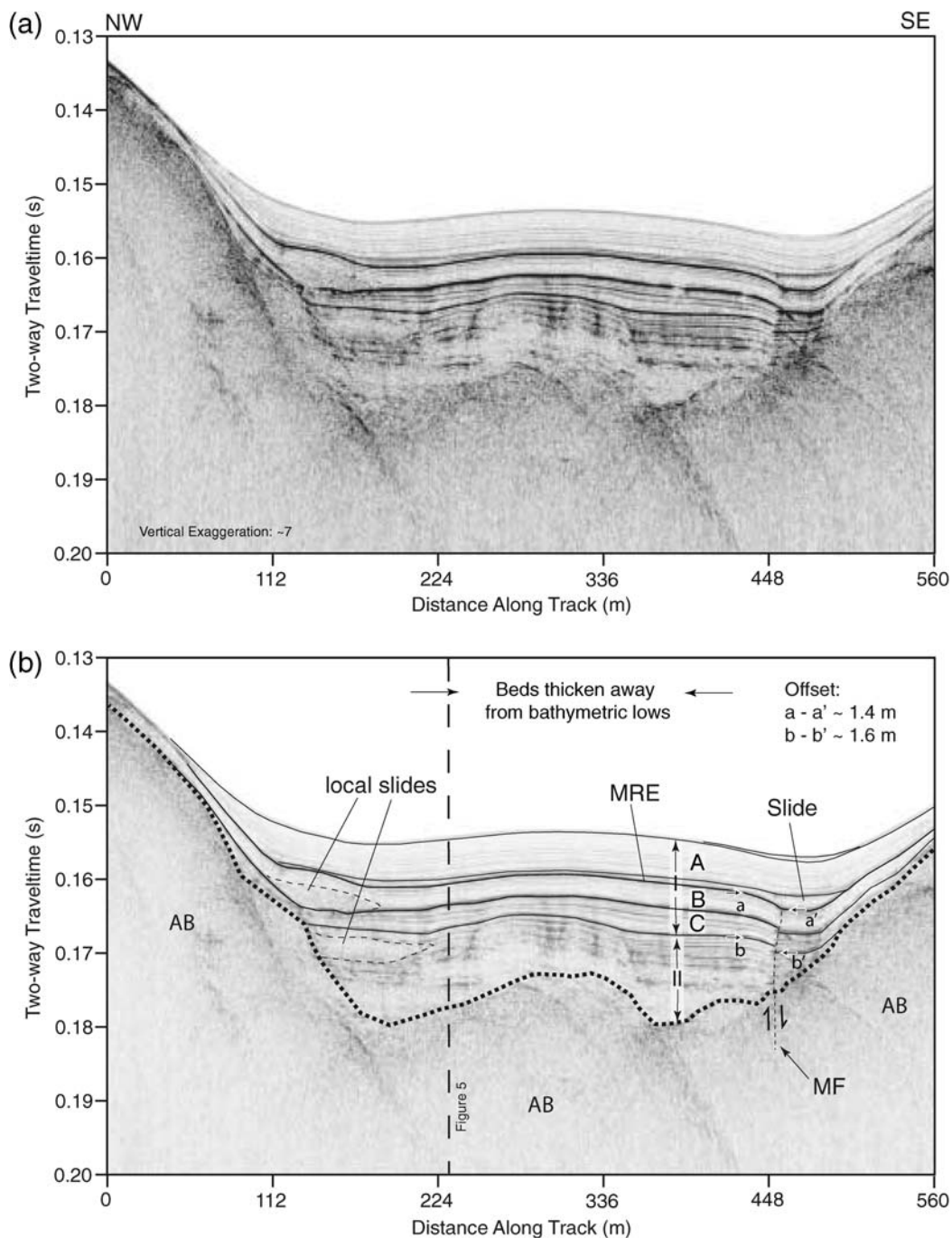


Figure 8. Northeast–southwest oriented profile over the MF and a series of debris slides along the western slope. The MRE horizon and overlying slide are the equivalent layers observed across the WTDPF. Displacement is down-to-the-east and increases from ~ 1.4 m across the MRE horizon to ~ 1.6 m down section. Packages A, B, and C represent lenticular shaped drift deposits (low amplitude) that mantle the underlying topography, but also thicken away from the basin margins. Each unit is separated by thin, coarse-grained gravity slides, one of which is the slide directly above the MRE horizon. Contact surfaces between coarse- and fine-grained deposits result in high-impedance (i.e., high-amplitude) boundaries in the seismic stratigraphy.

estimates for coseismic slip that occurred during the MRE. Overall, nine precise measurements across the MRE horizon ranged between 1.5 and 2.8 m and eight measurements across deeper horizons ranged between 3.0 and 3.7 m (Table 2). The secondary splay (Figs. 5–7), located very near the slope break, is evident in six profiles by small synclinal fold-

ing and infill above the MRE horizon. Offset measurements over the splay ranged from 0.6 to 1.3 m. Although the nature of the splay is poorly imaged, it is possible that the two faults merge at depth and their slip is additive, increasing the total offset produced during the MRE to between 3.6 and 4.5 m, with an average of ~ 4.1 m.

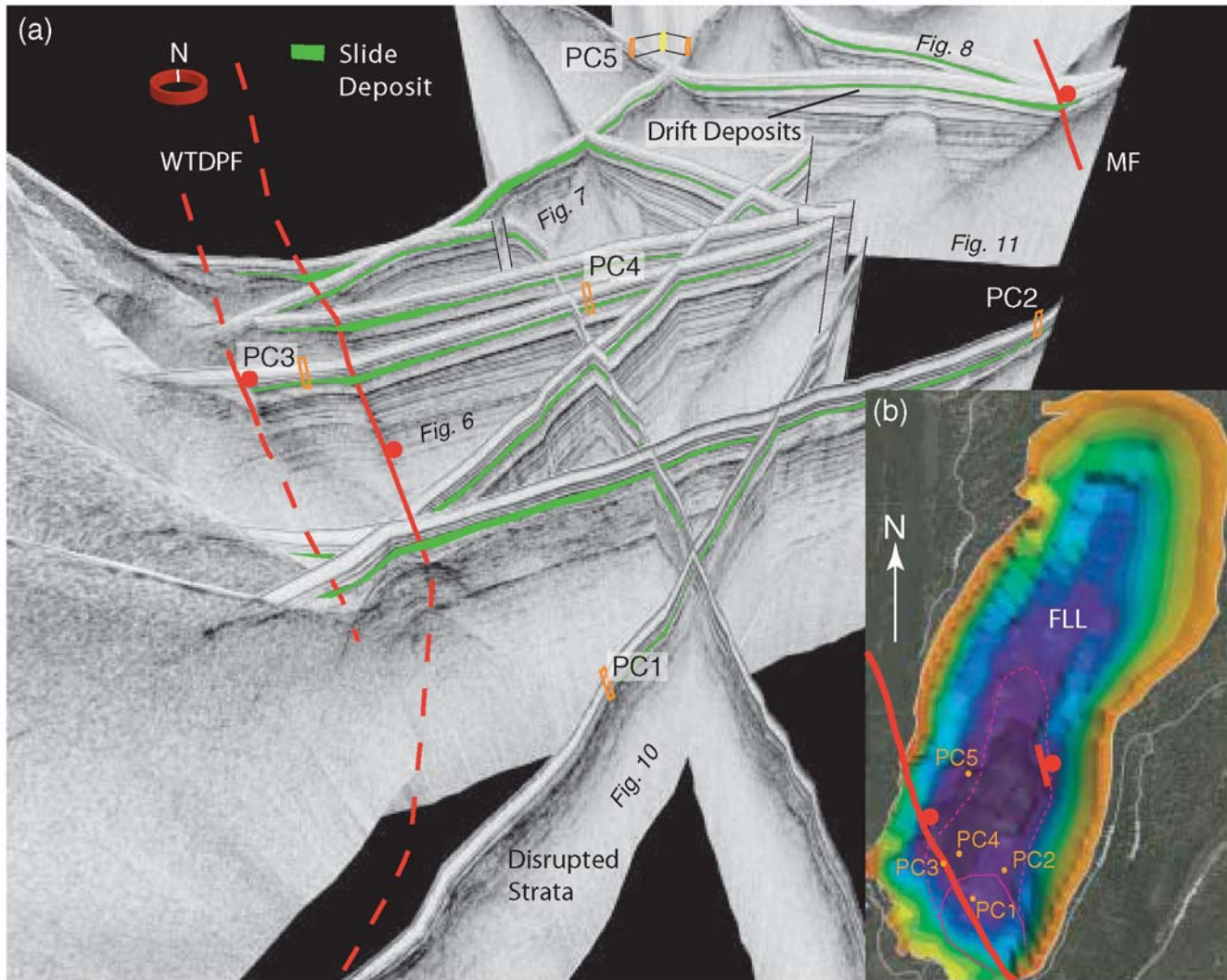


Figure 9. (a) Fence diagram of CHIRP profiles and core locations illustrating the 3-dimensional structure, stratigraphy, and core locations. The diagram illustrates the utility of using acoustic stratigraphy to correlate sediments throughout the basin. PC5 is projected onto the two nearest profiles, but all other cores are within 20 m of the nearest profile. The slide deposit directly above the MRE horizon (green layer) can be traced from its coarse-grained proximal extent to its fine-grained distal reach at the far side of the southern basin. The run-out length is over 1 km. Faults are depicted by red lines (solid red lines, where known and dashed red lines, where inferred). (b) Bathymetric grid of FLL based on CHIRP soundings. Thick red lines are the WTDPF and MF; thin red lines outline the inferred extent of slide deposit (solid red line, proximal and dashed red line, distal).

Approximately 35 m below the lake floor, the stratigraphy abruptly changes in character and has a marked 4° increase in dip toward the fault (Fig. 6). The data quality diminishes down-section due to attenuation and interference from diffractions off the AB and adjacent slopes, but the dipping strata are observed in several profiles and are unlikely to be a three-dimensional artifact or sideswipe from a nearby slope. A dipping horizon that spans the deeper portion of the basin was used as a piercing line and depth was measured at both ends (cc' in Fig. 6). Some ambiguity exists when picking the edges of the horizon resulting in large uncertainty, but the measured difference is $\sim 7 \pm 2$ m (Fig. 5).

The MF is observed in two profiles ~ 1 km northeast of the WTDPF (Figs. 8, 9, and 11). The MRE horizon at the MF

was vertically folded by 1.4 m and is overlain by a divergent wedge similar to that observed across the WTDPF. Offset increases slightly down-section to ~ 1.6 m. The trend of the fault, determined over a length of ~ 100 m, appears parallel to the WTDPF. However, the nearest profile north of the projected trend lacks convincing evidence for faulting. Farther north, disrupted sediments and slide deposits provide weak evidence for a north-south trending fault.

Onshore Mapping

Onshore field reconnaissance mapping south of FLL, near Osgood Swamp (Figs. 2 and 14), revealed a 2.6 km long section of down-to-the-east fault scarps. The scarps offset

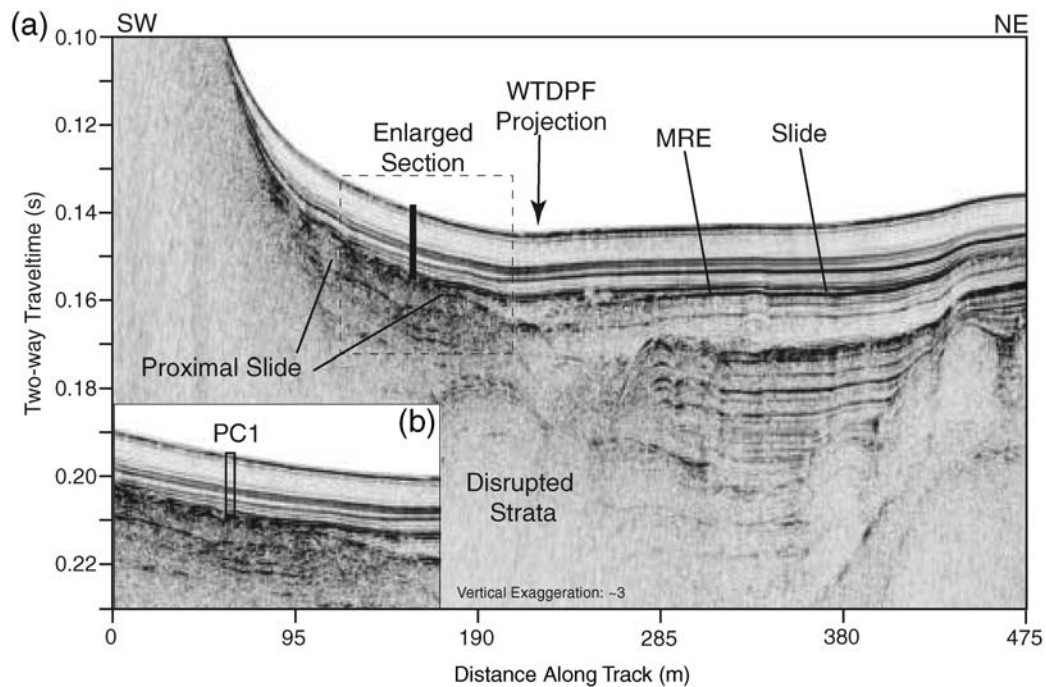


Figure 10. Northeast–southwest oriented type section that confirmed the correlation between the slide material sampled at the base of PC1 (Fig. 4) and highly disrupted, chaotic bedding that grades distally into the divergent bed observed above the MRE horizon.

unconsolidated alluvial and glacial sediments and have relaxed slope profiles. Heights varied depending on the age of the offset material, where some scarps north of Osgood Swamp are 10–15 m high, while others to the south of Osgood Swamp are 2–4 m high (Fig. 14). Between Osgood Swamp and Angora Lakes (Fig. 2) steep slopes and dense vegetation preclude identification of the fault. An ~400 m long, ~3 m high scarp was mapped perpendicular to the Angora Ridge moraine crest (Fig. 2) and aligns with the trend beneath FLL and another ~500 m long scarp mapped on the opposite side of FLL valley. North of FLL, the landscape again becomes covered with dense vegetation and complex fluvial and glacial overprint. A potential ~1 km long scarp was mapped ~2 km south of Baldwin Beach along the edge of a small meadow (Fig. 2). The scarp height in the meadow varies between 3 and 10 m depending on the age of the surface material. Overall, the onshore expression of the WTDPF is poorly constrained, particularly in the region between FLL and Lake Tahoe. Because of the complex geomorphology, subsurface studies are needed to discern fault scarps from glacial or fluvial scarps.

Baldwin Beach

CHIRP data collected along the shallow sandy shelf immediately offshore Baldwin Beach (Fig. 3) show evidence for faulted sediments. A tightly folded syncline (Fig. 15) traced between three profiles and trending north–south aligns with pockmarks and possible lake-floor disruption down the adjacent steep basin slope (Dingler, 2007). The deformation is less obvious than in FLL, possibly due to an absence of

internal bedding in the unconsolidated, medium- to coarse-grained sand.

Several submerged, but rooted trees have been identified near Baldwin Beach and are thought to reflect climatic variability during the mid-Holocene (Lindstrom, 1990). A sample from the deepest submerged tree (Fig. 3), rooted at ~4 m depth and located to the east of the inferred fault (Fig. 3), was radiocarbon dated (Table 1) to test for coincident timing between the MRE on the WTDPF and the tree's inundation. Its age (5.3–5.6 k.y. B.P.; Table 1) is slightly greater than the MRE age range determined at FLL but is consistent with the range of dates determined by Lindstrom (1990).

Rubicon Point to Dollar Point

Several CHIRP profiles discussed by Dingler (2007) were reexamined to define the Rubicon and Dollar Point sections of the WTDPF. Deformation similar to that in FLL is observed across a CHIRP profile at the base of the shelf offshore Rubicon (Figs. 3 and 16). An ~1.4–2.0 m thick section of nearly transparent, unfaulted material overlies a divergent bed that thickens into the fault and infills the small accommodation (Fig. 17). As in FLL, the divergent bed rests directly above the MRE horizon and has a high-amplitude basal reflector suggesting it is a coarse-grained deposit, possibly a gravity slide. The MRE horizon is offset down-to-the-east by 1.0 m (possibly along a synthetic splay of the WTDPF) but farther down-section the offset increases to 2.0 m. Folding is observed ~150 m east of the main fault with horizons offset vertically up to 0.3 m. A piston core located ~800 m from the eastern end of the profile in Figure 3

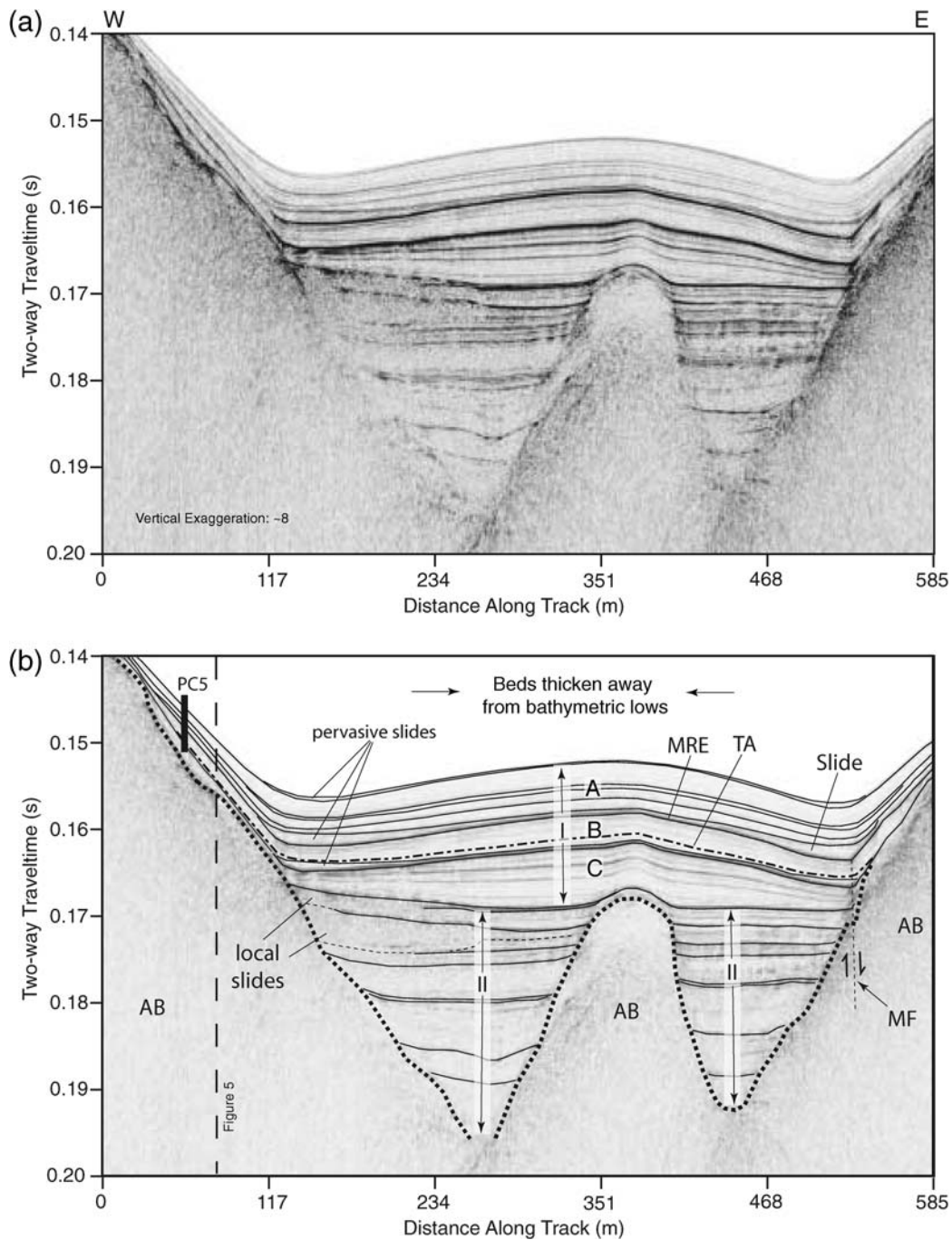


Figure 11. East-west oriented profile highlighting the interplay between current-controlled deposition that forms contourite drifts and down-slope deposits that infill bathymetric low points. Units A, B, and C of section I are separated by coarse-grained slide deposits, resulting in the high-amplitude contacts. The MRE horizon is traced from profiles to the south. Piston core PC5 (~50 m to the north of its projected position shown in the figure) samples the 7.6–8.0 k.y. B.P. Tsoyowata Ash (Fig. 4; Bacon, 1983). The stratigraphic position of the TA is projected onto the seismic section and correlated basin wide. Several thin slides are observed on several profiles, and other local slides are observed to disrupt underlying strata. Evidence for drift deposits is not observed in section II, but small slide complexes are observed along the basin slopes and uniform deposition in topographic lows.

sampled two distinct slide deposits, one at ~0.6 m and the other at ~1.2 m, that have been correlated with several cores to the north and have been dated at 4.1–4.5 k.y. B.P. and 5.3–5.6 k.y. B.P., respectively (Smith *et al.*, 2007). Despite the equivalent age of the upper slide in the core and the MRE

timing along the Fallen Leaf section, we cannot verify that the thin slide imaged above the MRE in Figure 17 correlates with the slide in the core because their relationship is speculative. Nevertheless, using this slide as a marker bed provides a minimum sedimentation rate for this area of ~0.1 mm/yr.

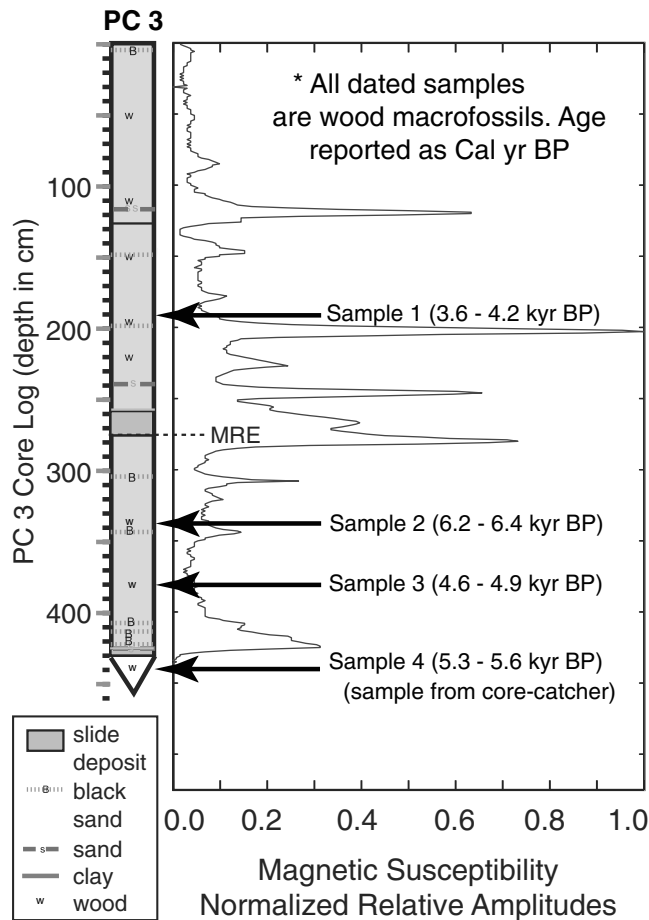


Figure 12. Piston core PC3 lithology and magnetic susceptibility logs. Each of the lithological layers logged can be correlated between all cores except PC5 (Fig. 4). The slide layer, consisting of highly disturbed sand, silt, and clay mixed with several twigs and organics, directly overlies the MRE horizon. Four radiocarbon samples (black arrows; Table 1) were dated to constrain the timing of the MRE. Sample 4, a pine needle, was taken from the core catcher and may have been slightly deeper than 4.3 m due to overpenetration.

The MRE horizon nearest the core in Figure 17 is at ~1.4 m depth, resulting in an age of ~10 k.y. Sedimentation rates may be expected to increase closer to the basin margins, thus reducing the MRE age estimate. Elsewhere in Lake Tahoe sedimentation rates in the upper 2 m have been estimated as high as ~0.4 mm/yr (Smith *et al.*, 2007), which would result in an age for the MRE of ~3.5 k.y. B.P.

Offshore Sugar Pine Point the WTDPF offsets a fan delta forming a 10.5 m high scarp observed in both bathymetry and CHIRP data (Fig. 16 and Fig. 18 for the scarp profile). Just north of Sugar Pine Point, the scarp is ~90 m tall then disappears at the main run-out area of the MBS debris apron. The Dollar Point section begins at the southern edge of the TCS, where the fault has an ~100 m tall scarp and possible slumping and secondary faulting in both the footwall and hanging wall (Fig. 16; Dingler, 2007). The scarp continues along the east edge of the TCS to Dollar Point. The scarps on

either side of the MBS are approximately the same height. The age of the MRE is not constrained on this section.

Discussion

Fallen Leaf Lake Morphology and Stratigraphic Character

FLL has formed through a combination of glacial and tectonic forces. The undulating and hummocky nature of the AB imaged in the northern two-thirds of the lake suggests that a series of recessional and lateral moraines create topography that is being filled with lacustrine sediments (Fig. 4). Formation of the steep slope bounding the basin depocenter may have facilitated glacial erosion along the WTDPF. Any preglacial structure in the bedrock, including an increased fracture density due to faulting, may have created a zone of preferential quarrying along the hanging-wall block on the lee side of glacial flow. The glacial history in the LTB provides rough estimates for the sedimentary history in FLL where it is assumed that Tioga glaciation reworked the inner walls of the moraine-bounded valleys and reset lacustrine sedimentation at ~14 ka, when the glaciers recessed (Benson *et al.*, 1998).

The stratigraphy observed in package I (Figs. 6, 8, and 11) reveals that a combination of down-slope and along-slope processes have formed intercalated drift deposits and gravity driven slope deposits. The lenticular beds that thicken toward the center of FLL resemble current controlled deposits that are swept basinward by bottom currents (Driscoll and Laine, 1996). Bathymetric lows along the basin slopes have been filled with coarse-grained beds that onlap the underlying strata. High-amplitude contacts between the lenticular beds and onlapping beds support the notion that coarser-grained down-slope deposits are emplaced on top of finer-grained drift deposits. Contourite drifts are often observed in marine environments along continental margins (Driscoll and Laine, 1996; McGinnis *et al.*, 1997; Faugeres *et al.*, 1999) and in large-scale lacustrine basins (Gilli *et al.*, 2005), but less commonly in small confined basins such as FLL.

The coarse-grained layer above the MRE horizon is observed throughout the southern lake and appears to be a slide deposit. Although disrupted strata beneath the slide (Fig. 10) may be caused by soft sediment deformation during the MRE, the coincidence of coarser-grained (proximal) material in PC1 and the chaotic reflections in Figure 10 suggest the slide source is near the southeastern basin slope (Fig. 9b). The extensive run out (> 1000 m) away from the source region and the absence of coherent internal reflectors indicate the slide deposit was most likely emplaced by a hyperpycnal flow with high velocity. Based on the stratal relationship between the slide and the MRE horizon, it is possible that the slide was triggered by the last major event on the WTDPF. Several smaller slides are identified throughout the basin

Table 1
Radiocarbon Ages Derived from Macrofossil Samples

Location	Lab ^a	Sample Number, Description ^b	Stratigraphic Depth ^c (m)	Lab Identification Number	$\delta^{13}\text{C}$ ^d	Uncalibrated ¹⁴ C Age (yr B.P.)	Calibrated Calendric Age ^e	% Confidence	Rounded Age ^f (k.y. B.P.)
Core 3 (FLL)	UofA	1, wood	1.90	AA76371	-21.9	3580 ± 110	4159–3585 4201–4227	94.1 1.0	3.6–4.2
		2, wood	3.40	AA76375	-26.3	5506 ± 41	4171–4178 6270–6400	0.2 86.5	6.2–6.4
		3, wood	3.83	AA76374	-25.6	4235 ± 44	6214–6242 4785–4869	8.9 45.6	4.6–4.9
Core 4 (FLL)	LLNL	4, pine needle	4.30	128008	-25	4795 ± 45	4620–4765 5458–5607	49.8 89.3	5.3–5.6
		5, fiber	4.10	128009	-25	7995 ± 40	5331–5375 8717–9008	6.1 94.6	8.7–9.0
Core 5 (FLL) Baldwin Beach Tree (LT)	UofA LLNL	6, wood	2.36	AA76376	-26.2	6003 ± 48	6730–6975	95.4	6.7–7.0
		7, wood	N/A	12628	-25	4705 ± 35	5510–5581 5438–5485	23.1 21.1	5.3–5.6
							5321–5420	51.2	

^aSample analysis was performed at the University of Arizona Accelerator Mass Spectrometry Laboratory (UofA) and the Lawrence Livermore National Laboratory Center for Accelerator Mass Spectrometry (LLNL).

^bAll samples were larger than 5 mg.

^c $\delta^{13}\text{C}$ values equal to -25 were not measured, but are the assumed values according to Stuiver and Polach (1977). All other values were measured.

^dMeasured from top of core.

^eAll dates given as a max–min date range. Raw ¹⁴C ages were calibrated using *OxCal v4.0.5* (Ramsey, 2001) and the *IntCal04* atmospheric curve (Reimer *et al.*, 2004). Calibrated ages are reported as % confidence under the 95% probability distribution.

^fRounded ages are reported as a max–min range. Final age ranges are rounded to the nearest 0.1 k.y.

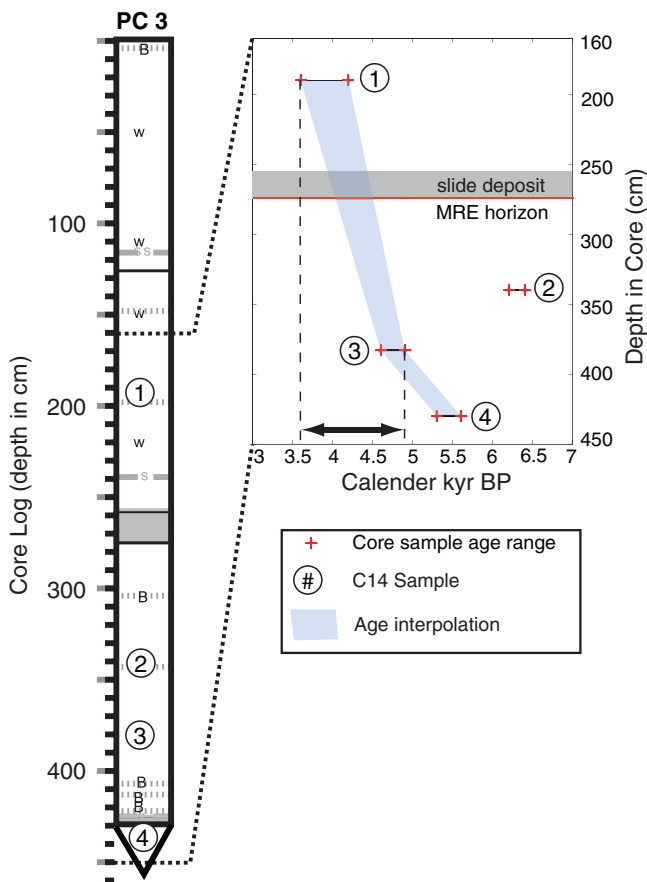


Figure 13. Plot of piston core PC3 sediment depth as a function of age. The age of the MRE was estimated by removing the thickness of the slide then linearly interpolating between samples 1 and 3. Sample 2 appears anomalously old based on its stratigraphic position and was not used in the analysis. The blue region represents the interpolated age range, and the black double-sided arrow indicates the absolute range of ages. The section between samples 1 and 3 is 173 cm and the MRE is at 65 cm after removing the 20 cm thick slide deposit. Interpolating between the upper and lower age ranges results constrains the MRE to between 4.1 and 4.5 k.y. B.P.

based on their acoustic character and range in size from very localized to regional.

Updated Fault Locations

Results from the onshore and offshore fault mapping have improved our understanding of fault locations along the Fallen Leaf section of the WTDPF and add important constraints on the potential rupture length. The southernmost extent of the fault is uncertain as the scarp merges with a steep hillside ~1 km south of Osgood Swamp, but based on the 2–3 m scarp height near this location (Fig. 14), the fault may continue southward for several kilometers. Evidence for faulting offshore Baldwin Beach based solely on CHIRP profiles is ambiguous but, when combined with mapped scarps to the south (meadow scarp) and the lake-floor disruption to the north, suggests that the WTDPF extends offshore near Baldwin Beach. Although the coseismic vertical offset

observed in FLL (Table 2) would be sufficient to drown near-shore vegetation situated east of the fault, the age of the submerged tree offshore Baldwin Beach is slightly older than the age estimate of the MRE. Nonetheless, given the timing of the MRE, it is likely that down-to-the-east motion associated with this event played a role in the ultimate preservation of the submerged trees, and we cannot reject the possibility that an older event submerged the trees but did not rupture through FLL. The mapped extent of the MF in FLL is limited but appears to project northward toward the meadow scarp (Fig. 2). We do not observe offset strata in CHIRP data collected in Emerald Bay, but acoustic penetration was limited toward the mouth of the bay by glacial sediment. North of FLL, the fault may trend towards the eastern shore of Cascade Lake, then across the mouth of Emerald Bay into the Rubicon section. The apparent complexity may be due to inconclusive mapping onshore, a relay zone between sections, or the existence of a broader basin-bounding fault zone, in which multiple faults accommodate extension. The fault's proximity to the steep basin slope creates acoustic interference and hinders our ability to image the sub-bottom using the CHIRP system; therefore, the Rubicon and Dollar Point sections are generally delineated by bathymetric expression.

The minimum estimate for the total length of the combined sections, from the southern terminus of our field mapping to where the Dollar Point section steps onshore in Carnelian Bay, is ~46 km. The fault likely extends onshore at least another 5 km north of Carnelian Bay (Saucedo *et al.*, 2005) and possibly a similar amount south of Osgood Swamp, producing a length of ~55 km. Overall, the length and morphology of the WTDPF is strikingly similar to that of the GF (Fig. 19).

Earthquake Timing, Magnitude, and Slip Rates

The MRE age estimates for the Fallen Leaf (4.1–4.5 k.y. B.P.) and Rubicon (~3–10 k.y. B.P.) sections are in rough agreement and imply the fault may rupture as a single strand. Offset measurements should be considered minimum estimates as the apparent offset (based on constant velocity) is expected to increase in the deeper, more compacted, higher velocity sediments. At FLL, the maximum observed offset of the lacustrine sediments is 3.7 m on the main trace and 1.3 m on the secondary splay, producing a maximum possible offset of 5.0 m. The MF has a 1.6 m of offset but remains poorly understood and may have recorded local deformation following an event on the WTDPF. The ~2 m offset observed along the Rubicon section (Fig. 17) is about half the maximum but within the range of offset values measured beneath FLL (e.g., Fig. 5). The fault observed in Figure 17 may represent a splay off the WTDPF, with a second fault along the base of the slope where acoustic diffractions preclude imaging with the CHIRP system. However, along strike variation in slip is common along normal fault ruptures, in particular near geometric complexities (Witkind *et al.*, 1962; Crone *et al.*, 1987; Ramelli *et al.*, 1999). More

Table 2
 WTDPF Offset Measurements from Chirp Profiles in Fallen Leaf Lake

Profile	MRE Horizon				Depth Horizon				Secondary Splay				Total* (m)
	Footwall (sec)	Hanging wall (sec)	Offset (m)	±(m)	Footwall (sec)	Hanging wall (sec)	Offset (m)	±(m)	Footwall (sec)	Hanging wall (sec)	Offset (m)	±(m)	
Perp01	0.1570	0.1592	1.7	0.2	0.1661	0.1702	3.0	0.2	0.1536	0.1562	1.0	0.2	4.0
Perp02	0.1530	0.1550	0.15	0.2	?	?	?	?	?	?	?	?	
Perp04	0.1589	0.1617	2.0	0.2	0.1780	0.1827	3.5	0.2	0.1575	0.1583	0.6	0.2	4.1
Perp05	0.1577	0.1604	2.0	0.2	0.1733	0.1779	3.5	0.2	0.1574	0.1584	0.8	0.2	4.3
Perp06	0.1604	0.1631	2.0	0.2	0.1736	0.1776	3.0	0.2	?	?	?	?	
Line4	0.1579	0.1611	2.4	0.2	0.1737	0.1780	3.2	0.2	0.1581	0.1598	1.3	0.2	4.5
Line04all [†]	0.1589	0.1626	2.8	0.2	0.1875	0.1923	3.7	0.2	0.1585	0.1597	0.8	0.2	4.5
D3L08 [‡]	0.1577	0.1602	1.9	0.2	0.1779	0.1820	3.1	0.2	0.1602	0.1614	0.9	0.2	3.9
Line03b	0.1568	0.1592	1.7	0.2	0.1679	0.1704	3.0	0.7	?	?	?	?	
Measurements			9				8				6		
Average			2.0				3.3				0.9		
Maximum			2.8				3.7				1.3		
Minimum			1.5				3.0				0.6		

Offset is measured at three places: the MRE horizon, a horizon at greater than 10 m depth, and the MRE horizon of the WTDPF splay. Piercing points on either side of the fault are listed as two-way travel times then converted to depth using a constant 1500 m/sec seismic velocity. All uncertainties are the vertical resolution of the CHIRP source. Offset measurements on Line03b (not shown) have higher uncertainty due to chaotic bedding near the fault.

[†]The sum of measurements across the depth horizon and the secondary splay.

[‡]See Figure 5.

[‡]See Figure 6.

seismic data and coincident coring are required along the Rubicon and Dollar Point sections to evaluate the precise timing and slip during the MRE.

Length and displacement estimates can be used to reconstruct the rupture magnitude for the MRE. The greatest sources of uncertainty in the magnitude calculation arise from measuring the coseismic slip and the total length of rupture, especially in regions with sparse data coverage such as the two northern sections. However, several factors allow us to calculate a worst case scenario magnitude estimate in

which the entire WTDPF ruptured during the MRE: (1) overlap between the MRE timing between the Fallen Leaf and Rubicon sections leads us to believe they could rupture in concert, (2) the Rubicon and Dollar Point sections combined have a linear trend and do not appear to have any major structural discontinuities that would terminate propagation, (3) through-going ruptures are reported on the GF despite a 1.5 km stepover (Ramelli *et al.*, 1999), and (4) ruptures along strike-slip faults suggest the limiting stepover dimension is between 3 and 4 km (Wesnousky, 2006). A range of theoretical moment magnitudes (Hanks and Kanamori, 1979) can be calculated using the minimum slip and minimum rupture length and the maximum slip and maximum rupture length estimates. Assuming all sections rupture concomitantly, we believe the uncertainty in total fault length does not exceed 10 km (20%). However, our maximum slip measurement is along the southernmost 15 km of the fault, which may actually be a better estimate of the average slip because displacement is generally the greatest at fault midpoints (Scholz, 2002). Therefore, we assume slip measured at FLL represents an average value for the entire WTDPF and calculate a theoretical moment magnitude. Using a 4.5 m maximum offset (the combined offset across the WTDPF and secondary splay in FLL), a 55 km fault length and 15 km fault width produces an M 7.33 event. Because we do not understand the nature of the splay and we cannot rule out the possibility for multiple events between the MRE horizon and the deeper offset measurements, a minimum estimate of M 6.81 is calculated using the 2.8 m maximum offset measured across the MRE horizon and a fault length of 15 km for the Fallen Leaf section. However, based on the previous dis-



Figure 14. Photograph of the WTDPF scarp ~500 m south of Osgood Swamp (see Fig. 2 for location). Mapped scarps typically have relaxed profiles with slopes between 20° and 40°, suggesting that significant time has passed since the last surface rupture. White arrow delineates the approximate base of the scarp.

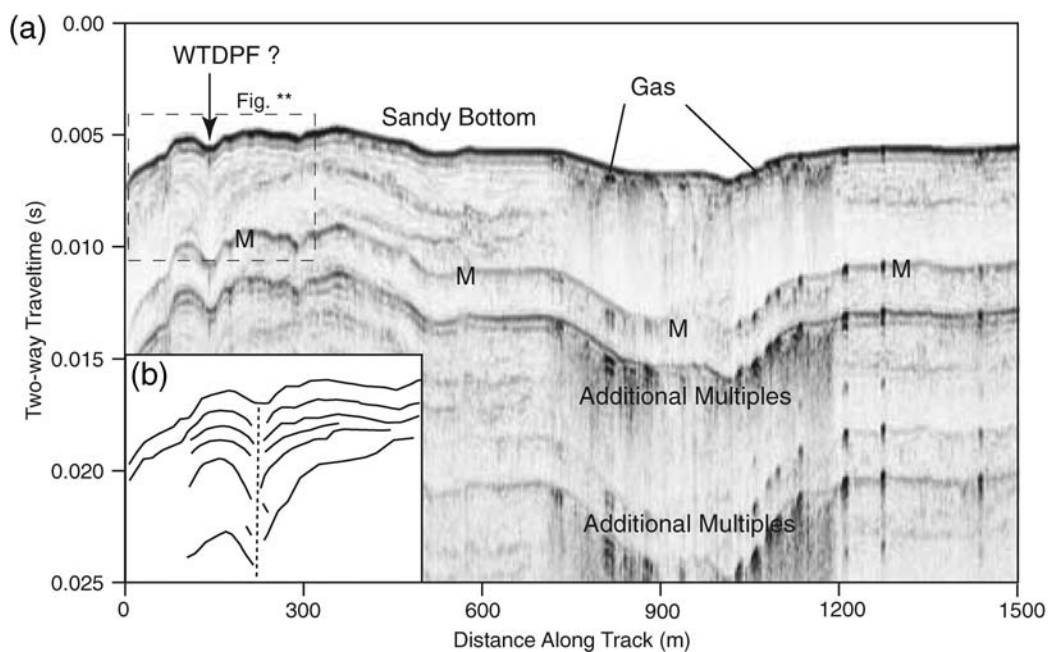


Figure 15. (a) Northwest–southeast oriented profile directly offshore Baldwin Beach (see Fig. 3 for location). Three profiles image a tightly folded syncline that is inferred to be a strand of the WTDPF. Coarse-grained sandy sediments and shallow water multiples limit penetration to ~4 m below the lake floor. There is no penetration beneath the first multiple (M). (b) Interpreted structure within the dashed box.

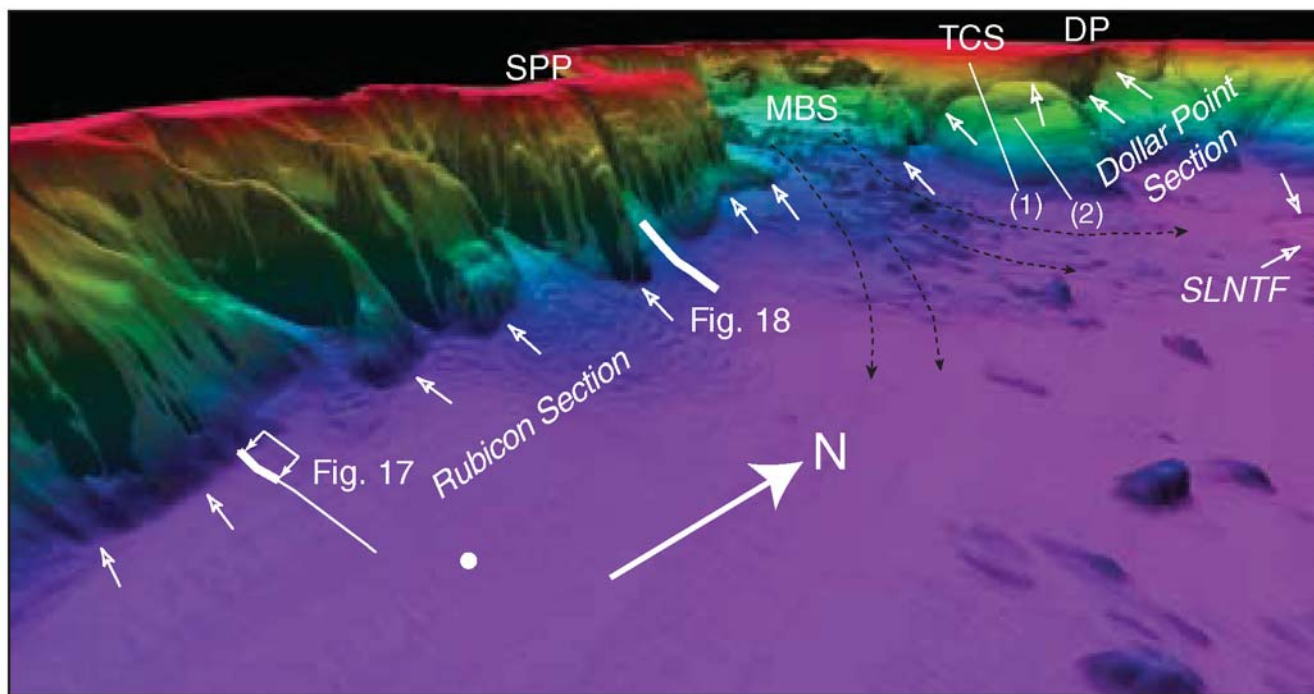


Figure 16. Three-dimensional rendering of Lake Tahoe bathymetry looking northwest along the Rubicon and Dollar Point sections of the WTDPF. Small, open arrows point to fault locations and observed lake-floor scarps; thin black arrows are the approximate transport direction of the MBS debris flow and fan systems. (1) and (2) highlight slumping head scarps and secondary deformation in the hanging wall of the WTDPF. Abbreviations: Sugar Pine Point, SPP; McKinney Bay slide, MBS; Tahoe City shelf, TCS; Dollar Point, DP; West Tahoe–Dollar Point fault, WTDPF; and Stalentine–North Tahoe fault, SLNTF.

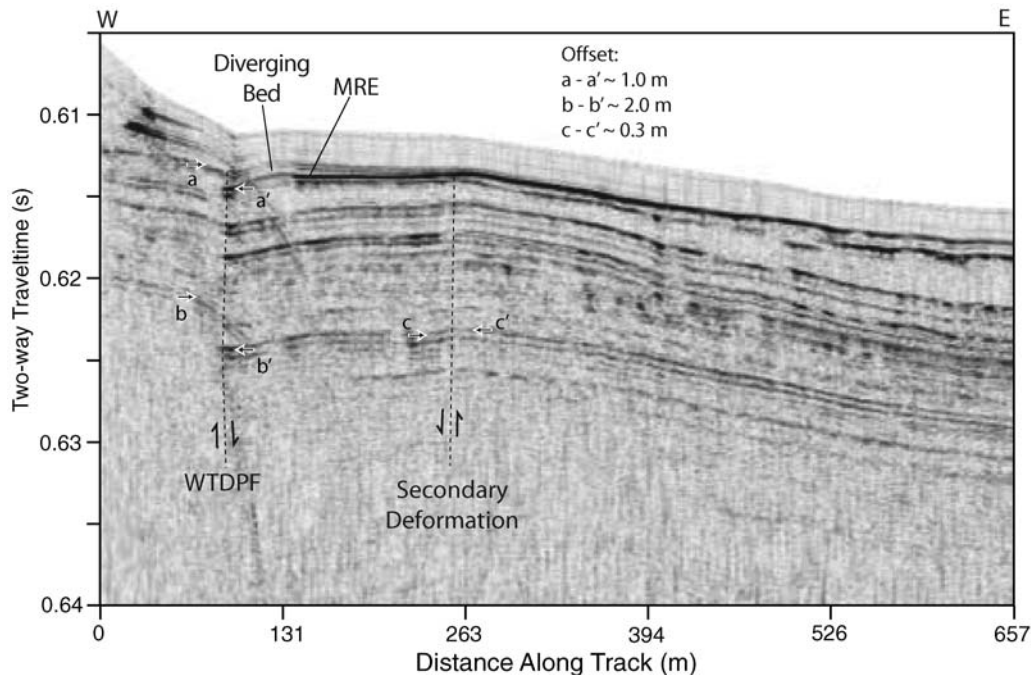


Figure 17. East-west trending profile in Lake Tahoe (see Fig. 3 for location) over the Rubicon section of the WTDPF highlighting offset lake stratigraphy. The MRE horizon is delineated by the sudden change in dip and overlying divergent wedge that thickens into the fault (similar to the deformation observed beneath FLL). Piercing points (white arrows with black interior) measure ~ 1 m down-to-the-east offset across the MRE horizon (aa') and up to ~ 2 m on a deeper horizon (bb'). Note secondary deformation ~ 150 m to the east of the WTDPF, where bedding dip abruptly changes from down-to-the-west to down-to-the-east and layers are slightly folded (> 0.5 m). This may represent secondary deformation associated with either an antithetic fault or hanging-wall collapse. A piston core ~ 800 m to the east of this profile (Smith *et al.*, 2007) provides a rough estimate of the sedimentation rates, and an MRE age between ~ 3.5 and 10 k.y. B.P., which is consistent with the age determined in FLL.

cussion, our best estimate for the magnitude of the MRE employs a fault length of 55 km and an average slip of 3.7 m (the maximum measured across the primary WTDPF splay in FLL), producing an $M 7.27$ event. Using the same parameters

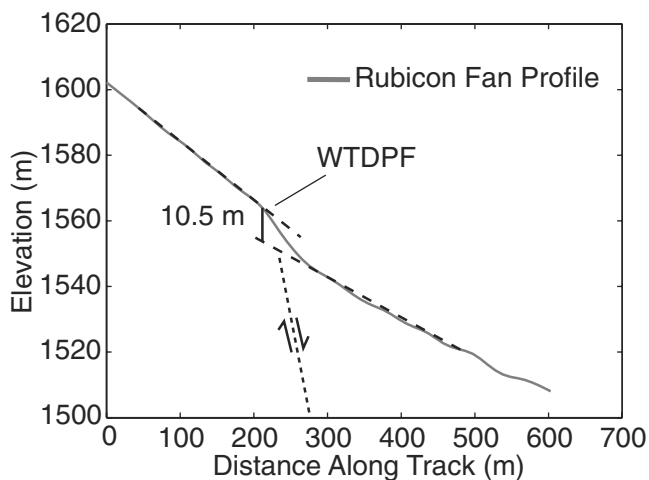


Figure 18. Topographic profile across the Rubicon Fan, offshore Sugar Pine Point (see Fig. 16 for location). A 10.5 m high scarp has formed along the WTDPF and appears to record coseismic deformation since the recession of the Tioga-aged glaciation ~ 14 ka. 10.5 m slip during this period results in an average slip rate between 0.7 and 0.8 mm/yr.

in an empirical magnitude estimate (Wells and Coppersmith, 1994) produces an event between $M 6.89$ and 7.35. In summary, the MRE magnitude estimates are between $M 6.8$ and 7.3, with the latter being the best estimate. This magnitude range is similar to historical large-magnitude earthquakes in the northwestern Basin and Range (Bell *et al.*, 2004; Wells and Coppersmith, 1994), as well as paleoseismic based estimates for the GF (Ramelli *et al.*, 1999).

Slip rates can be calculated in two ways, both of which involve the timing of Tioga glacial retreat. First, if lacustrine sediments in FLL were deposited after the Tioga glacier receded up the valley, we can apply the age of glacial retreat as an upper bound on the age of the tilted strata in Figure 6. We assume the dipping strata were originally deposited horizontally and then subsequently tilted toward the fault during multiple events. Tioga glaciation ceased in the eastern Sierra Nevada between 13 and 14 k.y. B.P. (Phillips *et al.*, 1996; Clark and Gillespie, 1997; Benson *et al.*, 1998), an age range also supported by climate proxies from piston cores collected in Lake Tahoe (Smith *et al.*, 2007); therefore, the 7 ± 2 m offset measured across the dipping beds produces a minimum late-Pleistocene slip rate between 0.4 and 0.7 mm/yr. The seismic velocity used to convert from travel time to depth in the measured section may be as high as 1800 m/sec, which would increase the offset to ~ 10.5 m (upper bound) and the slip rate to ~ 0.8 mm/yr over the last 13 k.y. In the

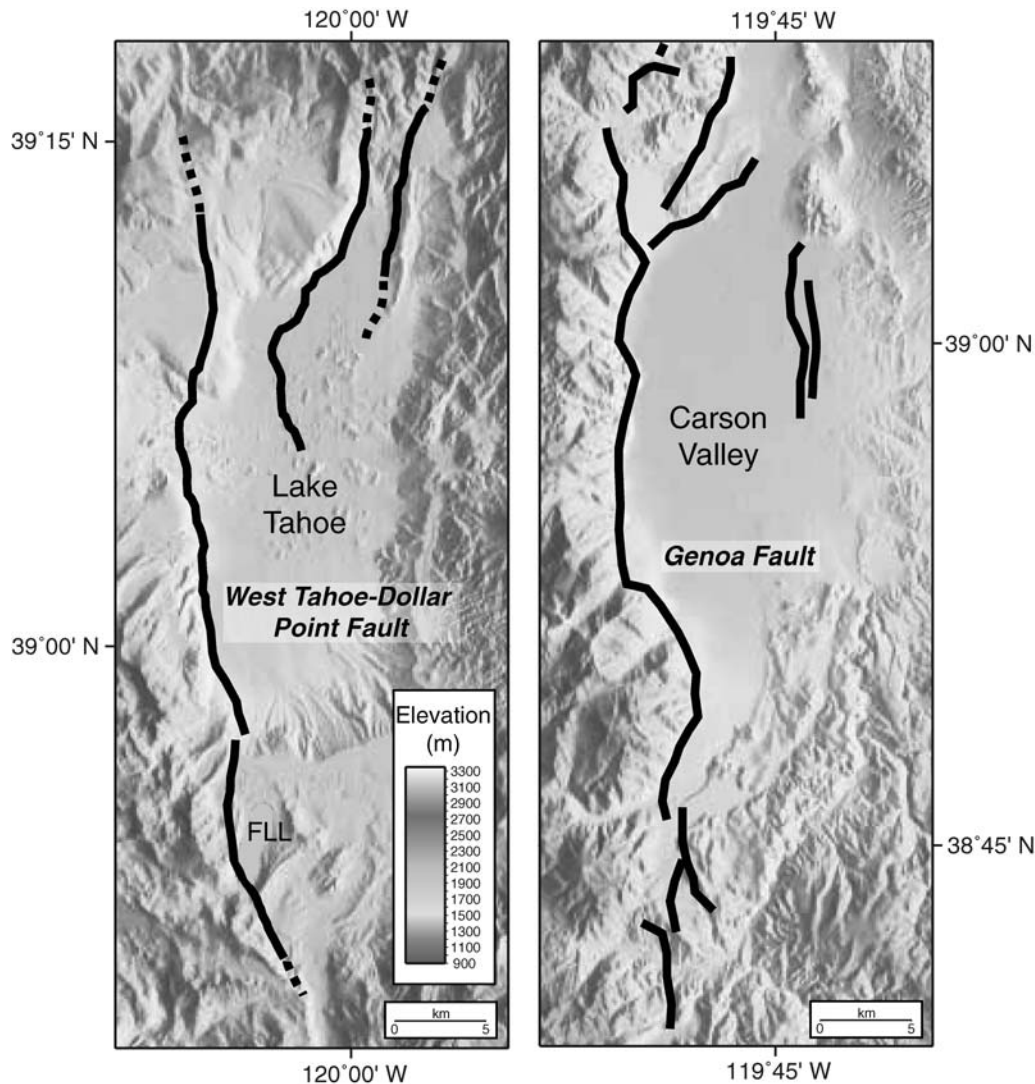


Figure 19. Comparison of the West Tahoe fault and the GF; both faults exhibit similar range front morphology, strike, and length. Together, these faults appear to be accommodating most of the extension (2–3 mm/yr) occurring within the northern Walker Lane at the latitude of Lake Tahoe.

second method, the offset fan surface offshore Sugar Pine Point (Figs. 16 and 18) is presumed to be inactive since the Tioga glacial retreat (Dingler, 2007). The 10.5 m offset (Fig. 18) since 13 k.y. B.P. also produces a maximum vertical slip rate of ~ 0.8 mm/yr. Overall, these data give rise to a vertical displacement rate between 0.4 and 0.8 mm/yr since the end of Tioga glaciation, which is slightly higher than the 0.5 mm/yr minimum slip-rate estimate (over the last ~ 20 ka) reported by Kent *et al.* (2005). An extension rate can be estimated from vertical slip rate assuming simple fault geometry. For a 60° dipping normal fault, the vertical deformation rate is transformed into an extension rate between 0.3 and 0.5 mm/yr. The slip rate along the WTDPF may be higher than estimated because the MRE occurred at 4.1–4.5 k.y. B.P. and, presumably, additional strain has accumulated during the quiescent interval. With a slip rate between 0.4 and 0.8 mm/yr, it is possible that ~ 3 m of elastic strain

has accumulated across the WTDPF. Coseismic slip of 3 m on the WTDPF could generate an $M \geq 7$ event. The GF (Fig. 19) has a vertical deformation rate of 2–3 mm/yr over the last 2 k.y. (Ramelli *et al.*, 1999), which can be converted to a 1.2–1.7 mm/yr extension rate (also assuming 60° dip). The combined extension rates of the GF and the WTDPF are consistent with the 2–3 mm/yr GPS derived extension rates across the Sierra Nevada frontal fault zone (Hammond and Thatcher, 2004, 2007).

Earthquake triggering associated with normal fault earthquakes and resulting static stress changes have been used to explain normal fault event sequences (Nostro *et al.*, 1997); therefore, it is important to compare paleoearthquake records between neighboring faults. Events on the IVF and GF at ~ 500 yr B.P. (Ramelli *et al.*, 1999; Dingler, 2007) suggest a possible relationship in the rupture timing, but the age uncertainty is large and coincident timing could also be re-

lated to dynamic and viscoelastic stress changes. We do not observe any evidence for an event 500 yr B.P. along the Fallen Leaf or Rubicon sections of WTDPF. Although the MRE timing along the SLNTF has not been determined, the proximity (~3 km) of the SLNTF to WTDPF suggests either of these faults may adversely affect stress conditions on the other following a large rupture.

Conclusions

Based on fault length and coseismic slip determined for the MRE, the WTDPF has the potential to generate $M \geq 7.0$ ruptures. The vertical slip rate determined in this study (0.4–0.8 mm/yr) suggests that the WTDPF is amongst the most active normal faults in the western Basin and Range and the northern WLB. With the westward encroachment of extensional faulting since the middle Miocene (Surpless *et al.*, 2002), the faults in the LTB, may eventually take on higher (2–3 mm/yr) slip rates comparable to that of the GF (Ramelli *et al.*, 1999). Although the northern sections require additional studies, and only one paleoearthquake has been precisely identified on the WTDPF, the new constraints on timing and slip across the WTDPF are important for hazard assessment in the LTB as well as Carson City and Reno, Nevada. Beyond the loss of life and damage associated with ground shaking in large earthquakes, Ichinose *et al.* (2000) predict ~10 m high seiche waves in Lake Tahoe can be generated by 2.83 m (average) of coseismic slip on the WTDPF. If the WTDPF were to produce an $M \geq 7.0$ rupture, the resulting seiche waves would present a significant hazard to lake-front areas.

Data and Resources

The authors collected all seismic CHIRP data and piston cores used in this study. To request data, contact author Daniel Brothers.

Acknowledgments

We would like to acknowledge Captain Brant Allen of the Tahoe Environmental Research Center, John Kleppe, John Rich of the Fallen Leaf Marina, Jenna Hill, Leah Hogarth, and Elizabeth Johnstone for their assistance with fieldwork in Fallen Leaf Lake and Lake Tahoe. We would also like to thank Rich Koehler of the University of Nevada, Reno, for thorough and helpful reviews. This project was funded through U.S. Geological Survey National Hazards Reduction Program (USGS NEHRP) Grant Number 06HQGR0064.

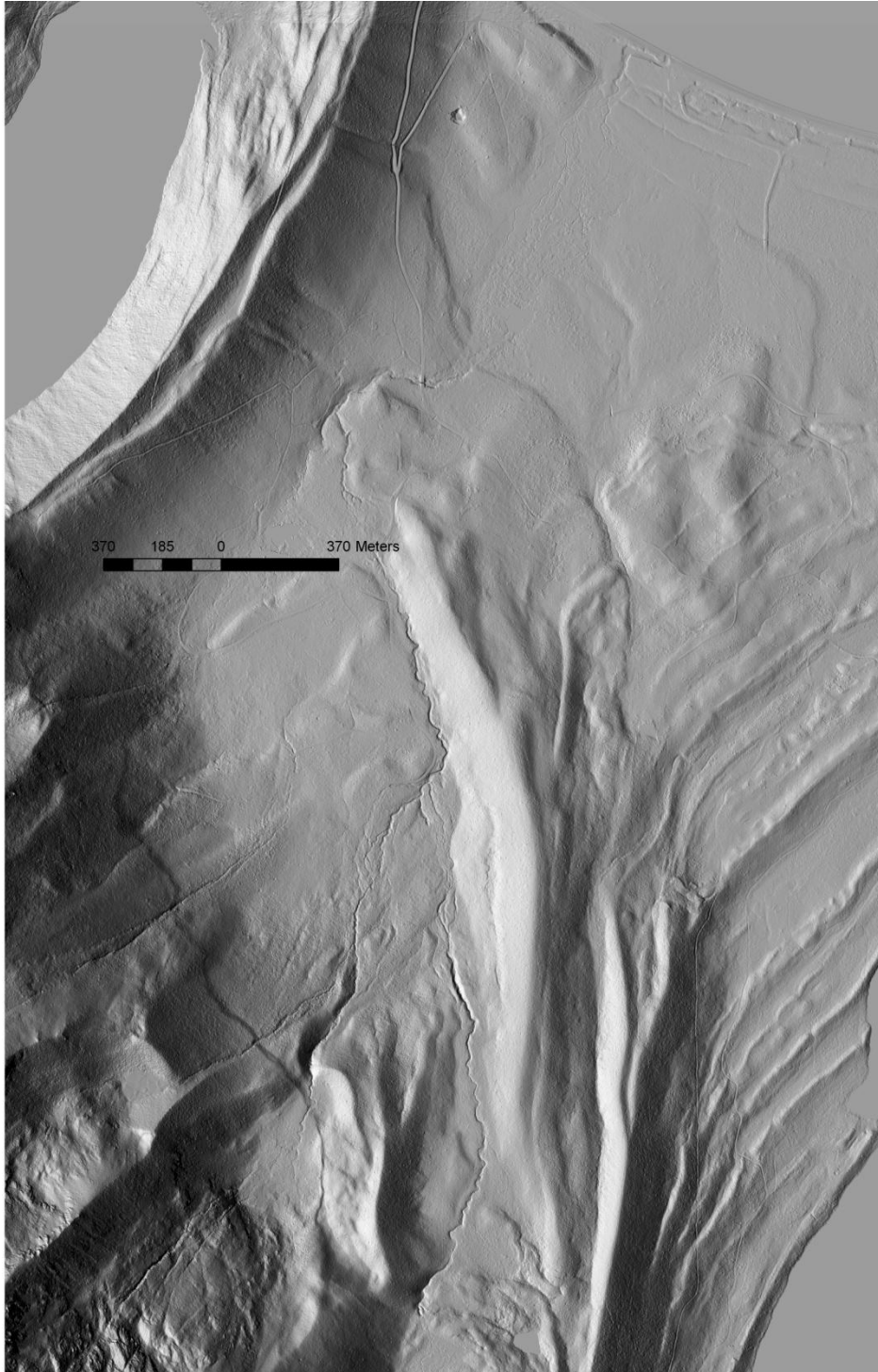
References

- Argus, D. F., and R. G. Gordon (2001). Present tectonic motion across the Coast Ranges and San Andreas fault system in central California, *Geol. Soc. Am. Bull.* **113**, 1580–1592.
- Bacon, C. R. (1983). Eruptive history of Mount Mazama and Crater Lake Caldera, Cascade Range, USA, *J. Volcanol. Geotherm. Res.* **18**, 57–115.
- Bell, J. W., S. J. Caskey, A. R. Ramelli, and L. Guerrieri (2004). Pattern and rates of faulting in the central Nevada seismic belt, and paleoseismic evidence for prior beltlike behavior, *Bull. Seismol. Soc. Am.* **94**, 1229–1254.
- Bennett, R. A., B. P. Wernicke, N. A. Niemi, A. M. Friedrich, and J. L. Davis (2003). Contemporary strain rates in the northern Basin and Range province from GPS data, *Tectonics* **22**, no. 2, 1008, doi 10.1029/2001TC001355.
- Benson, L. V., H. M. May, R. C. Antweiler, T. I. Brinton, M. Kashgarian, J. P. Smoot, and S. P. Lund (1998). Continuous lake-sediment records of glaciation in the Sierra Nevada between 52,600 and 12,500 C-14 yr BP, *Quat. Res.* **50**, 113–127.
- Birkeland, P. W. (1963). Pleistocene volcanism and deformation of the Truckee area, north of Lake Tahoe, California, *Geol. Soc. Am. Bull.* **74**, 1453–1463.
- Bischoff, J. L., and K. Cummins (2001). Wisconsin glaciation of the Sierra Nevada (79,000–15,000 yr BP) as recorded by rock flour in sediments of Owens Lake, California, *Quat. Res.* **55**, 14–24.
- Briggs, R. W., and S. G. Wesnousky (2004). Late Pleistocene fault slip rate, earthquake recurrence, and recency of slip along the Pyramid Lake fault zone, northern Walker Lane, United States, *J. Geophys. Res.-Solid Earth* **109**, B8402, doi 10.1029/2003JB002717
- Briggs, R. W., and S. G. Wesnousky (2005). Late Pleistocene and Holocene paleoearthquake activity of the Olinghouse fault zone, Nevada, *Bull. Seismol. Soc. Am.* **95**, 1301–1313.
- Clark, D. H., and A. R. Gillespie (1997). Timing and significance of late-glacial and Holocene cirque glaciation in the Sierra Nevada, California, *Quat. Int.*, **38–9**, 21–38.
- Crone, A. J., M. N. Machette, M. G. Bonilla, J. J. Lienkaemper, K. L. Pierce, W. E. Scott, and R. C. Bucknam (1987). Surface faulting accompanying the Borah Peak earthquake and segmentation of the Lost River fault, Central Idaho, *Bull. Seismol. Soc. Am.* **77**, 739–770.
- Dingler, J. A. (2007). New geophysical approaches to study neotectonics and associated geohazards, *Ph.D. Thesis*, University of California at San Diego.
- Dixon, T. H., M. Miller, F. Farina, H. Z. Wang, and D. Johnson (2000). Present-day motion of the Sierra Nevada block and some tectonic implications for the Basin and Range province, North American Cordillera, *Tectonics* **19**, 1–24.
- Driscoll, N. W., and E. P. Laine (1996). Abyssal current influence on the southwest Bermuda Rise and surrounding region, *Mar. Geol.* **130**, 231–263.
- Faugeres, J. C., D. A. V. Stow, P. Imbert, and A. Viana (1999). Seismic features diagnostic of contourite drifts, *Mar. Geol.* **162**, 1–38.
- Faulds, J. E., C. D. Henry, and N. H. Hinz (2005). Kinematics of the northern Walker Lane: an incipient transform fault along the Pacific–North American plate boundary, *Geology* **33**, 505–508.
- Gardner, J. V., L. A. Mayer, and J. E. H. Clarke (2000). Morphology and processes in Lake Tahoe (California–Nevada), *Geol. Soc. Am. Bull.* **112**, 736–746.
- Gawthorpe, R. L., I. Sharp, J. R. Underhill, and S. Gupta (1997). Linked sequence stratigraphic and structural evolution of propagating normal faults, *Geology* **25**, 795–798.
- Gilli, A., F. S. Anselmetti, D. Ariztegui, M. Beres, J. A. McKenzie, and V. Markgraf (2005). Seismic stratigraphy, buried beach ridges and contourite drifts: the Late Quaternary history of the closed Lago Cardiel basin, Argentina (49 degrees S), *Sedimentology* **52**, 1–23.
- Hammond, W. C., and W. Thatcher (2004). Contemporary tectonic deformation of the Basin and Range province, western United States: 10 years of observation with the Global Positioning System, *J. Geophys. Res.-Solid Earth* **109**, B08403, doi 10.1029/2003JB002746.
- Hammond, W. C., and W. Thatcher, (2007). Crustal deformation across the Sierra Nevada, northern Walker Lane, Basin and Range transition, western United States measured with GPS, 2000–2004, *J. Geophys. Res.-Solid Earth*, **112**, B05411, doi 10.1029/2006JB004625.
- Hanks, T. C., and H. Kanamori (1979). Moment magnitude scale, *J. Geophys. Res.* **84**, 2348–2350.
- Hardy, S., and K. McClay (1999). Kinematic modelling of extensional fault-propagation folding, *J. Struct. Geol.* **21**, 695–702.

- Hearn, E. H., and E. D. Humphreys (1998). Kinematics of the southern Walker Lane belt and motion of the Sierra Nevada block, California, *J. Geophys. Res.-Solid Earth* **103**, 27033–27049.
- Henry, C. D., and M. E. Perkins (2001). Sierra Nevada-Basin and Range transition near Reno, Nevada: two-stage development at 12 and 3 Ma, *Geology* **29**, 719–722.
- Hyne, N. J., P. Chelmins, D. S. Gorsline, C. R. Goldman, and J. E. Court (1972). Quaternary history of Lake Tahoe, California–Nevada, *Geol. Soc. Am. Bull.* **83**, no. 5, 1435–1448.
- Ichinose, G., J. Anderson, K. Satake, R. Schweickert, and M. Lahren (2000). The potential hazard from tsunami and seiche waves generated by large earthquakes within Lake Tahoe, California–Nevada, *Geophys. Res. Lett.* **27**, no. 8, 1203–1206.
- Ichinose, G. A., J. G. Anderson, K. D. Smith, D. dePolo, R. Anooshehpour, R. A. Schweickert, and M. L. Lahren (1999). The seismotectonics of the 30 October 1998 Incline Village, Nevada earthquakes from regional moment tensor inversion, *Bull. Seismol. Soc. Am.* **70**, 297–305.
- Ichinose, G. A., J. G. Anderson, K. D. Smith, and Y. H. Zeng (2003). Source parameters of eastern California and western Nevada earthquakes from regional moment tensor inversion, *Bull. Seismol. Soc. Am.* **93**, 61–84.
- Kent, G. M., J. M. Babcock, N. W. Driscoll, A. J. Harding, J. A. Dingler, G. G. Seitz, J. V. Gardner, L. A. Mayer, C. R. Goldman, A. C. Heyvaert, R. C. Richards, R. Karlin, C. W. Morgan, P. T. Gayes, and L. A. Owen (2005). 60 k.y. record of extension across the western boundary of the Basin and Range province: estimate of slip rates from offset shoreline terraces and a catastrophic slide beneath Lake Tahoe, *Geology* **33**, 365–368.
- Lindstrom, S. G. (1990). Submerged tree stumps as indicators of mid-Holocene aridity in the Lake Tahoe region, *J. Calif. Gt. Basin Anthropol.* **12**, 146–157.
- McGinnis, J. P., D. E. Hayes, and N. W. Driscoll (1997). Sedimentary processes across the continental rise of the southern Antarctic Peninsula, *Mar. Geol.* **141**, 91–109.
- Nostro, C., M. Cocco, and M. E. Belardinelli (1997). Static stress changes in extensional regimes: an application to southern Apennines (Italy), *Bull. Seismol. Soc. Am.* **87**, 234–248.
- Oldow, J. S. (2003). Active transtensional boundary zone between the western Great Basin and Sierra Nevada block, western US cordillera, *Geology* **31**, 1033–1036.
- Phillips, F. M., M. G. Zreda, L. V. Benson, M. A. Plummer, D. Elmore, and P. Sharma (1996). Chronology for fluctuations in late Pleistocene Sierra Nevada glaciers and lakes, *Science* **274**, 749–751.
- Ramelli, A. R., J. W. Bell, C. M. dePolo, and J. C. Yount (1999). Large-magnitude, late Holocene earthquakes on the Genoa fault, west-central Nevada and eastern California, *Bull. Seismol. Soc. Am.* **89**, 1458–1472.
- Ramsey, C. B. (1995). Radiocarbon calibration and analysis of stratigraphy: the OxCal program, *Radiocarbon* **37**, 425–430.
- Ramsey, C. B. (2001). Development of the radiocarbon calibration program, *Radiocarbon* **43**, no. 2A, 355–363.
- Reimer, P. J., M. G. L. Baillie, E. Bard, A. Bayliss, J. W. Beck, C. J. H. Bertrand, P. G. Blackwell, C. E. Buck, G. S. Burr, K. B. Cutler, P. E. Damon, R. L. Edwards, R. G. Fairbanks, M. Friedrich, T. P. Guilderson, A. G. Hogg, K. A. Hughen, B. Kromer, G. McCormac, S. Manning, C. B. Ramsey, R. W. Reimer, S. Remmele, J. R. Southon, M. Stuiver, S. Talamo, F. W. Taylor, J. van der Plicht, and C. E. Weyhenmeyer (2004). IntCal04 terrestrial radiocarbon age calibration, 0–26 cal kyr BP, *Radiocarbon* **46**, 1029–1058.
- Sarna-Wojkicki, A. M., K. R. Lajoie, C. E. Meyer, D. P. Adam, and H. J. Rieck (1991). Tephrochronologic correlation of upper Neogene sediments along the Pacific margin, conterminous United States, in *Quaternary Non-Glacial Geology: Conterminous United States*, in The Decade of North American Geology, R. B. Morrison (Editor), Geological Society of America, Boulder, Colorado, Vol. **K-2**, 117–140.
- Saucedo, G. J., J. D. Little, S. E. Watkins, J. R. Davis, M. T. Mascorro, V. D. Walker, and E. W. Ford (2005). Geologic map of the Lake Tahoe Basin, California and Nevada, California Geological Survey, scale 1:100,000.
- Scholz, C. H. (2002). The mechanics of earthquakes and faulting, Second Ed., Cambridge U. Press, Cambridge, UK, 439 pp..
- Schweickert, R. A., M. M. Lahren, K. D. Smith, and R. Karlin (1999). Preliminary fault map of the Lake Tahoe Basin, California and Nevada, *Seism. Res. Lett.* **70**, 306–312.
- Smith, K. D., D. von Seggern, G. Blewitt, L. Preston, J. G. Anderson, B. P. Wernicke, and J. L. Davis (2004). Evidence for deep magma injection beneath Lake Tahoe, Nevada–California, *Science* **305**, 1277–1280.
- Smith, S. B., R. Karlin, G. G. Seitz, and G. M. Kent (2007). Clastic sedimentation in Lake Tahoe as a record for submarine landsliding and seismic shaking (Abstract OS33A-1000), *Eos. Trans. AGU* **88**, OS33A-1000.
- Stewart, J. H. (1988). Tectonics of the Walker Lane belt, western Great Basin–Mesozoic and Cenozoic deformation in a zone of shear, in *Metamorphism and Crustal Evolution of the Western United States*, W. G. Ernst (Editor), Vol. **VII**, Prentice-Hall, Englewood Cliffs, New Jersey, 683–713.
- Stuiver, M., and H. A. Polach (1977). Reporting of C^{14} data, *Radiocarbon* **19**, no. 3, 355–363.
- Surpless, B. E., D. F. Stockli, T. A. Dumitru, and E. L. Miller. (2002). Two-phase westward encroachment of Basin and Range extension into the northern Sierra Nevada, *Tectonics* **21**, no. 1, doi 10.1029/2000TC001257.
- Svarc, J. L., J. C. Savage, W. H. Prescott, and A. R. Ramelli (2002). Strain accumulation and rotation in western Nevada, 1993–2000, *J. Geophys. Res.-Solid Earth* **107**, no. B5, doi 10.1029/2001JB000579.
- Unruh, J., J. Humphrey, and A. Barron (2003). Transtensional model for the Sierra Nevada frontal fault system, eastern California, *Geology* **31**, 327–330.
- Wells, D. L., and K. J. Coppersmith (1994). New empirical relationships among magnitude, rupture length, rupture width, rupture area, and surface displacement, *Bull. Seismol. Soc. Am.* **84**, 974–1002.
- Wesnousky, S. G. (2006). Predicting the endpoints of earthquake ruptures, *Nature* **444**, 358–360.
- Witkind, I. J., W. B. Myers, J. B. Hadley, W. Hamilton, and G. D. Fraser (1962). Geologic features of the earthquake at Hebgen Lake, Montana, August 17, 1959, *Bull. Seismol. Soc. Am.* **52**, 163–180.
- Scripps Institution of Oceanography
University of California, San Diego
9500 Gilman Drive
La Jolla, California 92093-0225
dbrother@ucsd.edu
(D.S.B., G.M.K., N.W.D., J.A.D., A.J.H., J.M.B.)
- Department of Geological Sciences/172
University of Nevada, Reno
1664 N. Virginia St.
Reno, Nevada 89557-0138
(S.B.S., R.K.)
- Department of Geological Sciences
San Diego State University
5500 Campanile Drive
San Diego, California 92182
(G.G.S.)

Manuscript received 4 January 2008

Day 1, Stop 4 – West Tahoe Fault

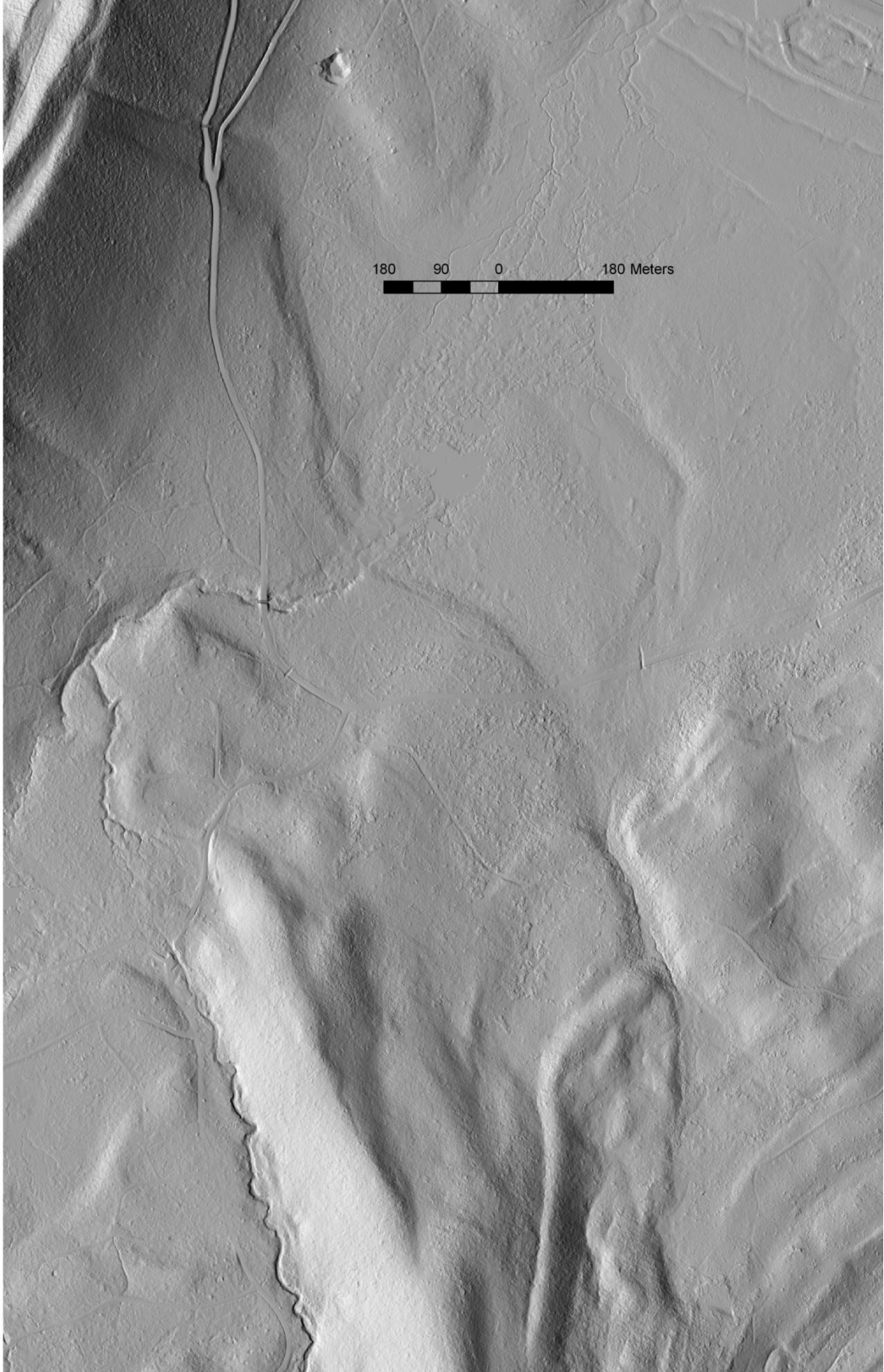


This site is located about half way between Lake Tahoe and Fallen Leaf Lake. It is located in a

small valley largely formed by coalescing recessional Tioga-age moraines. The well-defined linear scarp is continuous over several hundred meters. Although this scarp is bounded by a moist meadow on which some runoff occurs, the scarp shows only minor signs of fluvial modification. The meadow is essentially level so there is not much stream energy at this location. It appears that this meadow was once a pond, that has become filled with fluvial and colluvial material. There has been no recent incision of this “valley” as evidenced by the non-existence of an opposite-facing paired fluvial scarp. The existence of fine-grained deposits on the hanging wall block has several positive aspects. First, these fine grain deposits are almost certainly C-14 datable, as they generally preserve organic matter quite well. In fact, it would not be surprising to encounter buried peat layers that provide unparalleled dating accuracy, because they contain in situ formed organic matter. Secondly, finer grained deposits simplify the excavation and logging greatly, and often provide a clearer observation of the event deformation, because large boulders have a tendency to generate hard to interpret deformation features both during earthquakes and during excavations. I had targeted this site for a paleoseismic trench, however, the recently collected LiDAR has led me to reconsider. The main reason for these doubts is the newly discovered western strand at the base of Mount Tallac, which appears to be active at a similar level. So any paleoseismic record from this strand may be incomplete in events and certainly in long-term slip.



Oblique View of the West Tahoe fault between Lake Tahoe and Fallen Leaf Lake.



Proposed trench site identified years before we viewed LiDAR. At that time we interpreted this strand to be located near the highest onshore slip rate portion of the WTF.



Proposed Trench Site shown above . Trench Location outlined in black, top and bottom of the fault scarp indicated by white lines. Scarp height is ~ 4 meters with beveled portion, which is most likely the result of 2 or more events.



Day 1, Stop 5 – Taylor Creek Amphitheater

GPS Measurement of Active Crustal Deformation of the Lake Tahoe Basin and Vicinity

Extended Abstract and Figures

William C. Hammond, Corné Kreemer, Geoff Blewitt, Jayne Bormann
Nevada Geodetic Laboratory
Nevada Bureau of Mines and Geology
University of Nevada, Reno

Geodetic measurements provide data on the rate, pattern and style of crustal deformation, and constrain the slip rate budget across active faults systems. We present a new published synoptic strain rate map of Nevada and California that places the Lake Tahoe basin into the context of the province-scale plate boundary crustal deformation field (Figure 1- *Kreemer et al.*, 2012), and detailed measurements that record deformation across faults in the Lake Tahoe basin.

Across Lake Tahoe, GPS velocity gradients are consistent with the pattern and style of deformation throughout the western Great Basin. Velocities are directed northwest with respect to stable North America and increase to the west until reaching the Sierra Nevada/Great Valley microplate (SNGV - Figure 2 and Figure 3a). These velocities, and the strain implied from the gradients in velocity, are consistent with those seen elsewhere in the San Andreas system in western California, suggesting that deformation of the Tahoe basin is an active component helping to accommodate Pacific/North America plate boundary motion in a wide system of intracontinental transtension. The SNGV is a near-rigid block (to within ~ 1 mm/yr) that forms a northwest translating rigid boundary condition to the west of the Sierra Nevada crest.

Examination of the details in GPS velocities measured between the crest of the Sierra Nevada (west side of the Tahoe basin) and the crest of the Carson Range (east side of basin) shows that rates vary by a total of ~ 1.8 mm/yr (Figure 4). This velocity difference is most precisely estimated when viewed through station pairs that span the lake (e.g. stations WARD and SLID - Figures 3 & 4). Looking at examples of individual components shows that WARD moves north with respect to SLID at 0.4 mm/yr, and west 1.7 mm/yr. P141 moves north with respect to P142 at 1.1 mm/yr and west 1.4 mm/yr. The formal uncertainties in these rates are too small since they are smaller than the changes in rates we infer by considering different time segments of the data. We expect the uncertainties are at least 0.2 mm/yr, possibly higher. The relative size of the east component compared to the north component translation rates between WARD - SLID might lead one to conclude that extension is dominant over shear, but this difference is not significant in other pairs (e.g. P141 - P142). These EarthScope Plate Boundary Observatory stations are farther afield of the Basin and may capture deformation associated with other faults (e.g. Genoa fault).

Because much of the signal in GPS velocities in a North America frame is attributable to motion east of our area of interest, and includes a component of

rigid body rotation, we subtract the mean velocity for 4 stations east of Carson Valley, to highlight features in the deformation field (Figure 3b). This allows us to better interpret the patterns of strain in all of the high-precision GPS stations in the Tahoe region. The deformation style is characterized by east-west extension in addition to north-south contraction implying shear that is broadly consistent the pattern seen throughout the rest of the Pacific/North America plate boundary in California and Nevada (Figure 1). The rate of extension across the basin is ~ 1.8 mm/yr.

Strain accumulation measured by GPS can be compared to evidence for strain release present in the geologic record. In the case of the West Tahoe, North Tahoe, and Incline Village faults that strike roughly north-south, the expected sense of slip is east-west normal extension and north-south dextral slip. The true rake of oblique slip depends on the real local strike of the fault and local block rotations that may not be perfectly aligned to regional patterns. However, total modeled slip rates should vector sum to at least 1.8 mm/yr including both the dextral strike slip and east-west horizontal extension components. Thus agreement between geodetic slip rates and local measurements of fault slip from offset markers depends on the local strike of the fault segment, fault system complexity, and possibly real variations in rate of block motions over the period of observation.

To more accurately estimate patterns of likely future strain release rate from geodetic measurements we model the long-term motion with blocks. The presentation by *Bormann et al* (in this guide) is an effort to model block motions in detail on a regional scale, including the Tahoe Basin. That modeling accounts for local vertical axis rotations, the locking of faults from seismogenic depths to the surface, and first order geometric complexities in the fault systems.

A Geodetic Strain Rate Model for the Pacific-North American Plate Boundary, Western United States

Corné Kreemer¹
 William C. Hammond¹
 Geoffrey Blewitt¹
 Austin A. Holland²
 Richard A. Bennett²

¹Nevada Bureau of Mines and Geology,
 University of Nevada Reno
²Department of Geological Sciences,
 University of Arizona
 2012

SUMMARY

The map presents a model of crustal strain rates derived from Global Positioning System (GPS) measurements and geologic information. The model domain covers the Pacific-North American plate boundary in the western United States. The model is based on GPS measurements and geologic information. The model is based on GPS measurements and geologic information. The model is based on GPS measurements and geologic information.



GPS DATA

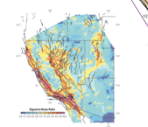
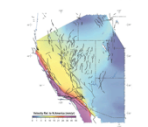
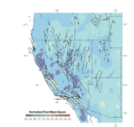
The GPS stations were selected according to the study of the GPS network in the western United States. The GPS stations were selected according to the study of the GPS network in the western United States. The GPS stations were selected according to the study of the GPS network in the western United States.

GPS stations and an area covered within which the GPS stations are located. The GPS stations are located in the western United States. The GPS stations are located in the western United States. The GPS stations are located in the western United States.

MODELING DETAILS

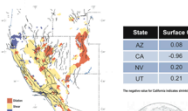
For the strain rate calculations, we used GPS stations with available velocity and geologic information. The model is based on GPS measurements and geologic information. The model is based on GPS measurements and geologic information.

A method for the continuous Strain Rate Model (SRM) is described. The SRM is based on GPS measurements and geologic information. The SRM is based on GPS measurements and geologic information.



BIBLIOGRAPHY

Allen, M. R., & England, P. (2001). Global plate motions and strain rates. *Journal of Geophysical Research*, 106, 14663-14686.
 Blewitt, G., Hammond, W. C., & Kreemer, C. (2002). GPS measurements of the Pacific-North American plate boundary in the western United States. *Journal of Geophysical Research*, 107, 4103.
 Kreemer, C., Hammond, W. C., Blewitt, G., & Holland, A. A. (2012). A geodetic strain rate model for the Pacific-North American plate boundary, western United States. *Journal of Geophysical Research*, 117, B03302.



State	Surface Growth (mm/yr)
AZ	0.08
CA	0.06
NV	0.20
UT	0.21

GEODETIC VELOCITIES RELATIVE TO NORTH AMERICA
 (mm/yr)
 - Continuous GPS
 - IGS permanent GPS
 - Other studies

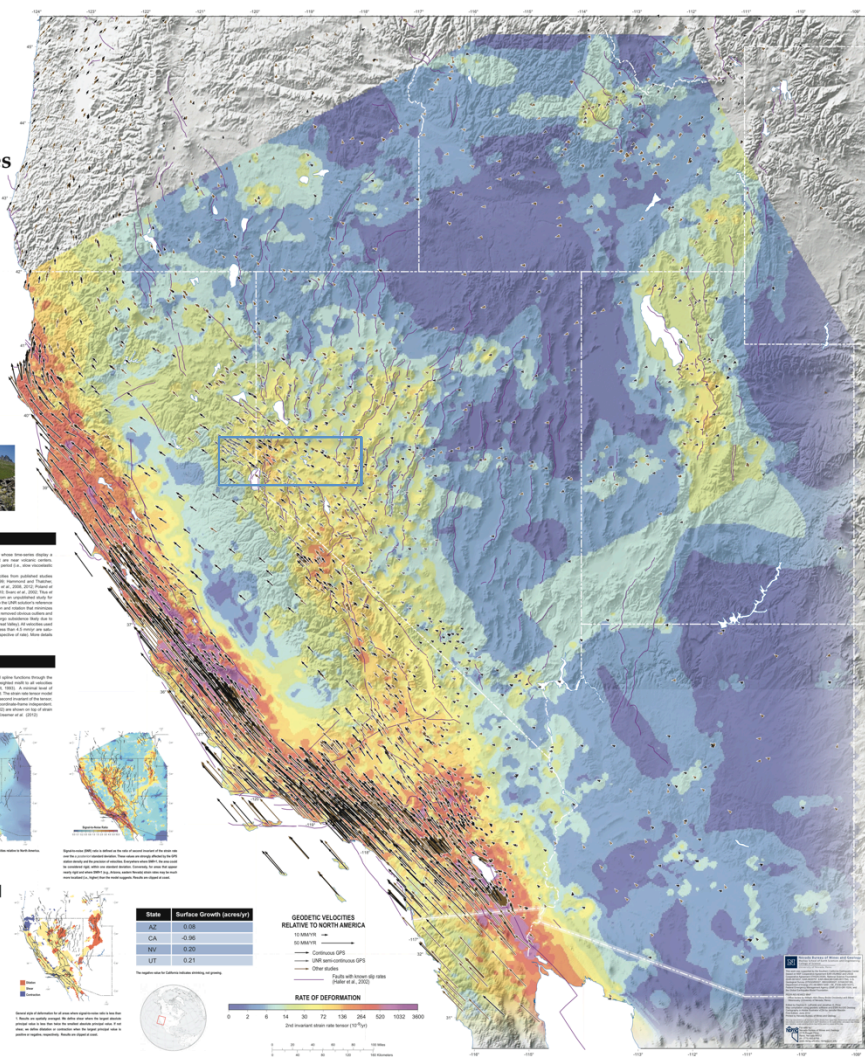


Figure 1. Strain rate map of California and Nevada (Kreemer et al., 2012). Based on GPS measurements, this map shows the intensity of deformation rate at all locations in the model domain. Velocities used to construct the model are shown as vectors in a North America reference frame. Approximate location of GPS velocity profile in Figure 2, near Lake Tahoe is shown with light rectangle near the center of the map.

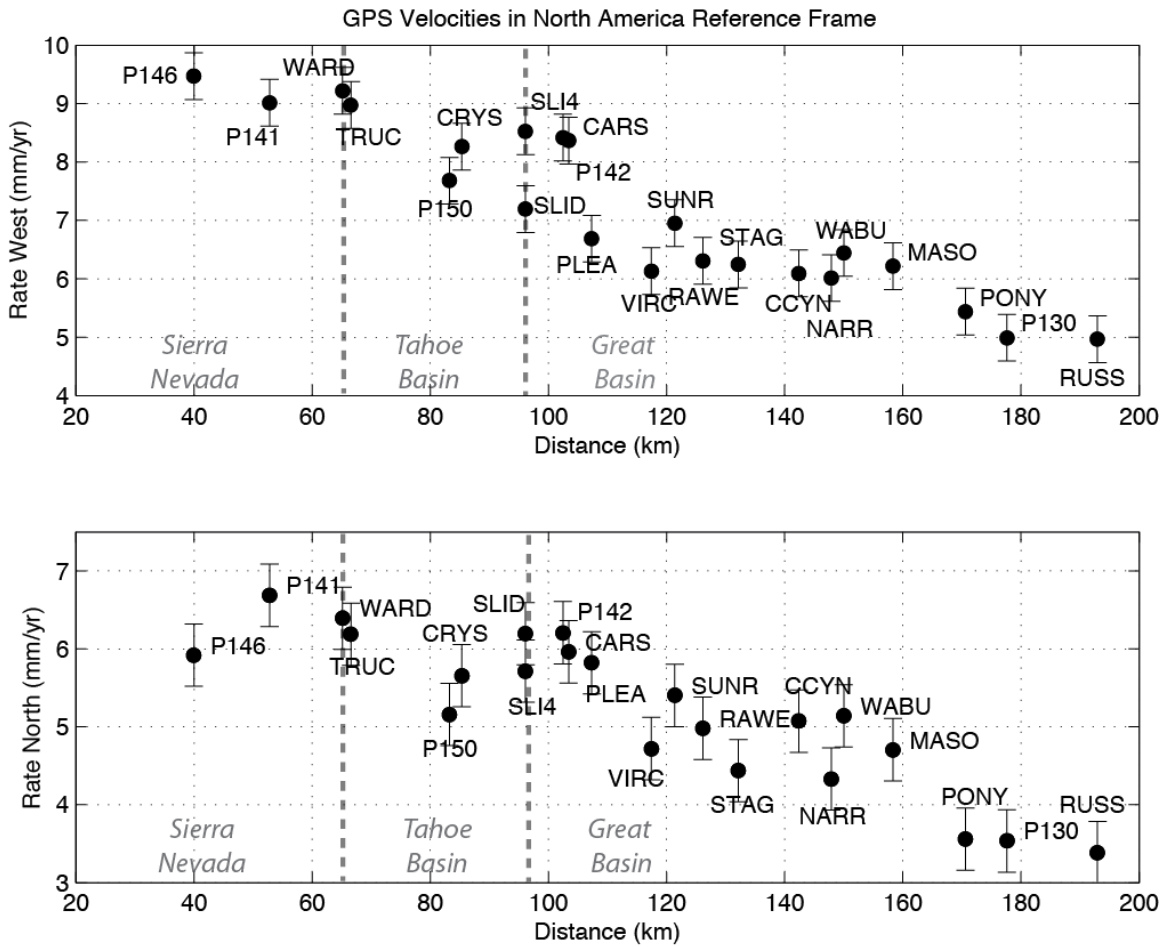


Figure 2. GPS velocity profile across Sierra Nevada, Walker Lane, Great Basin transition, in vicinity of lake Take Basin. See Figures 1 for approximate location of profile and Figure 3 for velocities plotted in map view. A floor in rate uncertainties of 0.2 mm/yr was applied because formal uncertainties are unrealistically small.

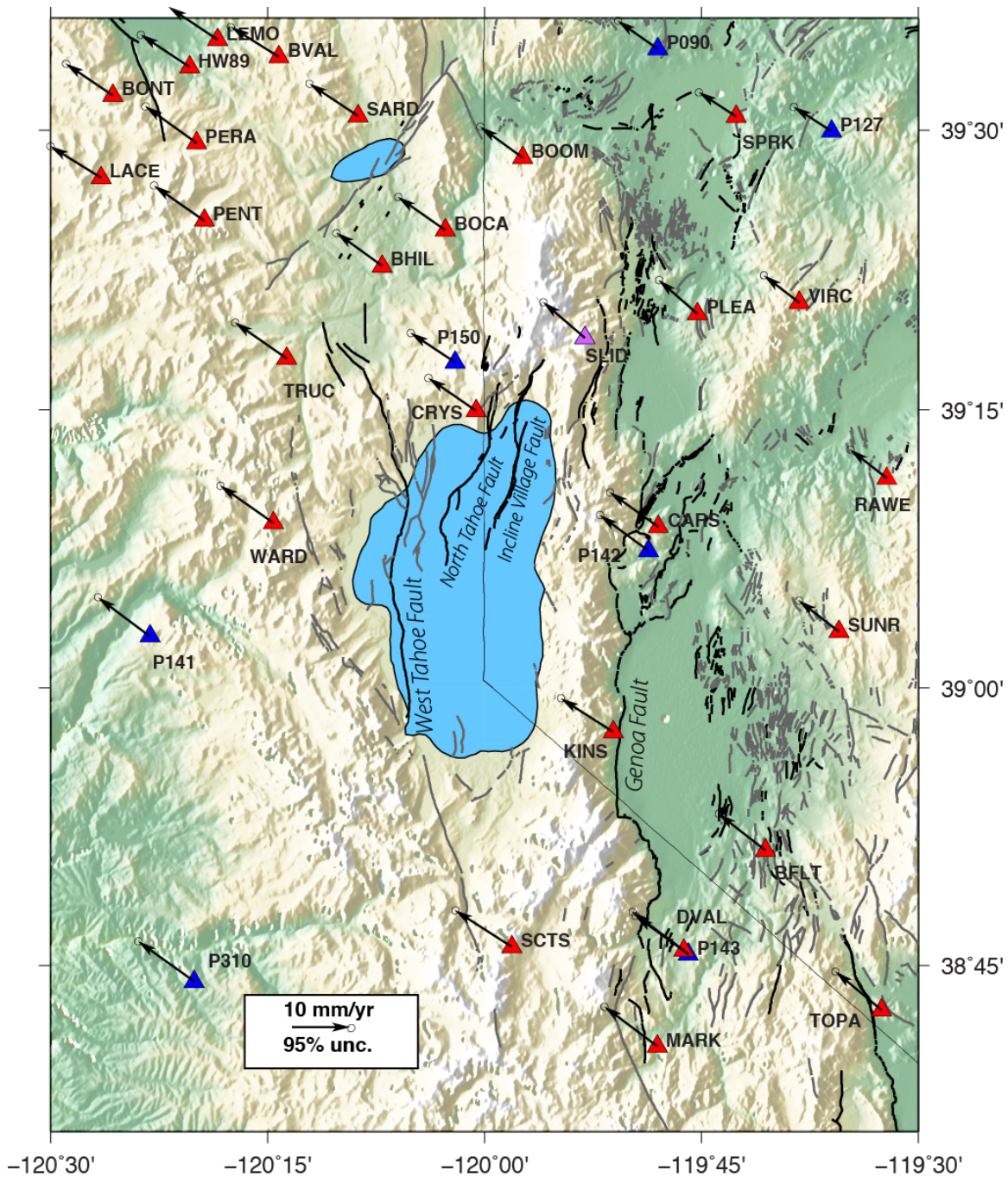


Figure 3a. GPS velocities in North America fixed reference frame and topography around Lake Tahoe. Red triangles=MAGNET (Mobile Array of GPS for Nevada Transtension operated by UNR), Blue=EarthScope Plate Boundary Observatory, Maroon=BARGEN network (only SLID for this figure). The station WARD is a MAGNET site near the Sierra Nevada crest at the summit of Alpine Meadows ski area. SLID is a continuous station at the summit of the Mt. Rose ski area on Slide Mountain, NV.

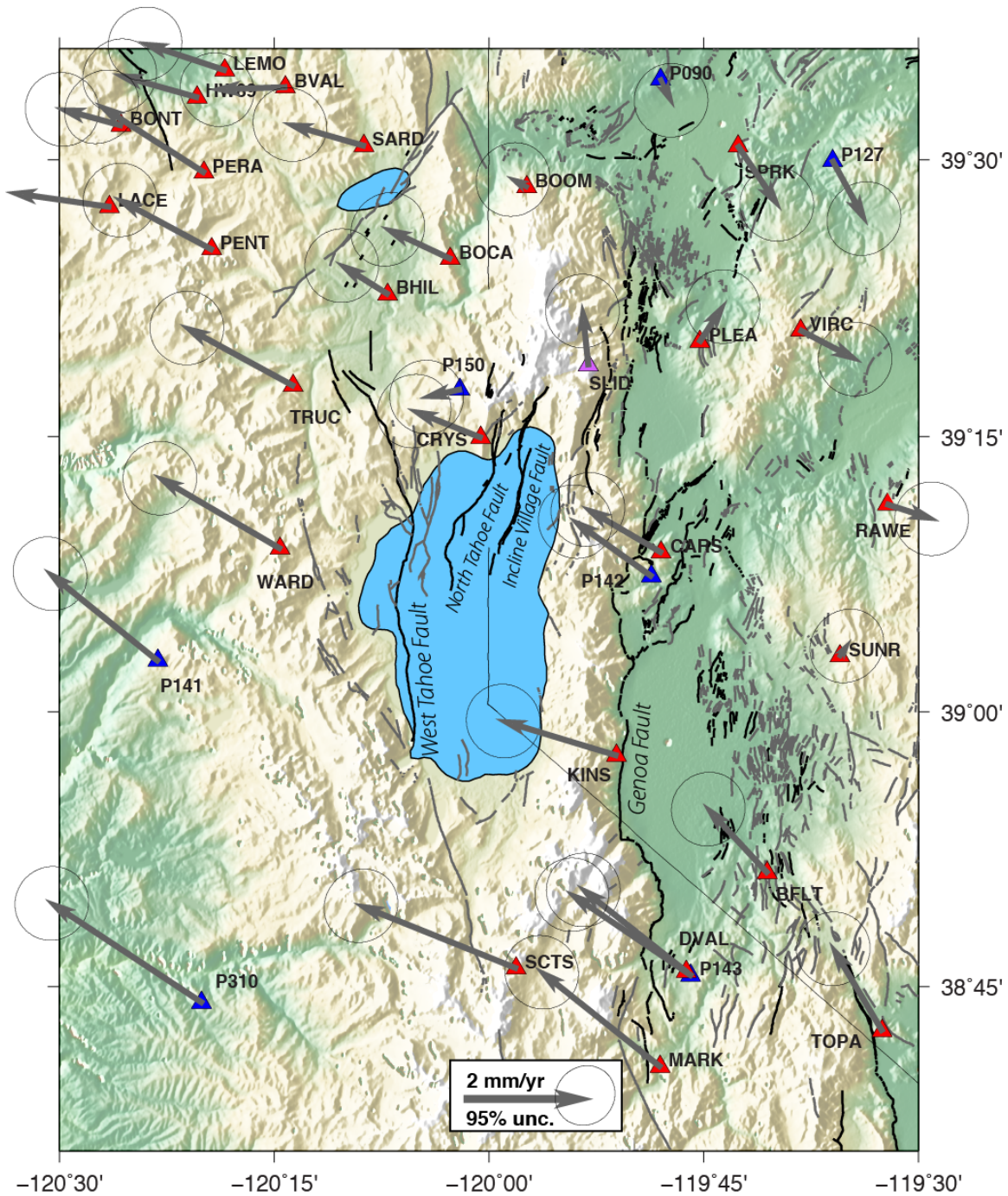


Figure 3b. Same as Figure 3a, but velocities are placed in a reference frame whose mean velocity east of Carson Valley is zero (mean of stations SUNR, RAWE, BFLT, PNUT). This improves our ability to see variations in the velocity field. Strain rate field is predominantly shear with east-west component of extension. Note change in vector velocity scale compared to Figure 3a.

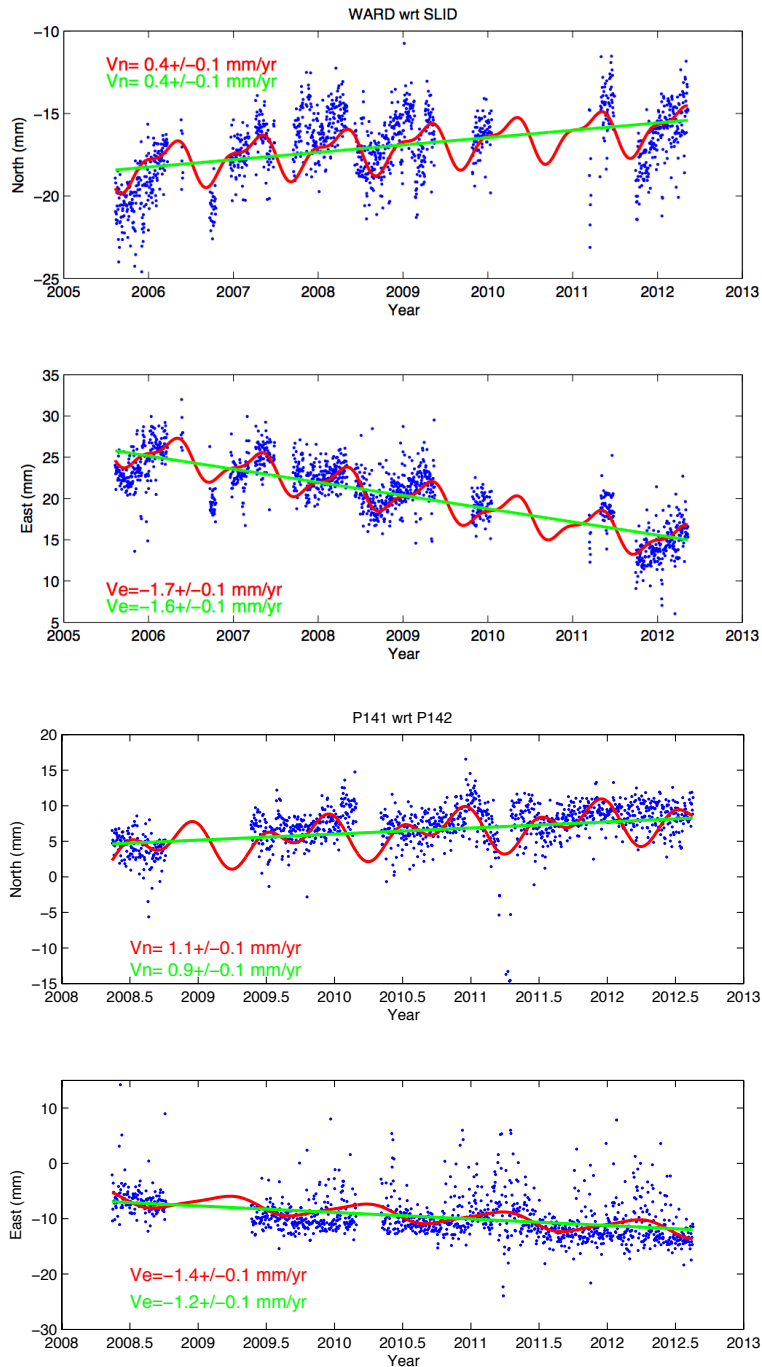


Figure 4. Top Two Panels) North and east component time series of position of GPS site WARD (Sierra Nevada crest at Alpine Meadows) with respect to GPS site SLID. Bottom Two Panels) North and east component time series of P141 with respect to P142. Both baselines span the Tahoe Basin. Location of GPS sites are shown in Figure 3. Red rates and curves show model with annual and semi-annual terms included in time series model, green include linear terms only. A floor in rate uncertainties of 0. mm/yr was applied because formal uncertainties are unrealistically small.

References

Kreemer, C., W.C. Hammond, G. Blewitt, A. Holland, R.A. Bennett, 2012, A geodetic strain rate model for the southwestern United States, Nevada Bureau of Mines and Geology, M178. Available free for download, see NBMG online publication sales.

Holocene Subaqueous Paleoseismology of Lake Tahoe

Submitted to the Geological Society of America Bulletin: Accepted: final submission on 9/12/2012.

Shane B. Smith¹, Robert E. Karlin¹, Graham Kent², Gordon Seitz³, Neal Driscoll⁴

¹*Department of Geological Sciences, University of Nevada, Reno, Reno, Nevada 89557-0172, USA*

²*Nevada Seismological Laboratory, University of Nevada, Reno, Reno, Nevada 89557-0174, USA*

³*California Geological Survey, 345 Middlefield Road, MS 520, Menlo Park, California 94025, USA*

⁴*Scripps Institution of Oceanography, UCSD, 9500 Gilman Drive, La Jolla, California, 92093, USA, Mail Code 0244*

ABSTRACT

Gravity flow deposits recovered in a suite of sediment cores in Lake Tahoe were examined to determine if the event deposits may have been triggered by strong shaking from earthquakes on active faults within and in close proximity to the Lake Tahoe Basin. The acoustic character and distribution of individual lacustrine deposits as well as potential source regions were constrained by very high resolution CHIRP seismic reflection and multi-beam bathymetric data. Between 14 and 17 Holocene event deposits have been identified in Lake Tahoe and examination of their source areas suggests they are sourced from different initiation points along the steep margin with some being synchronous around the basin as opposed to flood-related deposits. Lithologic characteristics, magnetic susceptibility, carbon and nitrogen isotopic signatures, opal content, and ¹⁴C dating indicate that these event deposits are reworked lacustrine material. Radiocarbon dates indicate that the emplacement of these event deposit sediments correlates well with the late Holocene paleoseismic earthquake record developed for the Tahoe Basin. When taken alone, the causality of these events may appear ambiguous, but when the evidence is examined comprehensively, it suggests that strong shaking may likely be the primary trigger for many of the event deposits observed in the lake throughout the Holocene. For example, four event deposits are assigned to the Tahoe Basin faults. The most recent earthquakes is on the Incline Village Fault (between 630 and 120 calBP); the southern segments of the West Tahoe Fault (between 4510 and 4070 calBP); on the central and northern segments of the West Tahoe Fault and the North Tahoe Fault (5600-5330 calBP); and on the West Tahoe Fault (between 7890 and 7190 calBP). The oldest of the Tahoe Basin events coincides with the beginning of an extended period when Lake Tahoe was likely not spilling or spilling intermittently, and suggests active faulting and footwall uplift cut off the outlet at this time, exaggerating drought conditions downstream. Likewise, the event between 5600 and 5330 calBP on the West Tahoe Fault may have exaggerated a smaller drought reflected downstream in Pyramid Lake. This event may also be the most recent event (MRE) on the largest segment of the West Tahoe fault. If correct, the period since the last rupture is approximately twice the estimated average recurrence interval for the Rubicon segment of the West Tahoe Fault. A more complete Holocene record of strong shaking greatly extends the paleoseismic record in the region and indicates a combined recurrence interval of between 750 and 800 years for all faults in the region.

1. 0 INTRODUCTION

Seismic triggering of submarine/subaqueous landslides, debris flows, and turbidity currents is well documented for historic earthquakes (e.g. Heezen and Ewing, 1952, 1955; Ryan and Heezen, 1965; Krause et al., 1970; Inouchi et al, 1996; Nakajima and Kanai, 2000); however, identifying a triggering mechanism for these gravity flow deposits in the geologic record may be controversial (e.g., Shanmugam, 2009, Goldfinger et al., 2008, 2009, Atwater 2011). Numerous mechanisms may lead to gravity-driven deposits observed in the submarine/subaqueous environment: storm wave loading, water level change, hyperpycnal flow, sediment loading, volcanic eruptions, and earthquake ground motions (Hampton et al., 1996, Locat and Lee, 2002). Any distinction between these varying triggering mechanisms in the sediment record is difficult to ascertain as the gravity deposits record their transport and emplacement history rather than the triggering mechanism.

Several researchers have argued for seismic triggers for episodic deposits based on varying criteria. Turbidites offshore the Cascadia subduction zone margin and the northern San Andreas Fault have been attributed to seismic triggering on the basis of synchronous ages, stratigraphic relationships, and a confluence test (Adams, 1990, Goldfinger et al., 2003, 2007, 2008, 2009). Subaqueous landslides and associated turbidites in Lake Washington, Seattle have been suggested as seismic in origin due to the near-simultaneous slumping of multiple sources and areal distribution of the deposits (Karlin and Abella, 1992,

Karlin et al., 2004). Subaqueous landslides and associated chaotic deposition in Lake Lucerne and Lake Zurich, Switzerland have been associated with earthquakes based on the synchronous failure of multiple slumps on non-deltaic slopes, and in one case correlating to a historic earthquake (Schnellmann et al., 2002, Schnellmann et al., 2005, Strasser et al., 2006, Strasser et al., 2007). The common theme in all of these locations is occurrence of synchronous slope failures over broad areas without obvious other triggers leading to event deposits that can be correlated basin-wide by geophysical imaging and core analyses. These criteria imply a widespread trigger such as earthquake shaking.

The Lake Tahoe basin (Fig. 1) provides an excellent environment to investigate event deposits due to the presence of a large permanent lake with a high sedimentation rate in a steep walled basin with readily identifiable landslide zones (Fig. 2) and stream inputs. Direct sediment contribution by streams to the deep basin is limited to a few sources. This provides an opportunity to track changes in sedimentation across the lake basin and determine sediment source areas. Also, the earthquake recurrence interval of faults in and near the basin is expected to be greater than the uncertainty in radiocarbon dating, which is an advantage over relatively short-recurrence areas such as the Cascadia subduction zone (e.g., Goldfinger et al., 2008), as it allows for the temporal separation of anomalous sedimentation events. Unlike submarine deposits, carbon reservoir corrections are not required in Lake Tahoe because short-lived plant macrofossils are used for dating. As in any submarine/subaqueous environment, a downside to Lake Tahoe is that basin-wide sedimentation events may be triggered by many different mechanisms.

Episodic deposits were first identified in the lake as sand layers (Hyne et al., 1972), later identified as graded beds (Palmer et al., 1979), and then labeled as turbidites (Karlin et al., 2005, Kent et al., 2005), however no origin for the deposits was hypothesized. Turbidite and debris flow deposits in Fallen Leaf Lake to the south were linked to active faulting within the Tahoe basin (Brothers et al., 2009). Osleger and others (2009) conducted a data-limited two core study and interpreted these deposits as primarily hyperpycnal flow deposits resulting from extreme flood events with one seismically induced debris flow and turbidite in the past ~7800 yrs calBP. Additionally, a singular event in the past ~7800 yrs calBP is not consistent with slip rates on faults in and near the basin (Ramelli et al., 1999a, Ramelli et al., 1999b, Kent et al., 2005, Brothers et al., 2009, Dingler et al., 2009), which suggest that the basin should undergo far more frequent strong shaking.

Here we examine a suite of 21 gravity and piston cores collected throughout the lake basin in an effort to better distinguish between possible seismic or flood triggering. The cores are supplemented by high-resolution seismic CHIRP sub-bottom surveys (Kent et al., 2005, Brothers et al., 2009, Dingler et al., 2009) as well as swath bathymetry (Gardner et al., 2000). We are able to correlate episodic deposits with the limited paleoseismic data onshore and other offshore studies in and around the basin. Our results suggest that many of the event deposits in the Holocene appear to be contemporaneous with documented local earthquakes in the basin and may extend the paleoseismic record for the region far beyond that of standard onshore methods.

1.1 Background and Geologic Setting

Lake Tahoe basin is located in the northern Walker Lane, a northwest-trending zone of right lateral strike-slip faults and north-south trending normal faults (Oldow, 2003; Unruh et al., 2003) that occupy the area between the relatively stable Sierra Nevada block to the west and the central Basin and Range to the east (Fig.1). The Walker Lane accommodates ~20-25% of North America-Pacific plate motion as the Sierra Nevada—Great Valley block migrates northwestward relative to stable North America at a rate of between 9 and 13 mm/year (Thatcher et al., 1999; Dixon et al., 1995; Bennett et al., 2003; Hammond and Thatcher, 2004, 2007). The Tahoe Basin lies between the Sierra Nevada range to the west and the Carson range to the east, and is the westernmost basin in a series of north striking basins and ranges. The basin is an asymmetric half-graben with westward dipping lake deposits (Hyne et al., 1972, Schweickert et al., 1999, Surpless et al., 2002, Dingler et al., 2009) that has been tectonically active for at least the past 3 Ma (Surpless et al., 2002, Faulds et al., 2005). The Sierra Nevada batholith is composed of granodiorite mantled by Tertiary basaltic flows and comprises most of the two bounding mountain ranges around Lake Tahoe (Saucedo et al., 2005). Metamorphic roof pendants are found on the east side of the basin and south of Fallen Leaf Lake at the southern end of the basin, while younger volcanics are located along the western shore near Tahoe City and at the north end of the basin. Pleistocene lake sediments are predominantly found in the southern and western sections of the basin.

Steep slopes ranging between 30 and 70 degrees characterize the west, north, and eastern margins of Lake Tahoe (Fig. 2, Gardner et al., 2000). The southern margin has a gentler slope and is largely overprinted by sediment input. The basin is rimmed by a narrow wave-cut terrace associated with a lake

lowstand, which has been offset down to the east due to active faulting (Kent et al., 2005, Dingler et al., 2009). Broad platforms in the north and west are sediment starved and are part of this same paleoterrace (Dingler et al., 2009). Deltaic formations within the lake are predominantly limited to the Upper Truckee River inlet (Fig. 3) at the south end of the lake and along the eastern hanging wall. Clinofolds observed along the narrow shelf have yet to prograde to the shelf edge (Dingler et al., 2009). Debris aprons around the basin are associated with glacial valleys onshore (Gardner et al., 2000) and are being draped and covered by more recent sediments (Fig. 2).

Landslides are present along all the basin margins, as observed in the bathymetric data (Fig. 2a). The large blocks in the center of the lake are the result of a massive mega-slide failure that created the McKinney Bay reentrant on the west side of the lake (Hyne et al., 1972, Gardner et al., 2000). Single channel seismic reflection shows a thick chaotic layer that is up to 40 m thick across the basin, in which the large, back-tilted, sediment blocks identified in the bathymetry are rooted (Hyne et al., 1972, Karlin et al., 2000). The age of the main McKinney Bay slide is estimated to be ~60 ka (Kent et al., 2005), although this event may be slightly younger if Pleistocene sedimentation rates were greater than those determined for the Holocene. Multiple failures have occurred in the large reentrant of the bay based on the associated debris apron and readily identifiable secondary landslide features (Figs. 2B and 2C). Smaller landslides offshore Rubicon Point show evidence for local erosion and associated sedimentation (Dingler et al., 2009); several other landslides are readily identifiable in the bathymetry. One of the most recognizable landslides is the tongue-like landslide that originates off the lower bench along the Dollar Point (northern) segment of the West Tahoe fault. We will refer to this 1.3 x 2.2 km landslide as the Baby Landslide (BL). Several other landslides have also originated from the benches along the Dollar Point segment (Fig. 2). Landslides are also present along the steep slope created by the North Tahoe fault (NTS, Fig. 2) on the west side of Crystal Bay (Fig. 3), leaving behind a debris flow with a distinct toe on the lake floor. The spine along the Incline Village fault in Crystal Bay also exhibits slope failures on the west-dipping slope, e.g., IVS landslide (Fig. 2). The Rubicon (central) segment of the West Tahoe Fault is also lined with landslides that can be identified as clear subaqueous landslides with sediment mounds locally built up on the lake floor.

Three down to the east normal fault zones are located in the Lake Tahoe Basin; the West Tahoe, North Tahoe, and Incline Village faults (Seitz and Kent, 2004, Kent et al., 2005; Brothers et al., 2009; Dingler et al., 2009). The West Tahoe Fault, along the western margin, is ~50 km long and strikes roughly north-south. Seismic reflection profiles (Hyne et al., 1972), swath bathymetry (Gardner et al., 2000), and CHIRP surveys (Kent et al., 2005; Brothers et al., 2009; Dingler et al., 2009) show the fault offsetting debris aprons and landslides, while following the steep western escarpment. The most recent event (MRE) on the fault, between 4500 and 4100 calBP, is dated in Fallen Leaf Lake in the southern part of the basin, where a small landslide filled in the accommodation created during the down-to-the-east coseismic offset during the MRE and a debris flow and turbidite across the floor of the small lake are observed (Brothers et al., 2009). The vertical slip rate on the fault is between 0.43 and 0.81 mm/yr based on long-term geomorphic offsets (Dingler et al., 2009).

The North Tahoe (or Stateline) Fault is ~30 km long, and extends from north of the Crystal Bay escarpment south into the central lake offsetting recent sediments with a 15 m high, down to the east lake floor scarp (Hyne et al., 1972, Gardner et al., 2000, Kent et al., 2005, Dingler et al., 2009). The vertical slip rate on the fault is between 0.35 and 0.60 mm/yr (Dingler et al., 2009). As the majority of this fault is underwater, there are no onshore paleoseismic data. The Incline Village Fault to the east has been trenched, with the most recent event at ~500 calBP and the penultimate event between 20 and 30 ka calBP (Seitz and Kent, 2004). The fault is at least 25 km long and runs through Incline Village and offshore down the spine in the northeast portion of the lake (Kent et al., 2005, Dingler et al., 2009). The vertical slip rate is between 0.10 and 0.30 mm/yr based on geomorphic offsets (Dingler et al., 2009).

An analogous fault zone to the West Tahoe fault in terms of length and activity is the Genoa fault (Brothers et al., 2009) that lies ~10 km to the east of the basin (Fig. 1). The Genoa Fault has an estimated vertical slip rate of between 2 and 3 mm/yr based on trenching offsets (Ramelli et al., 1999a). Nevertheless, an outwash terrace of Tahoe age (~70 ka) and a terrace >100 ka offset by the Genoa Fault yield a lower estimated vertical slip-rate between 1 and 2 mm/yr (Ramelli et al., 1999b). The Genoa Fault has two well-constrained earthquakes identified in trenches, between 500 and 600 calBP and between 2000 and 2200 calBP (Ramelli et al., 1999a).

The Genoa fault is part of the Carson Range frontal fault system that also includes the Mount Rose fault zone to the north (Fig. 2) The MRE on the ~40 km long Mount Rose Fault, occurred between 700 and 900 calBP (Bell et al., 1984; Ramelli et al., 2002). The vertical slip rate on the entire Mount Rose Fault

zone, which consists of several smaller faults, is ~ 1.3 mm/yr though individual faults in the system are lower (DePolo and Ramelli, 1997).

Located on the northwest side of the lake, the Truckee River is the lake's only outlet and flows north from the lake before turning east to the terminal Pyramid Lake (Fig. 1). Pyramid Lake has been used to infer drought and wet periods in the western Great Basin during the Holocene and to identify times when Lake Tahoe was not spilling to the east (Benson et al., 2002; Mensing et al., 2004). Between 7530 and 6300 calBP Lake Tahoe was below the rim most of the time and only spilled periodically in short intense pulses (Mensing et al., 2004). A wetter period dominated between 6300 and 5000 calBP (Mensing et al., 2004), but lake spill from Tahoe was still limited and currently submerged trees in Lake Tahoe that date from this time may suggest a lower lake level (Lindstrom, 1990, Benson et al., 2002). Pyramid Lake experienced variable climate with distinct wet and dry phases between 5000 and 3400 calBP (Mensing et al., 2004); Lake Tahoe was not spilling over its rim during most of this time period (Benson et al., 2002). Sometime between 3400 and 2750 calBP, Lake Tahoe rose to sill level and began spilling continuously (Benson et al., 2002, Mensing et al., 2004), which is manifested as a marked transgression in Pyramid Lake at this time (Briggs et al., 2005). The past 2750 yrs calBP have been wetter, though punctuated by relatively short periods of drought and lower lake level (Benson et al., 2002, Mensing et al. 2004).

2.0 METHODS

Twenty-one piston cores and three gravity cores were collected in Lake Tahoe to establish a depositional and chronostratigraphic framework for the basin (Fig. 3). By establishing such a framework and comparing it to the established paleoseismic record for the region, we can examine whether certain event deposits are contemporaneous with documented earthquakes in the basin. In addition to the sediment cores, geophysical data (swath bathymetry, Geopulse, and CHIRP) are used to correlate event beds and define their areal distribution as well as their acoustic character and potential source regions. CHIRP results have been reported by Kent et al. (2005), Brothers et al. (2009), and Dingler et al. (2009). Sediment analyses and seismic profiles are incorporated with the existing bathymetry to assess potential triggering mechanisms and timing of the observed event layers.

Cores were acquired onboard the UC Davis *R/V LeConte* on three separate cruises in 2000, 2002 and 2006 using a modified Kullenberg piston corer and a gravity corer. Both the piston and gravity coring apparatus use a 250 to 500 kg weight stand. The piston coring apparatus has a 5 m long, 7.6 cm diameter core barrel and typically recovers between 3 and 5 meters of sediment. The gravity coring apparatus has a 1.5 m long, 10 cm diameter core barrel and typically recovers between 1 and 1.5 meters of sediment, with typically better recovery of the shallow-most half-meter of sediment when compared to piston coring. Core sites were selected to examine how sediment structure of the event beds varied with increasing distance away from possible source areas, including stream inputs, fault scarps and landslides in order to compare these with the geophysical data. Standard core handling procedures were followed.

Whole core magnetic susceptibility profiles were measured at 1 cm intervals using a Bartington ring sensor. Magnetic susceptibility is a proxy for terrigenous content in the sediments (Osleger, 2009) and allows for the distinction between terrigenous material and diatomaceous lacustrine material. The cores were then split, photographed, and logged before sampling. Smear slides were made of representative lithologies. Correlations between cores were established using visual changes in color, texture, lithology, relative stratigraphic positions, magnetic susceptibility trends, and radiocarbon ages. The Tsoyowata Ash (7930 to 7790 cal BP, Bacon, 1983, Sarna-Wojkicki et al., 1991) is the primary link between cores.

Detailed sediment analyses were done between 0.5 and 3 cm intervals on sediment cores 12, 15, and 18 to characterize the sediment and to develop identifiable tracers of event layers that could be used to correlate from core to core. Great care was taken not to integrate across depositional boundaries when sampling. Grain-size was measured with sieves on the >74 micron fraction and with a Micromeritics X-ray Sedigraph on the <74 micron fraction with the median grain size and the >74 micron fraction presented here. The comparison of the median grain size to the >74 micron fraction is one way to look at the grain size spectra, or the variation of grain size, within a single sample. To determine the lacustrine diatom content opal analyses were performed using a modified silica extraction technique (Mortlock and Froelich, 1989, Calvert et al., 2001). Stable isotope ($\delta^{13}\text{C}$ and $\delta^{15}\text{N}$) and total nitrogen and organic carbon measurements were conducted at the Nevada Stable Isotope Laboratory. The $\delta^{13}\text{C}$ isotopes were examined to distinguish between terrestrial and lacustrine sources of organic sediment into the lake and are reported relative to the VPDB standard. $\delta^{15}\text{N}$ may also be an indicator of organic matter sources as well as early diagenesis or changes in lake stratification and are reported relative to the air. Total organic carbon (TOC), total nitrogen (TN), and the C/N ratio may also be representative of organic matter inputs in the lake.

For chronologic control we use ^{14}C AMS supplemented by the Tsoyowata Ash (Table 1). We focused on dating a small subset of cores selected because they exhibited greater resolution as it was not efficient to date all cores. We also sampled other cores to date specific intervals of interest. Thirty-nine radiocarbon samples from Lake Tahoe were collected from several cores in intervals of 'normal' lacustrine sedimentation. To avoid problems with reservoir ages in sedimentary organic matter, plant macrofossils were isolated and extracted from the bulk material. Dates were run at the University of Arizona AMS laboratory and at Lawrence Livermore National Center for Applied Mass Spectrometry (CAMS) Laboratory. Forty-two samples had sufficient organic material to yield date estimates for Lake Tahoe sediment. Calibrated radiocarbon ages were determined using the program OXCAL v 4.0 (Bronk Ramsey, 2001), with the IntCal 04 calibration curve (Reimer et al., 2004). All ages are rounded to the decadal level, and are reported with 95% confidence intervals. For the best-dated core (18), the top of the core is between 1700 and 1250 cal BP. Nearly all piston cores are missing between 150 to 2000 yrs calBP of the most recent sediments due to overpenetration. Individual episodic event ages were modeled as a sequence in OXCAL V4.0 (Bronk Ramsey, 2001), with available bounding dates from multiple cores where possible. The sequence model uses stratigraphic order as an additional constant. The effect is seen in improved age control. Dates from within event deposits were assigned to lower boundaries as they contain reworked material and therefore represent maxima for the timing of deposition. No upper bounding date was available for the youngest episodic deposit, which was only identified in one core (21). As such, assuming the sedimentation rate is constant in the upper portion of the core, after subtracting the thickness of the event deposits from the core, we assign a calendar date of 1750 ± 110 A.D. to the top of the piston core and use this date as the upper bound on the youngest event deposit.

The volume of individual event deposits allows us to compare event size to sediment input into the lake via stream sources. Event deposit volumes were estimated by calculating the elevation of the top and bottom of each deposit in the cores. The lack of cores in the eastern part of the lake and the large distance between many of cores leads to a very rough estimate of volume. Nearest neighbor grids of the top and bottom of each event deposit were created in ArcGIS 9.1 with control points at the edges of the bottom of the lake to ensure that the two grids were at the same elevation. The estimated volume of the deposits reported here is the calculated volume between these two grids for each event deposit.

High-resolution CHIRP seismic reflection profiles aid in the identification of cross-lake variations in sediment deposition, subaqueous landslides, and potential source areas of these gravity deposits. Profiles were collected with the Edgetech SubScan CHIRP system. CHIRP profiles presented here use a 1–5.5 kHz pulse with a 10 ms duration, a 1–5.5 kHz pulse with 30 ms duration, or a 1–6 kHz pulse with a 50 ms duration (Dingler et al., 2009); CHIRP penetration was ~50 m. Depths are calculated based on two-way travel times and nominal water velocity of 1500 m/s. Select profiles that supplement coring results are presented in this paper (locations in Fig. 3).

3.0 SEDIMENTATION IN LAKE TAHOE

3.1 Seismic Stratigraphy

Sediments in Lake Tahoe are tilted and thicken to the west (Fig. 4, Dingler et al., 2009). Three distinct sediment packages are observed in CHIRP profiles (Fig. 4). The uppermost Holocene sediments in Lake Tahoe are acoustically transparent and thicknesses range between 1 and 4 m thick across the basin. These deposits generally drape older stratigraphy, and exhibit minor thickening toward the deeper northern basin as well as near fault zones along the western portion of the basin. Very weak reflectors are observed in this uppermost transparent layer and one weak reflector (between 40 and 70 cm depth) is present across much of the basin. Coring results suggest that this upper transparent layer represents the past ~11 ka calBP of sediments. The underlying sediment package is between 20 and 40 meters thick and is acoustically layered, with numerous strong reflectors (Fig. 4). The base of the longest cores contains homogeneous blue-gray thixotropic clay which is interpreted to be late Pleistocene glacial rock flour and delineates the upper portion of the underlying glacial sediment package.

Large-amplitude sediment waves observed in the bathymetry (Gardner, et al., 2000) consist of late Pleistocene graded outwash sands that underlie a thin layer of sediment as suggested by coring and seismic profiles in the southern portion of the basin. These layers appear to continue basin-wide, surrounding the large sediment blocks and are offset by faults. This sediment package is relatively thin in the footwall of the North Tahoe Fault as compared to the same package in the hanging wall, and is truncated at the West Tahoe Fault.

The deepest recognizable sediment package is a chaotic zone with no recognizable internal layering between 30 and 40 m thick (Hyne et al., 1972). This chaotic nature of the layer suggests rapid

deposition and considerable reworking of the entire central basin during a single depositional event. The sediment blocks readily identifiable in the bathymetry (Figs. 2 and 3) are rooted into this lenticular zone (Fig. 4) and are part of the McKinney Bay mega-slide (Hyne et al., 1972, Gardner et al., 2000, Kent et al., 2005, Dingler et al., 2009). The sediment blocks have tilted stratigraphy (Fig. 4) and a core from the top of the largest block recovered older lacustrine sediments that are similar to those observed along the western margin (Saucedo et al., 2005). The chaotic nature of the sediment package with tilted sediment blocks rooted into it is consistent with the result of the collapse of the McKinney Bay shelf.

3.2 Lithostratigraphy

Two dominant sediment types are identified in the cores, background lacustrine sediments and a sequence of six lithofacies; following previous authors, these are interpreted as a result of deposition in a single event. Background lacustrine deposits will be referred to here as normal sediments. Normal sediments are generally homogeneous and relatively uniform light olive gray, siliceous slightly sandy, slightly clayey silt with no apparent sorting. Few readily identifiable layers are observed, though occasional black and green banding less than 0.25 cm thick may be present. Black and green banding is not consistent across the basin from site to site. In the lower portion of the cores, deposition between episodic deposits is bluish green, slightly clayey silt consistent with glacial flour.

Normal sediments, in the upper portion of cores, contain numerous diatom microfossils and scattered organics in the form of small twigs, pine needles, and insect chitin. Median grain-size is typically between 4 and 10 microns, or in the fine silt range, with no discernable trends in the sand and clay fractions. The median grain size is somewhat finer (between 4 and 6 microns) in the bluish-gray, clayey silt layer observed in the bottom of the cores. Though still in the fine silt range overall, a higher percentage of both clay and sand is present. Macroplant fossils, such as those present higher in the core, are generally lacking and those that are identified are often very fragile and highly degraded. The transition between the upper and lower normal sediment regimes is abrupt, marked by an episodic deposit that contains a distinct diatomite layer that is between 5 and 10 cm thick throughout the basin and is topped by a bluish gray clay layer (Fig. 5).

Event deposits that interrupt normal sediments consist of six lithofacies that vary from the bottom of the deposit to the top (Fig. 5). All six of these subunits are present throughout the suite of cores; however as expected, not every deposit contains all six subunits in a single sequence. Subunit 1: chaotic slightly sandy, slightly clayey silt, is similar in composition to the normal sediments, but also contains rip-up clasts of previously deposited lake sediments, silt-sized to cobble-sized clay balls, and may have an irregular erosive base. Overlying Subunit 1 is chaotic, slightly clayey, slightly silty sand. Subunit 2: subrounded to subangular and coarse grained sand, with some medium and fine sand also present. Similar to Subunit 1, this chaotic subunit contains outsized rip-up clasts of previously deposited sediment, clay balls, and has an irregular, erosional base when not directly overlying Subunit 1. Though distinctly different due to grain size differences in the matrix, the first two subunits are here combined together using the broad term debris flow.

Subunit 3: slightly clayey, slightly silty sand, subrounded to subangular, ranging in size from medium or coarse sand at the base grading normally to fine sand at the top. Multiple graded sequences may be present within this subunit and may occasionally contain small sections of reverse grading (i.e., Osleger et al., 2009), however, the overall predominant trend across the entire subunit is normally graded sand with coarser sand at the base and finer sand at the top. This subunit is differentiated from Subunit 2 by the lack of rip-up clasts and gravel sized clay balls as well as the grading. This layer sometimes has an irregular erosional base that varies around the basin. Coarser sand is associated with the more irregular and erosional base. Terrestrial organics are occasionally present throughout this layer, though diatoms are also present, often attached to silt and clay balls (Fig. 6a). This subunit marks the bottom of a normally graded sequence that contains the remaining subunits. This sand layer typically ranges from between <1 and 4 cm thick and is coarser and thicker near basin margins and when directly overlying the debris flows.

Above the sand, Subunit 4, is normally graded, slightly clayey, sandy silt, and is medium olive gray in color, slightly darker than non-episodic sediments. Abundant scattered micaceous grains and occasional terrestrial organics are present in this layer that is also normally graded. Similar to the underlying sand layer, more than one graded sequence may be present within this subunit, though the overall trend remains a normally graded sequence with a higher percentage of sand at the base and a lower percentage of sand at the top. Subunit 5, a white to light gray, diatomaceous silt layer, is a thin layer that consists of fractured and broken diatom frustules in the fine silt range (Fig. 6b). Subunit 6 sits on top of the entire normal graded sequence and is comprised of a clay layer that is typically between 2 and 4

centimeters thick that transitions into normal sediment. Subunits 3 through 6 are together classified as turbidites based on the overall grading upward sequence. Cores that are closer to the basin margins and faults often contain the chaotic lower subunits as well as the upper subunits, while cores located farther into the basin often contain subunits 4 through 6 only.

The event deposit that marks the abrupt transition between lower and upper normal regimes is one of three basin-wide marker beds present in the cores. Radiocarbon dating suggests the transition took place ~12 ka calBP and we will refer to this as the lower marker bed. The second key marker bed identified in the cores is the Tsoyowata ash (Osleger et al., 2009), between 8000 and 7700 calBP (Bacon, 1983, Sarna-Wojkicki et al., 1991). The ash is coarse silt to sand sized. The ash and/or episodic deposit are present in all of the cores that penetrate to that depth with the exception of the far northern core. The ash is not a discrete layer in 8 cores, but ash rip-ups and balls are observed in chaotic Subunits 1 and 2 of one episodic deposit that is prominent in the southwestern section of the lake. The third and youngest marker bed consists of white, clastic silt that is distinctly different when compared to normal Holocene sediments. This bed is subtle when compared to the massive lower marker bed and the ash layer. At first glance, the silt appears to be a thin diatomite layer between 1 and 3 cm thick; however, the layer is lacking in diatoms relative to normal sediments and consists of clastic material that appears to be derived from older Pleistocene lake sediments that make up a significant portion of the western lake walls. This layer is underlain by a turbidite or debris flow in many of the northern cores consistent with a nearby source.

4.0 SEDIMENT ANALYSES

4.1 Magnetic susceptibility and grain size

Prominent peaks in magnetic susceptibility are directly correlated to peaks in the percentage of sand throughout the cores (Fig. 7) and the highest values correspond to event deposit Subunit 2 (sandy debris flow) and Subunit 3 (sandy turbidite base). As magnetite is present in the sand size fraction, susceptibility drops off as the percentage of sand decreases throughout the graded silt (Subunit 4) and continues to drop through the upper subunits of the turbidite. The sand fraction of the grain size shows similar trends, though the whole core susceptibility measurements lead to a more smoothed appearance in the magnetic susceptibility curve than in the sand fraction. The lowest values of magnetic susceptibility are associated with periods of normal sedimentation, though the lowest sand fraction samples are those in Subunit 6, the uppermost part of each turbidite. Normal sediments show higher susceptibilities in the Pleistocene, which corresponds with higher detrital content. Magnetic susceptibility drops very slightly throughout the Holocene, though there is no readily identifiable coincident drop in sand size.

4.2 Biogenic Opal

Concentrations of biogenic opal, a measure of diatom abundance in sediments, inversely correlate to grain size and magnetic susceptibility in Lake Tahoe event deposits (Fig. 7). The basal turbidite sands contain the lowest percentages (<10%), while the diatomaceous clay capping layers at the tops of turbidites typically contain opal percentages >35%. Interestingly, the white, diatomaceous silt layers are typically between 30 and 35% opal. No overall trend in biogenic opal is observed in normal sediments, though Holocene sediments contain higher opal percentages than those in the Pleistocene. Changes in % opal identified within normal sediments do not correspond with grain size or magnetic susceptibility, though they roughly correlate with $\delta^{13}\text{C}$ and total carbon and total nitrogen.

4.3 Carbon and Nitrogen

Total carbon (Fig. 7) and total nitrogen track each other on a one to one basis throughout core 18 and, as with opal, are inversely correlated to grain size and magnetic susceptibility in the event deposits. Values drop to near zero in the basal sandy turbidite layers and increase throughout the turbidite. In normal sediments, carbon and nitrogen are relatively uniform during the Pleistocene, but both increase at the lower marker bed and steadily increase throughout the remainder of the Holocene. This corresponds to a decrease in magnetic susceptibility, possibly associated with increased organic material input to the basin. The C/N ratios are relatively constant in normal sediments, with the Pleistocene ratios between 9 and 11 and Holocene ratios between 10 and 12. A shift to higher values occurs above the lower marker bed. Sporadic peaks are found in the Holocene episodic deposits where total C and N are otherwise at their lowest values.

$\delta^{13}\text{C}$ positively correlates to grain size and magnetic susceptibility, and inversely correlates to opal concentration, total carbon, and total nitrogen (Fig. 7). The $\delta^{13}\text{C}$ signal is less negative in the basal sandy turbidite and more negative at the top of the turbidite. In normal sediments, no easily recognizable pattern is present, $\delta^{15}\text{N}$ shows trends that are different than all the other proxies (Fig. 7), with evidence for both inverse and positively correlated spikes in the episodic deposits. Normal sediment values are more positive

prior to the Tsoyowata ash, and become continuously less positive after the ash with a rapid decrease occurring immediately following the deposition of the ash.

4.4 Radiocarbon dating

Radiocarbon dates from the normal sediments are in stratigraphically correct order as opposed to dates from event deposits which are anomalously old. The Tsoyowata ash (7930 to 7790 cal BP, Bacon, 1983, Sarna-Wojkicki et al., 1991) fits well on the age depth curves for cores where it is present with R^2 values of 0.94 and higher. The tops of most of the cores are between 750 and 3000 cal BP, indicating that the uppermost sediments were lost due to the piston coring process.

Sedimentation rates vary across the basin (Table 2) and suggest a complex interaction between episodic deposits, normal sedimentation, and bathymetry. Higher total sedimentation rates (between 35.9 and 39.0 cm/ky) are located in the northern depocenter. Core 2, offshore Rubicon Point in the southwestern portion of the lake, has an extremely high total sedimentation rate (between 71.4 and 71.5 cm/kyr) as a direct result of a massive, very thick event deposit. The normal sedimentation rates (~9.8 cm/kyr) at the same location are among the lowest observed in the lake. The lowest observed total (between 11.8 and 11.9 cm/kyr) and normal (~7.0 cm/kyr) sedimentation rates are located in the south-central portion of the basin (core 7), equidistant from the eastern and western margins and on a small bathymetric high outboard from the Upper Truckee River inlet. Other low total sedimentation rates are observed where sediment thins over the North Tahoe Fault (core-17, between 15.5 and 15.7 cm/kyr), in the footwall of the North Tahoe Fault in northwest (core -19, between 19.2 and 19.5 cm/kyr), and in the southwest (core -1, between 17.6 and 18.7 cm/kyr) where the dated samples are above the youngest observed episodic deposit and represent a more recent sedimentation rate than most of the other cores (see depths of radiocarbon dates in Figure 9). Both normal and total sedimentation rates are highest near faults where deposits fill in the accommodation created on the hanging wall and are lowest away from faults and in the footwall.

5.0 CROSS-BASIN CORRELATION

5.1 Core correlation

Layers recovered in sediment cores can be correlated across the basin on the basis of whole core magnetic susceptibility (Fig. 8), lithology, radiocarbon dating and marker horizons. Magnetic susceptibility profiles show relatively uniform susceptibility that is punctuated by peaks of higher susceptibility that can be correlated between cores based on their patterns and amplitudes. Three distinct marker beds serve as tie points between the cores, the lower marker bed (Figure 9, Deposit O, ~12 ka calBP), the Tsoyowata ash (between 7950 and 7730 calBP), and the white, clastic silt (Figure 9, Deposit F). These lithologic tie points, in conjunction with the magnetic susceptibility profiles, allow for the development of an event deposit framework for the entire basin (Fig. 9). These relations are consistent with radiocarbon dating, as intervals of normal sediments in the same stratigraphic position have similar dates (Table 1).

Individual event deposits are labeled from A (the youngest identified) to O (the lower marker bed). A debris flow representing the proximal deposit of a gravity flow appears to be associated with every turbidite somewhere in the basin (except event C), regardless of turbidite size or continuity. The white, clastic silt layer (F) is the youngest layer present basin-wide. Deposit F is associated with debris flow and turbidite deposits in the north only, thins away from the location of the Baby Landslide, and becomes finer grained to the south. Event deposits younger than deposit F are primarily identified in the northern basin, and vary in size and continuity. The northernmost core, at the deepest point in the basin contains the youngest sediments recovered.

The Tsoyowata ash is present as a prominent layer throughout much of the northern basin and is overlain by deposit J containing a turbidite but no underlying debris flow. In the southern part of the lake, the ash is primarily found as rip-up clasts in the debris flow portion of deposit J, which is >1 m thick in core 2. In core 4, the debris flow containing ash clasts directly overlies the ash bed indicating the debris flow is younger than the ash. Deposit J is highly erosive in the southwest and southeast parts of the lakes and is quite thick (between 20 and 30 cm) in the west-central portion of the lake. In the southwest portion of the lake, multiple debris flows occur in a very short period of time, but only a single turbidite is associated with deposit J in the central and northern cores, possibly indicative of a single trigger.

Deposit O is present basin-wide, however only fourteen cores were able to penetrate and recover sediments that deep below the lake floor. Six cores bottomed out in this deposit. In the core located on the sediment waves in the south (core 3), deposit O is 114 centimeters thick with a clean gravel base grading up to the clay-capping layer. The deposit sits atop a major liquefaction feature. The associated debris flow

is present in the south central portion of the basin and the turbidite maintains its thickness through much of the northern basin.

Fifteen (preferred) to eighteen event deposits can be identified basin-wide (Fig. 9). Three of those seventeen deposits, F', F'', and I' are interpreted as near-simultaneous sub-events of F and I, leading to our preferred interpretation. F' and F'' are only identified in the northernmost depocenter, and deposit F, where in close proximity to the Baby Landslide (BL; Fig. 2) north of McKinney Bay, shows up to seven stacked turbidites, indicating several slope failures occurred over a very short period of time. Modeled ages of deposits A-N, 14 in the last ~ 11,200 years, yields a long-term recurrence interval of one episodic deposit per 750 to 800 years.

5.2 Coring and seismic stratigraphic correlation

The upper-most transparent layer in the CHIRP data contains a weak reflector typically occurring between 40 and 70 cm depth (Figs. 10 and 11), which is consistent with the depth of deposit F (~4300 yrs calBP, Fig. 9, Table 1) in cores. This weak reflector (Fig. 10) appears to originate from the debris pile of the Baby Landslide (BL, Fig. 2) north of McKinney Bay and is present basin-wide. Deposit F consists of white, clastic silt, consistent with Pleistocene lacustrine sediments observed along the western shore, which is likely a result of the failure and redistribution of lake sediments in the Baby Landslide. In the two cores directly basinward from the Baby Landslide (cores 17 and 18) multiple <1 cm stacked turbidites are present. These two cores are the only ones in which a debris flow is observed associated with deposit F (Fig. 9).

On one seismic profile (not shown, see Fig. 11a in Dingler et al., 2009), two separate debris flow deposits overlie one another in the southwest portion of the lake offshore Rubicon Point. The younger of the two corresponds to the large debris flow (deposit G) observed in core 5. The debris flow portion of deposit G thins quickly away from a landslide scar present on the outside of one of the paleochannels along the western wall, though the turbidite is quite thick in the central and northern portions of the basin (Fig. 9). The debris flow is overlain by a small sediment wedge along a strand of the West Tahoe Fault. The older debris flow identified offshore Rubicon Point corresponds to the large debris flow (deposit J) observed in core 2 (Fig. 11b). This debris flow is quite thick over much of the southern basin and originates from a sediment pile off a landslide scar observed in the bathymetry. Deposit O correlates with the strong reflector between 2 and 3 m depth.

6.0 DISCUSSION

Lake Tahoe sedimentation is affected by tectonic and climatic influences. The regional westward tilt of sediments in the lake is because of tectonic deformation along the West Tahoe and North Tahoe faults. In the late Pleistocene, glacially derived sediments filled bathymetric lows that resulted from fault related down-drop of the basin along the western margin and northern portion of the lake. Glacial outwash debris aprons, built on top of McKinney Bay mega-slide deposits and inter-layered with glacio-lacustrine flour, led to remnant topography that Holocene sediments drape and in-fill. The relatively high topography created by the debris aprons in the south combined with active faulting along the western margin and in the northern basin led to asymmetric Holocene deposition.

6.1 Event Deposition

Event deposition in Lake Tahoe consists of a continuum of gravity flow deposits ranging from subaqueous landsliding (block slides and slumps) to debrites (unsorted debris flows) to turbidites (sand to silt graded beds sorted during flow and settling). Debris flow deposits encountered in many of the cores are immediately topped by normally graded turbidites suggesting that they were rapidly deposited during the same event. The debrites often contain clasts and rip-up beds of reworked lacustrine sediment indicating that the landslides or block slumps cause erosion, deformation, and transport of preexisting lake deposits that are incorporated in the debris flows. The graded turbidites range from coarse to fine sand to silt in their presumptive basal layers depending on distance to source. The overlying silty layers are graded, with clay and often diatom layers, due to density and grain size separation during settling, on top. These deposits can be traced areally based on their relative grain sizes and thicknesses (e.g., Figs. 4, 9, 10, and 11).

Source areas for the individual events can be approximated by the location of proximal debris flows and systematic changes in thickness and grain size of the more distal turbidites. The debris flows are clear evidence of subaqueous slope failure and mass redistribution by gravity flow on the lake bottom. Several source areas can be recognized. McKinney Bay is an area in which several landslides are easily identified in the bathymetry (Fig. 2, Gardner et al., 2000), and cores taken from around the base of the bay often show evidence of proximal deposits. Several debris flows and thick turbidites are also present in the northernmost section of the lake around Crystal Bay and landsliding is evident in the bathymetry (Fig. 3).

The slope off Rubicon Point and the Pleistocene debris apron near Emerald Bay appear to be source areas in the southwestern portion of the lake. Large subaqueous slumps offshore Zephyr Cove are the likely source of debris flows found in several of the nearby cores. Source areas may occur along other parts of the eastern slope, but limited core coverage precludes further identification.

6.2 Causes of Event Deposits

Event deposits in Lake Tahoe may be triggered from tectonic, climatic, or sedimentological processes. Strong ground motion as the result of earthquakes on faults within the region is one way in which large landslides and associated event deposits can be emplaced. Holocene earthquakes have been documented from paleoseismic trenches and other studies on several Walker Lane faults in the area. These include the West Tahoe and Incline Village faults within the basin, and the Genoa and Mt. Rose faults to the east and northeast, respectively (Fig. 1). The North Tahoe Fault within the basin is also likely to have had similar style offsets in the Holocene, although the MRE is unknown at this time. Landslides may be triggered by the initial onset of shaking and/or a rise in pore pressure with extended periods of ground motion (Hampton et al., 1996). Hanging wall downdrop on faults within the lake basin could lower lake level and potentially trigger slope destabilization and upper slope landslides in the lake. This would be particularly plausible along the West Tahoe Fault, which stretches along the entire western margin. In addition, gas escaping along faults within the basin following large earthquakes may lead to slope instability and failure (e.g. Field, 1990). Pockmarks are observed in the bathymetry in the southern end of the lake, possibly associated with the West Tahoe Fault (Brothers et al., 2009). Additional evidence for gas accumulation within some sediments is observed near the Tahoe City Shelf (Dingler et al., 2009).

Climatic triggers of episodic mass flows may include storms, flooding, and/or water level fluctuations (Hampton et al., 1996). Storms may increase erosion in the watershed and wave-induced erosion along the shoreline. Wave loading may increase pore pressure and weaken shallow-water slopes (Seed and Rahman, 1978). Periodic floods could rapidly introduce large quantities of sediment to the lake, potentially triggering delta collapse and landslides due to oversteepening or pore pressure loading as well as hyperpycnal flows at stream mouths (Piper and Normark, 2009). Changes in lake level could conceivably trigger landslides as lake level drops during extended periods of drought would cause sediment input to occur along the shelf-upper slope area and would also expose shelf-edge deposits to increased wave action (Lee, 2009).

Unfortunately, we expect many of the depositional characteristics of event deposits in Lake Tahoe to be similar regardless of the triggering mechanism. However, we can place additional constraints on the source region by examining the deposits, their areal distributions, and whether they are proximal or distal. Storminess and flooding have been suggested as a cause for most of the Holocene episodic deposits in Lake Tahoe based on two cores which show many turbidites, and only one debris flow deposit (Osleger et al., 2008), however, we find this interpretation to be unlikely for several reasons discussed in more detail in later sections. Taken individually, these lines of evidence would not be enough to establish a relationship between event deposits and earthquakes; however, when the evidence is examined together, strong shaking becomes the most viable triggering mechanism.

(1) The distribution of most debris flows and turbidites suggests they are sourced from areas of subaqueous landslides, not river or stream sources. The largest stream input sediment source to Lake Tahoe is the Upper Truckee River in the southernmost part of the lake (Fig. 3), providing ~25% of the terrestrial sediment supply (Simon et al., 2003). Several other small streams flow into Lake Tahoe, including Blackwood Creek, Second Creek, Trout Creek, Third Creek, and Ward Creek (Fig. 3). Rapid stream input due to floods could trigger slope landslides. If event deposits were caused by increased sediment input from floods, we would expect to see thicker and coarser grained deposits offshore of stream mouths and evidence of erosion from hyperpycnal flow along the lake margin. Most of the Holocene deposits in the southern portion of the lake are thin and fine-grained, if present at all. The only two exceptions are debris flow deposits found in cores 3 and 4 (Fig. 3) located on the debris apron offshore of the Upper Truckee River. However, these two deposits, J and M, are sourced by landslides in the southwest and central parts of the lake and are not associated with streams. Deposit M is both thicker and coarser in the central portion of the lake, directly downslope from the well-established landslides of McKinney Bay, however, the debris flow in core 3 suggests an additional southern source. The uppermost deposits, A-E are not present at the southern end of the lake, as they appear to be sourced at a lower elevation than those in the southern part of the lake. These uppermost deposits become more distal to the south throughout the central cores as a result of the topography.

Deposit O at the Pleistocene/Holocene boundary does appear to be sourced from the southern delta as suggested by the clean gravel base and >1 m thick turbidite found in core 3. The underlying liquefaction feature may result from rapid emplacement or from earthquake shaking. As such, it is difficult to ascertain a causal mechanism for this particular deposit.

(2) Episodic deposits consist of reworked lake sediments containing diatoms with little to no additional input from terrestrial sources. Sedimentological studies indicate that Lake Tahoe turbidites and debris flows contain significant fractions of reworked lacustrine sediment. Radiocarbon dates in the event deposits are consistently older for their stratigraphic position than dates obtained in normal lacustrine sediments on either side of the deposits (Table 1). Debris flows contain clay balls and outsized layered and tilted lacustrine clasts. Turbidites show strong effects of grain size sorting, with coarse terrigenous material at the base and high abundances of diatom-derived opal and a more negative $\delta^{13}\text{C}$ signal in the overlying fining upward sequence. This suggests that the reworked material is sourced within the lake as opposed to from stream inputs.

Normal sediments are a mixture of terrigenous sediment and diatoms. Terrigenous sediment consists of sand, silt, and clay washed into the lake from the surrounding basin and has a less negative $\delta^{13}\text{C}$ signal than diatoms. $\delta^{13}\text{C}$ profiles show relatively less negative values in the base of the event deposits as opposed to higher in the event deposits or in normal sedimentation. This has been interpreted as new terrigenous material input from a different carbon source (Osleger et al., 2009). However, when $\delta^{13}\text{C}$ is compared with median grain size and the >74 micron sand fraction, it is apparent that the signal is not a reflection of new input, but is simply a function of hydraulic sorting. The terrigenous material which is already present in the lake is coarser grained and hydraulically heavier than the diatoms and fine silt/clay. As the turbidite develops, this more terrestrial material is the first to settle or in some cases may never fully be incorporated into the turbidity current. Though the base of the turbidite is obviously more terrigenous, coarser grained and has a less negative $\delta^{13}\text{C}$ signal, than stratigraphically higher in the same event, when the grain size spectra of the complete event package is considered, size distribution is not significantly different than that of normal sediments on either side of the event deposit. The increased grain size and less negative $\delta^{13}\text{C}$ signal may be simply explained by pre-existing normal sediments being redistributed as a result of hydraulic sorting during event deposition, rather than the introduction of significant amounts of new material to the lake floor during event deposition as required by the flood model.

Occasional reverse grading in the base of the turbidites, subunit 3, has been used to imply increasing sediment input and storm runoff through time (Osleger et al., 2009). Reverse grading is most commonly found in subunit 3 when multiple graded sections are present in a single event. Reverse grading at the base of Lake Tahoe turbidites has developed when the deposition rate exceeds the escape rate of fines. The escape rate of the fines is proportional to the fluid expulsion rate from the portion of the flow that may not be fully turbid. As fluid is expelled from Subunit 3, fine sediments are also expelled. When the deposition rate out of the overriding turbidity current exceeds this expulsion rate, fines that are removed from the underlying flow are unable to fully integrate into the turbidity current before being redeposited (Sylvester and Lowe, 2004). Coarser material is essentially raining out faster than the turbidity current can incorporate finer material while continuing to travel downslope. Reverse grading within individual deposits is the result of this same process, as multiple turbidity currents from multiple sources converge or turbidity currents that have reflected off basin walls return over the same location.

(3) The total amount of sediment deposited in each event deposit is at least an order of magnitude larger than total annual sediment input to the lake. Volumetrically, the event deposits are quite large (Table 3), particularly when compared to annual sediment budgets. The debris flows/turbidites have volumes between 10^4 and 10^7 m^3 , which is from one to four orders of magnitude greater than the annual sediment input via the Upper Truckee River and up to 3 orders of magnitude greater than the average annual total sediment load delivered to Lake Tahoe (Simon et al., 2003).

(4) None of the Holocene episodic deposits apparently originate from the southern delta, which is the only delta in the basin built out beyond the Pleistocene shelf. Rapid deposition and delta collapse are not likely, as deltaic progradation beyond the paleoterrace is not observed. Only two significant deltas are currently observed in the bathymetry (Fig. 3). The delta at Ward Creek does not reach the narrow shelf edge. The inundation of the submerged shelf has been dated at ~19.2 ka (Kent et al., 2005), and there is no geomorphic evidence for a landslide derived from the Ward Creek delta, or at any other stream inputs, in the bathymetry data. The Upper Truckee River delta is the only delta that has built out beyond the paleoshelf and as previously discussed, episodic deposits do not appear to originate from this source, at

least in the Holocene. One exception, debris flow M in core 3, suggests deposit M may have a southern delta origin; however, this event has multiple source areas.

Large shallow platforms found off the south shore, Sugar Pine Point, Tahoe City, and Agate Bay could potentially provide sediment to the deep lake. However, seismic reflection profiles show that these are relict wave-cut platforms that are bare of sediment accumulation (Kent et al., 2005, Dingler et al., 2009), and thus would not be a major turbidite source. CHIRP lines show that sediment is building out onto the shelves (Dingler et al., 2009), but has yet to build out to the edge. It is unlikely that wave loading or collapses of sediment platforms are contributing significantly to event deposition.

(5) Simultaneous failure at multiple source areas occurs in most of the deposits. The presence of debris flow and subunit 3 turbidite basal layers, as well as total turbidite thickness may be used to determine source areas across the basin (Figure 9). Deposit C consists of proximal turbidites in cores 14, 15, and 16 as well as in core 21 to the north, with cores 17, 18, and 19 showing distal deposits. The deposit E debris flow is present in core 12 in the central basin as well as core 21 in the far north and a proximal turbidite is present in core 19 as well, suggestive of three different source areas. Deposit F consists of debris flow deposits in cores 17 and 18 directly basinward of the Baby Landslide in Lake Tahoe and corresponds in time to the landslide and event deposit identified to the south in Fallen Leaf Lake (Brothers et al., 2009). Event G consists of debris flow deposits and proximal turbidites in cores 5, 14, 17, 19, and 21 indicative of widespread local failures. Debris flow deposits in Event H are present in cores 6, 8, and 13 with proximal turbidites present in 6, 14, and 19 as expected in multiple failures. Event J consists of a massive debris flow in the southern end of the lake, a large proximal debris flow in cores 14 and 15 consistent with multiple source areas. Debris flow deposits in event K are present in cores 12, 15, 16, and 21 suggestive of multiple failures. Event M debris flow deposits are found in the south in cores 3 and 7, and in the central basin in cores 14, 15, and 16 which indicates at least two source areas. Deposit O is widespread with a large turbidite and debris flow deposit in the south, however, as previously discussed, the character of this deposit leads to an ambiguous interpretation with regards to causal mechanism.

(6) The six youngest episodic deposits correlate well with significant paleoseismic events on Tahoe basin faults and Carson Range frontal faults (Fig. 12, Table 3). The six youngest episodic deposits and possibly deposit K all correlate well with known paleoseismic events. The most recent event deposit, A, correlates in time (between 630 and 120 calBP) with three paleoseismic events all estimated at M 7 or larger that are indistinguishable in age, including the MRE on the Incline Village Fault (Seitz and Kent, 2004), two segments of the Genoa Fault that are likely the same event (Ramelli et al., 1999a), and the Carson range frontal fault in Carson City (Ramelli et al., 1999b). Given the northern origin of event A, the Incline Village Fault MRE is the most likely trigger. Event deposit B (between 1520 and 1150 calBP) is the weakest of these correlations, but the thick Subunit 6 debris flow (core 21) suggests a northern origin for the flow, consistent with the oldest of the Mt. Rose fault MRE dates at Callahan Ranch (Ramelli et al., 2002) and younger than the Mt. Rose Davis Creek penultimate event (DePolo, 2006). Deposit C (between 2320 and 2160 calBP) can be correlated to the penultimate event on the Genoa Fault (Ramelli et al., 1999a). Deposit D (between 2610 and 2250 calBP) may be related to the penultimate event at White's Creek on the Mount Rose Fault zone, an event that has no lower constraining age, but is older than 2330 calBP (Bell et al., 1984). Deposit E (between 3540 and 2990 calBP) may be related to the third event back identified in the Sturgis trench on the Genoa Fault, which also has no lower constraining age, but is older than 2870 calBP (Ramelli et al., 1999a). Deposit F (between 4510 and 4070) corresponds to the MRE on the Fallen Leaf Lake segment of the West Tahoe Fault (Brothers et al., 2009). Event K (between 9450 and 8770) may be related to third event back on the Mt. Rose Fault zone at White's Creek, which is older than 8410 calBP (Bell et al., 1984). Given these correlations, these event deposits are most consistent with strong shaking on the Tahoe Basin faults and the faults that are part of the Carson Range frontal fault system to the east although specific faults are difficult to identify.

For some time periods, there were apparently more local paleoearthquakes than event deposits. This suggests that the sedimentary record in the lake may not be a perfect recorder of regional seismicity, but may indeed record only nearby large earthquakes. Alternatively, slope failure may require preconditioning, that is maybe two or three earthquakes are required to make the margin susceptible to slope failure. After a failure the slope stability clock is reset and another series of earthquakes is required to induce additional slope failures. Along the same lines an earthquake-triggered failure could lead to a succession of later retrogressive failures along the margin as observed in McKinney Bay.

6.3 Paleoseismic implications

If one accepts the supposition that all of the event deposits with the exception of event O are the result of strong shaking, a long-term Holocene regional shaking record can be constructed for the Tahoe basin; especially if more distant earthquakes do not appreciably affect the record. Seventeen Holocene episodic deposits have been identified. Three of those seventeen deposits, F', F'', and I' are interpreted to be multiple turbidites associated with events F and I respectively. Thus, 14 event deposits have occurred in the last ~11,200 years. This yields a long-term average recurrence interval of shaking every ~750 to 800 years. Estimated average recurrence intervals are not uniform throughout time. The estimated average recurrence interval from event A to E is between 470 to 690 years, from event F to J is between 530 and 770 years, from event K to N is between 250 to 630 years. The recurrence interval between individual events is also not uniform. For example, the interval between Events A and B is between 520 and 1400 years whereas the interval between Events C and D is 450 years or likely less.

Episodic deposits A, F, G, and J may be tied directly to fault segments within the Tahoe basin; the younger two correlate to previously identified paleoseismic events in the basin and the other two are older than existing paleoseismic history. Deposit A correlates well with the preferred age of the MRE on the Incline Village fault from trenching results and is the youngest paleoseismic event identified in the basin. The offset in the trench on the Incline Village fault was 3+ meters, requiring a M7 earthquake, and it is unlikely that the relatively short Incline Village fault could produce such an earthquake alone (Seitz and Kent, 2004). It is more probable that the North Tahoe fault ruptured as well (Seitz and Kent, 2004). It is possible that Deposit A dates an earthquake that ruptured both faults either very close in time or at the same time. Deposit F, directly related to the Baby Landslide north of McKinney Bay (Fig. 9 cores 17 and 18, Fig. 10), correlates with fault offset and landslide infilling as identified in Fallen Leaf Lake to the south; this relationship dates the MRE on the Fallen Leaf segment and possibly the Rubicon and Dollar Point segments of the West Tahoe fault to the north (Brothers et al., 2009). Deposit G comprises a debris flow that grades laterally into turbidites and is likely sourced offshore Rubicon Bay. This deposit can be tied directly to a debris flow observed in CHIRP imagery (Fig. 11a). Its age matches that of the drowned trees offshore Baldwin Beach (Fig. 3) on a downthrown block of the West Tahoe Fault. Previously, these trees were inferred to record climatic variability (Lindstrom, 1990, Benson et al., 2002), though tectonic drowning had also been proposed (Lindstrom, 1990, Dingler et al., 2009). The correlation between the age of deposit G and the deepest submerged trees is curious and requires additional investigation. The trees were likely growing at a lower elevation due to climatic influences that led to a lower lake level; however an earthquake on the West Tahoe fault at this time would have dropped the hanging wall perhaps submerging the trees (an efficient mechanism for preservation). Oxygen isotope data from Pyramid Lake indirectly support the hypothesis of lake level being lower as Lake Tahoe was not spilling to Pyramid Lake during this time period (Benson et al., 2002).

Deposit J comprises the largest debris flow and with the broadest distribution in the lake sedimentary record. The debris flow is present in many of the southern cores and correlates by the large debris flow identified in CHIRP offshore Rubicon (Fig. 11) along the West Tahoe fault. This suggests shaking on this fault triggered the flow, though it is possible that a nearby earthquake triggered a mass movement on an unstable fault scarp.

Deposits F, G, and J likely represent three events on the West Tahoe Fault and may suggest segmented rupture. The Fallen Leaf segment and possibly the Rubicon segment ruptured in a M 7+ earthquake between ~4500 and 4100 calBP (Brothers et al., 2009). This correlates with the emplacement of the Baby Landslide north of McKinney Bay and the event deposit F in Lake Tahoe. The debris flow is restricted to the immediate vicinity of the Baby Landslide and the turbidite is relatively thin across the basin, with only Subunit 6 (clay layer) present in the southern basin. Because of the restricted distribution of this deposit, it may represent an earthquake on a fault further away or segmentation limited to the Fallen Leaf Segment of the West Tahoe Fault. Deposit G likely records a MRE rupture from between ~5600 and 5330 calBP on the Rubicon segment of the West Tahoe Fault and corresponds to the drowning of the trees off Baldwin Beach. In Fallen Leaf Lake, to the south, there is no evidence for a rupture during this time period (Brothers et al., 2009), which indicates that if this does result from a West Tahoe fault earthquake, only the northern segments ruptured. From the thickness distribution of the deposits, deposit J (between ~7890 and 7190 calBP) is likely sourced along the West Tahoe Fault from just north of Emerald Bay to Rubicon Bay.

Assuming three events on the West Tahoe Fault in the past ~7890 to 7190 yrs calBP yields an average recurrence interval (when all segments are included) of between 2630 and 2390 years. This average recurrence interval is slightly longer than similarly sized faults to the east along the Carson Range

front, ~1500 to 1700 years for the Genoa fault (Ramelli et al., 1999a) and ~1800 years for the Mount Rose fault zone (Ramelli et al., 1999b). The longer average recurrence interval on the Tahoe basin faults is consistent with terrace-offset long-term slip rates that are slightly lower than slip rates on the Carson Range faults.

6.4 Paleoclimate implications

The dominance of event deposits relative to normal sediments in the sediment record of Lake Tahoe leads to a difficult paleoclimate interpretation. By examining the periods of normal sedimentation, we can reach some broad paleoclimate conclusions, but finer scale interpretations are questionable due to low sedimentation rates and the erosive nature of the event deposits. The most obvious paleoclimate signal identified in the cores is the change from Pleistocene blue glacial silt below glacial silt/organic laminae to uniform light olive gray Holocene silt at event deposit O, between ~12490 and 11200 calBP. This change is accompanied by changes from a lower opal content to a higher opal content, indicative of higher productivity in the lake during the Holocene (Fig. 7). This boundary also marks the start of a slight increase in C/N ratio, as more terrestrial plants as well as diatoms occupied the basin, increasing the total carbon in the Holocene. Source areas are likely to be the remnant debris fans seen in the bathymetry (Fig. 2) for at least some of the event deposits older than O. It is possible that some of these event deposits are the result of outwash pulses, oversedimentation of the slope and delta collapse; however, active faulting cannot be ruled out.

Intriguingly, the $\delta^{15}\text{N}$ signal (Fig. 7) is the only signal examined that does not reflect the event deposits and also does not reflect the change at marker bed O. However, $\delta^{15}\text{N}$ is less enriched following deposition of the Tsoyowata ash and deposit J. This change is accompanied by a slightly lower opal content and a slightly higher C/N ratio (Fig. 7), though the effects are short-lived in these two measures, likely a result of stresses placed on the system due to the introduction of the ash and a large earthquake. $\delta^{15}\text{N}$ continues to become less enriched throughout the Holocene. This is consistent with Lake Tahoe remaining below the rim (Mensing et al., 2004) likely due to climate influences, though footwall uplift across the West Tahoe Fault may further exacerbate the situation downstream. The strengthening of the stratification within the lake may lead to longer periods without overturn and increased usage of $\delta^{15}\text{N}$. The trend continues until the time period between deposits G and H, between 6390 and 5330 calBP, consistent with a period in which there was not much lake spill (Benson et al., 2002). The age of the drowned trees (Lindstrom et al., 1990, Benson et al., 2002, Brothers et al., 2009) also records tectonic deformation and a down drop in the hanging wall along the West Tahoe Fault as outlined in the previous section. A short, intense drought between 5200 and 5000 has been inferred from Pyramid Lake, but is not observed elsewhere (Mensing et al., 2004). The drowned trees may be a result of faulting and consequent lake lowering on the West Tahoe fault rather than a climatic influence. The $\delta^{15}\text{N}$ becomes more enriched between deposits F and G and holds steady until between deposits C and D, between 2610 and 2160 calBP, at which point there is another decrease in $\delta^{15}\text{N}$, again consistent with a drought identified in Pyramid Lake (Mensing et al., 2004).

7.0 CONCLUSIONS

The determination of exact causal mechanisms for debris flows and turbidites is difficult. However, by examining composition, inferring source areas, and making comparisons to the existing paleoseismic record, we are able to determine that the Holocene episodic deposits in Lake Tahoe are likely the result of strong shaking due to earthquakes on active faults within the basin and within close proximity to the basin—although not a perfect record of shaking as only one event deposit is observed in Lake Tahoe in the last 630 years, whereas three known earthquakes with $M > 6.5$ have occurred on the Incline Village, Genoa, and Carson faults, though multiple turbidites which are merged and indistinguishable is also a possibility. Fourteen Holocene event deposits were emplaced over the last 11260 to 10480 calBP years. This yields an average shaking recurrence interval of between ~750 and 800 years for episodic deposits in the Lake Tahoe basin. If we assume that all the Holocene event deposits are the result of strong shaking on nearby faults, then this is also the combined average recurrence interval for the region. The central and northern segments of the West Tahoe fault may not have ruptured in the past 5600 years, which is approximately twice the average estimated recurrence interval. If these event deposits are the record of strong shaking on local faults, this study extends the paleoseismic record for the region through the entire Holocene, though it is clear that more work needs to be done on specific faults in order to determine their individual contributions to seismic hazard both within and outside the basin.

ACKNOWLEDGEMENTS

The authors thank Captains Brant Allen and Bob Richards of the R/V John Le Conte at the UC Davis Tahoe Environmental Research Center for their experience and aid in the collection of sediment cores and CHIRP profiles as well as the rest of the scientific crew aboard during data collection cruises. We would also like to thank Simon Poulson and his staff in the Nevada Stable Isotope Laboratory for their contributions to this work as well as the numerous undergraduate lab technicians who participated in the project. Thanks to Alan Heyvaert, Sudeep Chandra, Daniel Brothers, and Jeff Dinger for thoughtful discussion. Partial support for this project was received from the USGS National Earthquake Hazards Reduction Program (02HQGR0072, 04HQGR00017 and 07HQGR0014) and the Geological Society of America Student Grant Program.

REFERENCES CITED

- Adams, J., 1990, Paleoseismicity of the Cascadia Subduction Zone: Evidence from turbidites off the Washington-Oregon Margin, *Tectonics*, v. 9, no. 4, p. 569-583.
- Atwater, B.F., 2011, A Landlubber's Thoughts on Cascadia Turbidites, National USGS Marine Geohazards Workshop, Menlo Park, CA.
- Bacon, C.R., 1983, Eruptive History of Mount Mazama and Crater Lake Caldera, Cascade Range, USA: *Journal of Volcanology and Geothermal Research*, v. 18, p. 57-115.
- Bell, J.W., Slemmons, D.B., and Wallace, R.A., 1984, Reno to Dixie Valley-Fairview Peak earthquake areas, in Lintz, J., Jr., ed., *Western geological excursions: Reno, Nevada*, University of Nevada, Mackay School of Mines, 1984 Annual Meetings of the Geological Society of America, Guidebook, v. 4, p. 425-472.
- Bennett, R.A., Wernicke, B.P., Niemi, N.A., Friedrich, A.M., and Davis, J.L., 2003, Contemporary strain rates in the northern Basin and Range province from GPS data: *Tectonics*, v. 22.
- Benson, L., Kashgarian, M., Rye, R., Lund, S., Paillet, F., Smoot, J., Kester, C., Mensing, S., Meko, D., and Lindstrom, S., 2002, Holocene Multidecadal and Multicentennial Droughts Affecting Northern California and Nevada: *Quaternary Science Reviews*, v. 21, p. 659-682.
- Briggs, R.W., S.G. Wesnousky, K.D. Adams, 2005, Late Pleistocene and late Holocene lake highstands in the Pyramid Lake subbasin of Lake Lahontan, Nevada, USA, *Quaternary Research*, v. 64, issue 2, p. 257-263.
- Bronk, Ramsey, C., 2001, Development of the radiocarbon calibration program OxCal, *Radiocarbon*, v. 43, p. 355-363.
- Brothers, D.S., G.M. Kent, N.W. Driscoll, S.B. Smith, R. Karlin, J.A. Dinger, A.J. Harding, G.G. Seitz, J.M. Babcock, 2009, New constraints on deformation, slip rate, and timing of the most recent earthquake on the West Tahoe Fault, Lake Tahoe Basin, California, *Bull. Seismol. Soc. Amer.*, 99, no. 2A, pp. 499-519.
- Calvert, S.E., T.F. Pedersen, R.E. Karlin, 2001, Geochemical and isotopic evidence for post-glacial palaeoceanographic changes in Saanich Inlet, British Columbia, *Marine Geology*, v. 174, issues 1-4, p. 287-305.
- DePolo, C.M., 2006, Estimating Uncertainties of Seismic Hazard Parameters for Nevada Faults, Formations of a Quaternary Nevada Fault Working Group, and Gaining Consensus Fault Parameters, U.S. Geological Survey Earthquake Hazards Reduction Program Final Technical Report.
- Dinger, J., G. Kent, N. Driscoll, J. Babcock, A. Harding, G. Seitz, B. Karlin, and C. Goldman, 2009, A high-resolution seismic CHIRP investigation of active normal faulting across Lake Tahoe Basin, California-Nevada, *Geological Society of America Bulletin*, v. 121, no. 7-8, p. 1089-1107.
- Dixon, T.H., S. Rabaud, J. Lee, and M.C. Reheis, 1995, Constraints on present-day Basin and Range deformation from space geodesy, *Tectonics*, v. 14, no. 4, p. 755-772.
- Faulds, J.E., Henry, C.D., and Hinz, N.H., 2005, Kinematics of the northern Walker Lane: An incipient transform fault along the Pacific-North American plate boundary: *Geology*, v. 33, p. 505-508.
- Field, M.E., 1990, Submarine landslides associated with shallow seafloor gas and gas hydrates off northern California, *AAPG Bulletin*, v.74, no. 6
- Gardner, J. V., Mayer, L. A., and Hughs Clarke, J. E., 2000, Morphology and processes in Lake Tahoe (California-Nevada): *Geological Society of America Bulletin*, v. 112, no. 5, p. 736-746.
- Goldfinger, C., C.H. Nelson, J.E. Johnson, 2003, Holocene earthquake records from the Cascadia Subduction Zone and Northern San Andreas Fault based on precise dating of offshore turbidites, *Annual Review of Earth and Planetary Sciences*, v. 31, p. 555-577.
- Goldfinger, C., A.E. Morey, C.H. Nelson, J. Gutiérrez-Pastor, J.E. Johnson, E. Karabanov, J. Chaytor, A. Eriksson, and Shipboard Scientific Party, 2007, Rupture lengths and temporal history of significant

- earthquakes on the offshore and north coast segments of the Northern San Andreas Fault based on turbidite stratigraphy, v. 254, issues 1-2, p. 9-27.
- Goldfinger, C., K. Grijalva, R. Bürgmann, A.E. Morey, J.E. Johnson, C.H. Nelson, J. Gutiérrez-Pastor, A. Ericsson, E. Karabanov, J.D. Chaytor, J. Patton, and E. Gràcia, 2008, Late Holocene Rupture of the Northern San Andreas Fault and Possible Stress Linkage to the Cascadia Subduction Zone, *Bulletin of the Seismological Society of America*, v. 98, p. 861-889.
- Goldfinger, C., J. Patton, A.E. Morey, and C.H. Nelson, 2009, Reply to Comment on "Late Holocene Rupture of the Northern San Andreas Fault and Possible Stress Linkage to the Cascadia Subduction Zone" by Chris Goldfinger, Kelly Grijalva, Roland Bürgmann, Ann E. Morey, Joel E. Johnson, C. Hans Nelson, Julia Gutiérrez-Pastor, Andrew Ericsson, Eugene Karabanov, Jason D. Chaytor, Jason Patton, and Eulàlia Gràcia, *Bulletin of the Seismological Society of America*, v. 99, no. 4, p. 2599-2606.
- Hammond, W.C., and W. Thatcher, 2004, Contemporary tectonic deformation of the Basin and Range province, western United States: 10 years of observation with the Global Positioning System: *Journal of Geophysical Research-Solid Earth*, v. 109.
- Hammond, W.C., and W. Thatcher, 2007, Crustal deformation across the Sierra Nevada, northern Walker Lane, Basin and Range transition, western United States measured with GPS, 2000-2004: *Journal of Geophysical Research-Solid Earth*, v. 112.
- Hampton, M.A., H.J. Lee, J. Locat, 1996, Submarine landslides, *Reviews of Geophysics*, v. 34, issue 1, p. 33-60.
- Heezen, B.C., and W.M. Ewing, 1952, Turbidity currents and submarine slumps, and the Grand Banks [Newfoundland] earthquake, *American Journal of Science*, v. 250, p. 849-873.
- Heezen, B.C., and W.M. Ewing, 1955, Orleansville earthquake and turbidity currents, *AAPG Bulletin*, v. 39.
- Hyne, N. J., P. Chelminski, J. E. Court, D. Gorsline, and C. R. Goldman, 1972, Quaternary history of Lake Tahoe, California-Nevada, *Geological Society of America Bulletin*, v. 83, p. 1435-1448.
- Inouchi, Y., Y. Kinugasa, F. Kumon, S. Nakano, S. Yasumatsu, and T. Shiki, 1996, Turbidites as records of intense palaeoearthquakes in Lake Biwa, Japan, *Sedimentary Geology*, v. 104, issues 1-4, p. 117-125.
- Karlin, R.E., and S.E.B. Abella, 1992, Paleearthquakes in the Puget Sound Region Recorded in Sediments from Lake Washington, U.S.A., *Science*, v. 258, no. 5088, p. 1617-1620.
- Karlin, R., R.A. Schweickert, M.M. Lahren, K.D. Smith, 2000, High-Resolution Seismic Reflection Survey of Holocene Faults, Deformation, and Landslides in Lake Tahoe, *Abstracts with Programs, Geological Society of America* 32 (7): 244.
- Karlin, R.E., M. Holmes, S.E.B. Abella, R. Sylwester, 2004, Holocene landslides and a 3500-year record of Pacific Northwest earthquakes from sediments in Lake Washington, *Geological Society of America Bulletin*, v. 116, no. 1-2, p. 94-108.
- Karlin, R.E., S. Smith, G. Seitz, G. Kent, and N. Driscoll, 2005, Landslides, Active Faulting, and Paleoseismicity in Lake Tahoe, *Seismological Research Letters*, March, Annual Meeting Abstracts.
- Kent, G.M., Babcock, J.M., Driscoll, N.W., Harding, A.J., Dingler, J.A., Seitz, G.G., Gardner, J.V., Mayer, L.A., Goldman, C.R., Heyvaert, A.C., Richards, R.C., Karlin, R., Morgan, C.W., Gayes, P.T., and Owen, L.A., 2005, 60 k.y. record of extension across the western boundary of the Basin and Range province: Estimate of slip rates from offset shoreline terraces and a catastrophic slide beneath Lake Tahoe, *Geology*, v. 33, p. 365-368.
- Krause, D.C., W.C. White, D.J.W. Piper, and B.C. Heezen, 1970, Turbidity currents and cable breaks in the Western New Britain trench, *Geological Society of America Bulletin*, v. 81, no. 7, p. 2153-2160.
- Lee, H.J., 2009, Timing and occurrence of large submarine landslides on the Atlantic Ocean margin, *Marine Geology*, v. 264, issues 1-2, p. 53-64.
- Lindstrom, S., Submerged tree stumps as indicators of Mid-Holocene aridity in the Lake Tahoe Basin, 1990, *Journal of California and Great Basin Anthropology*, v. 12, p. 146-147.
- Locat, J., and H.J. Lee, 2002, Submarine landslides: advances and challenges, *Canadian Geotechnical Journal*, v. 39, no. 1.
- Mensing, S.A., Benson, L.V., Kashgarian, M., and Lnd, S 2004. A Holocene pollen record of persistent droughts from Pyramid Lake, Nevada, USA *Quaternary Research*, 62(1): 29-38.
- Mortlock, R.A., and Froelich, P.N., 1989, A simple method for the rapid determination of biogenic opal in pelagic marine sediments. *Deep-Sea Research*, 36, 1415-1426.

- Nakajima, T., and Y. Kanai, 2000, Sedimentary features of seismoturbidites triggered by the 1983 and older historical earthquakes in the eastern margin of the Japan Sea, *Sedimentary Geology*, v. 135, issues 1-4, p. 1-19.
- Oldow, J.S., 2003, Active transtensional boundary zone between the western Great Basin and Sierra Nevada block, western U.S. Cordillera, *Geology*, v. 31, no. 12, p. 1033-1036.
- Osleger, D.A., A.C. Heyvaert, J.S. Stoner, and K.L. Verosub, 2009, Lacustrine turbidites as indicators of Holocene storminess and climate: Lake Tahoe, California and Nevada, *Journal of Paleolimnology*, v. 42, no. 1, p. 103-122.
- Palmer, D.F., T.L. Henyey, and R.E. Dodson, 1979, Paleomagnetic and sedimentological studies at Lake Tahoe, California-Nevada, *Earth and Planetary Science Letters*, v. 46, issue 1, Pages 125-137.
- Piper, D.J.W. and W.R. Normark, 2009, Processes that initiate turbidity currents and their influence on turbidites: a marine geology perspective, *Journal of Sedimentary Research*, v. 79, no. 6, p. 347-362.
- Ramelli, A. R., Bell, J.W., dePolo, C.M., and Yount, J.C., 1999a Large-magnitude, late Holocene earthquakes on the Genoa fault, west-central Nevada and eastern California, *Bulletin of the Seismological Society of America*, v. 89, p. 1458-1472.
- Ramelli, A.R., dePolo, C.M., and Bell, J.W., 1999b, Paleoseismic studies of the northern Sierra Nevada Frontal fault zone: Final Technical Report to the National Earthquake Hazards Reduction Program.
- Ramelli, A.R., dePolo, C.M., and Bell, J.W., 2002, Paleoseismic studies of the Little Valley fault; U.S.G.S. Earthquake Hazards Reduction Program Final Technical Report.
- Reimer, P.J., Baillie, M.G.L., Bard, E., Bayliss, A., Beck, J.W., Bertrand, C.J.H., Blackwell, P.G., Buck, C.E., Burr, G.S., Cutler, K.B., Damon, P.E., Edwards, R.L., Fairbanks, R.G., Friedrich, M., Guilderson, T.P., Hogg, A.G., Hughen, K.A., Kromer, B., McCormac, G., Manning, S., Ramsey, C.B., Reimer, R.W., Remmele, S., Southon, J.R., Stuiver, M., Talamo, S., Taylor, F.W., van der Plicht, J., and Weyhenmeyer, C.E., 2004, IntCal04 terrestrial radiocarbon age calibration, 0-26 cal kyr BP: *Radiocarbon*, v. 46, p. 1029-1058.
- Ryan, W.B.F. and Heezen, B.C., 1965, Ionian sea submarine canyons and the 1908 Messina turbidity current, *Geological Society of America Bulletin*, v. 76, no. 8, p. 915-932.
- Sarna-Wojkicki, A.M., Lajoie, K.R., Meyer, C.E., Adam, D.P., and H.J., R., 1991, Tephrochronologic correlation of upper Neogene sediments along the Pacific margin, conterminous United States. In: Morrison R.B. (ed.), *Quaternary Non-Glacial Geology: Conterminous United States: Geological Society of America, Decade of North American Geology*, v. K-2, p. 117-140.
- Saucedo, G.J., Little, J.D., Watkins, S.E., Davis, J.R., Mascorro, M.T., Walker, V.D., and Ford, E.W., 2005, Geologic map of the Lake Tahoe Basin, California and Nevada: California Geological Survey, scale 1:100,000.
- Schnellmann, M., F.S. Anselmetti, D. Giardini, J.A. McKenzie, and S.N. Ward, 2002, Prehistoric earthquake history revealed by lacustrine slump deposits, *Geology*, v. 30, p. 1131 – 1134.
- Schnellmann, M., F.S. Anselmetti, D. Giardini, J.A. McKenzie, and S.N. Ward, 2005, Mass movement-induced fold-and-thrust belt structures in unconsolidated sediments in Lake Lucerne (Switzerland). *Sedimentology*, v. 52, p. 271–289.
- Schweickert, R.A., Lahren, M.M., Smith, K.D., and Karlin, R., 1999, Preliminary fault map of the Lake Tahoe Basin, California and Nevada: *Seismological Research Letters*, v. 70, p. 306-312.
- Seed, H.B., and M.S. Rahman, 1978, Wave induced pore pressure in relation to ocean floor stability of cohesionless soils, *Marine Geotechnology*, v. 3, p. 123-150.
- Seitz, G.G. and G. Kent, 2004, Closing the gap between on and offshore paleoseismic records in the Lake Tahoe Basin, Final Technical Report to the National Earthquake Hazard Reduction Program.
- Shanmugam, G., 2009, Comment on "Late Holocene Rupture of the Northern San Andreas Fault and Possible Stress Linkage to the Cascadia Subduction Zone" by Chris Goldfinger, Kelly Grijalva, Roland Bürgmann, Ann E. Morey, Joel E. Johnson, C. Hans Nelson, Julia Gutiérrez-Pastor, Andrew Ericsson, Eugene Karabanov, Jason D. Chaytor, Jason Patton, and Eulàlia Gràcia, *Bulletin of the Seismological Society of America*, v. 99, no. 4, p. 2594-2598.
- Simon, A., Langendoen, E, Bingner, R., Wells, R, Heins, A., Jokay, N, and Jaramillo, I, 2003, Lake Tahoe Basin Framework Implementation Study: Sediment Loadings and Channel Erosion, USDA ARS Technical Report.
- Michael Strasser, Flavio S. Anselmetti, Donat Faeh, Domenico Giardini, and Michael Schnellmann, 2006, Magnitudes and source areas of large prehistoric northern Alpine earthquakes revealed by slope failures in lakes, *Geology (Boulder)*, v. 34, no. 12, p. 1005-1008.

- Strasser, M. S. Stegmann, F. Bussmann, F.S. Anselmetti, B. Rick and A. Kopf, 2007, Quantifying subaqueous slope stability during seismic shaking: Lake Lucerne as model for ocean margins, *Marine Geology*, v. 240, issues 1-4, p. 77-97.
- Surpless, B.E., Stockli, D.F., Dumitru, T.A., and Miller, E.L., 2002, Two-phase westward encroachment of Basin and Range extension into the northern Sierra Nevada: *Tectonics*, v. 21.
- Sylvester, Z., and Lowe, D.R., 2004, Textural trends in turbidites and slurry beds from the Oligocene flysch of the East Carpathians, Romania, *Sedimentology*, v. 51, issue 5, pages 945-972.
- Thatcher, W., G. R. Foulger, B. R. Julian, J. Svarc, E. Quilty, and G. W. Bawden, 1999, Present-Day Deformation Across the Basin and Range Province, Western United States, *Science*, v. 283, p. 1714-1718.
- Unruh, J., Humphrey, J., and Barron, A., 2003, Transtensional model for the Sierra Nevada frontal fault system, eastern California: *Geology*, v. 31, p. 327-330.

TABLE 1: RADIOCARBON SAMPLES

Core-Sample	Sample Depth (cm)	14C age	Max* (calBP)	Min* (calBP)	Mean (calBP)	Episodic Deposit Notes
21-1	27	470 ± 130	690	-10	530 ± 100	Pre A
21-3	33	1278 ± 48	1300	1080	1190 ± 60	Pre A/Post B
17-1	9	1380 ± 30	1350	1260	1300 ± 20	Post C
21-4	62	1605 ± 35	1550	1400	1500 ± 50	Pre B/Post C
9-1	13	2175 ± 35	2320	2060	2210 ± 70	Post C?
17-2	23.5	2210 ± 30	2330	2140	2230 ± 50	Pre C/Post E
12-2	52	2215 ± 30	2330	2150	2230 ± 50	Post C
1-2	30	2421 ± 36	2700	2350	2500 ± 100	Post F
16-1	28	2440 ± 120	2750	2150	2500 ± 150	in C
12-3	71	2500 ± 30	2740	2460	2590 ± 80	Pre D/Post E
21-5	106	2515 ± 40	2750	2450	2600 ± 100	Pre D/Post E Reworked, out of sequence
12-1	48	2549 ± 37	2750	2500	2650 ± 100	
19-1	55	2885 ± 30	3150	2890	3020 ± 60	Pre D/Post E
21-6	131	3290 ± 38	3650	3400	3500 ± 50	Pre E/Post F
15-1	52	3550 ± 50	3950	3700	3850 ± 100	Pre E/Post F
18-1	44	3630 ± 120	4350	3650	3950 ± 150	Pre E/Post F
1-3	57	3661 ± 38	4150	3900	4000 ± 50	Pre E/Post F
12-5	96	3790 ± 100	4450	3900	4200 ± 150	Pre E/Post F
7-1	41	3976 ± 44	4550	4300	4450 ± 50	Pre F/Post G
18-2	62	4189 ± 39	4850	4600	4700 ± 50	Pre F/Post G
18-3	71	4660 ± 100	5600	5050	5350 ± 150	Pre F/Post G
15-2	73	4780 ± 40	5600	5350	5500 ± 50	Pre G/Post H
15-3	88	5120 ± 50	6000	5750	5850 ± 50	in G
7-2	67	5710 ± 110	6750	6300	6500 ± 100	Pre H/Post I
16-2	140	5880 ± 180	7150	6300	6750 ± 200	Pre H/Post I
2-1	83	6095 ± 79	7150	6750	7000 ± 100	Pre I/Post J
18-4	109	6160 ± 110	7300	6750	7050 ± 150	in I
16-3	151	6400 ± 190	7650	6900	7300 ± 200	Pre I/Post J

TA	^	7015	± 45	7950	7730	7850	± 60	Pre J/Post K
15-6	182	7970	± 50	9000	8650	8850	± 100	Pre Ash/Post K
15-4	118	8140	± 60	9300	8800	9100	± 100	in I or I'
15-5	145.5	8260	± 40	9400	9100	9250	± 100	in J
2-2	268	8263	± 66	9450	9050	9250	± 100	Pre J/Post K/L?
18-5	160	8350	± 360	10250	8450	9350	± 450	Pre L/Post M
15-7	199	8410	± 50	9500	9300	9450	± 50	Pre K/Post L
15-9	215	8550	± 230	10200	9050	9600	± 300	Pre L/Post M
18-6	174	8590	± 110	10100	9300	9650	± 150	Pre M/Post N
15-8	215	8780	± 130	10200	9550	9850	± 200	Pre L/Post M
2-3	278	8861	± 50	10150	9750	10000	± 100	Pre J/Post K/L?
7-3	114	9357	± 51	10700	10400	10600	± 50	Pre K/L?/Post O
15-10	241.5	9460	± 60	11050	10550	10750	± 150	in M
15-11	260	9600	± 250	11750	10250	10950	± 400	Pre M/Post O
18-7	204	9804	± 53	11300	11150	11200	± 50	Pre N/Post O
16-4	267	10320	± 280	12800	11250	12050	± 450	in O
15-12	297.5	12160	± 40	14150	13900	14000	± 50	in O
15-13	297.5	12200	± 110	14600	13800	14100	± 200	in O
18-8	261.5	13990	± 170	17300	16100	16700	± 300	in 2nd below O
1-1	7	***	***	***	***	***	***	Post F
21-2	32	***	***	***	***	***	***	Pre B/Post C

TA=Tsoyowata Ash

*=95% confidence interval

^=see table 2 and Figs. 8 and 9 for depths

*** =Not enough material for dating

TABLE 2: SEDIMENTATION RATES FOR CORES WITH MULTIPLE SAMPLES

Core #	Total Sed. Rate (cm/kyr)	Normal Sed. Rate (cm/kyr)	Samples Used*^
1	17.6-18.7	17.6-18.7	1-1, 1-2
2	71.4-71.5	~9.8	2-1, 2-2, 2-3
7	11.8-11.9	~7.0	7-1, 7-2, 7-3
12	~21.9	~14.5	12-2, 12-3, 12-5, TA-178
15	28.2-31.8	13.9-14.9	15-1, 15-2, 15-6, 15-8a, 15-10, TA-167
16	18.2-33.8	11.5-22.1	16-2, 16-3, TA-166
17	15.5-15.7	11.4-11.6	17-1, 17-2, TA-111
18	22.3-22.9	11.2-11.4	18-1, 18-2, 18-3, 18-5, 18-6, 18-7, TA-137
19	19.2-19.5	9.9-10.0	19-1, TA-148
21	35.9-39.0	15.5-17.0	21-1, 21-2, 21-3, 21-4, 21-5

*Refer to table 1 for sample information

^Only cores with multiple samples were averaged. Sed. rates are averaged over different intervals based on sample depths

TA is the Tsoyowata Ash and the number is the associated depth of the ash in cm

TABLE 3: ESTIMATED VOLUMES AND ASSIGNED FAULTS FOR INDIVIDUAL EPISODIC DEPOSITS

Episodic Deposit	Estimated Volume (m ³)	Modelled 2σ Age (calBP)	Fault
A	2.5x10 ⁴	630-120	Incline Village, Carson City or Genoa
B	2.5x10 ⁴	1520-1150	Possibly Mount Rose
C	2.2x10 ⁵	2320-2160	Genoa
D	7.2x10 ⁴	2610-2250	Mount Rose
E	5.0x10 ⁶	3540-2990	Carson City or Genoa
F	2.3x10 ⁶	4510-4070	Fallen Leaf segment of West Tahoe
G	1.7x10 ⁷	5600-5330	Rubicon segment of West Tahoe
H	9.7x10 ⁶	6390-5480	Undetermined
I	1.9x10 ⁶	7080-6560	Undetermined
J	2.3x10 ⁷	7890-7190	Rubicon segment of West Tahoe
K	4.8x10 ⁶	9450-8770	Possibly Mount Rose
L	3.1x10 ⁶	9730-9320	Undetermined
M	1.3x10 ⁷	10160-9800	Undetermined
N	1.2x10 ⁶	11260-10480	Undetermined
O	3.1x10 ⁷	12490-11200	Undetermined, possibly not earthquake related

See Figures 9 and 12

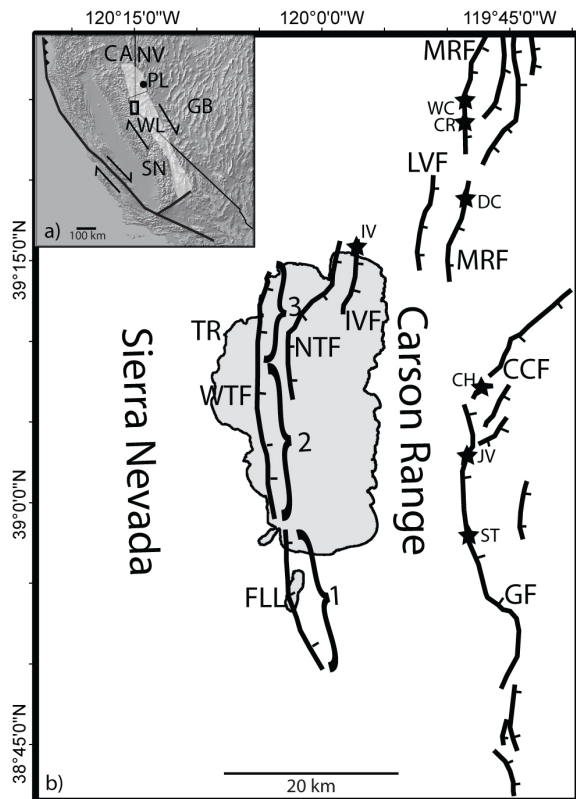


Figure 1

Figure 1: Location map of the study area along the California and Nevada border. A. (inset) Shaded relief map highlighting major features. The Walker Lane (WL) is highlighted with the Sierra Nevada (SN) along its western boundary and the Great Basin (GB) on its eastern boundary. Pyramid Lake (PL), the terminal lake in the Lake Tahoe/Truckee River system is also noted with a dot. B) The Tahoe Basin fault system is identified as three separate faults; the West Tahoe Fault (WTF), North Tahoe Fault (NTF), and the Incline Village Fault (IVF). The WTF comprises three segments: the Fallen Leaf Lake segment (1), the Rubicon segment (2), and the Dollar Point segment (3). The Carson Range frontal fault system is identified as several separate faults; the Genoa Fault (GF), the Mount Rose Fault system (MRF), the Carson City Fault (CCF), and the Little Valley Fault (LVF). The Truckee River (TR) and Fallen Leaf Lake (FLL) are also noted. Trench sites with radiocarbon ages used in this study are identified with stars; Incline Village (IV), Whites Creek (WC), Davis Creek (DC), Callahan Ranch (CR), Carson Hill (CH), Jacks Valley (JV), and Sturgis (ST).

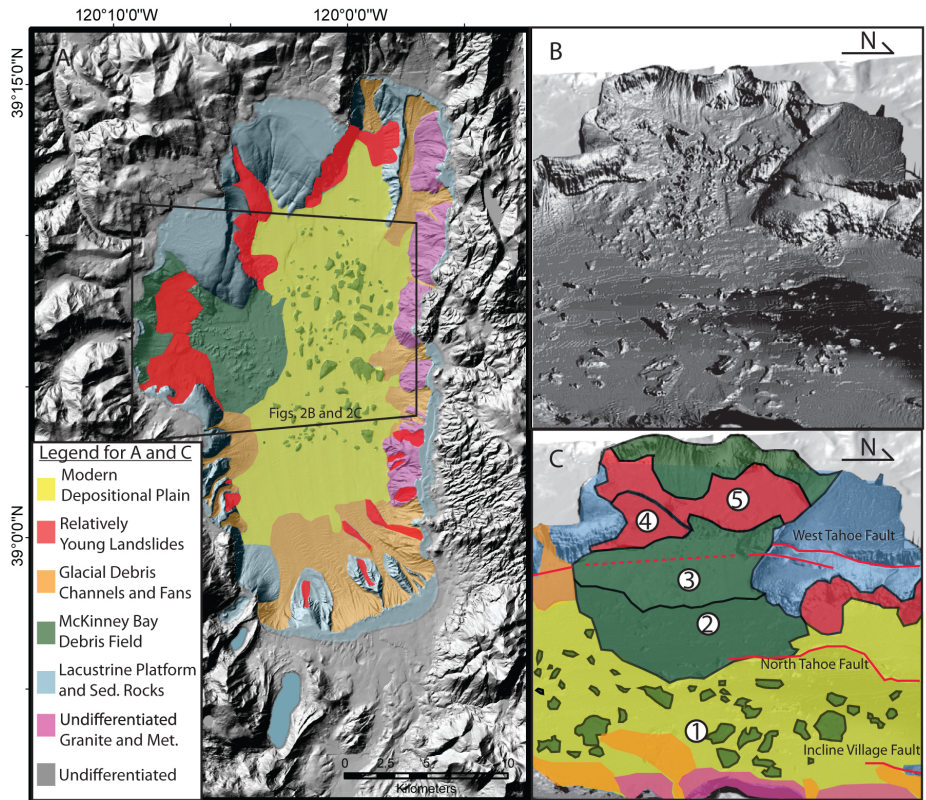


Figure 2: Landslides and geology in Lake Tahoe. A. Shaded bathymetry and topography with a geologic map of Lake Tahoe highlighting the modern depositional plain, glacial erosional channels and debris aprons, the lacustrine platform and older lacustrine rocks and sediments, Mesozoic granite and metamorphic rocks as well as the McKinney Bay (MB) debris field and several relatively recent landslides. Other key landslides discussed throughout the text are also noted; the baby landslide (BL), Rubicon (R), North Tahoe Slope (NTS), and Incline Village Spine (IVS). B. Perspective view looking west toward the McKinney Bay slide area without interpretation. C. Perspective view of the McKinney Bay reentrant that highlights at least 5 different episodes of sliding. The mega-slide that distributed large debris blocks over the floor of the lake is marked with a 1. Two younger large debris aprons are identified with a 2 and a 3, and two younger landslides are identified with a 4 and 5.

Figure 3: Shaded topography and bathymetry showing core locations and selected CHIRP seismic reflection profiles. Cores are marked by black dots and labeled. Selected seismic reflection profiles are identified as black lines and are shown in Figures 4, 10, and 11. Several locations are also noted; Agate Bay (AB), Crystal Bay (CB), Truckee River (TR), Tahoe City (TC), Tahoe City Shelf (TCS), Ward Creek Delta (WCD), Blackwood Creek (BC), Second Creek (SC), Third Creek (TC1), Trout Creek (TC2), McKinney Bay (MB), Rubicon Bay (RB), Emerald Bay (EB), Baldwin Beach (BB), Zephyr Cove (ZC), Sugar Pine Point (SPP), Upper Truckee River (UTR), and Fallen Leaf Lake (FLL).

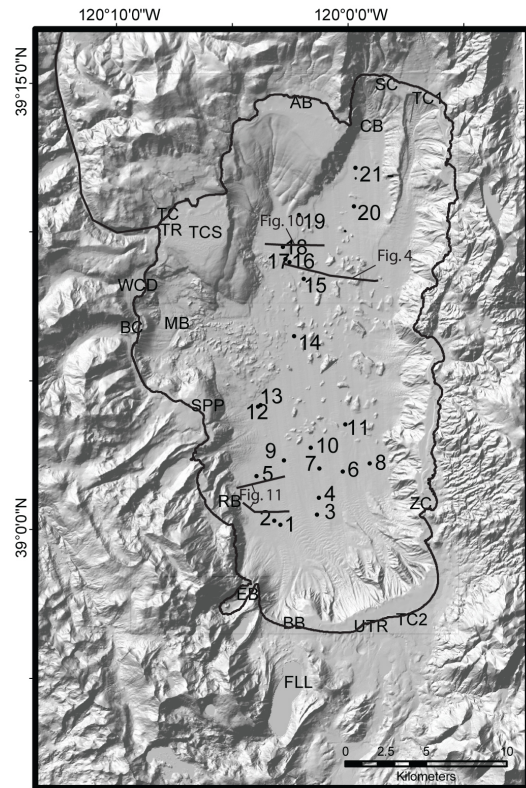


Figure 3

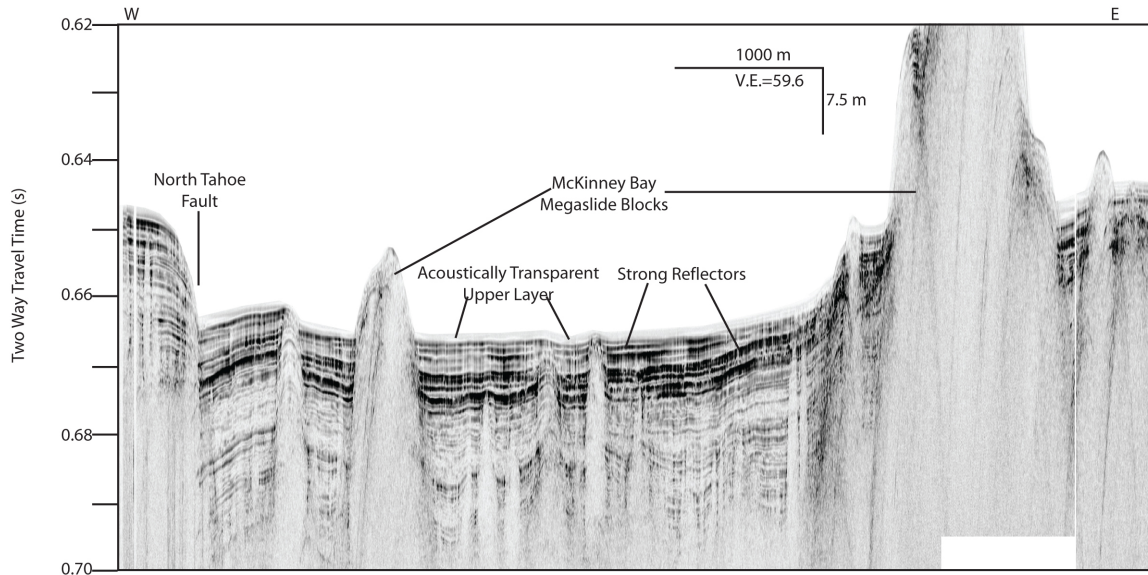


Figure 4

Figure 4: East-west oriented CHIRP profile (see Fig. 3 for location) that images an acoustically transparent layer mantling a series of high-amplitude reflectors. The large blocks are part of the McKinney Bay Slide. The North Tahoe Fault is also shown. In the profile, note that the sediments across the basin generally tilt and thicken to the West, though some east dipping layers are present possibly due to localized sedimentation around McKinney Bay landslide blocks.

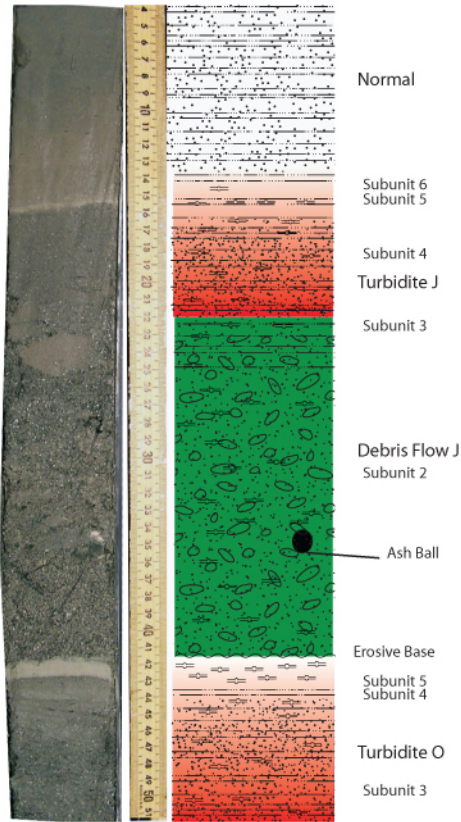


Figure 5

Figure 5: Example of Lake Tahoe sediments from core 8, 104-150 cm. In the right hand column, the white represents “normal” sedimentation, the red denotes a turbidite and the green a debris flow. Note lithofacies subunits 2-6 are present in the deposit J, though subunit 1 is not present in this case. The debris flow has incorporated ash balls, clay balls, and other reworked material. Subunit 3 is only weakly developed in this case, though the turbidite O does have a well-developed subunit 3. Turbidite O subunit 5 is eroded by a Holocene debris flow and is a distinctively thick layer that marks the upper portions of a key marker bed.

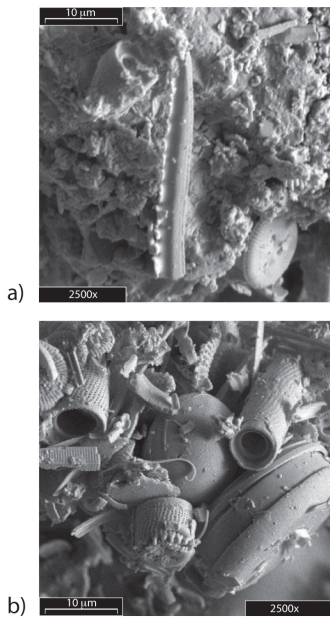


Figure 6

Figure 6: SEM photographs of diatoms in subunit 3 (a) and subunit 5 (b), from core 15. Both photographs are at 2500X magnification. A. One clay ball from subunit 3 contains sand-sized clay balls that have diatoms attached to them and account for the presence of diatoms in this coarse layer. B. Subunit 5 contains abundant fractured diatoms indicative of transport.

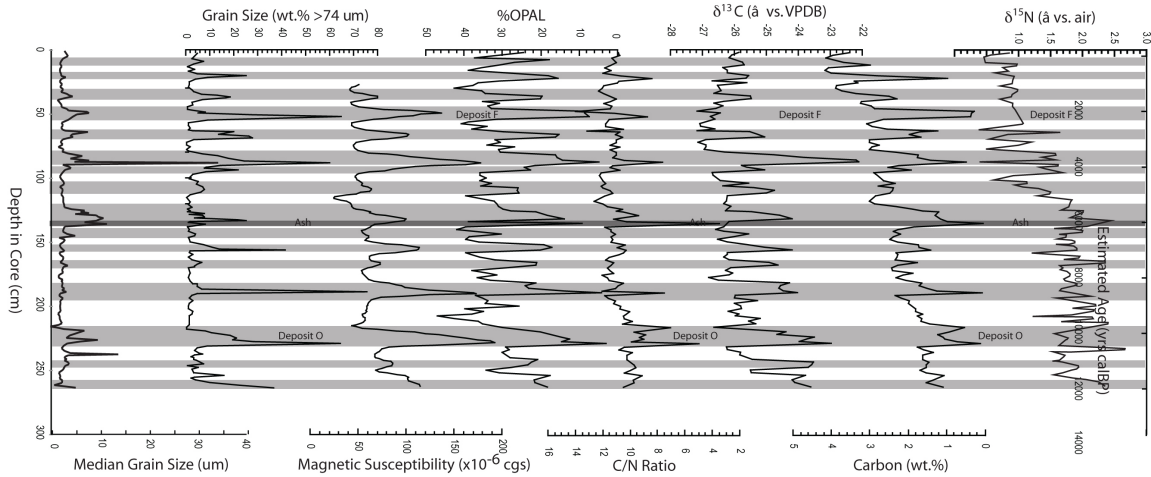


Figure 7

Figure 7: Comparison of median grain size, weight % of sand >74 microns, whole core magnetic susceptibility, diatom content as measured by %Opal, C/N ratio, $\delta^{13}\text{C}$, Total Carbon, and $\delta^{15}\text{N}$ in core 18. Gray bars represent event deposits. The darker gray bar at ~140 cm represents the location of the Tsoyowata Ash. Note that the axes of %Opal, C/N ratio, and total Carbon are inverted. Also note that the event deposits dominate the signal except in the $\delta^{15}\text{N}$. The age estimate on the upper x-axis is for rough reference only, and is not meant to be definitive and should not be taken as such. Sedimentation rates do vary with time in the lake and the erosion of debris flows and turbidity currents also affects the age model.

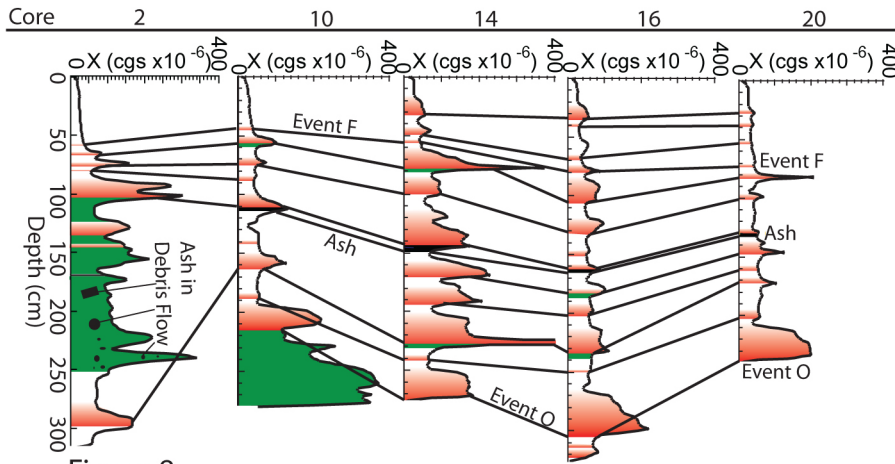


Figure 8

Figure 8: Correlation of selected cores (see Fig. 3 for location) by whole core magnetic susceptibility profiles. As in Figure 4, the white represents “normal” sedimentation, the red denotes a turbidite and the green is a debris flow. Black represents the Tsoyowata ash, which is a discreet layer in many of the northern cores, but has been reworked and incorporated into a debris flow in the southern cores. When combined with lithologic descriptions and stratigraphic relationships, magnetic susceptibility allows us to correlate deposits across the basin (see figure 9).

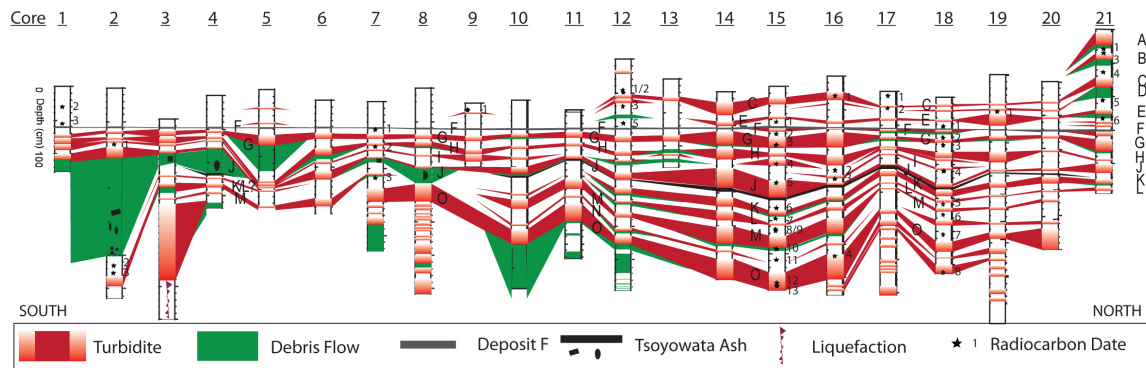


Figure 9

Figure 9: Correlation of all cores from this study arranged from south (left) to north (right). Please refer to Figure 3 for core locations. The cores are hung on episodic deposit F, represented here in gray, the youngest deposit identified in every core and one of the three key marker beds. As in earlier figures, the white represents “normal” sedimentation, the red denotes a turbidite and the green is a debris flow. The ash is shown in black while radiocarbon samples are shown with black stars with the sample number to the right (see Table 1). Liquefaction in the base of core 3 lies directly below a massive turbidite and the cause is unclear, as it could either be earthquake related or a result of dewatering when the turbidite was deposited.

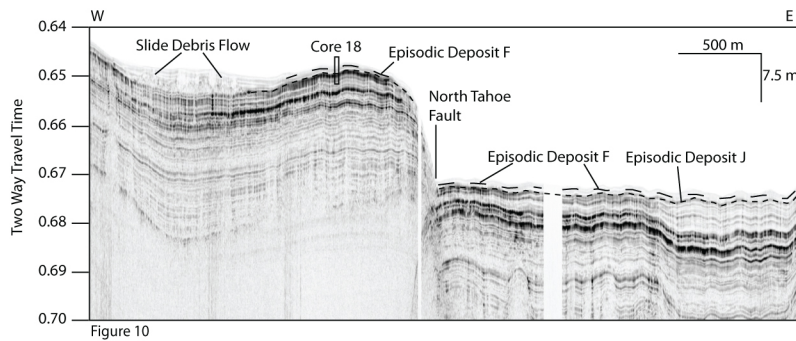


Figure 10

Figure 10: CHIRP seismic reflection profile (see Fig. 3 for location) with the baby landslide (BL) debris flow and associated episodic deposit F (larger dashed line). The line is located north of the blocks seen in the bathymetry and the debris flow is confined to the western side of the back tilted sediment block between the West Tahoe and North Tahoe faults. The debris flow has eroded down to deposit J (smaller dashed line) and thins quickly to the east into deposit F. Subunits 3-6 are present in core 18.

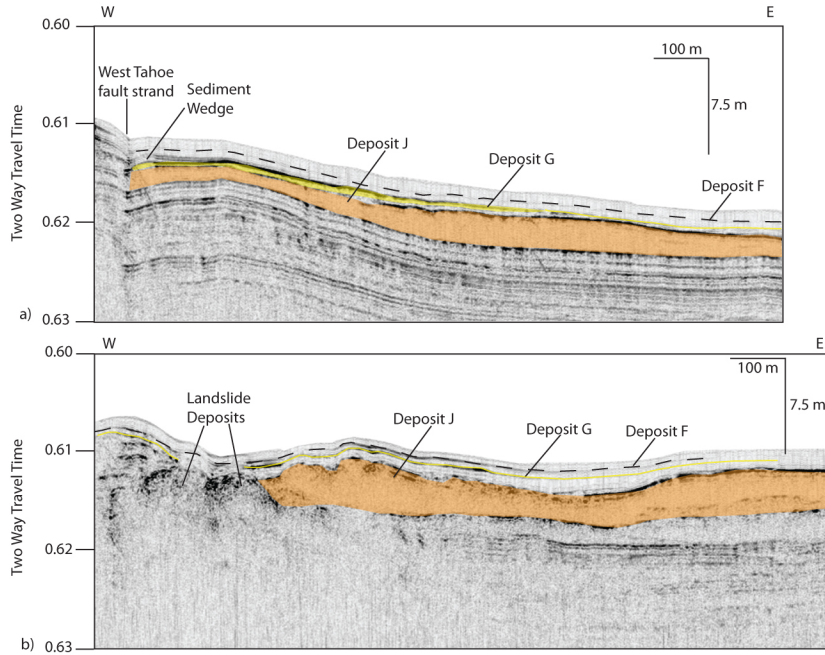


Figure 11

Figure 11: CHIRP seismic reflection profiles (see Fig. 3 for locations) with debris flows offshore Rubicon highlighting activity on the West Tahoe fault. In both figures, deposit F is a dashed line, deposit G is shown in yellow, and deposit J is shown in orange. A: Debris flow J, 1+ m thick across this profile, is truncated and possibly offset at the strand of the West Tahoe fault shown here. Deposit G is thinner than J, but still identifiable as a debris flow in the western portion of the profile and thins to the east. Deposit F is potentially associated with the colluvial wedge and likely marks the MRE on the Rubicon segment of the fault. B: Deposit J is much thicker in the southern of the two profiles. J is present off the toe of a landslide that has come off the western wall. Deposit G and deposit F are discreet reflectors at this location.

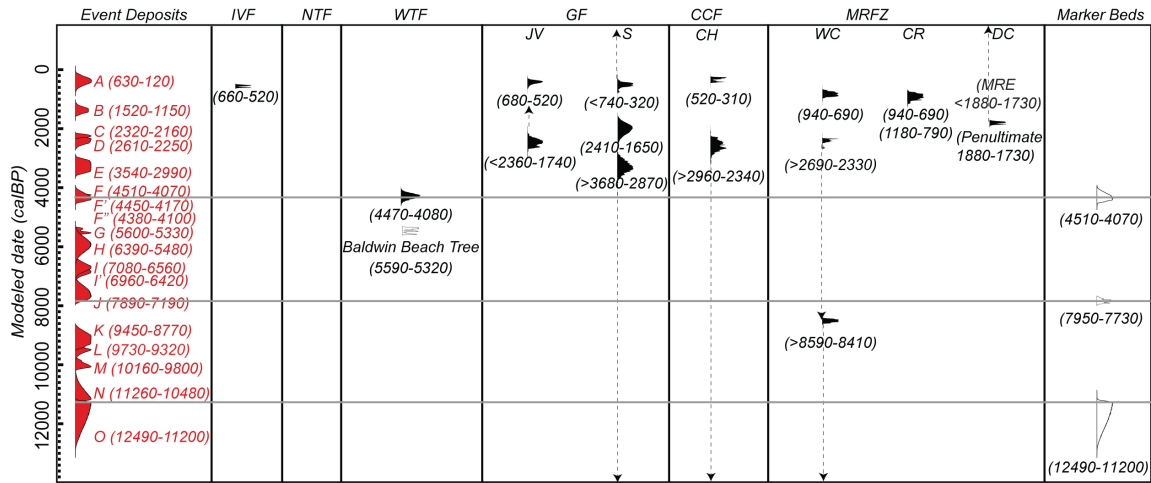


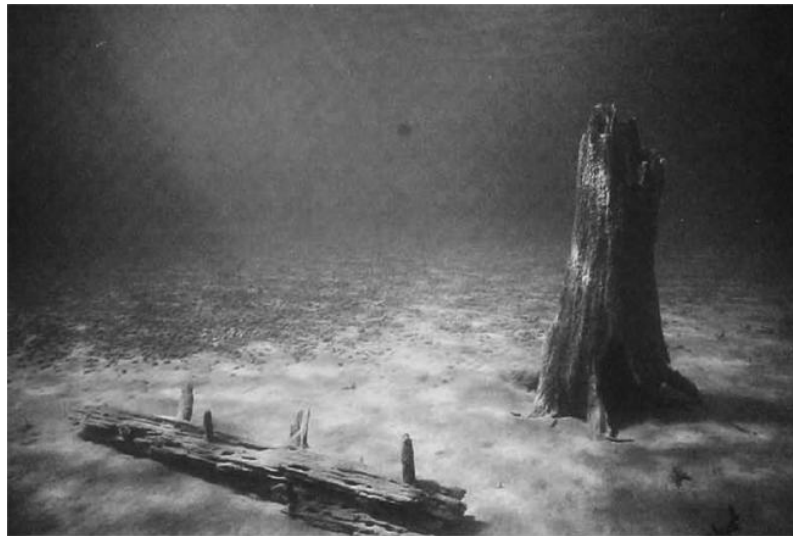
Figure 12

Figure 12: Correlation of modeled ages of episodic deposits and preexisting paleoseismic histories of nearby faults. Probability distribution curves for event deposits are in red, preexisting paleoseismic investigations (see Fig. 1 for locations) on the Incline Village Fault (IVF), West Tahoe Fault (WTF), Genoa Fault Jacks Valley and Sturgis (GF, JV, S), Carson City Fault C Hill (CCF, CH), Mount Rose Fault Zone White's Creek, Callahan Ranch, and Davis Creek (MRFZ, WC, CR, and DC), are shown in black. Many of the events only have one bounding date. In these cases, a dashed line with an arrow indicating the potential age of the event is shown. The Tsoyowata Ash and Baldwin Beach sunken trees are shown in white outlined in black. The Carson Range frontal fault system is better studied than the Tahoe Basin fault system and accounts for the majority of preexisting data (Bell et al., 1984, Ramelli et al., 1999a, Ramelli et al., 1999b, Ramelli et al., 2002, DePolo, 2006). The Incline Village Fault is the only trench site in the Tahoe basin (Seitz and Kent, 2004) and the subaqueous landslide in Fallen Leaf Lake (Brothers et al., 2009) is the only other known paleoseismic study in the basin. Preexisting data are labeled based on the trench or fault strand associated with the individual faults. Note that there is not an MRE listed for the Davis Creek segment of the Mount Rose fault system, but there is a penultimate event (Ramelli et al., 2002). One younger event on that fault exists but there is no data available to constrain the date.

Day 1, Stop 6 – Submerged Tree Stumps

We will attempt to swim out about 75 m into the lake and observe the submerged tree stumps. We sampled and C-14 dated one stump, the outer layer provided a C-14 date of ~5450 years BP, documented in the provided Brothers et al. 2009 paper.

Summary: By design Stop 6 will provide cooling off, as needed. You'll have the opportunity to get wet and examine submerged tree stumps, which we have sampled and radiocarbon dated. Although the stumps appear to be limited to the WTF hanging wall block, non-tectonic interpretations have been published. We'll swim out to the submerged tree stumps—be as prepared for ~65-70 degree water at the surface (perhaps a bit colder if you want to touch the ~4 ka stumps). You may wish to pack goggles, maybe some fins, and a towel. Below from Lindstroem 1990.



“So singularly clear was the water, that where it was only twenty or thirty feet deep the bottom was so perfectly distinct that the boat seemed floating in the air! Yes, where it was even eighty feet deep. Every little pebble was distinct, every speckled trout, every hand's- breadth of sand. Often, as we lay on our faces, a granite boulder, as large as a village church, would start out of the bottom apparently, and seem climbing up rapidly to the surface, till presently it threatened to touch our faces, and we could not resist the impulse to seize an oar and avert the danger. But the boat would float on, and the boulder descend again, and then we could see that when we had been exactly above it, it must still have been twenty or thirty feet below the surface. Down through the transparency of these great depths, the water was not merely transparent, but dazlingly, brilliantly so. All objects seen through it had a bright, strong vividness, not only of outline, but of every minute detail, which they would not have had when seen simply through the same depth of atmosphere. So empty and airy did all spaces seem below us, and so strong was the sense of floating high aloft in mid-nothingness, that we called these boat-excursions 'balloon-voyages.'” - Mark Twain

Day 2, Stop 1 – Eagle Rock

60 k.y. record of extension across the western boundary of the Basin and Range province: Estimate of slip rates from offset shoreline terraces and a catastrophic slide beneath Lake Tahoe

G.M. Kent

J.M. Babcock

N.W. Driscoll

A.J. Harding

J.A. Dingler

Scripps Institution of Oceanography, University of California, San Diego, La Jolla, California 92093, USA

G.G. Seitz Department of Geological Sciences, San Diego State University, San Diego, California 92182, USA

J.V. Gardner

L.A. Mayer

Center for Coastal and Ocean Mapping, University of New Hampshire, Durham, New Hampshire 03824, USA

C.R. Goldman

A.C. Heyvaert

R.C. Richards

Department of Environmental Science and Policy, University of California, Davis, California 95616, USA

R. Karlin Department of Geological Sciences, University of Nevada, Reno, Nevada 89557, USA

C.W. Morgan AVALEX Inc., South Lake Tahoe, California 96155, USA

P.T. Gayes Center for Marine Studies and Wetlands, Coastal Carolina University, Conway, South Carolina 29526, USA

L.A. Owen Department of Geology, University of Cincinnati, Cincinnati, Ohio 45221, USA

ABSTRACT

Deformation across three major fault strands within the Lake Tahoe basin has been mapped by using a novel combination of high-resolution seismic chirp, airborne laser and acoustic-multibeam-derived bathymetry, and deep- and shallow-water sediment cores. Submerged erosional terraces of late Pleistocene age (19.2 ± 1.8 ka) record vertical deformation across fault strands that ranges between 10 and 15 m; offset of 10 m is observed across the southern part of the West Tahoe fault. Avalanche deposits from the catastrophic McKinney Bay slide (ca. 60 ka) are offset across the Stateline fault by at least 21–25 m. The submerged shoreline terraces and debris avalanche provide marker beds with which to constrain the extensional history of the region for the past 60 k.y. This history is then used to assess the future seismic hazard of the region. Data on deformation across these two important marker beds, combined with chronological control from ^{14}C and optically stimulated luminescence measurements, yield an estimate of extension across the Lake Tahoe basin that is 0.4–0.5 mm/yr. On the basis of these measurements, there exists the potential for a large, seiche wave-generating M7 earthquake every ~ 3 k.y. Late Pleistocene and Holocene vertical deformation rates within the Tahoe basin are characteristic of Basin and Range faulting and place the Tahoe basin within the western limits of the extensional Basin and Range province.

Keywords: Lake Tahoe, normal faulting, seismic imaging, earthquakes, slip rate, seiche.

INTRODUCTION

Lake Tahoe occupies the largest of several fault-controlled basins that define the western edge of the Walker Lane deformation belt (Oldow et al., 2001; Unruh et al., 2003), a distributed zone of transtensional structures that marks the boundary between the central Great Basin and the relatively stable northern Sierra Nevada block. Geodetic measurements indicate that nearly 10 mm/yr of dextral shear occurs along faults within the western margin of the Basin and Range, with smaller amounts of extension, 2–3 mm/yr, across north-trending Sierra Nevada frontal faults (Bennett et al., 2003; Dixon et al., 2000; Hammond and Thatcher, 2004). These measurements, based on global positioning system data, highlight the potential for modest slip rates across faults in the Lake Tahoe region. Paleoseismic inves-

tigation of the Genoa fault, the easternmost bounding normal fault of the Tahoe-Carson Range (Fig. 1), has revealed that there were two large-displacement events in the late Holocene, suggesting a recurrence rate of less than a few thousand years (Ramelli et al., 1999). Considering the estimated 3–5.5 m of displacement per event (over a fault segment length of 25–40 km), these two events were comparable in size to some of the largest historical Basin and Range earthquakes. The amount of extension west of the Genoa fault and across the fault-bounded Lake Tahoe basin is the focus of this paper.

The characterization of fault architecture and history within the Tahoe basin has been difficult in large part because of the lake, which covers nearly 40% of the basin. The bounding faults that form the basin are be-

neath ~ 300 –500 m of water, ruling out any conventional approach to estimating slip history such as paleoseismic trenching. Water depth is also an important factor when considering the consequences of a large earthquake within the Tahoe basin; these include the potential for a tsunami or seiche wave associated with either coseismic deformation or earthquake-triggered landslides. Swath mapping of lake-floor bathymetry beneath Lake Tahoe imaged at least one catastrophic landslide and several fault-related scarps offsetting the lake floor (Gardner et al., 2000), highlighting the potential for seismic and related hazards. On the basis of numerical simulations, coseismic deformation from an M7 normal-fault-generated earthquake has the potential to spawn tsunami or seiche waves with wave heights ranging between 3 and 10 m (Ichinose et al., 2000). Footwall collapse along Lake Tahoe's western shoreline (i.e., McKinney Bay slide) is thought to have generated wave heights of nearly 100 m in the past (Gardner et al., 2000).

TECTONIC MARKERS

Two markers that form tectonic baselines have been identified that are critical for unraveling the late Pleistocene–Holocene fault history of the Tahoe basin: (1) a submerged shoreline terrace and (2) the expansive McKinney Bay slide complex. By coregistering lidar-based bathymetry and seismic chirp images (see Appendix DR1¹), a suite of sub-

¹GSA Data Repository item 2005068, Table DR1 and Figures DR1 and DR2, dating results, core photographs, chirp profiles; Appendix DR1, data and methods; and Appendix DR2, optically stimulated luminescence dating, is available online at www.geosociety.org/pubs/ft2005.htm, or on request from editing@geosociety.org or Documents Secretary, GSA, P.O. Box 9140, Boulder, CO 80301-9140, USA.

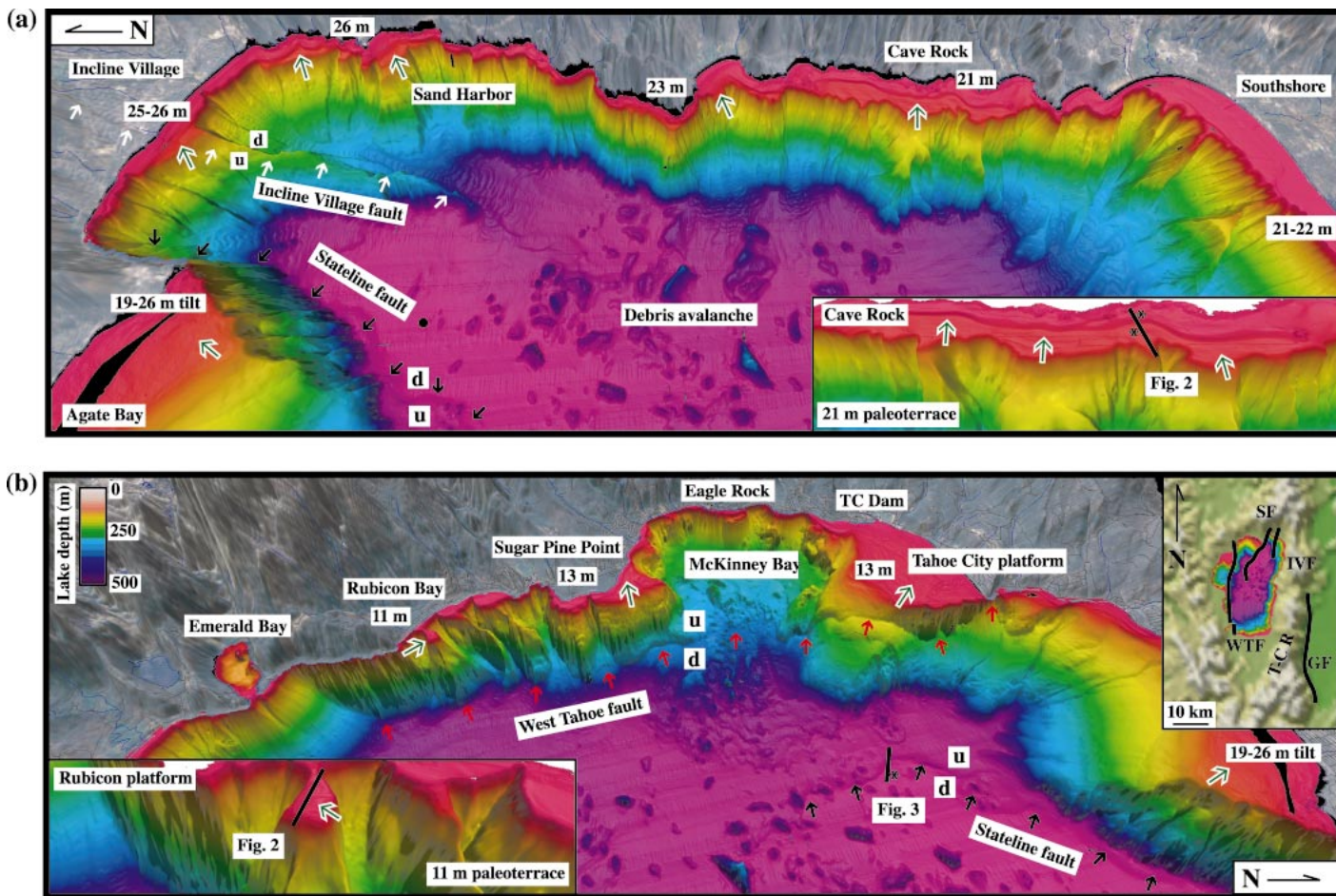


Figure 1. Three-dimensional renderings of eastern (A) and western (B) shorelines beneath Lake Tahoe, highlighting wave-cut terraces and fault structure within basin. Sediment-corrected depths of terraces (silhouetted green arrows) are displayed at various locations around lake. Simplified fault traces (see simple arrows) for major basin faults are shown (white—Incline Village; black—Stateline; red—West Tahoe); throw of normal faults is indicated by u (up) and d (down). Also shown are locations of chirp profiles (black lines in insets) across submerged terraces (Fig. 2), Stateline fault (Fig. 3), sediment cores (asterisks), and wave-cut caves at Eagle Rock (1967 m) and Cave Rock (1937 m). Box inserts in A and B show enlargement of Cave Rock and Rubicon platform, respectively. Inset of regional geography is marked by active traces (black) of West Tahoe (WTF), Stateline (SF), Incline Village (IVF), and Genoa (GF) faults; Tahoe-Carson Range (T-C R) is also shown. Lake Tahoe is ~35 km in length and 20 km in width; its maximum depth (black dot) is 499 m.

merged terraces marking a lower lake stand has been revealed (Figs. 1 and 2). This surface is now deformed, as evidenced by clear vertical offsets and tilting across the West Tahoe and Stateline faults, with only minimal offset observed across the Incline Village fault. In addition, multibeam sonar (Gardner et al., 2000) and seismic chirp images across the McKinney Bay slide, an acoustically transparent sedimentary sequence deposited in the deepest regions of the lake, enable an estimate of vertical deformation across the Stateline fault (Fig. 3). Taken together, these observations of fault-induced deformation, combined with dated sediment cores, record a rate of extensional deformation across the Tahoe basin that is similar in magnitude to the rates documented in other regions of the Basin and Range province (e.g., Friedrich et al., 2003).

The clearest evidence for a prolonged low-stand of lake level is truncated strata around the shallowest parts of the lake. Chirp profiles collected along the eastern shoreline reveal modern prograding deltaic deposits

overlying erosional terraces, which are characterized by oblique clinoforms (Fig. 2). Conversely, erosion and truncation along the western shores of Lake Tahoe are more prevalent as a consequence of east-side-down fault geometry. Several trends are observed within both shallow-water chirp (Fig. 2) and airborne lidar bathymetry data sets that assist in the determination of slip rates for the West Tahoe and Stateline faults: (1) a systematic vertical displacement of 10–15 m exists between shoreline terraces on the east and west sides of the lake, and (2) to the north toward Incline Village, the eastern shoreline erosional terrace deepens by 5 m.

Independent evidence for late Pleistocene–Holocene slip on faults within the Tahoe basin comes from the Stateline fault (Hyne et al., 1972), where chirp profiles show the McKinney Bay slide complex has been displaced by at least 21 m (Fig. 3). The overlying stratigraphic record shows preferential thickening of sediments on the downfaulted eastern block, indicating a long-term period of ongo-

ing slip. Moreover, thickening and divergence of the uppermost few meters of hanging-wall sediments toward the Stateline fault zone is indicative of Holocene fault-related slip. When on-fault measurements are combined with an age estimate for the McKinney Bay slide and the observed pattern of terrace deformation, slip rates across the three most active faults in the Tahoe basin can be estimated.

CHRONOLOGICAL CONTROL

Coarse-grained sediments overlying the paleoterrace along the eastern shoreline near Cave Rock were sampled in 2002. Three Vibracores measuring 0.5, 6.5, and 8.0 m were collected through the deltaic complex overlying the erosional surface. Accelerator mass spectrometry (AMS) ^{14}C -dated and optically stimulated luminescence (OSL)-dated samples provide an age estimate between 17.3 and 19.2 ka for the abrasion surface (Appendix DR2, Table DR1, Fig. DR1; see footnote 1). These dates are also consistent with an inundation mechanism that would allow lake level

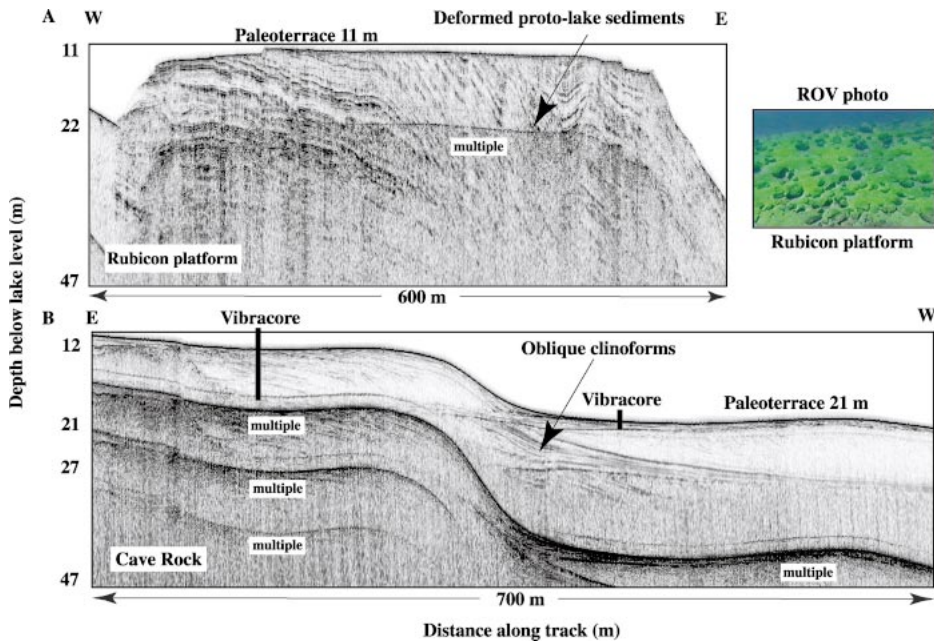


Figure 2. Submerged erosional surfaces imaged by using seismic chirp at Rubicon (A) and Cave Rock (B); depths to surfaces were measured at 11 m (A) and 21 m (B) below present lake level. Sediment-corrected terrace depths vary along eastern shoreline from 21 to 26 m between Cave Rock and Incline Village, corresponding to at least 5 m of additional east-side-down movement in northern part of lake across Stateline and Incline Village faults. Remotely operated vehicle (ROV) submersible image of erosional terrace at Rubicon reveals a beveled platform overlain with rounded cobbles.

to rise and thus flood the paleosurface. Tioga glacial damming that filled the outflow channel would provide such a mechanism (Fig. DR2; see footnote 1). Estimates for Tioga glaciation vary from 13.6 to 24.5 ka (Phillips et al., 1996) throughout the Sierra, with a glacial maximum near 20 ka.

The timing of failure for the McKinney Bay slide complex is difficult to estimate directly. The depth of the lake floor is nearly 500 m, and the slide is buried by ~15–25 m of sediment. The top of the slide is vertically offset across the Stateline fault by a minimum of 21

m, and some profiles record as much as 25 m. During the summers of 2000 and 2002, nearly 12 piston cores ranging in length from 3 to 5 m were collected. A piston core located in the hanging wall of the Stateline fault has provided the best estimate of sedimentation rates during the Holocene and allows an estimate of slide age to be made through extrapolation of early to middle Holocene rates. We dated 11 carbon samples within a 3-m-long core, suggesting an early to middle Holocene sedimentation rate of ~0.4 mm/yr or an extrapolated slide age of ca. 60 ka. Pre-Holocene rates may

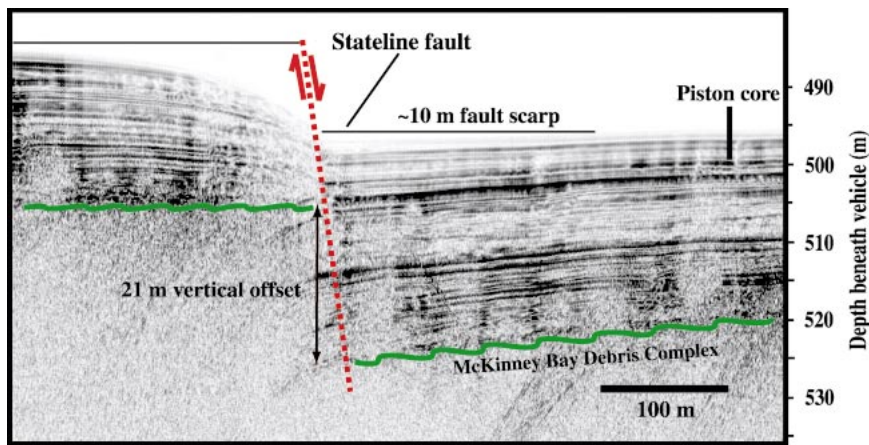


Figure 3. Chirp profile across Stateline fault. McKinney Bay debris avalanche (below green wavy line) is acoustically transparent. Top of this thick unit provides excellent marker bed on which to measure 21 m of vertical deformation. Other chirp profiles crossing Stateline fault show between 21 and 25 m of offset. No antithetic deformation was imaged in hanging wall of Stateline fault; top-of-slide topography is several meters in amplitude.

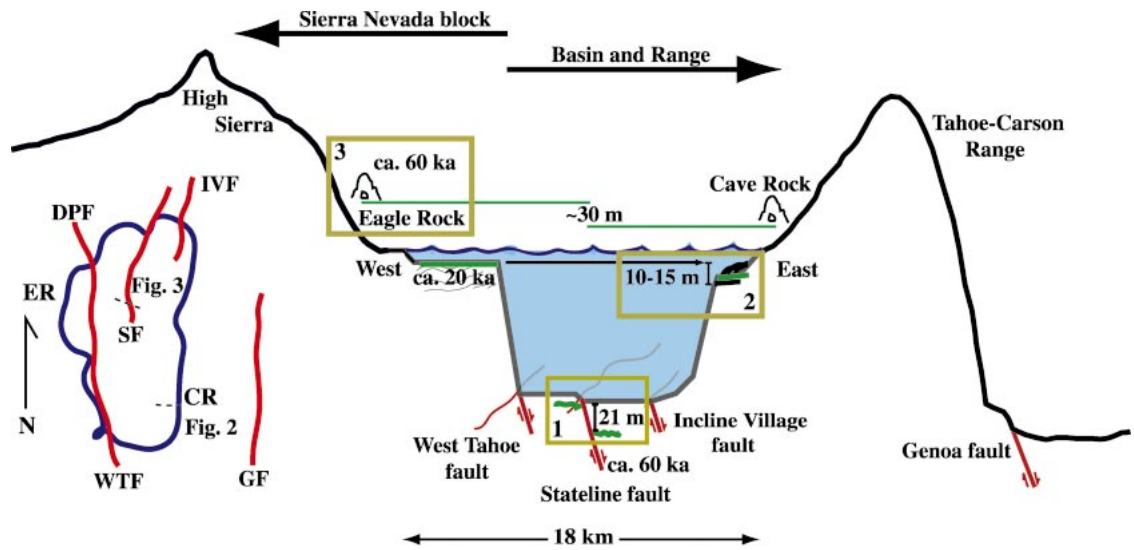
have been greater during the melting of Tioga glaciers, suggesting that the timing of failure could be younger.

ESTIMATION OF VERTICAL DEFORMATION RATE

The combination of tectonic markers and chronological control provided by ^{14}C and OSL measurements enable an estimate of vertical deformation rate across the primary faults in the Tahoe Basin, over time intervals spanning the late Pleistocene and Holocene. Additionally, the en echelon geometry of normal faults in the Tahoe basin (Schweickert et al., 1999) can be used to separate the contributions of vertical displacement for individual faults. Comparison of terrace elevations at Rubicon and Cave Rock (Fig. 4) give a vertical displacement estimate due solely to the West Tahoe fault. Any vertical offset contribution from either the Stateline or Incline Village fault is not recorded in southern Lake Tahoe because these faults die out ~10–15 km to the north. The Rubicon and Cave Rock terraces have been vertically offset by 10 m in slightly less than 20 k.y.: these data give rise to a vertical displacement rate of ~0.5 mm/yr. There is additional evidence regarding longer time windows of vertical displacement across the West Tahoe fault; wave-cut caves located above current lake level found at Eagle Rock and Cave Rock (Fig. 4) are vertically offset by 29.7 m. These caves were likely cut during younger Tahoe glaciation, while the lake was significantly higher because of damming during the most extensive period of glaciation in the Lake Tahoe region (Birkeland, 1964). If confirmed, these measurements suggest an average ongoing vertical deformation rate of ~0.5 mm/yr across the West Tahoe fault over the past 60 k.y.

Rate estimation of vertical displacement across the Stateline fault to the north is more complicated because of the overlapping nature of the West Tahoe and Stateline faults. Here, the observed offset of the McKinney Bay slide complex, in addition to northward deepening of submerged shoreline terraces along the eastern shore, helps to separate the individual contributions from each fault. Inspection of terraces along the eastern shore reveals an additional 5 m of displacement toward Incline Village during the past 20 k.y. If the observed 5 m northward tilt was due solely to additional east-side-down displacement across the Stateline fault, this amount of tilt would extrapolate to 15 m of displacement in 60 k.y., the estimated age of the slide complex. This value is close to the measured 21–25 m of offset across the Stateline fault. The deepening of shoreline terraces attributable to displacement across the Incline Village fault is minimal, amounting to no more than 2 m, during the past 20 k.y. Thus, for a 60 ka slide age, the rate of vertical offset for the Stateline fault ranges between 0.35 and 0.4 mm/yr. Over this

Figure 4. Schematic cross section across Tahoe Basin highlights geometrical relationships among various markers used in this study. (1) Offset McKinney Bay slide deposits reveal 21–25 m of vertical separation across Stateline fault; slide was emplaced ca. 60 ka. (2) Offset shoreline terraces are vertically displaced ~10 m across West Tahoe fault, with greater offsets to north owing to cumulative east-side-down slip on all three normal faults. Optically stimulated luminescence-dated and ¹⁴C-dated cores yield age date for this surface at or near Last Glacial Maximum (ca. 20 ka). (3) Located above present lake level, shoreline caves are vertically displaced 30 m; preliminary studies suggest younger Tahoe age for this higher excursion of lake level. See map-view inset of active fault traces. Locations of Cave Rock and Eagle Rock are also provided. Abbreviations: West Tahoe (WTF), Stateline (SF), Incline Village (IVF), Dollar Point (DPF), and Genoa (GF) faults; Cave Rock (CR); Eagle Rock (ER).



period, the offshore Incline Village fault records ~0.1 mm/yr vertical offset based on the height of the fault scarp preserved on a paleoterrace.

SLIP-RATE ESTIMATION

Slip rates can be readily estimated from vertical-offset rates, under the assumption of simple fault geometries. For a 60° dipping normal fault, the vertical deformation rates across the West Tahoe and Stateline faults are transformed into slip rates of 0.57 and 0.40–0.46 mm/yr, respectively. The combined extension across both faults, based on the integrated deformation of the submerged terraces, is ~0.4–0.5 mm/yr, or ~20% of total extension observed across the Sierra Nevada frontal faults (e.g., Hammond and Thatcher, 2004). Errors in these estimates can arise from several factors, including the depth of terraces and or slides, the age models of marker beds, fault dip, and the extrapolation of sedimentation rates back in time. Errors in measuring terrace depth are <10%, or no more than a change of ±0.05 mm/yr in slip rate. The OSL dating errors of submerged terraces are also ~10%, or when added to depth estimates for the West Tahoe fault, are no more than ±0.1 mm/yr. Slip-rate error estimation for the Stateline fault is more difficult because of the extrapolation of sedimentation rate. Although AMS ¹⁴C measurements are very accurate, sedimentation rates during Pleistocene time were likely greater owing to melting glaciers, resulting in extrapolation errors. Consequently, the 0.4–0.46 mm/yr slip-rate estimate for the Stateline fault may be viewed as a minimum end-member value.

DISCUSSION

The existence of significant fault scarps on the lake floor (10–15 m in height) suggests

that extension is accommodated by a small number of larger-magnitude earthquakes, because ground rupture is typically associated with events that are M6 or greater in size (Wells and Coppersmith, 1994). If we use the 4 m maximum slip model of Ichinose et al. (2000) as a characteristic Basin and Range event, then the time needed to accumulate the equivalent amount of strain (or ~2.75 m of average slip) on the West Tahoe and Stateline faults is ~4.8 k.y. and 6.8 k.y., respectively. Thus, the potential of an event capable of generating a 10-m-high tsunami event, when averaged over time, is roughly every 3 k.y. yr. Although the characteristic size (and hence recurrence interval) has not been directly estimated for faults within the Tahoe basin, the long-term averaged slip rates are similar to those measured for the Genoa fault (Ramelli et al., 1999) to the east, where deformation is concentrated in a few larger normal events that measure between 3 and 5.5 m.

ACKNOWLEDGMENTS

The Lake Tahoe research was funded through grants from the National Science Foundation (EAR-0003839), Lawrence Livermore National Laboratory (02-GS-008), and National Earthquake Hazard Reduction Program (U.S. Geological Survey; 02HQGR0072). We thank Donald Wells and an anonymous reviewer for their thoughtful comments.

REFERENCES CITED

- Bennett, R.A., Wernicke, B.P., Niemi, N.A., Friedrich, A.M., and Davis, J.L., 2003, Contemporary strain rates in the northern Basin and Range province from GPS data: *Tectonics*, v. 22, no. 2, p. 1008, doi: 10.1029/2001TC001355.
- Birkeland, P.W., 1964, Pleistocene glaciation of the northern Sierra Nevada, north of Lake Tahoe, California: *Journal of Geology*, v. 72, p. 810–825.
- Dixon, T.H., Miller, M., Farina, F., Wang, H., and Johnson, D., 2000, Present-day motion of the Sierra Nevada block and some tectonic implications for the Basin and Range province, North America Cordillera: *Tectonics*, v. 19, p. 1–24.
- Friedrich, A.M., Wernicke, B.P., and Niemi, N.A., 2003,

- Comparison of geodetic and geologic data from the Wasatch region, Utah, and implications for the spectral character of Earth deformation at periods of 10 to 10 million years: *Journal of Geophysical Research*, v. 108, no. B4, 2199, doi: 10.1029/2001JB0006823.
- Gardner, J.V., Mayer, L.A., and Hughs Clarke, J.E., 2000, Morphology and processes in Lake Tahoe (California–Nevada): *Geological Society of America Bulletin*, v. 112, p. 736–746.
- Hammond, W.C., and Thatcher, W., 2004, Contemporary tectonic deformation of the Basin and Range province, western United States: 10 years of observation with the global positioning system: *Journal of Geophysical Research*, v. 109, B0843, doi: 10.1029/2003JB002746.
- Hyne, N.J., Chelminski, P., Court, J.E., Gorsline, D.S., and Goldman, C.R., 1972, Quaternary history of Lake Tahoe, California–Nevada: *Geological Society of America Bulletin*, v. 83, p. 1435–1448.
- Ichinose, G.A., Anderson, J.G., Satake, K., Schweickert, R.A., and Lahren, M.M., 2000, The potential hazard from tsunami and seiche waves generated by large earthquakes within Lake Tahoe, California–Nevada: *Geophysical Research Letters*, v. 27, p. 1207–1210.
- Oldow, J.S., Aiken, C.L.V., Hare, J.L., Ferguson, J.F., and Hardyman, R.F., 2001, Active displacement transfer and differential block motion within the central Walker Lane, western Great Basin: *Geology*, v. 29, p. 19–22.
- Phillips, F.M., Zreda, M.G., Benson, L.V., Plummer, M.A., Elmore, D., and Sharma, P., 1996, Chronology for fluctuations in late Pleistocene Sierra Nevada glaciers and lakes: *Science*, v. 274, p. 749–751.
- Ramelli, A.R., Bell, J.W., dePolo, C.M., and Yount, J.C., 1999, Large-magnitude, late Holocene earthquakes on the Genoa fault, west-central Nevada and eastern California: *Seismological Society of America Bulletin*, v. 89, p. 1458–1472.
- Schweickert, R.A., Lahren, M.M., Smith, K., and Karlin, R., 1999, Preliminary fault map of the Lake Tahoe basin, California and Nevada: *Seismological Research Letters*, v. 70, p. 306–312.
- Unruh, J., Humphrey, J., and Barron, A., 2003, Transtensional model for the Sierra Nevada frontal fault system, eastern California: *Geology*, v. 31, p. 327–330.
- Wells, D.L., and Coppersmith, K.J., 1994, New empirical relationships among magnitude, rupture length, rupture width, rupture area, and surface displacement: *Seismological Society of America Bulletin*, v. 84, p. 974–1002.

Manuscript received 24 September 2004
 Revised manuscript received 13 January 2005
 Manuscript accepted 17 January 2005

Printed in USA

Geological Society of America Bulletin

A high-resolution seismic CHIRP investigation of active normal faulting across the Lake Tahoe Basin, California-Nevada

J Dingler, G Kent, N Driscoll, J Babcock, A Harding, G Seitz, B Karlin and C Goldman

Geological Society of America Bulletin published online 24 Apr 2009;
doi:10.1130/B26244.1

- E-mail alerting services** click www.gsapubs.org/cgi/alerts to receive free e-mail alerts when new articles cite this article
- Subscribe** click www.gsapubs.org/subscriptions/index.ac.dtl to subscribe to Geological Society of America Bulletin
- Permission request** click <http://www.geosociety.org/pubs/copyrt.htm#gsa> to contact GSA

Copyright not claimed on content prepared wholly by U.S. government employees within scope of their employment. Individual scientists are hereby granted permission, without fees or further requests to GSA, to use a single figure, a single table, and/or a brief paragraph of text in subsequent works and to make unlimited copies of items in GSA's journals for noncommercial use in classrooms to further education and science. This file may not be posted to any Web site, but authors may post the abstracts only of their articles on their own or their organization's Web site providing the posting includes a reference to the article's full citation. GSA provides this and other forums for the presentation of diverse opinions and positions by scientists worldwide, regardless of their race, citizenship, gender, religion, or political viewpoint. Opinions presented in this publication do not reflect official positions of the Society.

Notes

A high-resolution seismic CHIRP investigation of active normal faulting across Lake Tahoe Basin, California-Nevada

J. Dingler^{1,§}, G. Kent¹, N. Driscoll¹, J. Babcock¹, A. Harding¹, G. Seitz², B. Karlin³, and C. Goldman⁴

¹*Scripps Institution of Oceanography, University of California, San Diego, La Jolla, California 92093, USA*

²*Department of Geological Sciences, San Diego State University, San Diego, California 92182, USA*

³*Department of Geological Sciences, University of Nevada, Reno, Nevada 89557, USA*

⁴*Department of Environmental Science and Policy, University of California, Davis, California 95616, USA*

ABSTRACT

We measured extension rates across Lake Tahoe Basin for the last 60 ka. based on measured displacement of offset marker surfaces across three active faults beneath Lake Tahoe. Seismic chirp imaging with submeter accuracy, together with detailed multibeam and light detection and ranging (LIDAR)-derived bathymetry, was used to measure fault offset, thickness of earthquake-derived colluvial wedges, depth of wave-cut paleoterraces, and other geomorphic features. An analysis of these features provides refined estimates of extension rates and new information on Holocene faulting, and places Tahoe Basin deformation into the larger context of Walker Lane and Basin and Range tectonics. Measured offset marker surfaces include submerged wave-cut paleoterraces of Tioga age (19.2 ± 1.8 ka), McKinney Bay slide deposits (ca. 60 ka), and a winnowed boulder surface of Tahoe age (ca. 62 ka). Estimated vertical offset rates across submerged geomorphic surfaces are 0.43–0.81 mm/a for the West Tahoe fault, 0.35–0.60 mm/a for the Stateline–North Tahoe fault, and 0.12–0.30 mm/a for the Incline Village fault. These offset rates indicate a combined east-west extension rate across Lake Tahoe Basin, assuming 60° fault dips, of 0.52–0.99 mm/a. This estimate, when combined with the Genoa fault-slip rate, yields an extension rate consistent with the magnitude of the extension deficit across Carson Valley and Lake Tahoe Basin derived from global positioning system (GPS) velocities. The Stateline–North Tahoe, Incline Village, and West Tahoe faults all show evidence for

individual Holocene earthquake events as recorded by either colluvial wedge deposits or offset fan-delta stratigraphy.

INTRODUCTION

This paper updates extension rates in Lake Tahoe Basin through the measurement of fault offset, thicknesses of earthquake-derived colluvial wedges, depths of wave-cut paleoterraces, and other geomorphic features. These results are important for placing Holocene to late Pleistocene deformation in the context of the present strain field as measured by global positioning system (GPS), and they may permit a reassessment of slip budgets for the region. The changing stress field in the Walker Lane region during the Pliocene and Pleistocene (Zoback, 1989; Wesnousky and Jones, 1994; Bellier and Zoback, 1995) is still a matter of debate, and it cannot be completely resolved by GPS studies alone. As slip rates for each of the active faults in the basin are refined, the residual difference between GPS and fault slip will provide new insight into strain partitioning and the potential displacement deficit that may exist between GPS and fault-slip data in Lake Tahoe Basin and Carson Valley. This analysis, in turn, will provide greater understanding of strain partitioning and extension in high dextral shear regions, and the role of off-fault diffuse strain.

High-resolution light detection and ranging (LIDAR) and multibeam mapping conducted in 1998 (Gardner et al., 1998, 2000) combined with high-resolution seismic chirp imaging (Kent et al., 2005) provide a tool for measuring deformation across faults in Lake Tahoe Basin. These results can be related to the overall strain field through comparison with modern GPS measurements (Hammond and Thatcher, 2004). Our onshore-offshore study employed high-resolution seismic CHIRP imaging, lake-bottom sediment cores, and onshore paleoseismic trench-

ing, which together provide new constraints on deformation within Walker Lane at an unprecedented scale (Fig. 1). These data have the resolution required to accurately measure Holocene and late Pleistocene fault displacement and deformation. While previous seismic studies have revealed important structural features in the lake (Hyne et al., 1972), they lack the resolution needed to define fault offsets of late Pleistocene and Holocene sequences at a resolution approaching onshore paleoseismic measurements. Throughout this paper, the term “active fault” refers to a fault that has exhibited deformation during the Holocene. The CHIRP profiles acquired between 1999 and 2006 allow us to examine the surface geomorphology and subsurface expression of three active faults beneath Lake Tahoe (i.e., the West Tahoe–Dollar Point, Stateline–North Tahoe, and Incline Village faults), as well as other important tectonic offset markers and geomorphic features.

Seismic CHIRP profiles also provide independent evidence of faults mapped into, or striking toward the lake, indicating whether they are actual faults or misidentified glacial or fluvial features. Active faults extending into the lake should show subsurface deformation offshore. A comparison of CHIRP profiles to previously published articles and geologic maps, such as the official State of California geology map for the Lake Tahoe region (Saucedo, 2005), allows us to independently confirm or refute the existence of offshore faults. For example, over 25 km of seismic CHIRP data in Emerald Bay show that the mapped Tahoe–Sierra frontal fault zone, as purported by Schweickert et al. (2004), does not have an associated offshore expression, even though the fault is claimed to be active, off-setting moraines on both sides of Emerald Bay. Based on the distribution of CHIRP profiles throughout Lake Tahoe, we are able to characterize active faulting beneath most portions of the lake (Fig. 2).

[§]Current address: BP America, Inc., Houston, TX 77079, USA; E-mail: jeffrey.dingler@bp.com.



Figure 1. Map of the central and northern Walker Lane showing major fault zones and global positioning system (GPS) velocities (after Hammond and Thatcher, 2004; Table 1). Normal and dextral faults shown outside Lake Tahoe have deformation rates >0.2 mm/a (USGS, 2005). Sinistral faults shown have deformation rates <0.2 mm/a. The white on black GPS arrow to the west of Lake Tahoe shows a calculated relative velocity difference of 2.7 ± 0.9 mm/a between stations UU83 and A270, which are located to the north-northwest of Lake Tahoe and on the east side of the Carson Valley, respectively. At the eastern margin of Walker Lane, normal faults strike north-northeast and include the Central Nevada seismic belt. Dextral faults dominate away from the margin of the Sierra Nevada microplate and strike north-northwest. Sinistral faults strike northeast and are primarily located perpendicular to dextral faults in Northern Walker Lane. Individual fault segments (USGS, 2005) have been combined to form one approximate fault trace for each fault zone. 1—Lone Mountain fault zone; 2—Toiyabe Range fault zone; 3—Western Toiyabe Range fault zone; 4—Fairview fault zone; 5—region with numerous unnamed sinistral faults; 6—Fish Lake Valley fault zone; 7—Bettles Wells—Petrified Springs fault zone; 8—Benton Springs fault; 9—Dixie Valley fault zone; 10—Rainbow Mountain fault zone; 11—Wassuk Range fault zone; 12—White Mountains fault zone; 13—Owens Valley fault zone; 14—Round Valley fault; 15—Hilton Creek fault; 16—Hartley Springs—Silver Lake faults; 17—Mono Lake fault; 18—Robinson Creek fault; 19—West Walker River fault; 20—Antelope Valley fault; 21—Smith Valley fault zone; 22—Carson lineament; 23—unnamed faults SE of Truckee Range; 24—Pyramid Lake fault zone; 25—Olinghouse fault; 26—Honey Lake fault zone; 27—unnamed fault west of Hungry Valley; 28—Mount Rose fault zone; 29—Kings Canyon fault; 30—Genoa fault; 31—Deep Springs fault; 32—Emigrant Peak fault zone; 33—Mohawk Valley fault.

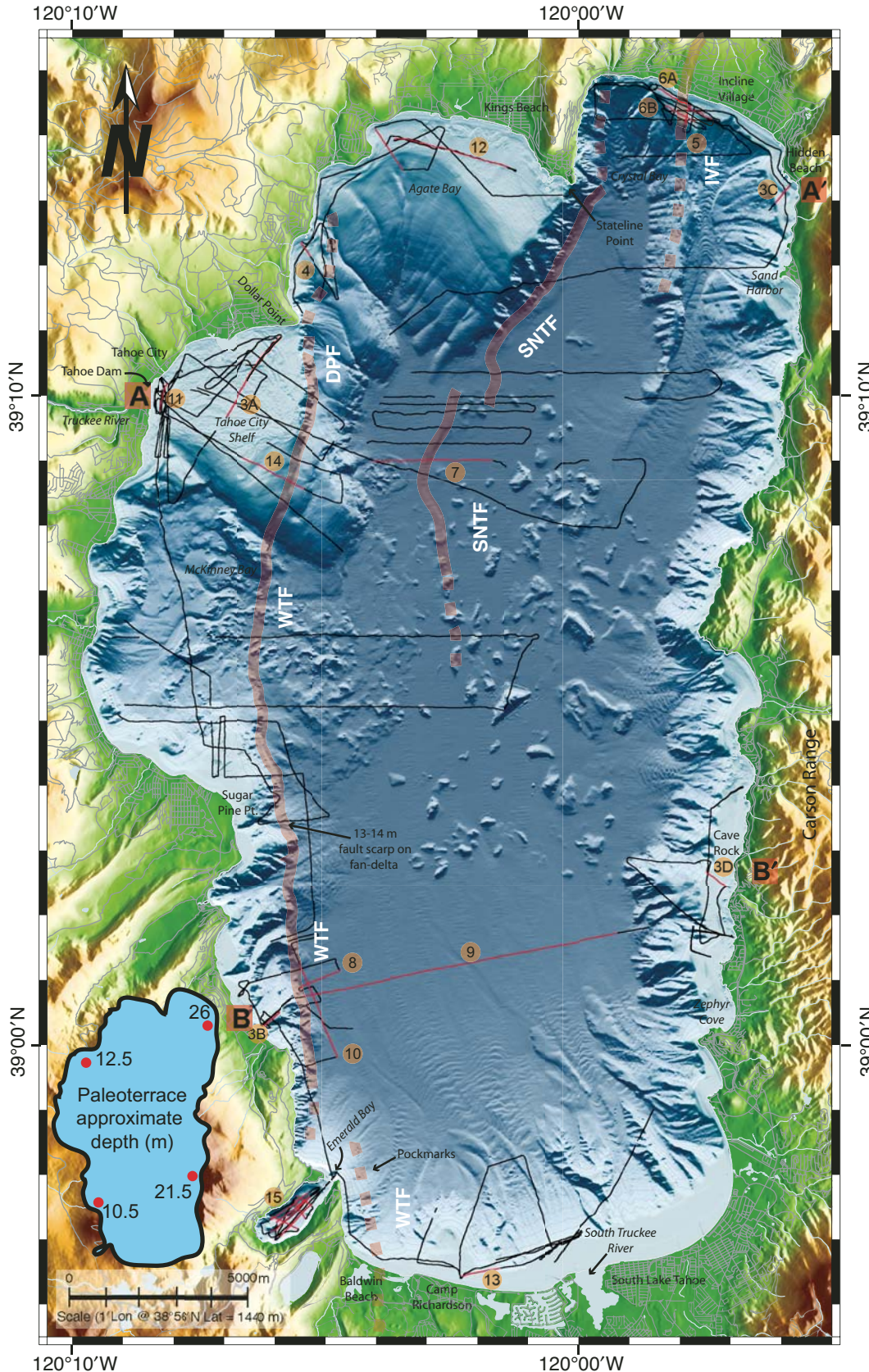


Figure 2. Combined bathymetry and topography map of Lake Tahoe highlighting active faults and chirp profiles. Active faults are represented by semi-transparent thick red lines, dashed where fault locations are inferred; WTF—West Tahoe fault; DPF—Dollar Point fault; SNTF—Stateline–North Tahoe fault; IVF—Incline Village fault. Thin brown lines delineate CHIRP profiles and are labeled with figure numbers for profiles presented in this paper. Thin, gray bathymetric contours are in 50 m intervals. The lake sill, at the Lake Tahoe Dam at the mouth of the Truckee River, is at ~1899 m, and the deepest point is ~1300 m, corresponding to a maximum lake depth of ~499 m. Bathymetry is a combination of SHOALS LIDAR (light detection and ranging) and EM1000 multibeam bathymetric surveys (Gardner et al., 1998, 2000), with a horizontal resolution of 10 m. Topography is interpolated from 10 m U.S. Geological Survey digital elevation model (DEM). Small inset of Lake Tahoe outline displays the approximate depth of the wave-cut paleoterrace at four locations throughout the lake. The paleoterrace increases in depth from west to east and from south to north.

The 19.2 ± 1.8 ka wave-cut paleoterrace (Kent et al., 2005) is an ideal marker surface for measuring fault offset and lake-level change. Relative depth change of the paleoterrace across individual faults can be used to determine fault offset and slip rate, while depth changes parallel to faults provide insight into along-strike slip variations and fault termination. The paleoterrace can be traced nearly continuously around the lake in the LIDAR-derived bathymetry and is also well imaged in numerous CHIRP profiles. Constraints can also be placed on lake-level changes and inundation of the paleoterrace by analyzing geomorphic features such as incised channels, or overlying sedimentary sequences observed in the CHIRP profiles. Age estimates of submerged trees above the paleoterrace along the south shore of Lake Tahoe by Lindström (1990) provide additional evidence that the paleoterrace may have been offset by tectonic deformation and may provide constraints on the most recent event (MRE) on the West Tahoe fault.

GEOLOGIC HISTORY OF THE LAKE TAHOE REGION

Lake Tahoe Basin lies on the boundary between two distinctly different tectonic provinces, the relatively stable Sierra Nevada–Great Valley block (Argus and Gordon, 2001) and the deforming Walker Lane belt (Svarc et al., 2002). The ~ 12.4 mm/a rate of relative motion between the Sierra Nevada–Great Valley block and North America (Bennett et al., 2003) suggests a kinematic linkage between the San Andreas fault system and the Eastern California shear zone, which has transferred up to 23%–29% of the relative plate motion northward into this deformation belt (Dokka and Travis, 1990; Miller et al., 2001). Details of Walker Lane deformation continue to emerge from regional geodetic studies, and they exhibit a marked difference compared to Basin and Range deformation farther to the east (Dixon et al., 2000; Svarc et al., 2002; Bennett et al., 2003; Hammond and Thatcher, 2004). Paleoseismic slip rate estimates by Wesnousky et al. (2005) support the geodetic measurements and suggest that paleoearthquake rupture rates are greater at the margins of the Great Basin than in the interior; however, these authors noted that comparison to geodetic surveys is hindered by relatively large uncertainties in the geologic rate estimates. To the north and east of Lake Tahoe, the axis of maximum extension is rotated counterclockwise with respect to locations farther east. These new measurements also show that in the vicinity of Lake Tahoe, deformation is a combination of dextral shear and extension, and there is 2.7 ± 0.9 mm/a of mo-

tion across Carson Valley and Lake Tahoe Basin relative to stable North America (Fig. 1; white arrow is adapted from Hammond and Thatcher, 2004). The velocity of the Sierra Nevada–Great Valley microplate does not parallel the eastern margin of the block, resulting in boundary-normal displacement (Oldow, 2003), which may explain the increased extension in the vicinity of Lake Tahoe and along the eastern margin of the Sierra Nevada.

The Sierra Nevada frontal fault system delineates the eastern boundary of the Sierra Nevada–Great Valley microplate (Fig. 1). Based on fault orientation and the predominantly dextral shear deformation, Unruh et al. (2003) suggested that Walker Lane is a separate tectonic province and is not just the westward continuation of the Basin and Range Province. Deformation in the Basin and Range Province is the result of extension perpendicular to the range axis with a more northeast structural trend. In the Lake Tahoe region, the Sierra Nevada frontal fault system consists of two main branches, one of which runs through the Lake Tahoe region and is the focus of this paper; the other branch passes to the east through Carson Valley and is primarily represented by the Genoa fault along the eastern front of the Carson Range (Wakabayashi and Sawyer, 2001; Unruh et al., 2003). These deformation patterns suggest that Tahoe Basin is the result of a releasing step along the microplate margin, where active deformation is transferred westward to the dextral Mohawk Valley fault to accommodate Sierra Nevada–North America microplate motion (Unruh et al., 2003). The primary faults responsible for this westward deformation transfer are the Mohawk Valley fault and the Pyramid Lake fault (Unruh et al., 2003; Briggs and Wesnousky, 2004; Faulds et al., 2005) (Fig. 1, faults 24 and 33). Paleovalley dextral offsets across the Pyramid Lake fault are significantly less than dextral offsets farther south; this suggests that Northern Walker Lane is probably the youngest part of the transform boundary, and possibly the future plate boundary (Faulds et al., 2005).

Four identifiable glaciations, Tioga, Tahoe, Donner, and Hobart, have had a pronounced influence on the preserved landscape of Lake Tahoe Basin and a profound impact on lake level. Sedimentation and lake-level changes related to these glaciations provide marker horizons within Tahoe Basin that place important constraints on late Quaternary faulting and offset rates. The lake rose by as much as 600 ft (183 m) during the Donner glaciation (Birkeland, 1964). Rapid decreases in lake level have also been documented and are attributed to jökulhlaups in the Truckee River during the Hobart, Donner, and Tahoe glaciations (Birkeland, 1964; Hyne

et al., 1972). The most recent significant glaciation was the Tioga glaciation beginning ca. 24,500 yr B.P. and ending by 13,600 yr B.P. (Phillips et al., 1996; Benson et al., 1998). Since that time, climate in the Sierra has been too warm and/or arid to support large glaciers (Clark and Gillespie, 1997). Increased erosion in glacial-covered basins (Hallet et al., 1996) suggests that sedimentation rates since the end of the Tioga glaciation (and melting of glaciers) have been significantly lower than during glacial periods. The most extensive glacial activity occurred on the western, northern, and southern sides of the basin (Hyne et al., 1972). The resulting overlying mantle of glacial moraines makes it difficult to trace individual faults on land.

The only significant seismic-reflection survey of Lake Tahoe Basin prior to 1999 imaged three potential fault scarps based on bedrock ridges and escarpments cutting recent sediments, as well as large mounds in the middle of the lake (Hyne et al., 1972, 1973). High-resolution seismic systems such as CHIRP had not been developed at the time, so the survey was not intended to quantify small-scale sediment deformation or fault offset. Because of the relatively low resolution of the survey, numerous important features were imaged but incorrectly identified. In 1998, the first modern multibeam bathymetry was collected in the lake (Gardner et al., 1998), which was combined two years later with a scanning hydrographic operational airborne LIDAR survey (SHOALS) to create a comprehensive bathymetry data set with ~ 10 m horizontal resolution at all depths (Gardner et al., 1998, 2000). This survey identified six steep-sided linear trends in the bathymetry, but subsequent work by Kent et al. (2005) determined that only three of these linear trends were indeed active faults (WTF, SNTF, IVF; Fig. 2). The survey also suggested that a catastrophic failure at McKinney Bay was responsible for the large sedimentary blocks strewn throughout the center of the lake (Gardner et al., 2000). Building on this comprehensive bathymetric data set, high-resolution seismic CHIRP and sediment cores were acquired between 1999 and 2006 to define the deformational history across all three major fault strands within Lake Tahoe Basin. These measurements yield a minimum extension rate of 0.4–0.5 mm/a across the basin and provide the most robust measurements to date of extension across Lake Tahoe Basin.

DATA COLLECTION

CHIRP Overview

The seismic CHIRP profiler used in this study was an Edgetech SubScan system. The system, herein referred to as CHIRP, includes

a number of predefined pulses in the frequency range from 500 Hz to 16 kHz. The CHIRP profiles presented in this paper predominantly use a 1–5.5 kHz pulse with a 10 ms duration, a 1–5.5 kHz pulse with 30 ms duration, or a 1–6 kHz pulse with a 50 ms duration. The SIOSEIS processing package developed by Paul Henkart at Scripps Institution of Oceanography was used to process the data. Processing included the following steps: data conversion to standard SEG-Y, manual or automatic water-bottom picking, trace mix, amplitude gain starting at the water-bottom, and display. Two-way traveltimes were converted to depth assuming a water velocity of 1500 m/s. This conversion provides an accurate representation of the lake bottom and a minimum bound on sediment thicknesses.

RESULTS

Survey Overview

We acquired over 400 line kilometers of CHIRP data in Lake Tahoe both on- and off-fault, covering most of the geographical regions of the lake, including nearshore and deep-water environments. The on-fault profiling imaged the offset of individual sediment layers or sequences across a fault, while the off-fault profiles allowed us to compare the relative depth of the ca. 19.2 ka wave-cut paleoterrace around Lake Tahoe. We also identified other geomorphic features, such as infilled river channels, submarine landslides, and clinof orm sequences that provided additional information about the tectonic activity of the basin. Here, we will present the observed stratigraphy in Lake Tahoe from youngest to oldest, and then we will discuss vertical offset across the fault systems from west to east.

LAKE TAHOE STRATIGRAPHY

Wave-Cut Paleoterrace (W_1)

The paleoterrace (W_1) is a shallow, relatively flat surface observed in the high-resolution bathymetry (Fig. 2), and it has been dated at 19.2 ± 1.8 ka near Cave Rock on the east shore (Kent et al., 2005). In CHIRP profiles, the paleoterrace is evident as a well-defined unconformity when mantled with sediment, or as a truncation surface when no sediment mantle is present. Varying amounts of sediment mantle this surface. For example, in many locations, prograding deltas or clinof orms extend out onto the paleoterrace surface and infill accommodation space created by a rise in lake level and/or tectonic subsidence of the surface since its formation (Figs. 3, 4, 5, and 6). Where buried, the paleoterrace has a similar flat appearance in CHIRP profiles.

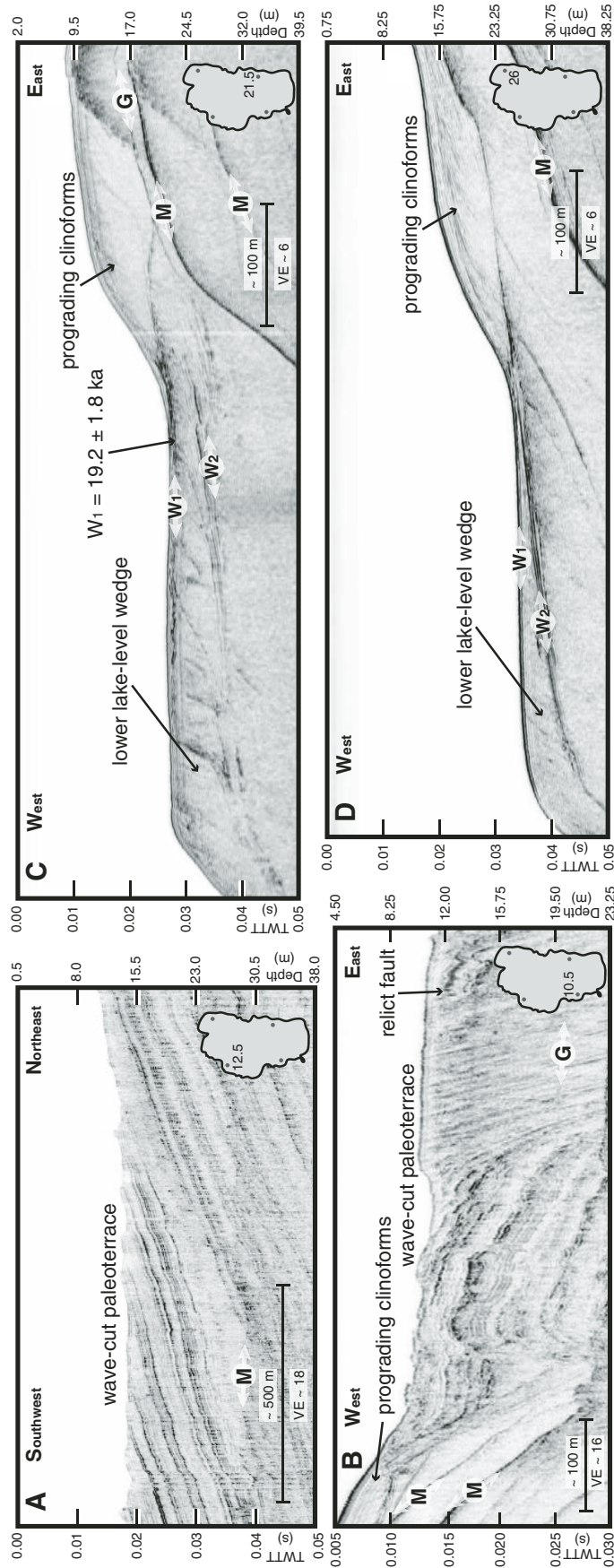


Figure 3. Chirp profiles crossing the ca. 19.2 ka wave-cut paleoterrace along the east and west shores of Lake Tahoe. The approximate depth of the wave-cut paleoterrace in meters is indicated next to the location of the current profile in the inset Lake Tahoe outline. The location of the other three profiles is marked with a dot, but no depth. (A) Profile across the Tahoe Shelf. Dipping reflectors are truncated in this profile. The depth of the paleoterrace is 12.5 ± 2.0 m. (B) Profile offshore of Rubicon. The paleoterrace is at a depth of 10.5 ± 0.5 m. Prograding clinof orms are building out onto the terrace from the west, and they unconformably overlie the paleoterrace. A relict fault is evident to the east, but it does not offset the surface of the paleoterrace. (C) Profile offshore Cave Rock. Two wave-cut surfaces and prograding clinof orms as C, except W_1 has an age of 19.2 ± 1.8 ka. (D) Profile offshore Hidden Beach, which shows the same wave-cut surfaces and prograding clinof orms as C, except W_1 is at a depth of 26.0 ± 1.0 m. TWTT—two-way traveltime; VE—vertical exaggeration; M—water-bottom multiple; G—CHIRP ghost water-bottom multiple.

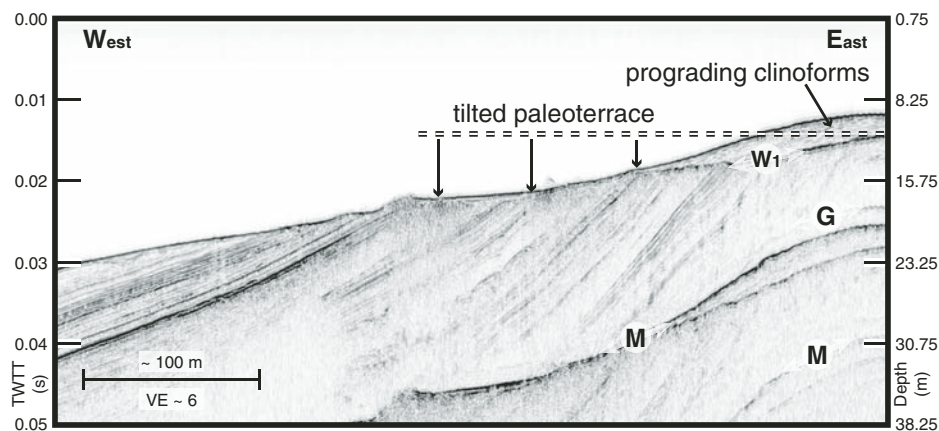


Figure 4. Chirp profile images the wave-cut paleoterrace along the west shore of Agate Bay, ~2 km north of Dollar Point. The ca. 19.2 ka wave-cut paleoterrace is labeled W_1 and is interpreted to have formed at the same time as the terrace observed south of Cave Rock, along the eastern shore (Fig. 3C). This dipping paleoterrace is at a depth ranging from 9.7 to 18.6 m. Modern clinoforms also prograde out onto the wave-cut paleoterrace in this location. TWT—two-way traveltime; VE—vertical exaggeration; M—water-bottom multiple; G—CHIRP ghost water-bottom multiple.

The offset between the paleoterrace on the east and west sides of the lake provides an indirect, approximate off-fault method to measure minimum vertical deformation associated with Tahoe Basin faults since the cutting and inundation of the paleoterrace. On the east shore, the change in slope between the paleoterrace and paleoforeshore is at 21.5 ± 0.5 m near Cave Rock and systematically deepens to 26.0 ± 1.0 m near Hidden Beach (Fig. 3). On the west shore, the paleoterrace is at 12.5 ± 1.0 m on the Tahoe City Shelf and shoals slightly to the south as measured offshore of Rubicon (10.5 ± 0.5 m). The Tahoe City Shelf is the widest section of shelf in the lake, and it is underlain by a series of dipping reflectors that are truncated at the lake floor (Fig. 3A). The truncated reflectors have eroded at different rates, resulting in a rough surface that is not as flat or featureless as the paleoterrace's other locations. The depth of the eastern paleoterrace in the southern half of the lake is dominantly controlled by offset across the West Tahoe fault, while in the northern half, it records motion on all three faults (e.g., West Tahoe, Stateline–North Tahoe, and Incline Village faults; Fig. 2).

Tahoe Age Surface (WBs and W_2)

The second, and oldest, marker surface is a ca. 62 ka Tahoe-age, winnowed boulder surface (WBs, Fig. 6). This age estimate comes from cosmogenic dating of Tahoe-age moraine boulders (R. Finkel, 2002, personal commun.) and correlation of onshore Tahoe glacial deposits in

the vicinity of Incline Village with offshore boulder deposits. Around the Incline Village fault, the marker surface is expressed as a winnowed boulder surface that transitions into a wave-cut unconformity. Tioga glacial deposits terminate ~2.5 km north of the present-day shoreline (Saucedo, 2005). Tahoe glacial outwash deposits extend from the Tioga deposits to the present-day shoreline. The greater extent of the Tahoe glaciation in Incline Village is also supported in a general sense by Birkeland (1964), who reported that Tioga glaciers north of Lake Tahoe were shorter and thinner than Tahoe glaciers. He also noted that the Tahoe glaciation consisted of only one major advance based on the stacking patterns and arrangement of moraines. These results, combined with the age of onshore glacial boulders, suggest that the boulder surface was deposited by the Tahoe glaciation, ca. 62 ka. The winnowed boulder surface may also correlate in time with a second truncation surface seen along east-shore profiles, W_2 (Fig. 3).

McKinney Bay Slide

The top of the debris apron from the McKinney Bay slide provides a third marker surface for estimating fault-related deformation (Fig. 7). Radiometric carbon ages from an ~3-m-deep sediment core, to the east of the Stateline–North Tahoe fault, indicate an early to mid-Holocene sedimentation rate of ~0.4 mm/a (Kent et al., 2005). Extrapolation of these shallow ^{14}C ages down to the top of the slide suggests an age of ca. 60 ka for the emplacement of the McKinney

Bay slide deposits. As mentioned earlier, climate in the Sierra since the end of the Tioga glaciation has been too warm and/or too arid to support large glaciers (Clark and Gillespie, 1997). Increased erosion in glacial-covered basins (Hallet et al., 1996), such as the Tahoe Basin, during the melt periods of the Tioga and Tahoe glaciations would have produced a higher sediment rate and imply a younger age for the slide. Based on the high probability of increased sedimentation rates, relative to those measured in the 3 m core, we believe that the ca. 60 ka age is a maximum, and the McKinney Bay slide is probably somewhat younger.

However, we do not agree with Moore et al. (2006), who claimed that Kent et al. (2005), and by association this work, discount the possibility of megaturbidites and therefore significantly overestimate the age of the slide. Slides and/or mass-movement deposits are observed near the West Tahoe fault (Figs. 8, 9, and 10), and recent slides are observed near the Stateline–North Tahoe fault (Fig. 7), but they are of limited spatial extent, have chaotic acoustic character, and unconformably overlie older, layered sediment, and they can be clearly correlated between profiles. Thin turbidites have been observed in the sediment core (Kent et al., 2005), but these are no thicker than ~0.15 m. Based on the CHIRP profiles collected throughout the lake, we are able to detect slides/mass movement deposits that are thicker than ~0.30 m. While thin turbidites are clearly present in the sediment core, we detect no evidence of megaturbidites, slides, or debris flows that are significantly thicker than 0.30 m between the base of the core and the top of the McKinney Bay slide.

Paleochannels and Jökulhlaups

Rapid decreases in lake level have been attributed to jökulhlaups in the Truckee River during the Hobart, Donner, and Tahoe glaciations, based on 10 m boulders in Truckee River Canyon and giant gravel bars that rise 12 m above adjacent terrace surfaces (Birkeland, 1964; Hyne et al., 1972). A north-south CHIRP profile over the shallow Tahoe City Shelf, less than 1 km east of the dam, images an ~2.5-km-wide incised channel that is at least 9 m deep (Fig. 11). The dam has a hydraulic height of ~3 m, and it has controlled lake level since its construction in 1913. Closer to the dam, a narrower, 13-m-deep incised channel was well imaged in the CHIRP data (Kent et al., 2005). Two episodes of downcutting and incision can be observed (Fig. 11). The south side of the channel exhibits an extremely sharp channel contact and only chaotic, unstratified channel fill. The northern side of the channel has laminated channel fill overlain

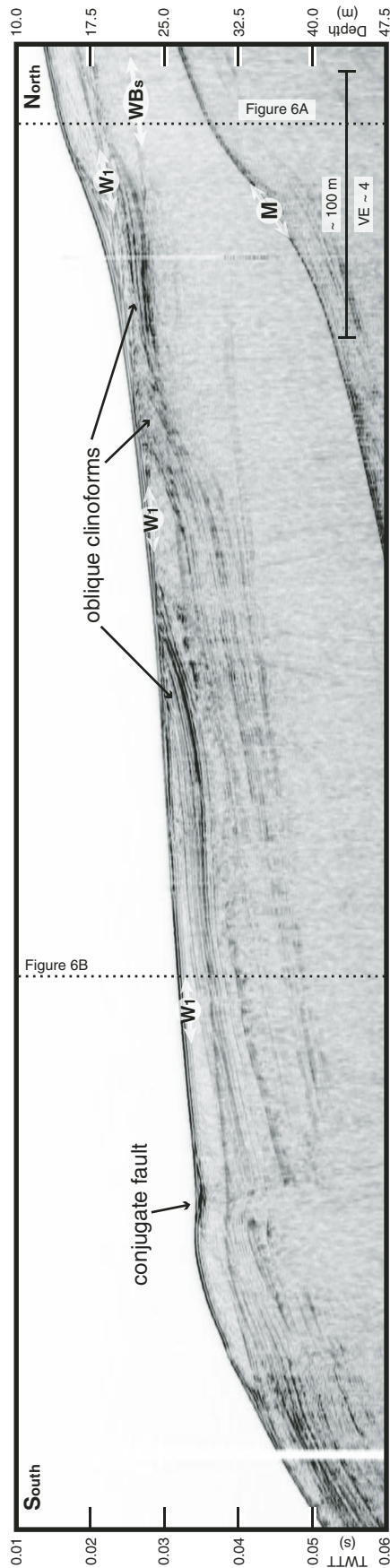


Figure 5. Chirp profile acquired east of, and parallel to, the Incline Village fault. Dashed vertical lines indicate where CHIRP profiles (Figs. 6A and 6B) perpendicular to the fault trace intersect this profile. Winnowed boulder surface (W_1) is seen beneath surface W_1 at 22 m (right side of figure). W_1 —ca. 19.2 ka wave-cut paleoterrace; TWTT—two-way traveltime; VE—vertical exaggeration; M—water-bottom multiple.

by chaotic, unstratified channel fill. Upsection, there is another incision mantled by a laminated sequence. The base depth of the channels is approximately equal to the depth of the paleoterrace on the Tahoe City Shelf. Sediment cores acquired for construction of Lake Tahoe Dam recovered at least two tephra layers at depths of ~5–7 m and ~10 m. The tephra layers were chemically similar to ash deposits from the Long Valley Caldera that had ages between 0.73 and 1.0 Ma (Hawkins et al., 1986). Based on the age estimates, it is likely that the cores sampled inter-fluvial sediments or slump deposits along the cut-bank and failed to sample the channel fill.

On the south shore of Lake Tahoe (Hyne et al., 1972), Tioga, Tahoe, and pre-Tahoe glacial deposits lie adjacent to Pleistocene lacustrine terrace deposits and Holocene floodplain deposits (Saucedo, 2005). One profile offshore of Camp Richardson shows a 200-m-wide paleochannel that has been truncated by a wave-cut surface (Fig. 12). The base of the paleochannel extends below the bottom of the profile at a depth of 39 m. Sediment fill in the paleochannel has also been truncated by the wave-cut surface, indicating that infilling of the channel predates the wave-cut surface, as is also the case for a paleochannel observed in Agate Bay (Fig. 13). The base of the channel in Agate Bay is obscured by the acoustic multiple, but where observed, it cuts down to a depth of 32 m. The depth of the incision associated with the channels offshore Camp Richardson and in Agate Bay is roughly equivalent to the depth of W_2 (Fig. 3).

LAKE TAHOE FAULT NETWORK

West Tahoe–Dollar Point Fault

On the basis of bathymetry and CHIRP sub-bottom data, the West Tahoe fault appears to extend along the eastern edge of the Tahoe City Shelf (referred to as the Dollar Point fault in this location) south across McKinney Bay and along the base of the west-shore slope until it steps to the east, bypassing Emerald Bay (Fig. 2). The fault scarp, where observed, is located at the base of the steep slope or offsets dipping fan-delta deposits (Fig. 14). When the CHIRP instrument images steep slopes, more pulse energy is reflected at the water-sediment interface because of the high grazing angle, and less energy penetrates into the lake floor. As a result, penetration dramatically decreases over steep slopes. Even though the CHIRP penetration is limited over significant portions of the West Tahoe fault, it is still possible to image the fault or synthetic faults where they step east away from the base of the slope, or where they cross fan-delta deposits. The fan delta offshore of

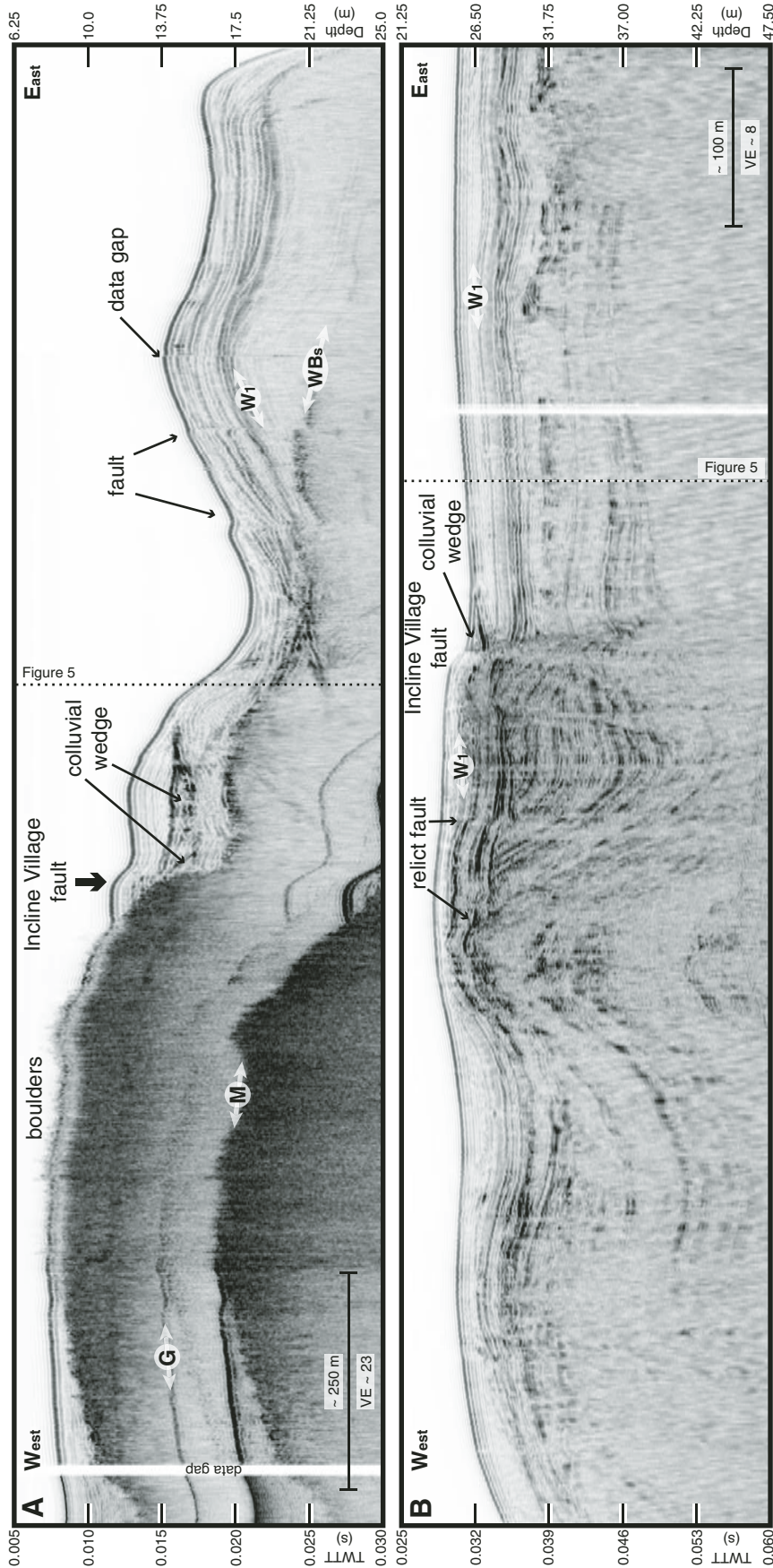


Figure 6. Chirp profiles across the Incline Village fault. (A) Shallower of the two fault-crossing profiles. The west side of the profile shows an acoustically opaque lake-bottom reflector with an extremely rough surface. This surface, imaged by remotely operated vehicle (ROV), is a boulder surface that has been winnowed (WBs) and was probably deposited during the Tahoe glaciation, ca. 62 ka. The WBs is offset ~14 m across the Incline Village fault at this location. Two colluvial wedges are evidence for large normal faulting events. (B) Deeper of the two fault-crossing profiles. Surface morphology shows an ~1-m-high fault scarp that offsets bedding layers for almost 20 m beneath the surface. W_1 is the ca. 19.2 ka paleoterrace, which is offset 3.0–3.5 m across the fault. The colluvial wedge in the top few meters of sediment suggests vertical offset during the Holocene. To the west of the Incline Village fault, there is a zone of deformation that contains two relict faults that do not offset the top 1–2 m of sediment. Dashed vertical line indicates where CHIRP profile Figure 5, parallel to the fault trace, intersects this profile. TWTT—two-way traveltime; VE—vertical exaggeration; M—water-bottom multiple; G—CHIRP ghost water-bottom multiple.

Sugar Pine Point is cut by the West Tahoe fault, and it displays a fault scarp that is 10.5 ± 0.5 m high. CHIRP profiles were collected over the scarp at this location, but they do not penetrate deep enough into the sediment to correlate offset layers across the fault.

The CHIRP profile at the base of the shelf offshore Rubicon Point displays up to 2 m of vertical sediment displacement (Fig. 8) and is the first published seismic profile that exhibits measurable Holocene displacement on the West Tahoe fault. The fault does not appear to displace

the top ~ 1.9 m of sediment. Vertical offset ~ 10 m below the surface is ~ 2 m, while offset of the most recently faulted surface is ~ 1.6 m. Diffractions off the steep west-shore shelf obscure the ~ 100 – 200 m of lake floor closest to the base of the shelf, which makes it difficult to image

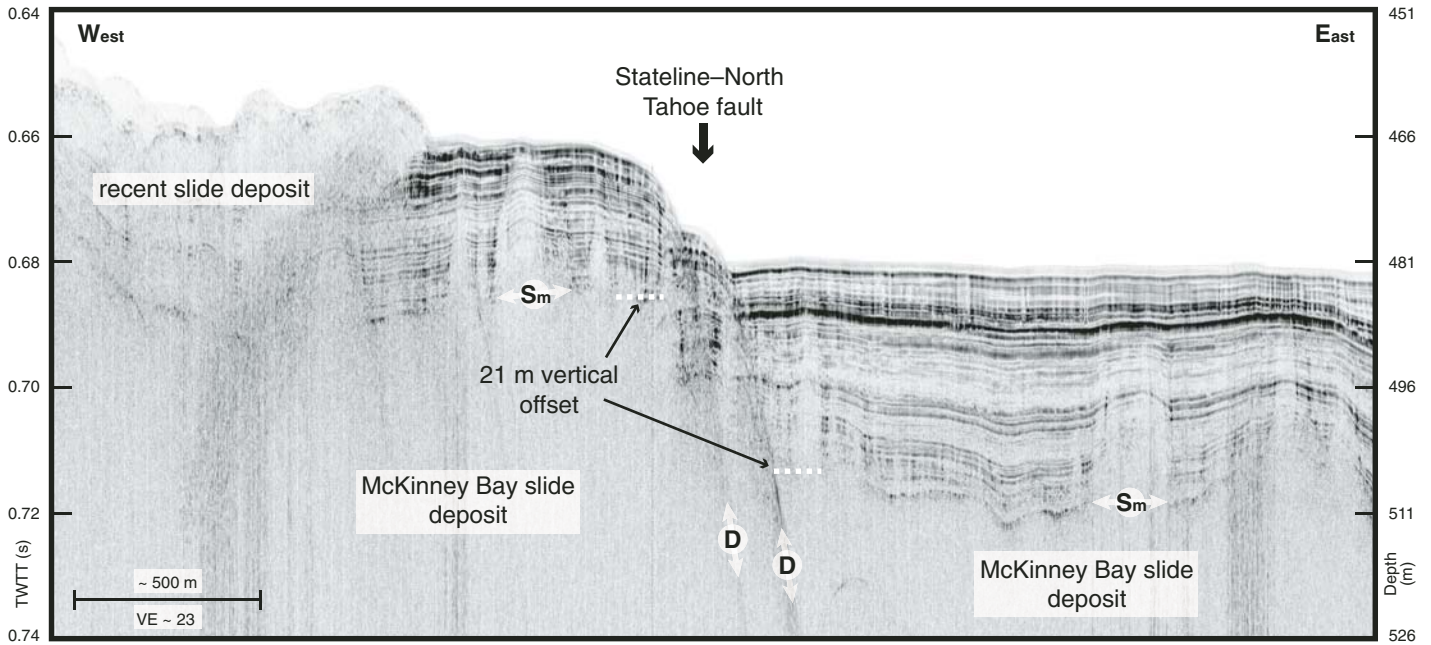


Figure 7. Chirp profile across the Stateline–North Tahoe fault. McKinney Bay slide deposits underlie the entire profile and are offset across the fault. Vertical offset between the dashed white lines is 21 m using a 1500 m/s sound velocity. The rough surface of the slide deposit contributes to some uncertainty. Postslide sediment is thicker on the down-dropped east side of the fault. A younger slide deposit is observed in the western portion of the profile and obscures the underlying stratigraphy. Sm—top of McKinney Bay slide deposit; D—diffraction; TWTT—two-way traveltime; VE—vertical exaggeration.

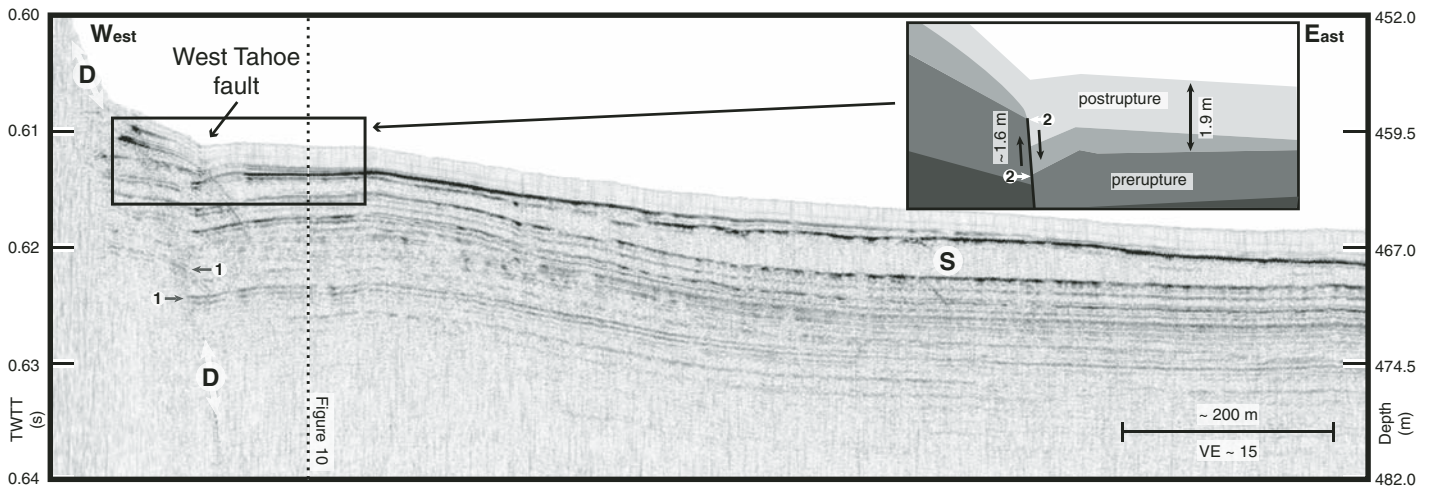


Figure 8. Chirp profile across synthetic splay of the West Tahoe fault. The sedimentary layer labeled 1 is vertically offset ~ 2 m. The inset image shows another sedimentary layer labeled 2 that is offset ~ 1.6 m across the fault. The dip of sedimentary layers above this surface decreases and is part of a sedimentary package that pinches out away from the fault. The top ~ 1.9 m of sediment represent postrupture sediment. The slide deposit to the east can be correlated in Figures 9 and 10, where it appears to thicken to the south. Dashed black line indicates approximate intersection of Figure 9. 1—offset sedimentary layer; 2—youngest offset sedimentary layer; S—slide deposit; D—diffraction; TWTT—two-way traveltime; VE—vertical exaggeration.

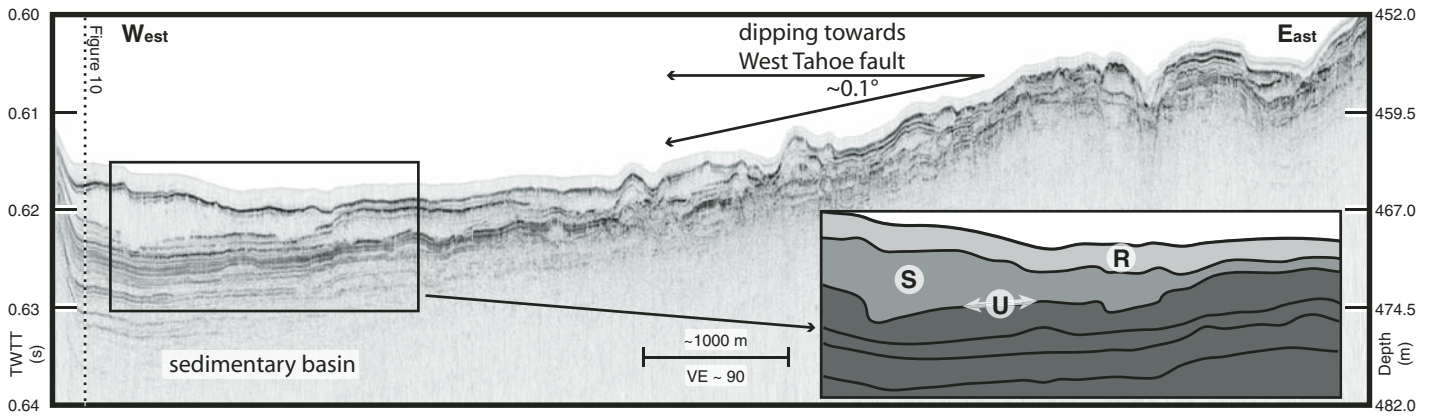


Figure 9. Chirp profile across the southern part of the lake. Inset figure shows interpretation of the same slide deposit imaged in Figures 8 and 10 and a well-defined unconformity at the base of the slide deposit. A 0.5–1.0 m layer of relatively acoustically transparent sediment (R) is present at the lake floor. The overall layered sediment sequence, in the top 7–10 m, is dipping to the west at $\sim 0.11^\circ$. Rough calculations based on the sediment dip indicate that actual West Tahoe fault offset may be larger than offset measured on the east-shore paleoterrace. R—recent, acoustically transparent sediment; U—unconformity; S—slide deposit; TWTT—two-way traveltime; VE—vertical exaggeration.

the fault in this location. The cross-lake profile (Fig. 9) shows that the lake floor slopes to the west by $\sim 0.1^\circ$ and that sediment thickens toward the West Tahoe fault, which records the normal-slip component across the fault (e.g., Driscoll et al., 1995). CHIRP profiles on the west- and east-shore paleoterraces are located on either side of the West Tahoe fault, and they also record some fraction of the vertical deformation since its formation (W_1 ; Fig. 3).

The sedimentary basin along the base of the west-shore shelf contains a recent slide deposit that extends at least 1500 m toward the center of the lake, and it is imaged in parallel and crossing profiles (Figs. 8, 9, and 10). The slide appears to be associated with multiple mass-movement deposits to the north and south, and it is imaged as a chaotic, unlayered deposit in CHIRP profiles (e.g., Fig. 10). The top 1.5–2.0 m of layered sediment are conformable with the slide and chaotic deposits. A shallow sediment core ~ 1.5 km to the northwest yields a sediment rate of ~ 0.17 mm/a for the upper 1 m of sediment. Extrapolation of this rate to the layered sediment overlying the slide deposits suggests an age of ca. 8.5–12.0 ka for these large, chaotic, slide deposits. Nevertheless, this rate may overestimate the age of the slide because postslide sedimentation rates are likely higher at this location due to the focusing nature of deposition near the scarp.

Direct measurement of the West Tahoe fault scarp provides an independent estimate of fault offset that complements estimates derived from wave-cut paleoterrace measurements. Offshore Sugar Pine Point, the fault cuts across a fan delta, creating a scarp that is 10.5 ± 0.5 m high. No cores were acquired from the fan delta, so radiometric ages are not available,

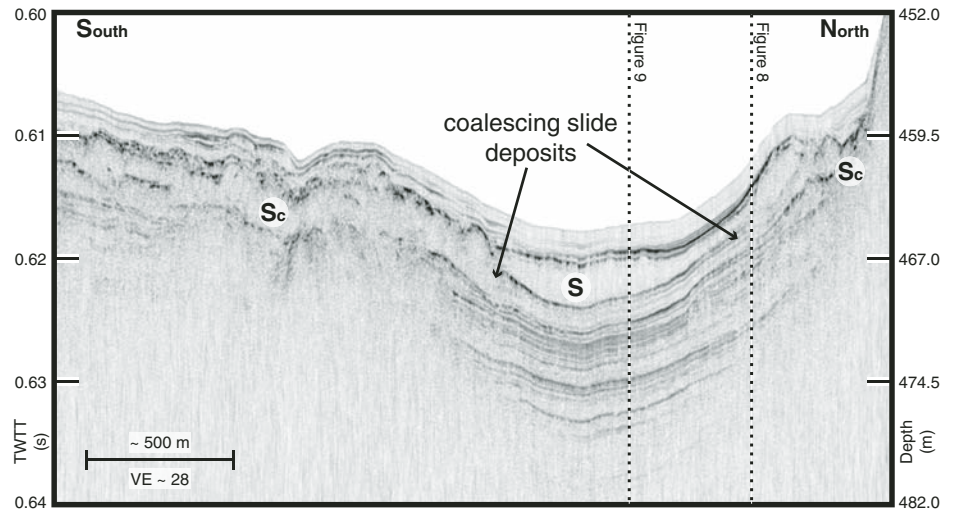


Figure 10. Chirp profile parallel to the West Tahoe fault and the base of the west-shore slope, offshore of Rubicon. An acoustically laminated sequence in the basin may be the distal portion of two proximal slide deposits, distinguished by their chaotic, unlayered sediment packages. Such geometry suggests that the slide events may have occurred at the same time. The slide deposit near the top of the basin (S) can be correlated in Figures 8 and 9. Dashed black line indicates approximate intersection of Figures 8 and 9. Sc—coalescing slide deposits; S—slide deposit; TWTT—two-way traveltime; VE—vertical exaggeration.

but we estimate that the growth of the fan delta was associated with Tioga glaciation that began ca. 24,500 yr B.P. and ended by ca. 13,600 yr B.P. (Phillips et al., 1996; Benson et al., 1998). At present, no major fluvial system exists at the head of the fan delta, and the shallow wave-cut paleoterrace has little to no sediment cover. The onshore valley to the southwest contains lateral moraine deposits from the Tioga, Tahoe, and Donner glaciations, which suggest that a large amount of sediment was funneled down the valley

during glacial periods, especially during glacial melting. Based on these arguments, it is reasonable to assume that the last significant pulse of sedimentation into this fan delta occurred during the end of the Tioga glaciation, subsequent to the cutting of the ca. 19.2 ka paleoterrace.

The fault scarp extends to the north, where it crosses the northern and southern edges of the McKinney Bay slide. North of Sugar Pine Point, the scarp is ~ 90 m high, and then is obscured in the runout area of the McKinney Bay slide.

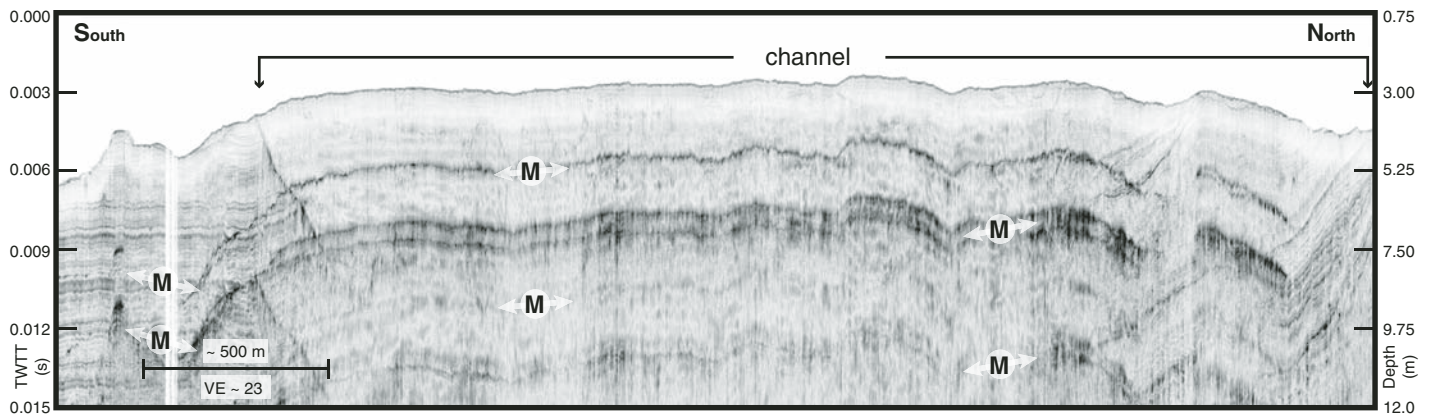


Figure 11. Chirp profile east of the Lake Tahoe Dam on the Tahoe City Shelf. Continuous layers are interrupted by a 9-m-deep valley that is ~3.0 km wide. Another profile (Kent et al., 2005, their supplemental material) closer to the dam reveals a narrower, but well-imaged, 13-m-deep incised channel that is filled with unstratified fill. The southern side of the channel cuts through laminated layers, a result of catastrophic jökulhlaup failure farther down the Truckee River (Birkeland, 1964; Hyne et al., 1972). M—water-bottom multiple; TWTT—two-way traveltime; VE—vertical exaggeration.

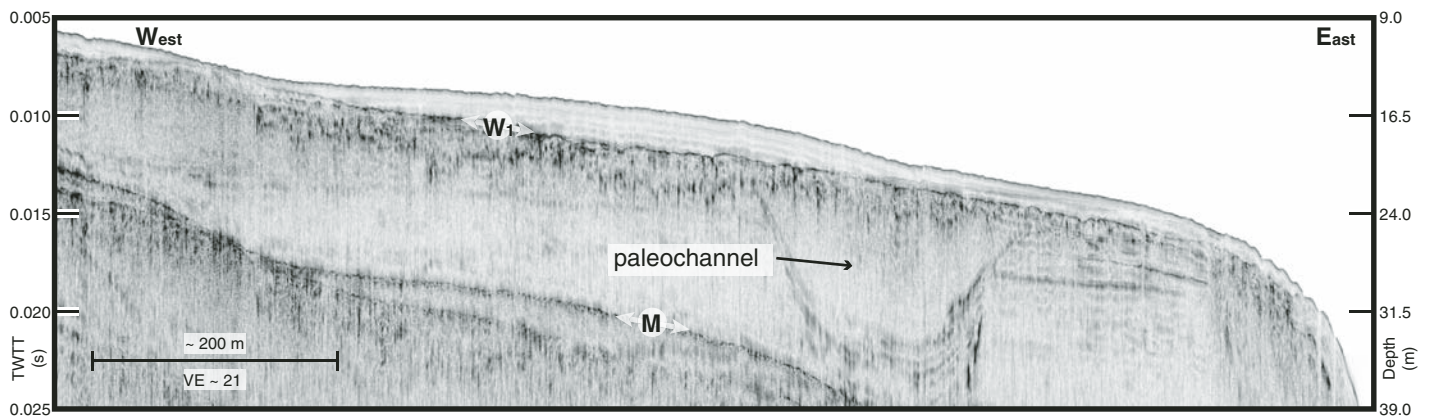


Figure 12. Chirp profile on the shelf offshore Camp Richardson. The ca. 19.2 ka paleoterrace is observed across the profile, but it is difficult to confidently identify a paleoshoreline depth because the profile is oblique to shore. The ~200-m-wide, ~15-m-deep paleochannel is truncated by the paleoterrace and may be an older channel associated with the Upper Truckee River. The truncation of the channel fill indicates that this channel is older than the paleoterrace, thus recording more down-to-the-east tectonic deformation. W₁—ca. 19.2 ka wave-cut paleoterrace; M—water-bottom multiple; TWTT—two-way traveltime; VE—vertical exaggeration.

Farther north along the southern edge of the Tahoe City Shelf, the scarp is ~100 m high, and there is possible slumping and faulting in the footwall block (Fig. 14). The scarp continues along the east edge of the Tahoe City Shelf to Dollar Point. The scarps exhibit similar relief to the north and south of the McKinney Bay slide, indicating that they are older than the slide itself and have been overprinted by the McKinney Bay slide.

Stateline–North Tahoe Fault

The Stateline–North Tahoe fault scarp exhibits multiple en echelon segments from offshore of Stateline Point to the middle of the lake,

where the surface expression is obscured by the McKinney Bay slide deposits (Fig. 2). The fault trace changes strike with each eastward step for an overall ~30° strike change from south to north. The profile in Figure 7 is representative of the multiple east-west profiles collected across the fault, all of which image parallel-layered deposits conformably overlying McKinney Bay slide deposits. The western part of the profile also crosses a more recent slide deposit, which is clearly visible in the bathymetry off the eastern edge of the Tahoe City Shelf (Fig. 2). Six kilometers to the south, there is no evidence for offset across the Stateline–North Tahoe fault, but large slide blocks may obscure the fault trace. Continuing south (Fig. 9), where there are fewer slide

blocks, there are no fault or fault-related features, suggesting that the Stateline–North Tahoe fault dies away in the center of Lake Tahoe (Fig. 2).

The post-McKinney Bay slide sediment sequence is offset by two parallel traces of the Stateline–North Tahoe fault (Fig. 7). Sedimentation rates for the upper 3 m of sediment are ~0.4 mm/a, based on radiocarbon dating of organic material recovered in a 3-m-long piston core from the hanging wall (Kent et al., 2005). The top of the McKinney Bay slide deposit is offset ~21 m across the two fault traces. The surface of the slide deposit has relief as a result of the catastrophic emplacement, so the 21 m estimate is based on the measured offset of the slide deposits directly adjacent to the fault. The postslide



Figure 13. Chirp profile across Agate Bay. Saucedo (2005) showed that the inferred Agate Bay fault strikes through Agate Bay at the location of the resistant outcrop. Gardner et al. (2000) also listed an inferred Kings Beach fault following a similar trace. Change in bedding to the west of the resistant outcrop could be misinterpreted as a fault zone, but the roughness appears to be the result of a paleochannel that was filled in prior to erosion of the wave-cut shelf. The channel extends to a depth of at least 37 m and indicates a longer record of down-to-the-east deformation because no other evidence in the bathymetric record indicates a lake stand below the one documented in this paper. The base depth of the channel is similar to the channel depth observed off Camp Richardson. The anticline and associated folding indicate tectonic deformation that predates the wave-cut paleoterrace. M—water-bottom multiple; TWTT—two-way traveltime; VE—vertical exaggeration.

sediment sequence is thicker on the hanging-wall block, suggesting that the fault scarp may also be affecting lake-bottom sediment deposition. The general strike of the fault rotates ~30° clockwise in the vicinity of this profile.

The younger slide deposit evident in the western portion of the profile (Fig. 7), which obscures the underlying stratigraphy, may be the consequence of recent earthquakes in the basin. The chaotic surface of the younger slide debris prevents accurate thickness measurements of overlying thin sediment drape, but up to 1.7 m of sediment occur against the toe of the slide.

Incline Village Fault

CHIRP profiles acquired on the shallow shelf offshore of Incline Village image an active normal fault with fault-derived colluvial wedges. Up to ~14 m of vertical deformation across the Incline Village fault are recorded by an offset boulder-layer (WBs) and associated synthetic faulting. A densely spaced grid of seismic data was collected in the vicinity of the fault (Fig. 2). Two fault-normal profiles and one fault-parallel profile, ~150 m to the east of the scarp on the hanging wall, are presented here (Figs. 5 and 6). Paleoseismic trenching onshore confirms that the Incline Village fault offsets young sediment horizons.

The shallower of the two fault-normal profiles shows an acoustically opaque lake-bottom reflector with an extremely rough surface (Fig. 6A). This surface was imaged by a remotely operated vehicle (ROV), and it is a winnowed boulder surface. Another wave-cut surface, believed to be the same ca. 19.2 ka wave-cut paleoterrace surface observed at other locations, is present above the winnowed boulder surface on the down-dropped hanging wall toward the east. The boulder surface is offset 13–14 m across the fault, and there is an ~1.5-m-thick colluvial wedge present above the paleoterrace. In the profile to the south, the paleoterrace is offset ~3.0 m across the fault, and an ~1-m-thick colluvial wedge is present in the overlying sediment (Fig. 6B). The surface expression of the fault scarp diminishes toward the shelf break to the south. After passing over the shelf break, the fault passes slightly to the west of the ridge that extends for ~8 km south into Crystal Bay (Fig. 2).

In addition to the main fault trace, small-scale synthetic faulting is observed in the hanging wall within several small relay zones between en echelon offsets of the fault zone (Fig. 6A). No additional active faulting is observed to the east on the shelf between the end of the profile in Figure 6A and the profile in Figure 3D. At least two relict faults, which do not offset the truncated paleoterrace, are present in the

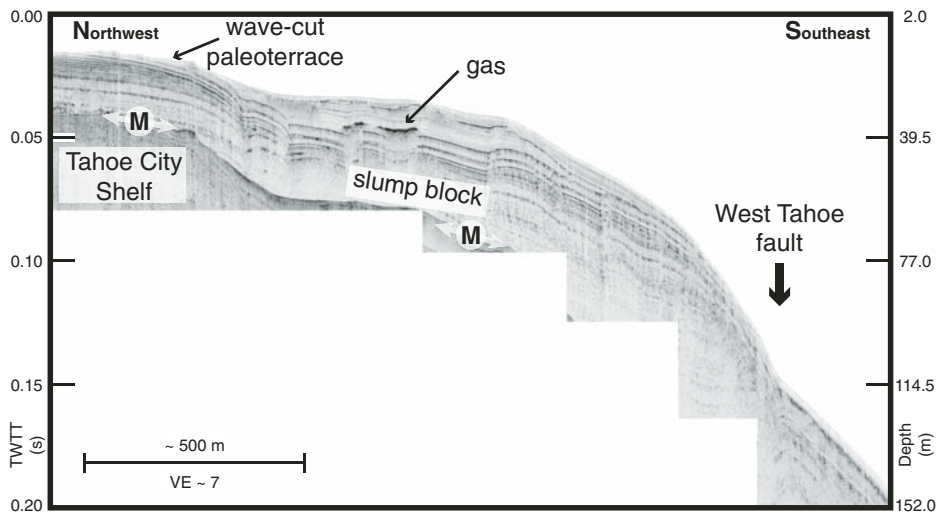


Figure 14. Chirp profile across the southeast corner of the Tahoe City Shelf. A thin layer of sediment, 1–2 m in thickness, overlies the wave-cut surface (left). The West Tahoe–Dollar Point fault, at the southeast end of the profile, exhibits up to ~100 m of vertical offset in the bathymetry data between the hanging wall and Tahoe City Shelf paleoterrace. M—water-bottom multiple; TWTT—two-way traveltime; VE—vertical exaggeration.

footwall and are visible in six of the nine fault-normal and fault-oblique profiles. The relict faults are not visible in the three profiles closest to shore because the footwall sediment is obscured by the acoustically opaque boulder surface (Fig. 6). While the westernmost fault does not offset the winnowed boulder surface, the relict fault to the east, closer to the present-day fault trace, offsets this surface but not the ca. 19.2 ka paleoterrace surface. The winnowed boulder surface, in shallower water closer to the shoreline, prevents imaging of underlying sedimentary features because the CHIRP system cannot penetrate through the granitic boulders. Farther offshore to the south, the boulders taper out and are not imaged.

Initial results from a paleoseismic trench ~1 km onshore, combined with the offset surfaces and colluvial wedges, indicate that the Incline Village fault has been active during the late Holocene. Preliminary ^{14}C analysis of fissure-filled cracks overlying a 3+-m-thick colluvial wedge in the paleoseismic trench indicates a Holocene age, possibly as young as ca. 500 yr B.P., for the youngest surface rupture (Dingler, 2007). Two older colluvial wedges of similar thickness are also observed beneath the most recent event (MRE).

At least four distinct sets of prograding clinoform sequences are present within the hanging-wall block (Fig. 5). A similar clinoform sequence is not present on the footwall. The clinoform sequences beneath the wave-cut paleoterrace, W_1 , have been truncated, while the sequence above

the paleoterrace appears to postdate the truncation and was deposited on both the hanging-wall and footwall block. These clinoform sequences record changes in accommodation space, which is affected by changes in lake level and by tectonic down-drop of the footwall block.

Tahoe–Sierra Frontal Fault?

Emerald Bay is located at the southwest corner of Lake Tahoe where the shoreline steps approximately 1 km to the east (Fig. 2). This eastward shoreline step south of Emerald Bay has been purported to delineate a segment boundary along the West Tahoe fault (Saucedo, 2005). On-shore field mapping southeast of Emerald Bay suggests that the fault trace trends from Fallen Leaf Lake to Baldwin Beach in alignment with pockmarks found offshore of Baldwin Beach. These pockmarks appear to be fault controlled and are consistent with the predicted trend of the fault (Fig. 2). In this region, Schweickert et al. (2004) proposed that the Tahoe–Sierra frontal fault is located a few kilometers farther west of the West Tahoe fault, and it is mapped crossing the central portion of Emerald Bay. CHIRP data provide an ideal opportunity to test the validity of this fault zone, which is mapped as a series of left-stepping offsets across Tahoe- and Tioga-aged moraines. Contrary to the predicted slip rates in excess of 1 mm/a, no evidence of late Pleistocene or Holocene faulting is observed in a grid of seven profiles acquired throughout Emerald Bay (Fig. 15).

We also imaged glacial deposits in Emerald Bay. In the southwest part, they are mantled by up to ~22 m of younger deposits, whereas in the northeast part of the bay, there is little to no recent deposition observed above the glacial sediments. This pattern of deposition suggests that glaciers scoured the bay during the Tioga glaciation. At the deepest point in the basin, there is ~8.5 m of acoustically transparent sedimentation, with continuous layers of post-Tioga laminated mud that form the top of the basin sediment package (Fig. 15). The acoustically transparent sediment thins to the northeast. An ~4.5-m-thick sediment core collected in the center of the sedimentary basin was dated near the bottom at ca. 4000 yr B.P. The inset in Figure 15 shows an enlarged view of the southwest half of the basin. The layered sediment, starting at a depth of 8.5 m below the lake floor, has a sharp vertical contact with chaotic, unlayered sediment to the northeast, which is different than the sediment-draped contacts on the other sides of the basin.

DISCUSSION

Chronology and Offset of the Wave-Cut Paleoterrace (W_1)

Estimates of vertical deformation across Lake Tahoe were determined by comparing offsets of the 19.2 ± 1.8 ka paleoterrace and the ca. 62 ka boulder surface across individual fault strands and measurements of fault offset, scarp height, and thickness of colluvial wedges. Offset measurements of marker surfaces (horizons) across specific fault strands can be an important tool for comparing deformation across multiple fault strands, and for quantifying far-field vertical fault slip. Offset of a specific marker surface at different lake locations may record deformation due to a single fault strand acting alone or due to a combination of the West Tahoe, Stateline–North Tahoe, and Incline Village faults acting in concert (Fig. 2). Measurement of scarp height, from bathymetry alone, provides an important constraint on fault deformation, but it is limited in accuracy because differential sedimentation on the hanging wall or erosion of the footwall will downward bias the true vertical displacement across the fault. CHIRP profiles across individual fault segments provide the best mechanism to determine the relative contributions of each fault because offset of marker beds can be mapped across the fault.

Based on the geophysical and geological data, the recent deformation appears to be predominantly dip-slip, and there is little to no evidence for strike-slip deformation along the three main fault strands in Lake Tahoe Basin.

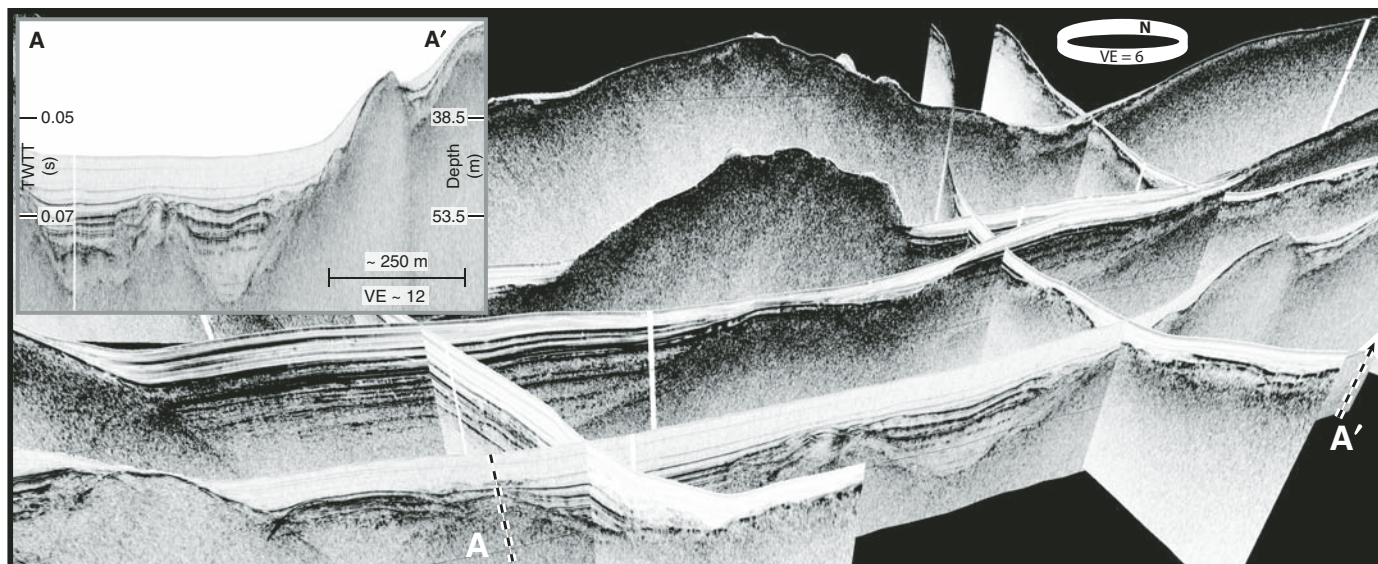


Figure 15. Three-dimensional fence diagram of seven chirp profiles in Emerald Bay. No evidence of fault offset is observed within the sedimentary section overlying basement. The lighter-colored, almost acoustically transparent surficial layer of sediment is interpreted to be deposited post-Tioga glaciation. Darker, more reflective, sediment is interpreted to be Tioga glacial deposits based on the Tioga lateral moraines that are exposed onshore in Emerald Bay. The location of the inset profile, A–A', is marked by white lettering and white dashed lines. The white orientation ring indicates the oblique view angle relative to north, as well as the vertical exaggeration (VE). TWTT—two-way traveltime.

Extensive analysis of both sides of the onshore Incline Village paleoseismic trench corroborates this interpretation. Furthermore, no transtensional or transpressional structures are visible in the high-resolution bathymetry or CHIRP seismic data along releasing or constraining bends along the Stateline–North Tahoe fault since the emplacement of McKinney Bay slide (ca. 40–60 ka). Consequently, the vertical deformation measurements presented here likely record true deformation because of the lack of strike-slip motion indicators at multiple locations throughout the basin.

The depth of the paleoterrace shows a progressive down-to-the-east vertical displacement across each of the three active faults, and displacement systematically increases northward along the eastern shore (Figs. 16 and 17). Offset across the West Tahoe fault can be directly measured by comparing the paleoterrace depth at Rubicon Point and Cave Rock (Figs. 2, 3, and 16). The 11.0 ± 0.5 m difference between these two terraces largely records movement on the West Tahoe–Dollar Point fault because the Stateline–North Tahoe and Incline Village faults terminate well north of this transect (Fig. 2). Vertical deformation on the West Tahoe fault since the cutting of the ca. 19.2 ka paleoterrace is therefore estimated at 0.44–0.68 mm/a. The uncertainty for this rate assumes $\pm 10\%$ error in measuring the vertical offset, and $\pm 10\%$ age error related to the Vibracore optically stimulated luminescence (OSL) age. A 30 m offset

between wave-cut caves at Eagle Rock along the west shore and Cave Rock on the east shore records a longer-term offset across the West Tahoe fault (Kent et al., 2005); however, there are no accompanying age or lake-level constraints (although Tahoe-aged high lake stands are likely responsible).

Faults are finite, are typically divided into segments, and usually do not terminate abruptly. Instead, fault offset decreases toward the ends of segments, and maximum offset usually occurs near the center of the segment (Cowie and Scholz, 1992; Dawers et al., 1993). The three wave-cut paleoterrace measurements along the footwall of the West Tahoe fault exhibit relatively little variability in depth (2 m) between Rubicon Point and the Tahoe City Shelf (Fig. 16). This suggests that cumulative extension from south to north along the three fault strands in Lake Tahoe is roughly similar.

North of Dollar Point, in Agate Bay, the paleoterrace is on the hanging-wall block, and it exhibits a southerly dip. The southward-dipping reflectors in Agate Bay tilt toward the maximum displacement on the fault farther south (Schlische, 1992), suggesting that Agate Bay is near the northern termination of the West Tahoe fault. When formed by wave erosion, the paleoterrace in Agate Bay was most likely a relatively flat surface with little dip, similar to the erosional surfaces farther south along the Tahoe City Shelf or at Rubicon (Fig. 2). Subsequent to formation of the paleoterrace, extensional

deformation across the West Tahoe fault to the south tilted the paleoterrace in the same manner as the underlying sediment. Note that the depth of the paleoterrace would be ~ 8 – 10 m if the southerly tilt were removed.

The two measurements of the paleoterrace on the east shore, near Cave Rock and Hidden Beach, indicate that the paleoterrace increases in depth to the north (Figs. 3, 16, and 17). The paleoterrace offshore Hidden Beach has a depth of 26.0 ± 1.0 m, ~ 4.5 m deeper than the paleoterrace at Cave Rock. The latitude of the paleoterrace offshore Hidden Beach is near the northern termination of the West Tahoe–Dollar Point fault, so the vertical contribution from the Dollar Point fault should be significantly smaller than that from the Stateline–North Tahoe fault and Incline Village fault. An additional factor that must also be considered is asymmetry in the hanging-wall block. For example, the measured paleoterrace at Hidden Beach is ~ 3 km from the nearest fault, while the paleoterrace at Cave Rock is ~ 13 km from the nearest fault. Vertical deflection decreases with increasing distance from an asymmetric normal fault, so the paleoterrace at Hidden Beach potentially records a higher percentage of the per-event vertical offset than the paleoterrace at Cave Rock (Fig. 16). Without deeper penetrating seismic data, it is impossible at present to precisely determine how much of the additional ~ 4.5 m of vertical offset in the north on the east shore paleoterrace can be attributed to

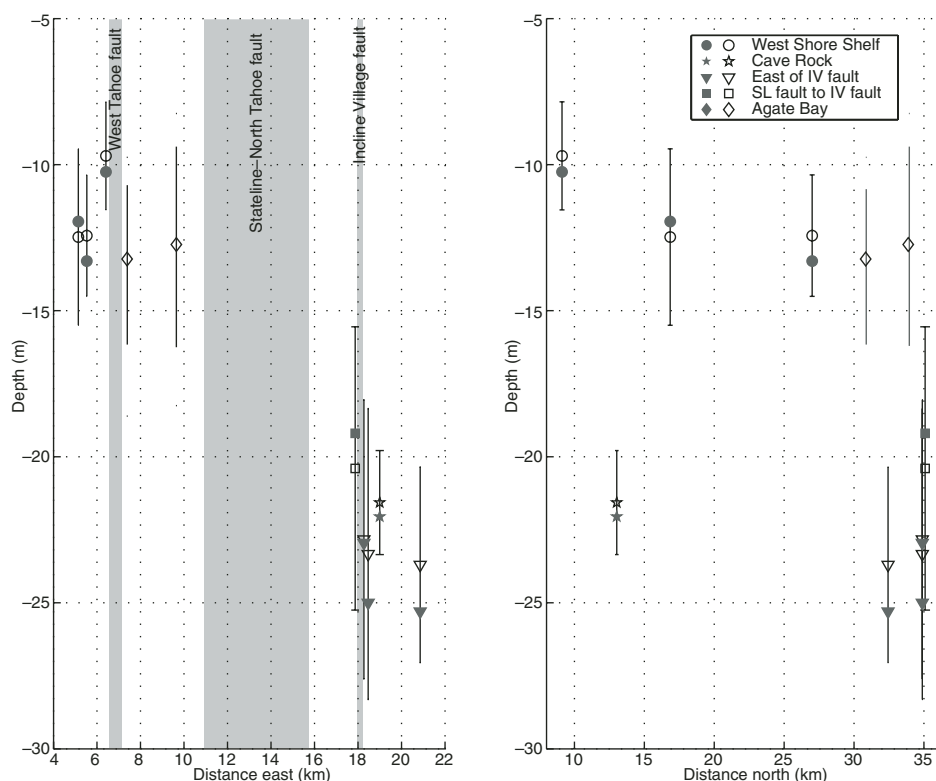


Figure 16. Graph of ca. 19.2 ka wave-cut paleoterrace depths based on chirp profiles. **Left graph** shows paleoterrace depth vs. location in kilometers north of 120°10.5'W longitude, just inboard of the west shore of Lake Tahoe. Approximate relative locations of West Tahoe, Stateline (SL)–North Tahoe, and Incline Village (IV) faults are shown as gray boxes. Paleoterrace depth systematically increases to the east after crossing each fault. **Right graph** shows paleoterrace depth vs. location in kilometers north of 38°55.5'N latitude, just inboard of the south shore of Lake Tahoe. Solid symbols represent best estimate for paleoterrace depth, while open symbols represent average paleoterrace depth. Black vertical lines represent maximum and minimum bounds for paleoterrace depth.

offset on the Stateline–North Tahoe and Incline Village faults or the proximity of the paleoterrace to the relevant fault. Next, we will now discuss the observed offset across the individual faults strands in Lake Tahoe from west to east.

McKinney Bay Slide Offset

Deposits from the McKinney Bay slide are offset by at least 21 m and possibly by as much as 24 m across the Stateline–North Tahoe fault, depending on the selection of the top of the McKinney Bay slide deposits (Fig. 7). This offset, combined with the ca. 40–60 ka age for McKinney Bay slide, suggests a vertical deformation rate on the Stateline–North Tahoe fault of 0.35–0.60 mm/a. The uncertainty for this rate assumes up to +30% overestimation of age due to the likelihood of increased sedimentation rates during the Tahoe and Tioga glaciations, +15% error in measuring the ver-

tical offset, and up to +30% underestimation of sediment velocities due to increasing sediment velocity with depth. In the north portion of the lake, it appears that the Stateline–North Tahoe fault plays a dominant role in controlling the half-graben basin architecture because the deepest region of the lake is on the hanging wall of the Stateline–North Tahoe fault, and seismic data by Hyne et al. (1972) image deep sedimentary layers dipping toward the Stateline–North Tahoe fault.

Paleochannels and Tree Stumps: Evidence for Tectonic Deformation

Paleochannels and submerged trees provide additional evidence for tectonic offset across the West Tahoe–Dollar Point fault. Two paleochannels, with similar width and depth, are present offshore of Camp Richardson on the south shore and Agate Bay on the north shore.

Both paleochannels have a channel depth of at least ~40 m, and they were filled with sediment prior to truncation by the ca. 19.2 ka paleoterrace (Figs. 12 and 13). These paleochannels were formed subaerially some time between the Donner and Tahoe glaciations at an elevation equal to or higher than the west shore paleoterrace and were then down-dropped by multiple tectonic events. The lowstand wedge sediment observed beneath the ca. 19.2 ka wave-cut paleoterrace on the east shore shelf is further evidence that the east shore was subaerially exposed (Figs. 3C and 3D). Eleven of the twelve submerged tree stumps on the south shore are at a depth of 0.0–1.2 m below the predam lake sill and range in age from 4.8 to 5.6 ka (Lindström, 1990). The twelfth tree, dated at 6.3 ka, is 3.7 m below the predam lake sill. The depth of these submerged trees can be explained by tectonic down-drop instead of climate-controlled changes in lake level as suggested by Lindström (1990). The 6.3 ka tree may be deeper than the younger trees due to a 2+ m rupture event on the West Tahoe fault between 6.3 and 5.6 ka. After this event, no further tree growth could occur on this newly submerged surface, so the shallowest depth at which subsequent tree growth could occur was at the new shoreline. The age of this possible 2+ m rupture event roughly correlates with the synthetic faulting observed in the West Tahoe fault CHIRP profile (Fig. 8). Otherwise, normal faulting would help preserve existing tree stumps emplaced by climatic conditions by further submerging them below lake level.

West Tahoe–Dollar Point Fault

Direct measurement of fault offset is possible for the West Tahoe fault based on an offset fan delta near Sugar Pine Point (Fig. 2). However, poor age constraints make a rate estimate based on this offset less certain than those derived from the offset paleoterrace or other dated fault offsets. The fault is expressed in the bathymetry as a fault scarp 10.5 ± 0.5 m high. No significant source of sediment currently supplies this fan delta. If we assume that the last consistent and sustained supply of sediment was related to the Tioga glaciation, which ended by 13,600 yr B.P. (Phillips et al., 1996; Benson et al., 1998), then the fault-offset rate is similar to the paleoterrace-offset rate, including a greater uncertainty due to poorer age constraint. The estimated vertical deformation rate from scarp height is 0.43–0.81 mm/a. The uncertainty for this rate assumes ±5% error in measuring the vertical offset, and up to –40% age error if the displacement occurred since the end of the Tioga glaciation. Direct coring and dating of this fan delta could significantly improve age constraints.

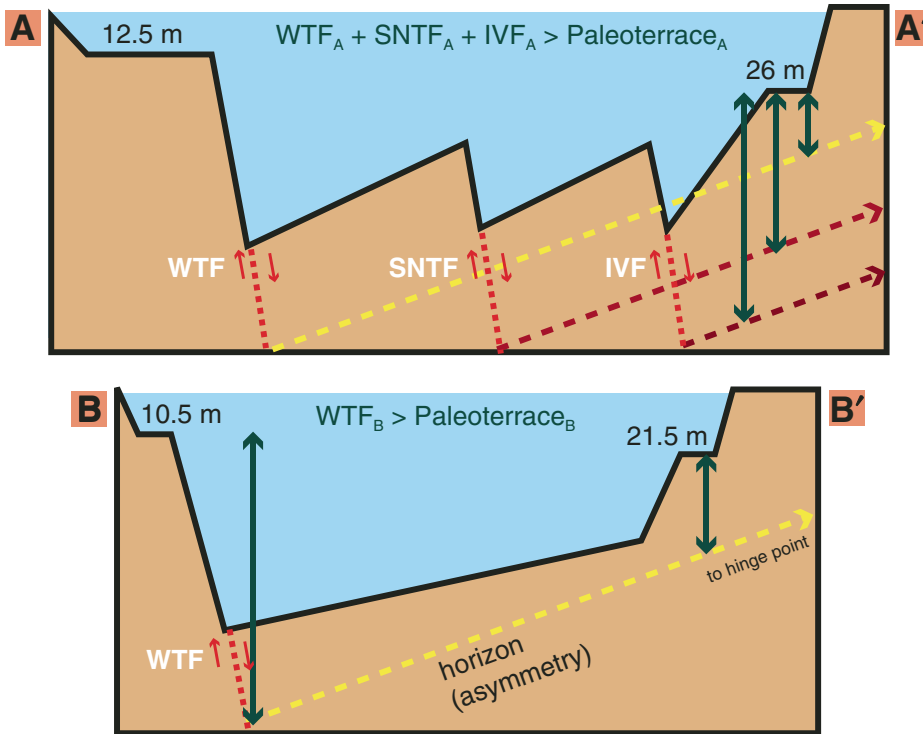


Figure 17. Schematic cross sections illustrate the approximate fault geometry in the northern (left, A–A') and southern (right, B–B') parts of the lake (see Fig. 2 for cross-section location). Green vertical arrows represent the relative vertical displacement measured across individual faults or on the wave-cut paleoterrace. The yellow dashed line is an idealized sedimentary horizon extending from the fault to the hinge point. Vertical deformation decreases with increasing distance away from the faults, so east-shore paleoterrace offset is a minimum estimate of fault offset. WTF—West Tahoe fault, SNTF—Stateline–North Tahoe fault, and IVF—Incline Village fault.

Subbottom deformation and faulting associated with the West Tahoe fault was imaged in a single CHIRP profile (Fig. 8). The probable location of the main fault trace is obscured by seismic diffractions in parallel CHIRP profiles to the north and south. Based on the strike of the West Tahoe fault where it crosses a fan delta to the north (Fig. 2), the actual West Tahoe fault trace is probably 100–300 west of the synthetic fault imaged in Figure 8. The inferred synthetic fault displays ~2 m of vertical offset 10 m below the surface, and the most recent offset reflectors display an offset of ~1.6 m at a depth of ~1.9 m below the surface. The synthetic fault offsets the ca. 8.5–12.0 ka slide mentioned earlier, so the most recent rupture event (MRE) must postdate this age. If sedimentation rates at this location, which is closer to the shelf, are higher than those at the core site used to determine the slide age, then the age of the last rupture event could be younger. Because this fault splay appears to be a synthetic fault, we cannot definitively determine whether this rupture event coincided with the last rupture event on the main trace of the fault.

The sedimentary structure observed in the cross-lake profile provides important constraints on basin architecture (Fig. 9). The CHIRP profiles confirm that sediment layers dip westward in conjunction with the overall dip of the lake floor (Figs. 9 and 17). This observation suggests that the West Tahoe fault is the controlling normal fault for the half-graben in the southern half of the lake. The ~0.1° slope of the lake floor along the cross-lake profile in the southern half of the lake allows a rough calculation of fault asymmetry and the approximate difference between an on-fault measurement on the West Tahoe fault and off-fault measurement on the east shore paleoterrace (Fig. 17). Assuming the lake floor was flat after the ca. 60 ka McKinney Bay slide, then the ~0.1° westward dip translates into increased offset on the West Tahoe fault (since 19.2 ka), compared to the ~11 m vertical offset measured on the east-shore paleoterrace. A comparison of the maximum slip rates for the paleoterrace and the fan-delta scarp from Table 1 also shows a higher maximum slip rate for the on-fault measurement at

the fan delta. This is a rough measurement that could be refined in the future by deeper seismic imaging of the top of the McKinney Bay slide debris and more precise measurement of the change in dip of that surface. On the basis of these measurements, it is clear that vertical offset of the paleoterrace serves as an absolute minimum bound on fault offset.

Coalescing slide deposits from adjacent fan deltas indicate that some slides or other mass-wasting events may be earthquake triggered, because their initiation points are spatially separated, but the coalescing deposits indicate that they are concomitant. Additional CHIRP profiles and associated sediment cores will help constrain the origin and timing of the different slides. Sediment cores throughout the lake record turbidite sequences that may be related to these and other earthquake-triggered mass-wasting events.

Incline Village Fault

On the Incline Village fault, the vertical deformation rate is 0.18–0.30 mm/a since the formation of the winnowed boulder surface (WBs) ca. 62 ka, based on the 13–14 m vertical offset (Fig. 17). The estimated vertical deformation rate includes ±10% measurement error, +20% due to increased sediment velocity, and ±10% for error in dating of the winnowed boulder surface. The western of the two relict faults does not offset an older truncation surface, while the eastern relict fault offsets this surface, but not the ca. 19.2 ka paleoterrace (Fig. 6B). Though speculative, such an offset pattern suggests that the fault rupture has migrated eastward through time, which may record the long-term regional deformation that is measured by a slight counterclockwise rotation of GPS velocities (Hammond and Thatcher, 2004) across Carson Valley and Lake Tahoe Basin (Fig. 1, white arrow).

The second wave-cut surface, W_2 , imaged beneath the ca. 19.2 ka paleoterrace in the two CHIRP profiles on the east shore would provide additional constraints on vertical deformation if accurate dates were available (Figs. 3C and 3D). Extrapolation of sedimentation rates based on the Vibracores in the vicinity of Cave Rock (Kent et al., 2005) is not feasible because the sedimentation rate is extremely variable due to changing lake levels. Deeper penetrating sediment cores and an improved lake-level chronology are needed to accurately date this surface.

The ca. 19.2 ka paleoterrace surface is offset by ~3.0–3.5 m across the Incline Village fault, which corresponds to a vertical deformation rate of 0.12–0.23 mm/a. The estimated vertical deformation rate includes ±10% measurement error, +20% due to increased sediment velocity,

TABLE 1. VERTICAL DEFORMATION, ERROR, AND SLIP RATES

	Vertical deformation On fault* (m)	Off fault† (m)	Age (ka)	Measurement error‡ (mm/a)	Age error (mm/a)	Velocity error¶ (mm/a)	Minimum slip rate** (mm/a)	Maximum slip rate†† (mm/a)
West Tahoe fault								
Paleoterrace	–	10.5–11.5	19.2	±0.06	±0.06	–	0.44	0.68
Fan delta	10.5 ± 0.5	–	13.6	±0.04	–0.31	–	0.43	0.81
Stateline–North Tahoe fault								
Fault offset	21	–	60	+0.03	+0.11	+0.11	0.35	0.60
Incline Village fault								
Paleoterrace	3–3.5	–	19.2	±0.02	±0.02	+0.03	0.12	0.23
Boulder surface	13–14	–	62	±0.02	±0.02	+0.04	0.18	0.30
Combined slip rate^{§§}							0.90	1.71
Extension rate (60° dip)							0.52	0.99

*On-fault measurements include direct measurement of continuous surfaces that are offset across the fault, as well as scarp height measurements.

†Off-fault measurements include surfaces that are offset across the fault but are not continuous from the measurement location to the fault.

‡Measurement error caused by roughness in offset surfaces.

¶Error caused by increase in velocity with increasing sediment depth. CHIRP profiles assume 1500 m/s velocity.

**Vertical deformation divided by age, then combined with all negative error values. Errors are cumulative.

††Vertical deformation divided by age, then combined with all positive error values except for asymmetry. Errors are cumulative.

§§Combined slip rate combines minimum value for each fault for minimum slip rate and maximum value for each fault for maximum slip rate.

and ±10% for error in dating of the paleoterrace. The colluvial wedges observed above the wave-cut paleoterrace are in similar positions relative to the lake floor and paleoterrace (Fig. 6), so we assume that they were formed by the same Holocene event.

Seismic-reflection data from Hyne et al. (1972) suggest that the 400+-m-high, south-trending ridge south of Incline Village is fault bounded and that the faulting is part of an en echelon system of faults. Our results on the shallow shelf offshore Incline Village confirm the explanation that the ridge represents long-term deformation on the Incline Village fault, but the present-day trace of the Incline Village fault is ~500 m to the west of and parallel to the ridge-line. A CHIRP profile just south of the termination of the ridge shows no evidence of shallow faulting, which, combined with the termination of the ridge to the north, suggests that the Incline Village fault dies out between the shelf break and the southern termination of the ridge.

Implications for Tahoe Deformation

No fault offsets or fault-related deformation in either Holocene sediment or unconsolidated glacial deposits are observed in over 25 km of CHIRP profiles acquired in Emerald Bay (Fig. 15). This network of profiles shows that any feature that could be considered a fault offset in any individual two-dimensional (2-D) profile cannot be correlated between profiles, or is obviously not fault-related when multiple profiles are viewed in a three-dimensional fence diagram. Based on these results, it is most probable that the West Tahoe fault steps eastward around Emerald Bay and comes ashore in the vicinity of Baldwin Beach (Fig. 2). The lack of observed Holocene faulting in Emerald Bay is difficult to reconcile with the 1.6 + 0.35 mm/a slip rate on the postulated Tahoe–Sierra frontal fault zone

suggested by Schweickert et al. (2004), which is interpreted to offset several moraines extending from Emerald Bay to Meeks Bay and beyond.

It is unclear from our measurements whether strain in the northern and southern portions of the lake is equal or increases from south to north. Vertical deformation in the northern part of the lake, as measured on the offset paleoterrace, is slightly larger than in the south, but this may be due to the combined offset on three active faults (or asymmetry) as opposed to one active fault in the south. The paleoterrace offset measurements serve as a minimum bound on deformation because throw measurements decrease with increasing distance onto the hanging wall from the fault (Fig. 17).

The combined deformation rate across the lake, from west to east, is similar throughout the lake, providing important clues as to the way in which strain is partitioned. The Sierra frontal fault system consists of two branches, one through Lake Tahoe and the second to the east through Carson Valley (Fig. 1). North of Lake Tahoe, active deformation is transferred westward to the dextral Mohawk Valley fault to accommodate Sierra Nevada–North America plate motion (Unruh et al., 2003). Deformation in this region can be explained by extension across north-striking faults combined with shear on N35°W-striking dextral faults (Hammond and Thatcher, 2004). The three principal fault strands in Lake Tahoe are roughly north-striking normal faults, while the general strike of the Mohawk Valley fault is N20–45°W. For the purpose of analyzing regional deformation, overlapping segmented fault systems can be viewed as one fault and their offset rates can be summed (Dawers and Anders, 1995). In the following discussion, the Tahoe faults are treated as a single fault, but data are insufficient at present to determine if the three faults rupture in unison or separately. Improved rupture-event chronology

from onshore-offshore paleoseismology and additional lake sediment cores will be required to determine the timing and extent of past earthquakes in Lake Tahoe Basin.

If we combine the extension rates for the three principal faults in Lake Tahoe with the rate for the Genoa fault, we can compare them with current GPS extension rates. The late Holocene extension rate for the Genoa fault (Ramelli et al., 1999), assuming a 60° fault dip, is 1.15–1.73 mm/a. The Genoa rate combined with the sum of the West Tahoe–Dollar Point, Stateline–North Tahoe, and Incline Village fault extension rates, also assuming a 60° fault dip, provides a rate of 1.67–2.72 mm/a. A velocity difference of 2.7 ± 0.9 mm/a was measured between GPS sites in Carson Valley and northwest of Lake Tahoe (Fig. 1). The fault extension rates calculated from this study are consistent with rates derived from GPS velocities for the region, and they suggest that extension in Lake Tahoe might account for the residual GPS strain between Carson Valley and Lake Tahoe Basin after Genoa fault-slip rates are removed. A number of caveats must be taken into account when considering this extension rate comparison. First, GPS measurements record current deformation rates, while the results from Lake Tahoe integrate multiple earthquake cycles of deformation averaged over tens of thousands of years. Second, the two GPS stations used in this comparison are near the northern end of Lake Tahoe. Based on similarity with surrounding GPS sites at the latitude of Lake Tahoe, we are operating under the assumption that the GPS-derived extension rates apply for the entire Lake Tahoe Basin.

CONCLUSION

The results of this study confirm that Lake Tahoe has been an actively deforming basin at the western edge of the Walker Lane since

at least the late Pleistocene. Revised vertical deformation rates for the three main active faults in the lake and their associated sources of error are summarized in Table 1. The combined east-west extension rate across Lake Tahoe basin, assuming 60° fault geometry, is estimated 0.52–0.99 mm/yr. These refined slip rates, when combined with the Genoa fault-slip rate (Ramelli et al., 1999), are consistent with the magnitude of extension derived from GPS velocities across Carson Valley and Lake Tahoe Basin (Hammond and Thatcher, 2004). In addition, in-depth analysis of the offset and dip of the wave-cut paleoterrace throughout the lake, combined with other high-resolution CHIRP profiles, indicates that Lake Tahoe is a westward-tilted, asymmetric half-graben in the south, and it transitions to three en echelon asymmetric half-grabens in the north. The Stateline–North Tahoe, Incline Village, and West Tahoe–Dollar Point faults all show evidence for large (2+ m) Holocene rupture events. Faulting in Lake Tahoe is on the scale of faulting observed to the east in Walker Lane, and this suggests that Lake Tahoe Basin should be considered the western edge of the actively deforming Walker Lane.

ACKNOWLEDGMENTS

Our research at Lake Tahoe has been ongoing since 1999. Several people during that time deserve special recognition for their assistance. Bob Richards, the former captain of the R/V *LeConte*, constantly worked overtime to accommodate our ever-changing schedules. His knowledge of the lake was extremely important and aided in the planning of our CHIRP surveys. His successor, Brant Allen, carried on the tradition of hard work and was instrumental in the success of our Lake Tahoe research. Shane Smith provided valuable assistance during CHIRP data collection, and his lake sediment cores provided important constraints to our CHIRP data. Craig Morgan was a constant source of advice about the geology and regulatory agencies in Lake Tahoe Basin. Danny Brothers, Allison Dingler, Fiona Sutherland, Liz Johnstone, Leah Hogarth, and Jenna Hill all helped out with data collection and helped J. Dingler explore the forests and mountains around Lake Tahoe. All the members of the Scripps Institution of Oceanography Ocean Bottom Seismometer (SIO OBS) laboratory, Paul Georgief, Mark Gibaud, Martin Rapa, and Ernest Aaron, assisted with equipment loading and preparation during the multiple trips to Lake Tahoe. A special thanks is due to Geoff Schladow and the Tahoe Environmental Research Center for advancing and supporting our research in Lake Tahoe Basin. We also thank Jim Phelan at the Tahoe City Marina and Matt Daniels who supplied the barge for Vibracoring; their constant help throughout the years was invaluable. The Lake Tahoe research was funded through grants from the National Science Foundation (EAR-0003839), University of California Academic Senate (RA821-S), Lawrence Livermore National Laboratory (02-GS-008), and National Earthquake Hazard Reduction Program of the U.S. Geological Survey (02HQGR0072, 04HQGR007, and 06HQGR0064).

REFERENCES CITED

- Argus, D.F., and Gordon, R.G., 2001, Present tectonic motion across the Coast Ranges and San Andreas fault system in central California: *Geological Society of America Bulletin*, v. 113, no. 12, p. 1580–1592, doi: 10.1130/0016-7606(2001)113<1580:PTMATC>2.0.CO;2.
- Bellier, O., and Zoback, M.L., 1995, Recent state of stress change in the Walker Lane zone western Basin and Range Province, United States: *Tectonics*, v. 14, no. 3, p. 564–593.
- Bennett, R.A., Wernicke, B.P., Niemi, N.A., Friedrich, A.M., and Davis, J.L., 2003, Contemporary strain rates in the northern Basin and Range Province from GPS data: *Tectonics*, v. 22, no. 2, doi: 10.1029/2001TC001355.
- Benson, L.V., May, H.M., Antweiler, R.C., Brinton, T.I., Kashgarian, M., Smoot, J.P., and Lund, S.P., 1998, Continuous lake-sediment records of glaciation in the Sierra Nevada between 52,600 and 12,500 ¹⁴C yr B.P.: *Quaternary Research*, v. 50, no. 2, p. 113–127, doi: 10.1006/qres.1998.1993.
- Birkeland, P.W., 1964, Pleistocene glaciation of the northern Sierra Nevada, north of Lake Tahoe, California: *The Journal of Geology*, v. 72, no. 6, p. 810–825.
- Briggs, R.W., and Wesnousky, S.G., 2004, Late Pleistocene fault slip rate, earthquake recurrence, and recency of slip along the Pyramid Lake fault zone, northern Walker Lane, United States: *Journal of Geophysical Research*, v. 109, B08402, doi: 10.1029/2003JB002717.
- Clark, D.H., and Gillespie, A.R., 1997, Timing and significance of late-glacial and Holocene cirque glaciation in the Sierra Nevada, California: *Quaternary International*, v. 38–39, p. 21–38, doi: 10.1016/S1040-6182(96)00024-9.
- Cowie, P.A., and Scholz, C.H., 1992, Displacement length scaling relationship for faults—Data synthesis and discussion: *Journal of Structural Geology*, v. 14, no. 10, p. 1149–1156, doi: 10.1016/0191-8141(92)90066-6.
- Dawers, N.H., and Anders, M.H., 1995, Displacement-length scaling and fault linkage: *Journal of Structural Geology*, v. 17, no. 5, p. 607, doi: 10.1016/0191-8141(94)00091-D.
- Dawers, N.H., Anders, M.H., and Scholz, C.H., 1993, Growth of normal faults; displacement-length scaling: *Geology*, v. 21, no. 12, p. 1107, doi: 10.1130/0091-7613(1993)021<1107:GONFDL>2.3.CO;2.
- Dingler, J.A., 2007, *New Geophysical Approaches to Study Neotectonics and Associated Geohazards* [Ph.D. thesis]: San Diego, University of California, 190 p.
- Dixon, T.H., Miller, M., Farina, F., Wang, H., and Johnson, D., 2000, Present-day motion of the Sierra Nevada block and some tectonic implications for the Basin and Range Province, North American Cordillera: *Tectonics*, v. 19, no. 1, p. 1–24, doi: 10.1029/1998TC001088.
- Dokka, R.K., and Travis, C.J., 1990, Role of the Eastern California shear zone in accommodating Pacific–North American plate motion: *Geophysical Research Letters*, v. 17, no. 9, p. 1323–1326, doi: 10.1029/GL017i009p01323.
- Driscoll, N.W., Hogg, J.R., Christie-Blick, N., and Karner, G.D., 1995, Extensional tectonics in the Jeanne d'Arc Basin, offshore Newfoundland: Implications for the timing of break-up between Grand Banks and Iberia: *Geological Society of London Special Publication* 90, p. 1–28.
- Faulds, J.E., Henry, C.D., and Hinz, N.H., 2005, Kinematics of the northern Walker Lane: An incipient transform fault along the Pacific–North American plate boundary: *Geology*, v. 33, no. 6, p. 505–508, doi: 10.1130/G21274.1.
- Gardner, J.V., Mayer, L.A., and Hughes-Clarke, J., 1998, The bathymetry of Lake Tahoe, California–Nevada: U.S. Geological Survey Open-File Report OF-98-509, 22 p.
- Gardner, J.V., Mayer, L.A., and Hughes-Clarke, J.E., 2000, Morphology and processes in Lake Tahoe (California–Nevada): *Geological Society of America Bulletin*, v. 112, no. 5, p. 736–746, doi: 10.1130/0016-7606(2000)112<0736:MAPILT>2.3.CO;2.
- Hallet, B., Hunter, L., and Bogen, J., 1996, Rates of erosion and sediment evacuation by glaciers: A review of field data and their implications, *in* Solheim, A., Riis, F., Elverhoi, A., Faleide, J. I., Jensen, L. N., and Cloetingh, S., eds., *Global and Planetary Change*, v. 12, p. 213–235.
- Hammond, W.C., and Thatcher, W., 2004, Contemporary tectonic deformation of the Basin and Range Province, western United States: 10 years of observation with the Global Positioning System: *Journal of Geophysical Research*, v. 109, no. B8, doi: 10.1029/2003JB002746.
- Hawkins, F.F., Laforge, R., and Hansen, R.A., 1986, Seismotectonic Study of the Truckee/Lake Tahoe Area, Northern Sierra Nevada, California: U.S. Department of the Interior, Bureau of Reclamation, no. 85-4, 210 p.
- Hyne, N.J., Chelminski, P., Court, J.E., Gorsline, D.S., and Goldman, C.R., 1972, Quaternary history of Lake Tahoe, California–Nevada: *Geological Society of America Bulletin*, v. 83, no. 5, p. 1435–1448, doi: 10.1130/0016-7606(1972)83[1435:QHOLTC]2.0.CO;2.
- Hyne, N.J., Goldman, C.R., and Court, J.E., 1973, Mounds in Lake Tahoe, California–Nevada—Model for landslide topography in subaqueous environment: *The Journal of Geology*, v. 81, no. 2, p. 176–188.
- Kent, G.M., Babcock, J.M., Driscoll, N.W., Harding, A.J., Dingler, J.A., Seitz, G.G., Gardner, J.V., Mayer, L.A., Goldman, C.R., Heyvaert, A.C., Richards, R.C., Karlin, R., Morgan, C.W., Gayes, P.T., and Owen, L.A., 2005, 60 k.y. record of extension across the western boundary of the Basin and Range Province: Estimate of slip rates from offset shoreline terraces and a catastrophic slide beneath Lake Tahoe: *Geology*, v. 33, no. 5, p. 365–368, doi: 10.1130/G21230.1.
- Lindström, S.G., 1990, Submerged tree stumps as indicators of Mid-Holocene aridity in the Lake Tahoe region: *Journal of Geology and Great Basin Anthropology*, v. 12, no. 2, p. 146–157.
- Miller, M.M., Johnson, D.J., Dixon, T.H., and Dokka, R.K., 2001, Refined kinematics of the Eastern California shear zone from GPS observations, 1993–1998: *Journal of Geophysical Research*, v. 106, no. B2, p. 2245–2264, doi: 10.1029/2000JB900328.
- Moore, J.G., Schweickert, R.A., Robinson, J.E., Lahren, M.M., and Kitts, C.A., 2006, Tsunami-generated boulder ridges in Lake Tahoe, California–Nevada: *Geology*, v. 34, no. 11, p. 965–968, doi: 10.1130/G22643A.1.
- Oldow, J.S., 2003, Active transtensional boundary zone between the western Great Basin and Sierra Nevada block, western U.S. Cordillera: *Geology*, v. 31, no. 12, p. 1033–1036, doi: 10.1130/G19838.1.
- Phillips, F.M., Zreda, M.G., Benson, L.V., Plummer, M.A., Elmore, D., and Sharma, P., 1996, Chronology for fluctuations in late Pleistocene Sierra Nevada glaciers and lakes: *Science*, v. 274, no. 5288, p. 749–751, doi: 10.1126/science.274.5288.749.
- Ramelli, A.R., Bell, J.W., dePolo, C.M., and Yount, J.C., 1999, Large-magnitude, late Holocene earthquakes on the Genoa fault, west-central Nevada and eastern California: *Bulletin of the Seismological Society of America*, v. 89, no. 6, p. 1458–1472.
- Saucedo, G.J., 2005, *Geologic Map of the Lake Tahoe Basin, California and Nevada*: California Department of Conservation California Geological Survey, California Geological Survey Regional Geologic Map Series, Map no. 4, scale 1:100,000.
- Schlische, R.W., 1992, Structural and stratigraphic development of the Newark extensional basin, eastern North America—Evidence for the growth of the basin and its bounding structures: *Geological Society of America Bulletin*, v. 104, no. 10, p. 1246–1263, doi: 10.1130/0016-7606(1992)104<1246:SASDOT>2.3.CO;2.
- Schweickert, R.A., Lahren, M.M., Smith, K.D., Howle, J.F., and Ichinose, G., 2004, Transtensional deformation in the Lake Tahoe region, California and Nevada, USA: *Tectonophysics*, v. 392, no. 1–4, p. 303–323, doi: 10.1016/j.tecto.2004.04.019.
- Svarc, J.L., Savage, J.C., Prescott, W.H., and Ramelli, A.R., 2002, Strain accumulation and rotation in western Nevada: *Journal of Geophysical Research*, v. 107, no. B5, 2090, doi: 10.1029/2001JB000579.

- Unruh, J., Humphrey, J., and Barron, A., 2003, Transtensional model for the Sierra Nevada frontal fault system, eastern California: *Geology*, v. 31, no. 4, p. 327–330, doi: 10.1130/0091-7613(2003)031<0327:TMFTSN>2.0.CO;2.
- U.S. Geological Survey (USGS), 2005, Quaternary fault and fold database for the United States, 18 May 2005: <http://earthquake.usgs.gov/regional/qfaults> (April 2006).
- Wakabayashi, J., and Sawyer, T.L., 2001, Stream incision, tectonics, uplift, and evolution of topography of the Sierra Nevada, California: *The Journal of Geology*, v. 109, p. 539–562, doi: 10.1086/321962.
- Wesnousky, S.G., and Jones, C.H., 1994, Oblique slip, slip partitioning, spatial and temporal changes in the regional stress field, and the relative strength of active faults in the Basin and Range, western United States: *Geology*, v. 22, no. 11, p. 1031–1034, doi: 10.1130/0091-7613(1994)022<1031:OSSPSA>2.3.CO;2.
- Wesnousky, S.G., Barron, A.D., Briggs, R.W., Caskey, S.J., Kumar, S., and Owen, A.L., 2005, Paleoseismic transect across the northern Great Basin: *Journal of Geophysical Research*, v. 110, B05408, doi: 10.1029/2004JB003283.
- Zoback, M.L., 1989, State of stress and modern deformation of the northern Basin and Range Province: *Journal of Geophysical Research*, v. 94, no. B6, p. 7105–7128, doi: 10.1029/JB094iB06p07105.

MANUSCRIPT RECEIVED 10 APRIL 2007

REVISED MANUSCRIPT RECEIVED 16 OCTOBER 2008

MANUSCRIPT ACCEPTED 13 NOVEMBER 2008

Printed in the USA

Day 2, Stop 2 – Incline Village Fault Trench Site

Large Magnitude Holocene Earthquakes Recorded on the Incline Village Fault, Lake Tahoe, California-Nevada

Seitz, Gordon, California Geological Survey, Menlo Park, CA

Introduction

Although the geologic setting for assessing the activity of faults are challenging in the Tahoe basin, the combination of off and onshore observations have made it possible. The Lake Tahoe basin is the result of ongoing normal faulting along three basin-parallel faults that step en echelon across the width of the basin. Although onshore faulting is obscured by a Pleistocene-age glacial overprint that has resulted in many fault-appearing scarps, basin-wide bare-earth LiDAR has largely eliminated the uncertainties in identifying landform origins. High-resolution Chirp seismic profiles confirmed the onshore fault location of the Incline Village fault, expressed as a laterally continuous scarp. In many circumstances, offshore seismic imaging can allow an unambiguous distinction of tectonic versus fluvial or glacial landforms, by providing a subsurface image of the feature's sedimentary structure. Furthermore this imaging method is very efficient, tens of kilometers of profiles can be collected per day. Prior to the study presented here there was no direct observation from which to gauge the expected earthquake magnitudes and associated recurrence intervals that occur on Lake Tahoe basin faults. Estimated vertical slip rates based on the displacement of a submerged terrace dated at 19.2 ± 1.8 ka are 0.12-.3 mm/year for the

Incline Village fault (Dingler et al., 2009).

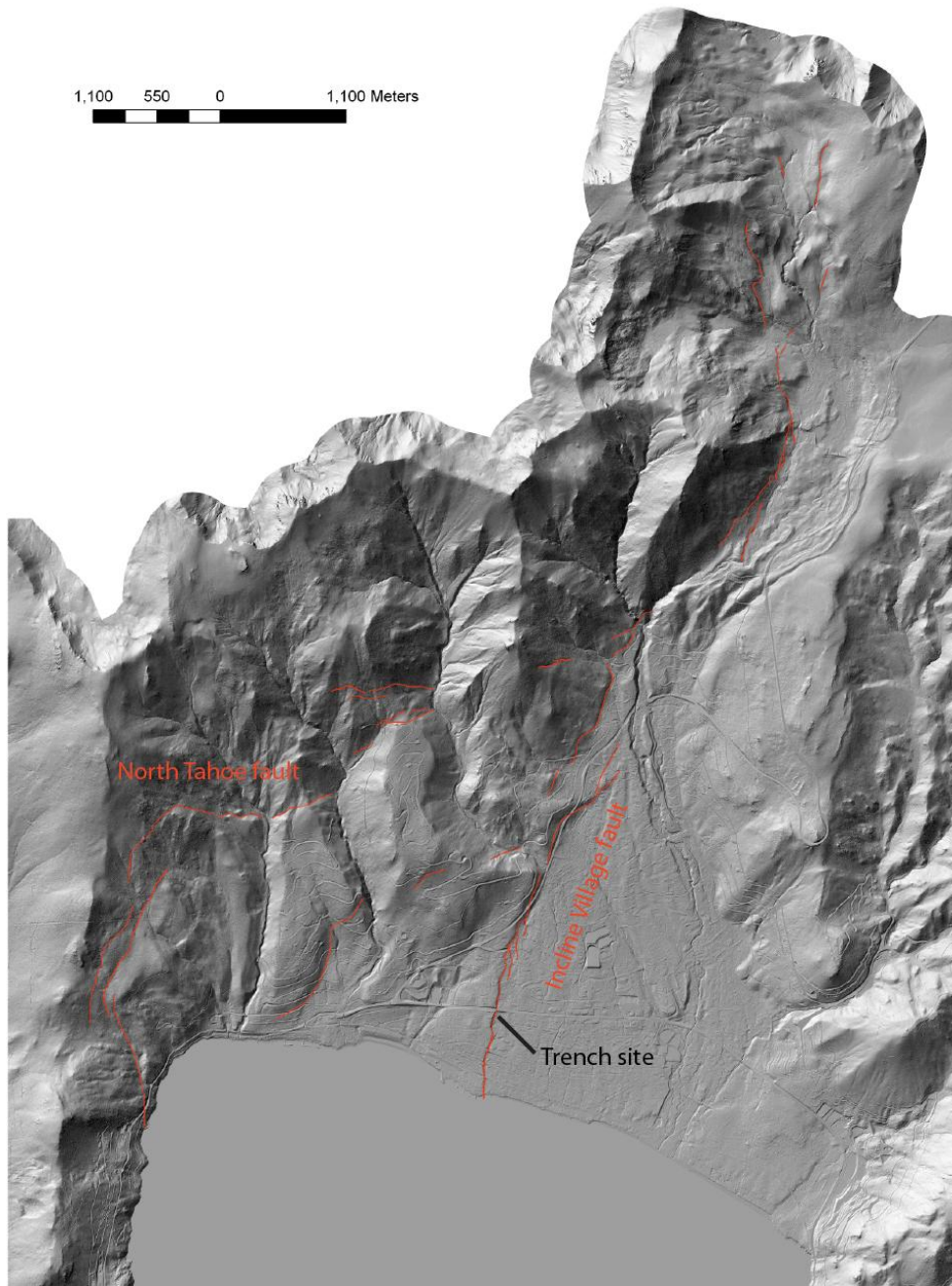


Figure 1 Incline Village fault map on bare-earth LiDAR. The trench site is located on the IV fault, whereas the fault strands merging into the IV fault north of the trench site from the west belong to the North Tahoe/Stateline fault.

Onshore Fault Investigation

For the onshore investigation, we selected a site where the scarp is laterally continuous over a 50 m stretch with a uniform character in terms of scarp height and slope. The scarp profile suggests multiple events, with a lower angle bevel near the top of the scarp. We extended an 8.4 m deep and 22 m long trench across this 4.75 meter-high scarp.

The uplifted footwall fault block consists of Tahoe-age or older consolidated near shore lacustrine layered sands and gravels faulted against Holocene/Pleistocene-age scarp-derived colluvial and fault-parallel transported colluvial and fluvial sediments consisting of layered gravels and sands in the hanging wall (Figure 2). The structure consists of a 7 m wide zone of parallel down-to-the-east normal faults that extend the width of the scarp face. There are six fault surface breaks along which most of the displacement has occurred. Only a subset of these fault splays were active during each individual event. The footwall block is comprised of three characteristic colluvial wedges (CW), each bounded by a soil. These sedimentary packages have the following characteristics: 1) a wedge shaped geometry, thickening towards the scarp, and abutting the faulting-generated free faces, and extending above the base of the scarp; 2) the clast size and concentration decreases from the fault zone to the east, with clasts ranging in sizes of over 1 m to less than 20 cm; 3) each CW package is capped by a soil, indicating a long period of landscape stability.

The most recent event deposits infill two fissures, a smaller fissure at about 3.5 meters height from the base of the scarp, and a larger fissure at the base of the scarp. The most recent event (MRE), CW deposits consist of two units, scarp-collapse derived fissure fill [unit 18] consisting of coarse layered gravels in the eastern 3 m deep fissure [faults E,D] with individual clasts up to 1 m and a smaller 1 m deep fissure filled with A-horizon soil at fault A. These fissure fills are overlain by a unit [unit 16] that fines to the east. We interpret this unit to grade from scarp collapse derived coarser material in the fault zone to finer grained fault-parallel transported silty sands on the eastern distal portion.

The penultimate CW deposits consist of two distinct gravel units, a basal unit [22] which is clast supported and contains almost no fines, overlain by a unit [20] which is matrix supported with a silty sand with an increasing large clast content towards its top. In the eastern portion of the trench this unit is capped by a well-developed soil, approximately 30 cm thick.

The third event CW is comprised of a coarse sand unit overlying a gravel unit. The top unit [30] capped by the oxidized soil and is in depositional contact with the penultimate CW along a buried scarp face of fault B. The CW is only partially exposed at the bottom of the exposure.

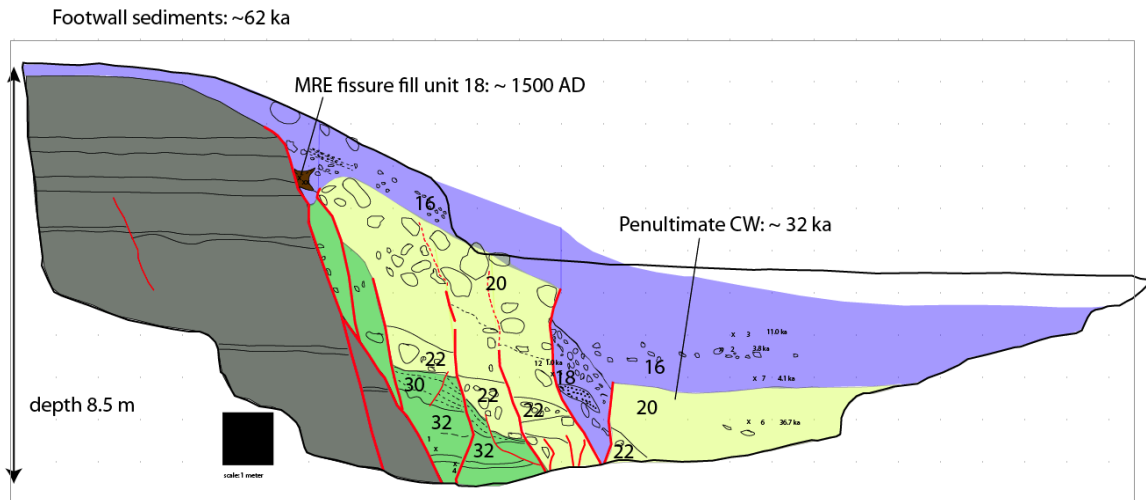


Figure 2 Incline Village Fault Trench Log. This is the south wall inverted, event ages are indicated, along with the sample locations.

Earthquake Chronology

The earthquake chronology is constrained by AMS C-14 samples from the trench and AMS C-14 and OSL dates obtained from an offshore sediment core. We interpret the age of the MRE at approximately 1500AD constrained by the youngest sample (1299-1424 AD) from the upper fissure fill [unit 18]. This fissure fill formed at the westernmost fault strand near the center of the scarp. The fissure fill material consists of organic rich A-horizon soil material from which 4 samples were dated. The charcoal sampled from this fissure consisted of large angular pieces, several cm in size, that have experienced minimal transport. Offshore we observe a submerged lake terrace deformed only by the MRE dated at 19.2 ka. The 19.2 ka age of this surface is based on a sediment core taken on the east shore of Lake Tahoe and correlated to this location based on the LiDAR bathymetry and seismic stratigraphy (Kent et al., 2005, Dingler et al., 2009). Onshore the penultimate event colluvial wedge deposits contain a single C-14 sample dated at 36.7 ka. The overlying MRE colluvial wedge deposits contain samples ranging up to 11 ka in age.

Considering that we have a more reliable age estimate from the youngest fissure fill C-14 dates at 1500 AD, we can conclude that reworking of charcoal in this distal portion of the CW is common. The majority of C-14 samples in the distal portion of the MRE CW are 3-4 thousand years older than the MRE event, and applying this lag time to the penultimate CW age estimate results in an age estimate of ~ 32 ka for the penultimate event. The third event is bracketed between the penultimate event age and the age of the footwall sediments. We were unable to obtain C-14 samples from these deposits. These footwall sediments are shallow water lacustrine deposits that are consistent with lake level high stand. A chronological candidate for this high stand can be found in the highest and oldest moraine at Meeks Bay is 62 ka old based on Be cosmogenic surface exposure dating of large boulders (Howle et al., 2005). Supporting evidence for this event chronology is the extent of soil development on the top of each CW deposit, and

complete lack thereof everywhere else except the stable footwall surface. The buried soil on the distal portion of the penultimate wedge consists of a ~ 30 cm thick soil. The soil development on the third event CW extends throughout the entire deposit. By far the greatest amount of soil development is observed at the top of the scarp on the stable footwall, where soil development extends to a depth of over 2 meters. Although difficult to quantify these buried soils attest to long periods of relative landscape stability between earthquakes.

Our preferred event ages are 0.5 ka for the MRE, 32 ka for the penultimate event and 36.7 ka to 62 ka for the third event (Figure 3).

Earthquake Magnitude and Vertical Slip Rate

The most robust measurement that we can contribute bearing on the earthquake magnitudes is that the Incline Village fault produces 3.7 m average vertical slip per event with a minimum of 3.5 m and a maximum of 4.2 m for individual events, measured onshore at a single point. Combined with the recurrence rate this results in a vertical slip rate of 0.11 mm/year, that is consistent with the low end of the 19.2 ± 1.8 ka estimate of 0.12-.3 mm/year. The difference of these rates can be understood in two ways: 1) the onshore rate is based on a narrow aperture observation and may not include all the slip; 2) the onshore rate may be more representative because it is over a longer term of ~ 32 ka, and includes a full seismic cycle. The offshore rate is an overestimation because it does not take into account ~ 13 ka portion of the interseismic cycle from 32 ka to 19 ka. The maximum vertical displacement of the IVF must be greater than 4.2 m. None of the well documented historical Basin and Range earthquakes with a maximum throw greater than 4.2 m was less than 7.2 Mw. Based on comparisons to historical ruptures and their

average and maximum displacements (Wesnousky, 2008) the Incline Village fault releases its strain in Mw 7.1 earthquakes (Mw 6.8 –7.4). The minimum magnitude required to produce these displacements appears better constrained than the maximum magnitude. Empirical earthquake rupture relationships on Basin and Range normal faults (Wesnousky, 2008) predict that this magnitude of slip is associated with a rupture length of 41 km; the mapped length of the IVF is 15 km.

Summary

The observation that the last three events on the IVF resulted in large displacements from 3.5 to 4.2 m, indicates that strain release is accomplished in large magnitude earthquakes in the 6.8 to 7.4 Mw range. As this is the shortest and least active of three major faults in the basin with little paleoseismic data, one should expect potentially higher magnitudes on the NTF and WTF. The long recurrence adequately explains the lack of large historical earthquakes in the Lake Tahoe basin.

The predicted rupture length of 41 km is significantly longer than the mapped IVF (15 km) and considering the proximity and overlapping orientation of the NTF and MRF zones at normal distances to the semi parallel oriented fault strands of 0.8 km, and 4.5 km, respectively (Figure 1). Based on these step distances one cannot dismiss the possibility of multiple segment ruptures (Wheeler, 1987, Wesnousky, 1994, Zhang et al., 1999). The NT to WTF distance is 1 km. The overlapping fault lengths of the IVF and NT faults is 27 km. Fault mapping utilizing the recent bare earth LiDAR, combined with field validation shows the NT extending onshore as laterally discontinuous fault scarps

that intersect the IVF. The geomorphic expression of these scarps suggests they may have formed during the IVF MRE \sim 500 yrs ago. The combined overlapping lengths including the WTF are over 59 km. The Mount Rose Fault zone has a length of 20 km. Although there is no direct MRE estimate for the NTF, the RI is on the order of 10 ka based on the cumulative vertical displacement for the past 60 ka of 21 m (Kent et al., 2005, Dingler et al., 2009). Considering that the IVF appears to have a rupture length that is significantly greater than its length, it appears most likely that the Incline Village fault does not rupture alone, and likely in concert with the NT, WTF and possibly MRF. Considering that the IVF has a long RI, it seems notable that the MRE age range, at 500 years BP, is permissible to be the same as the Genoa fault MRE (Ramelli et al, 1999), and the Mount Rose fault MRE (Bell et al., 1984). Whether or not the IVF MRE was part of a multi-segment rupture that included other faults it certainly suggests that earthquake behavior in this region may be temporally and spatially clustered analogous to the Central Nevada Seismic Belt, where between 1915 and 1954, a sequence of 7 large magnitude earthquakes occurred (Bell et al., 2004).

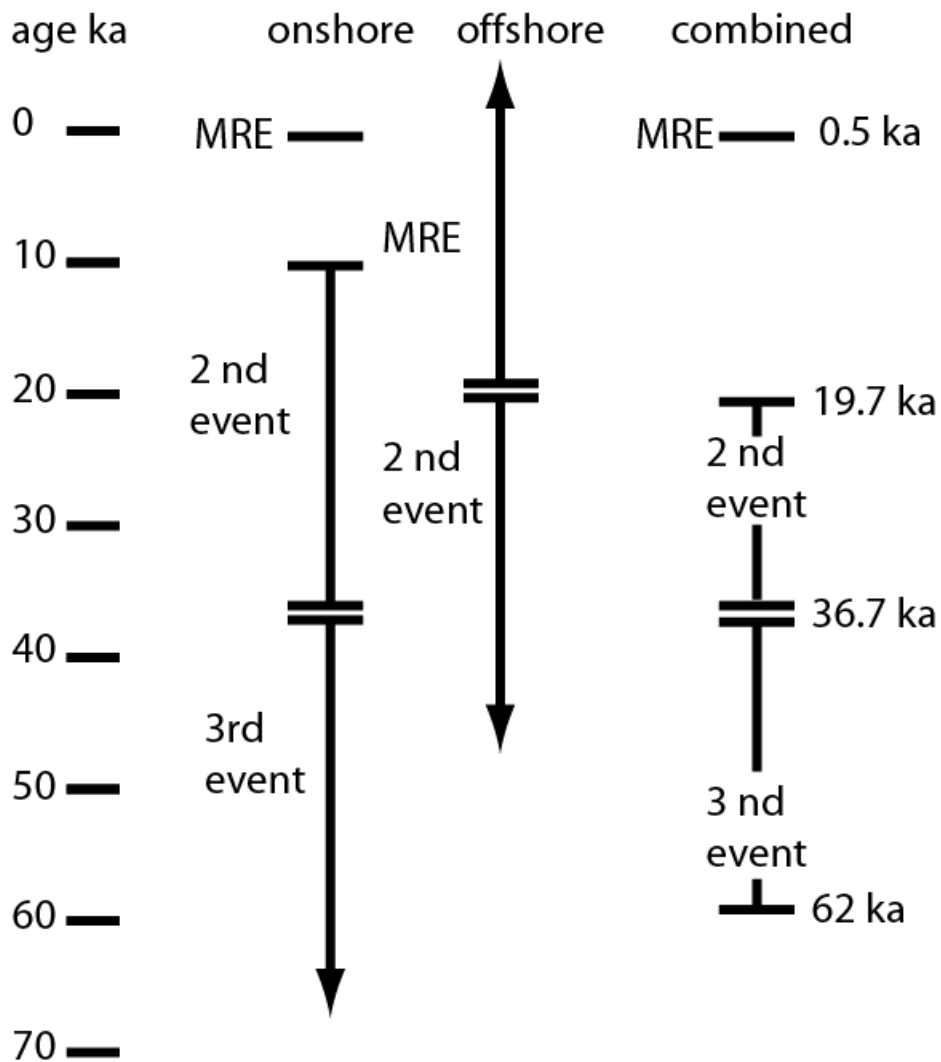


Figure 3 Event Chronology. The age ranges of the observed events are shown for the onshore, offshore and combined records. Improvements at different age bounds are realized.

References

Bell, J.W. Slemons, D.B., and Wallace, R.E., 1984, Roadlog for Neotectonics of Western Nevada, fieldtrip 18, ed. J. Lintz, Jr., Geol. Soc. Amer., annual meeting guidebook, v.5, p. 425-472.

Bell J. W., Caskey, S. J., Ramelli, A. R., Guerrieri, L. 2004, Pattern and Rates of Faulting in the

Central Nevada Seismic Belt, and Paleoseismic Evidence for Prior Beltlike Behavior Bulletin of the Seismological Society of America, Vol. 94, No. 4, pp. 1229–1254.

Brothers, D. S., Kent, G. M., Driscoll, N. W., Smith, S. B., Karlin, R., Dingler, J. A., Harding, A. J., Seitz, G. G., and Babcock, J. M., 2009, New constraints on deformation, slip rate, and timing of the most recent earthquake on the West Tahoe---Dollar Point Fault, Lake Tahoe Basin, California: Bulletin of the Seismological Society of America, v. 99, no. 2A, p. 499---519.

Dingler, J., Kent, G., Driscoll, N., G., Babcock, J., Harding, Seitz, G., A., Karlin, B., Goldman, C. 2009, A high-resolution seismic CHIRP investigation of active normal faulting across the Lake Tahoe basin, California-Nevada, Geol. Soc. of Amer. Bul., v.121, no.7/8, p. 1089-1107.

Howle, J. F., Finkel, R. C., Seitz, G., 2005, Cosmogenic exposure ages for Tioga and Tahoe age moraines at Meeks Bay, Lake Tahoe, California, abstr., Geol. Soc. Amer., v. 37, 7, pp. 2321.

Kent, G. M., Babcock, J. M., Driscoll, N. W., Harding, A. J., Dingler, J. A., Seitz, G. G., Gardner, J. V., Mayer, L. A., Goldman, C. R., Heyvaert, A. C., Richards, R. C., Karlin, R., Morgan, C. W., Gayes, P. T., and Owen, L. A., 2005, 60 k.y. record of extension across the western boundary of the Basin and Range province: Estimate of slip rates from offset shoreline terraces and a catastrophic slide beneath Lake Tahoe: Geology, v. 33, no. 5, p. 365-368.

Ramelli, A. R., Bell, John W., dePolo, Craig M., Yount, James C., 1999, Large-magnitude, late Holocene earthquakes on the Genoa Fault, west-central Nevada and eastern California: Bulletin of the Seismological Society of America, v. 89, no. 6, p. 1458-1472.

Wesnousky, S. G., and Jones, C. H., 1994, Oblique slip, slip partitioning, spatial and temporal changes in the regional stress field, and the relative strength of active faults in the Basin and Range, western United States: Geology, v. 22, no. 11, p. 1031-1034.

Wesnousky, S. G., 2008, Displacement and Geometrical Characteristics of Earthquake

Surface Ruptures: Issues and Implications for Seismic Hazard

Analysis and the Process of Earthquake Rupture, Bulletin of the Seismological Society of America, Vol. 98, No. 4, pp. 1609–1632.

Wheeler, R.L., 1989. Persistent segment boundaries on Basin and Range normal faults. U.S. Geol. Surv. Open-File Rep. 89-315, 432–444.

Zhang a P., F. Mao , D.B. Slemmons, 1999, Rupture terminations and size of segment boundaries from historical earthquake ruptures in the Basin and Range Province, Tectonophysics 308, 37–52.

LiDAR-Assisted Identification of an Active Fault near Truckee, California

by L. E. Hunter, J. F. Howle, R. S. Rose, and G. W. Bawden

Abstract We use high-resolution (1.5–2.4 points/m²) bare-earth airborne Light Detection and Ranging (LiDAR) imagery to identify, map, constrain, and visualize fault-related geomorphology in densely vegetated terrain surrounding Martis Creek Dam near Truckee, California. Bare-earth LiDAR imagery reveals a previously unrecognized and apparently youthful right-lateral strike-slip fault that exhibits laterally continuous tectonic geomorphic features over a 35-km-long zone. If these interpretations are correct, the fault, herein named the Polaris fault, may represent a significant seismic hazard to the greater Truckee–Lake Tahoe and Reno–Carson City regions. Three-dimensional modeling of an offset late Quaternary terrace riser indicates a minimum tectonic slip rate of 0.4 ± 0.1 mm/yr. Mapped fault patterns are fairly typical of regional patterns elsewhere in the northern Walker Lane and are in strong coherence with moderate magnitude historical seismicity of the immediate area, as well as the current regional stress regime. Based on a range of surface-rupture lengths and depths to the base of the seismogenic zone, we estimate a maximum earthquake magnitude (M) for the Polaris fault to be between 6.4 and 6.9.

Introduction

The U.S. Army Corps of Engineers (USACE) owns and operates an inventory of more than 600 dams across the United States (Halpin and Ferguson, 2007) and recently implemented the Dam Safety Assurance Program (DSAP) to evaluate risks to the public posed by these dams as a consequence of potential failure. The Martis Creek Dam, located ~6 km east of Truckee, California (Fig. 1a) and ~56 km upstream from Reno, Nevada, is one of ten dams nationwide that received a Dam Safety Action Class I ranking, indicating urgent and compelling safety concerns.

Completed in 1972, the Martis Creek Dam is a zoned earthen embankment with an impervious blanket on the upstream side. Glacial outwash underlies most of the dam's foundation and left abutment, while layered volcanic rock underlies the right abutment (U.S. Army Corps of Engineers, 1966, 1972; Latham, 1985; and Sylvester *et al.*, 2007). A history of excessive seepage during reservoir test fillings, including sand boils along the downstream toe and seepage along stratigraphic contacts adjacent to the spillway, have prevented the USACE from allowing the dam to fulfill its full design function of flood control and limited water storage. These leakage problems are compounded by a significant seismic hazard (I. Wong *et al.*, unpublished report, 2008, see Data and Resources), based on the presence of two fault zones within 10 km of the dam that may be capable of generating horizontal ground motion near $1.0g$, thereby exceeding the seismic-design criteria of $0.1g$.

As part of the DSAP evaluation, we acquired airborne LiDAR (Light Detection and Ranging) to provide a detailed digital elevation model to support geotechnical investigations, evaluate surface morphology, and provide data for potential inundation modeling. These data were augmented with aerial photographic imagery and demonstrate the presence of numerous geomorphic features suggestive of Late Pleistocene or Holocene fault surface rupture in the vicinity of Martis Creek Dam.

The LiDAR data presented in this paper were collected in two independent surveys. Merrick and Company flew approximately 260 km² in 2006 for the Truckee Donner Public Utility District (TDPUD); the LiDAR data they collected were to be used for infrastructure planning. The second dataset was collected in 2008 by Towell Surveying Mapping and GIS Services and extends from the southern portion of the Sierra Valley to the north shore of Lake Tahoe. The second dataset was collected specifically for tracing the Polaris fault to the northwest and southeast. Both Merrick and Towell generated bare-earth point-cloud datasets (classified ground data) using TerraScan software (see Data and Resources section). For the Merrick data, spot spacing of the laser first returns is approximately 4.3 ± 0.3 points/m², and the classified ground data are 2.4 ± 0.3 points/m², based on the average density of points from nine randomly selected 2.59-km² tiles. The Towell first-return data have a spot spacing of 3.4 ± 0.9 points/m², and the classified

ground data are 1.5 ± 0.4 points/m², based on the average density of points from eight randomly selected 0.84-km² tiles. The classified point-cloud data were imaged using Quick Terrain (QT) Modeler (see [Data and Resources](#) section) and modeled as a gridded surface. QT Modeler develops the surface by performing a Delaunay triangulation that mathematically creates a triangulated irregular network (TIN) from the original points. The software then creates the grid according to a user-defined grid spacing (here typically on the order of 1–2 m; however, for large scale maps, we used a spacing of up to 5 m). Elevations from the TIN are then assigned to the vertices of the grid and are retriangulated to create a smoothed topographic surface. No additional processing was applied to the data.

Analysis of these data, using pseudosun angles, vertical exaggeration of 2–2.5 times, oblique perspectives, and extracted profiles revealed a series of linear features across

the landscape that extends from southeast of the Martis Valley for at least 35 km northwest past Kyburz Flat (Fig. 1). Along this trace are conspicuous geomorphic and hydrologic features such as scarps in unconsolidated alluvium, elongate depressions aligned with adjacent linear mounds, anomalously deep hillside troughs with little or no contributing drainage area, closed depressions, linear swales, mole tracks, offsets of fluvial terrace risers, right-lateral deflections of creeks and river courses, and shutter ridges, as well as springs and linear seeps. We interpret these features as evidence for a previously unrecognized right-lateral strike-slip fault associated with the northern Walker Lane fault zone and herein refer to this likely active fault as the Polaris fault. Polaris is the name of a 19th-century townsite that was located along the Truckee River, where we have identified progressive tectonic displacement of late Pleistocene terrace risers and other tectonic geomorphic features. The goal of

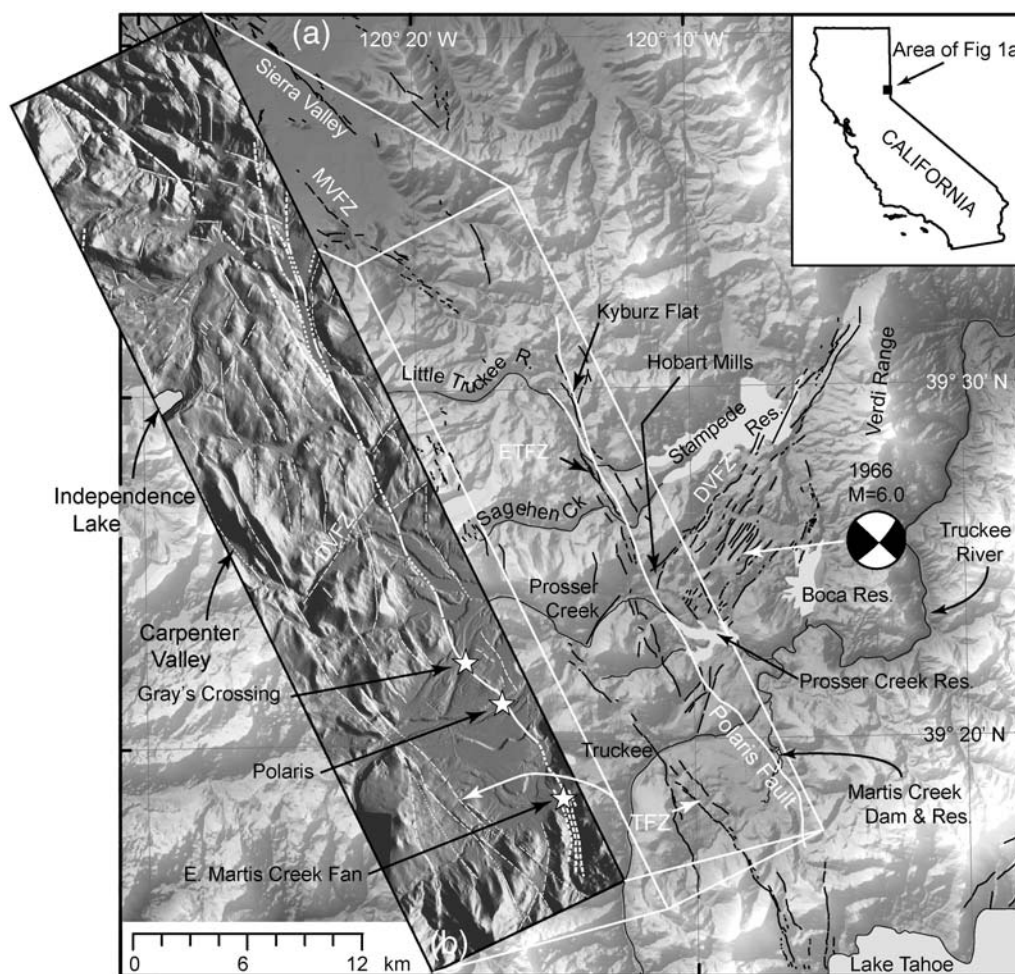


Figure 1. (a) Regional map showing location of the Polaris fault and selected regional faults from the U.S. Geological Survey (USGS) Quaternary Fault and Fold Database (see [Data and Resources](#)) and from I. Wong *et al.* (unpublished report, 2008, see [Data and Resources](#): MVFZ, Mohawk Valley fault zone (#25b, from USGS); TFZ, Truckee fault zone (A005, from Wong *et al.*); ETFZ, Eastern Truckee fault zone (A005b, from Wong *et al.*); and DVFZ, Dog Valley fault zone (#27, from USGS). Also shown are the focal plane mechanism and epicenter location of the 1966 Truckee *M* 6.0 earthquake. (b) Inset topographic map showing high-resolution airborne LiDAR imagery, the Polaris fault (bold white line) and subordinate structures (broken white lines) mapped using bare-earth LiDAR. Stars indicate the locations of the East Martis Creek fan, Polaris, and Gray's Crossing sites; also shown are the Martis Creek Dam, and selected geographic features. Illumination is from the east–northeast.

this paper is to characterize the Polaris fault and the previously unrecognized regional extent, provide a preliminary estimate of the minimum tectonic slip rate, discuss the local fault patterns with respect to the regional tectonic setting, and discuss the length of the Polaris fault and seismic hazard implications.

Regional Tectonic Setting

Geodetically measured right-lateral motion between the Pacific and North American plates is primarily accommodated on the San Andreas fault system, with ~20%–25% of the deformation occurring east of the Sierra Nevada microplate (SNP) in the western Basin and Range Province (Dixon *et al.*, 1995; Thatcher *et al.*, 1999; Bennett *et al.*, 2003; Hammond and Thatcher, 2004, 2007). Space geodesy reveals that the SNP is translating northwestward (N40°–45°W) at ~14 mm/yr (Dixon *et al.*, 2000), relative to the stable North American plate (Fig. 2a). The SNP slip vector is oblique (~45°W) to the roughly north-striking normal faults along the eastern escarpment of the SNP and subparallel to the dextral faults of the Walker Lane (Stewart, 1988; Faulds *et al.*, 2005; Wesnousky, 2005b), creating a zone of dextral shear or dextral transtension (Unruh *et al.*, 2003; Schweickert *et al.*, 2004; Wesnousky, 2005a). Thus, the northwest-striking dextral faults of the Walker Lane are favorably oriented to accommodate the large-scale Pacific–North American plate motion east of the SNP. The broader Walker Lane–eastern California shear zone (ECSZ in Figure 2a) is thought to represent an incipient transform plate boundary (Faulds *et al.*, 2005; Wesnousky, 2005a; Faulds and Henry, 2008), and the complexity of faulting within this

region is largely attributed to the immature stage of this evolution (Schweickert *et al.*, 2004; Wesnousky, 2005b).

The Truckee basin lies on the boundary between the SNP and the northern Walker Lane (NWL), also known as the Sierra Nevada—Great Basin boundary zone (SNGBBZ in van Wormer and Ryall, 1980; Zoback, 1989; Schweickert *et al.*, 2004). At the latitude of the Truckee basin, the NWL is a ~100-km-wide zone of spatially overlapping and kinematically linked northwest-trending right-lateral strike-slip faults, northeast-trending left-lateral strike-slip faults, and north-striking normal faults (Bennett *et al.*, 2003; Schweickert *et al.*, 2004; Faulds *et al.*, 2005; Wesnousky, 2005a). It is in this complex zone that ~20% of the dextral shear between the Pacific and North American plates is accommodated with a pronounced increase occurring west of 119° in the NWL (Thatcher *et al.*, 1999; Bennett *et al.*, 2003; Hammond and Thatcher, 2004, 2007). Between the SNP and ~119°W, this increased rate equates to 6 ± 2 mm/yr of dextral shear in the general vicinity of the Truckee basin and Polaris fault (Thatcher *et al.*, 1999; Dixon *et al.*, 2000; Hammond and Thatcher, 2004, 2007).

In the NWL and the region surrounding the Lake Tahoe and Truckee basin, the dextral transtension appears to be accommodated by spatially and temporally alternating modes of faulting (Wright, 1976; Stewart, 1988; Zoback 1989; Ichinose *et al.*, 1998; Schweickert *et al.*, 2004). In the current-mode conjugate zones of high-angle strike-slip faults (northeast-trending left-lateral and northwest-trending right-lateral) accommodate north–south shortening and east–west extension. In the alternate mode, extension generally perpendicular to the range fronts is accommodated by the normal faults (Ichinose *et al.*, 2003). In the current stress regime (for zones of conjugate strike-slip faulting like the Truckee basin), the maximum principal stress vector (S_1 , or P -axis) is oriented horizontally (S_H) in a north–south vertical plane, the intermediate stress vector (S_2) is vertical (S_V) in the same north–south plane, and the minimum principal stress (S_3 , or T -axis) is oriented east–west perpendicular to the latter plane ($S_H > S_V > S_3$). In the normal faulting mode, the relative magnitudes of S_1 and S_2 switch within the north–south vertical plane (S_1 vertical), while the T -axis remains oriented east–west ($S_V > S_H > S_3$). According to Zoback (1989), the magnitudes of S_1 and S_2 are similar (i.e., $S_H \approx S_V$), which is consistent with temporally and spatially alternating modes of strike-slip and normal faulting that collectively accommodate the regional transtension over geologic time scales.

Glacial and Alluvial Stratigraphy

The fault-bounded Truckee basin, including the Martis Valley and main stem of the Truckee River east of the town of Truckee, is filled with a succession of Pleistocene ground moraines in the western half and coeval glacial outwash terraces in the eastern half (Birkeland, 1963, 1964). The oldest recognized glacial deposit and corresponding outwash in

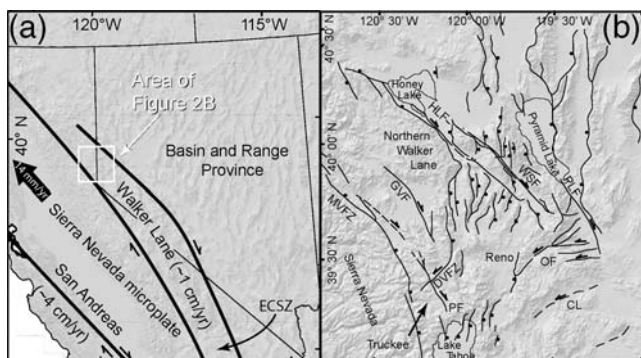


Figure 2. (a) Generalized location map showing the Walker Lane–eastern California shear zone (ECSZ) in relation to the Basin and Range Province, the Sierra Nevada microplate, and the San Andreas fault system, as well as relative motions and rates. (b) Generalized fault map of the northern Walker Lane: PF, Polaris fault; DVFZ, Dog Valley fault zone; MVFZ, Mohawk Valley fault zone; GVF, Grizzly Valley fault; HLF, Honey Lake fault; WSF, Warm Springs Valley fault; PLF, Pyramid Lake fault; OF, Olinghouse fault; and CL, Carson lineament. Barbed arrows show relative motion of strike-slip faults, and black dots show down-thrown side of normal faults. Parts (a) and (b) are modified from Faulds and Henry (2008).

the Truckee basin is the locally named Donner Lake age deposits, followed by the Tahoe age deposits, and finally the youngest Tioga age deposits (Table 1). During the various glacial stages, sediment-laden braided streams aggraded thick sequences of alluvium (fill terraces) that blanketed the bottom of the basin downstream of the corresponding glacial margin, leaving a relatively smooth outwash plain. During deglaciations, these streams incised their channels, leaving prominent terrace risers. Because each successive glaciation was significantly smaller (climatically and spatially) than the previous one (Birkeland, 1964), a nested fill-terrace sequence is preserved in the eastern Truckee basin. Hence, the highest outwash terrace on the basin margins corresponds with the oldest Donner Lake glaciation, and the subsequent Tahoe and Tioga glacial deposits are inset at progressively lower elevations (Birkeland, 1964), as shown in the profile in Figure 3. It is in these deposits that the Polaris fault has geomorphic expression, which is imaged by the high-resolution LiDAR data.

Polaris Fault Characterization

The Polaris fault strikes northwest across the Truckee basin and deforms multiple middle-to-late Pleistocene glacial and fluvial deposits, providing a means to assess important fault characteristics. Our studies focus on three areas that present the most obvious data for evaluating the Polaris fault: (1) the East Martis Creek fan, where the fault is characterized by discontinuous north–northwest (NNW)-trending scarps; (2) the Polaris site, where middle-to-latest Pleistocene terrace risers are right-laterally offset; and (3) the tectonically

complex Gray's Crossing site, where the primary north-west-striking Polaris fault right-laterally displaces an early-to-middle Pleistocene terrace riser, a northeast-trending conjugate strike-slip fault left-laterally offsets the same terrace riser, and small thrust faults accommodate north–south shortening along a westerly bend in the Polaris fault (Fig. 1).

East Martis Creek Fan

The East Martis Creek fan is located ~2.5 km south of Martis Creek Dam. *Sylvester et al. (2007)* has mapped the fan as Holocene alluvium, while I. Wong *et al.* (unpublished report, 2008, see [Data and Resources](#)) suggest that the fan is late Pleistocene in age based on the relative stratigraphic position (Figs. 1, 4, and 5). Initial inspection of the LiDAR data revealed a linear feature that cuts across the alluvial fan and continues in bedrock for at least 2 km to the south. At the head of the fan, the fault is expressed as a set of discontinuous, west–southwest-facing scarps aligned in a NNW orientation (Figs. 4 and 5). The scarps project northwest through a closed depression and linear graben. At the closed depression, the fault splays and the subparallel fault strands diverge along strike, bounding a linear graben. The eastern strand displays down to the southwest separation, where it projects southeast across the head of the East Martis Creek fan in the vicinity of small thermal springs and seeps. Near the northwestern end of the graben, springs discharge from both fault strands (Figs. 4 and 5). Over the length of the graben, the western strand displays down to the northeast morphology and projects northwest through a narrow topographic notch and across Martis Creek Reservoir toward the Martis Creek Dam and spillway (Figs. 4 and 5).

In the fall of 2008, the main fault strand at the head of the fan and the lower fault strand with the prominent vegetation lineament (Fig. 4) were trenched in a paleoseismic investigation (see Fig. 5 for trench locations). Both trenches exposed faults revealing thickening of the stratigraphy across the fault, which is interpreted as indicating strike-slip displacement (*Crampton et al., 2009* and *Hunter et al., 2009* trench logs). The upper trench documents ~1.5 m of apparent vertical separation from at least three events, while the lower trench revealed ~0.4 m of apparent vertical separation from two events. Structural and stratigraphic relationships in the trenches (near vertical faults at depth that flower near the surface and across fault thickening of the alluvial deposits) are indicative of lateral displacement, but the amount of displacement is unknown. In both trenches, chronologic control was inconclusive; however, in the lower trench, latest Pleistocene to early Holocene alluvium was displaced.

From the graben southeast of Martis Creek reservoir (trending northwest across the reservoir bottom), the only geomorphic evidence of the fault is a broad swale (Fig. 4) that is roughly aligned with the next geomorphic expression of the fault between the western abutment of the dam just north of the spillway. Here, a lineament exposed in the Donner Lake outwash terrace is on strike with the lineament

Table 1
Stratigraphic Relationships of Selected Quaternary Map Units, Correlation to Marine Oxygen Isotope Stages (If Applicable), and Age Constraints

Map Unit	Marine Oxygen Isotope Stages (MIS) and Age Estimates (ka)
Qtio—Tioga outwash	MIS 2 (13–32) * > 14.0 [†] to < 25.2 ± 2.5 [‡]
Qtao—Tahoe outwash	MIS 4 (64–75) **§ > 62.0 ± 3.1 ~70 ± 5 [§] 64.0 ± 3.5 to 76.4 ± 3.8 [#]
Qdl—Donner Lake glacial deposits	≥ MIS 6? (128–195)* > 131**
Qdlo—Donner Lake outwash	~400 to 600 ^{††}
Qpc—Prosser Creek alluvium	≤ 1.3 Ma ^{‡‡}

*Shackleton and Opdyke (1976).

[†]Clark and Gillespie (1997).

[‡]Bursik and Gillespie (1993).

[§]Gillespie (1991).

^{||}Howle *et al.* (2005).

[#]James *et al.* (2002).

**Yount and La Pointe (1997).

^{††}Birkeland (1964).

^{‡‡}Birkeland (1963).

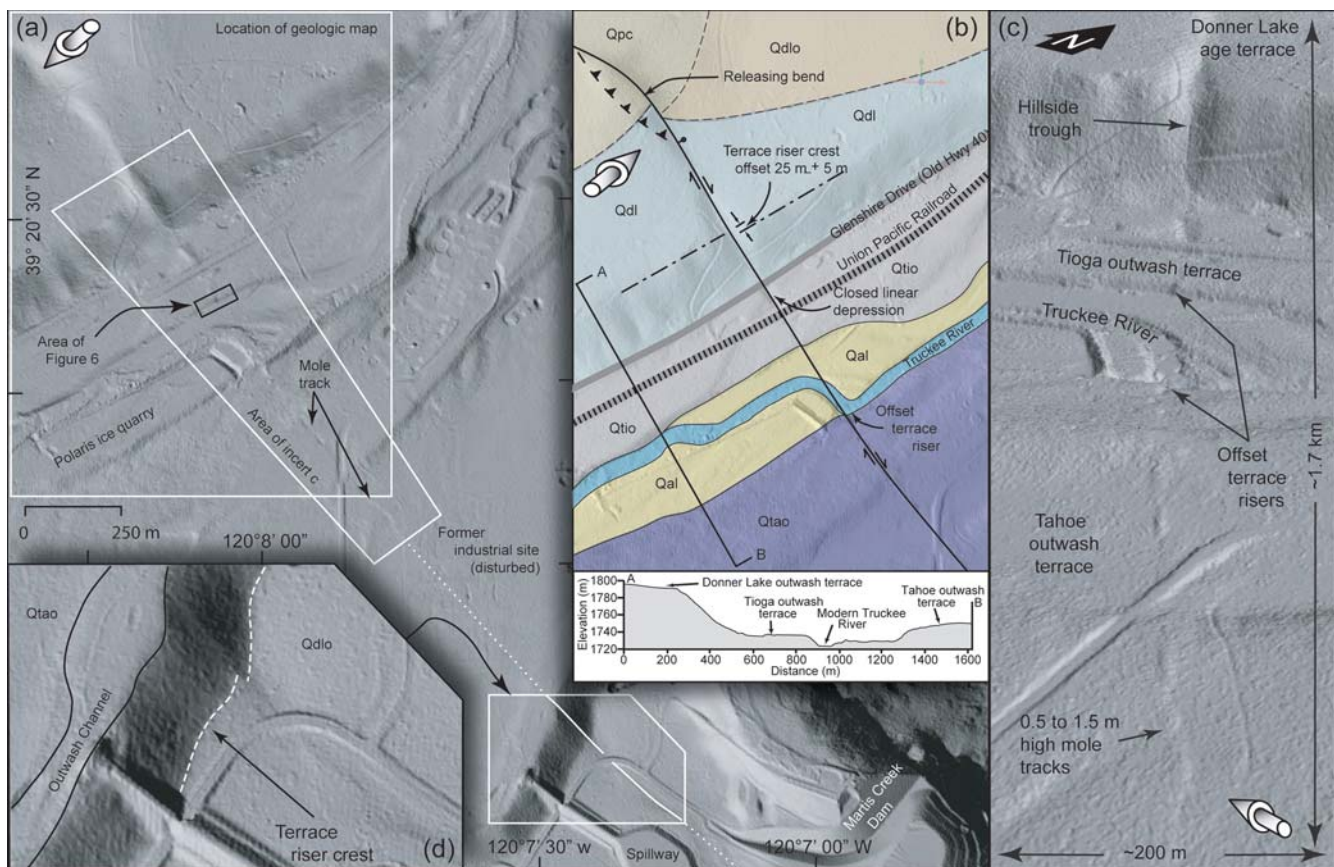


Figure 3. (a) Plan view bare-earth LiDAR image extending from the Martis Creek Dam spillway to the Polaris site (vertical exaggeration is 2). White boxes show the locations of insets (b, c, and d), and black box shows location of Figure 6. The shaded-gray arrow indicates illumination angle. (b) Geologic map modified from Birkeland (1964) superimposed on a LiDAR image. Map units: Qal, Holocene alluvium undifferentiated; Qtio, Tioga age glacial outwash; Qtao, Tahoe age glacial outwash; Qdl, Donner Lake age glacial outwash; Qdlo, Donner Lake age glacial outwash; Qpc, Prosser Creek alluvium, see Table 1 for ages. Solid lines in (a) and (b) are mapped fault traces (dashed where approximately located, dotted where inferred, barbs on up-thrown side, ball and bar on down-dropped side). Also shown are fault related geomorphic features and selected geographic features. Profile A-B shows the nested relationship of Late Pleistocene fill terraces. (c) Oblique aerial view of bare-earth LiDAR imagery showing along strike fault-related geomorphic features through the Polaris site. View is looking northwest. (d) High-resolution enlargement of subtle scarp cutting across Donner Lake-age glacial outwash terrace and terrace riser, as well as offset terrace riser crest.

southeast of the reservoir (Figs. 3 and 4). A northwest-striking down to the southwest scarp cuts the flat-lying terrace before crossing down the ~38-m-high terrace riser to the Tahoe age outwash terrace (Fig. 3d). From the base of the Donner Lake terrace riser, along strike to the northwest, the trace of the fault is obscured for ~400 m where it passes through a former industrial site that has been graded. Northwest of this disturbed area, approaching the Polaris site, the fault is expressed as a 450-m-long linear mole track (Fig. 3a,c). This narrow linear feature stands 0.5–1.5 m above the smooth Tahoe outwash surface and is probably a product of coseismic deformation of the outwash alluvium.

Polaris Site

At the Polaris site (Figs. 1 and 3), the modern Truckee River is flanked by a Tioga-age glacial outwash terrace on the north side and Tahoe-age outwash terrace on the south

side (Birkeland, 1964). These fill terraces have been incised by glacial melt water that formed linear fluvial terrace risers (Fig. 3b). The Polaris fault orthogonally offsets the terrace risers on both the northern and southern sides of the Truckee River in a right-lateral sense. The modern Truckee River is right-laterally deflected to the southeast, along the trace of the fault, and has eroded the offset terrace risers on the south side of the river, modifying the tectonic morphology and thus negating a reliable strain analysis. However, on the north side of the Truckee River, the offset terrace riser has been largely unaffected by Holocene stream processes. At this site, we utilize the relatively pristine morphology and a maximum age of the terrace to estimate a minimum tectonic slip rate.

Using Offset Terrace Risers to Determine a Slip Rate. Because of their simple geometry, offset fluvial terrace risers are one of the most common landforms used to determine rates of strike-slip faulting (Harkins and Kirby, 2008; Gold *et al.*,

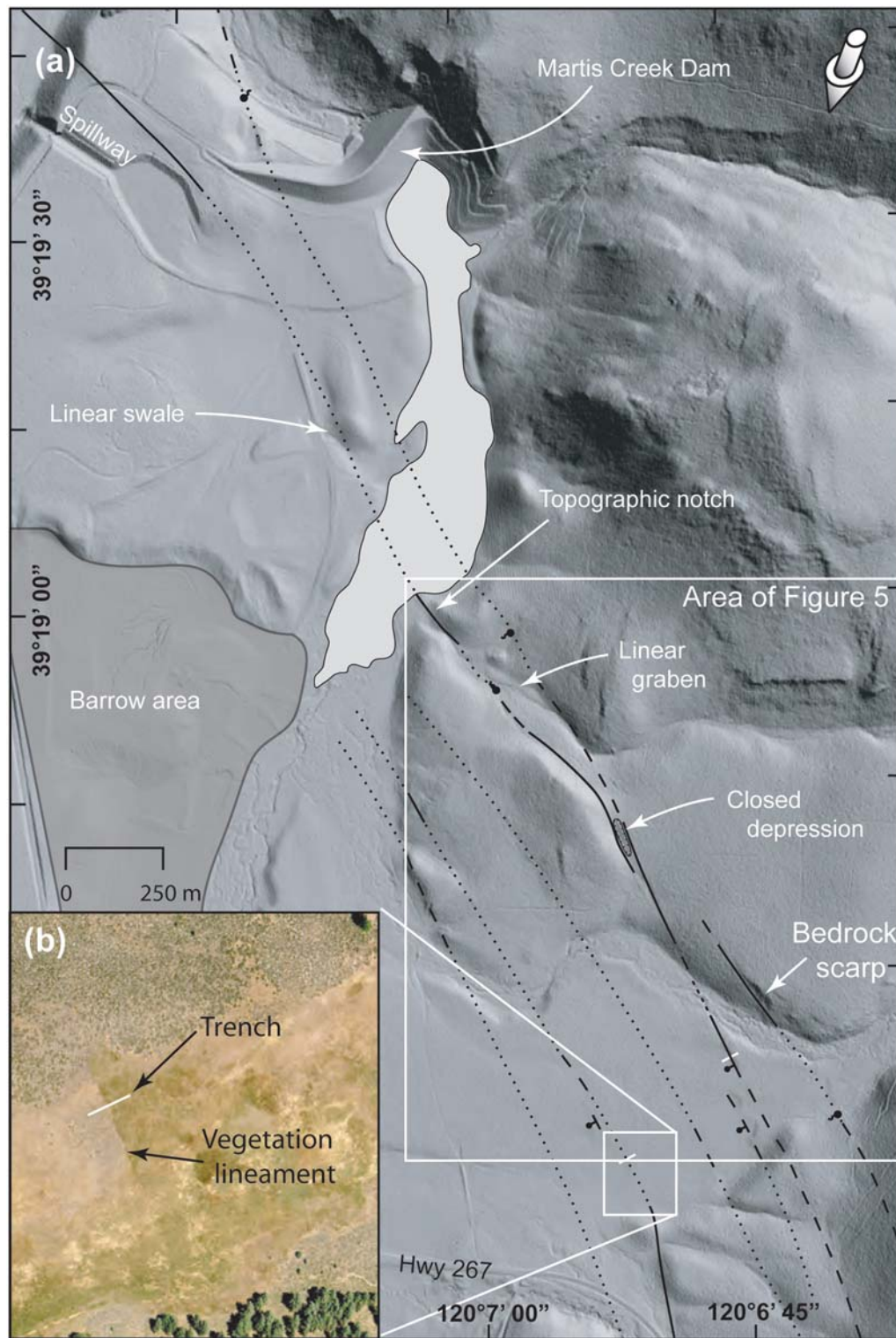


Figure 4. (a) Plan-view bare-earth LiDAR image, extending from the East Martis Creek fan to the Martis Creek Dam spillway (vertical exaggeration is 2). See Figure 1 for regional location. Gray-shaded arrow (upper right) indicates direction of illumination. Also shown are mapped fault traces (dashed where approximately located, dotted where inferred, ball-and-bar on down-dropped side), as well as fault-related geomorphic and hydrologic features described in the text. Locations of two paleoseismic trenches are depicted by thin white lines, and white boxes show the area of inset (b) and Figure 5. (b) Plan-view aerial photograph, showing vegetation lineament on south side of the East Martis Creek fan and location of trench (see text and Fig. 5).

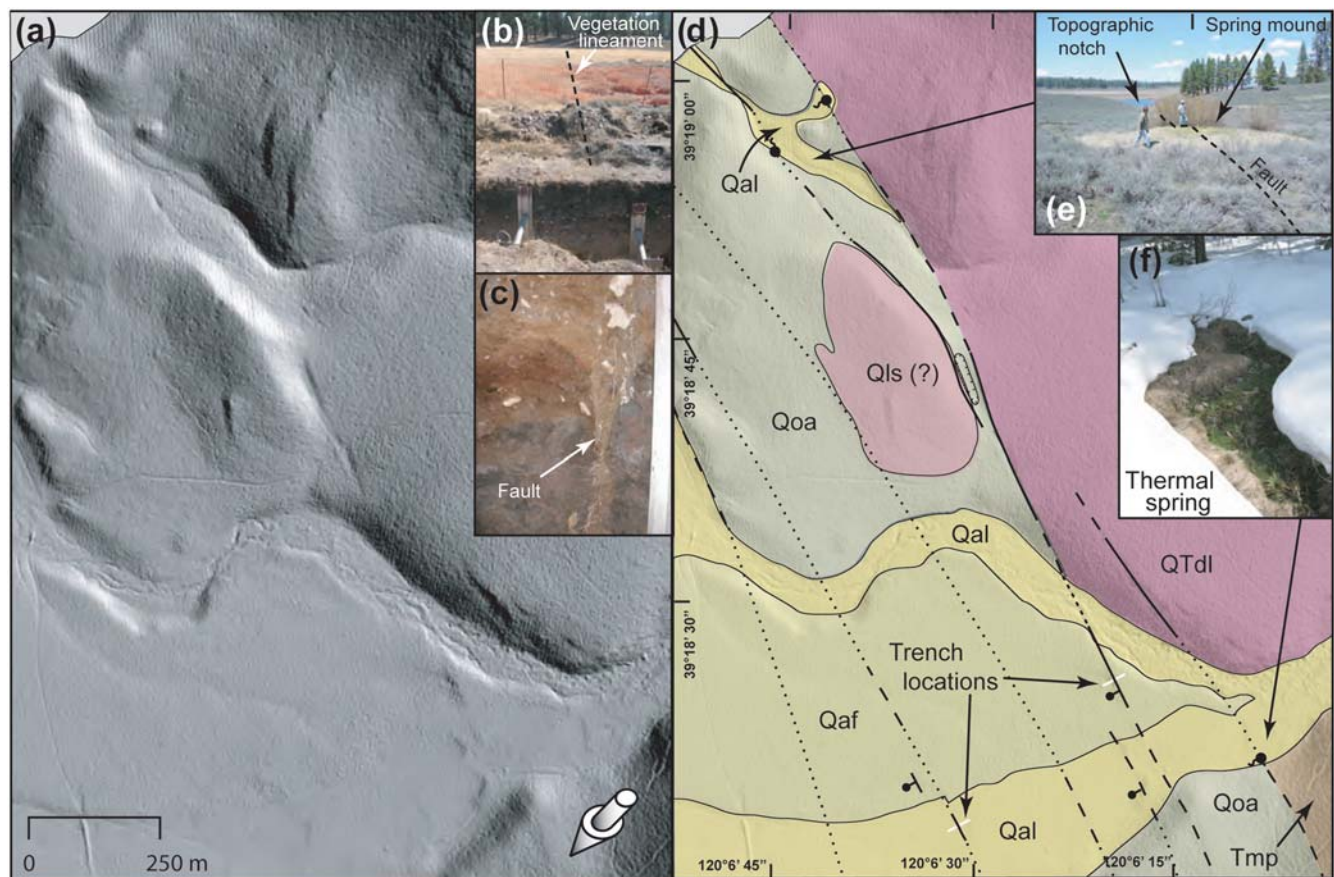


Figure 5. (a) Plan-view bare-earth LiDAR image of the East Martis Creek fan (vertical exaggeration is 2). Gray-shaded arrow indicates direction of illumination. (b) View of vegetation lineament on fan surface in background and trench in foreground. (c) Vertical fault exposed in trench and aligned with vegetation lineament on fan surface. Aluminum shoring on the right side of insets (b) and (c) are the same. (d) Geologic map (modified from [Sylvester et al., 2007](#), and [Crampton et al., 2009](#)) superimposed on LiDAR image. Qal, Holocene alluvium undifferentiated; Qaf, alluvial fan deposits (see text for age discussion); Qoa, dissected older alluvium; Qls, landslide deposit; QTdl, Dry Lake andesitic flows; Tmp, Martis Peak pyroclastic andesite. Solid black lines are mapped fault traces (dashed where approximately located, dotted where inferred, ball and bar on down-dropped side). Photograph insets: (e) spring mound located on fault trace at northwest end of linear graben and (f) thermal spring near the head of the East Martis Creek fan.

2009, and references therein). “Determining a rate of strike-slip faulting is simple in principle because only two measurements are needed: a magnitude of offset and the time over which this displacement accrued” ([Cowgill, 2007](#), p. 240). The terrace riser genesis is described in the next paragraph, and the underlying assumptions for using the offset Tioga-age terrace risers as a geomorphic strain marker are listed in the following section ([Geomorphic Criteria for Using Offset Terrace Risers as Strain Markers](#)).

First, aggradation of the Tioga-age glacial outwash terrace (fill terrace) occurred during the glaciation due to glacial quarrying that increased the sediment flux, as well as increasing the sediment size (i.e., cobbles and boulders) to the proglacial stream ([Birkeland, 1964](#) and [Hallet et al., 1996](#)). Subsequently, deglaciation melt water increased the stream discharge while, at the same time, sediment size and flux decreased, causing the stream to incise the risers and abandon the terrace ([Birkeland, 1964](#) and [Repka et al., 1997](#)). Thus, we assume that the terrace riser formed by the end of the Tioga deglaciation and that the abandonment

age of the Tioga outwash terrace represents a maximum limiting age of the tectonic displacement (i.e., the riser formed first, followed by tectonic displacement).

Age of Offset Tioga Deposit. In the central Sierra Nevada, the Tioga deglaciation is constrained at 14.5 ± 0.5 ka, based on radiocarbon dating of basal sediments impounded by terminal moraines ([Clark and Gillespie, 1997](#)). In the northern Sierra Nevada, 35 km west of the Polaris site, [James et al. \(2002\)](#) demonstrate that the Tioga deglaciation occurred by 14.1 ± 1.5 ka, using cosmogenic beryllium-10 (^{10}Be) exposure dating of a glacially striated bedrock valley. [Benson et al. \(1990\)](#) provide detailed radiocarbon data constraining fluctuations of Pleistocene Lake Lahontan. These data, specific to the Truckee River drainage, suggest that locally the Tioga deglaciation may have ended at 13.3 ± 0.3 ka. Based on these studies, we consider the maximum age of the terrace riser to be 14 ± 1.5 ka (i.e., the maximum limiting age of tectonic displacement). This scenario of constraining the slip rate with a maximum limiting age or an upper terrace

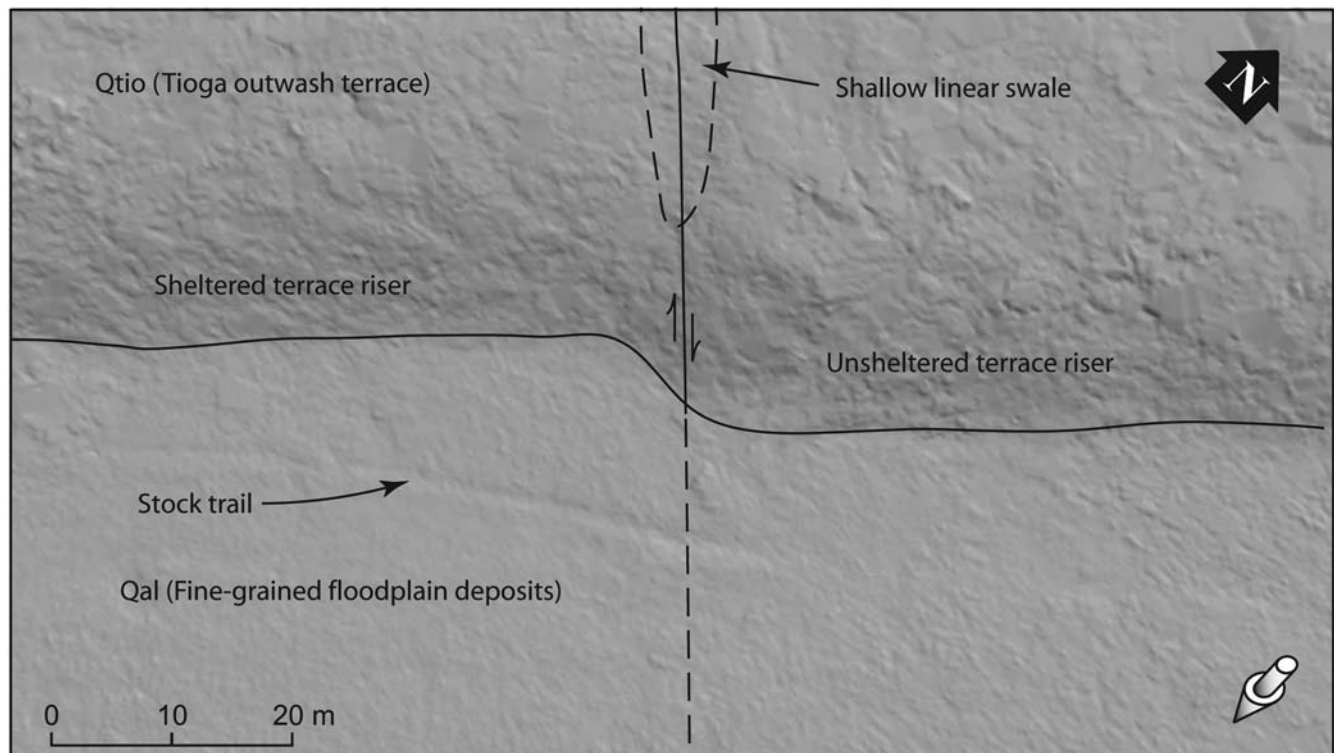


Figure 6. Plan-view bare-earth T-LiDAR image of offset Tioga-age terrace riser at the Polaris site, showing the linear and parallel offset terrace risers on either side of the fault trace and abrupt truncation of the risers in a narrow fault zone. See Figure 3 for location. There is no vertical exaggeration. Shaded-gray arrow indicates illumination angle.

reconstruction produces a conservative minimum slip rate estimate (Cowgill, 2007; Gold *et al.*, 2009).

Geomorphic Criteria for Using Offset Terrace Risers as Strain Markers. At the Polaris site, the modestly degraded morphology of the Tioga terrace riser is attributed to the youthful age that makes this locality well suited as a geomorphic strain marker. Geomorphic criteria that support the use of these offset risers as a strain marker are: (1) The offset terrace risers are linear for ~60 m on either side of the fault. (2) The terrace risers are abruptly and orthogonally truncated in a narrow fault zone ~10 m wide. (3) The riser faces (planar section below the degraded riser crest and above the colluvial wedge at the base) on either side of the fault are nearly parallel (strikes differ by $< 6^\circ$) and have very similar dips (dips vary by $1\text{--}1.5^\circ$). (4) Across-fault correlation of terrace risers is straightforward because there is only one on either side, they are equal in height on either side of the fault, and the curvature of the degraded riser crests are similar. In addition, we assume that no Holocene lateral erosion of the risers has occurred because the modern Truckee River flows away from the offset riser (Fig. 3). Furthermore, during major flood events, relatively slow and weak overbank flow has deposited a veneer of fine sand and silt that has partially buried the colluvial wedge at the base of the terrace riser rather than eroding the riser base. If the unsheltered riser (downstream riser nearest the active channel) were laterally eroded by Holocene stream processes, then the magnitude of

the displacement would be reduced, further making the slip rate estimate a minimum.

Reconstructing Offset Terrace Risers. Displacements of fluvial terrace risers are usually reconstructed in a two-dimensional (2D) plan-view map from total station and/or GPS survey data (e.g., Cowgill, 2007; Harkins and Kirby, 2008). Surveyed points typically represent field interpretations of the riser crest and/or base location that are best fit to a line, which is then projected to an intersection with the fault trace to determine piercing points on a plan-view map. Uncertainties in the cumulative displacement associated with this type of 2D reconstruction range from 3 to 7 m (Cowgill, 2007; Harkins and Kirby 2008; Gold *et al.*, 2009).

At the Polaris site, Howle *et al.* (2009) utilized high-resolution ground-based LiDAR imagery of the offset terrace risers (Fig. 6) to mathematically reconstruct pristine terrace-scarp morphologies on both sides of the fault, define coupled sets of piercing points, and extract a corresponding displacement vector (Fig. 7). By using ground-based or terrestrial LiDAR (T-LiDAR), thousands of points per square meter were collected over an ~12,000-m² area surrounding the offset terrace risers. Vegetation was removed from the point-cloud data using TerraScan software (see [Data and Resources](#) section) and large protruding boulders were manually deleted to generate a bare-earth point-cloud dataset with an average data density of over 240 points per square meter.

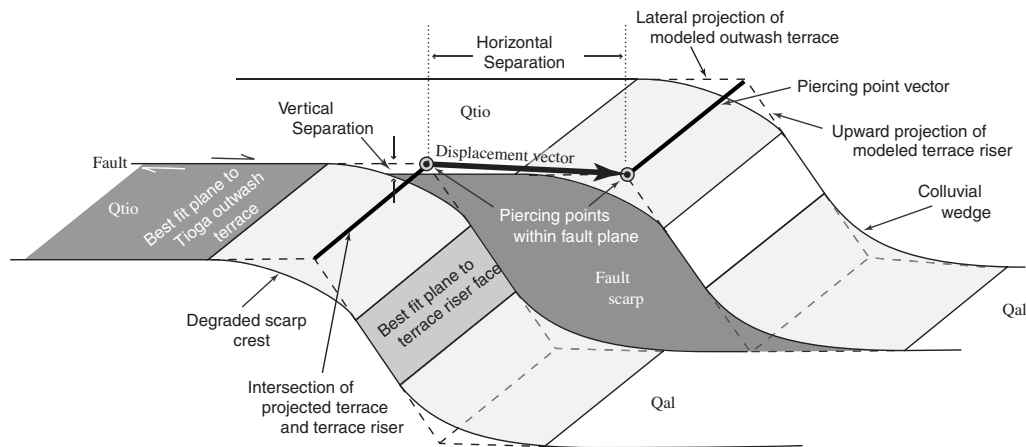


Figure 7. Oblique schematic of offset terrace riser depicting the mathematical 3D reconstruction used to define piercing points and to extract a corresponding displacement vector. See text for discussion. (Figure is not to scale.)

The orientation of the Polaris fault was approximated in the 3D data as a vertical plane that bisects the offset terrace risers, as well as linear swales and tectonic depressions along strike in the Tioga outwash terrace. Using the 3D T-LiDAR image, piercing points to the vertical fault plane were mathematically extracted from the geometry of the geomorphic elements on either side of the fault. On each side of the fault, equal area planes were best fit (with a linear regression) to the outwash terrace as well as the terrace riser face, excluding points on the degraded scarp crest and colluvial wedge at the riser base (Fig. 7). Then, on each side of the fault, the model outwash terrace plane was projected laterally and the modeled terrace riser face was projected upward to a virtual intersection, creating vectors. These constructed vectors were projected to an intersection with the fault plane, defining statistically significant piercing points. The distance between the coupled set of piercing points, within the plane of the fault, yields the cumulative displacement vector (Fig. 7).

To assess the variability of the modeled tectonic displacement due to surface roughness and nonlinearity of the landform, Howle *et al.* (2009) generated a suite of ten displacement models by systematically incorporating larger areas into the model domain symmetrically about the fault. The area modeled for individual outwash terraces on either side of the fault ranged from 800 m² to 2200 m², and the area modeled for individual terrace risers ranged from 240 m² to 440 m². On average, for the ten displacement models, 95% of the point cloud (laser ground points) was within ± 0.06 m of the best-fit modeled plane.

This numerically robust technique has the statistical advantage of integrating hundreds of thousands of data points collected over a broad area, which collectively yield the cumulative displacement vector. The total number of ground points used to constrain the displacement vectors in the ten models ranges from over 163,000 to nearly 303,000. Results of the ten displacement models yields an average cumulative displacement of 5.6 m (1 Std Dev = 0.31 m). The 3D modeling reveals a small down to the east component of displace-

ment that is not readily apparent in the field. The average ratio of horizontal-to-vertical displacement at this site is $\sim 12:1$. However, this is not a far-field strain (i.e., not representative of regional transtention) but rather a localized feature related to a releasing bend along the Polaris fault (see discussion in the section [Progressive Deformation at the Polaris Site](#)).

Using the 5.6 ± 0.3 m of cumulative displacement and the maximum limiting age of 14 ± 1.5 ka discussed previously in this article, Howle *et al.* (2009) estimate a preliminary minimum fault slip rate of 0.4 ± 0.1 mm/yr for the Polaris site since the Pleistocene–Holocene boundary. While this estimate is not a long-term time-averaged rate, it currently represents the only slip-rate estimate for the Polaris fault.

Progressive Deformation at the Polaris Site. Along strike, 300 m northwest of the Tioga-age offset, there is a larger dextral offset of an ~ 35 -m-high terrace riser (Fig. 3) eroded into middle(?)-Pleistocene Donner Lake ground moraine. Because of the large uncertainties in the absolute age of the Donner Lake age deposits (Table 1), no slip rate estimate is inferred here. However, the scarp crest and terrace riser are right-laterally offset by 25 ± 5 m, demonstrating progressive deformation relative to the post-Tioga offset. In addition, ~ 5 m of down to the east displacement is observed in the relatively flat upper terrace of Donner Lake ground moraine (Fig. 3).

In between these offset scarp crests, the fault is expressed as an anomalously deep and broad hillside trough that has no appreciable colluvium at the base but rather a closed linear depression (Figs. 3 and 8). These anomalous features and the previously mentioned down to the east displacement are interpreted as being caused by collapse of the unconsolidated deposits into the fault zone along a releasing bend in the fault. Just north of this hillside trough is a westerly bend in the fault trace (Figs. 3 and 8). Along the convex east side of the bend (releasing bend), right-lateral displacement opens a void, creating a localized zone of extension that allows for the collapse of unconsolidated deposits into the

fault zone and produces oblique normal separation of the Donner Lake terrace. Conversely, on the concave west side of the bend (restraining bend), right-lateral displacement creates a localized zone of shortening, highlighted here by an elongated contractional ridge in the Prosser Creek alluvium, which we interpret to be a product of a shallow-thrust fault.

The Gray's Crossing Site

The Gray's Crossing site is located approximately 2.5 km northwest of the Polaris site and 4 km northeast of Truckee, California (Figs. 1, 8, and 9). The site is on a relatively flat upland surface comprised of early-Pleistocene Prosser Creek alluvium, which is thought to be coeval with the 1.3-Ma Hirschdale basalt (Birkeland, 1963; Sylvester *et al.*, 2007). Incised into the Prosser Creek alluvium is a linear north–northeast-trending paleochannel (Figs. 8 and 9) mantled with Donner Lake–age outwash, indicating the abandoned channel was cut during the Donner Lake glaciation (Birkeland, 1964).

At the Gray's Crossing site (Figs. 8 and 9), the airborne LiDAR imagery reveals a prominent west–northwest (WNW)-trending lineament that is expressed as a series of aligned, elongated depressions (as much as 4 m deep) and linear

mounds up to 5 m high (mole tracks). These features could be the result of small-scale fault-plane undulations where releasing bends create depressions and restraining bends cause contraction, forming the linear mounds. Of special interest are (1) the offset terrace risers along the western side of the paleochannel (Fig. 9), where the northwest-striking Polaris fault right-laterally offsets the fluvial terrace riser by 58 ± 4 m, and (2) to the south is a 43 ± 5 m left-lateral offset of the same terrace riser on a northeast-trending conjugate strike-slip fault (Fig. 9). Because of the large uncertainties in the absolute ages of the upper-terrace Prosser Creek alluvium (age based on stratigraphic correlation) and the lower Donner Lake outwash (Table 1), no slip rate estimates are inferred at this site. I. Wong *et al.* (unpublished report, 2008, plate 2; see [Data and Resources](#)) recognize this conjugate lineament and depict it in the southwestern corner of the broadly distributed and discontinuous Dog Valley fault zone (DVFZ in Fig. 1a).

The Gray's Crossing site lies at the western end of an ~2-km-long section of the Polaris fault that strikes more westerly than northwesterly (Figs. 1 and 8). Right-lateral motion creates a localized zone of contraction along this bend in the Polaris fault. Localized shortening is evident in the north and

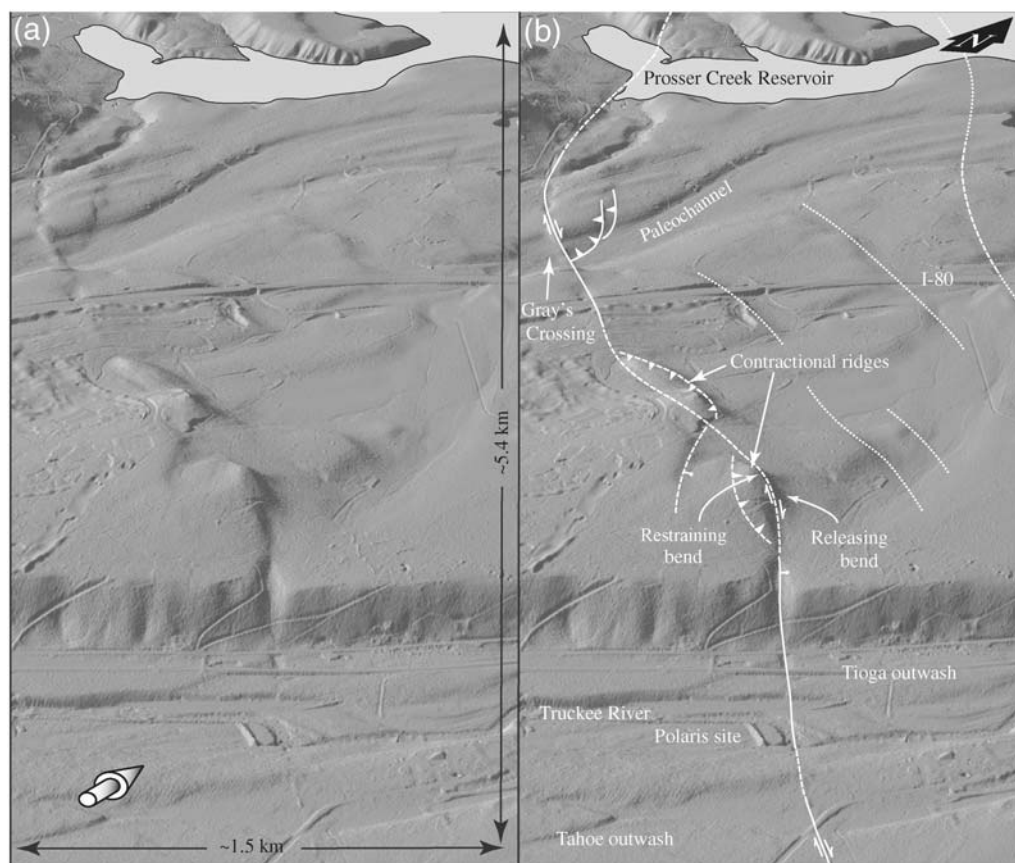


Figure 8. (a) Oblique aerial view of bare-earth LiDAR imagery, extending from the Polaris site to Prosser Creek Reservoir. (View is looking to the northwest.) Shaded-gray arrow indicates illumination angle (vertical exaggeration is 2). (b) Solid white lines are mapped fault traces (dashed where approximately located, dotted where inferred, bars on up-thrown side, ball and bar on down-dropped side). Also shown are fault-related geomorphic features and selected geographic features. See text for discussion of releasing and constraining bends.

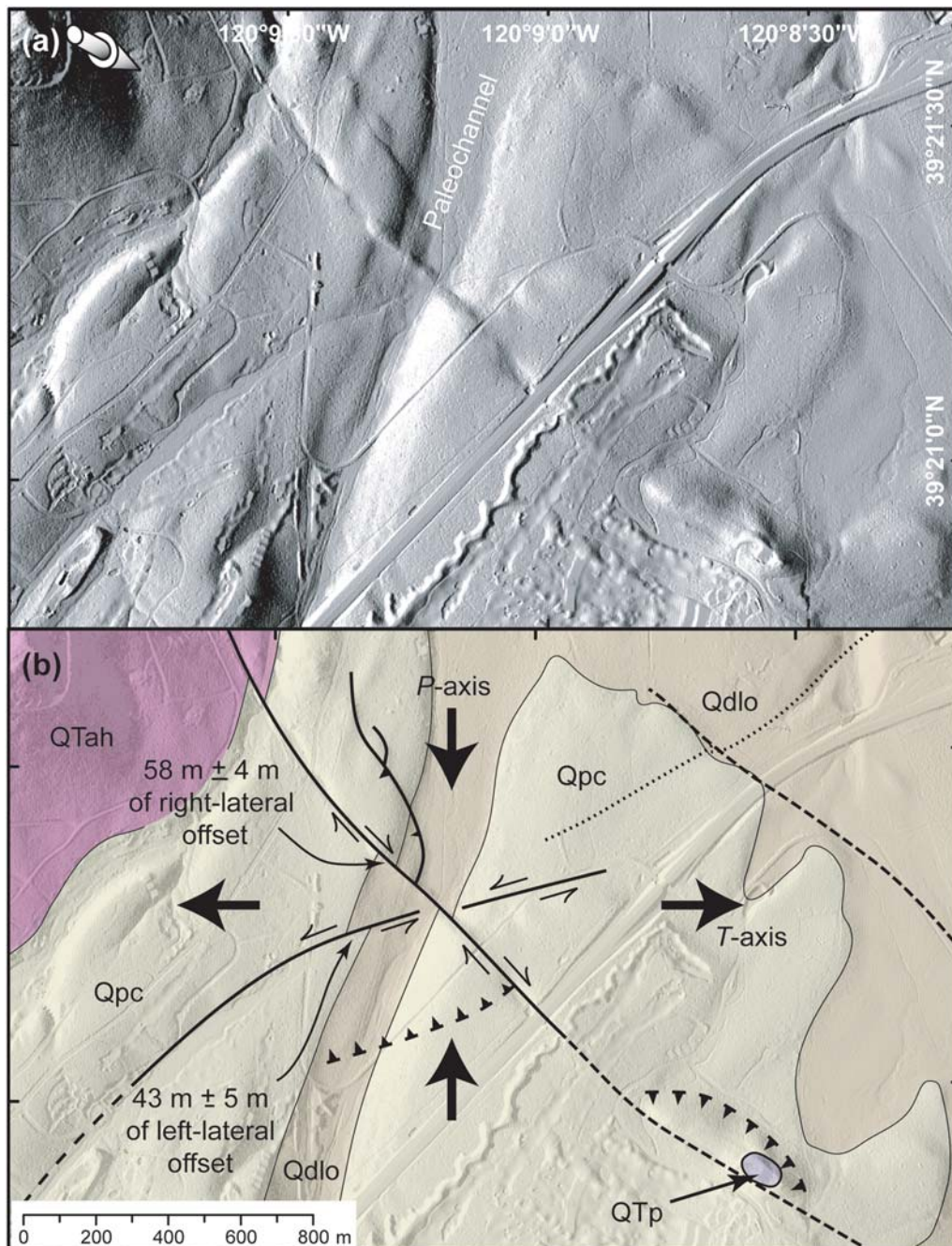


Figure 9. (a) Plan-view bare-earth LiDAR imagery of the Gray's Crossing site. Shaded-gray arrow indicates illumination angle (vertical exaggeration is 2). (b) Geologic map modified from Birkeland (1964) and superimposed on a LiDAR image. Map units: Qdlo, Donner Lake age glacial outwash; Qpc, Prosser Creek alluvium; QTp, Polaris basalt; and QTah, Alder Creek olivine basalt. Solid black lines are mapped fault traces (dashed where approximately located, dotted where inferred, barbs on up-thrown side), and bold arrows indicating the orientation of the maximum principal stress (*P*-axis) and minimum principal stress (*T*-axis) vectors. (See text for discussion.)

south quadrants, defined by the intersection of the Polaris fault and its conjugate (Fig. 9). Along the west side of the northern quadrant, an apparent reverse fault is represented by a sharp, arcing topographic lobe that intersects the main fault at almost a right angle before turning to the northwest and extends for several hundred meters in an orientation that is subparallel to the main fault (Fig. 9). In the southern fault-bounded quadrant, just east of the paleochannel, is a conspicuous 5-m-high

rise in the otherwise flat-lying Prosser Creek alluvium. We interpret this rise (or fold?) as a product of a blind thrust fault that accommodates the localized north–south contraction.

Northwest of the Gray's Crossing site, the Polaris fault strikes north–northwesterly and is expressed as a 7-m-high northeast-facing scarp coincident with a sharp tonal–vegetation lineament south of Prosser Creek Reservoir (Figs. 8 and 10g). Where Alder Creek enters the southwest



Figure 10. (a) Location map showing plan-view bare-earth LiDAR imagery from Prosser Creek Reservoir to Sagehen Creek northwest of Hobart Meadow. White boxes show the locations of insets (b and c), (d and e), and (g). Bare-earth images have a vertical exaggeration of 2.5, and shaded-gray arrows indicate illumination angle. Solid black lines are mapped fault traces (dashed where approximately located, dotted where inferred, ball and bar on down-dropped side). (b) Enlargement of bare-earth image near Hobart Mills with (c) annotations of features discussed in the text. (d) Enlargement of the bare-earth imagery along the west side of Prosser Creek Reservoir with (e) annotations of features discussed in the text and topographic profile of the scarp in alluvium, showing location of linear seep shown in (f). (g) Aerial photograph showing tonal-vegetation lineament coincident with the fault scarp southwest of Prosser Creek Reservoir. (DVFZ, Dog Valley fault zone; ETFZ, Eastern Truckee fault zone.)

arm of Prosser Creek Reservoir, a fault-shunted ridge right-laterally deflects the course of Alder Creek to the south (Fig. 10d,e). On the south and north sides of the peninsula between the arms of Prosser Creek Reservoir, the Polaris

fault is expressed as a set of deeply incised gullies with little or no contributing drainage areas (Fig. 10e). These anomalously deep gullies are aligned with the fault and have preferentially developed along it. Between these conspicuous

drainages is an ~8-m-high northeast-facing scarp in unconsolidated alluvium (see profile in Fig. 10e). Along the base of the scarp is an ~200-m-long linear seep with lush grass surrounded by sage brush (Fig. 10f). Dissecting the peninsula, east of the fault, is a beheaded former channel of Prosser Creek that apparently was abandoned due to right-lateral displacement along the Polaris fault (e.g., Oskin *et al.*, 2007). Along strike to the northwest and southeast of Hobart Mills, the modern course of Prosser Creek is fault-controlled before it enters the northwest arm of Prosser Creek Reservoir (Fig. 10a). Just south of Hobart Mills, the 25-m-high terrace riser flanking the north side of Prosser Creek is dextrally offset ~100 m where the Polaris fault makes a slight bend to the NNW (Fig. 10c). At Hobart Mills is a 400-m-long NNW-striking linear scarp with a spring issuing from the base that is aligned with the offset terrace riser to the south-southeast SSE. Where the scarp projects to the NNW, it is aligned with subtle breaks in slope on intervening ridges and a tonal-vegetation lineament that continues NNW along the linear west side of Hobart Meadow (Fig. 10c).

Complex Zone of Spatially and Kinematically Linked Faults. Between Hobart Mills and Hobart Meadow is a complex zone where three faults with different orientations and senses of displacement intersect (Fig. 10a). Just north of Hobart Mills, the main trace of the northeast-striking left-lateral DVFZ, as mapped by Hawkins *et al.* (1986), abruptly terminates where it intersects the NNW-striking right-lateral Polaris fault on the south side of Billy Hill (Fig. 10a). To the WNW of Hobart Mills, there is an apparent 1.5 km gap in the DVFZ (Hawkins *et al.*, 1986; Olig *et al.*, 2005) before resuming along the northeast-trending reach of Prosser Creek (Fig. 1). Using the high-resolution LiDAR imagery, we interpret that the main trace of the DVFZ is right-laterally offset ~0.9 km by the Polaris fault between Hobart Mills and Hobart Meadow (Fig. 10a,c). Approximately 1 km south of Hobart Meadow and west of Hwy 89, the fault trace resumes and continues for 2 km along the southeast flank of the Sagehen Hills before it rejoins the northeast-trending reach of Prosser Creek, as originally mapped by Hawkins *et al.* (1986).

At Hobart Meadow, the Polaris fault intersects the Eastern Truckee fault zone (ETFZ in Figs. 1a and 10). To the south of this intersection, the ETFZ has been mapped (Birkeland, 1963; Latham, 1985) as a down to the east normal fault evidenced by ~200-m-high triangular facets on the eastern side of Alder and Prosser Hills (Fig. 10a). However, at Hobart Meadow, the strike and sense of displacement of the ETFZ changes from a north-striking down to the east normal fault to a NNW-striking fault with dextral features (Figs. 10 and 11).

Hobart Meadow is a triangular-shaped fault-bounded closed depression and forms a prominent saddle on the topographic divide between Prosser and Sagehen Creeks. A paleoseismic trench at Hobart Meadow (Melody, 2009) documents a north-striking normal fault with ~1 m of down

to the east vertical separation. Radiocarbon dating constrains one and possibly two Holocene events (<7 ka). This data demonstrate the recency of faulting in this complex zone of intersecting faults bounding the closed depression.

Tectonic Geomorphology along the Northern Extent of the Polaris Fault. From Hobart Meadow NNW to Kyburz Flat, the ETFZ as mapped by Olig *et al.* (2005) is mostly coincident with our mapping. Along this northern section, the fault leaves the Pleistocene deposits of the Truckee basin and traverses Tertiary volcanic bedrock, where it is primarily expressed as larger scale offsets and alignments of creeks and rivers (I. Wong *et al.*, unpublished report, 2008, see [Data and Resources](#)).

Northwest of Hobart Meadow, the general west-to-east trend of Sagehen Creek is offset ~1.6 km to the southeast along a fault-controlled reach on trend with the Polaris fault (Figs. 11 and 12). To the north, this lineament projects through a bedrock notch and another prominent ridge-crest saddle where Highway 89 crosses Sagehen Summit (Fig. 12). North of Sagehen Summit, the west-to-east trend of the Little Truckee River is similarly right-laterally offset for ~5 km along a NNW-trending reach (Fig. 11). The offsets and alignment of Sagehen Creek and the Little Truckee River along a NNW trend was originally recognized by William Page (cited as a written communication circa 1995 in Olig *et al.*, 2005). Along the northwest-trending reach of the Little Truckee River, I. Wong *et al.*, (unpublished report, 2008, see [Data and Resources](#)) retrodeform 5 km of right-lateral displacement based on a planimetric reconstruction of an east-west trending andesite-basalt contact, which is roughly coincident with the offset east-flowing reaches of the Little Truckee River to the northwest and southeast (Fig. 11). Along this reach of the Little Truckee River north of Sagehen Summit to Kyburz Flat are conspicuous NNW-striking geomorphic features, such as linear valley edges and linear ridges. Just north of Sagehen Summit is a narrow linear graben that is over 80 m deep with only a minor stream draining it to the north (Fig. 12). On the west side of this triangular-shaped valley is the beginning of a fault-bounded hillside bench that continues for 4 km to the NNW above the Little Truckee River valley. Near the northern end of this linear hillside bench and 45 m above the river is a small thermal spring that flows from the mapped fault trace (Fig. 12).

Where the Little Truckee River turns east and exits the northwest-trending reach, the channel character changes from a sediment-choked braided channel to a narrow bedrock channel coincident with a mapped fault trace (Fig. 12). The ponding of sediment, upstream of the mapped fault trace, can be explained by right-lateral displacement (possibly right oblique) where bedrock on the east side of the fault is shunted across the active channel, damming the river and effectively raising the bedrock sill. A right-lateral component along this mapped fault trace is demonstrated by the right-lateral deflection the Little Truckee River and the right-lateral offset of the Sagehen Creek valley to the south. Here, on the north side of

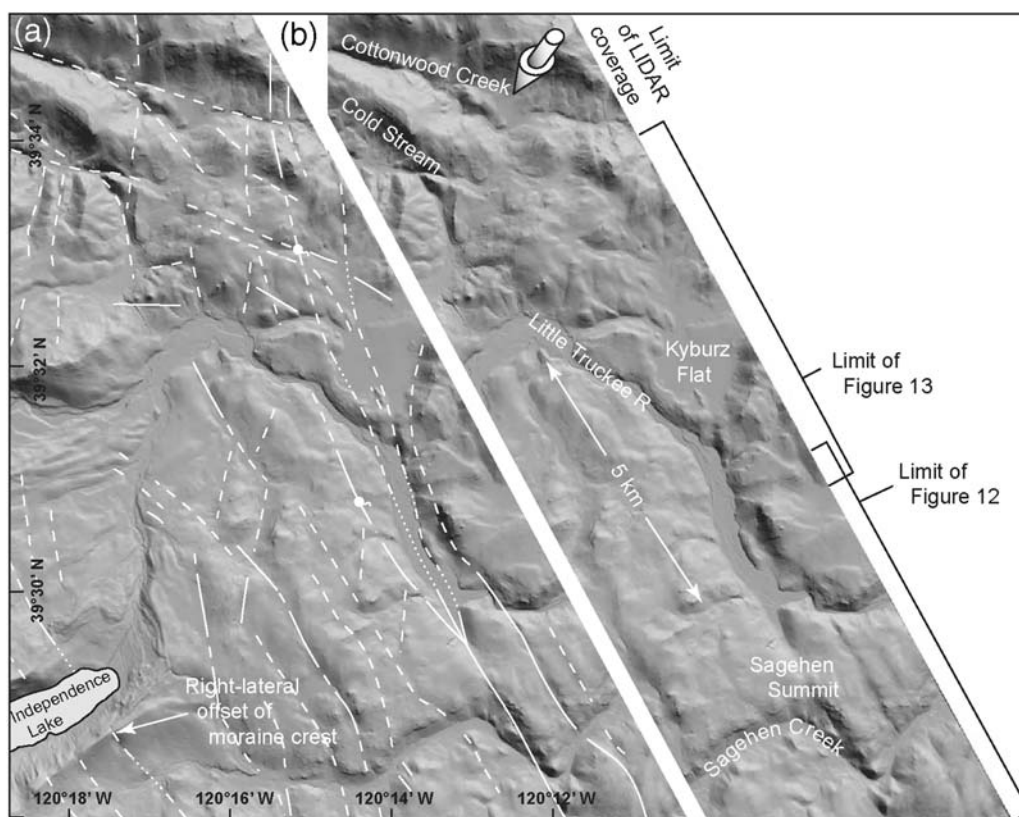


Figure 11. (a) Plan-view bare-earth LiDAR image showing overview of structural interpretations from Sagehen Creek to Cottonwood Creek. Shaded-gray arrow indicates direction of illumination (vertical exaggeration 2.5). (b) Geographic features described in the text, and northwest to southeast extent of Figures 12 and 13.

Sagehen Creek, the linear valley edge and valley wall is right-laterally juxtaposed. In addition, this northeast-trending reach of Sagehen Creek appears to be a left-lateral structure. Sinistral motion is inferred here by the northeast orientation of the linear drainage and the opposing bedrock scarps along the northwest-striking dextral fault on either side of Sagehen Creek. Left-lateral motion would induce a down to the southwest normal component north of the creek and down to the northeast normal component south of the creek, as highlighted by the illumination in Figure 12.

Collectively, these geomorphic, geologic, and hydrologic observations from Kyburz Flat to Hobart Meadow strongly suggest a structural connection with the Polaris fault to the southeast.

Distributed Nature of Faulting along the Northern Extent of the Polaris Fault. At Sagehen Summit, the Polaris fault splays with the western strand, continuing NNW, and the subparallel eastern strands striking more northerly towards Kyburz Flat, where they diverge to the north and northeast (Figs. 11, 12, and 13). The western strands display east down normal components, and the eastern strands have west down normal components, creating an extensional trough. This scenario of a splaying strike-slip fault with inward-facing normal components is an example of extensional or negative flower structure. This fault-bounded extensional trough helps

explain the wide underfit appearance of the Little Truckee River along the ~5 km NNW-trending reach.

The complex nature of the faulting at the northern end of the Polaris fault (i.e., a strike-slip fault splaying into normal faults) is noted elsewhere in the NWL, where dextral strike-slip faults are observed to end in arrays of north-striking normal faults (Faulds *et al.*, 2005; Faulds and Henry, 2008) that are similar to both the northern and southern ends of the Polaris fault.

Local Fault Patterns Relative to Regional Tectonics

At the latitude of the Truckee basin, the Polaris fault and subparallel strands (described in the following section) represent the westernmost dextral structures of the NWL. The Polaris fault fills a recognized ~35-km-long gap between the Mohawk Valley fault zone (MVfZ in Figs. 1 and 2) to the northwest and Lake Tahoe basin faults to the south (S. Olig *et al.*, unpublished report, 2005, see [Data and Resources](#)). Together, the ~85-km-long MVfZ (Page *et al.*, 1993; Olig *et al.*, 2005) and the Polaris fault define an ~120-km-long zone of dextral faults in the westernmost part of the NWL.

Throughout the NWL, where dextral strike-slip faults end, they are commonly observed to make an echelon left-steps to adjacent strike-slip faults (Faulds *et al.*, 2005;

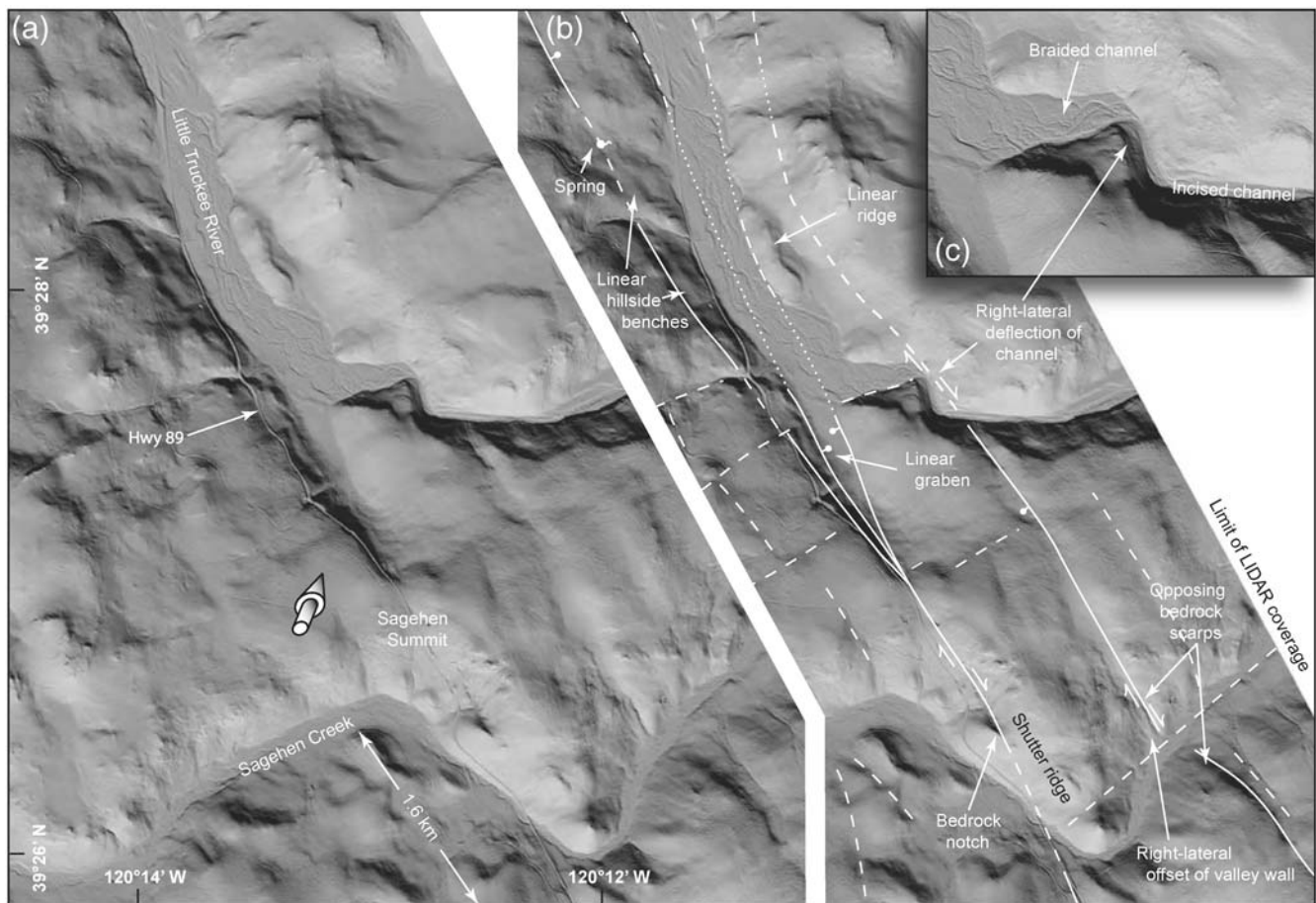


Figure 12. (a) Plan-view bare-earth LiDAR image of the area near Sagehen Summit and selected geographic features. Shaded-gray arrow indicates direction of illumination (vertical exaggeration 2.5). (b) Solid white lines are mapped fault traces (dashed where approximately located, dotted where inferred, ball and bar on down-dropped side). Also shown are fault-related geomorphic features described in the text. (c) Detailed inset showing right-lateral offset of channel coincident with mapped fault and change from braided channel to incised bedrock channel.

Faulds and Henry, 2008). However, the structural connection between the MVFZ and the Polaris fault is notably different. In this case, the MVFZ and Polaris fault appear to intersect at about 45° in a structurally complex zone between the Sierra Valley and Kyburz Flat (Fig. 1). At the northern extent of the Polaris fault, north of Kyburz Flat, the mapped NNW lineaments die out where they intersect topographically strong WNW-trending lineaments at the head waters of Cottonwood and Cold Stream Creeks (Fig. 11). These lineaments projecting out of the Sierra Valley to the SSE are the southeasternmost mapped structures of the MVFZ (Sawyer *et al.*, 1995; Grose, 2000; Sawyer and Briggs, 2001; Sawyer *et al.*, 2005), and where they die out is only 5 km from Kyburz Flat. This structurally complex zone between the Sierra Valley and Kyburz Flat is dissected by short NNW-trending lineaments that are crosscut by pervasive WNW-trending lineaments forming northwest-oriented rhombohedral shaped blocks on the scale of a few hundred meters up to ~ 2 km in length (Figs. 11 and 13). The northwest alignment of the Little Truckee River immediately west of Kyburz Flat and the southeastward projection of the linear headwaters of Cold

Stream and Cottonwood Creek (Figs. 1b and 11) are suggestive of an incipient through-going structure. Because this part of the NWL is the youngest (Faulds *et al.*, 2005; Faulds and Henry, 2008) and least well developed (Wesnousky, 2005a, 2005b), this possible connection between the MVFZ and Polaris fault is structurally immature, and it is unclear how strain is partitioned across it.

In the MVFZ to the northwest and Honey Lake fault zone to the northeast (HLF in Fig. 2b), as well as numerous other locations throughout the Walker Lane and ECSZ (Fig. 2a), regional dextral shear is partitioned across subparallel faults. At these locations the western strands form range-front normal faults (accommodating localized extension approximately perpendicular to the range front; Ichinose *et al.*, 2003), and the more active eastern strands are dextral strike-slip faults that accommodate Pacific–North American plate boundary-related shear (Wesnousky and Jones, 1994; Unruh *et al.*, 2003; Sawyer *et al.*, 2005; Wesnousky, 2005a). This same pattern is evident between the dextral Polaris fault and the normal Truckee fault zone (TFZ in Fig. 1) 7 km to the southwest, which runs between Truckee across the head of

Independence Lake 16 km to the NNW (Olig *et al.*, 2005; S. Olig *et al.*, unpublished report, 2005, see [Data and Resources](#)) and continues another 16 km NNW into the southernmost corner of the Sierra Valley (Grose, 2000).

Truckee, California lies near the southwest corner of a broad shatter zone of high-angle conjugate strike-slip faults that is roughly bounded by the Little Truckee River on the north, the main stem of the Truckee River on the south, the TFZ on the west, and the Verdi Range on the east (Fig. 1). This area is central to a broader zone referred to as the Truckee transition zone (Schweickert *et al.*, 2004) that is defined by historic northwest- and northeast-oriented seismic trends (van Wormer and Ryall, 1980; Hawkins *et al.*, 1986; Ichnose *et al.*, 1999; Schweickert *et al.*, 2004; Smith *et al.*, 2008) that generally lack surface expression. At the core of this zone are the through-going Polaris fault and the conjugate DVFZ (Figs. 1a and 2b). Near Hobart Mills (Fig. 10), the dextral Polaris fault intersects north-striking east down normal faults of the ETFZ and the northeast-trending sinistral DVFZ (Fig. 10), demonstrating the complex nature of the spatially overlapping and kinematically linked faults that collectively accommodate the dextral transtension in this westernmost and structurally complex part of the NWL.

The Polaris and DVFZ are favorably oriented to accommodate the current regional stress field wherein the maximum

principal stress (S_1 or P axis) is oriented horizontally in a north–south vertical plane and the minimum principal stress (S_3 or T axis) is oriented east–west, perpendicular to the north–south vertical plane (Wright, 1976; Zoback, 1989; Ichnose *et al.*, 2003; Schweickert *et al.*, 2004). At the Gray’s Crossing site (Fig. 9), the intersection of high-angle conjugate faults defines fault-bounded quadrants that highlight the current regional stress field with contraction (previously described thrust faults) in the opposing north–south quadrants (P axis) and extension in the east–west quadrants (T axis). Furthermore, the orientation of the intersecting high-angle conjugate faults at the Gray’s Crossing site (Fig. 9) matches the nodal plane orientation of moderate magnitude historical seismicity in the immediate area and the broader Truckee transition zone (Fig. 1; also Greensfelder, 1968; Tsai and Aki, 1970; van Wormer and Ryall, 1980; Hawkins *et al.*, 1986; and Schweickert *et al.*, 2004).

The largest historical earthquake in the vicinity of the Polaris fault happened on 12 September 1966 (Kachadoorian *et al.*, 1967). The M_L 6.0 Truckee earthquake occurred ~10 km northeast of Truckee on a nearly vertical north-east-striking fault with left-lateral displacement, as defined by the aftershock sequence (Greensfelder, 1968; Tsai and Aki, 1970). Surface manifestations of the earthquake included pressure ridges, mole tracks, and lurch cracks in alluvium

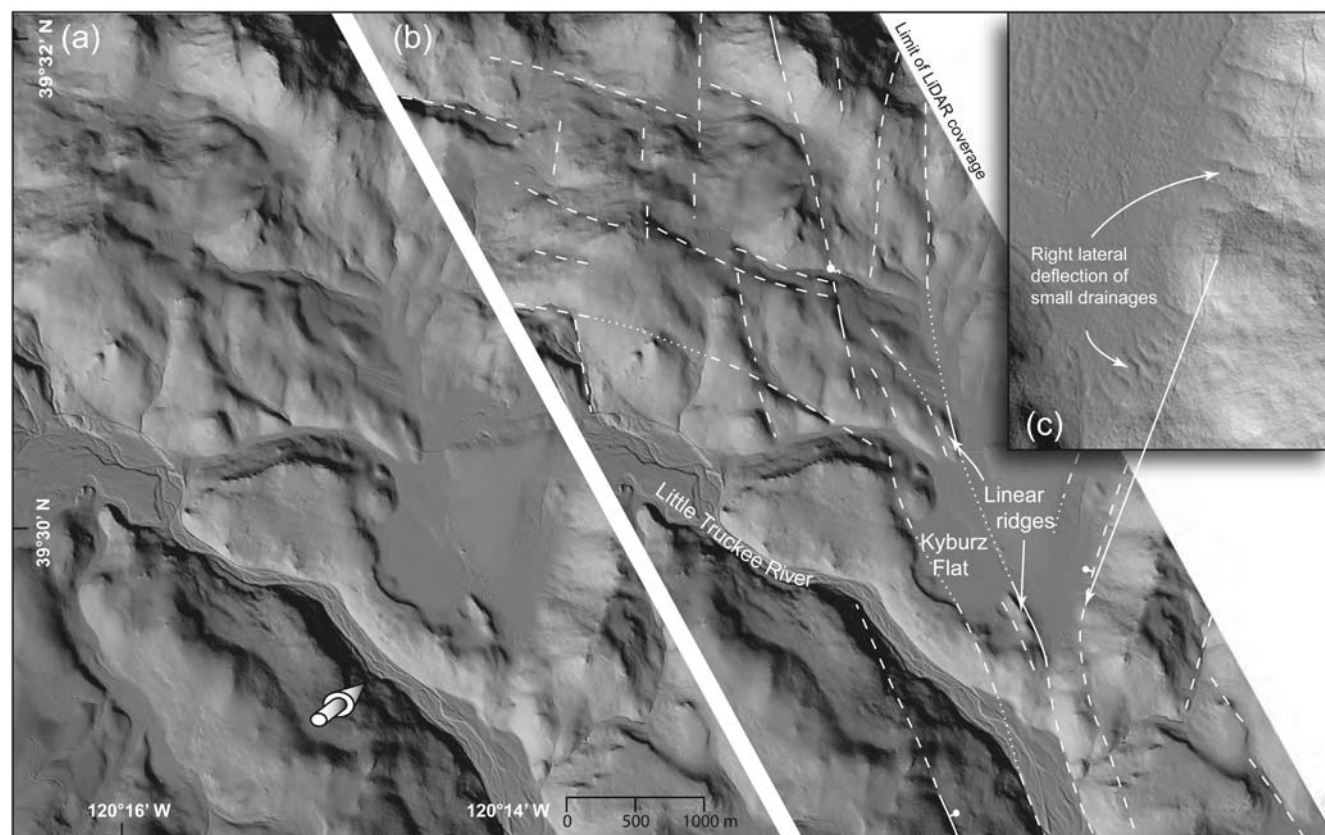


Figure 13. (a) Plan-view bare-earth LiDAR image of the area near Kyburz Flat. Shaded-gray arrow indicates direction of illumination (vertical exaggeration 2.5). (b) Solid white lines are mapped fault traces (dashed where approximately located, dotted where inferred, ball and bar on down-dropped side). (c) Enlargement showing right-lateral deflections of drainages along fault trace shown in (b).

along a ~16-km-long northeast-trending zone (Greensfelder, 1968), and Hawkins *et al.* (1986) associated the event with the DVFZ (Fig. 1a). Fault-plane mechanisms for the immediate area consistently show right-lateral motion on northwest-trending vertical planes and/or left-lateral motion on northeast-trending vertical planes (Tsai and Aki, 1970; van Wormer and Ryall, 1980; Hawkins *et al.*, 1986; Schweickert *et al.*, 2004).

Length of the Polaris Fault and Seismic Implications

As currently mapped using the airborne LiDAR imagery (Fig. 1), the previously unrecognized section of the Polaris fault extends for ~19 km from southeast of the Martis Valley, northwest across the Martis Creek reservoir and the Truckee basin, to Hobart Meadow north of Truckee. Geomorphic and geologic evidence suggests that the Polaris fault may extend an additional 17 km northwest. If so, the Polaris fault would be at least 36 km in length from a point 2 km south of the East Martis Creek fan to a point 6 km north of Kyburz Flat.

The ~35-km fault length makes the Polaris fault potentially capable of producing damaging large-magnitude earthquakes that could significantly threaten the Martis Creek Dam, which lies adjacent to the fault. Assuming a range of surface-rupture lengths (25, 30, and 35 km) and a range of depths to the base of the seismogenic zone (10, 14, and 18 km; Hawkins *et al.*, 1986 and Smith *et al.*, 2004), we estimate a range of earthquake magnitudes for the Polaris fault using the empirical relationships of Wells and Copper-smith (1994) and Hanks and Bakun (2002); these are listed in Table 2. These equations (Table 2) yield a range of possible maximum earthquake magnitudes (moment magnitude, M) for the Polaris fault from 6.4 to 6.9.

In addition, the southeasternmost mapped lineaments of the Mohawk Valley fault zone (Fig. 1) are only 5 km northwest of Kyburz Flat and may possibly connect or rupture coseismically with the Polaris fault, potentially making

the previously mentioned estimates lower than credible maximums.

Geodetic versus Geologic Constraints of Deformation in the Northern Walker Lane

Numerous authors have noted the large differences between geodetically and geologically determined strain rates (by a factor of 2–3 times or greater) in the NWL (Thatcher and Wesnousky, 2001; Briggs and Wesnousky, 2001; Hammond and Thatcher, 2004; S. Olig *et al.*, unpublished report, 2005, see Data and Resources; Hammond and Thatcher, 2007). Geodetically constrained dextral motion for the westernmost part of the NWL (i.e., the MVFZ and Polaris fault trend) ranges from 2.3 ± 0.3 mm/yr (Hammond and Thatcher, 2007) to $\sim 6 \pm 3$ mm/yr (Dixon *et al.*, 2000). Geologically determined dextral slip rates for this westernmost part of the NWL are given by Sawyer *et al.* (2005), who reports a Holocene slip rate 0.3–0.5 mm/yr along an eastern strand of the MVFZ in the southern Sierra Valley (Fig. 1) and Howle *et al.* (2009), who reports a latest Pleistocene–Holocene slip rate of 0.4 ± 0.1 mm/yr for the Polaris fault east of Truckee. Geologic estimates of right-lateral slip across this westernmost part of the NWL are sparse which may largely explain the disparity between the geodetic and geologic strain rates.

Thatcher and Wesnousky (2001) conclude that discrepancies between geodetic and geologic rates in the Great Basin are due to a large fraction of the strain being distributed off of the main range-front bounding faults on smaller broadly distributed structures and unrecognized faults such as the Polaris fault. This assessment may well be the case for this westernmost part of the NWL where a significant fault has gone undetected, as well as adjacent subparallel structures.

From the north side of Truckee River ~1 and 3 km northeast of the Polaris site are at least two northwest-trending subparallel fault strands that cut flat-lying Donner Lake–age

Table 2
Calculated Maximum Earthquake Magnitudes for the Polaris Fault, Assuming a Range of Rupture Lengths and Depths*

Rupture Length (km)	Rupture Depth (km)	Rupture Area (km ²)	M^{\dagger} Equation 1 [‡]	M^{\dagger} Equation 2 [§]	M^{\dagger} Equation 3
25	10	250	6.7	6.4	6.4
25	14	350	6.7	6.6	6.5
25	18	450	6.7	6.7	6.6
30	10	300	6.8	6.5	6.5
30	14	420	6.8	6.6	6.6
30	18	540	6.8	6.7	6.7 [#]
35	10	350	6.9	6.6	6.5
35	14	490	6.9	6.7	6.7
35	18	630	6.9	6.8	6.8 [#]

*See text for discussion.

[†]Values of M are moment magnitudes.

[‡] $M = 5.08 + 1.16[\log(\text{surface-rupture length})]$; figure 9 in Wells and Copper-smith, 1994.

[§] $M = 4.07 + 0.98[\log(\text{rupture area})]$; figure 16 in Wells and Copper-smith, 1994.

^{||} $M = \log(\text{rupture area}) + 3.98$; Hanks and Bakun, 2002.

[#]Where rupture area is greater than 537 km², $M = \frac{4}{3}[\log(\text{rupture area}) + 3.07]$; Hanks and Bakun, 2002.

outwash before crossing Prosser Creek Reservoir and forming prominent arms (linear drainages) on the north side of the reservoir (Figs. 1 and 8). Further north, these structures are expressed as aligned drainages that cut across the topographic divides between Prosser Creek, Sagehen Creek, and the Little Truckee River (Figs. 1 and 11). The NNW-trending scarps become more pronounced along strike to the north, where they bound the eastern margin of the Little Truckee River along the NNW-trending fault-controlled reach (Fig. 11). Similarly, west of the Polaris fault from Truckee to Independence Lake are numerous subparallel structures. Some of these have been mapped by Olig *et al.* (2005) and S. Olig *et al.* (unpublished report, 2005, see [Data and Resources](#)) as the ETFZ along the Highway 89 corridor, as well as the faults of the Truckee fault zone (TFZ in Fig. 1). However, west of Prosser Hill and east of the TFZ, the airborne LiDAR imagery reveals strong north-to-NNW-trending lineaments traversing the steep and densely vegetated terrain (Fig. 1). These structures do not display significant normal components, suggesting dextral motion is accommodated through this zone west of Highway 89 and east of the TFZ (Fig. 1). Dextral motion is also suggested in this area by the southeast-trending course of Prosser Creek through Carpenter Valley (west of the northeast-trending reach, DVFZ, in Fig. 1b), which is remarkably similar in appearance to the right-laterally offset reaches of Sagehen Creek and the Little Truckee River. The prominent NNW-trending fault that shutters Prosser Creek at Carpenter Valley (Fig. 1) also right-laterally offsets Tahoe-age lateral moraines at Independence Lake 10 km along strike to the NNW (Fig. 11a; Olig *et al.*, 2005). Between the west end of Independence Lake and Sagehen summit (~7 km to the east) are at least eight subparallel structures (Figs. 1 and 11). While most of these structures do not display the through-going nature of the Polaris fault to the east, their orientation is unmistakably related to the Polaris trend, and they are likely accommodating regional dextral transtension across this zone. The airborne LiDAR data could help direct future geologic investigations that in time might close the gap between geodetic and geologic strain rates. This in turn highlights the utility of bare-earth airborne LiDAR data in identifying and constraining tectonic geomorphology in densely vegetated terrain (e.g., Haugerud *et al.*, 2003; Carter *et al.*, 2007; Prentice *et al.*, 2009).

Conclusions

The utilization of high-resolution bare-earth airborne LiDAR imagery greatly assisted in identifying, constraining, and visualizing the fault-related geomorphology in densely vegetated and otherwise inaccessible terrain. The likely active Polaris fault exhibits youthful and laterally continuous tectonic geomorphic features along the 35-km length currently mapped utilizing the LiDAR imagery.

Based on maximum limiting age constraints and statistically robust 3D modeling of an offset terrace riser, a preliminary minimum estimate of the latest Pleistocene–

Holocene slip rate is 0.4 ± 0.1 mm/yr at the Polaris site east of Truckee.

Considering the favorable regional orientation as well as the strong and pervasive geomorphic character, the Polaris fault may be a prominent regional structure in accommodating dextral transtension in this westernmost part of the northern Walker Lane between Lake Tahoe and the Sierra Valley.

Conjugate fault patterns between the Polaris and Dog Valley fault zones are in strong coherence with moderate-magnitude historical seismicity of the immediate area, as well as the current regional stress regime.

Given the 35-km length, the Polaris fault is potentially a significant seismic hazard to the region and in particular to the Martis Creek Dam, with the capability of generating a magnitude 6.4–6.9 earthquake.

Data and Resources

The initial LiDAR data were collected by Merrick & Company for the Truckee Donner Public Utility District (TDPUD). The U.S. Army Corps of Engineers (USACE) gained access to these data under contract with TDPUD with a stipulation that USACE would not release the data to the public. These data remain proprietary to TDPUD.

The LiDAR data collected by Towell Surveying Mapping and GIS Services were acquired under contract with the USACE. These data are being used by USACE and its contractors to map and characterize faults in the region. These data will be released to the public at the conclusion of these studies, but the repository has not been determined as yet.

Ground-based LiDAR data reported in this paper were collected by J. F. Howle and are proprietary pending publication in a follow-up paper.

Faults referenced in the text are defined in the USGS Quaternary Fault and Fold Database, available at <http://earthquake.usgs.gov/hazards/qfaults/> and from updated fault maps presented in a report by I. Wong, T. Dawson, P. Thomas, S. Olig, M. Dober, and F. Terra. This unpublished report, “Seismic Hazard Analyses and Development of Design Ground Motions for Martis Creek Dam, California,” was prepared by URS Corp. Seismic Hazards Group on 6 March 2008 for the U.S. Army Corps of Engineers, Sacramento District. It is available upon request to the first author of this paper, L. E. Hunter.

The unpublished report by S. Olig, T. L. Sawyer, D. Wright, and F. Terra, “Preliminary Seismic Source Characterization of Faults near Stampede and Prosser Creek Dams–Washoe Project and Boca Dam–Truckee Storage Project,” was prepared by URS Corp. Seismic Hazards Group on 28 June 2005 for the U.S. Bureau of Reclamation. It is available upon request to L. E. Hunter.

The classified point-cloud data were imaged using Quick Terrain (QT) Modeler by Applied Imagery (<http://www.appliedimagery.com/qtmain.htm>). Vegetation was removed from the point-cloud data using TerraScan software by TerraSolid (<http://www.terrasolid.fi/en/products/terrascan>).

Other data used in this paper came from published sources listed in the references.

Acknowledgments

This work has been conducted under the U.S. Army Corps of Engineers' Dam Safety Assurance Program (DSAP). We thank DSAP program manager Richard Britzman and Martis Creek project manager Veronica Petrovsky for their continued support of our investigations, as well as the dam site manager, Dale Verner, who has provided logistical support through all phases of the project. The authors wish to thank Keith Kelson, Michael Rymer, Carol Prentice, and two anonymous reviewers for their constructive reviews of earlier drafts of this paper. The use of firm and/or brand names in this report is for identification purposes only and does not constitute endorsement by the United States government.

References

- Bennett, R. A., N. A. Wernicke, A. Niemi, A. M. Friedrich, and J. L. Davis (2003). Contemporary strain rates in the northern Basin and Range province from GPS data, *Tectonics* **22**, no. 2, 1008, doi [10.1029/2001TC001355](https://doi.org/10.1029/2001TC001355).
- Benson, L. V., D. R. Currey, R. I. Dorn, K. R. Lajoie, C. G. Oviatt, S. W. Robinson, G. I. Smith, and S. Stine (1990). Chronology of expansion and contraction of four Great Basin lake systems during the past 35,000 years, *Palaogeography, Palaeoclimatology, Palaeoecology* **78**, 241–286.
- Birkeland, P. W. (1963). Pleistocene volcanism and deformation of the Truckee area, north of Lake Tahoe, California, *GSA Bull.* **74**, 1453–1464.
- Birkeland, P. W. (1964). Pleistocene glaciation of the northern Sierra Nevada, north of Lake Tahoe, California, *J. Geol.* **72**, 810–825.
- Briggs, R. W., and S. G. Wesnousky (2001). The Basin and Range-Sierra Nevada transition along the northern Walker Lane: Geology vs. geodesy, *Seismol. Res. Lett.* **72**, no. 2, 280.
- Bursik, M. I., and A. R. Gillespie (1993). Late Pleistocene glaciation of Mono Basin, California, *Quat. Res.* **39**, 24–35.
- Carter, W. E., R. L. Shrestha, and K. C. Slatton (2007). Geodetic laser scanning, *Phys. Today* **60**, 41–47.
- Clark, D. H., and A. R. Gillespie (1997). Timing and significance of late-glacial and Holocene cirque glaciation in the Sierra Nevada, California, *Quat. Int.* **38/39**, 21–28.
- Cowgill, E. (2007). Impact of riser reconstructions on estimation of secular variation in rates of strike-slip faulting: Revisiting the Cherchen River site along the Altyn Tagh Fault, NW China, *Earth Planet. Sci. Lett.* **254**, 239–255.
- Crampton, T., R. Rubin, C. Slack, and W. McCormick (2009). Preliminary results of paleoseismic trenching and geomorphic mapping of the Polaris fault, Truckee, CA, 2009 Association of Environmental and Engineering Geologists Annual Meeting, Program with Abstracts, *AEG News* **52**, 65.
- Dixon, T. H., M. Miller, F. Farina, H. Wang, and D. Johnson (2000). Present-day motion of the Sierra Nevada block and some tectonic implications for the Basin and Range Province, North American Cordillera, *Tectonics* **19**, 474–486.
- Dixon, T. H., S. Robaudo, J. Lee, and M. C. Reheis (1995). Constraints on present-day Basin and Range deformation from space geodesy, *Tectonics* **14**, 755–772.
- Faulds, J. E., and C. D. Henry (2008). Tectonic influences on the spatial and temporal evolution of the Walker Lane: An incipient transform fault along the evolving Pacific—North American plate boundary, *Arizona Geol. Soc. Digest* **22**, 437–470.
- Faulds, J. E., C. D. Henry, and N. H. Hinz (2005). Kinematics of the northern Walker Lane: An incipient transform fault along the Pacific-North American plate boundary, *Geology* **33**, 505–508.
- Gillespie, A. R. (1991). Testing a new climatic interpretation for the Tahoe glaciation, *White Mountain Research Station Symposium* **3**, 383–398.
- Gold, R. D., E. Cowgill, J. R. Arrowsmith, J. Gosse, X. Chen, and X. F. Wang (2009). Riser diachroneity, lateral erosion, and uncertainty in rates of strike-slip faulting: A case study from Tuzidun along the Altyn Tagh fault, NW China, *J. Geophys. Res.* **114**, no. B04401, doi [10.1029/2008JB005913](https://doi.org/10.1029/2008JB005913).
- Greensfelder, R. (1968). Aftershocks of the Truckee, California, earthquake of September 12, 1966, *Seismol. Soc. Am. Bull.* **58**, no. 5, 1607–1620.
- Grose, T. T. L. (2000). Geologic map of the Sierraville 15' quadrangle, Sierra and Plumas counties, California, *CDMG Open-File Report 2000-24*.
- Hallet, B., L. E. Hunter, and J. Bogen (1996). Rates of erosion and sediment evacuation by glaciers: A review of field data and their implications, *Global Planet. Change* **12**, 213–235.
- Halpin, E. C., and K. A. Ferguson (2007). US Army Corps of Engineers dam safety program status and lessons learned in transitioning to risk informed approaches, *J. Dam Safety* **5**, no. 2, 24–36.
- Hammond, W. C., and W. Thatcher (2004). Contemporary tectonic deformation of the Basin and Range province, western United States: 10 years of observation with the Global Positioning System, *J. Geophys. Res.* **109**, no. B08403, 21 pp., doi [10.1029/2003JB002746](https://doi.org/10.1029/2003JB002746).
- Hammond, W. C., and W. Thatcher (2007). Crustal deformation across the Sierra Nevada, northern Walker Lane, Basin and Range transition, western United States measured with GPS, 2000–2004, *J. Geophys. Res.* **112**, no. B05411, 26 pp., doi [10.1029/2006JB004625](https://doi.org/10.1029/2006JB004625).
- Hanks, T. C., and W. H. Bakun (2002). A bilinear source-scaling model for $M - \log A$ observations of continental earthquakes, *Bull. Seismol. Soc. Am.* **92**, 1841–1846.
- Harkins, N., and E. Kirby (2008). Fluvial terrace riser degradation and determination of slip rates on strike-slip faults: An example from the Kunlan fault, China, *Geophys. Res. Lett.* **35**, L05406, doi [10.1029/2007GL033073](https://doi.org/10.1029/2007GL033073).
- Haugerud, R. A., D. J. Harding, S. Y. Johnson, J. L. Harles, and C. S. Weaver (2003). High-resolution LiDAR topography of the Puget Lowland, Washington—A bonanza for Earth science, *GSA Today* **13**, no. 6, 4–10.
- Hawkins, F. F., R. LaForge, and R. A. Hansen (1986). Seismotectonic study of the Truckee/Lake Tahoe area northeastern Sierra Nevada, California, *U.S. Bureau of Reclamation Seismotectonic Report Number 85-4*, 210 p.
- Howle, J. F., R. C. Finkel, and G. Seitz (2005). Cosmogenic exposure ages of Tioga and Tahoe age moraines at Meeks Bay, Lake Tahoe, California, *GSA Abstr. Programs* **37**, no. 7, 232.
- Howle, J. F., G. W. Bawden, L. E. Hunter, and R. S. Rose (2009). Modeling right-lateral offset of a Late Pleistocene terrace riser along the Polaris fault using ground-based LiDAR imagery, abstract no. G51B-0661, *American Geophysical Union*, Fall Meeting, 14–18 December 2009, San Francisco, California.
- Hunter, L. E., R. S. Rose, J. F. Howle, V. W. Brown, M. H. Powers, B. Hilton, and E. Hubbard (2009). *AEG 2009 Annual Meeting Field Trip Guidebook: Geotechnical and Paleoseismic Investigations of the Martis Creek Dam, Truckee, California*, Association of Environmental and Engineering Geologists, Denver, CO, 44 p.
- Ichinose, G., J. Anderson, K. Smith, D. dePolo, R. Anoshpoo, R. A. Schweickert, and M. M. Lahren (1999). The seismotectonics of the 30 October 1998 Incline Village, Nevada, earthquake and its effects, *Seismol. Res. Lett.* **70**, 297–305.
- Ichinose, G. A., J. G. Anderson, K. D. Smith, and Z. Yuehua (2003). Source parameters of eastern California and western Nevada earthquakes from regional moment tensor inversion, *Bull. Seismol. Soc. Am.* **93**, no. 1, 61–84.
- Ichinose, G. A., K. D. Smith, and J. G. Anderson (1998). Moment tensor solutions of the 1994 to 1996 Double Spring Flat, Nevada, earthquake sequence and implications for local tectonic models, *Bull. Seismol. Soc. Am.* **88**, no. 6, 1363–1378.
- James, L. A., J. Harbor, D. Fabel, D. Dahms, and D. Elmore (2002). Late Pleistocene glaciations in the northwestern Sierra Nevada, California, *Quat. Res.* **57**, 409–419.

- Kachadoorian, R., R. F. Yerkes, and O. A. Waananen (1967). Effects of the Truckee, California, earthquake of September 12, 1966, *USGS Circular* **537**, 14.
- Latham, T. S. (1985). Stratigraphy, structure, and geochemistry of Pliocene volcanic rocks of the western Basin and Range province, near Truckee, California, *Ph.D. dissertation*, University of California at Davis 341 pp.
- Melody, A. (2009). Holocene faulting and Late Quaternary paleohydrology in the northwestern Walker Lane north of Truckee, California, 2009 Association of Environmental and Engineering Geologists Annual Meeting, Program with Abstracts, *AEG News* **52**, 91.
- Olig, S., T. L. Sawyer, L. Anderson, D. Wright, I. Wong, and F. Terra (2005). Insights into Quaternary strain patterns in the northern Walker Lane from mapping and source characterization of faults near Truckee, California, *Seismol. Res. Lett.* **76**, no. 2, 251.
- Oskin, M. E., K. Le, and M. D. Strane (2007). Quantifying fault-zone activity in arid environments with high-resolution topography, *Geophys. Res. Lett.* **34**, L23S05, doi [10.1029/2007GL031295](https://doi.org/10.1029/2007GL031295).
- Page, W. D., T. L. Sawyer, M. K. McLaren, W. U. Savage, and J. Wakabayashi (1993). The Quaternary Tahoe-Medicine Lake trough: The western margin of the Basin and Range transition, NE California, *GSA Abstr. Programs* **25**, 131.
- Prentice, C. S., C. J. Crosby, C. S. Whitehill, J. R. Arrowsmith, and K. P. Furlong (2009). Illuminating Northern California's active faults, *Eos* **90**, 7, 55–56.
- Repka, J. L., R. S. Anderson, and R. C. Finkel (1997). Cosmogenic dating of fluvial terraces, Fremont River, Utah, *Earth Planet. Sci. Lett.* **152**, 59–73.
- Sawyer, T. L., and R. W. Briggs (2001). Stop 9: Kinematics and late Quaternary activity of the Mohawk Valley fault zone, *Pacific Cell Friends of the Pleistocene 2001 Fall Field Trip Guidebook*, Friends of the Pleistocene, Pacific Cell, San Francisco, California, 49–62.
- Sawyer, T. L., R. W. Briggs, and A. R. Ramelli (2005). Late Quaternary activity of the southern Mohawk Valley fault zone, Northeastern California, *Seismol. Res. Lett.* **76**, no. 2, 248–249.
- Sawyer, T. L., W. D. Page, and M. A. Hemphill-Haley (1995). Southern Mohawk Valley fault zone at the Calpine trench site, in W. D. Page (Editor), *Quaternary Geology along the Boundary between Modoc Plateau, Southern Cascade Mountains, and Northern Sierra Nevada: Friends of the Pleistocene 1995 Pacific Cell Field Trip Guidebook*, Friends of the Pleistocene, Pacific Cell, San Francisco, California.
- Schweickert, R. A., M. M. Lahren, R. E. Karlin, K. D. Smith, J. F. Howle, and G. Ichinose (2004). Transtensional deformation in the Lake Tahoe region, California and Nevada, USA, *Tectonophysics* **392**, 303–323.
- Shackleton, N. J., and N. D. Opdyke (1976). Oxygen-isotope and paleomagnetic stratigraphy of Pacific core V28-239 late Pliocene to latest Pleistocene, R. M. Cline and J. D. Hays (Editors), *Geol. Soc. Am. Memoir*, Vol. **145**, 449–464.
- Smith, K., D. von Seggern, D. dePolo, J. Anderson, G. Biasi, and R. Anoshehpour (2008). Seismicity of the 2008 Mogul—Somerset west Reno, Nevada, earthquake sequence, Fall Meet. Suppl. *Eos Trans. Am. Geophys. Union* **89**, no. 53, abstract S53C-02.
- Smith, K. D., D. von Seggern, G. Blewitt, L. Preston, J. G. Anderson, B. P. Wernicke, and J. L. Davis (2004). Evidence for deep magma injection beneath Lake Tahoe, Nevada—California, *Science* **305**, 1277–280.
- Stewart, J. H. (1988). Tectonics of the Walker Lane belt, western Great Basin: Mesozoic and Cenozoic deformation in a zone of shear, in W. G. Ernst (Editor), *The Geotectonic Development of California*, Prentice-Hall, Englewood Cliffs, New Jersey, 683–713.
- Sylvester, A. G., W. S. Wise, J. T. Hastings, and L. A. Moyer (2007). New digital geologic map of the northern Lake Tahoe-Donner Pass region, Sierra Nevada, California, *GSA Abstr. Programs* **39**, no. 5.
- Thatcher, W., and S. G. Wesnousky (2001). Character and origin of discrepancies between Holocene and GPS fault slip rate estimates in the interior western U.S., *Seismol. Res. Lett.* **72**, no. 2, 280.
- Thatcher, W., G. R. Foulger, B. R. Julian, J. Svarc, E. Quilty, and G. W. Bawden (1999). Present day deformation across the Basin and Range province, western United States, *Science* **283**, 1714–1718.
- Tsai, Y. B., and K. Aki (1970). Source mechanism of the Truckee, California earthquake of September 12, 1966, *Seismol. Soc. Am. Bull.* **60**, no. 4, 1199–1208.
- Unruh, J., J. Humphrey, and A. Barron (2003). Transtensional model for the Sierra Nevada frontal fault system, eastern California, *Geology* **31**, no. 4, 327–330.
- U.S. Army Corps of Engineers (1966). *Martis Creek Reservoir, Truckee River Basin, Nevada and California: Site Geology*, Design Memorandum No. 8, U.S. Army Corps of Engineers, Sacramento, California, 19 pp.
- U.S. Army Corps of Engineers (1972). *Martis Creek Lake Dam and Appurtenances, Truckee River Basin, Nevada and California: Foundation Report*, U.S. Army Corps of Engineers, Sacramento, California, 107 pp.
- van Wormer, J. D., and A. D. Ryall (1980). Sierra Nevada—Great Basin boundary zone: Earthquake hazard related to structures, active tectonic processes, and anomalous patterns of earthquake occurrence, *Seismol. Soc. Am. Bull.* **70**, 1557–1572.
- Wells, D., and K. J. Coppersmith (1994). New empirical relationships among magnitude, rupture length, rupture width, rupture area and surface displacement, *Bull. Seismol. Soc. Am.* **84**, 974–1002.
- Wesnousky, S. G. (2005a). The San Andreas and Walker Lane fault systems, western North America: Transpression, transtension, cumulative slip and the structural evolution of a major transform plate boundary, *J. Struct. Geol.* **27**, 505–512.
- Wesnousky, S. G. (2005b). Active faulting in the Walker Lane, *Tectonics* **24**, TC3009, 35 pp., doi [10.1029/2004TC001645](https://doi.org/10.1029/2004TC001645).
- Wesnousky, S. G., and C. H. Jones (1994). Oblique slip, slip partitioning, spatial and temporal changes in the regional stress field, and relative strength of active faults in the Basin and Range, western United States, *Geology* **22**, 1031–1034.
- Wright, L. (1976). Late Cenozoic fault patterns and stress fields in the Great Basin and westward displacement of the Sierra Nevada block, *Geology* **4**, 489–494.
- Yount, J. C., and D. D. La Pointe (1997). Glaciation, faulting, and volcanism in the southern Lake Tahoe basin, in: *Field Trip Guidebook for the National Association of Geoscience Teachers, Far West Section, 1997 Fall Conference*, Western Nevada Community College, Fallon, Nevada, II-1–II-22.
- Zoback, M. L. (1989). State of stress and modern deformation of the northern Basin and Range Province, *J. Geophys. Res.* **94**, 7105–7128.
- U.S. Army Corps of Engineers
Sacramento, California 95814
(L.E.H., R.S.R.)
- U.S. Geological Survey
Carnelian Bay, California 96140
(J.F.H.)
- U.S. Geological Survey
Sacramento, California 95819
(G.W.B.)

Manuscript received 2 September 2009

Day 2, Stop 3 – Grizzly Valley Fault

FOP 2012 Stop, Grizzly Valley fault system, Sierra Valley, CA

Coordinates: 39.705610N, 120.307405W

Presenter: Ryan Gold, US Geological Survey, Golden, CO

Collaborators: William Stephenson, Jack Odum, Rich Briggs, Anthony Crone, Steve Angster

Summary: The Grizzly Valley fault system (GVFS) strikes northwestward across Sierra Valley, California and is part of a network of active, dextral strike-slip faults in the northern Walker Lane (Figure 1). To investigate Quaternary motion across the GVFS, we analyzed high-resolution (0.25 m) airborne LiDAR data (Figure 2) in combination with six, high-resolution, P-wave, seismic-reflection profiles [*Gold and others*, 2012]. The 0.5- to 2.0-km-long seismic-reflection profiles were sited orthogonal to suspected tectonic lineaments identified from previous mapping and our analysis of airborne LiDAR data. To image the upper 400–700 m of subsurface stratigraphy of Sierra Valley (Figure 3), we used a 230-kg accelerated weight drop source. Geophone spacing ranged from 2 to 5 m and shots were co-located with the geophones. The profiles reveal a highly reflective, deformed basal marker that we interpret to be the top of Tertiary volcanic rocks, overlain by a 120- to 300-m-thick suite of subhorizontal reflectors we interpret as Plio-Pleistocene lacustrine deposits. Three profiles image the principle active trace of the GVFS, which is a steeply dipping fault zone that offsets the volcanic rocks and the basin fill (Figures 4 & 5).

We interpret the GVFS to have been active in Quaternary time because:

1) The LiDAR data reveal subtle surficial geomorphology indicative of youthful faulting, including a topographic lineament marked by a discontinuous, ~1-m-high, left-stepping ridge, which is interpreted to have been generated by strike-slip faulting (Figure 2).

2) The seismic-reflection profiles document shallow (≤ 400 m) faulting in the basin fill of Sierra Valley that coincides with the left-stepping ridge (Figures 4 & 5).

3) Vegetation lineaments and drainage patterns visible on aerial and satellite imagery indicate that geologic structures control the distribution of surface and ground water coincident with the left-stepping ridge (Figure 1b).

Stop summary

At this stop, we will stand on the principle trace of the GVFS. You will be able to observe the ~1-m-high topographic ridge, which has been interpreted to have resulted from Quaternary faulting along the GVFS (Figure 2). At this location, shallow-seismic reflection profile line 2a (Figure 4) was surveyed along the north-trending fence line. We will examine the seismic-reflection data.

Previous work

The GVFS was first queried as a Quaternary active structure in a California Department of Water Resources report [1963], presumably on the basis of regional geothermal hot springs, tonal vegetation lineaments, and drainage patterns. In this report, the fault strands are depicted as steeply dipping normal faults that are concealed by the uppermost portion of the lacustrine section. This mapping is also consistent with results from a local gravity survey of Sierra Valley that show a northwest-trending pattern of gravity highs, coincident with the mapped eastern traces of the GVFS [*Jackson and others*, 1961]. Reed

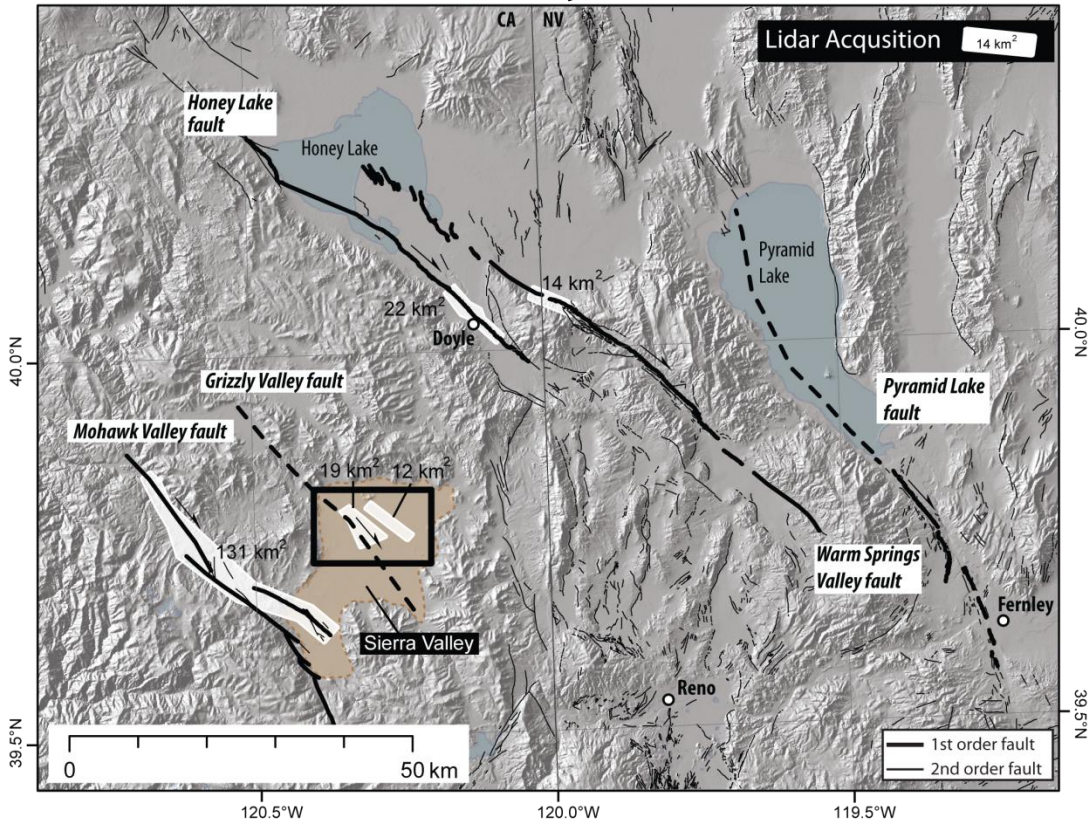
[1975] also depicts Quaternary faulting across Sierra Valley, noting NW-trending zones of tonal vegetation lineaments and disrupted water flow patterns. An update to the regional mapping was undertaken by Saucedo and Wagner [1992], and these authors simplified the mapping of the GVFS. More recent detailed mapping depicts faulting of the granitic basement and volcanics along the GVFS; however, this mapping explicitly notes a lack of evidence for active faulting along these structures [Grose, 2000a; 2000b; 2000c]. The 2010 Fault Activity Map of California [Jennings and Bryant, 2010] depicts the GVFS as a fault without recognized Quaternary displacement. It is not included in the U.S. Geological Survey's Quaternary Fault-and-Fold Database nor as a seismic source in the 2008 National Seismic Hazard Map [Petersen and others, 2008].

Timing of most recent fault

The presence of geomorphic features indicative of surface faulting is our strongest line of evidence for recent motion on the GVFS. We would expect surface processes including erosion from surface run-off and burial from eolian deposition to obliterate the GVFS lineament and scarps if they had been inactive during Quaternary time. We lack absolute age control for the faulted lacustrine deposits. However, Ramelli et al. [1999] suggest that a pluvial lake may have filled the basin as recently as 150 ka, which may provide a maximum bound on the timing of recent faulting. An additional line of evidence indicating recent faulting along the GVFS comes from a trenching study along the Mohawk Valley fault in the southwestern arm of Sierra Valley, where it was revealed that the Tsoyawata Mazama tephra [~7.8 ka, Bacon, 1983] has been faulted twice. Absolute age control on the faulted deposits across the GVFS are required to constrain the timing of the most-recent earthquake with certainty, but if the upper part of the Quaternary section in northern Sierra Valley also contains the Mazama tephra, then deformation of the surface along the GVFS may indicate Holocene faulting. Our preliminary analysis and comparison to regional studies lead us to assert with certainty that the fault has been active in the Quaternary,

almost certainly since 150 ka, and may have been active as recently as the middle-to-early Holocene.

(a) Northern Walker Lane, Study Area



(b) Grizzly Valley Fault, Sierra Valley, CA

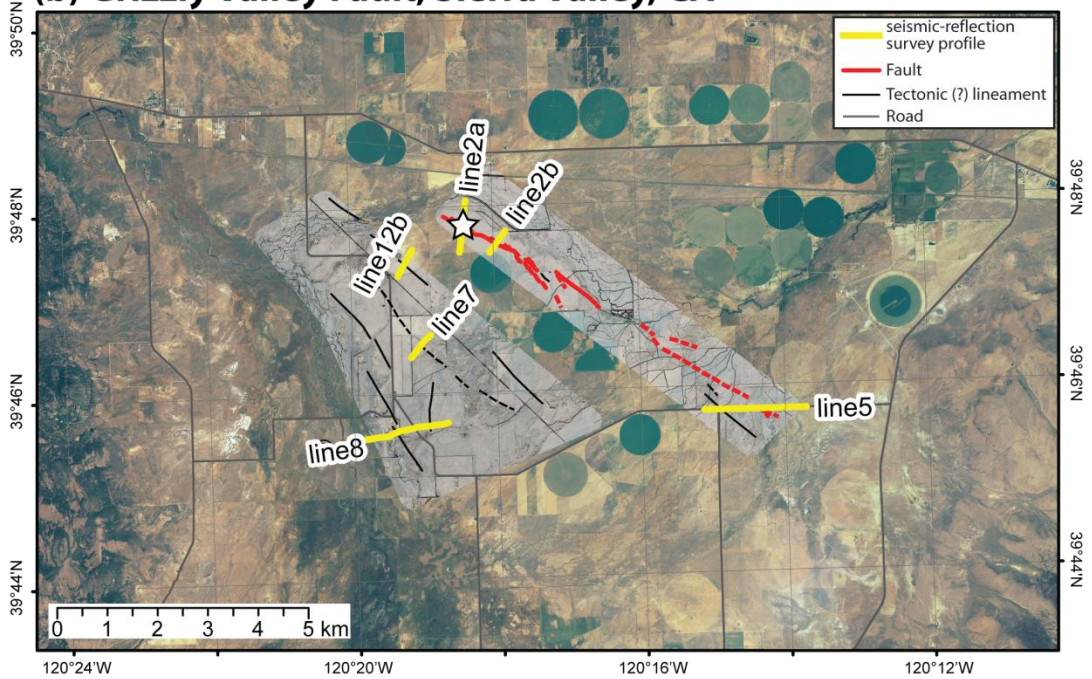


Figure 1. (a) Northern Walker Lane study area, showing areas of airborne LiDAR acquisition and regional faults. (b) Grizzly Valley fault system in Sierra Valley, CA., with map extent indicated in (a). LiDAR acquisition (white polygons), seismic-reflection

profiles, fault and tectonic lineaments are indicated by yellow, red, and black lines, respectively. Star shows location of FOP stop.

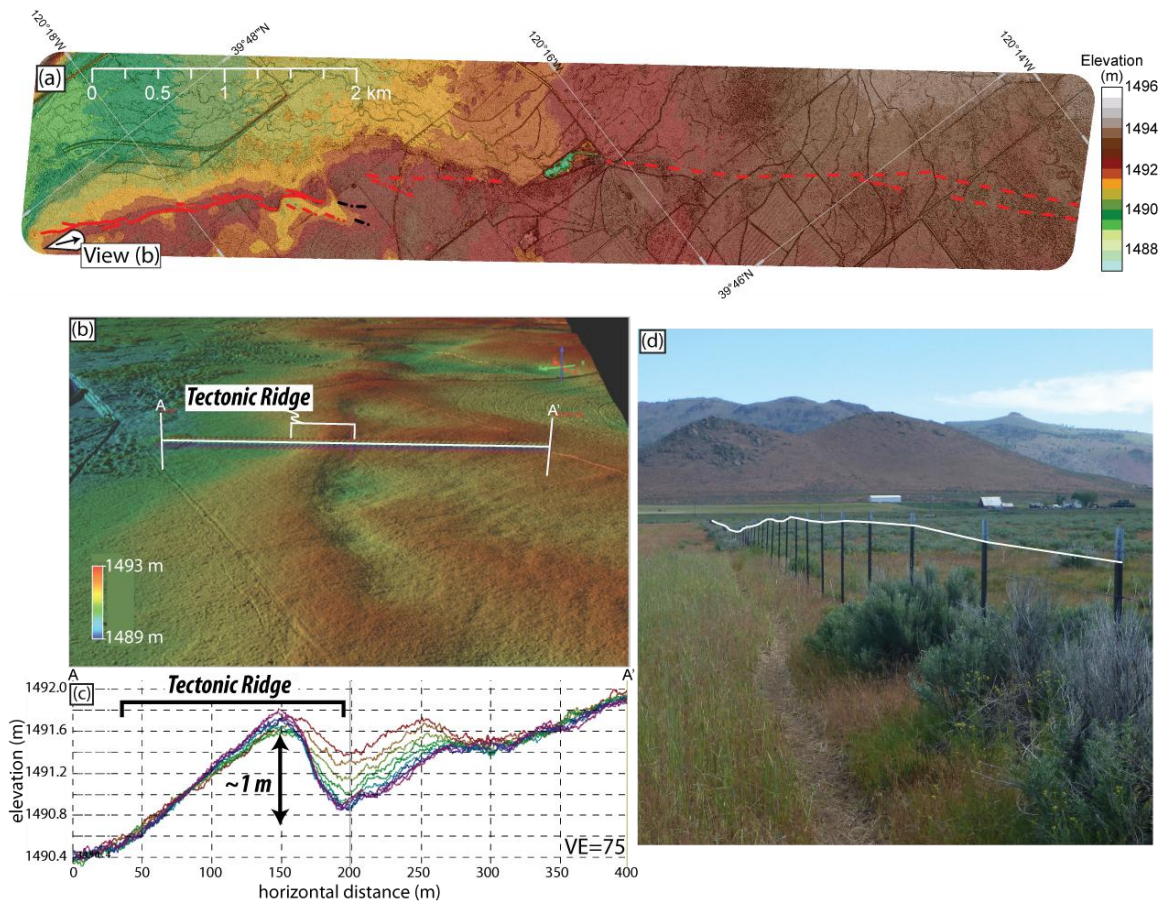
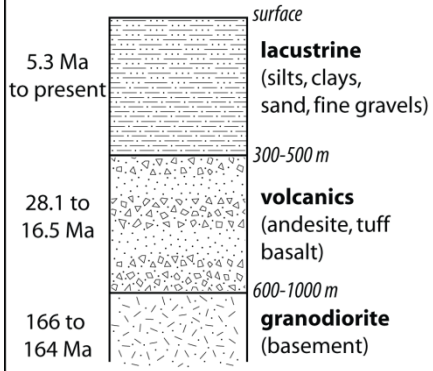


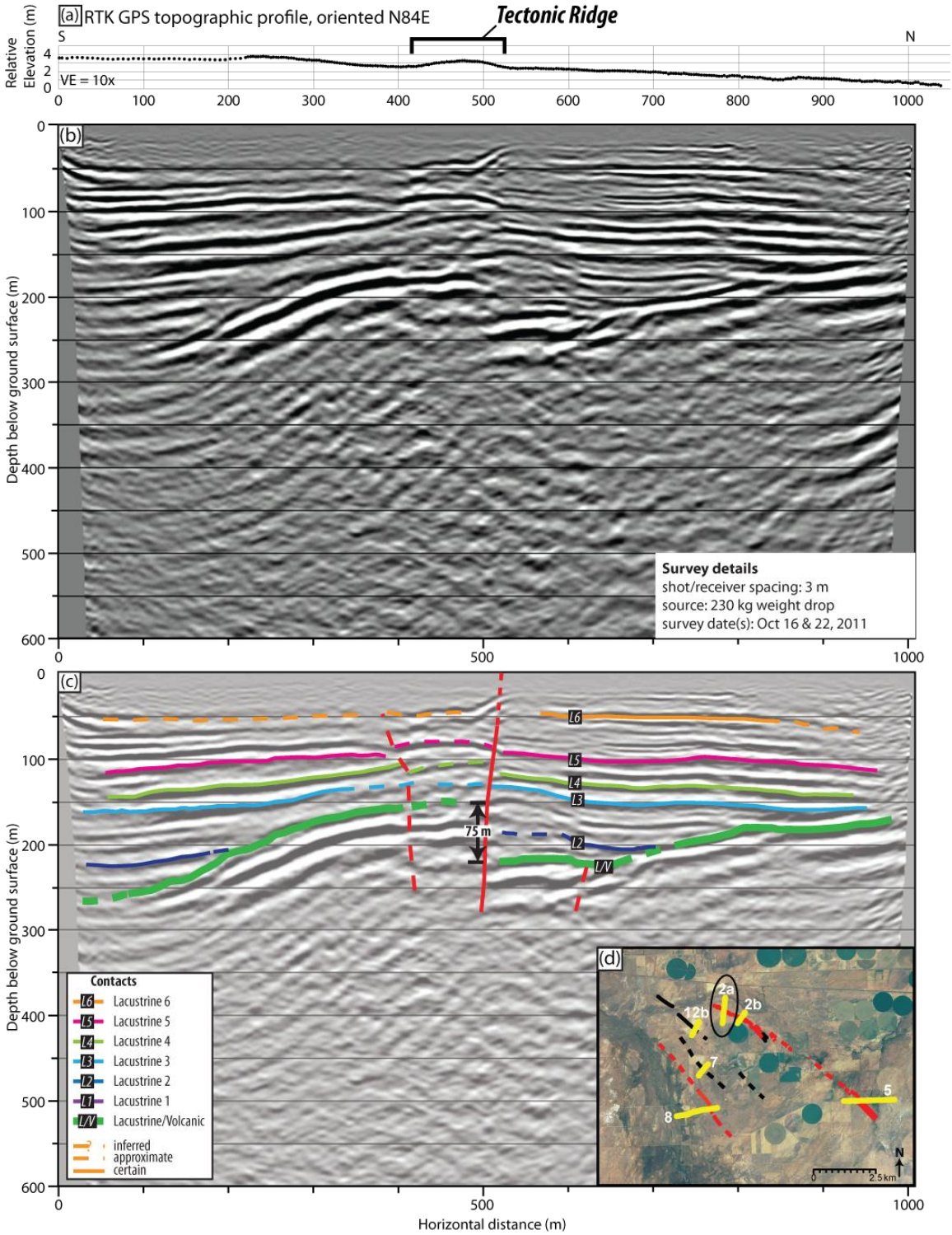
Figure 2. Topographic evidence for Quaternary faulting along the Grizzly Valley fault system. (a) Airborne LiDAR-derived digital elevation model (DEM) along the eastern strand of the Grizzly Valley fault system (red line). Ridge of topography in northwestern region of map (left) is interpreted to result from faulting. (b) Perspective view looking southeast along the Grizzly Valley fault system along tectonic ridge of topography. Location of topographic profiles presented in (c) indicated. (c) Topographic profiles across tectonic ridge, showing ~1 m high ridge that is asymmetric with a steeper slope to the southwest. (d) Photograph looking north from crest of ridge. Fence in photograph shows downward sloping surface.

Sierra Valley Basin Stratigraphy



- References
- California Department of Water Resources, 1963
 - Saucedo & Wagner, 1992
 - Grose, 2000
 - Well logs

Seismic-reflection survey - Line 2a



Seismic-reflection survey - Line 5

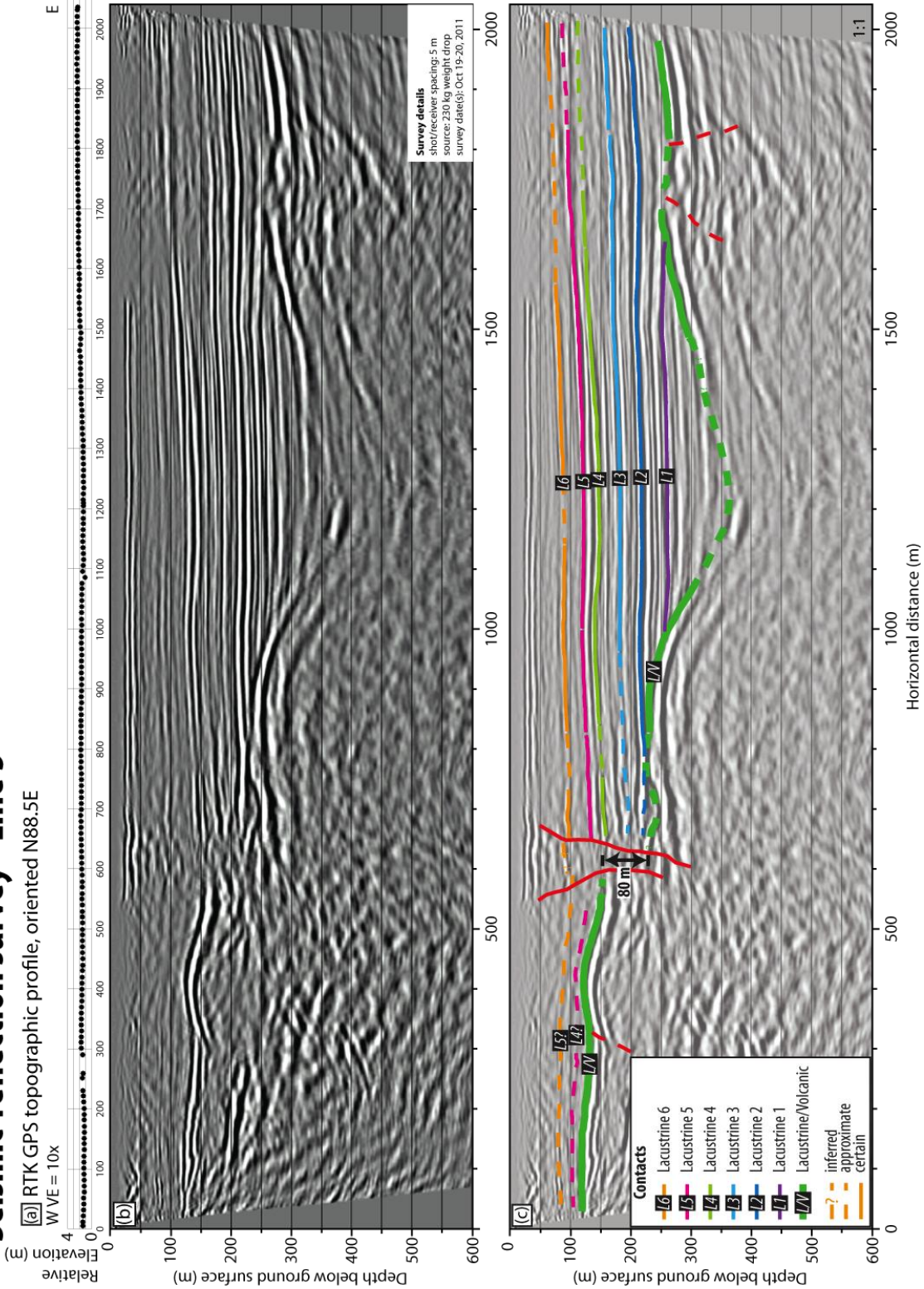


Figure 5. Seismic-reflection profile, line 5. (a) Topographic profile along profile line 5. (b) Uninterpreted and (c) interpreted reflection profile 5. See figure 1b for profile location.

References

- Bacon, C. R. (1983), Eruptive history of Mount Mazama and Crater Lake caldera, Cascade Range, USA, *Journal of Volcanology and Geothermal Research*, 18(1), 57-115.
- California Department of Water Resources (1963), Areal geology of Sierra, Mohawk, Humbug and Honey Lake Valleys ground water basins, in *Northeastern counties ground water investigation*, edited, p. 224, Bulletin 98.
- Gold, R. D., W. J. Stephenson, J. K. Odum, R. W. Briggs, A. J. Crone, D. Worley, J. Allen, S. Angster, and D. Bowden (2012), High-resolution seismic-reflection imaging profiles across the Grizzly Valley fault system, Northern Walker Lane, California, *Seismological Research Letters*, 83(2), 356.
- Grose, T. L. T. (2000a), Geologic map of the Blairsden 15' Quadrangle, Plumas County, California, California Department of Conservation, Division of Mines and Geology, Sacramento, CA.
- Grose, T. L. T. (2000b), Geologic map of the Portola 15' Quadrangle, Plumas county, California, California Department of Conservation, Division of Mines and Geology, Sacramento, CA.
- Grose, T. L. T. (2000c), Geologic map of the Loyalton 15' Quadrangle, Plumas and Sierra Counties, California, California Department of Conservation, Division of Mines and Geology, Sacramento, CA.
- Jackson, W. H., F. R. Shawe, and L. C. Pakiser (1961), Gravity study of the structural geology of Sierra Valley, CA, *Geological Survey Professional Paper 424-B, Geological Survey Research*, B254-B256.
- Jennings, C. W., and W. A. Bryant (2010), 2010 Fault Activity Map of California, California Geological Survey.
- Petersen, M. D., A. D. Frankel, S. C. Harmsen, C. S. Mueller, K. M. Haller, R. L. Wheeler, R. L. Wesson, Y. Zeng, O. S. Boyd, D. M. Perkins, N. Luco, E. H. Field, C. J. Wills, and K. S. Rukstales (2008), Documentation for the 2008 Update of the United States National Seismic Hazard Maps, 61 pp, U.S. Geological Survey OFR-1128.

- Ramelli, A. R., K. D. Adams, and J. C. Yount (1999), Probable short-lived middle Pleistocene spillover from pluvial Lake Beckwourth (Feather River/Pacific drainage system) into the Lake Lahontan basin; implications for biogeography, paper presented at Geological Society of America.
- Reed, M. J. (1975), Chemistry of thermal water in selected geothermal areas of California, 14 pp, California Division of Oil and Gas, TR-15.
- Saucedo, G. J., and D. L. Wagner (1992), Geologic map of the Chico Quadrangle, *Map No. 7*, California Department of Conservation, Division of Mines and Geology.

Using GPS measurements of active crustal deformation to estimate slip rates on the Honey Lake/Warm Springs and Mohawk Valley fault systems, Northern Walker Lane.

Jayne M. Bormann, William C. Hammond, Corné Kreemer, and Geoffrey Blewitt

Nevada Geodetic Laboratory
Nevada Bureau of Mines and Geology
University of Nevada, Reno

The Honey Lake/Warm Springs and Mohawk Valley faults are parallel, northwest striking, dextral fault systems separated by ~50 km in the westernmost part of the Northern Walker Lane (NWL). These faults work as a cooperative pair to accommodate 3-5 mm/yr of the total 6-8 mm/yr of right-lateral strain geodetically observed across the NWL (Figures 1 and 2), however it is unclear which fault is dominant. Geologic studies report right-lateral slip rates of 1-2.5 mm/yr on the Honey Lake fault (Turner et al., 2008; Wills and Borchardt, 1993) and a minimum of 0.3 mm/yr on the Mohawk Valley fault (Sawyer et al., 2003). In contrast, previous geodetic studies estimate slip rates of ~1 mm/yr on the Honey Lake fault and ~3 mm/yr on the Mohawk Valley fault (Hammond et al., 2011). Additionally, the Honey Lake and Mohawk Valley fault systems are separated by the subparallel Grizzly Valley fault. Geologic studies indicate that the Grizzly Valley fault has accommodated Quaternary dextral slip, however we are not aware of a published slip rate on the fault. To explore the discrepancy between the distribution of slip on the faults, the differences between sums of the geologically and geodetically estimated slip rates, and the effects of including the Grizzly Valley fault on geodetically estimated slip rates in the NWL, we use new GPS data to constrain an elastic block model developed specifically to study the Mohawk Valley and Honey Lake/Warm Springs fault systems.

We present a dense GPS velocity solution with velocities shown in a North American reference frame (~10 km average station spacing) that incorporates new semi-continuous MAGNET data with continuous data from the EarthScope Plate Boundary Observatory and other networks (Figure 1). The velocities are oriented to the northwest and increase smoothly from east to west across the NWL. Deformation is predominantly subparallel to the direction of Pacific-North America relative plate motion, with ~6 mm/yr of northwest-directed dextral shear in this region (Figure 2, lower profile) and <1 mm/yr of deformation perpendicular to the direction of shear. (Figure 2, upper profile).

Block modeling allows us to estimate long-term fault slip rates from GPS observations of contemporary crustal deformation, see Hammond et al. (2011) for methods. Block boundaries are drawn to coincide with active faults, patterns of seismicity, and major

topographic features (Figure 3). Long-term block motion is resolved by the best fit to GPS velocities, and fault slip rates are estimated from fault geometry and the relative motion of adjacent blocks. We solve for slip rates on the Honey Lake and Mohawk Valley fault systems and explore the effects of including the Grizzly Valley fault on predicted slip rates.

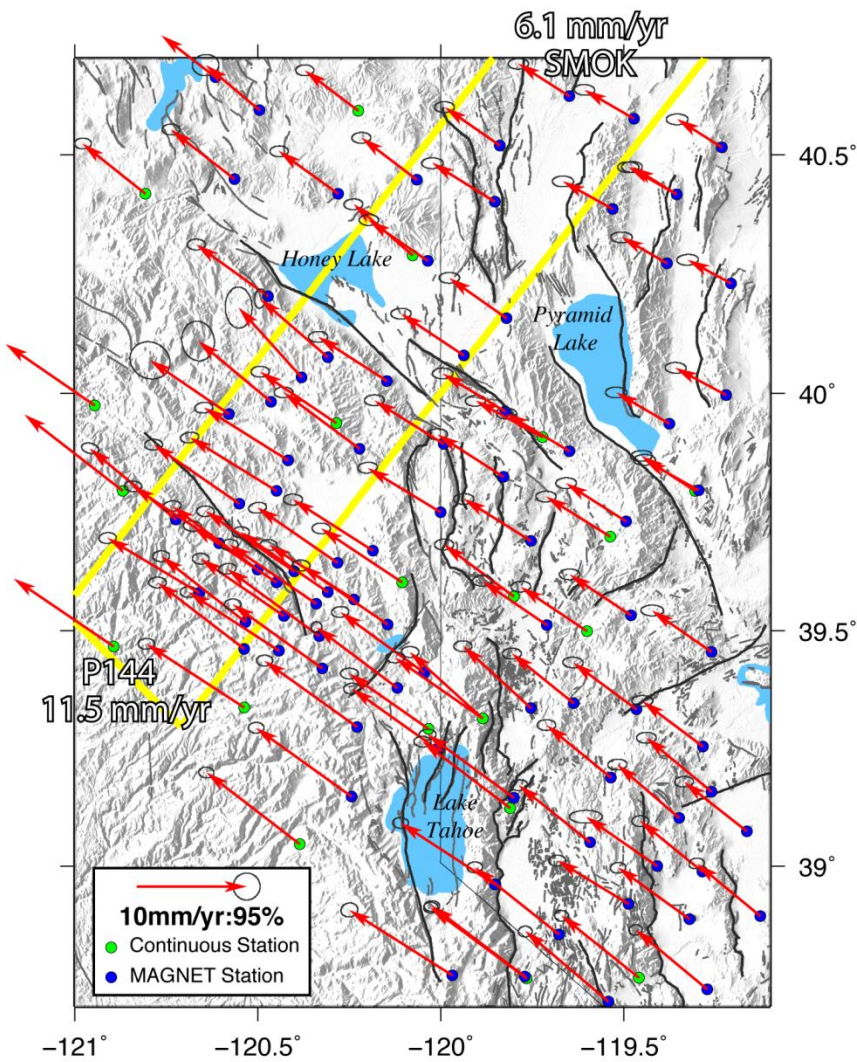
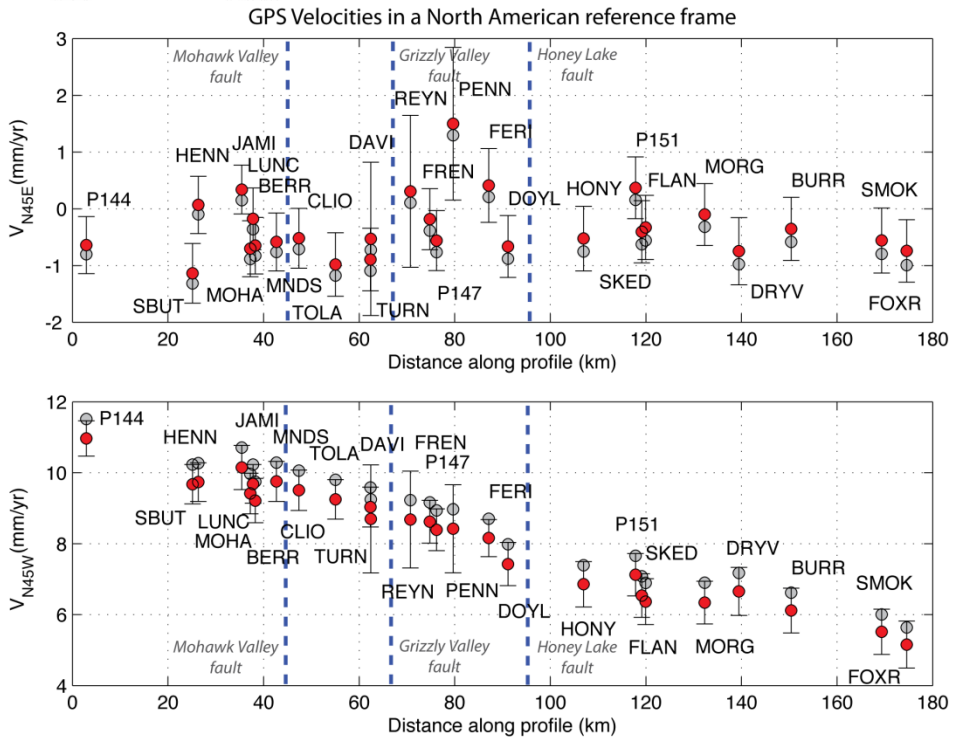


Figure 1. GPS velocities, topography, and major faults across the Sierra Nevada/Northern Walker Lane/Basin and Range Transition. Velocities are in a North America reference frame. PBO and other continuous stations are shown with green circles. Semi-continuous MAGNET stations are shown with blue circles. The yellow box shows the location of the velocity profiles in Figure 2.

Figure 2. GPS velocity profiles across the NWL. Profile location shown by yellow box in Figure 1. Uncertainties are 2-sigma confidence intervals. Velocities have been corrected for the effects of viscoelastic relaxation from earthquakes in central Nevada (red circles). Grey circles show the uncorrected velocities. **Note the vertical axis scale change between the two figures.**



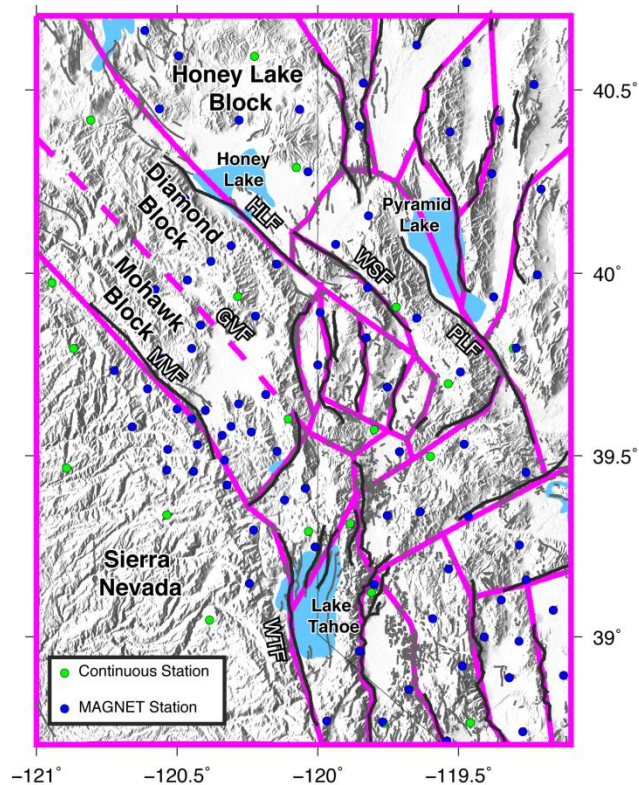


Figure 3. Block model geometry with faults, topography, and GPS station locations. Key blocks and faults are labeled. MVF=Mohawk Valley fault, GVF=Grizzly Valley fault, HLF=Honey Lake fault, WSF=Warm Springs Valley fault, PLF=Pyramid Lake fault, WTF=West Tahoe fault.

The block model results illustrate the change in style of deformation from extension on north-striking normal faults in Carson Valley and the Tahoe Basin in the southern portion of the model to dextral shear on northwest-striking strike-slip faults in the NWL (Figure 4a and 4b). Slip predicted on the Mohawk Valley, Honey Lake, Warm Springs Valley, and Pyramid Lake faults is almost purely strike-slip, whereas normal motion with significant oblique slip is predicted on the WTF.

Because the increase in shear across the NWL is very smooth and the shear is subparallel to the strike of the major faults (Figure 1 and Figure 2, lower profile), including the Grizzly Valley fault in the model strongly effects the slip rate predictions on the neighboring Mohawk Valley and Honey Lake faults. The model without the Grizzly Valley fault (Figure 4a) predicts dextral slip rates of 2.2 ± 0.2 mm/yr for the Mohawk Valley fault and 1.2 ± 0.2 mm/yr for the Honey Lake fault (Table 1). Including the Grizzly Valley fault reduces slip rates on the Mohawk Valley and Honey Lake faults to 1.6 ± 0.2 mm/yr and 0.7 ± 0.2 mm/yr, respectively, and results in 1.4 ± 0.3 mm/yr of dextral slip on the Grizzly Valley fault (Figure 4b and Table 1). The inclusion of the Grizzly Valley fault does not appreciably change the sum of slip accommodated across the NWL; rather, the additional fault causes the slip to be distributed among 3 faults. Including the Grizzly Valley fault results in a small but insignificant improvement to the model RMS residual velocities (Figure 4). We conclude that the geodetic data allows for up to ~ 1.5 mm/yr of dextral slip, but does not require any significant slip along the Grizzly Valley fault.

Our modeling shows that the Honey Lake, Grizzly Valley, and Mohawk Valley systems collectively accommodate ~ 3.5 mm/yr of shear deformation. Despite changes to block model geometry, the Mohawk Valley fault consistently accommodates ~ 1 mm/yr more slip than the Honey Lake fault. Our results support the conclusion of previous geodetic work (Hammond et al., 2011) that the Mohawk Valley fault in the westernmost NWL and possibly the Grizzly Valley fault are currently dominant in accommodating deformation in the NWL.

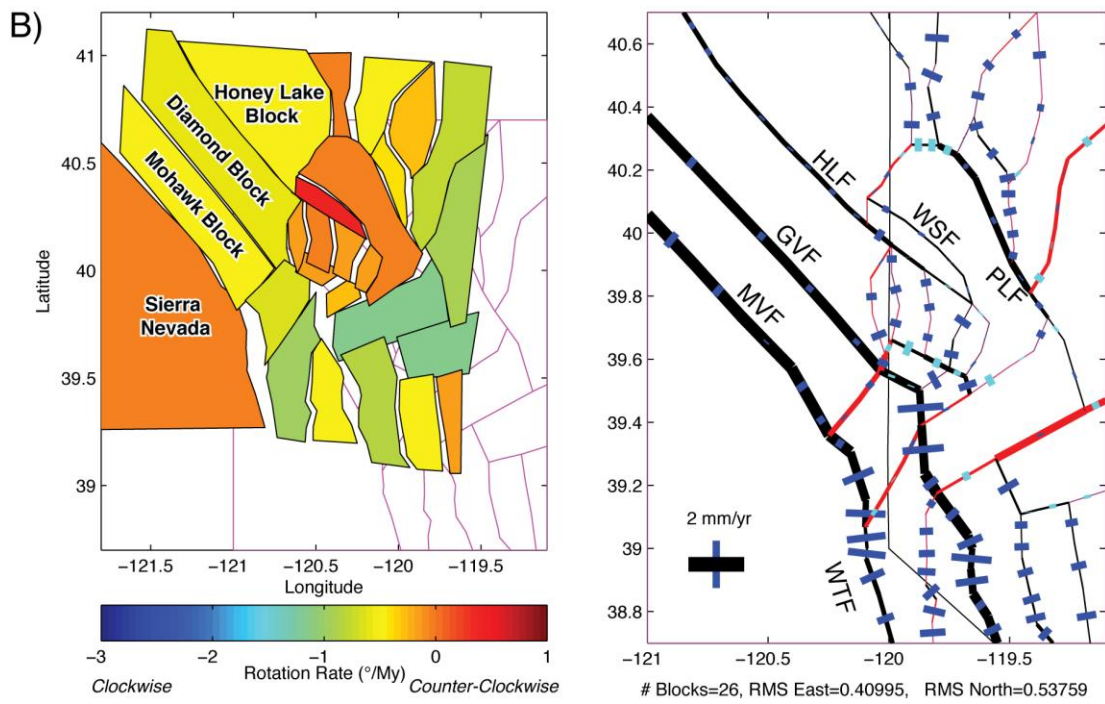
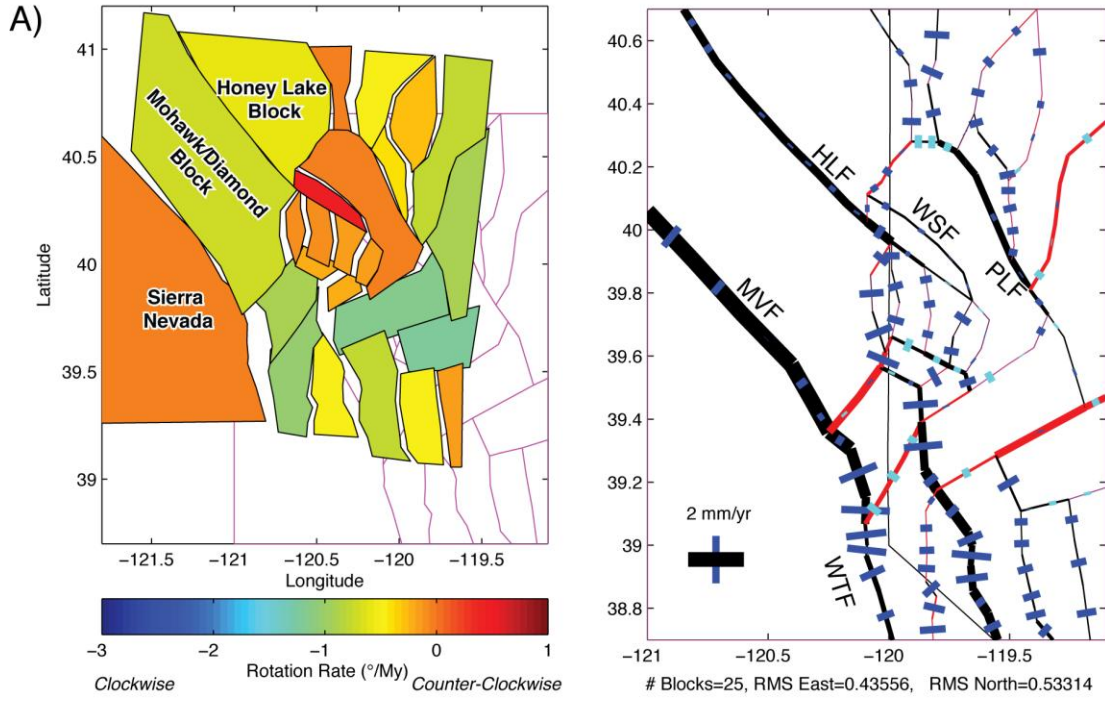


Figure 4. Block model predictions. (a) Results of model without the Grizzly Valley fault. (left) Rigid block (long-term) component of predicted motion is shown, exaggerated by a factor of 10^7 . Color of block indicates vertical axis rotation rate. (right) Slip rates on faults model. Thickness of black (red) line indicates dextral (sinistral) slip rates. Length of fault normal blue (cyan) line indicates normal (thrust) slip rate. (b) Results of model that includes the Grizzly Valley fault. Plots are same as in Figure 4a.

Table 1. Geologic and Geodetic fault slip rate estimates

Faults	Geologic Estimates	Geodetic Estimates	
		Without Grizzly Valley Fault	With Grizzly Valley Fault
Mohawk Valley	0.3 mm/yr minimum Holocene dextral slip (Saywer et al., 2005)	2.2 ± 0.2 mm/yr dextral slip	1.6 ± 0.2 mm/yr dextral slip
Grizzly Valley	Quaternary active dextral slip (Briggs and Wesnousky, 2003)	No estimate	1.4 ± 0.3 mm/yr dextral slip
Honey Lake	~1.7 mm/yr Holocene dextral slip (Turner et al., 2008)	1.2 ± 0.2 mm/yr	0.7 ± 0.2 mm/yr dextral slip
	1.1-2.6 mm/yr Holocene dextral slip (Wills and Borchardt, 1993)		
Warm Springs	Holocene-Latest Quaternary active dextral slip, <0.2 mm/yr slip rate category (USGS Quaternary fault and fold database, 2010)	0.3 ± 0.2 mm/yr dextral slip	0.3 ± 0.2 mm/yr dextral slip

References

- Hammond, W. C., G. Blewitt, and C. Kreemer (2011), Block modeling of crustal deformation of the northern Walker Lane and Basin and Range from GPS velocities, *J. Geophys. Res.*, 116, B04402, doi:10.1029/2010JB007817.
- Sawyer, T. L., R. W. Briggs, and A. R. Ramelli (2003), Paleoseismic investigations of the Mohawk Valley fault zone, Sierra County, northeastern California, Annual Project Summary, U.S. Geological Survey National Earthquake Hazards Reduction Program, Award 04HQGR0089, 4 pp.
- Turner, R., R. Koehler, R. W. Briggs, and S. G. Wesnousky (2008), Reevaluation of the fault slip rate and paleoseismic history of the Honey Lake fault zone, northeastern California, *Bull. Seismol. Soc. Am.*, 98, 1730–1736, doi:10.1785/0120070090.
- U.S. Geological Survey, Nevada Bureau of Mines and Geology, and California Geological Survey, 2010, Quaternary fault and fold database for the United States, accessed May 2012, from USGS web site: <http://earthquakes.usgs.gov/regional/qfaults/>.
- Wills, C. J., and G. Borchardt (1993), Holocene slip rate and earthquake recurrence on the Honey Lake fault zone, northeastern California, *Geology*, 21, 853–856.

Day 3, Stop 1 – Fort Sage Fault Trench

Sunday, September 16: Stop 1

Fort Sage South trench

Rich Briggs, Steve Wesnousky, Jim Brune, Matt Purvance, and Shannon Mahan

Where

Location: 40.057090, -120.089381

This stop is at the bottom of the Fort Sage Mountains, downhill from our campsite on Saturday night. The stop is ~500 m southeast of the access road to the Fort Sage OHV area. **Please park in single file well off the edge of the dirt road to allow traffic to pass into the OHV area.**

What

The main attraction is a trench excavated across the Fort Sage Mountains fault near Doyle, California. The trench exposes deformed alluvial fan deposits that record multiple paleoearthquakes.

Why

The Fort Sage fault is a short (<25 km), seemingly nondescript normal fault, but it is interesting for several reasons:

- The fault ruptured the surface during a M_L 5.6 earthquake in 1950. Scarps as high as 20 cm and surface warping of up to 60 cm were reported by Gianella (1957). This makes the 1950 event one of the smallest magnitude earthquakes associated with surface rupture in the global database. There is very little surficial evidence of the 1950 rupture today.
- The surface trace of the Fort Sage fault lies less than 1 km from a field of precariously balanced rocks (PBRs) (the other kind of PBR) previously identified and studied by Jim Brune and Matt Purvance. PBRs may help to forecast near-fault ground motions in this region, a problem for which there is very little data.

- Finally, in map view the Fort Sage fault appears to connect the Honey Lake and Warm Springs faults. This implies that rupture on the Fort Sage fault may at times be kinematically linked to ruptures on these neighboring major active strike-slip faults.

Trench highlights

The Fort Sage South trench (and its counterpart, the North trench, not visited today) exposed stratigraphic evidence for two large surface-rupture earthquakes prior to 1950. Each of these paleoearthquakes is associated with large colluvial wedges. Radiocarbon and optically-stimulated luminescence (OSL) dates provide fairly good constraints on the ages of the paleoearthquakes. Rupture at ~5.6 ka resulted in surface displacements of at least 0.8 - 1.5 m, implying earthquake moment magnitudes (M_w) of 6.7 – 7.1. An older rupture at ~20.5 ka displaced the ground at least 1.5 m, implying an earthquake of M_w 6.8 - 7.1. We'll discuss the stratigraphy and deformation exposed in the trench wall, including the apparent lack of evidence for prior, small 1950-like decimeter-scale displacements.

The Nitty Gritty

Following this short introduction is a paper in press with BSSA that presents the study in more detail. Check it out!

Things to ponder

- 1950-style ruptures: Are these the "characteristic" type ruptures for this short fault? If so, why don't we see more of them in the trench exposure? Is this a limitation of the resolution of mapping in coarse material? Or are they indeed absent?
- Shallow rupture: The decimeter-scale surface displacement associated with the relatively small M_L 5.6 earthquake in 1950 implies that rupture was very shallow. Is this a common mode of rupture, or did we capture something rare in 1950? The 2008 Mogul sequence near Reno, which culminated with a M_w 5.0 rupture at less than 4 km, also suggests that substantial shallow strain can be stored and released on Basin and Range faults independent of deeper ruptures.
- Larger paleoruptures: How can such a small fault produce such large displacements? Does the Fort Sage fault rupture with its larger neighbors during the large-displacement events?
- Range of displacements: Why is there no range of displacements between the meter-scale paleoruptures and the decimeter 1950 event, as might be predicted by a Gutenberg-Richter slip distribution?

- Precariously-balanced rocks (PBRs): If the PBRs were in their currently fragile states at 5.6 ka, how did they survive the large surface displacements recorded in the trench? What about in 1950?
- Evidence for oblique motion: Trench observations suggest a substantial component of right-oblique motion on the Fort Sage fault. Does this represent a transfer of right-lateral slip from the neighboring Honey Lake and Warm Springs faults? How can this be sustained kinematically in the long term?

Low Footwall Accelerations and Variable Surface Rupture Behavior on the Fort Sage Mountains Fault, Northeast California

Richard W. Briggs¹, Steven G. Wesnousky², James N. Brune³,
Matthew D. Purvance⁴, Shannon A. Mahan⁵

In press, BSSA

¹ Geological Hazards Science Center, US Geological Survey, Golden, CO 80401, USA
(corresponding author)

² Center for Neotectonic Studies, University of Nevada, Reno, Reno, NV 89557, USA

³ Seismological Laboratory, University of Nevada, Reno, Reno, NV 89557, USA

⁴ Itasca Consulting Group, Minneapolis, MN 55401, USA; also at Seismological Laboratory,
University of Nevada, Reno, Reno, NV 89557, USA

⁵ Crustal Geophysics and Geochemistry Science Center, US Geological Survey, Denver, CO 80225,
USA

Abstract

The Fort Sage Mountains fault zone is a normal fault in the Walker Lane of the western Basin and Range that produced a small surface rupture (< 20 cm) during a M_L 5.6 earthquake in 1950. We investigate the paleoseismic history of the Fort Sage fault and find evidence for two paleoearthquakes with surface displacements much larger than those observed in 1950. Rupture of the Fort Sage fault ~ 5.6 ka resulted in surface displacements of at least 0.8 - 1.5 m, implying earthquake moment magnitudes (M_w) of 6.7 - 7.1. An older rupture at ~ 20.5 ka displaced the ground at least 1.5 m, implying an earthquake of M_w 6.8 - 7.1. A field of precariously balanced rocks (PBRs) is located less than 1 km from the surface rupture trace of this Holocene-active normal fault. Ground-motion prediction equations (GMPEs) predict peak ground accelerations (PGAs) of 0.2 - 0.3g for the 1950 rupture and 0.3 - 0.5g for the ~ 5.6 ka paleoearthquake one kilometer from the fault surface trace, yet field tests indicate that the Fort Sage PBRs will be toppled by PGAs between 0.1 - 0.3g. We discuss the paleoseismic history of the Fort Sage fault in the context of the nearby precariously balanced rocks, GMPEs, and probabilistic seismic hazard maps for extensional regimes. If the Fort Sage PBRs are older than the mid-Holocene rupture on the Fort Sage fault zone, this implies that current GMPEs may overestimate near-fault footwall ground motions at this site.

Introduction

The Fort Sage Mountains fault zone is located within the northern Walker Lane, a zone of distributed dextral shear that accommodates 10%–15% of the ~50 mm/year of relative plate motion between the Pacific and North American plates (Fig. 1) (Thatcher et al., 1999; Hammond and Thatcher, 2007). The Fort Sage fault is a 20-km-long, arcuate normal-oblique fault bound by the strike-slip Warm Springs fault zone on the east and the Honey Lake fault zone on the west (Wills, 1990; also see Data and Resources Section). The focus of this study is the part of the Fort Sage fault that last ruptured in 1950 during a M_L 5.6 earthquake, producing scarps 12–20 cm high and surface warping of up to 60 cm (Fig. 2) (Gianella, 1957).

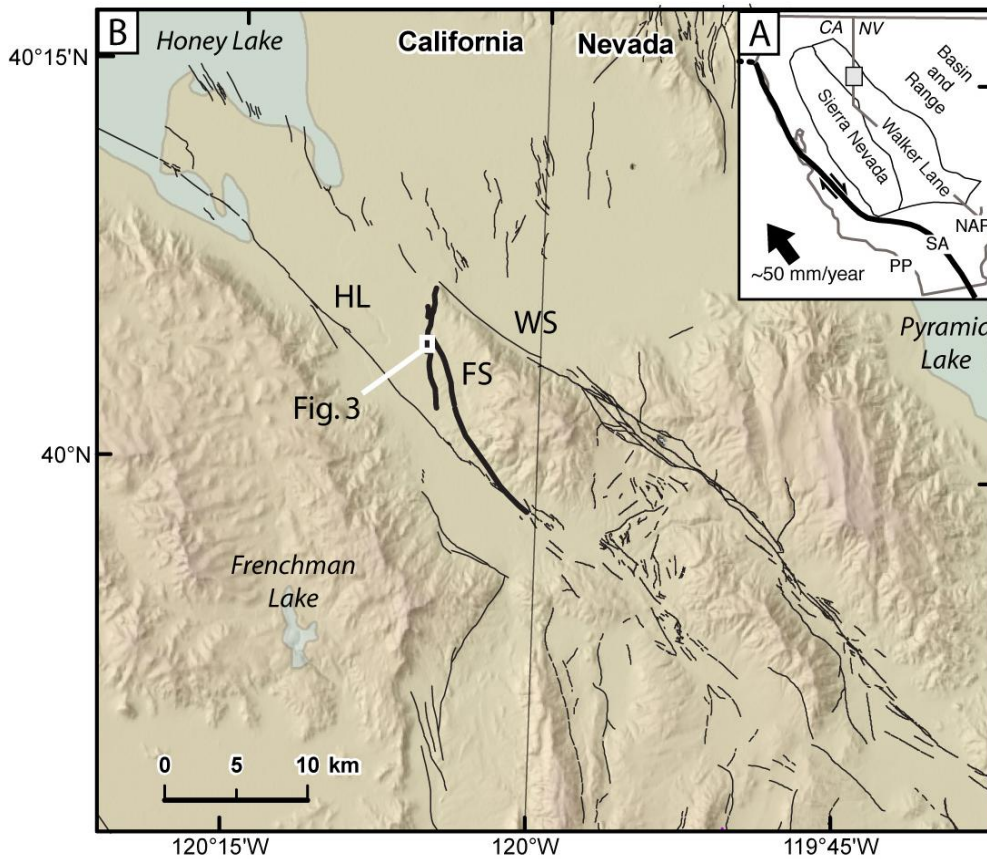


Figure 1. (A) Location of the Walker Lane with respect to the Pacific Plate (PP), San Andreas fault (SA), and North America Plate (NAP). Shaded square indicates extent of Figure 1B. (B) Location of the Fort Sage fault zone (FS). HL, Honey Lake fault zone; WS, Warm Springs fault zone. Faults are from USGS Quaternary Faults-and-Fold Database (Machette et al., 2003) and base map is generated from Shuttle Radar Topography Mission (SRTM) data (Farr et al., 2007). Shaded areas indicate lakes.



Figure 2. Previously unpublished field photos of the 1950 Fort Sage M_L 5.6 surface rupture. The photos were taken a few days after the earthquake by Ted Ramelli, a rancher from nearby Sierra Valley. Exact locations of photos are unknown. (A) Unweathered scarp in grus. Camera case for scale; estimated long dimension of case is 15 cm. (B) Scarp with associated fissure. No scale; estimated vertical offset is <15cm. (C) Sharp offset of swale edge, possibly in right-oblique sense. Leather wallet (arrow) is estimated 10 cm long in the longest dimension. (D) Unweathered scarp in grus. Wallet same as previous. (E) Scarp, fissure, and small slump block. Wallet same as previous.

The surface trace of the 1950 rupture lies within 1 km of a field of previously-identified precariously balanced granodiorite boulders (Brune, 2000; Brune, 2003) (Fig. 3). This study is

motivated by the survival of these boulders on the footwall of a historically-active fault. In this paper we report the number and timing of paleoseismic ruptures along the Fort Sage fault and discuss the fault rupture history in the context of the nearby precariously balanced rocks (PBRs). We also place our observations in the context of ground-motion prediction equations (GMPEs) for extensional regimes.

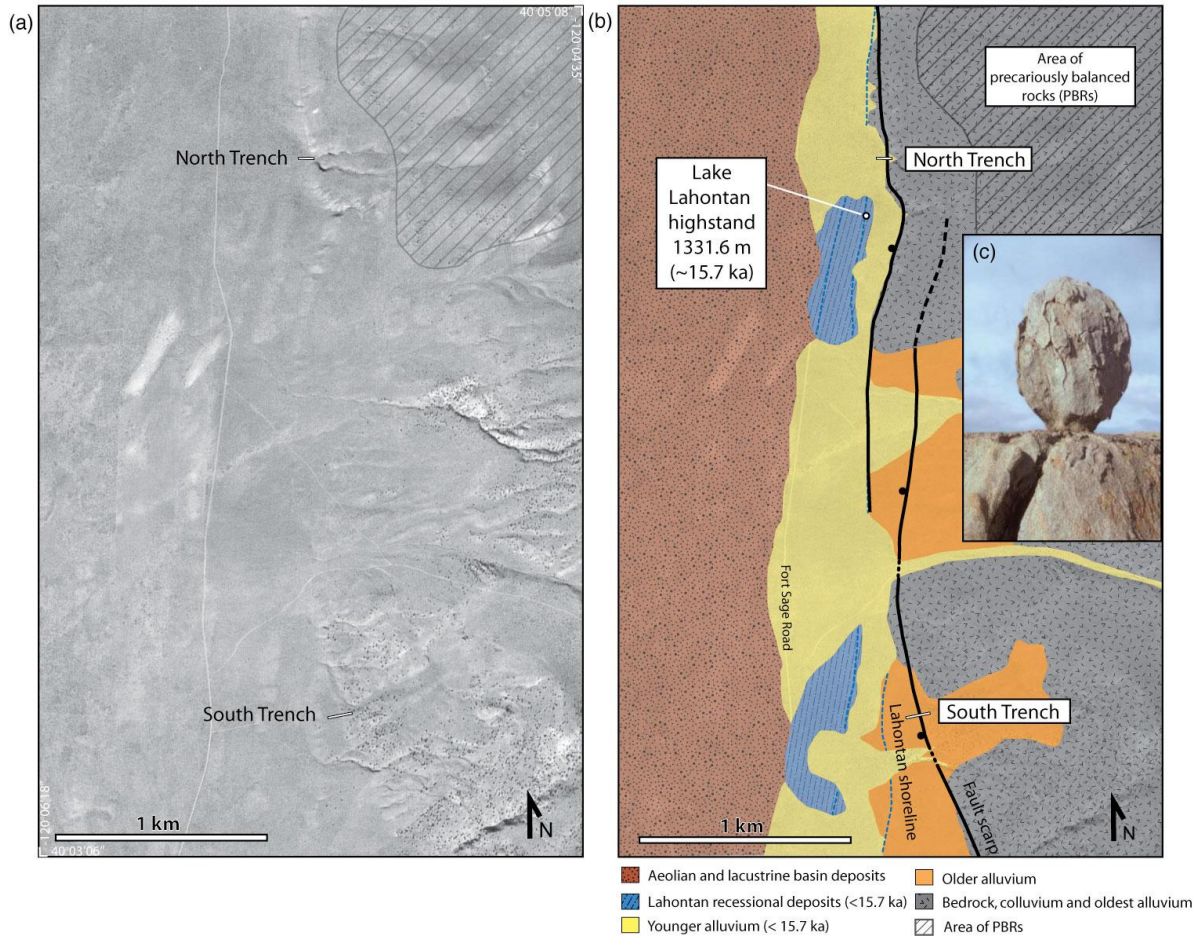


Figure 3. Paired vertical airphoto (A) and generalized surficial-deposit map (B) showing trench sites with respect to the zone of precariously balanced rocks. Photo (C) of precariously balanced rock is from Brune (2003). Individual rock locations are not shown for their protection and preservation (Anderson et al., 2011). Airphoto date is 1957.

Paleoseismic trench investigation

We excavated two trenches across scarps on the surface trace of the Fort Sage fault (Fig. 3). The Fort Sage North trench crosses a scarp on an alluvial fan that postdates the 15.7 ka highstand of pluvial Lake Lahontan (Adams and Wesnousky, 1998; Reheis, 1999). The Fort Sage South trench was excavated across a scarp formed on alluvium older than the Lake Lahontan 15.7 ka highstand (Fig. 3) and located directly above the highstand strandline. Both trenches are located along the mapped trace of the 1950 surface rupture (Gianella, 1957; Wills, 1990) and both preserve evidence of pre-1950 surface ruptures.

Fort Sage North trench

The North trench crosses a 1.6- to 2.1-m-high scarp at the head of a post-Lahontan alluvial fan (Figs. 3 and 4) and exposes loose, fine-grained alluvial grus derived from Cretaceous granodiorite upslope, with two primary depositional packages (Units 1 and 2) separated by a weak soil (Fig. 4). We observed very little internal stratigraphic structure in the massive grus units 1 and 2. The scarp-forming fault rupture, event P1, juxtaposes fan stratigraphy in the footwall against a single package of massive scarp-derived colluvium (unit C1) in the hanging wall. A weak soil (~20 cm of incipient B horizon) is forming at the present-day surface atop colluvial package C1.

The maximum age of event P1 in the North trench can be estimated from detrital charcoal in a weak soil beneath colluvial package C1 (Fig. 4). Sample FSN-C1 (Fig. 4 and Table 1) limits the time of the scarp-forming fault rupture to sometime after 6160 ± 130 cal. yr. B.P. (two-sigma 95% errors). The detrital charcoal is likely reworked from wildfires near the site and so this sample is interpreted as providing a maximum limiting age for earthquake P1. The age of sample FSN-C1 is stratigraphically consistent with the slightly older sample FSN-C2 (7165 ± 250 cal. yr. B.P.), which was obtained 50 cm lower in the exposure. OSL ages obtained from the South trench suggest that the maximum age of earthquake P1 may be slightly older than $\sim 6160 \pm 130$ cal. yr. B.P., and OxCal modeling (Bronk Ramsey, 2007, 2009) of radiocarbon and OSL ages from both trenches suggests an age range of 4.9-6.3 ka for earthquake P1 (see below).

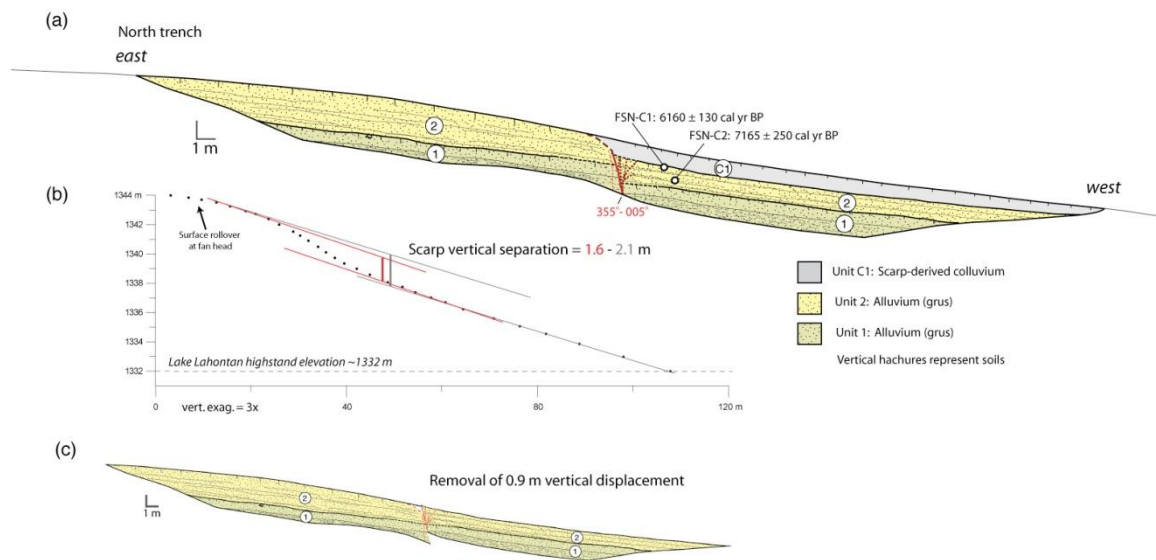


Figure 4. (A) Log of Fort Sage North trench exposure. Units 1 and 2 are weakly-bedded grus separated by an incipient soil, and C1 is scarp-derived colluvium. Fault zone and fault strike are shown in red. (B) Estimates of vertical separation across scarp. Range is due to variable far-field projection of surfaces into the fault zone. (C) Restoration of 0.9 m of vertical displacement removes colluvium C1 and aligns the contact between Units 1 and 2.

Surface offset from the pre-1950 earthquake P1 at the North trench site can be estimated from the scarp height, the thickness of colluvial package C1, and retrodeformation of the trench units (Fig. 4). The scarp appears to be a single-event feature based on its relatively small size and lack of compound character. The colluvial package C1 is 0.9 m thick and provides a minimum limit on surface displacement and allows a maximum of ~1.8 m, or twice the thickness of the wedge (Fig. 4a). Based on the scarp's topographic profile, the vertical separation across the scarp ranges from 1.6 - 2.1 m depending on whether far-field or near-field surface slopes are projected into the fault zone (Fig. 4b); this projection is complicated by the fan-head setting of the scarp and backtilting of the uphill surface toward the canyon mouth. Retrodeformation suggests that the surface offset was at least 0.9 m based on restoration of the contact between Units 1 and 2 (Fig. 4c). This reconstruction suggests that Unit 2 thinned downslope prior to the most recent surface rupture and that the fan deposits possibly draped a pre-existing scarp; if this is the case, the scarp height may overestimate fault displacement during event P1. However, a significant component of oblique slip during pre-1950 events (based on observations in the South trench described below) makes reconstructions based only on layer thicknesses suspect. Given these constraints, the most likely surface displacement during the penultimate earthquake P1 is 0.9 - 1.5 m, which is the minimum offset allowed by scarp-derived colluvium and the smaller estimate of vertical separation across the scarp, minus 12 cm of offset in 1950 at the site reported by Gianella (1957).

We did not recognize the 1950 surface rupture in the North trench exposure, possibly due to the small displacement along this stretch of the fault (approximately 12 cm, as inferred from Gianella, 1957) and relatively poor stratigraphy exposed in the trench. Field photos taken a few days after the 1950 rupture by Ted Ramelli (Fig. 2) show a sharp, decimeter-scale scarp and associated fissure. The granite grus of the fan surface is easily weathered and Gianella (1957) reported "(I)n June, 1956. . . little evidence of the (1950 scarps) remain." Rapid scarp degradation after 1950 is also evident in the 1958 field photos of Karl Steinbrugge, which show only discontinuous, low-angle scarps that are "the best remaining examples of faulting in this area" (See Data and Resources Section). No obvious surface expression of the 1950 earthquake remains along the Fort Sage range front today.

Fort Sage South trench

The South trench crosses an approximately 2.0-m-high scarp on an alluvial fan just above the 15.7 ka highstand of Lake Lahontan (Figs. 3 and 5). The trench exposes well-sorted fluvial sands and gravels (Units 1a-d) and poorly-sorted debris-flow deposits (Units 2a-c) derived from conglomerates, sandstones, and granodiorites upslope (Figure 5). These units are vertically offset by a main fault zone **a** and subsidiary fault zones **b-f**, resulting in the formation and preservation of colluvial packages C1 and C2.

The 1950 rupture is expressed in the South trench as the extension of shear zones to the surface and as a thickened Av soil horizon (approx. 5 cm) between the main fault zone **a** and secondary fault zone **b** (Fig 5). Aside from this zone of thickened silt, we did not observe a colluvial package associated

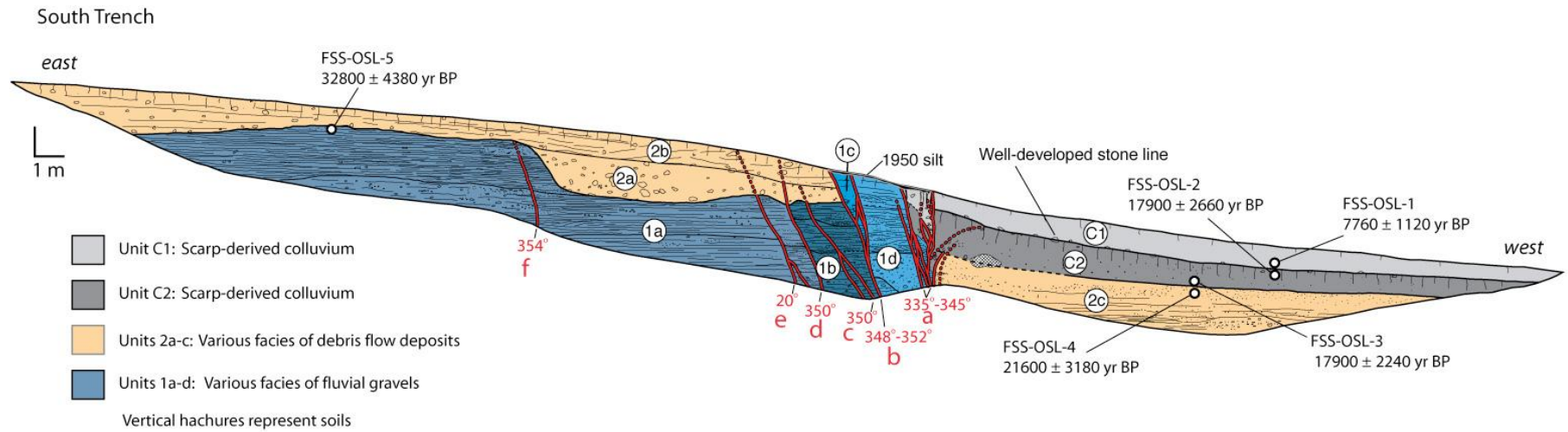


Figure 5. Log of Fort Sage South trench exposure. Units 1a-1d are well-sorted fluvial sands and gravels; units 2a-c are poorly-sorted debris flow deposits; and C1 and C2 are scarp-derived colluvium. Faults and fault strikes are shown in red.

with the small 1950 rupture here, and deformation appears to have occurred mainly in the form of warping and cracking as discussed by Gianella (1957).

Stratigraphic evidence shows that two surface-rupturing earthquakes, events P1 and P2, occurred at this site prior to the 1950 rupture (Fig. 5). The most recent pre-1950 earthquake, event P1, is indicated by the scarp-derived colluvial package C1 and by a fissure in underlying colluvial package C2 that is filled with unit C1. We correlate colluvial packages C1 in both the North and South trenches on the basis of their similar stratigraphic positions, thicknesses, close proximity of trenches, and soil development (~20 cm of incipient B horizon development at the modern surface). Vertical offset during event P1 in the South trench is at least 0.8 m, or the maximum thickness of the C1 colluvium.

Evidence for the second paleoearthquake in the South trench, paleoearthquake P2, is preservation of the scarp-derived colluvial package C2. A period of prolonged surface stability following this event resulted in the formation of a weak argillic B horizon on colluvium C2 and a well-defined stone line. This buried soil and prominent stone line allow easy differentiation between colluvial packages C1 and C2. The vertical offset from event P2 was at least 1.5 m based on the maximum thickness of colluvial package C2.

Age control for events P1 and P2 in the South trench is from optically stimulated luminescence (OSL) on quartz grains and infrared stimulated luminescence (IRSL) on feldspar grains. These dates are from bulk samples of fine-grained sediment (Fig. 5 and Table 2). The age of paleoearthquake P1 is constrained by samples FSS-OSL-1 and -2, which limit the time of P1 in the South trench to between 7.76 ± 1.12 ka and 17.9 ± 2.66 ka (two-sigma (95%) errors). This interval is slightly older than, and does not overlap with, the 6.1 ± 0.13 ka maximum age for paleoearthquake P1 obtained from the North trench. The OSL age from post-paleoearthquake P1 colluvium (C1) in the South trench (7.76 ± 1.12 ka) is slightly older than the radiocarbon date for the pre-earthquake buried surface in the North trench (6.1 ± 0.13 ka). The older, higher date may result from incomplete resetting of sample FSS-OSL-1. Paleoearthquake P2 occurred between 17.9 ± 2.24 and 21.6 ± 3.18 ka based on bounding samples FSS-OSL-3 and -4. Events P1 and P2 are both younger than 32.8 ± 4.38 ka, which is the minimum age of footwall deposits estimated from sample FSS-OSL-5.

To better constrain the ages of paleoearthquakes P1 and P2 with dates from both trenches, we model their probable age ranges using the program OxCal (Fig. 6) (See Data and Resources Section), which uses Bayesian statistics and stratigraphic ordering information to create probability distributions for boundaries between ordered, and often overlapping, dates (Lienkaemper and Bronk Ramsey, 2009). The assumptions of the model we developed in OxCal (see Appendix) are 1) paleoearthquake P1 is the same event in both trenches; 2) earthquakes are best modeled as boundaries in OxCal; and 3) OSL dates FSS-OSL-2 and -3 from the South trench are best combined to form a phase within the model, although combining these dates has very little effect on the model results.

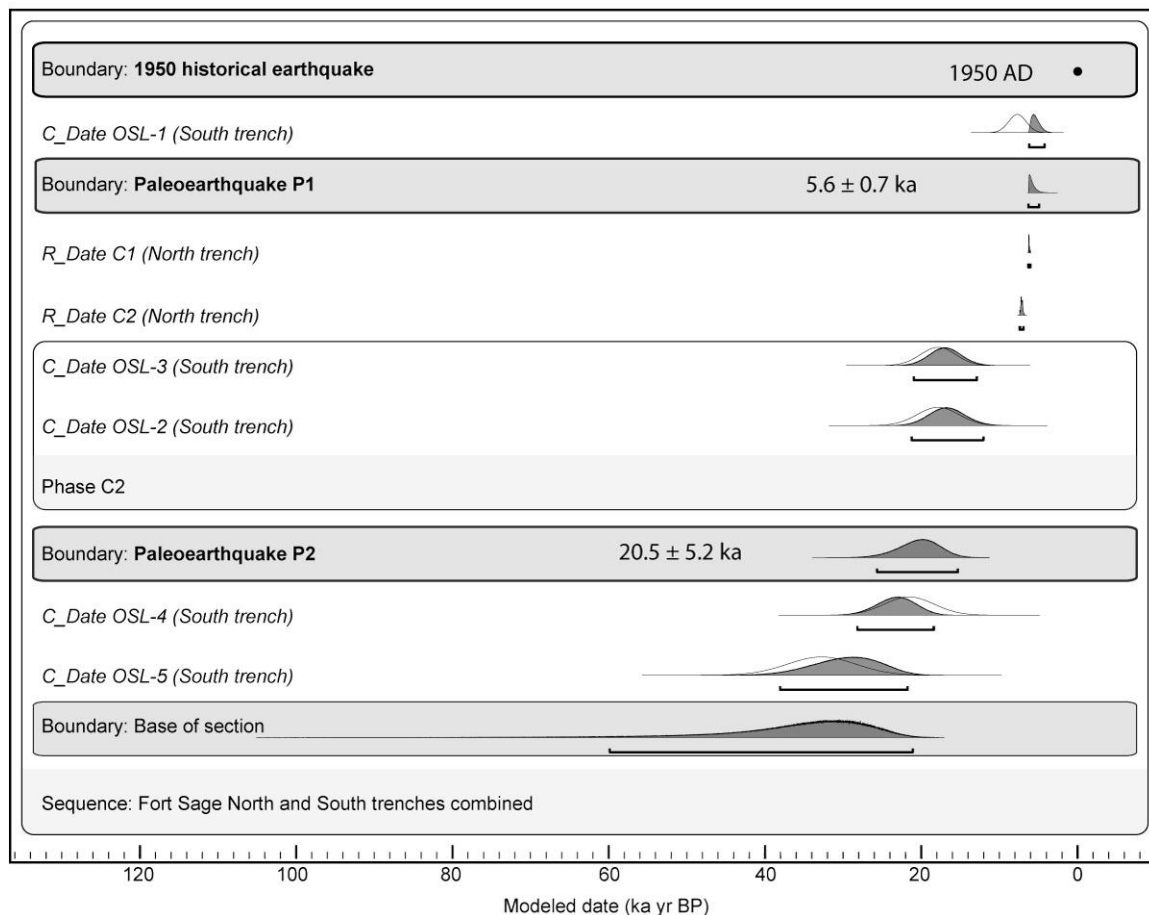


Figure 6. OxCal model of a sequence that combines North and South trench dates in a composite stratigraphy. Dates are shown as probability distribution functions (PDFs). Light grey distributions are the likelihood distributions of the OSL and radiocarbon dates, and darker distributions are modeled (posterior) PDFs. Bars below PDFs show the 95-percentile confidence ranges. Paleoearthquakes P1 and P2 are modeled as boundaries.

The main outcome of the OxCal modeling is that the most likely age of paleoearthquake P1 is 5.6 ± 0.7 ka (6275-4923 BP; two-sigma (95%) confidence interval) (Fig. 6). This interval includes the age range for an earthquake that occurred after 6.1 ± 0.13 ka (radiocarbon sample FSN-C1; North trench) but before the (apparently inverted) overlying OSL age of 7.76 ± 1.12 (FSS-OSL-1; South trench). Because the age of sample FSS-OSL-1 (South trench) is inverted with respect to the underlying radiocarbon ages of samples FSN-C1 and -C2 (North trench), the OxCal model returns a poor agreement index A value (19.9%) for the modeled age of the sample FSS-OSL-1 (6195-4220 BP). This is a formal indication that sample FSS-OSL-1 is an outlier. Alternatively, the underlying radiocarbon ages FSN-C-1 and FSN-C-2 may be too young if they were not obtained from detrital charcoal emplaced in successive debris-flow deposits as interpreted from the trench exposure. In any case, the combined OSL and radiocarbon dates and stratigraphic evidence point toward a large surface-rupture earthquake at ~ 5.6 ka in both trenches.

The age of paleoearthquake P2 obtained from the OxCal model is 20.5 ± 5.2 ka, similar to but slightly older than the ~ 19.8 ka age of P2 interpreted from OSL bounding ages in the South

trench alone. While a robust recurrence interval cannot be obtained from only two events, it appears that the Fort Sage fault ruptures in large ($>M$ 6.8) earthquakes at time scales of approximately 10-20 ka, similar to recurrence intervals obtained for typical Basin and Range normal faults (Wesnousky et al., 2005).

The footwall deposits east of the main fault zone in the South trench are deformed by several subsidiary shear zones **b-f**, and the stratigraphic packages they juxtapose are denoted as Units 1a-1d on Figure 5. Pronounced changes in layer thicknesses, facies mismatches, and apparent reverse displacement across these footwall shears suggest a substantial oblique component of deformation. The strike of the subsidiary faults is rotated 10-40 degrees in a clockwise direction with respect to the main fault zone, suggesting that they are R-type shears resulting from right-oblique offset (Fig. 5). The facies mismatch between the debris-flow deposits of the hanging wall (unit 2c) and the uppermost footwall (unit 2b) may also be evidence of oblique offset. However, no correlative laterally offset features were observed in the trench exposure. Shears that terminate in the footwall block, such as strands **c** and **f**, are probably evidence of older, undated events in the exposure.

Predicted paleoearthquake magnitudes

The moment magnitude (M_w) of an earthquake can be estimated from regressions that relate displacement to magnitude. Given that we only have displacement values obtained directly from trench exposures, we use these data to estimate paleoearthquake magnitude because independent limits on paleorupture length or area are not available. The trenches record vertical displacements from paleoearthquake P1 of 0.8 to 1.5 m, which correspond to M_w 6.9-7.1 using the regression of Wells and Coppersmith (1994), or M_w 6.8-7.1 using the approach of Biasi and Weldon (2006).

The regressions of Wells and Coppersmith (1994) and Biasi and Weldon (2006) use mean displacement values. It is difficult to obtain mean event displacements from our trenches because we have only two closely spaced sites along the fault, but if we take 1.15 m to represent mean offset during paleoearthquake P1 (the value midway between 0.8 and 1.5 m), both the Wells and Coppersmith (1994) and Biasi and Weldon (2006) methods predict a paleoearthquake magnitude of M_w 7.0. The full range of paleoearthquake magnitudes that might accompany 1.15 m of average surface offset, given that we have only 2 measurements that span less than 10% of the length of the fault, is M_w 6.7-7.9 (Hemphill-Haley and Weldon, 1999). The largest value, M_w 7.9, seems highly unlikely given that the mapped length of the Fort Sage fault zone is only about 20 km. Given the uncertainties in our displacement measurements and the displacement-to-magnitude regressions, we use M_w 6.7-7.1 as the most likely size of paleoearthquake P1.

A similar exercise for paleoearthquake P2 using the minimum displacement value of 1.5 m observed in the South trench leads to a paleoearthquake estimate of M_w 7.1 and a possible range of M_w 6.8-8.0. Using logic similar to above, we use M_w 6.8 - 7.1 as the most likely size of paleoearthquake P2.

Fort Sage precarious boulder field

The surface trace of the Fort Sage fault is less than 1 km from a field of precariously balanced rocks, or PBRs (Brune, 2000; Anderson et al., 2011) (Fig 3). PBRs are rocks balanced on

pedestals and that have high height-to-width ratios making them easily susceptible to toppling (Fig. 3c) (Brune, 1996). PBRs on granitic tors such as the Fort Sage Mountains are formed by chemical weathering and subsequent physical exhumation of relatively resistant corestones (Linton, 1955).

Precariously balanced rocks are natural ground-motion instruments (Brune, 1996), and numerous field and theoretical studies have demonstrated that untoppled PBRs place limits on ground motions near active faults (Brune, 1996; Shi et al, 1996; Anooshepoor and Brune, 2002; Brune et al., 2006). PBRs potentially record paleo-ground motions in regions with few instrumental records and PBR-derived ground-motion information may be of value in probabilistic seismic hazard analyses (PSHA) (Anderson and Brune, 1999; Stirling et al., 2002; O'Connell, LaForge, and Liu 2007; Purvance et al., 2008; Anderson et al., 2011).

Because the Fort Sage PBRs are very near the surface trace of an active normal fault, they present an opportunity to place limits on near-field, normal-fault, footwall ground motions (Brune, 2000). Theoretical studies predict that ground motions are asymmetric about dipping faults that juxtapose dissimilar material (Oglesby et al., 1998; Shi et al., 1997; Brune and Anooshepoor, 1999; O'Connell, Ma, and Archuleta, 2007; Ma and Beroza, 2008). Instrumental strong-motion records near the surface trace of a normal-fault earthquake are rare, with one exception being the observation that peak accelerations were nearly 50 percent lower on the footwall than the hanging wall during the 2006 M_w 5.4 Morelia, Mexico normal-fault earthquake (Munguía et al., 2009).

Quasi-static toppling tests of the Fort Sage PBRs show that they can be toppled by horizontal accelerations of 0.2 g , with a range of toppling accelerations of 0.1-0.3 g (Brune, 2000; Purvance, unpublished data). The age of the Fort Sage PBRs is unknown. By analogy with similar PBRs in Southern California that have been dated with cosmogenic surface exposure techniques (Bell et al., 1998; Balco et al., 2011), the Fort Sage PBRs are probably over ten thousand years old. Post-Lahontan (15.7 ka) erosion rates determined by cosmogenic nuclide analysis in the Fort Sage Mountains along catchment margins are 2-3 cm/ka (Granger et al., 1996; Riebe et al., 2000), making it unlikely that entire several-meter-high boulders and their pedestals have been exhumed since desiccation of Lake Lahontan. We estimate ages of 10 ± 5 ka for the Fort Sage PBRs in their present unstable form on the basis of present-day erosion rates and analogs in southern Nevada and California (Bell et al., 1998; Balco et al., 2011). Determination of the actual ages of Fort Sage PBRs will require a focused cosmogenic nuclide dating and modeling effort as recently demonstrated by Balco et al. (2011). While we consider it unlikely, the possibility that the Fort Sage PBRs represent a statistical remnant of a former larger population of toppled rocks (O'Connell, LaForge, and Liu 2007) should be addressed by a detailed mapping effort.

Predicted peak ground acceleration

Predictions of peak ground acceleration (PGA) are derived from models that estimate ground motions based on earthquake magnitudes, site conditions, faulting style, and attenuation relations. Several ground motion prediction equations (GMPEs) have been developed for extensional regions and normal faults (Power et al., 2008). We apply a representative sample of GMPEs (Chiou and Youngs, 2008; Abrahamson and Silva, 2008; Campbell and Bozorgnia, 2008; Boore and Atkinson, 2008; Spudich et al., 1999, Pankow and Pechmann, 2004) to the 1950 M_l 5.6 surface-rupture earthquake and to the range of paleoearthquake magnitudes (M_w 6.7-7.1) that we

calculate from fault offsets associated with paleoearthquake P1. For all models we calculate PGA at a hard rock site ($V_{s30} = 760$ m/s) on the fault footwall and assume a 45-degree dipping fault plane. We calculated distance with respect to the surface rupture trace. Calculations were performed using OpenSHA, an open-source platform for conducting seismic hazard analysis (Field et al., 2003; also see Data and Resources Section).

For the 1950 M_L 5.6 surface-rupture earthquake, the GMPEs predict median PGAs ranging from 0.2 - 0.3 g at 1 km, the distance from the 1950 surface rupture trace to the nearby PBR field (Fig. 7a). The Abrahamson and Silva (2008), Chiou and Youngs (2008), and Campbell and Bozorgnia (2008) GMPEs predict median PGAs of 0.3 g and above, sufficient to topple most of the Fort Sage PBRs. The Boore and Atkinson (2008) and Spudich et al. (1999) GMPEs predict median PGAs of 0.20 - 0.22, very near the 0.2 g toppling value for the Fort Sage PBRs derived from field tests. No field survey of the Fort Sage PBRs was conducted after the 1950 earthquake, but reconnaissance inspection of the Fort Sage PBR field does not show clear evidence for

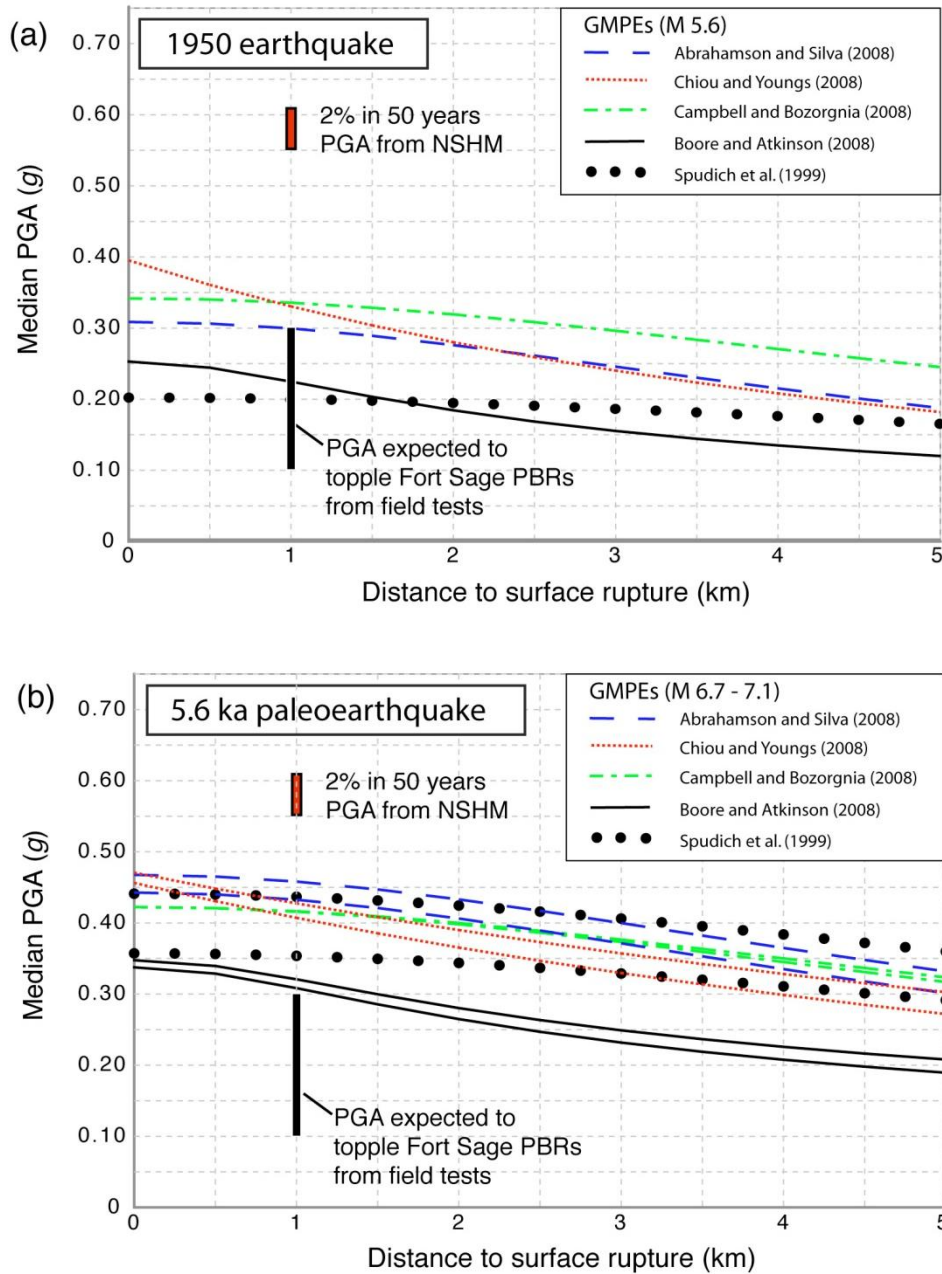


Figure 7. Median PGA (g) plotted against distance from the surface trace of the Fort Sage fault from ground-motion prediction equations (GMPEs). (A) Ground motion predictions for the 1950 M_L 5.6 surface-rupture earthquake. The Fort Sage PBRs are <1 km from the fault. PGA expected to topple Fort Sage PBRs is from Brune (2000). Two percent in 50 years PGA at PBR site is from the 2008 update of the National Seismic Hazard Maps (Petersen et al., 2008). Calculations performed with OpenSHA (Field et al., 2003). (B) Ground motion predictions for paleoearthquake P1 at ~5.6 ka, which is inferred to have ranged in magnitude from M_w 6.7 - 7.1.

significant numbers of boulders toppled in 1950. This observation suggests that the existing suite of GMPEs overpredicts near-fault footwall ground motions for this small-magnitude earthquake. A direct test of this hypothesis will require careful mapping of the Fort Sage PBR field.

For paleoearthquake P1 of estimated magnitude 6.7 - 7.1, the GMPEs predict PGAs ranging from 0.3 - 0.5 g at 1 km (Fig. 7b). The variation in the predicted ground motions arises from differing assumptions built into the models. Nonetheless, they all predict peak accelerations for the Fort Sage boulder field that are larger than the toppling accelerations derived from field measurements. The model of Boore and Atkinson (2008) predicts the lowest ground motions at all distances from the fault, but still predicts slightly higher accelerations (0.3 g) than would be required to topple most of the Fort Sage PBRs.

The US Geological Survey National Seismic Hazard Map (NSHM) depicts accelerations as the sum of probabilities of all potential sources that contribute to ground motion at a site (Petersen et al., 2008). At the location of the Fort Sage PBRs, the 2008 update of the NSHM estimates a PGA of 0.55-0.61 g at the 2% in 50 years level (\sim 2475 year return time) - a typical return time used for building design in low seismicity regions of the conterminous United States (Fig. 7). The NSHM does not provide site-specific hazard curves, but the hard-rock site conditions (granitic bedrock) at the location of the Fort Sage PBRs (Kalkan et al., 2010) are an appropriate application of the generic NSHM curves, which are calculated for $V_{s30} = 760$ m/s. Thus an important inference derived from the National Seismic Hazard Maps is that the PBRs at Fort Sage have been subject to \sim 0.6 PGA (2% in 50 years, or 2475 year return time) shaking at least twice due to all regional sources since \sim 5 ka.

Summary and conclusions

Rupture of the Fort Sage fault between 4.9-6.3 ka resulted in surface displacements of at least 0.8-1.5 m, implying a paleoearthquake of M_w 6.7–7.1. Based on a suite of commonly employed ground-motion prediction equations (GMPEs), the predicted range of footwall PGAs at 1 km distance from the surface paleorupture during this paleoearthquake is 0.3 - 0.5 g .

Precariously balanced rocks that can be toppled by accelerations of 0.1-0.3 g are located less than 1 km from the Fort Sage fault surface trace. The age of these rocks is unknown, but we estimate that they gained their currently unstable form at 10 ± 5 ka. If these PBRs are older than 4.9-6.3 ka (which is very likely), then they have survived at least one M 6.7 – 7.1 earthquake on a normal fault less than 1 km away. The presence of the Fort Sage PBRs argues for low PGAs at the site despite their close proximity to three Holocene-active faults (the Honey Lake, Warm Springs, and Fort Sage faults). Furthermore, survival of these rocks contrasts with the higher accelerations predicted deterministically by commonly used GMPEs and the probabilistic predictions of the NSHM.

There are at least three explanations for the apparent discrepancy between a large surface-rupture mid-Holocene earthquake on the Fort Sage fault and the presence of a PBR field less than one kilometer away. First, our paleoseismic results may be flawed and paleoearthquake P1 may be incorrectly dated, or the paleoearthquake magnitude may be overestimated. We consider this unlikely

because the 4.9-6.3 ka age of event P1 is well constrained by straightforward geomorphology and stratigraphy at two trenches with radiocarbon and OSL ages, and the vertical surface offsets observed in both trenches (0.8-1.5 m) are consistent with a large ($M 6.7 - 7.1$) earthquake. A second explanation may be that the assumed ages (10 ± 5 ka) and fragility (toppling at 0.1-0.3 PGA) of the PBRs might be incorrect. Third, the GMPEs commonly used for normal faults might not fully capture near-fault ground motions, or they may overestimate accelerations overall. To explain the apparent discrepancy between the paleoseismic information, PBR observations, and GMPEs, we recommend that the ages and fragilities of the Fort Sage PBRs be conclusively established and that the GMPEs be reevaluated in the context of the geologic field data.

An important result of this work for paleoseismic trenching studies is that evidence of the 1950 rupture is absent or obscure, which highlights the problem of recognizing small-offset earthquakes in relatively coarse-grained deposits. Because of its small displacement (Fig. 2) and the nature of sediment exposed in the trenches, it is unlikely that the M_L 5.6 1950 surface break would be recognized in the absence of historical information in this setting. We can't rule out the possibility that the fault has ruptured previously in multiple 1950-style events, but we can say that it does not characteristically rupture only in repeated, small-displacement 1950-style events. Instead, the fault has also produced less-frequent, much larger ruptures that are more typical of range-bounding Basin and Range normal faults. We do not observe a range in offsets between presumably more frequent 1950-type decimeter-scale ruptures and the rarer meter-scale surface offsets associated with paleoearthquakes P1 and P2. In this regard, the limited paleoseismic and historical evidence does not support either a strictly Gutenberg-Richter or characteristic earthquake model.

The reason for the variable surface-rupture behavior of the Fort Sage fault is not known, but a complicating factor is that this fault may at times break in conjunction with ruptures on nearby large strike-slip faults and thus may transfer slip between these larger structures (e.g. Caskey et al., 1996). For example, paleoearthquakes on the nearby Honey Lake fault zone (Fig. 1) occurred during the intervals 5.6 - 6.7 ka and 4.7 - 5.6 ka (Turner et al., 2008). Either of these Honey Lake events might correspond to paleoearthquake P1 documented in the Fort Sage trenches, but the present resolution of the ages of these events does not allow us to confidently correlate events between these adjacent faults.

Data and Resources

- OxCal calibration and modeling of radiocarbon dates used in this study are from Bronk Ramsey, C. (2007). OxCal Program, v. 4.0, Radiocarbon Accelerator Unit, University of Oxford, UK; <https://c14.arch.ox.ac.uk/oxcal.html> (lasted accessed October 2011).
- Faults depicted on Fig. 1 and discussed in the introduction are from Machette, M. N., K. M. Haller, R. L. Dart, and S. B. Rhea (2003). Quaternary fault and fold database of the United States, U.S. Geol. Surv. Open-File Rept. 03-417; <http://earthquake.usgs.gov/regional/qfaults/> (last accessed November 2011).
- Photographs of the 1950 Fort Sage Fault rupture discussed in the text are from Steinbrugge, K.V. (1958). Karl V. Steinbrugge Collection, University of California, Berkeley; http://nisee.berkeley.edu/visual_resources/steinbrugge_collection.html (last accessed September 2011).

- GMPE analyses were conducted using software downloaded from OpenSHA <http://www.opensha.org/> (last accessed September 2011).

Acknowledgments

Anthony Crone, Steve Personius, Ryan Gold, Senthil Kumar, and Andrew Barron assisted with fieldwork. Ted and Alan Ramelli graciously provided the surface rupture photos in Figure 2. Chris Wills kindly provided the airphoto used in Figure 3 and discussed the insights he gained from mapping the fault. Ken Adams helped pinpoint the Seho highstand elevation. Radiocarbon analyses were carried out by the Center for Accelerator Mass Spectrometry (CAMS) at Lawrence Livermore National Laboratory. This work was supported by the external grants program of the National Earthquake Hazards Reduction Program (NEHRP). Thoughtful reviews by Ryan Gold, Anthony Crone, Mark Stirling and Richard Koehler greatly improved the manuscript. Center for Neotectonic Studies Contribution #63.

References

- Abrahamson, N. and W. Silva (2008). Summary of the Abrahamson and Silva NGA ground-motion relations. *Earthquake Spectra* 24, 67-98.
- Adams, K. D., and S. G. Wesnousky (1998). Shoreline processes and the age of the Lake Lahontan highstand in the Jessup embayment, Nevada, *Bull. Geol. Soc. Am.* 110, 1318–1332.
- Anderson, J. G., and J. N. Brune (1999). Probabilistic seismic hazard analysis without the ergodic assumption. *Seismol. Res. Lett.*, 70, 19-28
- Anderson, J.G., Brune, J.N., Biasi, G., Anooshehpour, A., and M. Purvance (2011). Workshop Report: Applications of Precarious Rocks and Related Fragile Geological Features to U.S. National Hazard Maps. *Seismol. Res. Lett.*, 82, 431-441.
- Anooshehpour, A., and J. N. Brune (2002). Verification of precarious methodology using shake table tests of rocks and rock models. *Int. J. Soil Dynam. Earthquake Eng.*, 22, 917 -922.
- Balco, G., Purvance, M.D., and D.H. Rood (2011). Exposure dating of precariously balanced rocks. *Quaternary Geochronology*, 6, 295–303.
- Bell, J.W., Brune, J.N., Liu, T., Zreda, M. and Yount, J.C. (1998). Dating precariously balanced rocks in seismically active parts of California and Nevada. *Geology*, 26, 495-498.
- Biasi, G. P., and R. J. Weldon (2006). Estimating surface rupture length and magnitude of paleoearthquakes from point measurements of rupture displacement, *Bull. Geol. Soc. Am.* 96, 1612-1623.
- Boore, D.M. and G.M. Atkinson (2008). Ground-Motion Prediction Equations for the Average Horizontal Component of PGA, PGV, and 5%-Damped PSA at Spectral Periods between 0.01 s and 10.0 s. *Earthquake Spectra*, 24, 99-138.

Brune, J. N. (1996). Precariously balanced rocks and ground-motion maps for Southern California, *Bull. Seismol. Soc. Am.*, 86, 43-54.

Brune, J.N. (2000). Precarious rock evidence for low ground shaking on the footwall of major normal faults. *Bull. Seismol. Soc. Am.*, 90, 1107-1112.

Brune, J.N. (2003). Precarious rock evidence for low near-source accelerations for trans-tensional strike-slip earthquakes. *Phys. Earth Planet In.*, 137, 229-239.

Brune, J.N., Anooshehpour, A., Purvance, M.D., and Brune, R.J. (2006). Band of precariously balanced rocks between the Elsinore and San Jacinto, California, fault zones: Constraints on ground motion for large earthquakes. *Geology*, 34, 137-140.

Brune, J. N., and A. Anooshehpour (1999). Dynamic geometrical effects on strong ground motion in a normal fault model, *J. Geophys. Res.*, 104, 809 -815.

Bronk Ramsey, C. (2009). Bayesian analysis of radiocarbon dates. *Radiocarbon*, 51, 337-360.

Campbell, K.W. and Y. Bozorgnia (2008). NGA Ground Motion Model for the Geometric Mean Horizontal Component of PGA, PGV, PGD and 5% Damped Linear Elastic Response Spectra for Periods Ranging from 0.01 to 10 s. *Earthquake Spectra*, 24,139-171.

Caskey, S.J., Wesnousky, S.G., Zhang, P., and D.B. Slemmons (1996). Estimating prehistoric earthquake magnitude from point measurements of surface rupture. *Bull. Seismo. Soc. Amer.*, 86, 761-787.

Chiou, B.S.J. and R.R. Youngs (2008). An NGA model for the average horizontal component of peak ground motion and response spectra. *Earthquake Spectra*, 24, 173-215.

Farr, T. G., Rosen, P.A., Caro, E., Crippen, R., Durn, R., Hensley, S., Kobrick, M., Paller, M., Rodriguez, E., Roth, L., et al. (2007). The Shuttle radar topography mission, *Rev. Geophys.*, 45, RG2004, doi:10.1029/2005RG000183.

Field, E.H., T.H. Jordan, and C.A. Cornell (2003). OpenSHA: A developing community-modeling environment for seismic hazard analysis. *Seismol. Res. Lett.*, 74, 406-419.

Gianella, V. P. (1957). Earthquake and faulting, Fort Sage Mountains, California, December, 1950. *Bull. Seismol. Soc. Am.*, 47, 173-177.

Granger, D.E. Kirchner, J.W., and R. Finkel (1996). Spatially average long-term erosion rates measured from in situ-produced cosmogenic nuclides in alluvial sediment. *J. Geol.*, 104, 249-257.

Hammond, W. C. and W. Thatcher (2007). Crustal deformation across the Sierra Nevada, northern Walker Lane, Basin and Range transition, western United States measured with GPS, 2000-2004. *J. Geophys. Res.* 112, B05411, doi 10.1029/2006JB004625.

Hemphill-Haley, M. A., and R. J. Weldon, II (1999). Estimating prehistoric earthquake magnitude from point measurements of surface rupture. *Bull. Seismol. Soc. Am.* 89, 1264-1279.

Kalkan, E., Wills, C.J., and Branum, D.M. (2010). Seismic Hazard Mapping of California Considering Site Effects, *Earthquake Spectra*, 26, 1039-1055.

Lienkaemper, J. J., and C. Bronk Ramsey (2009). Oxcal: versatile tool for developing paleoearthquake chronologies—a primer. *Seism. Res. Letts.* 80, 431-434.

Linton, D.L. (1955). The Problem With Tors. *Geogr. J.*, 121, 420-487.

Ma, S., and G. C. Beroza (2008). Rupture dynamics on a bimaterial interface for dipping faults, *Bull. Seismol. Soc. Am.*, 98, 1642-1658.

Munguía, L., Glowacka, E., Suarez-Vidal, F., Lira-Herrera, H., and O. Sarychikhina (2009). Near-fault strong ground motions recorded during the Morelia normal-fault earthquakes of May 2006 in Mexicali Valley, B. C., Mexico. *Bull. Seismol. Soc. Am.*, 99, 1538-1551.

O'Connell, D.R.H., LaForge, R., and Liu, P. (2007). Probabilistic ground-motion assessment of balanced rocks in the Mojave Desert. *Seismol. Res. Letts.*, 78, 649-662.

O'Connell, D. R. H., S. Ma, and R. J. Archuleta (2007). Influence of dip and velocity heterogeneity on reverse- and normal-faulting rupture dynamics and near-fault ground motions. *Bull. Seismol. Soc. Am.*, 97, 1970-1989.

Ogelsby, D. D., R. J. Archuleta, and S. B. Nielsen (1998). Earthquakes on dipping faults: The effects of broken symmetry, *Science*, 280, 1055 -1059.

Pankow, K. L., and J. C. Pechmann (2004). The SEA99 ground-motion predictive relations for extensional tectonic regimes: Revisions and a new peak ground velocity relation, *Bull. Seism. Soc. Am.*, 94, 341 –348.

Petersen, M. D., A. D. Frankel, S. C. Harmsen, C. S. Mueller, K. M. Haller, R. L. Wheeler, R. L. Wesson, Y. Zeng, O. S. Boyd, D. M. Perkins, N. Luco, E. H. Field, C. J. Wills, and K. S. Rukstales (2008). Documentation of the 2008 update of the United States national seismic hazard maps. *Open File Rep. U. S. Geol. Surv.* 2008-1128.

- Power, M., Chiou, B., Abrahamson, N., Yousef Bozorgnia, Y., Shantz, T., C. Roblee (2008). An overview of the NGA project. *Earthquake Spectra* 24, 3-21.
- Prescott, J.R. and J.T. Hutton (1994) Cosmic ray contributions to dose rates for luminescence and ESR dating: large depths and long-term time variations. *Radiat. Meas.*, 23, 497–500.
- Purvance, M. D., J. N. Brune, N. A. Abrahamson, and J. G. Anderson (2008). Consistency of precariously balanced rocks with probabilistic seismic hazard estimates in southern California. *Bull. Seismol. Soc. Am.*, 98, 2,629 -2,640.
- Riebe, C. S., J. W. Kirchner, D. E. Granger, R. C. Finkel (2000). Erosional equilibrium and disequilibrium in the Sierra Nevada, inferred from cosmogenic ²⁶Al and ¹⁰Be in alluvial sediment. *Geology*, 28, 803–806.
- Reheis, M. (1999). Extent of Pleistocene lakes in the western Great Basin. *U.S. Geol. Surv. Misc. Field Studies Map* MF-2323, scale 1:800,000.
- Reimer, P.J., Baillie, M.G.L., Bard, E., Bayliss, A., Beck, J.W., Blackwell, P.G., Bronk Ramsey, C., Buck, C.E., Burr, G.S., Edwards, R.L., Friedrich, M., Grootes, P.M., Guilderson, T.P., Hajdas, I., Heaton, T.J., Hogg, A.G., Hughen, K.A., Kaiser, K.F., Kromer, B., McCormac, F.G., Manning, S.W., Reimer, R.W., Richards, D.A., Southon, J.R., Talamo, S., Turney, C.S.M., van der Plicht, J. and Weyhenmeyer, C.E. (2009). INTCAL 09 and MARINE09 radiocarbon age calibration curves, 0-50,000 years Cal BP. *Radiocarbon*, 51, 1111-1150.
- Spudich, P., W. B. Joyner, A. G. Lindh, D. M. Boore, B. M. Margaris, and J. B. Fletcher (1999). SEA99: a revised ground motion prediction relation for use in extensional tectonic regimes, *Bull. Seism. Soc. Am.*, 89, 1156 -1170.
- Shi, B., A. Anooshehpour, Y. Zeng, and J. N. Brune (1996). Rocking and overturning of precariously balanced rocks by earthquakes. *Bull. Seismol. Soc. Am.*, 86, 1,364 -1,371.
- Shi, B., Y. Zeng, J. N. Brune (1997), Numerical simulations of earthquake ruptures: A comparison between thrust, normal, and contained strike-slip faulting, *Seism. Res. Lett.* 68, 333.
- Stirling, M. W., A. Anooshehpour, J. N. Brune, G. Biasi, and S. G. Wesnousky (2002). Assessment of the site conditions of precarious rocks in the Mojave Desert, California. *Bull. Seismol. Soc. Am.*, 92, 2139 -2,144.
- Stuiver, M., and Polach, H. A. (1977). Discussion: reporting of ¹⁴C data. *Radiocarbon*, 19(3), 355-363.
- Thatcher, W., G. R. Foulger, B. R. Julian, J. Svarc, E. Quilty, and G. W. Bawden (1999). Present day deformation across the Basin and Range Province, Western United States, *Science*, 283, 1714–1718.
- Turner, R., Koehler, R., Briggs, R. W., and S. G. Wesnousky (2008). Paleoseismic and slip-rate observations along the Honey Lake fault zone, Northeastern California, USA. *Bull. Seismol. Soc. Am.*, 98, 1730-1736.

Wells, D. L., and K. J. Coppersmith (1994). New empirical relationships among magnitude, rupture length, rupture width, rupture area, and surface displacement, *Bull. Seismol. Soc. Am.*, 84, 974–1002.

Wesnowsky, S.G., Barron, A.D., Briggs, R.W., Caskey, S.J., Kumar, S., and L. Owen (2005). Paleoseismic transect across the northern Great Basin, USA. *J. Geophys. Res. B. Solid Earth Planets*, 110, B05408, doi:10.1029/2004JB003283.

Wills, C. J. (1990). Honey Lake and related faults, Lassen County, Calif.

Div. Mines Geol, Fault Eval. Rept, FER-214, scale 1:24,000, 17 pp.

Table 1. Radiocarbon ages from Fort Sage North trench

Sample name	CAMS # ^a	$\delta^{13}\text{C}^b$	Fraction modern	\pm	D^{14}C	\pm	^{14}C age (yr) ^c	$\pm 2\text{s}$	Cal yr BP ^d	$\pm 2\text{s}$
FSN-C1	121670	-25	0.5107	0.0020	-489.3	2.0	5400	35	6160	130
FSN-C2	121671	-25	0.4593	0.0052	-540.7	5.2	6250	100	7165	250

^a Samples analyzed at the Center for Accelerator Mass Spectrometry, Lawrence Livermore National Laboratory

^b $\delta^{13}\text{C}$ values are the assumed values according to Stuiver and Polach (1977) when given

without decimal places. Values measured for the material itself are given with a single decimal place.

^c The quoted age is in radiocarbon years using the Libby half life (5568 years) following the conventions of Stuiver and Polach (1977).

^d Calibrations are performed with the IntCal09 calibration curve (Reimer et al., 2009) and

OxCal version 4.1 (Bronk Ramsey, 2009).

Table 2. Quartz OSL and feldspar IRSL Ages from Fort Sage South trench

Sample Name	% Water		Cosmic dose ^c			Total Dose	Equivalent	n ^d
	content ^a	K (%) ^b	U (ppm) ^b	Th (ppm) ^b	additions (Gy/ka)	Rate (Gy/ka)	Dose (Gy)	
FSS-OSL-1	1 (27)	2.30 ± 0.08	2.41 ± 0.15	11.2 ± 0.29	0.12 ± 0.01	3.71 ± 0.07	28.8 ± 2.02	22 (30)
FSS-OSL-2	1 (27)	1.93 ± 0.12	2.45 ± 0.13	12.0 ± 0.30	0.09 ± 0.01	3.29 ± 0.07	58.9 ± 4.12	18 (20)
FSS-OSL-3	1 (28)	1.98 ± 0.12	2.59 ± 0.11	12.0 ± 0.30	0.04 ± 0.004	3.32 ± 0.07	59.3 ± 3.50	20 (25)
FSS-OSL-4	1 (28)	2.18 ± 0.12	2.25 ± 0.13	10.2 ± 0.31	0.03 ± 0.003	3.29 ± 0.07	71.1 ± 5.03	17 (25)
FSS-OSL-5	1 (34)	2.05 ± 0.13	2.39 ± 0.14	12.5 ± 0.26	0.12 ± 0.01	3.38 ± 0.06	111 ± 7.22	31 (35)

^aField moisture, with figures in parentheses indicating the complete sample saturation %.

Ages calculated at 15% of complete saturation for Holocene, 25% saturation for Pleistocene.

^bAnalyses obtained using laboratory Gamma Spectrometry (low resolution NaI detector).

^cCosmic doses and attenuation with depth were calculated using the methods of Prescott and Hutton (1994).

^dNumber of replicated equivalent dose (De) estimates used to calculate the mean.

Figures in parentheses indicate total number of measurements made including failed runs with unusable data.

^eDose rate and age for fine-grained 250-180 um quartz sand. Linear and exponential fit used on age, errors to two sigma.

Day 3, Stop 2 – Honey Lake Fault

FOP 2012 Stop, Honey Lake fault, Doyle, CA

Coordinates: 40.054411°N., 120.122401°W.

Presenter: Ryan Gold, US Geological Survey, Golden, CO

Collaborators: Richard Briggs, Anthony Crone, Steve Angster

Summary: The Honey Lake fault system (HLFS) strikes north-northwestward across Long Valley near Doyle, CA and is part of a network of active, dextral strike-slip faults in the northern Walker Lane (Figure 1). Geologic investigations of a right-laterally offset terrace riser along the north bank of Long Valley Creek, which we refer to as site 1 (Figure 2), indicate a latest Quaternary slip rate of 1.1-2.6 mm/yr [*Wills and Borchardt, 1993*] and 1.7 ± 0.6 mm/yr [*Turner and others, 2008*] (Table 1). These studies also document evidence of at least four post-6.8 ka surface-rupturing earthquakes at this site.

To further refine the Quaternary slip rate along the HLFS, we analyzed high-resolution (0.25 m) airborne LiDAR data [*Gold and others, 2011*]. On the basis of these new topographic data, we remeasured the offset of the terrace riser at site 1 along the north bank of Long Valley Creek ($18.9^{+7.6}_{-6.3}$ m) (Figure 3a). Furthermore, we identified two additional offset terrace risers at sites 2 and 3, with offsets of 36.6 ± 5.7 m and $6.5^{+1.0}_{-2.0}$ m, respectively (Figure 3b and 3c). All three terrace risers are bracketed by the same upper and lower terrace deposits. The upper terrace (Ql) is cut into Lahontan shorelines, which indicates that the terrace surface was abandoned after 15.8 ± 0.6 ka [*Adams and Wesnousky, 1998*]. Turner and others [2008] constrain abandonment of the lower terrace surface (Qt) to have occurred around 4.7 ± 0.1 ka.

We interpret the range in terrace riser offsets to result from variable amounts of lateral stream erosion to the cutbank, depending on the terrace position within stream meanders [e.g., *Cowgill, 2007*; *Gold and others, 2009*; *Harkins and Kirby, 2008*;

Lensen, 1964] (Figure 4). For example, the riser at site 2 is on the inside of a meander in Long Valley Creek and is therefore sheltered from lateral refreshment. Lateral offsets of this feature are interpreted to have been preserved following abandonment of the upper-terrace surface (Ql), suggesting a minimum slip-rate along the HLFS of 2.3 mm/yr since 15.8 ka (Figure 3b). In contrast, the riser at site 3 is located on the outside of a meander in Long Valley Creek, and lateral offsets of this feature are interpreted to have been recorded only since abandonment of the lower-terrace surface (Qt), suggesting a maximum slip rate of 1.4 mm/yr since 4.7 ka (Figure 3c). The previously characterized riser at site 1 is in an intermediate position along a relatively straight section of Long Valley Creek, and therefore we interpret the 18.9 m offset of this feature to reflect slip that occurred sometime between 4.7 ka and 15.8 ka (Figure 3a).

Summary results from this investigation:

- 1) Three laterally faulted terrace risers of Long Valley Creek along the HLFS have offsets ranging from 6.5 to 36.6 m. All of the terrace risers are bounded by the same upper and lower terrace surfaces that have abandonment ages of 15.8 ka and 4.7 ka, respectively.

- 2) The range of lateral offsets of the risers is interpreted to result from variable times when the riser was refreshed by meandering of Long Valley Creek. The riser position with stream meanders along Long Valley Creek dictate the time when the riser was last refreshed.

- 3) A minimum slip rate of 2.3 mm/yr since 15.8 ka is constrained at site 2 by the 36.6 m of right-laterally offset terrace riser. This slip-rate is nearly double the geodetically modeled slip-rate of 1.2 ± 0.3 mm/yr for the HLFS [Hammond and others, 2011]. However, at site 3, the laterally offset riser (6.5 m) indicates a maximum slip rate of 1.4 mm/yr since 4.7 ka, which closely agrees with the geodetically modeled slip rate.

Stop summary

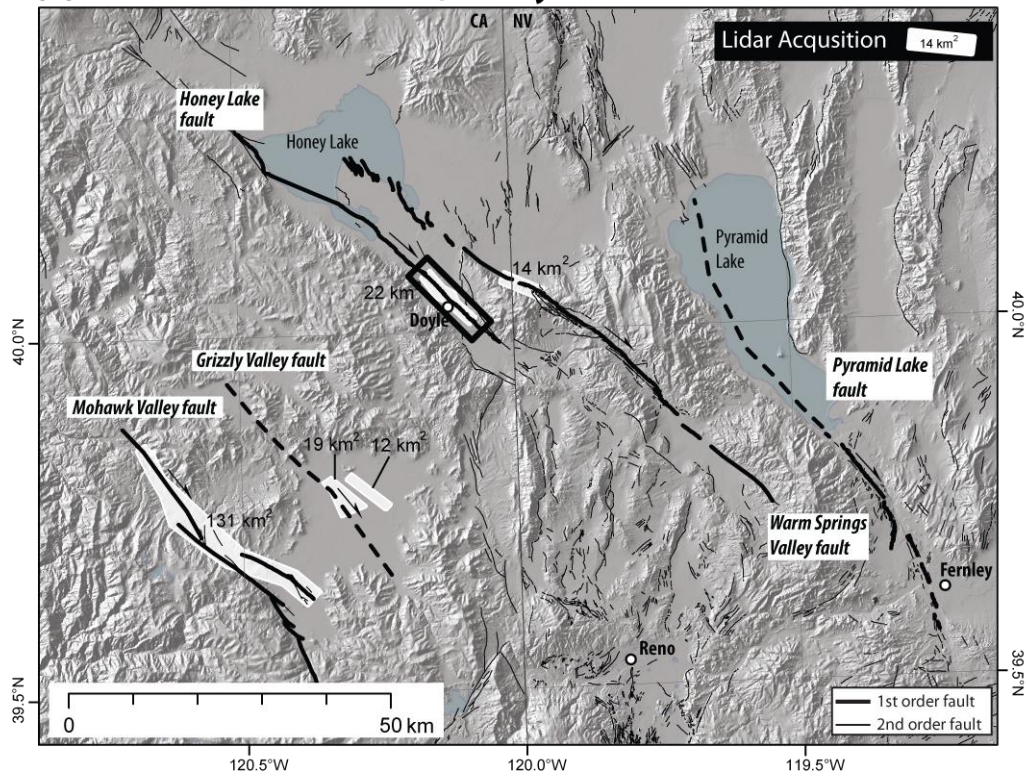
At this stop, we are on the principle trace of the HLFS where we can observe offset terrace riser at site 1, interpreted to have resulted from latest Quaternary faulting along the HLFS. We can examine the airborne LiDAR data collected along the HLFS and debate the quality of the terrace riser offset measurements. Do differing amounts of offset indicate temporal variability in fault slip rate? What geologic slip rate should be compared to geodetic slip rates?

Table 1. Summary of slip-rate calculations based on previous studies and our updated analysis.

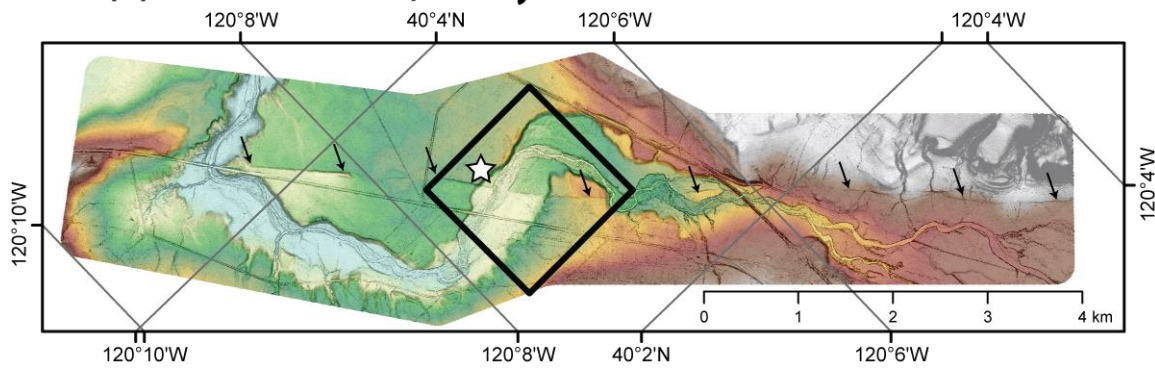
1. Previously published work		
Originally reported by Wills & Borchardt (1993)		
<i>offset</i>	16 ± 2 m	
<i>maximum age</i>	12.5 ka	(Ql, upper terrace; updated to 15.8 ka)
<i>minimum age</i>	7 ka	(Qt, lower terrace; updated to 4.67 ka)
<i>slip rate</i>	1.1 to 2.6 mm/yr	(with updated Ql age, 1.0 to 3.4 mm/yr)
Revised interpretation by Turner and others (2008)		
<i>offset</i>	5.3 to 10.6 m	(near field offset)
<i>maximum age</i>	none	(authors argue that upper terrace age is not appropriate)
<i>minimum age</i>	4.67± 0.145 ka	(Qt, lower terrace)
<i>slip rate</i>	1.7 ± 0.6 mm/yr	(authors argue this is a "minimum" slip rate)
2. Updated analysis		
Site 1 (same as Wills & Borchardt, 1993 and Turner and others, 2008)		
<i>offset</i>	18.9 ^{+7.6} / _{-6.3} m	
<i>maximum age</i>	15.8 ± 0.6 ka	(Ql, upper terrace; Adams and Wesnousky, 1998)
<i>minimum age</i>	4.7 ± 0.1 ka	(Qt, lower terrace; Turner and others, 2008)
<i>slip rate</i>	1.2 to 4.1 mm/yr	
Site 2		
<i>offset</i>	36.6 ^{+5.7} / _{-5.7} m	

<i>maximum age</i>	15.8 ± 0.6 ka	(Ql, upper terrace; Adams and Wesnousky, 1998)
<i>minimum age</i>	4.7 ± 0.1 ka	(Qt, lower terrace; Turner and others, 2008)
<i>slip rate</i>	2.3 to 7.8 mm/yr	<u>(2.3 mm/yr is minimum rate since 15.8 ka)</u>
Site 3		
<i>offset</i>	6.5 ^{+1.0} / _{-2.0} m	
<i>maximum age</i>	15.8 ± 0.6 ka	(Ql, upper terrace; Adams and Wesnousky, 1998)
<i>minimum age</i>	4.7 ± 0.1 ka	(Qt, lower terrace; Turner and others, 2008)
<i>slip rate</i>	0.4 to 1.4 mm/yr	<u>(1.4 mm/yr is maximum rate since 4.7 ka)</u>

(a) Northern Walker Lane, Study Area



(b) Airborne LiDAR, Honey Lake fault



Figure

1. (a) Northern Walker Lane study area, showing areas of airborne LiDAR acquisition and regional faults. (b) LiDAR coverage along the Honey Lake fault system (HLFS) near Doyle, CA., with map extent indicated in (a). Star shows location of FOP stop. Black arrows indicate the trace of the HLFS.

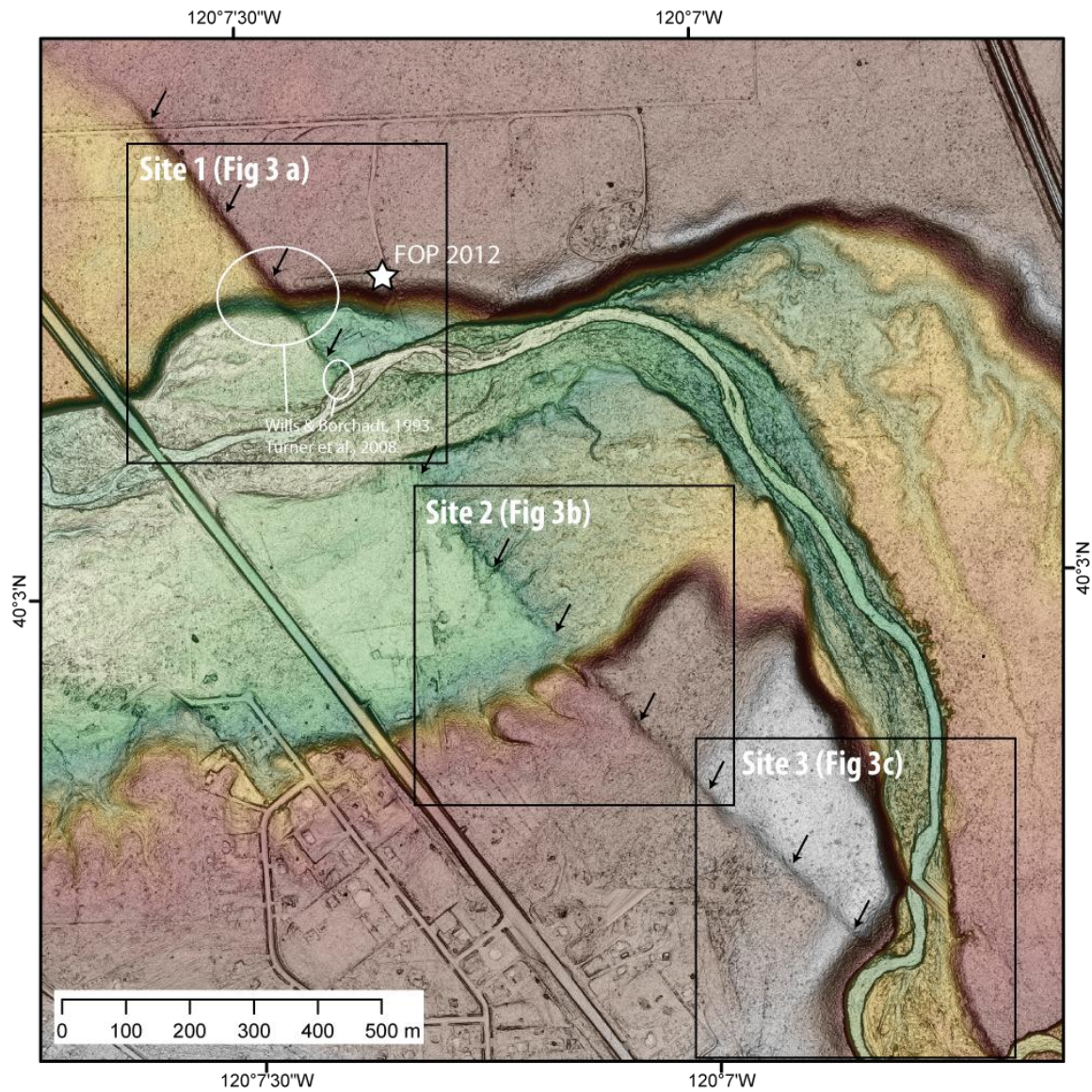


Figure 2. Airborne LiDAR-derived digital elevation model (DEM) along Long Valley Creek and the Honey Lake fault system (HLFS). Map extent indicated in Figure 1b. Detail measures of terrace riser offsets are shown in Figure 3. Black arrows show HLFS trace.

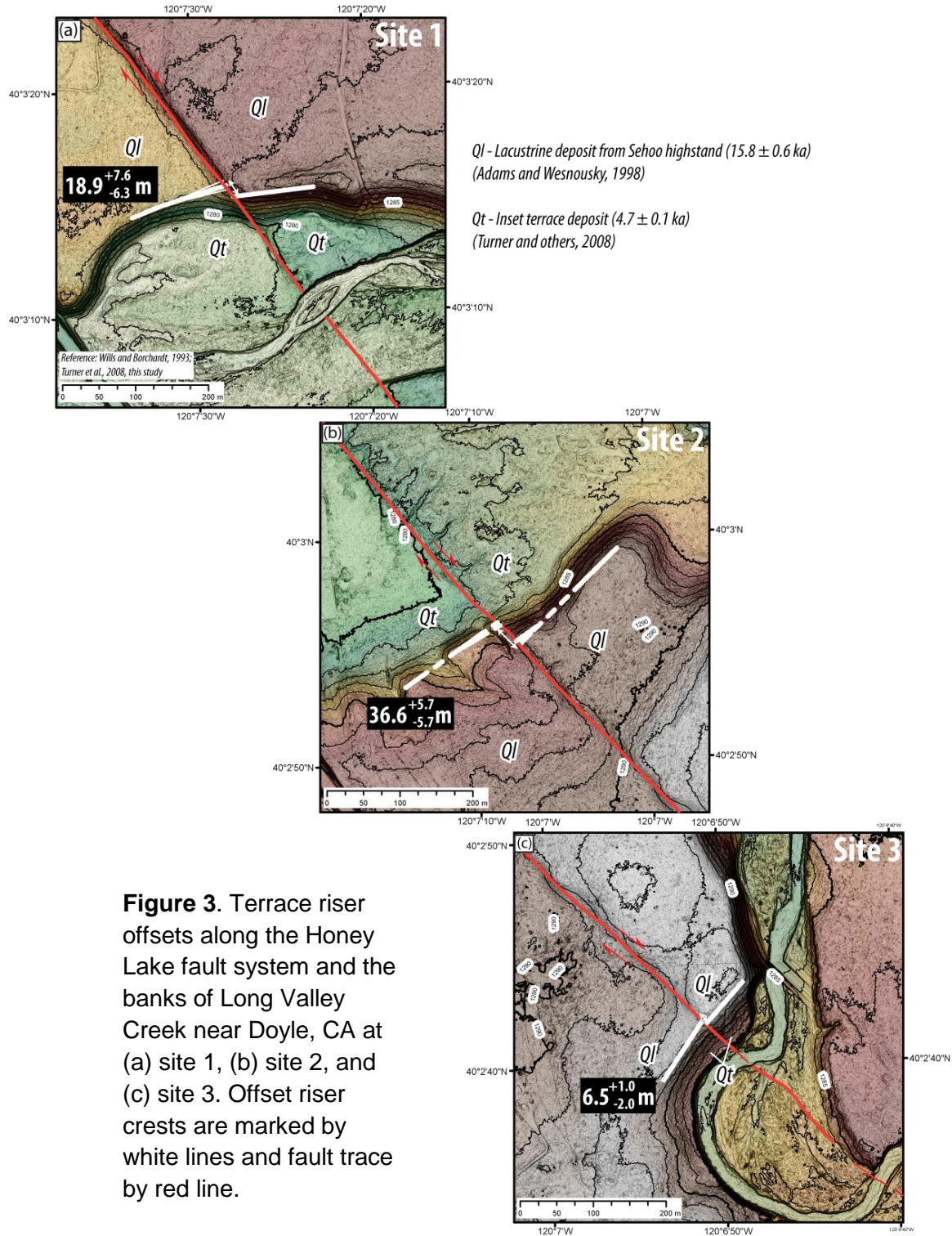
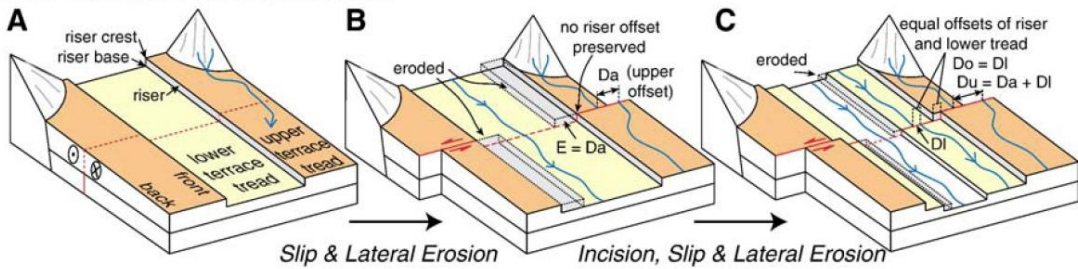
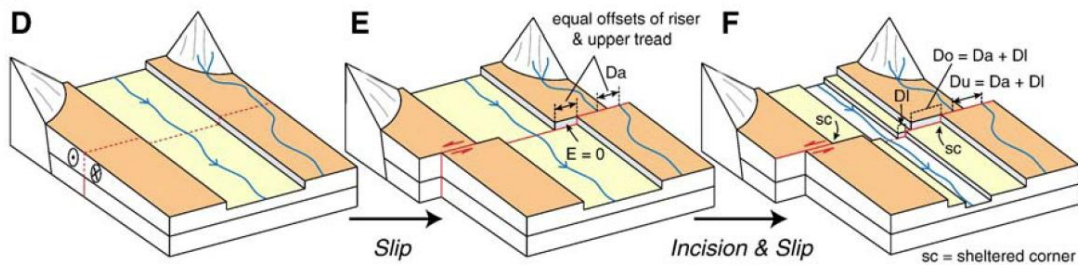


Figure 3. Terrace riser offsets along the Honey Lake fault system and the banks of Long Valley Creek near Doyle, CA at (a) site 1, (b) site 2, and (c) site 3. Offset riser crests are marked by white lines and fault trace by red line.

Lower-Terrace Reconstruction:



Upper-Terrace Reconstruction:



D_o = total observed riser displacement
 D_u = total displacement of the upper tread after its abandonment
 D_l = total displacement of the lower tread after its abandonment
 D_a = displacement of the upper tread after its abandonment but before incision of the lower tread
 E = lateral erosion of the displaced riser after abandonment of upper tread but prior to incision of the lower tread

Figure 4 (Figure and Caption from Cowgill [2007]). Block diagrams showing terrace nomenclature and two end-member models for linking riser offsets with terrace abandonment ages to determine rates of strike–slip faulting. Lower- and upper-terrace reconstructions are shown in panels (A–C) and (D–F), respectively. (A) Initial configuration, showing stream after incision of upper tread but before displacement of lower terrace. Blue line on upper tread is a primary feature that tracks total offset of upper tread (D_u). (B) Lower-terrace model presumes all riser offset is removed by lateral erosion ($E=D_a$) as long as stream occupies lower tread. As a result, stream channel must widen by at least D_a . At this stage $D_u=D_a$ and $D_o=0$. Gray boxes denote eroded material. (C) After incision of the lower tread, observed riser offset is equivalent to magnitude of slip that postdates lower tread incision ($D_o=D_l$). Total offset of upper tread is larger than D_o and is given by $D_u=D_a+D_l$. (D) Same as (A). (E) Upper-terrace model assumes no lateral erosion of riser ($E=0$). Thus riser offset and upper tread displacement (D_a) are equal. (F) Riser continues to accumulate slip after incision of lower tread such that $D_o=D_u=D_a+D_l$. Originally drafted by Ryan Gold after figures in Van der Woerd and others [2002] [28] and Mériaux and others [2004].

References

- Adams, K. D., and S. G. Wesnousky (1998), Shoreline processes and the age of the Lake Lahontan highstand in the Jessup embayment, Nevada, *Geological Society of America Bulletin*, 110(10), 1318-1332.
- Cowgill, E. (2007), Impact of riser reconstructions on estimation of secular variation in rates of strike-slip faulting: Revisiting the Cherchen River site along the Altyn Tagh Fault, NW China, *Earth and Planetary Science Letters*, 254(3-4), 239-255.
- Gold, R. D., C. M. dePolo, R. W. Briggs, and A. J. Crone (2011), Suppressed post-15.8 ka slip rate along the Warm Springs Valley fault, northern Walker Lane, California-Nevada border, paper presented at AGU Fall Meeting, San Francisco, CA.
- Gold, R. D., E. Cowgill, J. R. Arrowsmith, J. Gosse, X. Wang, and X. Chen (2009), Riser diachroneity, lateral erosion, and uncertainty in rates of strike-slip faulting: A case study from Tuzidun along the Altyn Tagh Fault, NW China., *Journal of Geophysical Research, B, Solid Earth and Planets*, 114(B04401), 24.
- Hammond, W. C., G. Blewitt, and C. Kreemer (2011), Block Modeling of Crustal Deformation of the Northern Walker Lane and Basin and Range from GPS velocities, *Journal of Geophysical Research, Solid Earth*, 116(B04402), 1-28.
- Harkins, N., and E. Kirby (2008), Fluvial terrace riser degradation and determination of slip rates on strike-slip faults: An example from the Kunlun fault, China, *Geophysical Research Letters*, 35(L05406), 6.
- Lensen, G. J. (1964), The general case of progressive fault displacement of flights of degradational terraces, *New Zealand Journal of geology and Geophysics*, 7, 864-870.
- Mériaux, A.-S., F. J. Ryerson, P. Tapponnier, J. Van der Woerd, R. Finkel, X. Xiwei, X. Xiwei, and M. Caffee (2004), Rapid slip along the central Altyn Tagh Fault: Morphochronologic evidence from Cherchen He and Sulamu Tagh, *Journal of Geophysical Research*, 109(B06401), 23.
- Turner, R., R. D. Koehler, R. W. Briggs, and S. G. Wesnousky (2008), Paleoseismic and Slip-Rate Observations along the Honey Lake Fault Zone, Northeastern California, USA, *Bulletin of the Seismological Society of America*, 98(4), 1730-1736.
- Van der Woerd, J., P. Tapponnier, F. J. Ryerson, A.-S. Meriaux, B. Meyer, Y. Gaudemer, R. C. Finkel, M. W. Caffee, G. Zhao, and Z. Xu (2002), Uniform

postglacial slip-rate along the central 600 km of the Kunlun fault (Tibet), from ^{26}Al , ^{10}Be and ^{14}C dating of riser offsets, and climatic origin of the regional morphology, *Geophysical Journal International*, 148, 356-388.

Wills, C. J., and G. Borchardt (1993), Holocene slip rate and earthquake recurrence on the Honey Lake fault zone, northeastern California, *Geology*, 21(9), 853-856.

Legal

Disclosure

WARNING! It was your choice. You opened to this page and now you are responsible for every word, in fact, every letter on this and some other pages.

ALL INDIVIDUALS USING, REFERRING TO, TALKING ABOUT, OR MERELY THINKING ABOUT THESE SUGGESTIONS MUST READ THIS!!!

We promise you nothing. This is no joke. The only law we aspire to is the “purity law” from 1516. These inaccurate instructions are based on dim recollections, half-baked guesses, gossip, blind speculation, and outright lies. In **NO WAY** do they tell the full story. You would probably be better off just trying to find your own way up the mountain, than you would be if you used these guides. But that statement in no way implies that we are in any way responsible if you don't use these instructions, and something bad happens anyway.

Nature is unpredictable and unsafe. Mountains are dangerous. Many books have been written about these dangers, and there's no way we can even list them all here, let alone discuss how to reduce risk from these dangers. Read the books, all of them. Do you have an advanced directive? Are you an organ donor?

The areas depicted by these maps and visited during this trip are covered in steep terrain with loose, slippery and unstable footing. The weather can make matters worse. Sheer drops are everywhere. You may fall, be injured or die. There are hidden holes. You could break your leg. There are overhanging outcroppings and low-growing tree branches where you could bump your head. There are wild animals, which may be vicious, poisonous, hungry or carriers of dread diseases. These may include poisonous amphibians, reptiles, and insects; insects to which you have allergies, or whose multiple stings can cause anaphylactic shock; mammals which may include skunks, badgers, marmots, lions, tigers, and bears; predatory birds, and all other manner of beasts. Plants can be poisonous as well, and even when not poisonous, can inflict serious injury like a sharp stick in the eye. Mushrooms growing in this area are very likely extremely poisonous even the good ones. These maps, and the authors of these maps and leaders of trip stops, will not do anything to protect you from any of this. We do not inspect, supervise or maintain the ground, rocks, cliffs, wildlife, vegetation, parking lots or other features, natural or otherwise. You are on your own. How many times do we have to say this to be legal? We're pretty sure this will do.

Real dangers are present even on approach trails. Trails are not sidewalks, and folks have died and been seriously injured even on sidewalks when they have tripped on cracked concrete, plunged into meter boxes with missing covers, been mugged, hit by cars, had pianos fall on them... Trails can be, and are, steep, slippery and dangerous. Trail features made or enhanced by humans, such as bridges, steps, walls and railings (if any) can break, collapse, or otherwise fail catastrophically at any time. We don't promise to inspect, supervise or maintain them in any way. They may be negligently constructed or repaired. Some trails in these areas are only maintained by Nelson Bighorn Sheep, who have little regard for human

life or human safety, or any humans whatsoever. In summary, trails are unsafe, period. Live with it or stay away.

Stay on the trails whenever possible. The terrain, in addition to being dangerous, is surprisingly complex. You may get lost. You probably WILL get lost. The chances of getting lost multiply geometrically after the sun goes down, due to poor visibility. The sun goes down at least once a day in these areas. Not to say that you won't get lost during daylight hours. In either event, carry a flashlight, extra bulb and batteries, compass, GPS, maps, altimeter, cellular phone, food, water, matches and first aid supplies at all times. Our advising you of this does not mean there are not other things you should be carrying. Carry them as well, and know how to use them. We are not responsible for the consequences if you fail to heed this advice. Don't think that fancy iPhone will save you. A slower more painful brain tumor will most likely result from its use. In fact, we are not responsible for the consequences even if you DO heed this advice, nor are we responsible if you carry so much stuff along that you end up moving so slowly that you get benighted. Tough luck.

Rocks and other objects can, and probably will, fall from the cliffs or simply from the universe, and these are faster and more energetic. The former ones can tumble down slopes, then later fly. This can happen naturally, or be caused by people above you, such as hikers, bikers or seemingly innocent bystanders. They're not. Rocks of all sizes, including huge boulders, can shift, move or fall with no warning. If you don't believe us check out the talus slopes at the base of some of the rock walls. They didn't just grow there. Use of helmets is advised for anyone approaching this general region. In fact, you shouldn't really be approaching any steep slopes anyway. It might be a good time to update your life insurance policy. That is a really stupid thing to do. If you do decide to approach these areas, shoulder pads, knee pads, elbow pads, athletic cups and supporters and other body armor may be handy as well as helmets. These items can be purchased or rented from mountaineering shops and athletic supply stores. They won't save you if you get hit by or scrape against something big or on another part of your body. A whole rock formation might collapse on you and squash you like a bug. Don't think it can't happen. It does, and it probably will.

Weather can be dangerous, regardless of the forecast. Be prepared with extra clothing, including rain gear. Hypothermia, heat stroke, dehydration, frostbite, lightning, ice and snow, runoff from rainstorms, flashfloods, etc. can kill you. Rain can turn easy terrain into a deathtrap, can drown you if you're looking up into the sky with your mouth open, and vastly decreases traction on pavement. Snow is even worse, the hazards ranging from snowball fight injuries to avalanches, attacking snowmen and perhaps even worse, snow women.

If you scramble in high places (scrambling is moving over terrain steep enough to use your hands) without proper experience, training and equipment, or allow children to do so, you are making a terrible mistake. Scrambling and CRN sampling amongst huge boulders can result in serious physical and/or emotional injury, or death. Even if you know what you're doing and are the most experienced and safest athlete/scientist the world has ever known, you are still making a terrible mistake: lots of things can and do go wrong and you may be injured or die. It happens all the time.

These areas, and these routes, are not patrolled by any rangers or security personnel on any regular basis. Other people in the area, including visitors, USFS employees, or misfits digging illegal pits without a

permit on USFS land—aimless and utterly misguided hand digging without the needed machinery or a clear plan for success, foreign agents, biologists and nature freaks, terrorists, geophysicists, and anyone else who might sneak in, be stupid, reckless, or dangerous. They may be mentally ill, criminally insane, drunk, using illegal drugs and/or armed with anything from nail clippers to deadly weapons and ready to use them. We're not going to do anything about that. We refuse to take responsibility.

Excessive consumption of alcohol, vitamins, probiotics, use of prescription drugs, over-the-counter medications, and/or controlled substances or even yoga while frequenting these areas can and probably will affect your mental state, alertness, and decision-making abilities, and could make an already dangerous situation even worse. Even hyperventilation or spinning around rapidly and repeatedly can affect your equilibrium to the point that even on a flat paved surface you may fall and injure yourself. Even abstinence from consciousness-altering substances and actions won't protect you from the actions of others under the influence of such substances or actions. That's your problem, and yours alone. Not our fault. Never was and never will be.

The driveways, freeways, highways, streets, alleys, back roads and unimproved 4WD tracks leading to these areas kill hundreds of folks each year. Many of these fatalities are folks who aren't even on their way to these areas, who in fact have never heard of them, but are simply innocent victims. Not so you. You have been warned. You could get killed driving to the next FOP stop. Wearing your seatbelt tightly fastened with the lap belt low across your waist improves your chances of survival, in most cases (except that one steep section of road) but does not and cannot guarantee your safety. Airbags may just accelerate the shortening of your life span. You might die before ever stepping out of your vehicle at the site, or on the way home. It can happen any time. If you think you are immune from this kind of thing, you're fooling yourself.

These are not sterile environments. Bacteria, viruses, protozoa, protoviruses, fungi and other forms of life and protolife which may or may not be currently included in either the plant or animal kingdom are capable of causing you serious bodily harm, illness, or death. These kinds of biological agents are both endemic in these areas or present in the plant and animal populations; and are also capable of being carried or transmitted by your hiking partners and travelling companions. We're not going to take responsibility for this, either. Our advice for you to treat drinking water, wash your hands before and after going to the bathroom and before eating, to not breathe hanta-virus-contaminated dust, and to not indulge in unprotected sex in these areas. The only safe fermented medium we stand behind, actually endorse in appropriate doses is based on the *Reinheitsgebot from 1516*. This in no way obligates us to be responsible for the consequences if you fail to do so, nor does it mean that even if you DO take these precautions and something happens anyway, that we are to blame. Not so. Forget it. Nada. Negativo.

If you hike, you may die or be seriously injured. And the longer you hike the greater your risk of bad luck, which may or may not be compounded by hubris, catching up to you. This is true whether you are experienced or not, trained or not, and equipped or not—though training, experience and equipment may help. It's a fact; hiking is extremely dangerous, especially with this crowd. If you don't like it, stay at home. You really shouldn't be doing it anyway. We do not provide supervision or instruction and even the classification as entertainment is a stretch. We are not responsible for, and do not inspect or maintain paths. As far as we know, any of them can and probably will suddenly fail without warning and send you plunging to your death with a bloodcurdling scream, likely pulling your partner to his or her doom as

well. There are countless tons of loose rocks ready to be dislodged and fall on you or someone else. There are any number of unobvious, extremely and unusually dangerous conditions existing on and around Lake Tahoe (remember Ward's tsunami modeling!) and elsewhere in this region. We probably don't know about any specific hazards, but even if we do, don't expect the trip leaders to try to warn you. You're on your own.

We won't even begin to discuss disagreeing with FOP trip leaders. If you are thinking of traveling here for the express purpose of questioning their superior judgment, do us all a favor: Just take a nice nap in the fast lane of an interstate truck route. But be advised that, if you do, we are in no way responsible for the consequences of that, either.

Rescue services are not provided by anyone near these stops, and may not be available quickly or at all. In fact, if anything really serious happens to you in these areas, you'll probably be dead before word ever reaches civilization. Local rescue squads may not be equipped for or trained in mountain rescue. They probably won't be. If you are lucky enough to have somebody try to rescue you or treat your injuries, they will probably be incompetent or worse. This includes doctors and hospitals. We assume no responsibility. Also, if you decide to participate in a rescue of some other unfortunate, that's your choice. Don't do it unless you are willing to assume all risks, and don't blame us when it goes bad and you end up getting yourself sued in the process.

By using, or even just looking at these guide materials, you are agreeing that we owe you no duty of care or any other duty, you agree to release us, our relatives, heirs, dependents, and anyone else we care to name, now and forevermore, from any and all claims of liability, even though our actions may be grossly negligent and/or be construed as reckless endangerment, manslaughter, or other misconduct up to and including premeditated murder. By consulting these maps, you agree to waive forever any rights that you, your partners, dependents, heirs, in-laws, and others known or unknown to you may have, to legal compensation resulting from anything that has anything to do with these maps, including but in no way limited to paper cuts from the edge of the map itself. If you try to sue us in spite of all this, you agree to pay our lawyers fees regardless of the outcome of the suit, and you expressly agree to reimburse us for any loss or injury, be it financial, physical, emotional, or **imagined**, which we may experience as a result of such lawsuit.

We do not and will not even try to keep these areas safe for any purpose. These areas are NOT safe for any purpose. This is no joke. We won't even try to warn you about any dangerous or hazardous condition, whether we know about it or not. If we do decide to warn you about something, that doesn't mean we will try to warn you about anything else. But you are warned here of crossing highway 89 from east to west at Eagle Rock, also all other roads that are along the trip path. Consider the chance of Commonwealth people reminiscing about driving on the wrong side, and in the wrong direction. If we do make an effort to fix an unsafe condition, we may not try to correct any others, and we may actually make matters worse! We may have done things in the area that are unwise and dangerous. We probably did, but we don't remember. Sorry, we're neither competent nor responsible. The maps give you bad advice. Don't listen. Or do listen. It's your choice, but you face the consequences either way, whatever they may be.

In short, attend AT YOUR OWN RISK. If you, or your heirs, relatives, dependents or others known or unknown to you; your partner or your partners heirs, relatives, dependents, or others known or unknown

to you OR your partner, are the slimy kind of lawyer-touting parasites who would try to sue the author of a map or guide, if you can't take responsibility for your own decisions, knowledge, route finding and plain dumb bad luck, PLEASE PLEASE PLEASE stay far far away from these routes and these areas, give up hiking, and die of some completely natural, painful, and slowly progressive disease.

Thank you, FOP friends, FOP foes, FOP agnostics, FOP doppelgangers and have fun, really!